UNIVERSIDADE DE LISBOA
FACULDADE DE CIÊNCIAS
DEPARTAMENTO DE QUÍMICA E BIOQUÍMICA

HENRIQUE POUSÃO'S OIL PAINTINGS: PIGMENT STUDY BY INFRARED AND RAMAN MICROSCOPY

Andreia Sofia Marcos Correia

DOUTORAMENTO EM QUÍMICA

(Química Analítica)

2010

UNIVERSIDADE DE LISBOA
FACULDADE DE CIÊNCIAS
DEPARTAMENTO DE QUÍMICA E BIOQUÍMICA

HENRIQUE POUSÃO'S OIL PAINTINGS: PIGMENT STUDY BY INFRARED AND RAMAN MICROSCOPY

Andreia Sofia Marcos Correia

Tese orientada por

Profª Doutora Maria Leonor Duarte
(Dep. Química e Bioquímica da FCUL da UL)

Engª Maria Isabel Ribeiro
(Laboratório de Conservação e Restauro José de Figueiredo)

DOUTORAMENTO EM QUÍMICA

(Química Analítica)

2010

This work was supported by the Operational Program "**Ciência e Inovação 2010** (POCI)" and by the European Social Fund.

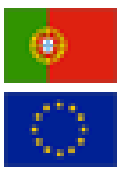

Resumo

A análise de obras de arte com recurso a técnicas analíticas tem demonstrado ser de elevada utilidade na determinação dos materiais e técnicas de trabalho usados pelos artistas, auxiliando em questões tais como autenticidade e escolha do tratamento de conservação ou restauro mais adequado.

Em Portugal, o principal responsável pelo estudo, conservação e restauro de obras de arte (de natureza pública e privada) é o Laboratório de Conservação e Restauro José de Figueiredo (LCRJF), Instituto dos Museus. Durante a última década foi requisitada a este laboratório a avaliação da autenticidade de várias pinturas atribuídas ao pintor Português do séc. XIX, Henrique Pousão (1859-1884). Tido como um dos mais importantes pintores do Naturalismo em Portugal, o seu estilo único e original levou a que, por vezes, fosse considerado pintor do Impressionismo.

Infelizmente, o número de referências bibliográficas dedicadas a este importante pintor é escarço e sobre os materiais e técnica por ele usados apenas se dispõe dos dados de um estudo, não publicado, conduzido no LCRJF em 1984.

Para colmatar esta lacuna, a presente investigação tem como um dos principais objectivos identificar os pigmentos e corantes usados por Pousão em diferentes períodos da sua carreira, ou seja estabelecer a sua paleta. Em simultâneo, pretende-se caracterizar a técnica usada pelo pintor e avaliar o estado de conservação das pinturas.

Com a ajuda de especialistas em História de Arte, foram seleccionadas para objecto desta investigação, 23 pinturas a óleo de Henrique Pousão, pertencentes ao Museu Nacional Soares dos Reis, Porto, cobrindo quatro períodos cronológicos (Inicial, Francês, Italiano e Final) e dois tipos de suporte (tela e madeira)

No estudo de 1984, recorrendo a testes microquímicos, foi possível concluir que as amostras das pinturas de Pousão são muito complexas, com uma estrutura em multicamadas, cada uma composta por um elevado número de pigmentos. A complexidade

das amostras tornou óbvia a necessidade de uma abordagem envolvendo várias técnicas analíticas. Além disso, dada a reduzida dimensão das amostras e, uma vez que se pretende analisar individualmente cada uma das camadas, as técnicas a utilizar devem ser microscópicas e envolver recolha de amostras.

Como os processos de análise são processos interactivos, ou seja novos resultados podem confirmar ou contrariar resultados antigos levantando novas questões, foi decidido iniciar esta investigação, usando duas técnicas analíticas principais e, sempre que necessário, recorrer a outras técnicas especificamente direccionadas para a solução das questões não resolvidas pelas primeiras.

De entre as várias técnicas disponíveis no LCRJF que podiam ser usadas para a análise deste tipo de amostras foi seleccionada, como uma das técnicas principais a usar, a microscopia de infravermelho (μ-IR).

A espectroscopia de infravermelho tem sido extensivamente utilizada há cerca de 50 anos para analisar compostos orgânicos e inorgânicos presentes em objectos de arte devido, entre outros atributos, à sua especificidade. Dadas as reduzidas dimensões das amostras de obras de arte, o desenvolvimento do microscópio de infravermelho e dos espectrómetros com transformada de Fourier, tornaram aquela técnica ainda mais adequada para este fim que, por isso, dispõe uma ampla base de dados.

Outra técnica de espectroscopia vibracional, relativamente recente e que tem gerado grande interesse devido a atributos tais como elevadas resolução espacial (ca. 1 μm) e espectral (ca. 1 cm^{-1}), excelente sensibilidade, especificidade e reprodutibilidade, relativo baixo custo, curto tempo de aquisição de dados e, principalmente por poder ser utilizada não destrutivamente é a espectroscopia de Raman, em particular a microscopia de Raman (μ-R).

Apesar de esta técnica ter sido considerada como uma das mais eficazes para a identificação de pigmentos, à data do início desta investigação e ainda presentemente, poucos foram os estudos realizados em pinturas de cavalete e, ainda em menor número os que consistiam na análise de estratigrafias daquele tipo de pinturas.

Uma vez que μ-R é a técnica vibracional complementar de μ-IR e que os resultados obtidos em alguns testes preliminares foram muito encorajadores, μ-R foi seleccionada como a segunda técnica principal a usar neste estudo, também com o propósito de averiguar se será vantajoso para o LCRJF adquirir um equipamento deste tipo.

Com o objectivo de responder às questões levantadas pelas técnicas principais (μ-IR e μ-R) foram seleccionadas três técnicas auxiliares, nomeadamente microscopia electrónica de varrimento com análise dispersiva de raios-X (SEM/EDS), micro-difracção de raios-X (μ-XRD) e microscopia de fluorescência (FM) com base no tipo de questões levantadas, acessibilidade e custo.

Para além destas técnicas, e como é usual nestes casos, a microscopia óptica (OM) foi também usada para determinar a estratigrafia de todas as amostras.

A complexidade das amostras, não só constitui um desafio para qualquer técnica analítica como permite testar a sua eficácia na identificação de pigmentos em amostras estratigráficas de pinturas a óleo.

Deste modo e porque, em particular μ-R ainda não foi suficientemente testada para a análise deste tipo de amostras, o segundo objectivo deste estudo consiste em avaliar a sua eficácia e compará-la com a de μ-IR para o mesmo fim.

153 amostras foram removidas das margens e lacunas das pinturas em estudo e preparadas como estratigrafias (μ-R) e como estratigrafias de camada fina (μ-IR). Mais de 800 espectros de μ-IR e 2000 espectros de μ-R foram adquiridos e interpretados.

Ambas as técnicas foram bem sucedidas na identificação dos compostos presentes nas amostras. μ-IR demonstrou ser mais eficaz na identificação de cargas e compostos associados, como por exemplo, caulino, gesso, quartzo, do que na identificação de pigmentos. Dos 18 compostos identificados por μ-IR apenas 11 são pigmentos. Contrariamente a μ-IR, μ-R demonstrou ser mais eficaz na identificação de pigmentos do que na identificação de cargas e compostos associados. Dos 41 compostos identificados por μ-R, 25 são pigmentos.

As vantagens e desvantagens das técnicas analíticas μ-IR, μ-R, SEM/EDS, μ-XRD e FM, no que respeita a preparação de amostras, tempo de análise, resolução espacial, interpretação de resultados e serem ou não destrutivas foram também detalhadamente analisadas.

Combinando os resultados obtidos por todas as técnicas analíticas foi possível estabelecer a paleta de Pousão como sendo constituída por 26 pigmentos e nenhum corante. Alguns dos pigmentos são pigmentos tradicionais, tais como óxido de ferro, oxihidróxido de ferro, celadonite, malaquite, amarelo de chumbo e antimónio, negro de osso/marfim, negro de carbono, realgar/pararealgar, vermelhão/cinábrio, laca de cochinilha, laca de garança, branco de chumbo e azul da Prússia, enquanto outros são pimentos do séc. XIX, tais como azul de cobalto, azul de cerúleo, ultramarino francês, amarelo de crómio, laranja de crómio, amarelo de estrôncio, amarelo de zinco, amarelo de cádmio, viridian, verde esmeralda, verde de Scheele, verde de crómio e branco de zinco.

Quanto à técnica usada pelo pintor, em geral, as pinturas são caracterizadas pela presença de uma camada de preparação de branco de chumbo, sobre a qual foram

aplicadas 1 até 10 camadas pictóricas. As camadas pictóricas, além de variarem significativamente em espessura (4 - 358 µm), em geral são constituídas por uma mistura complexa de pigmentos e foram aplicadas após secagem da camada de preparação ou da camada pictórica anteriormente aplicada.

Foi ainda observado que as pinturas se encontram em bom estado de conservação, uma vez que não existem rupturas, destacamentos, protuberâncias/saliências, ou algum sinal de descoloração dos pigmentos ou de decomposição.

Em relação ao segundo objectivo deste estudo, µ-R provou ser a técnica mais indicada para a identificação de pigmentos em amostras microscópicas, complexas de multicamadas devido aos atributos já referidos para esta técnica. Apesar disso, uma vez que cada técnica tem as suas próprias vantagens e desvantagens e provou ser útil em diferentes fases deste estudo, apenas uma abordagem envolvendo complementarmente várias técnicas permitiu obter o máximo de informação sobre as complexas misturas elaboradas por Henrique Pousão.

Palavras-chave: Henrique Pousão, pigmentos, Microscopia de Infravermelho, Microscopia de Raman.

Abstract

Twenty-three paintings by the Portuguese painter Henrique Pousão (1859-1884) were analysed by Infrared and Raman microscopy (μ-IR and μ-R) in order to establish the painter's palette and technique, as well as assess the paintings' conservation state. A total of 153 samples were removed from the paintings and prepared as thin sections and cross sections for analysis.

The analysis of Pousão's samples, composed by several layers of a complex mixture of compounds, was not always straightforward. Therefore, besides optical microscopy (OM), always used for the analysis of this type of samples, three auxiliary techniques, namely, scanning electron microscopy with energy-dispersive X-ray spectrometry (SEM/EDS), micro X-ray diffraction (μ-XRD) and fluorescence microscopy (FM) were used to confirm results which were uncertain and to identify compounds which were not identified by the μ-IR and μ-R techniques.

The high complexity of the samples under analysis constituted a case study that surveyed the advantages and limitations of these five techniques for pigment identification.

It was concluded that the paintings are in good state of conservation and that Pousão's palette is composed by 26 pigments, namely iron^{III} oxide, iron^{III} oxyhydroxide, celadonite, malachite, lead antimonate yellow, bone/ivory black, carbon-based black, realgar/pararealgar, vermilion, cochineal and madder lakes, lead white and Prussian blue, cobalt blue, cerulean blue, ultramarine blue, chrome yellow, chrome orange, strontium yellow, zinc yellow, cadmium yellow, viridian, emerald green, Scheele's green, chrome green and zinc white.

Regarding Pousão's technique, in general it consists in a lead white ground layer, over which 1 up to 10 paint layers, ranging from 4 - 358 μm and constituted by a complex mixture of pigments, were applied after the ground layer or previous paint layers had dried.

μ-R proved to be the most efficient technique to identify most individual pigment particles on minute, complex, multi-layered samples, when used on its own. However, only the use of a multi-technique approach allowed for the maximum information to be obtained.

Keywords: Henrique Pousão, pigments, Infrared microscopy, Raman microscopy.

Acknowledgements

Thanks are due to many people for their cooperation during this project. They are far too many to name everyone individually, so to those that are not listed here, I apologise and thank you.

First of all I want to thank my two supervisors, Professor Maria Leonor Duarte and Eng.ª Maria Isabel Ribeiro, for their support, encouragement, suggestions and friendship during these years.

Thanks are due to Laboratório de Conservação e Restauro José de Figueiredo at Instituto Português de Museus, and in particular to Ana Carmo, Helena Vargas, José Frade, Lília Esteves and Pedro Alves, who hosted me and provided a nice environment to work.

To Professor Robin J. H. Clark, Ingold Chemistry Laboratories, University College London, I want to thank for the warm reception and the opportunity to be part of his working group, the supervision during my stay in London and all the help and support to the publication of manuscripts.

I want also to thank a few other people who helped and supported me at UCL: Lucia Burgio, Maria Isabel Cardoso, Steve Firth, Tracey Chapman and Sonal Brown.

I am also thankful to Isabel Pombo Cardoso from Institute of Archaeology, University College London, and Isabel Nogueira, from the Instituto Superior Técnico, Lisboa for the SEM/EDS analysis; Maria José V. Oliveira from Laboratório de Conservação e Restauro José de Figueiredo, Lisboa, for the μ-XRD analysis; Dr. Lucia Burgio from Victoria & Albert Museum, London, for FM analysis.

I am grateful to Professor João Ferreira Duarte, Faculdade de Letras da Universidade de Lisboa and Eng.ª Tânia Correia for the support given during the revision of the thesis.

Finally, thanks are due to Fundação para a Ciência e a Tecnologia for the financial support SFRH/BD/14193/2003.

Andreia S. Marcos Correia

Contents

Resumo ..... **iii**

Abstract ..... **vii**

Acknowledgements ..... **ix**

List of Figures ..... **xvii**

List of Tables ..... **xxxv**

List of acronyms and abbreviations ..... **xxxvii**

Introduction **1**

Background to the research 2

Research aims and methodology 4

Thesis outline 6

1 On Henrique Pousão **9**

1.1 His life 10

1.2 His work 11

2 Easel paintings: structure, materials and analysis **13**

2.1 Structure and materials of easel paintings 14

2.1.1 Support 15

2.1.2 Ground layers 15

2.1.3 Paint layers 16

2.1.4 Varnish layer(s) 18

2.2 Painting analysis 18

2.2.1 Introduction to conservation science 18

2.2.2 Analytical analysis 20

2.3 Analytical techniques 23
2.3.1 Classification 23
2.3.2 Methodologies and analytical techniques for painting analysis 24
3 Sampling and sample preparation 37
3.1 Sampling strategy 38
3.2 Sample collection 40
3.3 Sample preparation 40
3.3.1 Cross sections 41
3.3.2 Thin sections 42
4 Optical microscopy analysis 45
4.1 The optical microscope 46
4.1.1 Resolution or resolving power 47
4.1.2 Depth of field and depth of focus 48
4.1.3 Optical microscopy techniques 49
4.2 Examination of painting's samples by OM 51
4.3 Experimental conditions 52
4.4 Results and discussion 53
4.4.1 Ground layer 53
4.4.2 Underdrawing 55
4.4.3 Paint layers 55
4.4.4 Questionable samples 57
4.4.5 Conservation state of the paintings 58
4.5 Conclusions 58
5 Introduction to vibrational microscopy 59
5.1 Principles of vibrational spectroscopy 60
5.1.1 Classical mechanics (CM) approach: normal modes of vibration 61
5.1.2 Quantum mechanics (QM) approach 67
5.2 Infrared spectroscopy 71
5.3 Normal Raman spectroscopy 72
5.4 Infrared and Raman activity 75
5.5 Interpretation of vibrational spectra 77
5.5.1 Functional Group Analysis 78
5.5.2 Factors affecting the vibrational spectra 81

5.5.3 Vibrations in crystals 83
5.6 Infrared and Raman microscopies 86
5.6.1 Instrumentation 86
5.6.2 Spatial and spectral resolution 91
6 Infrared and Raman microscopy analysis 95
6.1 Infrared microscopy 97
6.1.1 Experimental conditions 97
6.1.2 Results and discussion 98
6.1.2.1 Difficulties in sample's preparation and analysis 98
6.1.2.2 Interpretation of the infrared spectra 99
Arsenites 101
Carbonates 102
Chromates 104
Cyanides 107
Oxides and Oxyhydroxides 109
Phosphates, silicates and sulfates 111
Phosphates 112
Silicates 113
Sulfates 118
Difficulties in distinguishing phosphates, silicates and sulfates 121
Other compounds 124
6.2 Raman microscopy analysis 131
6.2.1 Experimental conditions 131
6.2.2 Results and discussion 132
Arsenites 135
Carbonates 136
Chromates 139
Cyanides 142
Oxides and Oxyhydroxides 143
Silicates 155
Sulfates 160
Sulfides 163
Other pigments 167
Other compounds 170
6.3 Infrared microscopy *vs.* Raman microscopy 173

6.3.1 Sample preparation 173
6.3.2 Spectra acquisition 174
6.3.3 Interpretation of the spectra 176
6.4 Conclusions 177
7 SEM/EDS, µ-XRD and FM analysis 181
7.1 Introduction 182
7.1.1 Scanning electron microscopy with energy-dispersive X-ray spectrometry (SEM/EDS) 182
7.1.2 Micro X-ray diffraction (µ-XRD) 186
7.1.3 Fluorescence microscopy (FM) 188
7.2 Experimental Conditions 190
7.2.1 SEM/EDS 190
7.2.2 µ-XRD 191
7.2.3 FM 192
7.3 Results and discussion 193
Restoration samples 193
Cadmium yellow 196
Carbon-based black pigments 197
Cobalt blue and cerulean blue 198
Copper pigment 200
Lead antimonate yellow and associated compounds 201
Red lake pigments 204
Rutile 207
Zinc white 209
Zinc yellow 217
7.4 SEM/EDS, µ-XRD and FM advantages and limitations 219
7.5 Comphreensive identification 224
7.6 Microchemical results *vs.* current study results 226
7.7 Conclusions 229
8 Pousão's palette and painting technique 231
8.1 Support and ground layer 232
8.1.1 Support 232
8.1.2 Ground layer 234
8.2 Painting technique 236

8.2.1 Underdrawing 236
8.2.2 Outlining 237
8.2.3 Paint structure 238
8.2.4 Palette 239
White pigments 240
Yellow and orange pigments 242
Red and brownish pigments 243
Blue pigments 244
Purple pigments 245
Green pigments 246
Black pigments 247
8.2.5 Main painting elements 247
8.2.6 Binder 250
8.2.7 Extenders, associated compounds/impurities and degradation compounds 250
8.2.8 Surface texture 252
8.2.9 Alterations to the original composition 253
8.3 Conservation state assessment of the paintings 254
8.4 Conclusions 256
9 Final conclusions and suggestions for future work 259
9.1 Final conclusions 260
9.2 Sugestions for future work 262
References 265
Appendix A 303
Appendix B 305
Appendix C 329
Appendix D 331
Appendix E 383
Appendix F 391

List of Figures

Figure 1.1 *Pousão, auto-portrait*. 1879. Oil on canvas, 78.5 x 51.7 cm (MNSR Invº 89). Photo: Museu Nacional Soares dos Reis, Porto..... 10

Figure 2.1 (a) Cross section of a sample removed from blue of the sea, viewed under reflected light. 5 paint layers and a white ground layer are visible; (b) cross section from a sample removed from the end of the canvas, viewed under reflected light. The white ground layer and the canvas support are visible; (c) **Casas Brancas de Capri**, 1882 (MNSR Invº 82). Oil on canvas, 70.5 x 141.0 cm. 15

Figure 2.2 *Rapariga de Anacapri* (MNSR 200), 1882, oil on canvas, 18.5 x 13.8 cm: (a) photography; (b) X-radiography, where it is possible to see the wooden stretcher frame, the metal staple securing the fabric to a wooden stretcher and restoration areas (black areas). Photo and radiography: LCRJF..... 26

Figure 3.1 Pousão's paintings analysed in this study: (a) ***Casa rústica de Campanhã***, (b) ***O mendigo Lapita***, (c) ***Paisagem - Abertura da Rua Alexandre Herculano***, (d) ***Jardim de Luxemburgo (estudo)***, (e) ***Aldeia de St. Sauves***, (f) ***Paisagem de St. Sauves***, (g) ***Cansada (Cachopa de Capri)***, (h) ***Casas brancas de Capri***, (i) ***Cecília***, (j) ***Escadas de um pardieiro - Roma***, (k) ***Esperando o sucesso***, (l) ***Fachada de casa soterrada - Roma***, (m) ***Miragem de Nápoles***, (n) ***Portão***, (o) ***Rapariga de Anacapri***, (p) ***Rua de Roma***, (q) ***Senhora vestida de preto***, (r) ***Janela das persianas azuis***, (s) ***Mulher da água***, (t) ***Paisagem de Anacapri***, (u) ***Rapariga deitada no tronco de uma árvore***, (v) ***Cais de Barcelona*** and (w) ***Flores Campestres***. The pictures (LCRJF) are not to scale. 39

Figure 3.2 a) Stereomicroscope, scalpel and needle, b) cross section's mould and cross section and c) scheme of a cross-section. 42

Figure 3.3 a) Rotary wheel for grinding and b) rotary wheel for polishing and c) cross section of sample W3 viewed by optical microscope under reflected light. 42

Figure 3.4 a) Silicone mould for sample preparation with four resin blocks and b) scheme of a resin block with the sample (adapted from *Andres MS.* et al. [140]). 43

Figure 3.5 a) Leica RM2155 rotary microtome and b) thin section of sample W3 viewed by optical microscope under reflected light (LCRJF laboratory). 43

Figure 4.1 Simplified configuration of a: (a) transmission microscope and (b) reflection microscope. The yellow traces represent the light path (adapted from *Davidson MW, et al.* [141]). 46

Figure 4.2 (a) Two resolved points; (b) two unresolved points. 47

Figure 4.3 Diffraction pattern of a uniformly-illuminated circular aperture. 47

Figure 4.4 Diffraction pattern of a uniformly-illuminated circular aperture and related intensity profile (point spread function). (a-c) Airy disk dimensions as related to the objective numerical aperture. As the numerical aperture increases from (a) to (c) the size of the Airy disk (and further diffraction orders) decreases; (d) Two Airy disks at the limit of resolution; (e) Two Airy disks so close together that their central spots overlap and are no longer resolved. (Reproduced with permission from *Davidson MW, et al.* [141]) 49

Figure 4.5 Leitz WETZLAR optical microscope used for the analysis of the samples. 53

Figure 4.6 Cross sections of the samples: (a) N5 - green foliage from *Portão* and (b) C4 - brown from the ground from *Paisagem - Abertura da Rua Alexandre Herculano*; viewed under reflected light. 54

Figure 4.7 Cross sections of the samples: (a) Q4 - black of the dress from *Senhora vestida de Preto*, and (b) F4 - brownish of the ground from *Paisagem de St. Sauves*; viewed under reflected light. 54

Figure 4.8 Cross sections of the samples: (a) **C2** - green of the tree from ***Paisagem - Abertura da Rua Alexandre Herculano*** and (b) **F6** - dark green of the ground from ***Paisagem de St. Sauves***; viewed under reflected light. 55

Figure 4.9 Cross section of the samples: (a) **H8** - dark green of the cactus from ***Casas brancas de Capri*** and **S2 -** green from the bushes from ***Mulher da água***; viewed under reflected light. 55

Figure 4.10 Cross section of the samples: (a) **K3** - yellow from the brush from ***Esperando o Sucesso***, (b) **H5** - blue from the sea from ***Casas brancas de Capri***, (c) **K9** - brown of the wood box from ***Esperando o Sucesso*** and (d) **H4** - blue from the sky from ***Casas brancas de Capri***; viewed under reflected light. 56

Figure 4.11 Cross section of the samples: (a) **T2 -** blue from the sea from ***Paisagem de Anacapri***, (b) **W4** - grey from the back from ***Flores Campestres***, and (c) **W7 -** light grey from the back from ***Flores Campestres***, viewed under reflected light. 57

Figure 4.12 Cross section of the sample **F1 -** blue from the sky from ***Paisagem de St. Sauves***, viewed under reflected light. 58

Figure 5.1 Degrees of freedom of an angular triatomic molecule (N=3). $T_{x,y,z}$ and $R_{x,y,z}$ are the translations and rotations of the molecule as a whole, respectively. v_a, v_s and δ are the normal modes of vibration (see below the meaning of these symbols) (adapted from *Schrader B.* [123])..... 61

Figure 5.2 Two point masses connected by a weightless spring. 61

Figure 5.3 Approximate form of the normal modes of a methylene (CH_2) group when attached to a molecule and respective frequencies. The + and - signals indicate upward and downward motion in the plane of the paper, respectively (adapted from *Nakamoto K.* [175], *Schrader B.* [177] and *Shurvell HF.* [178])..... 66

Figure 5.4 (a) Puckering and (b) breating modes of a four-membered ring (adapted from *Sathyanarayana DN.* [176])..... 67

Figure 5.5 Simplified scheme of the infrared absorption mechanism (adapted from *Ferraro JR, et al.* [163]). 71

Figure 5.6 (a) Energy level diagram illustrating the energetic transitions induced by infrared absorption, and Raman and Rayleigh scattering in a diatomic molecule (single vibration mode). (b) Infrared spectrum and (c) Raman and Rayleigh scattering simplified spectrum (the red dash square represents the usual Raman spectra). Figure adapted from *Nakamoto K.* [175] and *Keresztury G.* [185] (not to scale). 73

Figure 5.7 Simplified scheme of the Raman scattering mechanism (adapted from *Ferraro JR, et al.* [163]). 74

Figure 5.8 Infrared (top) and Raman (bottom) spectra of malachite. 76

Figure 5.9 The normal modes of vibration of a linear XY_2molecule (like CO_2). The + and - signals indicate upward and downward motion in the plane of the paper, respectively. The upper symmetric bending occurs in the plane of the paper (just like the two stretching modes), while the bottom symmetric bending occurs at right angles to the plane of the paper. 82

Figure 5.10 Wave motion for an infinite one-dimensional diatomic chain (adapted from *Ferraro JR, et al.* [163] and *Franke K, et al.* [199]). 85

Figure 5.11 FT-IR microspectrometer (Nicolet, LCRJF laboratory). Modulated broad-band IR light from a Michelson interferometer is focused onto the sample with a Cassegrainian objective. Light transmitted by the sample is collected by a Cassegrainian condenser and subsequently focused onto a MCT-A detector. 87

Figure 5.12 Raman microspectrograph (Renishaw, UCL laboratory). A laser source is focused onto the sample with an ordinary objective. Light reflected by the sample is collected by the same objective, passed through a holographic filter, following through a spectrograph and subsequently focused onto a CCD detector. 87

Figure 6.1 Representation of a transversal cut of the Thermo Spectra-Tech µSample Plan micro compression diamond cell set-up. 98

Figure 6.2 Unsuccessful thin section of sample **W3**, viewed under reflected light..... 98

Figure 6.3 Infrared spectra of: (a) layer 5 of sample **H8**, identified as a mixture of emerald green and lead white in oil, (b) layer 1 of sample **V1**, identified as a mixture of lead white and emerald green in oil, and (c) layers 3-5 of sample **H8**, identified as a mixture of emerald green, a chromate salt, a carbonate compound and a sulfate or silicate compound in oil... 101

Figure 6.4 Infrared spectra of: (a) ground layer of sample **O2**, identified as a mixture of lead white, lead carbonate and calcium carbonate - calcite form in oil, (b) layer 1 of sample **F1**, identified as calcium carbonate – calcite form in oil, (c) layer 1 of sample **E6**, identified as lead carbonate in oil and (c) layers 3 and 4 of sample **J2**, identified as a mixture of lead white and lead carboxylates in oil. 102

Figure 6.5 Infrared spectra of: (A)(a) the layer 2 of sample **E6**, identified as a mixture of lead carbonate, lead white and lead carboxylates in oil, and (b) sample **H2**, identified as a mixture of emerald green and lead white in oil; (B)(a) the layer 1 of sample **I2**, identified as a mixture of lead white and lead carboxylates in oil, and (b) the ground layer of sample **W1**, identified as a mixture of lead white and lead carbonate in oil. 103

Figure 6.6 Infrared spectra of: (A)(a) layer 2 of sample **O3**, identified as chrome orange in oil, (b) layer 5 of sample **H8**, identified as chrome yellow in oil, (c) the layer 1 of sample **Q5**, identified as strontium yellow in oil and (d) the layer 2 of sample **N5**, identified as zinc yellow in oil; (B) reference samples: (a) chrome orange, (b) chrome yellow, (c) strontium yellow, and (d) zinc yellow. 105

Figure 6.7 Infrared spectrum of: (A)(a) layers 3 and 4 of sample **C2**, identified as a mixture of a carbonate, a silicate or sulfate compound and a chromate compound in oil, (b) layer 7 of sample **C2**, identified as a mixture of a silicate or sulfate compound, strontium yellow and

lead carbonate in oil, and (c) layer 3 of sample **U1**, identified as a mixture of lead white, kaolin, chrome green (Prussian blue with chrome yellow) in oil; (B)(a) layer 4 of sample **H8**, identified as a mixture of emerald green, brochantite and zinc yellow in oil, and (b) sample **Q8**, identified as a mixture of lead white, lead carboxylates, gypsum and strontium yellow in oil. 107

Figure 6.8 Infrared spectra of: (a) layer 3 of sample **S2**, identified as a mixture of chrome green, lead white, lead carboxylates and a sulfate/silicate compound in oil, and (b) the layer 3 of sample **U9**, identified as a mixture of Prussian blue, lead white, lead carboxylates and maybe chrome yellow in oil. 108

Figure 6.9 Infrared spectra of: (a) layer 2 of sample **U4**, identified as a mixture of lead white, lead carboxylates and Prussian blue in oil, (b) layer 3 of sample **L2**, identified as a mixture of lead white, lead carboxylates and Prussian blue in oil, and (c) layers 2 and 3 of sample **K3**, identified as a mixture of lead white, lead carboxylates, and maybe calcium sulfate dihydrate and Prussian blue in oil. 109

Figure 6.10 Infrared spectra of: (a) layers 3-5 of sample **F6**, identified as a mixture of Prussian blue, viridian and carboxylates in oil, (b) layer 3 of sample **T3**, identified as viridian in oil, (c) reference sample of viridian (viridian - W&N) and (d) reference sample of viridian (vert émeraude - Lefranc). 110

Figure 6.11 Infrared spectra of the reference sample of viridian (viridian - W&N) (Nicolet 6700 spectrometer fitted with a DTGS detector, 4 cm^{-1} resolution, 128 scans). 111

Figure 6.12 Infrared spectra of: (A)(a) layer 2 of sample **B4**, identified as a mixture of bone/ivory black, lead carbonate, lead carboxylates in oil, (b) reference sample of bone/ivory black (Lefranc), and (c) reference sample of bone/ivory black (Winsor & Newton); (B)(a) layer 2 of sample **J3**, identified as bone/ivory black with a fraction of a proteinaceous material, (b) layers 2 and 3 of sample **G4**, identified as a mixture of lead white, lead carboxylates, gypsum, kaolin and bone/ivory black in oil, and (c) layer 2 of sample **G3**, identified as a mixture of lead white, lead carboxylates, kaolin and bone/ivory black in oil. 112

Figure 6.13 Infrared spectra of reference samples of: (a) celadonite and (b) glauconite.... 114

Figure 6.14 Infrared spectra of: (A)(a) sample **E4** (all layers), identified as a mixture of lead white, celadonite and maybe lead carbonate and (b) the layer 3 of sample **E7**, identified as a mixture of lead white, lead carboxylates, celadonite and Prussian blue in oil; (B)(a) layer 3 of sample **E7** (from a different thin section than spectrum Ab), identified as a mixture of lead white, lead carboxylates, lead carbonate, quartz and celadonite in oil, and (b) layer 2 of

sample **I4**, identified as a mixture of lead white, lead carboxylates, quartz and maybe barium sulfate, calcium carbonate – calcite form, and gypsum and/or celadonite in oil. 115

Figure 6.15 Infrared spectra of: (a) layer 1 of sample T2, identified as kaolinite in a proteinaceous binder, (b) the layer 2 of sample G2, identified as a mixture of lead white, lead carboxylates, quartz and kaolin in oil, (c) the layers 2-4 of sample U13, identified as a mixture of lead white, lead carboxylates, Prussian blue and kaolin in oil, and (d) the layers 5-8 of sample K9, identified as a mixture of lead white, lead carboxylates, gypsum, quartz and maybe kaolin in oil. The inset presents the enlargement of the quartz's doublet. 116

Figure 6.16 Infrared spectra of: (a) layers 1 and 2 of sample I1, identified as a mixture of barium sulfate, lead white, lead carboxylates and quartz in oil, (b) ground layer of sample G4, identified as a mixture of barium sulfate, lead white and lead carboxylates in oil, and (c) ground layer of sample H4, identified as a mixture of lead white, lead carboxylates and maybe barium sulfate in oil. 118

Figure 6.17 Infrared spectrum of layers 4 and 5 of sample H8 identified as a mixture of brochantite (bands assigned in blue), emerald green and lead white in oil. 119

Figure 6.18 Infrared spectra of: (A) (a) layer 3 of sample F3, identified as a mixture of gypsum, lead carbonate, lead carboxylates in oil, and (b) layer 2 of sample A2, identified as a mixture of lead white, lead carboxylates and gypsum in oil; (B) (a) layer 1 of sample E6, identified as a mixture of lead carbonate, lead carboxylates and maybe lead white and gypsum in oil, and (b) layers 2-6 of sample A4, identified as a mixture of lead white and maybe gypsum in oil. 121

Figure 6.19 Infrared spectra of: (A)(a) layer 1 of sample K3, identified as a mixture of lead white, lead carboxylates, quartz and a sulfate/silicate compound (probably gypsum) in oil, (b) layers 2 and 3 of sample I6, identified as a mixture of lead white, lead carboxylates, quartz, kaolin and maybe gypsum in oil, and (c) layer 4 of sample W4, identified as a mixture of lead white, lead carboxylates and a sulfate/silicate compound in oil; (B)(a) layer 2 of sample B2, identified as a mixture of lead white, lead carboxylates, quartz and a silicate/phosphate compound in oil, (b) layers 2 and 3 of sample K11, identified as a mixture of lead white, lead carboxylates, quartz, Prussian blue and a silicate/phosphate compound in oil, and (c) layer 4 of sample K12, identified as a mixture of lead white, lead carboxylates, quartz and a silicate/phosphate compound in oil. 122

Figure 6.20 Infrared spectra of: (A)(a) layers 2-5 of sample H1, identified as a mixture of lead white, lead carboxylates and a silicate compound in oil, (b) sample J4, identified as a mixture of lead white, lead carboxylates and a silicate compound in oil, and (c) sample M1, identified

as a mixture of lead white, lead carboxylates and a silicate compound in oil; (B)(a) reference sample of ultramarine blue (Winsor & Newton), (b) sample T1, identified as a mixture of lead white, lead carboxylates and a silicate compound in oil, and (c) layer 2 of sample S1, identified as a mixture of lead white and lead carboxylates in oil..... 123

Figure 6.21 Infrared spectra of: (a) ground layer 1 of sample F1, identified as calcium carbonate- 125

Figure 6.22 Infrared spectra of: (a) layer 2 of sample T7 identified as a mixture of viridian and metal carboxylate(s) in oil and (b) layer 2 of sample N2, identified as a mixture of zinc yellow, a carbonate compound and metal carboxylate(s) in oil..... 126

Figure 6.23 Infrared spectra of: (a) layers 3 and 4 of sample E5, identified as a mixture of lead carbonate, lead carboxylates and a polysaccharide material (probably starch), (b) layer 3 of sample F4, identified as a polysaccharide material (probably starch) and maybe wax, (c) layer 2 of sample Q5, identified as a polysaccharide material (probably starch) and strontium yellow, and (d) layers 2 and 3 of sample W4, identified as lead white and a sulfate/silicate compound or polysaccharide material..... 128

Figure 6.24 Infrared spectra of: (a) sample **R4**, identified as lead white and the embedding resin, and (b) the embedding resin..... 129

Figure 6.25 Infrared spectra of size layers: (a) layer 1 of sample U7, identified as animal glue, (b) layers 1 and 2 of sample T3, identified as animal glue and a polysaccharide material (probably cellulose, wavenumbers in purple), and (c) layer 1 of sample U1, identified as cellulose (wavenumbers in purple) and animal glue..... 130

Figure 6.26 Infrared spectra of: (a) layer 2 of the sample I3, identified as a carbonate, lead carboxylates and unknown compound 1 in oil, (b) layers 2 -3 of sample R1, identified as lead white, lead carboxylates and unknown compound 1 in oil, (c) sample R8, identified as lead white, lead carboxylates, inclusion resin (R) and unknown compound 1 in oil..... 130

Figure 6.27 Raman spectra of: (A) green pigment grains from: (a) layer 4 of sample H8 (40 scans, 0.63 mW) (b) layer 5 of sample H2 (12 scans, 0.63 mW) and (c) layer 2 of sample H7 (5 scans, 0.63 mW), all identified as emerald green; (B)(a) ground of layer 5 of sample H2, identified as a mixture of emerald green with chrome yellow (8 scans, 0.63 mW), (b) ground of layer 1 of sample L3, identified as a mixture of emerald green emerald green with chrome yellow and vermilion (4 scans, 0.63 mW), and (c) ground of layer 2 of sample H7, identified as a mixture of emerald green emerald green with lead white (5 scans, 0.63 mW)..... 135

Figure 6.28 Raman spectrum of: (a) green-grey pigment grain of layer 3 from sample H2, identified the as Scheele's green (40 scans, 0.63 mW) and (b) arsenolite (ID R050383) downloaded from RRUFF^{TM} Project library [314] (532 nm excitation line). 136

Figure 6.29 Raman spectrum of a brownish particle of layer 1 of sample **K13** (5 scans, 0.63 mW), identified as calcium carbonate - calcite form. 137

Figure 6.30 Raman spectra of: (a) white ground of layer 2 of sample P1, identified as lead carbonate (20 scans, 0.63 mW), (b) lead carbonate reference sample (10 scans, 2.00 mW), (c) a big white pigment grain of layer 2 of sample H7, identified as lead white (6 scans, 0.63 mW) and (d) lead white reference sample, the inset presents the hydroxyl band (12 scans, 2.00 mW). 138

Figure 6.31 Raman spectra of: (A)(a) dark green pigment grain of layer 4 of sample **H8** (15 scans, 0.63 mW), identified as malachite, (b) malachite reference sample 1 (80 scans, 2.00 mW) and (c) malachite reference sample 2 (20 scans, 1.00 mW); (B) hydroxyl stretching region of: (a) spectrum (Ab) and (b) spectrum (Ac). 139

Figure 6.32 Raman spectra of: (a) orange pigment grains of the white ground layer 3 of sample C5, identified as chrome orange (2 scans, 0.10 mW), (b) chrome orange reference sample (Winsor and Newton) (10 scans, 0.13 mW), (c) phoenicochroite reference sample (10 scans, 0.41 mW) and (d) orange pigment grain of sample K10, identified as chrome orange maybe mixed with chrome yellow (5 scans, 0.13 mW). 140

Figure 6.33 Raman spectra of: (a) yellow pigment grains of layer 3 of sample E4, identified as chrome yellow (3 scans, 0.63 mW), (b) brownish pigment grain of layer 2 of sample D1, identified as strontium yellow (15 scans, 0.63 mW), (c) green ground of layer 6 of sample H2, identified as zinc yellow (5 scans, 0.63 mW) and (d) a yellow-white pigment grain of layer 2 of sample Q2, identified as a mixture of chrome yellow (wavenumbers in orange) and strontium yellow (wavenumbers in blue) (4 scans, 0.32 mW). 141

Figure 6.34 Raman spectra of the green ground of layer 2 of sample S2, identified as chrome green (25 scans, 0.32 mW). Prussian blue bands are in blue, while chrome yellow bands are in orange. 142

Figure 6.35 Raman spectra of: (a) a dark blue particle of layer 2 of sample S7, identified as Prussian blue (16 scans, 0.32 mW), (b) a blue particle of layer 1 of sample I5, identified as Prussian blue (1 scan, 0.32 mW) and (c) the blue background of layer 2 of sample I5, identified as a mixture of Prussian blue and ultramarine blue (band wavenumbers in blue) (2 scans, 0.63 mW). 143

Figure 6.36 Raman spectra of: (a) green-bluish pigment grain of the green layer 4 of sample H8, identified as viridian (20 scans, 0.63 mW), (b) green pigment grain of the green layer 2 from sample I7, identified as viridian (50 scans, 0.63 mW) and (c) reference sample of viridian (Winsor & Newton) (10 scans, 0.10 mW). 143

Figure 6.37 Raman spectra of: (A)(a) blue pigment grains of layer 3 of sample H5, identified as cobalt blue (13 scans, 0.63 mW) and (b) blue ground of layer 2 of sample A3, probably cobalt blue (7 scans, 0.63 mW); (B) black particle of layer 2 of sample H7, identified as cobalt oxide (10 scans, 0.13 mW). 144

Figure 6.38 Raman spectra of: (a) yellow-brownish pigment grains of layer 3 of sample E5, identified as iron^{III} oxyhydroxide (23 scans, 0.63 mW) and (b) goethite reference sample (10 scans, 0.13 mW). 145

Figure 6.39 Raman spectra of: (a) red pigments grains of the reddish layer 4 of sample K7, identified as hematite (10 scans, 0.13 mW), (b) big brown particle of the brown layer 7 of sample K9, identified as hematite (17 scans, 0.32 mW) and (c) hematite reference sample (3 scans, 0.63 mW). 146

Figure 6.40 Raman spectrum of the reference sample of manganese oxide (30 scans, 2.00 mW). 147

Figure 6.41 Raman spectra of: (a) yellow pigment grain of the sample Q6 (5 scans, 0.63 mW), (b) yellow-green pigment grain of layer 2 of sample S7 (15 scans, 0.63 mW), (c) yellow pigment grain of layer 2 of sample S7 (10 scans, 0.63 mW), identified as lead antimonate yellow, and (d) reference sample of lead antimonate yellow (4 scans, 0.41 mW) (identity confirmed by μ-XRD and SEM/EDS). * marks the 253 cm^{-1} vermilion band in spectrum (a), and the 532 and 280 cm^{-1} bands of Prussian blue in the spectra (b) and (c). 148

Figure 6.42 (A) Raman spectra identified as a mixture of lead antimonate yellow with lead sulfate (wavenumbers in blue): (a) yellow pigment grain of layer 5 of sample K4 (12 scans, 0.63 mW), (b) yellow-greenish pigment grain of layer 6 of sample K7 (10 scans, 0.63 mW), (c) yellow pigment grain of layer 2 of sample S5 (16 scans, 0.63 mW), and (d) yellow pigment grain of layer 3 of sample T1 (6 scans, 0.63 mW); * marks the 253 cm^{-1} vermilion band; (B) Raman spectra identified as a mixture of lead antimonate yellow with basic lead sulfate (wavenumbers in purple): (a) yellow-greenish pigment grain of layer 6 of sample K7 (4 scans, 0.10 mW), (b) yellow-greenish pigment grain of layer 6 of sample K7 (10 scans, 0.63 mW) and (c) yellow pigment grain of layer 5 of sample K4 (10 scans, 0.13 mW); * marks ultramarine blue. 150

Figure 6.43 Raman spectrum of: (a) yellow-greenish pigment grain of layer 4 from the sample I1, identified as a mixture of $PbSb_2O_6$ and lead sulfate (10 scans, 0.63 mW) and (b) rosiaite (ID R070384) downloaded from RRUFF™ Project library [314] (532 nm excitation line). 150

Figure 6.44 Raman spectra of: (A)(a) white pigment grain of layer 3 of sample E4 (10 scans, 0.63 mW) and (b) yellow pigment grain of layer 4 of sample E4 (10 scans, 0.63 mW); (B)(a) yellow pigment grain of layer 3 of sample K14 (5 scans, 0.63 mW) and (b) yellow pigment grain of layer 2 of sample K14 (4 scans, 0.63 mW). 151

Figure 6.45 Raman spectra of: (a) yellow-orange pigment of layer 3 of sample T4 (8 scans, 0.13 mW) and (b) orange-red pigment grain of layer 2 of sample C5 (2 scans, 0.13 mW), both identified as $lead^{II,IV}$ oxide. 151

Figure 6.46 Raman spectra of: (A) black pigment grains of layer 2 of sample K4: (a) (16 scans, 0.13 mW) and (b) (4 scans, 0.63 mW), identified as orthorhombic $lead^{II}$ oxide; and (B) black pigment grain of layer 3 of sample E7 (2 scans, 0.63 mW) identified as carbon-based blak and orthorhombic $lead^{II}$ oxide. 152

Figure 6.47 The black pigments of the brown layer 2 from sample K4 visualised under the microscope of the Raman equipment (x1000): (a) before and (b) after acquisition of the spectrum of Figure 6.46Ab. 153

Figure 6.48 Raman spectra of: (a) white pigment grains of layer 2 of sample L3, identified as rutile (5 scans, 0.63 mW), (b) the yellowish pigments grains of layer 4 of sample K7, identified as anatase (5 scans, 0.13 mW), and (c) white pigment grain of layer 3 of sample K3, identified as brookite (5 scans, 0.32 mW). 154

Figure 6.49 Raman spectrum of: (a) the ground of layer 2 from the sample W5, identified as a mixture of zinc white and ultramarine blue (wavenumbers in blue) (272 scans, 0.63 mW) and (b) synthetic zinc oxide (ID R060027) downloaded from RRUFF™ Project library [314] (532 nm excitation line, 150 mW). 155

Figure 6.50 Raman spectra of: (A) (a) green pigment grain of the green layer 3 of sample E4 (50 scans, 0.63 mW), (b) celadonite reference sample (100 scans, 0.63 mW) and (c) hydroxyl stretching region of spectrum (b); (B) glauconite reference sample (80 scans, 0.63 mW). 155

Figure 6.51 Raman spectra of: (a) glauconite reference sample (300 scans, 0.9 mW) and (b) celadonite reference sample (100 scans, 0.9 mW) obtained using the argon-ion excitation

line. The insets (c) and (d) are the hydroxyl stretching region of the spectra presented in (a) and (b), respectively..... 157

Figure 6.52 Raman spectrum of the white of layer 1 of sample T2, identified as kaolinite (100 scans, 0.63 mW)..... 158

Figure 6.53 Raman spectrum of a whitish pigment grain of sample V1, identified as α-quartz (10 scans, 0.63 mW)..... 159

Figure 6.54 Raman spectrum of the blue pigment grains of layer 2 of sample S1, identified as ultramarine blue (5 scans, 0.63 mW)..... 159

Figure 6.55 Raman spectra of: (a) a white particle of layer 1 of sample K13, identified as barium sulfate (5 scans, 0.63 mW) and (b) a brownish particle of layer 1 of the sample K12, identified as a mixture of barium sulfate and calcium carbonate - calcite form (band wavenumbers in blue) (5 scans, 0.63 mW). 160

Figure 6.56 Raman spectra of: (a) a grey particle of layer 5 of sample K12, identified as basic lead sulfate (10 scans, 0.63 mW) and (b) lanarkite reference sample (35 scans, 2.00 mW)..... 161

Figure 6.57 Raman spectrum of the green-whitish background of layer 4 of sample H8, identified as brochantite (25 scans, 0.63 mW), the inset shows the hydroxyl region. 162

Figure 6.58 Raman spectra of: (a) a grey particle of layer 5 of sample I7, identified as lead sulfate (5 scans, 0.63 mW), the * marks a vermilion band and (b) lead sulfate reference sample (3 scans, 0.63 mW). 162

Figure 6.59 Raman spectra of: (a) yellow-greenish ground of the green layer 6 of sample K7, identified as a mixture of lead antimonate yellow (wavenumbers at orange) with probably lead sulfate (6 scans, 0.13 mW), and (b) green ground of the green layer 2 of sample I4, identified as a mixture of lead antimonate yellow (wavenumber at orange) with lead sulfate or basic lead sulfate and vermilion (wavenumber at red) (15 scans, 0.63 mW). 163

Figure 6.60 Raman spectra of: (a) red pigment grain of layer 2 of sample W5, identified as cadmium red (10 scans, 0.63 mW) and (b) pigment of layer 2 of sample U10, identified as cadmium yellow (18 scans, 0.63 mW); * marks a band probably due to ultramarine. 163

Figure 6.61 Raman spectrum of: (a) brown grain of layer 2 from the sample T1, identified as copper sulfide (10 scans, 0.32 mW); the band at 548 cm^{-1} is due to ultramarine blue and (b) covellite (ID R060306) downloaded from RRUFF™ Project library [314] (532 nm excitation line, 150 mW)..... 164

Figure 6.62 Raman spectrum of a red pigment of layer 3 of the sample K7, identified as mercury^{II} sulfide (1 scan, 0.13 mW). 165

Figure 6.63 (A) Raman spectra of: (a) orange/coral pigment grain of layer 2 of sample G4, identified as realgar (4 scans, 0.10 mW), and (b) coral pigment grain of layer 2 of sample G4 (2 scans, 0.13 mW) and (c) coral pigment grain of layer 1 of sample H1 (18 scans, 0.10 mW), identified as χ-phase and/or mixture of χ-phase and pararealgar; (B) Raman spectra of: (a) realgar reference sample and (d) pararealgar reference sample, both provided by *Burgio L.* [(398)]. 166

Figure 6.64 Raman spectra of carbon-based black pigments from: (a) the grey layer 3 of sample J1 (15 scans, 0.63 mW), (b) the brown layer 2 of sample G4 (3 scans, 0.13 mW), and (c) the blue layer 2 of sample D1 (6 scans, 0.32 mW); (d) Raman spectrum of a reference sample of ivory black from Windsor & Newton (40 scans, 1.00 mW). 167

Figure 6.65 Raman spectra of: (A)(a) red lake pigments of layer 2 of sample Q5, identified as cochineal lake (47 scans, 0.13 mW) and (b) carmine reference sample (372 scans, 0.02 mW); (B) purple pigment grain of layer 2 of sample W6, identified as madder lake (20 scans, 0.63 mW). 169

Figure 6.66 Raman spectra of a greenish grain of layer 4 of sample H8, identified as alumina water-slurry used for polishing (1 scans, 0.63 mW). 170

Figure 6.67 Raman spectra of: (a) black particle of layer 1 of sample P1 (2 scans, 0.13 mW) and (b) black ink reference sample (5 scans, 0.32 mW). 171

Figure 6.68 Raman spectra of a white grain of layer 2 of sample E6, identified as silicon carbide used for the grinding (7 scans, 0.32 mW). 171

Figure 6.69 Raman spectra of: (a) brown pigment of layer 2 of sample **U13** (15 scans, 0.32 mW), (b) black pigment of layer 2 of sample **P1** (3 scans, 0.32 mW), (c) black pigment of layer 2 of sample **P2** (13 scans, 0.32 mW) and (d) brown pigment of layer 2 of sample **H1** (10 scans, 0.63 mW). 172

Figure 6.70 Raman spectra of: (a) white pigment of layer 2 of sample K3 (4 scans, 0.32 mW), (b) white pigment of layer 4 of sample F3 (8 scans, 0.32 mW) (wavenumbers in black are due to chrome yellow), (c) grey pigment of layer 2 of sample S7 (20 scans, 0.63 mW) (wavenumbers: in orange is due to lead sulfate; in black are due to Prussian blue; in red is an unknown compound) and (d) white pigment of layer 2 of sample S5 (22 scans, 0.63 mW) (wavenumber in pink are from rosiaite and the wavenumbers in black are from Prussian blue) 172

Figure 7.1 The interaction volume and the regions from which secondary electrons, backscattered electrons and X-rays can be detected (adapted from *Goodhew PJ, et al.* [105] and *Leng Y.* [110]). 184

Figure 7.2 X-ray diffraction between adjacent Bragg planes (adapted from *FishbanePM, et al.* [428]). 187

Figure 7.3 Schematic diagram of the configuration of a reflected light fluorescence microscope, in which the filters are arranged in a fluorescence filter cube (adapted from *Murphy DB.* [145]). 189

Figure 7.4 Cross section of the samples: (a) T2 and (b) W4 under reflected light. Backscattered images of the samples: (c) T2 and (d) W4. 194

Figure 7.5 SEM/EDS spectra of: (a) white layer 1 of sample **W4**, (b) blue layer 2 of sample **T2** and (c) grey layer 3 of the sample **W4**. 194

Figure 7.6 X-ray diffraction pattern of: (a) the blue layer 2 of sample T2, (b) the grey layer 3 of sample W4 and (c) the grey layer 3 of sample W7. Phase abbreviations: K- kaolinite (JCPDS 080-0885), L-Lazurite-C (JCPDS 046-0103), M-muscovite ((a) JCPDS 006-0263; (b) 082-0576) and ZW-zinc white ((a) JCPDS 036-1451; (b) 005-0664). 195

Figure 7.7 SEM/EDS spectrum of the yellow pigments of green layer 2 from sample F6, identifying cadmium yellow. 196

Figure 7.8 (a) Cross section of sample Q4 under reflected light and (b) SEM/EDS spectrum of the black layer of sample Q4. 197

Figure 7.9 (a) Cross section of sample R1 under reflected light; SEM/EDS spectra of the blue pigments of: (b) blue layer 3 of sample R1 and (c) layer 2 of sample R1. 198

Figure 7.10 X-ray diffraction pattern of the blue layer 2 from the sample I3. Phase abbreviations: CB-cerulean blue (JCPDS 029-0514), LW-lead white (JCPDS 010-0401, 013-0131) and M-mercury^{II} sulfide (JCPDS 006-0256). 199

Figure 7.11 (a) Cross section of sample V3 under reflected light and (b) SEM/EDS spectrum of the green layer 3 of this sample. 200

Figure 7.12 X-ray diffraction pattern of the reference sample of lead antimonate yellow. Phase abbreviations: LY-lead antimonate yellow (JCPDS 074-1354, 042-1355) and R-titanium oxide-rutile form (JCPDS 021-1276). 201

Figure 7.13 X-ray diffraction pattern of: (a) layers 4 and 5 of sample I1, and (b) layer (2) of sample S5. Phase abbreviations: LW- lead white (JCPDS 013-0131, 010-0401), LS-lead

sulfate (JCPDS 036-1461), M-mercury^{II} sulfide (JCPDS 080-2192), BS-basic lead sulfate (JCPDS 018-0702), LY-lead antimonate yellow (JCPDS 018-0687), LC-lead carbonate (JCPDS 047-1734), R-rosiaite (JCPDS 049-1867), and C-cervantite (JCPDS 011-0694). . 202

Figure 7.14 (a) Cross section of sample I7 viewed under reflected light and (b) SEM/EDS spectrum of the yellow pigment marked with a red cross in (a). 203

Figure 7.15 Cross section of the sample W3 viewed under: (a) reflected light and (b) ultraviolet light (I 2/3 cube). 204

Figure 7.16 Cross-section of the sample (a) F4 and (b) Q5 viewed under reflected light; cross-section of the sample (c) F4 and (d) R5 viewed under ultraviolet light (I 2/3 cube). .. 205

Figure 7.17 (a) Cross section of sample F6 under reflected light; SEM/EDS spectra of the marked red pigments: (b) point 1, (c) point 2 and (d) point 3. 206

Figure 7.18 SEM/EDS spectrum of the red layer of sample Q5 (Figure 7.16b). 206

Figure 7.19 (A) Cross section of sample L3 under reflected light; (B) SEM/EDS spectra of the white layer 2 of sample L3: (a) area analysis, (b) point analysis and (c) point analysis. 208

Figure 7.20 X-ray diffraction pattern of the white layer 1 from the sample L3. Phase abbreviations: LW-lead white (JCPDS 010-0401, 013-0131) and LC-lead carbonate (JCPDS 047-1734). 208

Figure 7.21 a) Cross section of sample N3 viewed under reflected light and (b) SEM/EDS spectrum of the blue layer 2 from sample N3. 209

Figure 7.22 (a) Cross section of sample B3 viewed under reflected light and (b) X-ray diffraction pattern of the layers 2 and 3 from the sample B3. Phase abbreviations: LW-lead white (JCPDS 010-0401, 013-0131), LC-lead carbonate (JCPDS 047-1734) and ZW-zinc white (JCPDS 036-1451). 210

Figure 7.23 SEM/EDS spectrum of the grey layer 3 from the sample B3. 210

Figure 7.24 Cross-section of the sample K7 viewed under: (a) reflected light and (b) ultraviolet light (A cube); (c) SEM/EDS spectrum and (b) XRD pattern of the ground layer from sample K7. Phase abbreviations: LW-lead white (JCPDS 010-0401, 013-0131), B-barium sulfate (JCPDS 024-1035) and C-calcium carbonate - calcite form (JCPDS 005-0586). 211

Figure 7.25 (a) SEM/EDS spectrum of the ground layer of sample N3 and (b) X-ray diffraction pattern of the ground layer of the sample N5. Phase abbreviations: LW-lead white

(JCPDS 013-0131), LC-lead carbonate (JCPDS 047-1734), C-calcium carbonate-calcite form (JCPDS 005-0586) and ZW-Zinc white (JCPDS 036-1451). 212

Figure 7.26 Cross-section of the sample N5 viewed under ultraviolet light (A cube)..... 212

Figure 7.27 X-ray diffraction pattern of the ground layer of the sample N2. Phase abbreviations: LW-lead white (JCPDS 013-0131, 010-0401). 213

Figure 7.28 Cross section of the samples: (a) F1, (b) J2, and (c) T7, under reflected light. SEM backscattered image of the samples: (d) F1, (e) J2, and (f) T7..... 214

Figure 7.29 SEM/EDS spectra of: (a) an area of the blue layer 5 of sample F1 and (b) an area of the grey layer 4 of sample J2. 215

Figure 7.30 SEM/EDS spectrum of an area of the green layer 2 of sample T7..... 215

Figure 7.31 Cross section of the sample F1 viewed under: (a) reflected light and (b) ultraviolet light (A cube). 216

Figure 7.32 Cross section of the sample J2 viewed under: (a) reflected light and (b) ultraviolet light (A cube). 216

Figure 7.33 X-ray diffraction pattern of the grey layer 4 from the sample J2. Phase abbreviations: LW-lead white (JCPDS 010-0401, 013-0131) and LC-lead carbonate (JCPDS 076-2056). 216

Figure 7.34 X-ray diffraction pattern of the reference sample of zinc yellow. Phase abbreviations: ZY-zinc yellow (JCPDS 08-0202) and ZW-zinc white (JCPDS 036-1451). .. 217

Figure 7.35 (a) SEM backscattered image of sample K7 and (b) the SEM/EDS spectrum of the marked yellow pigment; (c) SEM backscattered image of L3 and (d) the SEM/EDS spectrum of the marked yellow pigment. 218

Figure 7.36 X-ray diffraction pattern of the green layer 4 from the sample **H8**. Phase abbreviations: LW-lead white (JCPDS 013-0131, 010-0401), LC-lead carbonate (JCPDS 047-1734), EG-emerald green (JCPDS 031-0448), M-mercury^{II} sulfide (JCPDS 080-2192) and ZY-zinc yellow (JCPDS 011-0275). 218

Figure 7.37 Raman spectra of: (a) yellow pigment grains of the green layer 4 of sample H8, identified as zinc yellow (5 scans, 0.63 mW) and (b) zinc yellow reference sample (Ferrario Colours) (1 scans, 0.13 mW). See experimental conditions on the previous chapter. 219

Figure 8.1 Detail of the paintings: (a) *Jardim de Luxemburgo (estudo)* and (b) *Senhora vestida de preto*, showing the wood panel support. Photo: LCRJF..... 234

Figure 8.2 Back-side of the painting ***Mulher da água***, showing the canvas stretched over the wooden frame (stretcher). Photo: LCRJF. 235

Figure 8.3 Cross section of sample **F2**, viewed under reflected light. 236

Figure 8.4 Detail of the painting: (a) *Rapariga deitada no tronco de uma árvore*, showing the black underdrawing pencil line used to define the tree logs and (b) *Mulher da água*, showing the carbon-based black strokes used to define the hand and jug. Photo: LCRJF. 237

Figure 8.5 Detail of the painting: (a) ***Casas brancas de Capri***, showing the blue outline of the cactus; (b) ***Mulher da água***, showing the blue outline of the woman's cloth; ***Janela das persianas azuis***, showing the blue outline of the roof; and (c) ***Rapariga deitada no tronco de uma árvore***, showing the brown outline to adjust the tree log dimensions. Photo: LCRJF. 237

Figure 8.6 Detail of the painting ***Mulher da água***, showing the reserve for the earthen pot done with a grey-black wash. Photo: LCRJF. 238

Figure 8.7 Detail of the painting ***Paisagem de Anacapri***, showing the black pencil line drawn over the paint layer. Photo: LCRJF. 238

Figure 8.8 Cross section of sample **H2** viewed under reflected light: the dark green layers 1, 3 and 5 are composed by emerald green, Scheele's green, lead white, chrome yellow, mercury^{II} sulfide and carbon-based black, the light green layers 2, 4 and 7 are composed by chrome green, emerald green, zinc yellow, lead white and mercury^{II} sulfide, and the brown layer 6 is composed by chrome yellow, emerald green and maybe cadmium yellow. 239

Figure 8.9 Cross section of sample **I1** viewed under reflected light: the white ground layer 1 is composed by lead white (extended with barium sulfate), the pink layer 2 is composed by lead white (with lead carbonate), mercury^{II} sulfide, iron^{III} oxide, cochineal lake, ultramarine blue and carbon-based black, the brown layer 3 is composed by iron^{III} oxide, mercury^{II} sulfide, chrome orange, ultramarine and viridian, the green layer 4 is composed by celadonite, mercury^{II} sulfide, lead antimonate yellow (with basic lead sufate) and carbon-based black, the pink layer 5 is composed by mercury^{II} sulfide, cochineal lake, lead white, iron^{III} oxyhydroxide, ultramarine blue and carbon-based black; the black layer 6 is composed by ultramarine blue, chrome yellow, vermilion, iron^{III} oxyhydroxide and carbon-based black. 239

Figure 8.10 Cross section of sample **A3** viewed under reflected light: the white ground layer 1 is composed by lead white with carbon-based black and ultramarine blue; the brown layer 2 is composed by lead white, mercury^{II} sulfide and chrome yellow, the blue layer 3 is

composed by lead white, cobalt blue, iron^{III} oxide and cochineal lake, and the orange layer 4 is composed by chrome orange, chrome yellow, iron^{III} oxide, lead white and carbon-based black. 242

Figure 8.11 Cross section of sample **H1** viewed under reflected light: the white layer 1 is composed by lead white, realgar, iron^{III} oxide, cadmium yellow and carbon based black; the brown layer 2 is composed by iron^{III} oxide, mercury^{II} sulfide and carbon-based black and the brown layer 3 is composed by lead white, mercury^{II} sulfide, iron^{III} oxide, cadmium yellow and carbon-based black. 244

Figure 8.12 Cross section of sample **M2** viewed under reflected light: the white ground layer 1 is composed by lead white and carbon-based black and the blue layer 2 is composed by cobalt blue and lead white..... 245

Figure 8.13 Cross section of sample **T4** viewed under reflected light: the white ground layer 1 is composed by lead white (extended with barium sulfate), iron^{III} oxide and carbon-based black; the purple layer 2 is composed by lead white, cobalt blue, cochineal lake, mercury^{II} sulfide and carbon-based black, the brown layer 3 is composed by ultramarine blue, cochineal lake, zinc yellow, lead white and carbon-based black and the blue layer 4 is composed by ultramarine blue, lead white, zinc yellow, mercury^{II} sulfide and carbon-based black. 245

Figure 8.14 Cross section of sample **E7** viewed under reflected light: the white ground layer 1 by lead white and zinc yellow, the blue layer 2 is composed by cobalt blue, zinc yellow, cochineal lake and carbon-based black and the green layer 3 is composed by celadonite, viridian, lead white (with lead carbonate), chrome yellow, chrome orange and Prussian blue. 246

Figure 8.15 Cross section of sample **G4** viewed under reflected light: the white ground layer 1 is composed by lead white (extended with barium sulfate) and the brown layer 2 is composed by bone/ivory black, iron^{III} oxide, mercury^{II} sulfide, realgar and χ-phase/pararealgar, cadmium yellow, cobalt blue and lead white. 247

Figure 8.16 Cross section of sample **C1** viewed under reflected light: the white ground layers 1 and 2 are composed by lead white (with lead carbonate and extended with calcium carbonate - calcite form, iron^{III} oxide and carbon-based black and the blue layer 3 is composed by lead white (with lead carbonate), cobalt blue and carbon-based black. 248

Figure 8.17 Cross section of sample **H5** viewed under reflected light: the white ground layer is composed by lead white (extended with barium sulfate) and carbon-based black, the blue layer 2 is composed by lead white and cobalt blue, the blue layer 3 is composed by lead

white, cobalt blue and mercury^{II} sulfide, the blue layer 4 is composed by lead white and cobalt blue and the white layer 5 is composed by lead white. 248

Figure 8.18 (a) Cross section of the sample **H7** viewed under reflected light: the white ground layer 1 is composed by lead white (extended with barium sulfate) and carbon-based black and the green layer 2 is composed by lead white, emerald green, chrome yellow, zinc yellow and cochineal lake; (b) Cross section of the sample **H8** viewed under reflected light: the white ground layer 1 is composed by lead white (extended with barium white) and carbon-based black, the brown layer 2 is composed by carbon-based black, the light green layer 3 is composed by ultramarine blue, chrome yellow, zinc yellow and carbon-based black, the green layer 4 is composed by malachite (with brochantite), emerald green, viridian, realgar, mercury^{II} sulfide and zinc yellow and the green layer 5 is composed by emerald green, viridian, malachite, lead white, chrome yellow, zinc yellow, realgar, vermilion, cobalt blue and carbon-based black. 249

Figure 8.19 Detail of the painting: (a) ***O mendigo lapita*** and (b) ***Cansada (Cachopa de Capri)***. Photo: LCRJF. 252

Figure 8.20 Detail of the painting *Casas brancas de Capri*. Photo: LCRJF. 253

Figure 8.21 Detail of the painting ***Paisagem - Abertura da Rua Alexandre Herculano***. Photo: LCRJF. 253

Figure 8.22 Detail of the painting ***Aldeia de St. Sauves***, showing the cracking pattern of the tree foliage. Photo: LCRJF. 254

List of Tables

Table 3.1 Key information on the paintings under analysis 38

Table 3.2 Number of samples taken from each painting 41

Table 5.1 Characteristic wavenumber ranges of the stretching vibrations of some organic functional groups. 79

Table 5.2 Narrower wavenumber ranges of the stretching vibrations of carbonyl groups of some classes of compounds. 79

Table 5.3 Main IR wavenumber ranges of some common inorganic ions. 80

Table 6.1 Compounds* identified by µ-IR in Pousão's paintings 100

Table 6.2 Overview of the IR band position of several zinc chromate compounds 106

Table 6.3 He-Ne laser (632.8 nm) power at the sample surface. 132

Table 6.4 Compounds* identified by µ-R in Pousão's paintings 133

Table 6.5 Raman band positions of lead antimonate yellow 148

Table 6.6 Compounds* identified by µ-IR and µ-R in Pousão's paintings 178

Table 7.1 Samples analysed by SEM/EDS 190

Table 7.2 Samples analysed by µ-XRD 191

Table 7.3 Samples analysed by FM 192

Table 7.4 Compounds* identified by µ-IR, µ-R, SEM/EDS, µ-XRD and FM in Pousão's paintings 225

Table 7.5 Pigments identified in Pousão's paintings*: 1984 study and current study 228

Table 8.1 Supports and dimensions of the paintings 233

Table 8.2 Pigments and extenders identified in the ground layers of the paintings 235

Table 8.3 Pousão's palette 241

List of acronyms and abbreviations

ATR	attenuated total reflectance
CCD	charge couple device
CI	colour index number
CM	classical mechanics
DRIFT	diffuse refection Fourier-transform infrared spectroscopy
DTA	differential thermal analysis
EELS	High-resolution electron energy loss spectroscopy
EDS	energy dispersive X-ray spectrometry
EPMA	electron probe microanalysis
ESEM	environmental scanning electron microscope
FM	fluorescence microscopy
FORS	fiber optic reflectance spectroscopy
FT	Fourier transform
FT-IR	Fourier transform infrared spectroscopy
FT-Raman	Fourier transform Raman spectroscopy
GC	gas chromatography
GC/MS	gas chromatography with mass spectroscopy
GL	grazing Light
HPLC	high performance liquid chromatography
HPLC/MS	high performance liquid chromatography with mass spectrometry
IETS	inelastic electron tunneling spectroscopy
INS	inelastic neutron scattering
IR	infrared or infrared spectroscopy
IR	infrared photography
μ-IR	infrared microscopy
IRFC	infrared false colour photography

IRR	infrared reflectography
IRS	internal reflection spectroscopy
LA	longitudinal acoustic phonon
LCRJF	Laboratório de Conservação e Restauro José de Figueiredo
LIBS	laser-Induced breakdown spectroscopy
LO	longitudinal optic phonon
MCT	Mercury cadmium telluride
MIR	mid-infrared
MS	mass spectrometry
m/z	mass-to-charge ratio
NA	numerical aperture
NAA	neutron activation analysis
NCA	normal coordinate analysis
Nd:YAG	neodymium-doped yttrium aluminium garnet
NIR	Near-infrared
NMR	nuclear magnetic resonance
OM	Optical microscopy
PIXE	particle-induced X-ray emission
PLM	polarized light microscopy
QM	quantum mechanics
R-A	reflection-absorption
RI	refractive index
RS	Raman spectroscopy
μ-R	Raman microscopy
SEM	scanning electron microscopy
SEM/EDS	scanning electron microscopy/energy dispersive X-ray spectrometry
SIMS	imaging secondary ion mass spectrometry
S/N	signal-to-noise ratio
SR	specular reflection
SR-μXRF	synchrotron radiation induced micro-X-ray fluorescence spectrometry
SR-XRD	synchrotron radiation induced X-ray diffraction
TA	transverse acoustic phonon
TEM	transmission electron microscopy
TG	thermal gravimetry
TO	transverse optic phonon
UV	ultraviolet

UVR	ultraviolet reflected photography
UVF	ultraviolet fluorescence photography
VIS	visible
WDS	wavelength dispersive X-ray spectrometry
XANES	X-ray absorption near edge structure
XPS	X-ray photoelectron spectroscopy
XRD	X-ray diffraction
µ-XRD	micro X-ray diffraction
XRF	X-ray fluorescence
µ-XRF	micro X-ray fluorescence
XRR	X-radiography

Introduction

The scientific analysis is a window through which we gain an appreciation of the structure of a painting just as paintings themselves are windows through which we may view ourselves and the world.

W.S. Taft and J.W. Mayer

Background to the research

Our historic and cultural heritage is extremely valuable, as it relates ours and future generations, to their roots and development. It makes it possible to know, for instance, how the pre-historic man hunted or Napoleon looked like.

Unfortunately, due to numerous factors, such as bad quality materials, wars, natural catastrophes, bad storage, vandalism, misguided conservation treatments and even accidents, part of that legacy is in poor condition or has been irretrievably lost. Nevertheless, thanks to conservation science, museums and public/private institutions have been able to keep a large number of works of art in good condition, which, owing to natural ageing, would have extensively deteriorated.

Conservation science is the term that became prevalent to describe the multidisciplinary use of analytical techniques, material science and environmental science, among others, in the study of artworks and archaeological objects, even if the study has not as its main purpose the conservation of the object [1,2]. In last decades conservation science has expanded enormously, as evidences that it provides a better understanding of how these works/objects were created, how they changed, and how should be preserved are made available [3-5].

By employing a wide range of analytical techniques, it has been possible to: i) achieve a better knowledge of technical developments at different regions and times, ii) achieve a better understanding of past societies and cultural development, iii) distinguish between different schools and periods, iv) determine causes of degradation and vulnerability to storage or exhibition conditions, v) choose the appropriate conservation or restoration procedures, avoiding incompatible materials, vi) study degradation phenomena and vii) establish authorship – authentication.

Authentication, in particular, is a very complex and controversial process [6-8]. Based on a scientific approach, a database with the materials and techniques of works with attested origin can be used for comparison. Incompatibilities between materials and techniques identified in suspected artworks and those known to have been used by the artists, or the presence of post materials, can indicate a non-original work, a forgery or a fake[1], but restoration and retouching works must also be taken in consideration [9,10].

Thanks to technologic and scientific developments, nowadays a large number of analytical techniques are available that can be applied to examination, characterization and analysis of artworks.

[1] According to Craddock P. [6] a forgery is a new object that is entirely the imitation of something else, while a fake is an object that has been altered so as to appear something else (generally more valuable).

Some of the most used techniques are: autoradiography, dendochronology, differential thermal analysis (DTA), electron probe microanalysis (EPMA), fiber optic reflectance spectroscopy (FORS), gas-chromatography with mass spectrometry (GC/MS), high-performance liquid chromatography (HPLC) and high performance liquid chromatography with mass spectrometry (HPLC/MS), imaging secondary ion mass spectrometry (SIMS), infrared spectroscopy (IR) and infrared microscopy (μ-IR), infrared reflectography (IRR), laser-Induced breakdown spectroscopy (LIBS), Mössbauer spectroscopy, nuclear magnetic resonance (NMR), neutron activation analysis (NAA), optical microscopy (OM), particle-induced X-ray emission (PIXE), polarized light microscopy (PLM), Raman spectroscopy (RS) and Raman microscopy (μ-R), radiocarbon dating, scanning electron microscopy with energy-dispersive X-ray spectrometry (SEM/EDS), thermal gravimetry (TG), thermoluminescence, thomography, ultraviolet reflected photography (UVR), X-radiography (XRR), X-ray absorption near edge structure (XANES), X-ray diffraction (XRD) and micro X-ray diffraction (μ-XRD), X-ray fluorescence (XRF) and X-ray photoelectron spectroscopy (XPS) [3,9,11-19].

In addition, a large number of analytical techniques used in this field are those used at the cutting edge of modern materials science, such as those that employ synchrotron radiation.

Of course, each technique has its own strengths, suitability, limitations and costs, thus, the selection of the most appropriate analytical method (both sample preparation and technique) to be used is an important task. It is well known that, for most cases, no single technique will provide all the necessary answers, therefore a multi-technique approach must be employed for a complete and trustworthy analysis [3,9].

In Portugal, the Laboratório de Conservação e Restauro José de Figueiredo (LCRJF) has been one of the major institutions active in the study, conservation and preservation of artworks, both of public and private ownership[2]. This laboratory has a strong know-how in analysis of materials and conservation interventions, due to the strong effort which has been made in the last decade to implement new methodologies and techniques. When this study set out (2003), LCRJF was equipped with a MuSIS 2007 multi-spectral imaging system (which includes a plurality of imaging modes, reflectance, fluorescence, with different spectral bands ranging from UV to NIR), XRF, μ-IR, HPLC/MS, and OM[3]. Recently, GC/MS and μ-XRD were also implemented. Additionally and, whenever necessary, other techniques,

[2] This public institution was created in 1967 under the name Instituto José de Figueiredo and was re-named Instituto Português de Conservação e Restauro from 1999 to 2006.

[3] LCRJF has currently three microscopes, one specific for minerals, another one for metals and a third for biological materials.

such as SEM/EDS and XPS have also been used, thanks to a close collaboration with university and research institutions.

During the last decade LCRJF has been requested to evaluate the authenticity of several paintings attributed to the Portuguese 19th century painter Henrique Pousão. However, due to the scarcity of studies devoted to this painter, as well as to the lack of information regarding materials and technique employed by the artist, except for a brief study conducted at LCRJF in 1884[4], this task became a challenge. In order to respond to it properly, the construction of a database of materials (especially the palette) and technique used by the painter was mandatory.

Henrique Pousão

Henrique Pousão (1859-1884) is one of the most important Portuguese Naturalist painters.

Possessing an extended academic background, filled with excellent grades and numerous prizes, it is the originality of his work, with luminous colours and a festive view of nature, especially during the last period of his life, which made him renowned. Despite his short life, Pousão produced a significant number of paintings and drawings, representing, among others, façades, streets and country landscapes [(20)] (see Appendix B).

The study of a few of Pousão's paintings undertaken at LCRJF in 1984 consisted in stratigraphic determination by OM, pigment identification by microchemical analysis, binder identification by dispersive infrared and identification of the support by OM[5].

Optical microscopy and microchemical analysis showed that Pousão's paintings are constituted by very complex mixtures of both traditional and new synthetic pigments brought about by the industrial revolution. However, a large number of pigments might not have been identified. On the one hand, new synthesized pigments are characterized by the presence of grains of reduced dimensions (0.1-0.5 µm), which are poorly resolved by optical microscopes [(21)]; on the other hand, the microchemical analysis is based on chemical reactions with metals or ions and in complex mixtures, different pigments may contain the same metals or ions in their composition, thus hampering the identification of some of the pigments.

Research aims and methodology

The first main objective of this study is to identity the pigments and dyes used by Pousão at different stages of his career, i.e. to establish his palette. This contributes to the

[4] This study was undertaken when some of the paintings belonging to the collection of Museu Nacional Soares dos Reis, Porto, were transferred to this laboratory to undergo a conservation intervention.

[5] This study was not published, but a summary of the results of pigment identification is presented in Appendix A.

understanding of both materials and technique used by the artist, by constructing a database for future reference purposes, such as authentication and, at the same time, helps to assess the state of conservation of the paintings.

Due to the complex nature of the samples of Pousão's paintings, which are composed by several layers, each layer in turn composed by a large number of pigments (as shown by the 1984 study), the need for a multi-technique analysis became immediately evident. In addition, in order to analyse each layer of the intricate multi-layered structure of Pousão's paintings, some of the analytical techniques to be employed should be invasive (involving sample collection) and microscopic, as the painting samples are of reduced size. Since the analytical process is interactive, because new results, either confirm or reject previous ones and new questions can arise, it was decided to start this study using two main analytical techniques, and to employ other analytical techniques, whenever necessary, geared to the specific questions to be answered.

A wide range of techniques has been used for pigment and dye analysis, some of the most common being: HPLC [22,23], IR and μ-IR [24-26], LIBS [27,28], PIXE [29-31], PLM [27,32], μ-R [10,33,34], SEM/EDS [35], SIMS [36-38], XPS [39-41], XRD [42,43] and XRF [44-46].

Among others, IR has been a well-established technique for about 50 years and one of the most widely applied to pigment identification and to the characterization of artworks' materials [26,47,48]. With the development of infrared microscopes, infrared microscopy (μ-IR) became much more suitable for the analysis of artworks' samples which are, in general, of reduced size. μ-IR offers several advantages, such as high specificity for both inorganic and organic compounds, good spatial resolution and the existence of comprehensive spectra databases of pigments and other materials used in artworks.

Due to its advantages and to the fact that it was available in-house (LCRJF), μ-IR was chosen as one of the two main analytical techniques for this study.

On account of its high spatial and spectral resolution, excellent sensitivity and molecular specificity and, most importantly, because it can be applied to samples non-destructively[6]

and to objects non-invasively and *in situ* [34], Raman microscopy (μ-R), among all the techniques used for pigment identification, has been the object of special interest. In fact, this technique has been considered to be the best single technique, among a large number of other techniques, for pigment identification [32,49,50]. However, until the publication of the first results which came out of this research [51], relatively few studies had been published on the analysis of wood panel and canvas paintings by μ-R [34,52] and fewer on the analysis of cross-

[6] Generally, the μ-R analysis does not produce destruction or alteration of the samples. In spite of the laser radiation may cause sample degradation, in general, there are ways to avoid it.

sectioned samples of this type of paintings [53,54]. In fact, even today, the number of publications on these topics is relatively small [55-58].Therefore, no conclusions about the suitability of this acclaimed technique (not available in-house) for the analysis of Pousão's paintings could be drawn.

Since μ-R is non-destructive and, furthermore, complements μ-IR, it was decided to test its advantages for pigment identification on the samples under study, especially in order to evaluate the possibility of purchasing μ-R equipment by LCRJF. As the first results turned out to be very encouraging, μ-R was chosen, in conjunction with μ-IR, as the main techniques for this study.

Although very helpful and used to examine all samples, OM was not considered a main technique in this study, since it was only employed to examine the stratigraphy of the samples and not to identify the pigments.

In order to address questions raised during the μ-IR and μ-R analysis, three auxiliary techniques, namely SEM/EDS, μ-XRD and FM were chosen, based on their suitability to the questions to be answered, accessibility and cost.

The complex nature of the samples under analysis constitutes a challenge to any analytical technique. Their study makes it possible to test the efficiency of different analytical techniques for pigment identification in oil painting's stratigraphic samples, especially of μ-R, which has not been significantly tested, as well as to compare their efficiencies for this purpose.

Therefore, the second main objective of this study is to evaluate how efficient μ-R is for pigment identification in oil paintings' cross sections and how it compares with μ-IR efficiency for the analysis of such samples.

This research is focused on the examination and analysis of 23 paintings by Pousão (Appendix B), painted between 1880 and 1884. The paintings are owned by the Museu Nacional de Soares dos Reis, Porto, and their authenticity is not questioned.

Thesis outline

This thesis is structured in 9 chapters plus 7 appendices. Chapter 1 presents a short biography of Henrique Pousão and major information regarding his work. Chapter 2 provides a brief introduction to the structure and composition of easel paintings and also a survey of some of the most frequently employed analytical techniques for its analysis. This chapter targets especially those outside the field of art, providing an insight into the making of

paintings and their analysis. Chapter 3 reproduces the paintings under study and describes the sampling procedures.

Chapter 4 provides a brief introduction to OM and presents the major results of the analysis of the cross-sectioned samples obtained by this technique. Chapters 5 and 6 are devoted to μ-IR and μ-R, the core of the analytical techniques of this project. Chapter 5 provides a brief introduction to these two vibrational techniques, which share the same theoretical background. Chapter 6 presents the results of the analysis of the paintings' samples by μ-IR and μ-R. The results and discussion are presented separately for each technique, μ-IR followed by μ-R, in order to analyse the major advantages and limitations of each one for the identification of the samples' components. At the end, a comparison of the efficiency of μ-IR and μ-R for the referred purpose is outlined. Chapter 7 presents the results of the analysis of some of the paintings' samples obtained by the auxiliary analytical techniques: SEM/EDS, μ-RXD and FM, employed to answer some questions raised during the μ-IR and μ-R analysis. In this chapter, a discussion of the main advantages and limitations of the auxiliary techniques for the analysis of the samples under study, as well as a comparison of these results with those previously obtained by the microchemical tests are also outlined.

Chapters 8 and 9 report the most important findings on Pousão's palette and technique. In chapter 8, targeting basically those outside the analytical field, an overall discussion of the analytical results presented in the previous chapters is undertaken. Additionally, a comparison of the final results with art history information about easel paintings and information culled from studies on other painters is sketched out. Finally, chapter 9 summarizes the main conclusions of the current work, either concerning the samples, or the employed analytical techniques. The thesis concludes by lining up some suggestions and guidelines for future work.

1 On Henrique Pousão

A sua obra [...] podendo sugerir muita 'literatura', em boa verdade, não aceita nenhuma. Existe por si, vive por si, fala por si.[7]

M. Figueiredo

This chapter presents a brief summary of the most relevant aspects of life and work of Henrique Pousão.

[7] His work […] suggesting a large number of 'literature', truly does not accept any one. Exists by itself, lives by itself, speaks by itself.

1.1 His life

Henrique César de Araújo Pousão (Figure 1.1) was born on 1 January 1859 in Vila Viçosa, Portugal, son of Francisco Augusto Nunes Pousão and Maria Teresa Alves de Araújo, who died victim of tuberculosis when Pousão was only three years old.

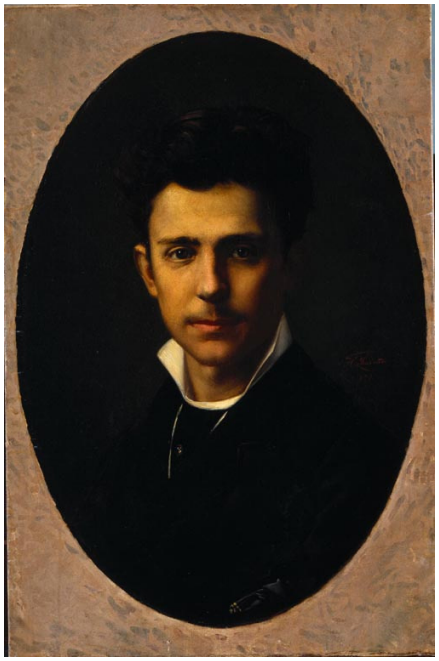

Figure 1.1 ***Pousão, auto-portrait***. 1879. Oil on canvas, 78.5 x 51.7 cm (MNSR Invº 89). Photo: Museu Nacional Soares dos Reis, Porto

He was eight years old, when, drawing an oil lamp globe, he revealed his skills, which his father encouraged, inscribing Pousão in a local classroom.

In 1872 he moved to Porto (to the house of a father's friend, Engº Evaristo Nunes Pinto) to frequent the atelier of António José da Costa (1840-1929), in order to prepare himself for the admission to the Academia Portuense de Belas-Artes, where he gets matriculated, in that same year, on a general course. Pousão proved to be a brilliant student, wining several prizes and honours and in completing the course in 1879.

In 1880 he wins the competition for a shoralship to study abroad in the landscape class (a speciality where he had no information neither experience) and moved to Paris. Arriving there, at the end of that year, he frequented the atelier of Alexander Cabanel (1823-1889) and worked intensely preparing himself for the examinations to enter to the École des Beaux-Arts (February of 1881), where he was admitted in 35th position out of the 70 entrants from 234 participants. At the École he frequented the atelier of Adolphe Yvon (1817-1893).

Supposedly, it was during one friezing morning that he went out to work that he got sick [59] being diagnosed with bronchitis. Therapeutically advised, he went to the watering-place La Bourbole-les-Bains, in Puy-de-Dôme, where he spent two months. However, his health did not improved and following a further medical suggestion, he moved to Rome that presents a more worm winter than Paris, at the end of 1881.

Although constantly moving between Rome, Naples, Pompeii, Capri and Anacapri, Pousão produced a largest number of paintings, including, some of his best paintings.

Despite every effort Pousão's health still failed to improve and consequently, he requested permission to return to Portugal. Although the trip was fatiguing, he painted all the way home. Back in Portugal, he stayed in the house of a cousin, in Vila Viçosa that presented a more favourable weather than the village where his father lived in. His health kept deteriorating, to the extent that he spent most of his time in the bedroom, where he painted his last works, before dying on 25 March 1884, victim of tuberculosis [20,59-63].

From the few references to his personality, it stands that Pousão was shy, modest, discrete, kind-hearted, with homely habits and devoted to work to the point of jeopardise his health [59,64].

1.2 His work

Despites is brief life, Pousão's work is composed by a considerable number or easel painting, covering a variety of subjects, from female nudes to elderly women, from bouquets of flowers to flowing country landscapes, and a large number of facades, streets and stairs (see, Appendix B) [20].

Pousão is now fully accepted as one exponent of Naturalism together with Columbano (1857-1929) and Malhoa [65], although the very particular expression found in his paintings had generated an open controversy between "impressionist Pousão" defended by Abel Salazar and Brás-Burity and "Mediterranean Pousão" defended by Diogo de Macedo [20,66].

Naturalism is an important movement of the 19th century that represents the transition from Romanticism to Impressionism. Its main characteristic is the use of the natural world as a direct source of artistic inspiration, not meaning a simple copy [62]. Landscapes, urban and rural scenes, habits, customs and portraits were some of the images captured by painters. Although some precursors can be referred, Naturalism arrived in Portugal in 1879 with Silva Porto (1850-1893) and Marques de Oliveira (1853-1927), the first scholars in Paris. The second generation of naturalism painters includes Artur Loureiro, Sousa Pinto and Henrique Pousão [62].

Unfortunately, if there is few art-historical literature devoted to Pousão, there is even less devoted to the materials he used in is paintings. His letters revealed nothing about the materials and technique [63] and, besides a report that part of his brushes and paints were left in Italy, where he was hoping to return after recovering is health [59], there is no other information source[8].

Often it is difficult to trace the history of a painting and even of its authenticity, as it passes from one collection to another over the years and even over the centuries. In fact, it is not uncommon to hear that a forgotten work by Picasso or Rembrandt was discovered, which sometimes is true, others not [11]. In the case of Henrique Pousão, however, the scenario is different, since most of his work has a known history. Some of the paintings were sent by Pousão to the Academia Portuense de Belas-Artes as proof of his improvement (academic test-pieces for schorlarship) and others were bequeathed to the same academy by his family, following his father wish [20,59]. The paintings were then transferred to Museu Nacional Soares dos Reis, in Porto, where they remain until nowadays.

Other works can be found in private collections, such as Paço Ducal in Vila Viçosa, Câmara Municipal de Vila Viçosa, Museu Nacional de Arte Contemporânea, Lisboa, Casa-Museu Anastácio Gonçalves and Escola Superior de Belas-Artes do Porto.

Scientific analysis

The only known scientific analysis of Pousão's paintings was the study conducted at Laboratório de Conservação e Restauro José de Figueiredo, Lisbon, in 1984, when some of the paintings belonging to the collection of Museu Nacional Soares dos Reis, Porto, were transfered to that laboratory to undergo a conservation intervention.

[8] There is a personal information that the archive of the shop were Pousão probably bought his materials (in Porto) still exists, but unfortunately, has not been researched.

2 Easel paintings: structure, materials and analysis

To achieve a certain degree of 'interpenetration of disciplines' some knowledge of each other's 'language' is required.

J. R. J. van Asperen de Boer

A previous comprehensive understanding of the painting structure and technique of analysis is essential to obtain the maximum information. This chapter provides a brief introduction to the structure, materials and analysis procedures of easel paintings, as well as a survey of the most frequently employed analytical techniques for its analysis.

Paintings are a relevant part of our cultural and artistic heritage. Although nowadays paintings are seen as an ornamental/decorative work, a large number of them have been executed with a definite and different purpose. Among many others examples, the wall paintings of the pre-historic cultures seem not have been painted to decorate the cave walls, since it is thought that these cultures believed that those paintings had a special power; and the biblical paintings, besides other purposes, were also used by the Catholic Church to teach those who were analphabetic [(67)].

Although visualised as a two dimension work (image), a painting is in fact a complex three-dimensional structure, created as the artist works up successive layers to develop subtle effects of tone, colour and surface structure. It may even involve a process of revision of the initial subject or a painting process over an unrelated image[9] [(12)]. Consequently, each painting is unique and a result of several factors, such as painter's education, painter's creativity and skill, painter's choice of materials and method, availability of materials and influence of the environment that surrounds the artist [(11)].

In the last decades the analytical studies of easel paintings has significantly increased. However, because easel paintings present an intricate multi-layered structure, colouring materials are presented in very small amounts and thoroughly mixed with many other compounds, their analysis represents a challenge for any analytical technique.

2.1 Structure and materials of easel paintings

When the paintings are not attached to an immovable object, being therefore portable, they are designed as easel paintings. Otherwise they are designed depending on of the type of support, such as for example, wall paintings, when painted on either walls from an architectural setting or natural cave walls, ceiling paintings when painted on ceilings[10]. Although there are several characteristics in common for all types of paintings, we will focuses on the structure and materials of easel paintings, since they are the ones under analysis in this study.

An easel painting is generally a very complex system. However, it presents a broadly similar layered structure composed by four main parts: 1) support, 2) ground layer, 3) paint layer(s) and 4) varnish layer, which can be seen in Figure 2.1. Further layers, such as additional paint and varnish layers applied by the painter, other painters or restorers, or layers of dirt and pollution can also be found.

[9] Alteration and amendment of works according to the in style, vogue or religious constrictions were very common.
[10] Wall paintings and ceiling paintings are commonly designed as mural paintings.

2.1.1 Support

The support, as its name indicates, is the structure over which the painting is produced. In the case of easel paintings, it can be a rigid material such as a wood panel, stone, metal, glass, ivory and plastic, or a flexible material like fabric - frequently canvas, leather or paper [11,12]. Canvas refers to fabric supports (linen, hup, cotton) that are stretched, either in the old wood strainers or in the wood stretchers [68].

In order to obtain a plain surface for the painting and ensure its preservation, the support is usually previously prepared applying a sealant, known as *size* and/or one to several ground layers, although exceptions are found.

Size

Because fabric support is very absorbent, it is normally impregnated with a sealant, known as *size*, whose function is to prevent the penetration of binder (and vehicles) from the ground and paint layers into it, as this can have a deleterious effect causing the weakening of the painting and shrinking the fabric to a taut, smooth membrane. Usually, size is diluted glue made from animal skin glue, but parchment glue, glue extracted from gloves and starch, were also used [11].

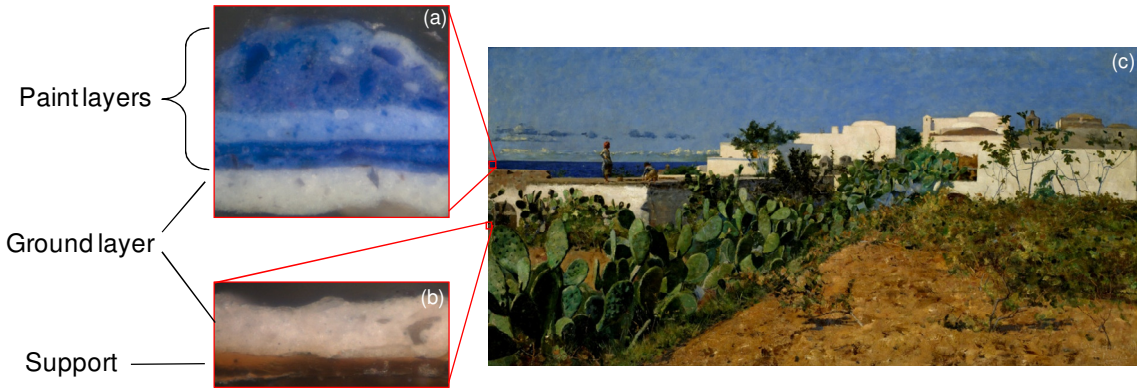

Figure 2.1 (a) Cross section[11] of a sample removed from blue of the sea, viewed under reflected light. 5 paint layers and a white ground layer are visible; (b) cross section from a sample removed from the end of the canvas, viewed under reflected light. The white ground layer and the canvas support are visible; (c) **Casas Brancas de Capri**, 1882 (MNSR Invº 82). Oil on canvas, 70.5 x 141.0 cm.

2.1.2 Ground layers

Like the *size*, the ground layer also protects the support from the adverse effects of binders, blocking the absorption of the binder into the support. However, the ground layer has other main functions: i) to fulfil the irregularities of the support living its surface plain; ii) to

[11] See page 22.

create an elastic base for the paint layers; iii) to assure the adherence between the paint layers and the support; iv) to act as a reflective surface beneath the paint film and v) determine the tonality of the whole painting.

These layers were applied either by the artist himself, by a pupil, a collaborator or by an independent primer, but from the 15th century onwards, supports could be bought already grounded [11,12,68]. Except for the paintings of 16th to 19th centuries, when coloured grounds (red, brown, yellow and green) were also used, the ground layer has generally a white colour, produced by gypsum or calcite with animal glue or lead white with oil.

Imprimitura

It is referred as *imprimitura*, a coloured isolation layer (pigments bound in oil medium), that covering the whole surface of the ground layer, reduces its absorbency and provides it with a colour (which can also be white).

This term is used to refer to the layer applied over a calcite or gypsum ground that prevents the medium in the subsequent paint layers of being absorbed by the ground layer, or in the case of more than one layer of distinct colour, to refer to the upper layer, which is the one that generally determines the tone of the painting.

The term 'double ground' can be used to referrer to the simultaneous presence of a ground layer and an *imprimitura* [69].

Underdrawing

To help in the paint execution, the painter might outline over the ground layer the design to be painted, using charcoal, black chalk, or using a pencil and an aqueous animal or vegetal black paint. As this drawing is covered by the paint layers, it is designated as *underdrawing* or *preparatory drawing*.

2.1.3 Paint layers

Paint layers are the coloured layers successively added in order to create the final image. Each paint layer is constituted by at least one colouring material (pigment or dye) dispersed into a binder, with or/without an extender, varying enormously, both in complexity and thickness.

Pigments and dyes

Pigments are known to have been used since prehistoric times, over 60,000 years ago, when natural ochre was used in the Ice Age as a colouring material. Although for a long time colouring materials were restricted to natural materials (minerals and plant or animal dyes),

synthesis of pigments started with about 2000 BC, with the burning of ochre, and from then to nowadays the number of the colouring materials has increased enormously [70].

We must refer that, although the word “pigment” is usually used to denominate the components we perceive as colour, independently of their origin (mineral, vegetal, animal or synthetic) and properties, in this context and according to the accepted standards, this word must be used only to denominate a substance consisting of small particles that is practically insoluble in the applied medium (binder) and is used on account of its colouring, protective or magnetic properties. The colouring substances that are soluble in the solvents and binders must be referred to as *dyes* [12,70].

Besides the “pure” pigments, which theoretically consist in a single compound, some pigments can consist in a mixture of compounds hence being referred to as mixed pigments. Mixed pigments, are pigments that have been mixed or ground with pigments or extenders in the dry state [70].

The specific selection of colours/pigments by the painter is generally referred to as his *palette*, which names also the rigid and flat surface on which the painter arranges and mixes paints.

Extender

Extender or *filler* is a colourless or slightly coloured substance, in a granular or powdered form that is insoluble in the medium in which it is applied just like pigments. However, an extender is not considered a pigment because it is not used with the purpose of a colorant substance. Extenders are used: i) to provide or modify the properties of the overall composition, such as viscosity, gloss, resistance to abrasion, resistance to weather conditions; ii) to increase its bulk (volume), forming a cheaper grade, iii) as a support for a lake and iv) to form ground layers [12,70].

Binder

The *binder* or *binding medium*, as the name suggest acts as a binding medium, promoting the cohesion of the pigment and the extender grains in each paint layer and a good adherence of each paint layer to the previous layer, after solidifying. Another function of the binder, while still liquid, is to allow the pigment to spread out.

It can be formed by animal glue, egg white, egg yolk, casein, linseed oil, walnut oil, poppy oil, plant gums, honey, starch, natural and animal resins, waxes and even a mixture of two of these, such as oil with resin or oil with egg [71]. By far, the most common binder is oil (linseed, poppy seed and walnut oil, being the most typical), which has long been considered the most versatile, as it presents a relatively slow drying, allowing colour mixing and the creation of

surface textures, and once dried, it forms a very durable, flexible and water resistant film. Solvents and additives, such as turpentine, lavender or spike oil, varnish, marble dust, waxes and resins have also been added to the binder in order to achieve certain properties [11,72].

Nowadays, a synthetic polymer, generally referred to as acrylic polymer emulsion, competes with the oil versatility, since the paints made with this binder, acrylic paints, have the ability to dry quickly producing a flexible film, and because water is used as solvent, there are no toxic fumes associated with the solvent and the cleanup of brushes and other equipment is much easier [11].

According to the binder, the painting is referred to as, for example, oil painting (oil), tempera painting (egg white, egg yolk), gouache and watercolor painting (plant gums), encaustic painting (wax with resin) and acrylic painting (acrylic polymer emulsion) [11,12].

2.1.4 Varnish layer(s)

Finally, the painting surface can be coated with a thin layer of *varnish*, which serves two primary purposes: i) to protect the paint film from dirt, moisture, pollutants, abrasions and UV radiation (if a UV absorber is present) and ii) to improve the appearance of the paint in accordance with the desired final visual effect. Reducing the scattering of the light, the paint surface becomes shinier and with increased colour intensity, but adding matting agents a less shiny paint surface is produced[12] [11,73].

Different components have been used as varnish. The most traditional were mixtures of a natural resin (dammar, mastic, copal, amber) with oil, or mixtures of resins, but plant gum or wax were also used [71,74]. Nowadays, varnishes are made of acrylic e vinyl resins that are easy to use. Unfortunately, varnishes can rarely be associated with a given artist since there is evidence that other artist or the restorer were often asked (by the purchaser) to varnish a painting for the first time [74] and, as it invariably discolour with time, it is often replaced by a new one to restore its original appearance.

2.2 Painting analysis

2.2.1 Introduction to conservation science

Based in two complementary approaches, analysis of documental sources and analysis of the object itself, a large knowledge about art objects, archaeologic samples and others with

[12] Painting's texture result of how light is reflected from the painting. A mirror like surface will reflect the light specularly, i.e. in the same direction and will appear shiny, while a rough surface will reflect the light diffusely, i.e. in a large number of directions and will appear matte.

significant historial value has been gained. Although analysis of documentary sources provides invaluable information, it is with the analysis of the object itself (and samples removed from it) or even related objects that a better understading is obtained. In fact, in the last decades, analytical techniques have been playing an increasing role on the conservation/restoration field.

In the first approach an art historian makes an exhaustive review of all the documental sources of information that can shed light on the investigation. These include, contemporary written technical sources, 'recipe books', surviving literature on painting process and materials (literature provides an insight into what the artists could have known about the materials, had they cared to seek it out and the opportunity to choose[13]), archives of artist's colourmen (buying notes), artist's correspondence (as is the case of Millais), contracts, diaries (as is the case of Ford Madox Brown), inventories of the studio contents by them death, unpublished papers, exhibition catalogues, records of natural accidents, records of transformations either due to changes of tastes, natural accidents or intervention [(74,75)].

The second approach, making use of the most diversified analytical techniques, from more traditional to more sophisticated ones, studies: the nature of the materials that were employed in the artwork or are a result of an alteration of the original materials, the methodology of application, possible alteration processes and most suitable intervention methods and materials. Besides the artwork itself, surviving materias, such as paintboxe(s) (as in the case of Columbano Bordalo Pinheiro) [(76)] or palette (as in the case of Turner) are also analysed.

The overall objectives of the analysis are [(12)].

1. determination of the materials and their application technique for dating, geographic localization, assigning to a painter, school, period, or region, and authentication;

2. diagnostic degradations/alterations and the study of associated sources and processes (e.g. accidents, previous conservation interventions, pollution). Recognising degradation process is fundamental to understand if a particular effect that the object presents nowadays was sought by the artist or is the result of a degradation process;

3. determination of the most correct preservation conditions;

4. determination of the most suitable intervention method to avoid complications or damage resulting from the treatment itself. Stability, reversibility and secondary effects of the materials used for the treatments are evaluated.

[13] With tube paints, artists no longer controled what they were using; Altough theory treatises, manuals and handbooks dealing with painting process and materials discourage the use of fugitive pigments, analytical results often demonstrate its use [(74)].

2.2.2 Analytical analysis

According to a published document [77], the earliest chemical analysis of paint samples seems to have occurred in 1781, when Johann Friedrich Gmelin, a pharmacist, identified the pigments of an Egyptian sarcophagus by the addition of various reagents, heat and flame.

Although after 1800 the majority of published analysis of painting materials was performed by pharmacists or chemists, some of the most eminent, such as Louis Nicolas Vauquelin (1763-1829), Sir Humphry Davy (1778-1829), Michel Chevreul (1786-1889), Michael Faraday (1791-1867) and Jean-Baptiste Dumas (1800-1884), until 1880 the analysis consisted generally in the application of a series of reagents, reactions to heat and solubility tests, which required a considerable amount of sample[14] [77]. Nowadays, although normally not developed specifically for this filed, almost every technique from any branch of science can yield some kind of information when employed for the study of an art object.

Ethic problems

Due to the high value of most of the artworks, several ethical problems have been raised regarding their analytical analysis. Firstly, there is the idea that the analysis of an artwork is the scrutinizing of it in every physical aspect and presenting it as a sum of analytical results, what reduces its magic and mystery. Secondly, there is a serious concern about alteration of the works by the analytical method, especially, if sampling (sample removal) is necessary.

Fortunately, the issues surrounding sampling, such as reasoning, methodology and ethic are formalised, from some years to now, into a code of ethics, as for example, the American Institute for Conservation (AIC) [78,79]. According to this code, samples are only removed if some kind of information can only be obtained by removing and analysing samples; the owner/custodian was informed about the need and the impact of sampling; samples are retained to allow future testing, either to replicate the results, to utilize new techniques, or to obtain additional information; the size of the sample must be the minimum required for current testing purposes [78]. Because samples are generally removed from edges or lacunae (areas of loss), and are characterized for having a microscopic size, much smaller than the detached flakes (detachment) often released from paintings, it has been recognized that the damage done by sampling is balanced with the information that their analysis can provide [78].

In fact, sampling presents some advantages. Firstly, it is possible to conduct stratigraphic analysis, i.e. to analyse independently each layer that constitutes the art object, secondly, it is not necessary to take the art object out of the holding building, which involves extreme insurance values, or moving the analytical equipment from the laboratory to the holding

[14] Samples had to be washing, dissolved and filtrated.

building, which, in the very few possible cases, generally requires a careful calibration and handling, and thirdly, more than one analytical method can often be employed, providing a much more complete analysis.

With the development of new techniques and analytical methodologies that are less and less invasive (producing less alteration), analytical analysis and consequent scientific studies is gradually gaining credibility and becoming commonplace.

Sampling

Sampling and sample preparation (if necessary) are integral and crucial parts of every analysis process, being tailored in accordance with the type of sample and the analytical technique to use.

As in any other field, sampling is conducted with the expectation that it will be representative of the area sampled, if not of the object itself. However, as a result of several factors such as: i) the artist's technique, ii) the artist's habit of cleaning the brush on the edge of the painting, iii) past conservation interventions, and iv) sampling restrictions[15], this does not always happens. To ensure representativeness of the results, sampling points should be carefully selected based on the results of non-invasive investigations, while a proper documentation of the points is also a critical factor for the correct interpretation of the analytical results [(80)].

Care must be taken during removal, storage, preparation and analysis of sample to prevent contamination and loss.

The amount of sample to be collected must, of course, be as small as possible, in order to avoid any visible damage to the artwork. This generally does not constitutes a problem for a large number of analytical techniques, such PLM, μ-R and μ-XRD, since a sample of ca. 0.1-0.5 mm^3, or 1 μg (dimensions of a typical layered paint sample mechanically removed using a scalpel) is more than enough and the gap left is almost invisible to the naked eye [(75,81)]. However, the minimal sample size is not equal for all analytical techniques, hence a concession between the allowed sample size and the size requirements of the technique to be used must be established.

Depending of the questions to be answered and of the analytical technique to be used, samples can be of three different types: *cross sections*, *particles*, and *swabs*.

[15] Due to the artwork value and conservation/deterioration state, number, size and localization of samples is normally very restricted.

Cross sections

Cross sections (or cross-sectioned samples) are samples with multilayers. These are obtained cutting extremely reduced samples of the object from the top down to the bottom, under magnification, using a scalpel, and can contain some or all the layers of the object. These samples are used to study the number and sequence (*stratigraphy*), condition and interaction of layers, painting technique, and for solubility, melting point and composition determinations.

Because cross sections, especially those removed from paintings, can present a heterogeneous and fragile consistency (besides the reduced size), whenever it is necessary to handle them for examination or sectioning, they must be previously mounted in a support material, most commonly, a resin[16], that will hold it together. The choice of the embedding material is very important, and depends on the sample and the analytical technique [(80)]. After the curing of the embedding resin, the surface is grounded down until the complete sample's stratigraphy reaches the surface to allow its analysis and then polished to reduce the scratched finish and make the exposed layers to a fine shine to be observed under the microscope [(80)] (Figure 2.1 a and b).

For transmission techniques, where the samples have to be thin enough to allow the passage of light, cross-sections are prepared as *thin cross sections*/*thin sections* (Figure 3.5b), which are simply thin slices (0.1 to 30 µm thickness) of the cross-sections. After the curing of the embedding resin, these can be sectioned: i) by hand-cutting, which is useful for sampling large materials, ii) using a microtome, or iii) grinding and polishing, which is useful for hard and brittle materials that cannot be embedded and/or microtomed [(80,82)]. Chapter 4 presents additional information regarding cross-section and thin section preparation.

Particle samples/isolated particles

Particle samples are samples that are only a portion of a particular layer and are used mainly for solubility, melting point and composition determinations. They can be obtained scrapping the surface of an exposed layer using a scalpel or a probe, or they can also be removed from a layered sample [(80,81,83)]. Unfortunately, this last procedure is time consuming and very difficult, if not impossible (unless the layers are very large), leading normally to the missing of small layers and seriously misunderstandings.

Particle samples are often prepared as dispersions (dispersion samples) for individual crystal characterization by PLM. Samples are crushed and separated for the analysis of component particles, transferred into a microscope slide with a small amount of a mounting medium of appropriated index of refraction and cover with a cover glass [(81,84,85)].

[16] Other types of support can also be used, such as cork, plastic sheets, soft metals and even carrots [(82)].

Swabs

Swabs are a particular case in which solvent-dipped swabs are used to rube the artwork surfaces and collect solvent-soluble coatings, such as patina or varnish [80].

2.3 Analytical techniques

2.3.1 Classification

Based on the impact that they have on the object, sample, or on their representativeness, the analytical techniques used in conservation science can be grouped into the following classes: *invasive*/*non-invasive* analysis, *destructive*/*non-destructive* analysis and *point/area* analysis [12].

Invasive/non-invasive are terms used to refer to the impact that the analytical method has in the object itself. *Invasive* stands for the analyses that require sampling, producing some alteration to the object, while *non-invasive* stands for analyses that do not require sampling.

As easily understood, preservation of the artwork (minimum alteration as possible) is the ultimate goal in any scientific study in this field. Consequently, non-invasive techniques are preferred and used in first place, while sampling is performed only when absolutely necessary and allowed.

Unfortunately, in general, non-invasive methods provide no discrimination between the layers that constitute the object and often restrict the analysis to the superficial layer(s). In cases, when specific answers will not be obtained by the non-invasive techniques, invasive techniques can be used right away, saving time and funds.

Although initially *destructive/non-destructive* was a term used by curators/conservators with the same meaning that *invasive/non-invasive* have nowadays, causing confusing and misunderstandings, since for analysts it has a different meaning [75], these terms are used to refer the impact that the technique has on the samples. *Destructive*, presumes alteration/consume of a sample during its preparation and/or analysis. *Non-destructive* means that sample does not suffer any kind of preparation and that is not consumed or changed during analysis.

Regarding its representativeness, an analytical technique can be classified as an *area* or *point analysis*. *Area analysis* is generally used to refer to the analyses that study the object as an all and are mainly photographic and surface mapping techniques, while *point analysis* is used to refer to analyses performed in a simple point or reduced area [12,86]. Although, initially, *point analysis* was related to the analysis of samples, nowadays it is possible to perform *point analysis* without sample removal, for example, with μ-XRF and μ-R.

Analytical techniques can be further classified based on the type of interaction with the sample, such as spectroscopic, chromatographic and thermal, or in the type of information they provide, such as elemental, molecular and phase transitions.

2.3.2 Methodologies and analytical techniques for painting analysis

As we have seen before, a painting is composed by a variety of materials, including, support, pigments, extenders, binder and varnish. The analysis of these materials and the way they were combined to build up the painting can provide valueless information. Some of the most used analytical techniques for painting examination and analysis are presented below.

Whatever the type of painting or questions to be answered, the first analysis of a painting is visual examination by an art historian, curator or conservator, which will detect alterations and/or interventions on the painting [12]. The next stage is normal photography, a non-invasive method, which is used to document the painting, the state of the painting and evaluation of the treatment processes and mark the sampling areas in the cases in which samples will be removed.

The range of analytical techniques currently available for conservation science is broad. However, since each technique has gives own type of information, suitability, strengths and weaknesses, a previous assessment is essential to avoid a disorientated and useless examination. Moreover, since no single analytical technique can determine the full composition and/or structure of an object and provide valuable conclusions, a compliance of the results from several complementary techniques must be employed.

A few works already presented an overview of different analytical techniques often used in conservation science [3,9,11-18,86], while other works presented a comparison among several analytical techniques [9,14,33,49,87]. Some of the most frequently used analytical techniques for the analysis of paintings (conservation science in general) are succinctly presented bellow.

Photographic techniques

Using different types of illumination, such as ultraviolet, grazing light and infrared, certain details of the art object or painting, which most frequently are hidden to the naked eye, are pointed out, without actually touching the object, i.e. in a non-invasive way.

For example, *Ultraviolet Fluorescence Photography* (UVF), which is based in the fact that an object subjected to ultraviolet light emits light in the visible region (fluoresce), is used in restoration interventions for varnish removal and for identification of the restoration areas. While an old varnish is strongly fluorescent (the resin that compose the varnishes develops fluorescence as they age), a recent restoration area and a varnish free surface will appear

dark against a fluorescent background. That technique is also of great help for identification of: i) the medium, as some natural materials such as drying oils, resins, waxes and proteins tend to develop distinct fluorescence, which increases with age and ii) the pigments employed in the upper paint layer, as a reduced number of pigments, such as zinc white, madder lake and Indian yellow, present a characteristic fluorescence [11,13,88,89].

As another example, when Grazing Light (GL), obtained setting the light source at a 5-30º angle with the painting, is used, the produced photography reveals the roughness and the irregularities of the painting surface, allowing an evaluation of the state of conservation of the painting. Lifting cracks in the paint, deformations and lack of adhesion and, sometimes, changes that an artist has made in paint, can be identified [12,90,91].

Other photographic techniques are: *Ultraviolet reflected photography* (UVR), less employed than UVF, this technique is useful for the identification of restoration interventions, pentimenti[17], and to distinguish between white pigments, *Infrared Photography* (IR), which proved to be useful to reveal underdrawings, though not as efficient as Infrared Reflectography (see below), and *Infrared False Colour Photography* (IRFC), so called because the green areas appear as blue, the red areas appear as green and the near infrared information appears as red, which has been useful for distinguish between blue pigments [13,75,86,92].

Infrared Reflectography (IRR)

Because near-infrared photon are not completely absorbed by most pigments, and consequently the paint layers are relatively transparent to it, this radiation penetrates the upper paint layers until it is absorbed by the carbon-containing pigments used in the underdrawings (the remaining radiation is reflected by the ground layer). This non-invasive technique has been effective for observation and evaluation of underdrawings and consequently, to study the working method, retouchings, pentimenti and also, hidden signatures [11,13,93,94].

X-Radiography (XRR)

The process is similar to that of medical x-radiography. Because x-rays are so intense, they can pass through a painting (or other object), being more or less absorbed by the materials that constitute the painting, depending on their atomic weight (electron density). Dense materials, i.e. materials with a high electron density, such as those containing lead or mercury, absorb more strongly the x-rays. Consequently, the corresponding area on the

[17] Changes in the composition made during the process of painting, such as, for example, reconsidering a figure's pose.

photographic film that is placed below the painting and that, when exposed to X-rays produces dark areas, will appear white. Low electron density materials, being more transparent to the X-rays, allow these to reach the film and produce grey or black areas. As the X-rays are scanned, an image of the painting is produced (Figure 2.2).

Figure 2.2 ***Rapariga de Anacapri*** (MNSR 200), 1882, oil on canvas, 18.5 x 13.8 cm: (a) photography; (b) X-radiography, where it is possible to see the wooden stretcher frame, the metal staple securing the fabric to a wooden stretcher and restoration areas (black areas). Photo and radiography: LCRJF.

X-radiography is a non-invasive area analysis technique that quickly and cost effective, enable to view the form and structure of the all painting and details of construction. It is possible to visualize the wooden stretcher frame, the nails securing a fabric to a wooden stretcher, alterations to size, and format of the support (e.g. union of panels or canvas), structural anomalies, lacks, insect attack, pentimenti, how the composition evolved, restoration areas and widen signatures [11-13,81].

X-ray Fluorescence (XRF) and Particle-Induced X-Ray Emission (PIXE)

Both X-ray fluorescence (XRF) and particle-induced X-ray emission (PIXE) are based in the induced emission of x-rays. Whenever atoms are bombarded with energetic photons or particles, such as X-rays or protons, characteristic x-ray energies are emitted from the atoms, allowing the identification of the elements present in the area of analysis. These two atomic spectroscopic techniques have the significant advantage of being non-invasive [11].

For XRF analysis there are portable units that eliminate the problems related with moving the painting out to the laboratory. However, this technique is subject to some intrinsic limitations: i) owing to the low fluorescence yield and low energy (fluoresce is absorbed by the sample itself) of elements having atomic number <14 (silicon), they are very difficult to detect in air (fluoresce is absorbed by air), ii) only a semi-quantitative analysis can be made due to matrix, iii) information is gathered simultaneously from all the paint layers, not

discriminating the elements present in each layer due to the penetration of X-rays and iv) the diameter of the X-ray spot is about 1 cm, thus a large area is simultaneously analysed [19,95-97].

In recent years, the development of high performance μ-XRF techniques, such as, synchrotron radiation induced micro-X-ray fluorescence Spectrometry (SR-μXRF), have revolutionised the capabilities of this technique [43], which is also capable of providing clearer and more detailed image of the hidden composition than the images obtained with XRR and IRR [98].

Unlike XRF, PIXE analysis requires the existence of a stationary particle accelerator (a highly expensive, massive installation) and the transport of the painting. However, it offers several advantages regarding XRF, such as a better spatial resolution (up to a few hundred of nanometres) [9,11], a greater sensitivity (up to 10 ppm for most elements) and, when differential measurements are conducted, elemental stratigraphic analysis [30,99].

Unfortunately, the techniques based in the use of X-ray fluorescence and emission can induce damage in the organic components of the samples, hence low flux, low power and short exposure time are required to minimize the extension of the damage [9]. Another drawback of these techniques is that they provide only information about the elements present in the samples, irrespectively of their state, chemical combination or the phases in which they might exist, thus, they are not able to distinguish among pigments with identical or, even, similar elemental composition.

Optical Microscopy (OM)

Optical Microscopy, also referred to as Light Microscopy, is probably the most used invasive technique in conservation science, since it provides valuable information regarding the paint technique and the materials that were used, in a relatively inexpensive way. Observing cross sectioned samples using a dark-field reflectance, information about the sequence (stratigraphy) and thickness of paint layers (detection of pentimenti and restoration layers), grain size and grain size distribution of the pigments is revealed. Regarding the compound identification, it requires a highly skilled operator and often fails to provide conclusive attribution [100]. Additional information about this technique is presented in chapter 4.

Using polarized light - *Polarized Light Microscopy* (PLM) - the crystalline compounds present in sample dispersions are identified by their unique appearance under that type of illumination. Essentially, a bright-field microscope with a rotating stage and plane-polarizing elements placed below (polarizer) and above the specimen (analyzer) is employed. In this

way, a crystal may be rotated and its refractive indices and birefringence may be determined along with other optical, physical, chemical and crystallographic properties [11,81,85,101].

Using ultraviolet light - *Fluorescence Microscopy* (FM) - interface of sample layers not visible under normal light, even those with similar composition, are visualised, helping in the identification of varnish, restoration and dirt layers. Based on the characteristic fluorescence that a small number of pigments exhibit, pigment tentative identification is also possible (as long as choices are limited) [32,78]. For additional information about this technique see chapter 7.

Reactions to heat (Thermomicroscopy [102]), solubility tests and staining[18] are other useful methods, conducted under a light microscope for identification of compounds, especially pigments.

Besides characterizing the sample, OM is also very useful for the selection of the following analytical technique and the most appropriated sample's area to use.

Microchemical tests

This invasive and somewhat destructive technique consists in the application of conventional 'wet' chemistry tests (chemical reactions that identify specific ions) in small clusters of particles or in layered samples, under a microscope. Using fine capillary, a liquid reagent is administered to the sample, that, by a specific chemical reaction (such as solubility tests, attack by acids and bases, calcination tests and reaction with specific compounds) produces a clear visible phenomena, such as colour change or fizzing, allowing the identification of particular elements or chemical groups [3,75].

Although relatively inexpensive and fast, these tests present a low capability to discriminate among the different materials within the same group [18] and, because they are based in elemental identification, they are not very suitable to differentiate among pigments with similar chemical composition [78].

Scanning Electron Microscopy (SEM)

When there is the need for greater detail that the one obtained with light sources by optical microscope, a scanning electron microscope is used. This microscope uses a narrow beam of electrons as source and provides topographic and compositional images at extremely high magnification (up to 10,000 times [103]). However, unfortunately the SEM images are monochromatic and must be assisted by a coloured photography to help interpretation.

[18] The majority of stains that have been applied to binder analysis stains, usually applied as solution, when reacting with a specific compound (most commonly with proteins or lipids) produce a visual effect that allows the identification the binding media. Unfortunately, only an idea of the general class of binder is provided [11,78].

When SEM is associated with an X-ray spectrometer that detects the X-rays emitted when the electron bean interact with the sample (SEM/EDS), determination of the elemental composition of tiny details, such as pigment grains and X-rays maps of the elements is possible, making this technique a very powerful tool [103-105].

Because this technique requires the removal of samples from the object, it is invasive, and because nonconducting samples have to be coated with a carbon or gold to avoid charging it, is also somewhat destructive. Additional information about this technique is presented in chapter 7.

X-Ray Powder Diffraction (XRD)

This is a highly specific technique for identification of solid compounds. However, since it is based on the diffraction of the x-rays by the crystalline structure of the compounds, it is limited to compounds with low crystallinity and not applicable to amorphous compounds.

When a monochromatic X-ray beam impinges on a crystal whose lattice dimensions are in the same order of the wavelength of the X-rays, diffraction of the beam occurs and a diffraction pattern is produced. The pattern obtained is very characteristic and is compared with those of standard for identification purposes [95,106,107].

In the traditional set-up, sampling is required and the sample (some grams) has to be reduced to a fine powder, eliminating any stratigraphy that it might have (invasive and destructive technique). In the microscopic set-ups, micro X-ray diffraction (μ-XRD) and synchrotron radiation induced X-ray diffraction (SR-XRD), objects can be analysed without sampling (non-invasive), as long as they fit the stage, and samples can be analysed without any preparation (non-destructive), as cross-sections or as thin sections [43,108-110]. Additional information about μ-XRD is presented in chapter 7.

Infrared Spectroscopy (IR)

Infrared spectroscopy (IR), also referred to as Fourier Transform Infrared Spectroscopy (FT-IR), since nowadays almost every IR spectrometer employs Fourier Transform (FT)[19] assisted interferometers, is a powerful molecular technique used for the identification of both organic and inorganic compounds and one of the most widely used techniques in the field of conservation science [3,26,48,87].

This technique is based in the fact that, when a beam of IR light, emitted as a range of frequencies (from a heated object) is incident on molecules/ions, absorption of discrete frequencies of the beam by molecules/ions takes place. This occurs because the chemical bonds present in molecules and ions are elastic, and the atoms they connect are constantly

[19] Fourier transforms is a mathematical process that transforms an interferogram into a spectrum.

vibrating (with a motion similar to that of a spring) around their equilibrium position with frequencies of the same order of magnitude of those of the IR radiation. When a frequency of the IR radiation is exactly the same of a particular vibration of the bond, it can be absorbed by the molecule/ion.

The selective absorbed or transmitted frequencies are graphically represented on an *infrared spectrum*, which is a plot of the intensity of absorption or transmission as a function of the frequency or wavenumber. Each spectrum is a very unique and characteristic pattern, which, by comparison with spectra of known compounds (reference spectra), can be used for identification purposes.

In a conventional set-up absorption/transmition mode, solid samples have to be reduced to a fine powder, which is then dispersed in a solid (commonly KBr) and compressed to form a pellet or dispersed in a liquid (commonly Nujol) to form a mull, or even dissolved into a solution, either way destroying the microstructure they present and requiring relatively large samples (1-3 mg) [(111)]. Therefore, conventional IR spectroscopy is not suitable for a large number of objects, whenever large samples cannot be removed or sampling is not allowed (is invasive and destructive).

However, the union of microscopy and IR spectroscopy - *Infrared Microscopy* (μ-IR) – originated a technique which allows the study of small and structured samples. In μ-IR, the samples are placed on the stage of a microscope that is coupled to the IR spectrometer, allowing the analysis of small samples (≈ 1 μg) without destroying their structure (since preparation of pellets is not necessary) and the analyse of specific areas of small samples [(83,112)].

When non-invasive[20] and/or non-destructive analyses are mandatory, instead of the transmission mode, a *reflection mode* is employed, which requires little or no sample preparation. The reflection modes can be of four types: specular reflection (SR), diffuse reflection (diffuse refection Fourier-transform infrared spectroscopy - DRIFT), reflection-absorption (R-A), and attenuated total reflectance (ATR) also called internal reflection spectroscopy (IRS) [(87)]. Specular reflection (SR), occurs when the incident radiation is reflected at the surface of the sample with an angle of reflection equal to the angle of incidence. Best spectra are achived for shiny surfaces, which requires the polishing of the sample if they do not have a lustrous surface [(82,87)]. Diffuse reflection (DRIFT) is based on the collection of radiation diffusly reflected by the sample, i.e. radiation reflected in all directions. However, because a significant amount of the incident radiation is, either lost in the sample, or specularly reflected, the efficiency of this mode is low (4 to 10%) and the bands can present distortion. In order to improve the efficiency, sample must be ground into small

[20] As long as the object can be placed on the microscope stage. Otherwise this technique is always invasive.

particles and diluted in a nonabsorbing matrix (such as KBr), which destroys sample's orientation and morphology [82,87].

Reflection-absorption (R-A) is based on the reflection of the radation by a nonabsorbing, reflective substracte (bellow the sample), such as a polished metallic piece. Depending of the angle of incidence R-A is divided in near-normal spectroscopy (12 to 35º) and grazing angle spectroscopy (65 to 85º). Both methods are advantageous for the analysis of films, the grazing angle spectroscopy in particular, for the study of sub-µm-thick films. Until nowadays, these methods had no significant employement in conservation science.

Attenuated total reflectance (ATR) is based on the phenomenon known as total internal reflection. When radiation passes from a high refractive index medium into a lower refractive index medium, part of the radiation is reflect and part is refracted. However, if the angle of the incident radiation at the interface of the two mediums exceeds a certain angle, referred to as the critical angle, the radiation is totally reflected from the interface. Yet, the electric field of the radiation (referred to as the evanescent wave) does penetrate the lower refractive index medium to a small distance and certain frequencies of the radiation can be partly absorbed. Therefore, the tottaly reflected radiation will be attenuated at the selectively absorbed frequencies, producing an infrared spectrum comparable to transmission specta.

An important advantage of ATR is the fact that the ATR crystal, which is a high refractive index medium, transparent to IR radiation, (also referred to as internal-reflection element (IRE)) has a magnification factor, allowing the analysis of even smaller areas [112,113]. Since it requires little or no sample preparation, and allows the analysis of small areas, ATR is probably the most used reflection method in conservation science.

However, ATR technique requires a good and uniform interfacial contact between the ATR crystal and the sample. Therefore, the ATR crystal has to be pressed over the sample or art object, and if too much pressure is applied, there is a high risk of the analysis becoming destructive or invasive. Another disadvantage is the fact that the cleaning of the ATR crystal is very tricky, easily causing its damage, while an inappropriate cleaning can cause cross contamination between samples.

A completely non-invasive, non-destructive approach, even *in situ*[21] (if a portable spectrometer is used), is obtained employing Fibre Optics Reflectance Spectroscopy (FORS), which consists on the coupling of fibre-optic probes to FT-IR bench unit [114-115]. This method allows the analysis of delicate and fragile objects [116].

Because in all reflection modes, the objective works both as condenser and objective, i.e. half of the objective condenses the radiation on the sample and the other half collects the

[21] *In situ*, refers to analysis conducted at the location of the object, e.g. museum, church, tomb. The object is not moved, it is the equipment that is transported.

reflected radiation, reflection measurements are generally conducted with 50% less signal. As result, a reflectance spectrum will be more noisy and complicated than a transmission spectrum, requiring longer scan times and/or larger apertures [82,113]. Shifts in band position, variations in the band intensity and changes in the band shape can frequently occur [87,116].

μ-IR has been successfully used in painting analysis (conservation science, in general) [3,25,35,87,117], since: i) with a single equipment it can virtually simultaneously provide information about inorganic (e.g. pigments) and the organic (e.g. binder) compounds present in the sample. Virtually, because often pigments and other inorganic constituents partially mask information regarding the binder, sometimes to the point that the binder cannot even be generally identified, ii) small samples can be viewed and analysed and iii) a small area of a sample, such as a single layer of a multi-layered paint sample, can be selectively analysed.

Unfortunately, because many organic compounds have similar chemical compositions and/or structures, they present similar spectra, not allowing discrimination. However, IR is useful for the quick identification of the general class of the binder (for example, oil, protein, gum), without the request of sample solubilization, volatilization or ionization, as other techniques, such as gas-chromatography (GC), does [118].

More detailed information about μ-IR is presented in chapter 5.

The development of synchrotron infrared microscopy (SR-μIR), whose source produces highly collimated and high-brightness IR radiation, is a new promising for the analysis of small and complex samples, which require apertures below ~20 μm [119,120]. Coupling the IR microscope to a synchrotron source, a higher spatial resolution (down to a spot of 6 x 6 μm^2) and signal-to-noise ratio are obtained, when compared with the conventional μ-IR [121,122]. Unfortunately, the synchrotron sources (electron storage ring) are of limited availability due to their large size and high cost.

Raman Spectroscopy (RS)

Raman spectroscopy (RS) is an analytical technique that, like IR provides molecular information as a result of the interaction of light with vibrating molecules/ions that constitute the samples. However, because a light scattering phenomena is involved rather than an absorption phenomena as in IR, the information provided by Raman spectroscopy is complementary to that obtained by IR. For example, strong polar bonds, like carbonyls, produce intense bands in the IR spectra, but considerably weaker bands in the Raman spectra; in contrast, skeletal bonds, such as unsaturated hydrocarbons, show stronger bands in Raman spectra than in the IR spectra.

In RS, the sample is illuminated with a monochromatic light source (single frequency, ν_0), typically a laser. As result of the interaction of light with the induced dipole moment of the molecules/ions, a small fraction of the scattered radiation can present (under certain conditions) a frequency different from the frequency of the incident source, $\nu = \nu_0 \pm \nu_\upsilon$, where ν_υ corresponds to the frequency of a vibrational mode of the molecules/ions. A plot of the intensity of scattered radiation as function of the frequency shift (shift relative to the incident frequency) is the *Raman spectrum*. Like the IR spectrum, also the Raman spectrum is very characteristic of each molecule/ion, and can be used for identification purposes [123].

It was not until the development of affordable Raman spectrometer equipped with microscopes that Raman spectroscopy, as *Raman microscopy* (μ-R), became an analytical technique employed to conservation science. Nevertheless, in the nearly two decades that have passed since then, this technique had become one of the most important in conservation science [10,33,34].

With μ-R samples of all forms and sizes can be virtually analysed, and as long as the object dimensions allow it to be placed on the microscope stage, it can be employed as a non-invasive technique [32]. *In situ* analyse of large or immovable art objects, using fibre optics, has also provided good sensitivity [52,124,125].

Because visible laser wavelengths are routinely used as source (lower diffraction limit), really reduced areas, such as pigment grains, can be easily analysed. This advantage associated with the ability to go down to low-wavenumber regions, extremely important for the characterization of inorganic pigments, made this technique widely used [33,100,126].

Identification of organic compounds, such as dyes, synthetic organic pigments, binders and varnishes, is also becoming an important area of application for μ-R [127,128]. However, when analysing organic compounds or samples containing organic compounds, there is often associated fluorescence emission, which can completely mask the Raman signal. To overcome this drawback, near-IR laser sources, whose energy is too low to excite fluorescence transitions, associated to FT spectrometers (since the Raman scattering efficiency of these laser sources is also low) are normally used [100]. For additional information about this technique see chapter 5.

Gas Chromatography (GC)/Mass Spectrometry (MS) and High Performance Liquid Chromatography (HPLC)

Chromatographic techniques are analytical techniques designed to separate a sample into its several components, which can then be identified and even quantified without interferences. The name of these widely used techniques comes from its first use, where the

separated compounds of various plant pigments appeared as different coloured bands when made to pass through a glass column packed with calcium carbonate [129].

The techniques basically consist on a stationary phase, generally hold in a column (narrow tube), a mobile phase and a detector. The sample is injected onto the head of the column and made to move throughout it by the mobile phase flow. In Gas-chromatography (GC), the mobile phase is an inert gas, while in High performance liquid chromatography (HPLC), also referred to as high pressure liquid chromatography, the mobile phase is a liquid. As the sample moves inside the column, its components are separated as result of a higher or lower affinity toward the stationary phase (and also toward the mobile phase, for HPLC), arriving at the end of the column at different times (retention time). The mobile and the stationary phases are selected so as to provide the best separation of the components. Exiting the column, the components are identified (comparing them retention times with the retention times of a standard, which was analysed under exactly the same conditions) and quantified by a sensible detector. The components that have a higher affinity for the stationary phase will move slowly and present a higher retention time, the components with a higher affinity towards the mobile phase will move quickly and present a short retention time [129].

Often, these chromatographic techniques are hyphened with another technique, Mass Spectrometry (MS), which is very specific for identification of molecules, ions and atoms, giving the GC/MS and HPLC/MS techniques. The components of the sample that are being separated by chromatography (each at a time) are ionized by a beam of electrons and electrically charged. The formed ions (either positive or negative ions) are then accelerated into the mass analyzer. There, the ions are deflected by a magnetic field, according to their mass-to-charge ratio (*m/z*). A *mass spectrum*, i.e. a graphical presentation of the relative abundances of the various ions, as a function of their *m/z* value is obtained. Comparing the mass spectrum with the masses of expected molecules or molecule fragments is possible to recognize or identify the separated components of the samples [130].

Gas-chromatography (especially GC/MS) is a quite useful technique for the identification of nearly all types of organic binder used in paintings, since these are a mixture of several different compounds. In fact, this is one of the best techniques for identification of the binder and varnishes and by far the most useful technique for the identification of resins and waxes [11,71,73,75,131-133].

Because the mobile phase in GC is a gas, the samples should be able to dissolve and the dissolved components of the sample should be able to be vaporized without disintegration or degradation, but unfortunately, some natural binder are not soluble and many of the

compounds of natural binder are not volatile. To overcome these difficulties, non soluble samples are placed in pyrolysis attachment that heats the sample rapidly to very high temperatures, causing its fragmentation in sizes small enough to pass through the gas chromatograph, while non-volatile compounds are often turned into a related compound that is volatile, by a process called derivatization [11,134,135].

Because HPLC requires that the samples are soluble but not that these are volatile, makes it a little more straightforward to apply to non-volatile or thermally fragile compounds. Even though HPLC can also be used for the analysis of binder, it is less used for this propose than GC [11,71]. HPLC has been instead, successfully used to identify and distinguish dyes and lake pigments [22,136-138].

Unfortunately, unless the layers can be mechanically isolated and analysed one at a time, these techniques are not able to allocate the sample components to a specific layer. More, since these techniques require the samples to be dissolved, pyrolysed or derivatized, being completely destroyed, they are invasive and destructive.

3 Sampling and sample preparation

Sample preparation is an integral part of the analysis process and is tailored in accordance with the sample itself and the analytical technique to use.

J. S. Martin

Sampling and sample preparation are very important steps in any analytical technique. This chapter reproduces the paintings under analysis and describes the sampling procedures.

3.1 Sampling strategy

In order to establish Pousão's palette and to verify how his materials and working method evolved through his life, a group of 23 paintings by Pousão (Table 3.1, Figure 3.1 and Appendix B) distributed through four chronological periods, belonging to the collection of the Museu Nacional de Soares dos Reis, whose authenticity is not questioned, were selected[22]. The four chronological periods were denominated as Early, French, Italian and Final, where the Early period refers to paintings executed in Portugal as a student of the Academia Portuense de Belas-Artes, the French and Italian periods refer to paintings executed in France and Italy, respectively and the Final period refers to paintings executed on the return trip to Portugal and during the last year of his life.

Table 3.1 Key information on the paintings under analysis

Period		Painting	MNSR[a]	Support	Date	Dimensions[b]	Fig.
Early	**A**	*Casa rústica de Campanhã*	109	wood	1880	20.2 x 12.8	4.1a
	B	*O mendigo Lapita*	101	wood	1880	23.5 x 14.2	4.1b
	C	*Paisagem - Abertura da Rua Alexandre Herculano*	183	canvas	1880	68.8 x 122.4	4.1c
French	**D**	*Jardim de Luxemburgo (estudo)*	96/11	wood	1880	16.5 x 9.0	4.1d
	E	*Aldeia de St. Sauves*	167	wood	1881	46.0 x 37.8	4.1e
	F	*Paisagem de St. Sauves*	158	canvas	1881	46.0 x 65.5	4.1f
Italian	**G**	*Cansada (Cachopa de Capri)*	94	canvas	1882	130.5 x 81.5	4.1g
	H	*Casas brancas de Capri*	82	canvas	1882	70.5 x 141.0	4.1h
	I	*Cecília*	106	canvas	1882	82.3 x 57.2	4.1i
	J	*Escadas de um pardieiro - Roma*	83	wood	1882	16.0 x 22.2	4.1j
	K	*Esperando o sucesso*	108	canvas	1882	131.5 x 83.5	4.1k
	L	*Fachada de casa soterrada - Roma*	107/36	wood	1882	9.9 x 16.5	4.1l
	M	*Miragem de Nápoles*	91/49	wood	1882	9.8 x 16.5	4.1m
	N	*Portão*	117/71	wood	1882	29.2 x 21.2	4.1n
	O	*Rapariga de Anacapri*	200	canvas	1882	18.5 x 13.8	4.1o
	P	*Rua de Roma*	96/24	wood	1882	16.5 x 9.9	4.1p
	Q	*Senhora vestida de preto*	114/39	wood	1882	28.3 x 18.4	4.1q
	R	*Janela das persianas azuis*	114/34	wood	1882-1883	28.5 x 25.0	4.1r
	S	*Mulher da água*	115	canvas	1883	144.0 x 135.5	4.1s
	T	*Paisagem de Anacapri*	432	canvas	1883	70.5 x 140.5	4.1t
	U	*Rapariga deitada no tronco de uma árvore*	86/88	canvas	1883	73.5 x 115.5	4.1u
Final	**V**	*Cais de Barcelona*	127/94	wood	1883	16.5 x 10.0	4.1v
	W	*Flores campestres*	117/96	canvas	1884	30.0 x 22.5	4.1w

[a] Museu Nacional Soares dos Reis - painting code; [b] height x width (cm x cm)

[22] Painting selection was done by agreement between Laboratório de Conservação e Restauro José de Figueiredo, Lisboa and Drª. Elisa Soares, Museu Nacional Soares dos Reis, Porto.

Figure 3.1 Pousão's paintings analysed in this study: (a) ***Casa rústica de Campanhã***, (b) ***O mendigo Lapita***, (c) ***Paisagem - Abertura da Rua Alexandre Herculano***, (d) ***Jardim de Luxemburgo (estudo)***, (e) ***Aldeia de St. Sauves***, (f) ***Paisagem de St. Sauves***, (g) ***Cansada (Cachopa de Capri)***, (h) ***Casas brancas de Capri***, (i) ***Cecília***, (j) ***Escadas de um pardieiro - Roma***, (k) ***Esperando o sucesso***, (l) ***Fachada de casa soterrada - Roma***, (m) ***Miragem de Nápoles***, (n) ***Portão***, (o) ***Rapariga de Anacapri***, (p) ***Rua de Roma***, (q) ***Senhora vestida de preto***, (r) ***Janela das persianas azuis***, (s) ***Mulher da água***, (t) ***Paisagem de Anacapri***, (u) ***Rapariga deitada no tronco de uma árvore***, (v) ***Cais de Barcelona*** and (w) ***Flores Campestres***. The pictures (LCRJF) are not to scale.

3.2 Sample collection

Although, ideally, for palette studies, at least two samples from each visually distinguishable hue and/or from important composition elements should be collected [(139)], due to the value and the good condition of the paintings, sampling was seriously constrained to edges and some cracks (see Appendix B).

To facility sample removal, the paintings were set out of their frames and lying flat over a table. Using a micro scalpel, a needle and a magnifying glass, cuts were executed in the edges and along the cracks of the paintings, and the microscopic samples removed. The objective is to remove a sample containing all the paint layers from the ground layer up to the surface coating one[23] and leave the sampling localization as invisible as possible. Each sample was then storage between two glass slices (one a depression slide and the other a normal one, set together by tape-hinges)[24], and properly identified by a tag where the process and the sample numbers were written. Since this process requires practice, samples were removed by a skilled technician from LCRJF.

Samples were set in two groups, those removed and studied in 1984 and those removed in 2005 to undertake this study (Table 3.2). Sampling sites were marked in the photographs of the paintings (see Appendix B) using yellow (samples taken in 1984) and red points (samples taken in 2005) and described in an analysis sheet (see an example of an analysis sheet in Appendix C).

In order to simplify the connection between sample and the painting from where they were collected, samples will be referred to by a code that consists in a letter, corresponding to the painting, and a number. For example, the blue sample removed from the sea in the Painting Casas Brancas de Capri (Figure 2.1a) has the code **H5**.

3.3 Sample preparation

Samples were prepared as cross sections and as thin sections, except for sample **O3**, due to its reduced size, which was prepared only as thin section. It was choosed to prepare sample **O3** as thin section due to the possibility of identifying its components by μ-IR.

[23] Samples that include the support can be collected. However, in practice the support can be examined from the back of the painting, hence, can be omitted from the cross sections.
[24] This type of container avoids the contamination of the sample by the container, even in long-term storage.

Table 3.2 Number of samples taken from each painting

Period		Painting	Support	N[a]	N[b]
Early	**A**	*Casa rústica de Campanhã*	wood		5
	B	*O mendigo Lapita*	wood		4
	C	*Paisagem - Abertura da Rua Alexandre Herculano*	canvas	4	
French	**D**	*Jardim de Luxemburgo (estudo)*	wood		6
	E	*Aldeia de St. Sauves*	wood		7
	F	*Paisagem de St. Sauves*	canvas		6
Italian	**G**	*Cansada (Cachopa de Capri)*	canvas	4	
	H	*Casas brancas de Capri*	canvas		9
	I	*Cecília*	canvas		8
	J	*Escadas de um pardieiro - Roma*	wood		4
	K	*Esperando o sucesso*	canvas	6	8
	L	*Fachada de casa soterrada - Roma*	wood		5
	M	*Miragem de Nápoles*	wood		5
	N	*Portão*	wood	5	
	O	*Rapariga de Anacapri*	canvas	3	
	P	*Rua de Roma*	wood		6
	Q	*Senhora vestida de preto*	wood	3	5
	R	*Janela das persianas azuis*	wood		8
	S	*Mulher da água*	canvas		7
	T	*Paisagem de Anacapri*	canvas		7
	U	*Rapariga deitada no tronco de uma árvore*	canvas	7	6
Final	**V**	*Cais de Barcelona*	wood		5
	W	*Flores campestres*	canvas	3	4

[a] number of samples taken in 1984; [b] number of samples taken in 2005

3.3.1 Cross sections

Samples collected in 1984 were already prepared as cross section. Samples taken in 2005 were prepared as follows.

Using a micro scalpel and a needle under a stereomicroscope (Figure 3.2a) a small piece of the native sample, containing all the layers was deposited perpendicularly in a well of a PVC plastic mould, over a small glue drop to keep sample orientation. The well was then filled up with epoxy polymeric resin (EpoFix, from Struers) and let to curry to room temperature. After curing, the cross-sections/resin blocks were mechanically grounded down

with silicon carbide (SiC) set in a rotary wheel with dripping water (Figure 3.3a), until the complete sample's stratigraphy reached the surface. Then they were polished with an alumina-water slurry FF (alumina suspension) over a cloth wheel (Figure 3.3b), to reduce the scratched finish and make the exposed layers to a fine shine to be observed under the microscope (Figure 3.3c), and finally, washed in current water to remove any alumina particles. Labelling was done, writing with a permanent pen the sample number in one of its sides.

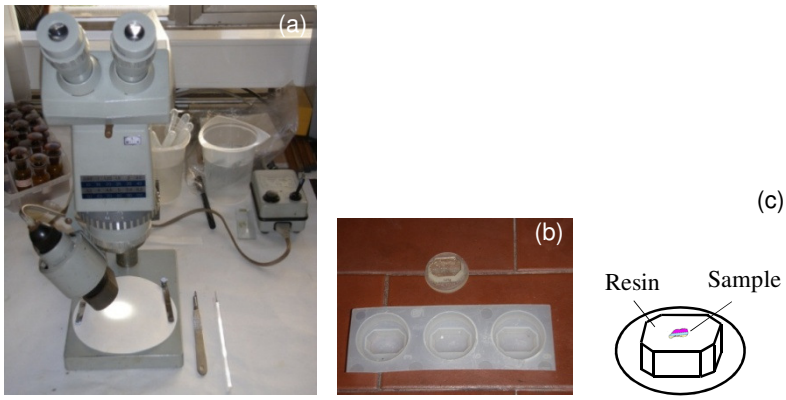

Figure 3.2 a) Stereomicroscope, scalpel and needle, b) cross section's mould and cross section and c) scheme of a cross-section.

Figure 3.3 a) Rotary wheel for grinding and b) rotary wheel for polishing and c) cross section of sample **W3** viewed by optical microscope under reflected light.

3.3.2 Thin sections

Using a micro scalpel and a needle under a stereomicroscope (Figure 3.2a) a small piece of the native sample, containing all the layers, was sectioned, placed (correctly oriented) in half-filled silicon rubber mould (Figure 3.4a) of polyester-styrene resin (SeriFix, from Struers) and topped up with new resin. The mold used for thin sections is much smaller than the mold used for cross sections, because excess of resin stresses the sample curing the slicing.

After curing, the resin blocks (Figure 3.4b) were set in a Leica RM2155 rotary microtome (Figure 3.5a), with a stainless steel blade and several thin-sections 15 µm thick (Figure 3.5b) were produced.

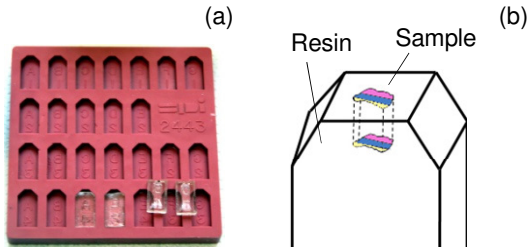

Figure 3.4 a) Silicone mould for sample preparation with four resin blocks and b) scheme of a resin block with the sample (adapted from *Andres MS.* et al. [140]).

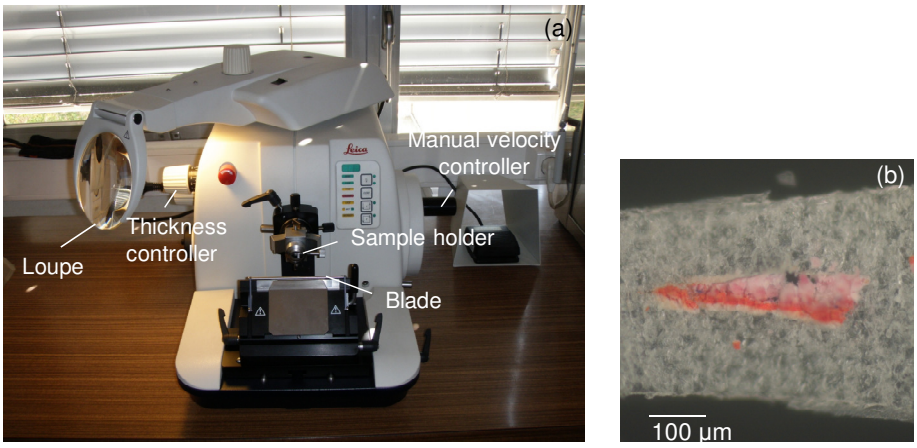

Figure 3.5 a) Leica RM2155 rotary microtome and b) thin section of sample **W3** viewed by optical microscope under reflected light (LCRJF laboratory).

4 Optical microscopy analysis

The best way to examine an 'unknown unknown' and decide how to examine it, is to use an optical microscope first. On occasion the sample remains mystifying, but generally microscopy will yield at least one point of useful information.

J. H. Townsend and K. Keune

Optical microscopy (OM) provides valuable information on the structure of the paintings (e.g. number and thickness of the paint layers). This chapter provides a brief introduction and presents the major results of the analysis of cross-sectioned samples obtained by this technique.

Although the human eye by itself can easily detect details only 0.2 mm in size [105], this ability is not enough to characterize painting's samples, since most painting layers and pigment particles have smaller dimensions. In this case, it is necessary to use a system capable of obtain a magnified and contrasted image of the sample, such as optical microscope.

4.1 The optical microscope

Optical microscopes, also referred to as light microscopes, can be equipped with a wide variety of reflected or transmitted illumination sources, objectives and accessories (such as for example, vertical illuminators, DIC prisms, polarizers, retardation planes), but all of them share the same basic components: eyepieces, objective lens, sample stage, condenser system and light source (Figure 4.1). Nowadays, most models allow alternating between reflected and transmitted illumination.

Examination of transparent samples is obtained using a transmission microscope (also referred to as diascopic illumination), Figure 4.1a. In this microscope, the condenser system (which consists in a number of lenses, diaphragms and accessories and is positioned bellow the sample stage) collects the light diverging from the source and focused it at the small area of the sample (set in the stage) to be analysed. The objective lens (positioned above the sample stage) then collects the light coming from the sample and combines it into a primary (imaginary) image. This image is then further magnified and inverted into the final image by the eyepieces and, detected directly by the eye, imagined in a photographic plate or captured digitally (and observed in a computer screen).

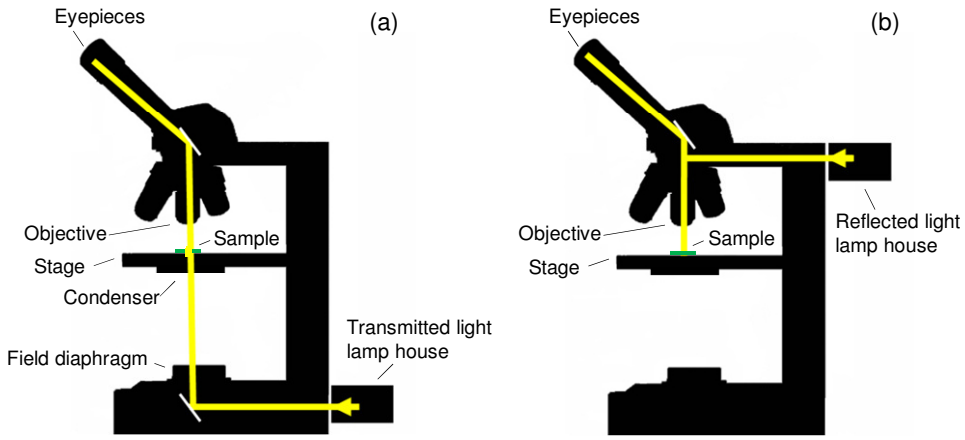

Figure 4.1 Simplified configuration of a: (a) transmission microscope and (b) reflection microscope. The yellow traces represent the light path (adapted from *Davidson MW, et al.* [141]).

When opaque samples are to be examined, because light is unable to pass through them, another type of microscope, known as reflected light microscope, (but also as incident light, episcopic illumination, epi-illumination, vertical illumination or metallurgical microscope) is used, Figure 4.1b. In this setup, illumination is directed (from above) to the sample's surface from the objective that acts also as a condenser. While the sample may absorb part of the incident illumination, other part can be reflect (specularly and/or diffusedly), being collected by the objective and combined it into a primary image. The rest of the image process is identical to that of transmitted microscopy [141].

4.1.1 Resolution or resolving power

The ability of a microscope to clearly separate small details of an object/sample is designated as **resolution** (Figure 4.2), or resolving power. This is not necessarily the same as the smallest point which can be seen with the microscope, which is often smaller than the resolution limit [105].

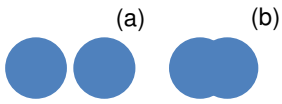

Figure 4.2 (a) Two resolved points; (b) two unresolved points.

Inevitably in any microscope, as light passes through restricted apertures, such as lenses, diffraction can occur, limiting the resolution of the microscope. When the width of the aperture is comparable to, or smaller than, the wavelength of the light passing through it, a diffraction pattern is produced. Instead of the expected point image, a series of alternating light and dark concentric circles (provide the aperture is circular) is formed (Figure 4.3). The central disk represents the direct light and is called the 0^{th} order (diffracted order) or Airy disk, while the following fainter circles are called the 1^{st}, 2^{nd}, 3^{rd}, etc., orders, respectively. Since the light from every small point in the sample suffers diffraction, even an infinitely small point becomes a small Airy disk in the image, reducing the capacity to differentiate between adjacent points.

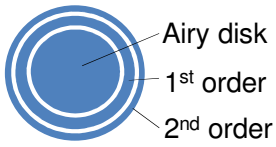

Figure 4.3 Diffraction pattern of a uniformly-illuminated circular aperture.

Because the central disk is much more intense than the others, containing 84% of the radiation, it is generally assumed that all the light falls in the central disk, of diameter d, all the other disks being ignored. Being so, spatial resolution, i.e. the minimum distance by which two of such d diameter adjacent disks can be distinguished, can be defined as [142-144] [25]:

$$\boldsymbol{d \approx \frac{1.22\,\lambda}{NA_{obj}+NA_{cond}}} \tag{4.1}$$

where λ is the wavelength of the incident radiation and NA_{obj} and NA_{cond} are the numerical aperture of the objective and condenser, respectively. Numeric aperture is a measure of the light collection, i.e. a measure of the gathering capabilities of the lens, and is defined as:

$$\boldsymbol{NA = \eta \sin \alpha} \tag{4.2}$$

where η is the refractive index of the medium between the objective (condenser) and the sample, and α is the half-angle of the most oblique rays that came into the objective (condenser).

From (4.2) it is possible to infer that the shorter the wavelength of the radiation and the higher the NA of the objective (and/or condenser), the better the resolution will be. High numerical aperture objectives capture more of the diffracted orders, produce smaller size disks, and consequently, the smaller the details of the sample that are clearly resolved.

4.1.2 Depth of field and depth of focus

When viewing a sample under a microscope, only the part of the sample that lies in the appropriated plane will be accurately in focus, while for the parts of the sample that lie above or below this plane, the equivalent part of the image will be out of focus. The range of positions of the sample for which no change in sharpness of the image is detected is known as *depth of field* or *axial resolving power*. In most microscopes *depth of field* is very short and therefore in order to produce sharp images the object must be very flat. Like horizontal resolution, the axial resolution is determined by the numerical aperture of the objective.

With the development of confocal light microscopes is possible to have images that present in focus a range of depths. The principle of confocal microscopy is very simple. Small apertures ensure that only the light from the in-focus region reaches the imaging part of the system. Since only one point of the sample can be at focus at a time, each point of the sample was to be illuminated at a time - a scanning system being used.

[25] In reflection mode, because the objective acts also as condenser, the denominator of this formula is $2NA_{obj}$.

Depth of field is often confused and interchangeably used with *depth of focus*. However, this last term refers to the range of positions that at which the image can be viewed without appearing out of focus, for a fixed position of the object.

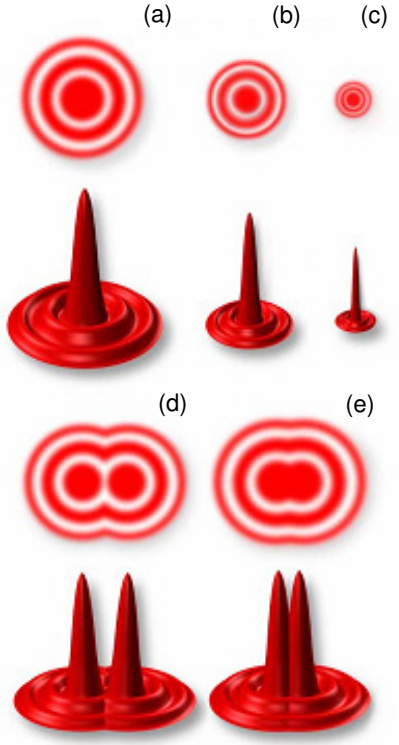

Figure 4.4 Diffraction pattern of a uniformly-illuminated circular aperture and related intensity profile (point spread function). (a-c) Airy disk dimensions as related to the objective numerical aperture. As the numerical aperture increases from (a) to (c) the size of the Airy disk (and further diffraction orders) decreases; (d) Two Airy disks at the limit of resolution; (e) Two Airy disks so close together that their central spots overlap and are no longer resolved. (Reproduced with permission from *Davidson MW, et al.* [141])

4.1.3 Optical microscopy techniques

Because there are several modes of illumination, and a wide variety of objectives, filters and accessories, reflected and transmission light microscopy leads to a large number of optical microscopy techniques, such as Brightfield microscopy, Darkfield microscopy, Polarized light microscopy, Differential interference contrast microscopy, Fluorescence microscopy, Phase contrast microscopy and Hoffman modulation contrast microscopy [141,145], each one presenting its one advantages and limitations.

From all the existing optical microscopy techniques, three are fundamental to the microscopic analysis of painting's samples, namely optical microscopy (OM), polarized light microscopy (PLM) and fluorescence microscopy (FM).

Optical microscopy

The most common and useful method for viewing samples in optical microscopy is darkfield illumination. This technique is based in the blocking out of the central light rays that normally pass through or around the sample, allowing only oblique rays to illuminate the sample [(141)]. The samples will appear bright illuminated against a dark background.

Darkfield microscopy is adequate for revealing outlines, edges and boundaries, thus serve for accurate identification of borders between various layers and differentiate various nuances within a given colour layer.

Polarized light microscopy

Polarized light microscopy permits the measurement of optical properties of transparent samples (e.g. thin sections, pigments and fibers) such as colour, opacity, pleochroism, birefringence, refractive index (RI)[26], and consequently can be used for identification purposes [(75)].

A polarizer is located in the light path below the sample stage and an analyser (a second polarizer), whose polarizing axis is perpendicular to the polarizer (cross polars) is located in the light path above the sample stage. If the incident light is unpolarized, the polarizer lets to pass only the light waves that vibrate perpendicularly to the polarizer transmission direction. If an isotropic[27] material is being analysed no alteration occurs and no light will be transmitted by the analyser. However, if an anisotropic material is under study, light is transmitted by the analyser and coloured patterns against the dark background are observed.

Particle samples are dispersed over a glass slide in a medium that reduces light scattering and has a known RI (generally 1.66), that works as a reference for measurement of the RI. Because inorganic materials have high refractive indices, they can be identified when visualized in a microscope under polarized light.

Fluorescence microscopy

Fluorescence microscopy is used to differentiate layers and particles that appear similar in visible light, but that fluoresce under ultraviolet light. Based on their primary fluorescence, or on the secondary fluorescence of fluorochromes used to mark them, materials can be identified [(32,145,146)].

[26] Refractive index refers to the ratio of the velocity of light in a vacuum to its velocity in the medium of interest.

[27] In an isotropic material, since all axes are equivalent, the optical properties are independent of the direction and orientation of the light to the crystal axes. In an anisotropic material, because these have crystallographically distinct axes, interaction with light is dependent of the material orientation respect to the incident light, thus, also the optical properties are dependent of the direction and orientation of the light to the crystal axes.

This technique is set adapting an ultraviolet source instead of the visible one and a filter that blocks the arrival of visible light to the detector. For additional information about this technique see chapter 7.

4.2 Examination of painting's samples by OM

Since the early 1900s that optical microscopy has been used as primary tool for examination of painting's samples and characterization of its components [78,146,147]. Using this relatively cheap technique, present in almost every laboratory, it is possible to achieve important results and select the most appropriate technique to carry on the study.

As referred before painting's samples can be layered samples, namely, cross sections and thin sections, which present the all the layers that constitute the painting, or particle samples. Examination of layered samples (denominated stratigraphic analysis) is central to the technical understanding of the painting and their preparation. It allows: i) to determine the structure of the painting, i.e. the chronologic sequence of the paint layers and them thickness; ii) to characterise the materials and techniques of an artist, such as planned use of opaque and transparent layers; iii) reveal the presence of pentimenti (small composition alterations done by the painter); iv) determine shape and size of the pigment grains and them distribution on each layer; v) to distinguish between original and overpaintings, restoration or alteration. It is also very important for assessing conservators/restorators in: vi) determining layer condition and adhesion; vii) planning and implementing a restoration or maintenance treatment interventions (when surface tests are ambiguous or fail to account for the behaviour of subsurface layers); viii) evaluating the progress of surface-related treatments, such as the removal of degraded varnish or overpaint, helping to decide how much, and how to clean it; ix) studying and evaluate a degradation phenomena, such as for example, the lead protrusions identified in oil paintings. Although identification of the components (pigments, dyes, extenders and medium) in cross sections is also possible, there are several limitations [21] and complementary techniques are often required for definitive identification [146].

Thin sections are examined under transmitted light, but because each layer is generally densely populated with absorbing particles (pigments) with a different refractive index from the binder, little light is transmitted through the cross sections and these are examined under (visible or ultraviolet) reflected light.

Analysis of particle samples is used to pigment identification (most traditional pigments exhibit a unique set of optical properties, these can be used for identification purposes), determination of the particle size of the pigment, particle size distribution, presence of

mineral inclusions. Particle samples are prepared as dispersions and characterized based on physical properties, such as size and shape and/or on optical properties, such as refractive index and birefringence (Polarized light microscopy - PLM), or even made to react with a series of chemical reagents and heat (microchemical tests) [147]. Unfortunately, identification requires a highly skilled operator, and even then fails to yield conclusive, or occasionally, accurate results.

Due to the complexity of the samples under analysis, manual separation of each layer (required for Polarized light microscopy) was very difficult, if not impossible, and since other, more specific techniques for identification purposes were going to be used, Optical microscopy analysis was limited to Darkfield Microscopy[28].

4.3 Experimental conditions

Samples

Samples were analysed as cross sections (see section 3.2.1 for sample preparation description), except for the sample removed from the red from the neckerchief (**O3**) of the painting ***Rapariga de Anacapri*** (Figure 3.1o), which was analysed in the bulk form.

Experimental set-up

Examination of the cross sections by optical microscopy was carried out using a Leitz WETZLAR microscope (10x ocular) under reflected visible light produced by a halogen lamp (Figure 4.5). Image acquisition was carried out with a coupled Leica DC500 digital camera and IM1000 software, using 6.5x, 11x and 22x objectives (corresponding to total magnifications of 65x, 110x and 220x, respectively). Layer dimension was measured using Leica Qwin software.

To ensure that the resin block surface (containing the sample) was completely horizontal to the microscope stage (perpendicularly to the objective axis), the block was pressed, using a parallel press, into a lump of plasticine on a metal plate. To reduce the amount of light scattered by the sample and rend its surface saturated, a thin glass cover slip was placed over the sample and held in place with a small drop of glycerol/water (50 % v/v). By this way, surface irregularities were remove and a better colour contrast and an easy differentiation between layers was obtained.

[28] During the study, it was found the necessity to use also Fluorescence microscopy to characterize a small number of the samples. The analysis and the results can be seen in chapter 8.

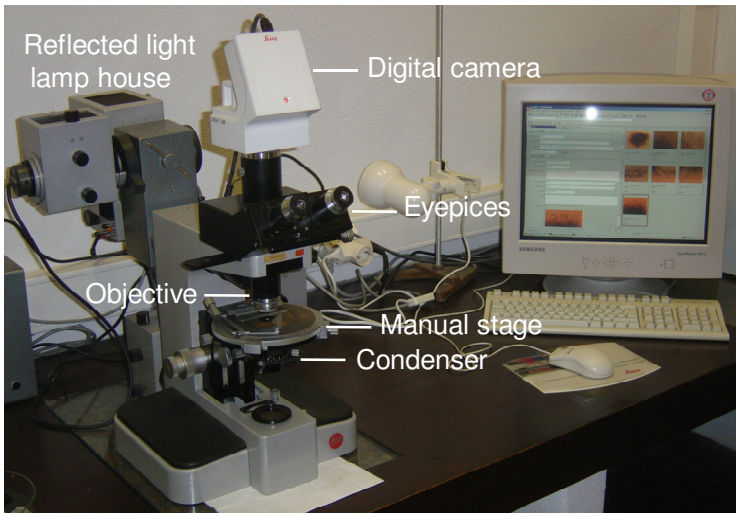

Figure 4.5 Leitz WETZLAR optical microscope used for the analysis of the samples.

4.4 Results and discussion

The results of the examination of the cross sections by OM, provided information regarding the structure of the paintings, such as characterization of the ground layer; existency of underdrawing; number[29], thickness and technique of the paint layers, as presented below. No attempt to pigment's identification was undertaken, since other more efficient techniques will be used for this purpose.

Only a few of the cross sections are presented in this chapter in order to clarify and/or exemplify the results presented, all of them being presented in Appendix D.

Since sample **O3**, was not mouted as a cross section, its stratigraphy was not determined. Nevertheless, since only two layers were visible on the thin section of this sample, one white and the other red, which were obseved by OM as the upper and lower layers (Figure D89), and the other samples removed from the same painting are also characterized by a white ground layer and a single paint layer, it likely probable that sample O3 is constituded by a white ground layer and a red paint layer.

4.4.1 Ground layer

Generally, the cross sections present a white ground layer (variable thickness), as presented in Figure 4.6a. One particularity was verified for the painting ***Paisagem - Abertura***

[29] Numeration of the layers is done from inside to outside, i.e. by their application order.

da Rua Alexandre Herculano, where the ground layer seem to be composed by three white layers of slightly different opacity (Figure 4.6b).

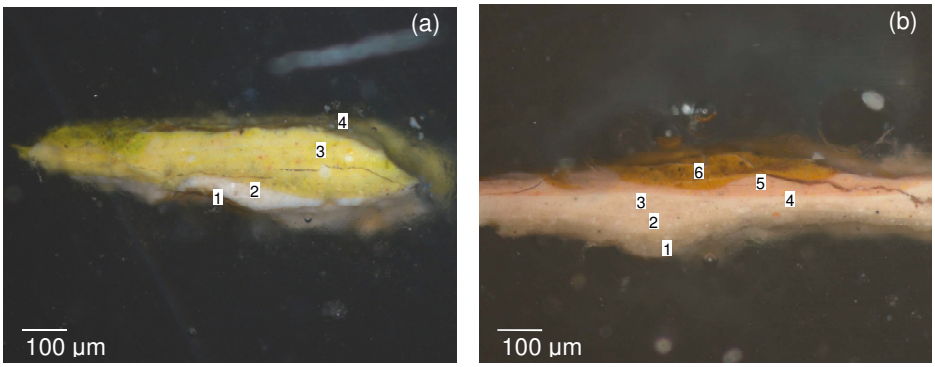

Figure 4.6 Cross sections of the samples: (a) **N5** - green foliage from ***Portão*** and (b) **C4** - brown from the ground from ***Paisagem - Abertura da Rua Alexandre Herculano***; viewed under reflected light.

Exceptions were found in, ***Estátua do jardim de Luxemburgo***, ***Senhora vestida de preto*** and ***Paisagem de St. Sauves***. Cross sections from ***Estátua do jardim de Luxemburgo*** and ***Senhora vestida de preto***, two wood panel paintings, present no ground layer (see for example, the cross section from ***Senhora vestida de preto*** presented in Figure 4.7a), while the cross sections from ***Paisagem de St. Sauves*** (canvas painting) present a brownish ground layer 1 and a white *imprimitura* (layer 2) (Figure 4.7b).

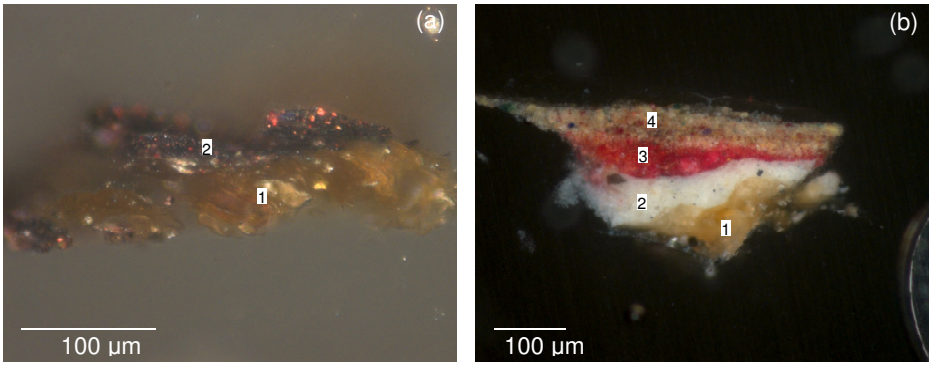

Figure 4.7 Cross sections of the samples: (a) **Q4** - black of the dress from ***Senhora vestida de Preto***, and (b) **F4** - brownish of the ground from ***Paisagem de St. Sauves***; viewed under reflected light.

Generally, the ground layer is clearly separated from the paint layers, indicating that the paint layers were applied after the ground layer had dried. However, in the sample **C2** of the green of the tree from ***Paisagem - Abertura da Rua Alexandre Herculano*** (Figure 4.8a) an infiltration of the ground layers 1 and 2 by the yellow paint layer 4 is clearly seen, and in the

sample **F6** of dark green of the ground from ***Paisagem de St. Sauves*** (Figure 4.8b), particles of the paint layer 2 are present in the ground layer.

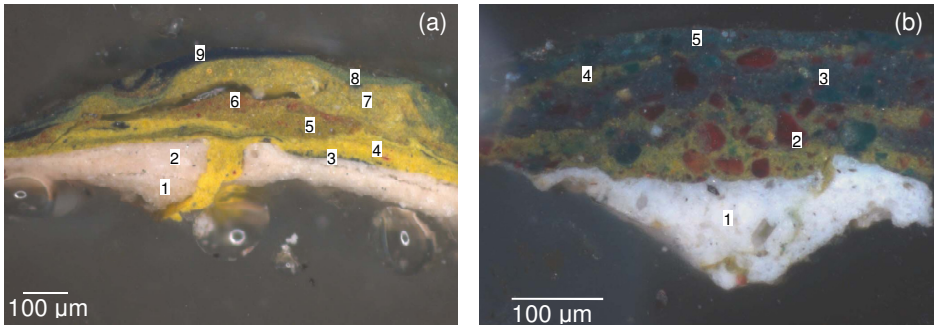

Figure 4.8 Cross sections of the samples: (a) **C2** - green of the tree from ***Paisagem - Abertura da Rua Alexandre Herculano*** and (b) **F6** - dark green of the ground from ***Paisagem de St. Sauves***; viewed under reflected light.

4.4.2 Underdrawing

In the sample **H8** of the dark green of the cactus from ***Casas brancas de Capri*** (Figure 4.9a) and the samples: **S2** of the green from the bushes (Figure 4.9b), **S5** the blue from the blouse and **S7** the blue from the skirt from ***Mulher da água***, it is possible to see a discontinuous and variable in thickness black layer 2 between the ground layer and the paint layers, which probably corresponds to a pencil/brush contour line.

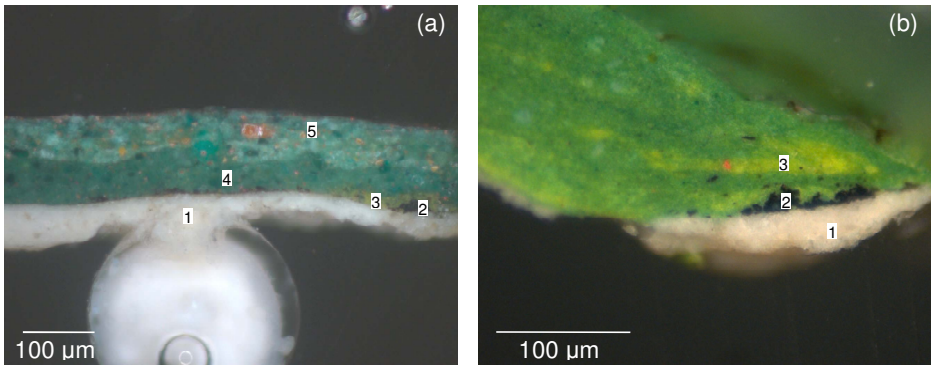

Figure 4.9 Cross section of the samples: (a) **H8** - dark green of the cactus from ***Casas brancas de Capri*** and **S2 -** green from the bushes from ***Mulher da água***; viewed under reflected light.

4.4.3 Paint layers

As shown in Figure 4.6-4.9 paint layers were verified to vary significantly in number (1 to 10), thickness (4 to 358 µm), pigment colour distribution and execution, even across the same painting. For example, while the sample removed from yellow from the brush from

Esperando o Sucesso (**K3**) has 9 paint layers (Figure 4.10a), the sample removed from the blue from the sky from ***Casas brancas de Capri*** (**H4**) (Figure 4.10b), has only one paint layer. In the same way, while layer 7 of sample **K3** is only 19 µm thick (Figure 4.10c), layer 1 of the sample removed from the brown of the wood box from ***Esperando o Sucesso*** (**K9**) is 184 µm thick (Figure 4.10d).

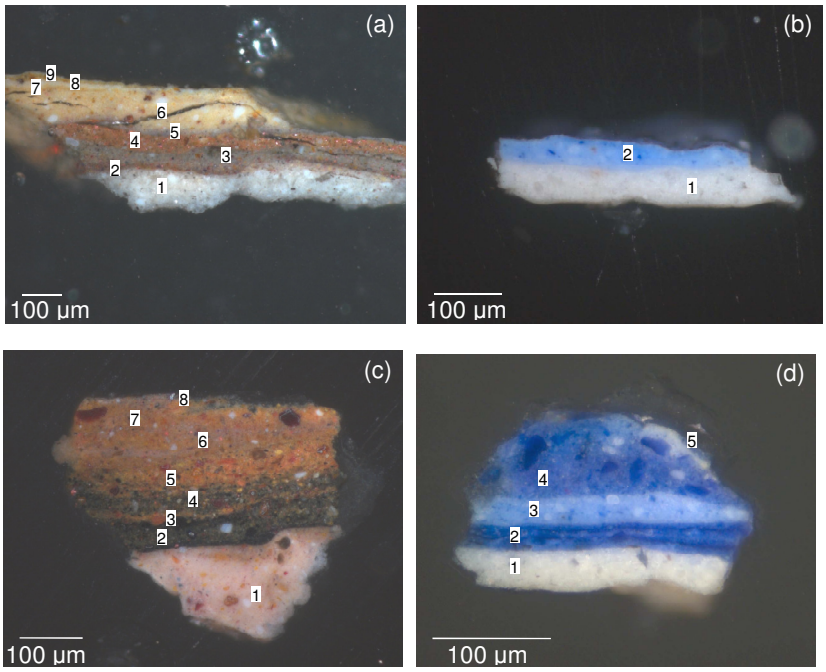

Figure 4.10 Cross section of the samples: (a) **K3** - yellow from the brush from ***Esperando o Sucesso***, (b) **H5** - blue from the sea from ***Casas brancas de Capri***, (c) **K9** - brown of the wood box from ***Esperando o Sucesso*** and (d) **H4** - blue from the sky from ***Casas brancas de Capri***; viewed under reflected light.

Relatively to the execution method, paint layers were normally added after the previous one had dried, although paint layers applied wet in wet (producing blending or half blending of the colours) were also identified, especially in vegetation and ground areas (Figure 4.8a and b and Figure 4.10c); similar hues were often obtained using different compositions, as demonstrated by the cross sections of the two samples removed from blue areas of the painting ***Casas brancas de Capri*** (Figure 4.10b and d). While the sample removed from the sky (b), presents a single blue paint layer, the sample removed from the sea (d) presents four bluish layers.

Regarding the pigment particles, these vary significantly both in colour and size, even across a single layer. The high variety of colours suggests that a large number of pigments is present, a result to be confirmed by infrared and Raman microscopy. The strongly heterogeneous size of some of the pigments, such as ochre pigments (see for example,

samples **K9** (Figure 4.9c) and **K14**) and cobalt blue (see for example sample **H4** (Figure 4.9d)) strongly suggest that these were hand-ground, while the uniform and reduced size of other pigments, such as ultramarine blue (see for example, samples **C2** (Figure 4.7) and **T1**), is indicative of a machine grounding[30]. Artists had known for centuries that some pigments give a more saturated (more intense) colour when they are not ground too finely and a more light colour is finely-ground, consequently is not odd to identify pigments sometimes coarsely-ground and others finely-ground [(21)].

Because this technique cannot discriminate between grains with 0.1-0.5 μm, is not possible to determine the size of the smallest particles, but the largest pigment particles have a size of about 54 μm (red lake particles of the dark green of the ground from ***Paisagem de St. Sauves***).

The varnish coating layer appeared to be thin and discontinuous.

4.4.4 Questionable samples

Three of the samples, namely those removed from: the blue of the sea from ***Paisagem de Anacapri*** (**T2**), the grey from the back from ***Flores Campestres*** (**W4**) and the light grey from the back from ***Flores Campestres*** (**W7**) (Figure 4.11) seem to show a ground layer 1 somehow different from that seen in the other samples, rising doubts regarding them origin, which will be address in the following chapters.

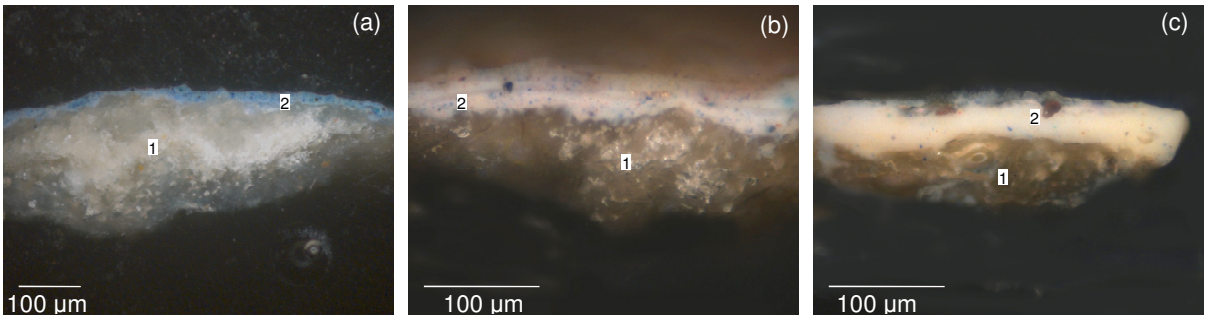

Figure 4.11 Cross section of the samples: (a) **T2 -** blue from the sea from ***Paisagem de Anacapri***, (b) **W4** - grey from the back from ***Flores Campestres***, and (c) **W7 -** light grey from the back from ***Flores Campestres***, viewed under reflected light.

Also strange is the brownish layer 4 (6 μm thick) between the two blue layers (layers 3 and 5), in the sample removed from the sky from ***Paisagem de St. Sauves*** (**F1**) (Figure 4.12). It seems as if the last blue layer was applied over a rest of the brownish layer, possibly

[30] Identification of pigments was achieved through other analytical techniques (see following chapters).

a varnish layer, being either a rework by Pousão or a result of a conservation intervention. Only after further analysis, will it be possible to confirm or to discharge these hypotheses.

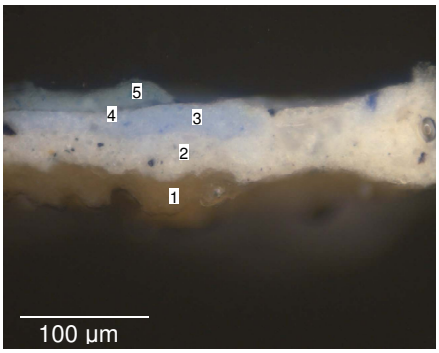

Figure 4.12 Cross section of the sample **F1 -** blue from the sky from ***Paisagem de St. Sauves***, viewed under reflected light.

4.4.5 Conservation state of the paintings

No signal of alteration or degradation of the paint layers or pigments is visible, assessing a good conservation state of the paintings.

4.5 Conclusions

The analysis by OM of 149 cross sections out of the 150 samples[31] removed from the 23 paintings under study, allowed valuable information to be obtained relatively to the painter's technique and the state of conservation of the paintings'. Preliminary examination of cross-sectioned samples under reflected light is essential to show graphically what went on under the painting surface.

In general, paintings are characterized by: i) the presence of one or more white ground layer(s). Exceptions are the paintings ***Estátua do jardim de Luxemburgo*** and ***Senhora vestida de Preto***, which do not present any ground layer at all and painting ***Paisagem de St. Sauves***, that has a browninsh ground layer and a white *imprimitura*; ii) well defined paint layers, indicating that these were applied after the ground layer or previous paint layers had been dried, iii) a variable number of paint layers (1 to 10) and respective thickness (4 to 358 µm), iv) the presence of a wide range of pigments colours, v) the absence of reworks, vi) a good state of conservation, as no signal of alteration or degradation of the paint layers or pigments were detected.

This technique also alerted to the possible existence of samples removed from restoration areas, as verified afterwards by other techniques.

[31] Excepted for sample **O3**, see page 40.

5 Introduction to vibrational microscopy

I am picking up Good Vibrations

Beach Boys

This chapter provides a brief introduction to Infrared and Raman microscopy (μ-IR and μ-R), the core of analytical techniques of this project. Only the necessary information to understand the analysis and interpretation of the results is provided.

Infrared and Raman microscopies are vibrational molecular spectroscopic techniques that have been extremely helpful to the analysis of various types of artworks and samples of archaeological interest, such as ceramics, painted pottery, frescos, wallpaper, illuminated manuscripts, glasses, paintings, etc. and to the identification of various materials: pigments, extenders, binder, degradation products, etc [16,48,148-159].

Coupling an optical microscope to an IR or Raman spectrometer, it is possible the determination of the molecular composition of microscopic heterogeneous samples, i.e. analyse of a reduced amount of sample with a good signal, and at the same time, provides their spatial distribution at a resolution close to the diffraction limit.

Although there are a large number of books about Infrared and Raman spectroscopies [160-163] and even some about Infrared and Raman microscopies [164-166], in order to understand these two analytical techniques and interpret the data they provide, we found it useful to present an introduction to the theoretical and practical background of these techniques.

5.1 Principles of vibrational spectroscopy

The atoms in molecules are represented at their equilibrium positions (ca. average positions). However, even in solids, atoms are constantly vibrating about their equilibrium positions, and consequently lengths and angles of all the chemical bonds in the molecule are constantly changing [167].

The vibrational frequency of a given chemical bond depends of its stiffness (force constant), the masses of the connected atoms, the molecular geometry and, to a less extent, of the neighbouring parts of the molecule. So, vibrational frequencies are specific of each chemical bond and can be used for identification purposes or for determination of important structural parameters, such as force constants, lengths and angles of the bonds and geometry.

The analytical techniques that provide this kind of information based on the vibrational frequencies are referred to as *vibrational spectroscopy techniques*. Although there are a new range of vibrational spectroscopic techniques[32], Infrared and Raman spectroscopies are still the most common, due to their availability/cost, well established knowledge and high number of reference spectra libraries/books.

[32] High-resolution electron energy loss spectroscopy (EELS) [168], inelastic electron tunneling spectroscopy (IETS) [169], inelastic molecular beam scattering [170] and inelastic neutron scattering (INS) [171].

5.1.1 Classical mechanics (CM) approach: normal modes of vibration

In space, every atom can move independently along the axes x, y and z of a cartesian coordinate system, i.e. each atom has 3 *degrees of freedom*. Therefore, a molecule with *N* atoms has 3*N* degrees of freedom. Any motion of the molecules can be considered as a linear combination of the 3*N* degrees of freedom.

In every molecule, 3 degrees of freedom describe the *translational* motion, i.e. the movement of the molecule as a whole, another 3 (or 2, if the molecule is linear[33]) describe the *rotational* motion, i.e. rotation of the molecule as a whole about its center of mass and the remaining 3*N*-6 (or 3*N*-5, for linear molecules) degrees of freedom describe the *normal modes of vibration.* Figure 5.1 presents the degrees of freedom of an angular triatomic molecule (*N*=3).

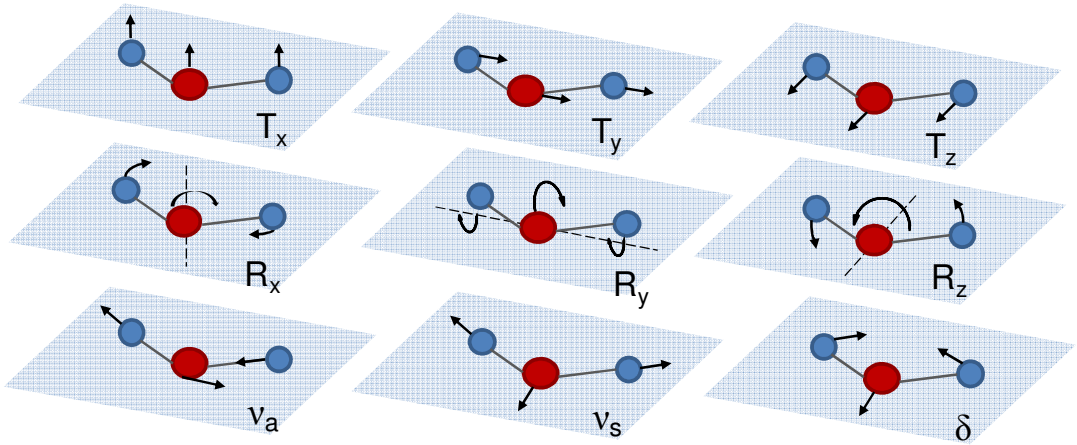

Figure 5.1 Degrees of freedom of an angular triatomic molecule (N=3). $T_{x,y,z}$ and $R_{x,y,z}$ are the translations and rotations of the molecule as a whole, respectively. ν_a, ν_s and δ are the normal modes of vibration (see below the meaning of these symbols) (adapted from *Schrader B.* [(123)]).

Because the bonds are elastic, molecules can be visualized, to a first approximation, as point masses connected by springs (Figure 5.2) and most of the characteristics of their vibrations can be understood in terms of classical harmonic motion (harmonic oscillator model).

Figure 5.2 Two point masses connected by a weightless spring.

[33] Because rotation of a linear molecule about the axis of the bond does not involve the displacement of any of the atoms, one of the three coordinates is not necessary.

When by a force action F_1, a point mass attached to a spring is displaced from their equilibrium position, the spring itself inflicts a restoring force F_2, in order to bring the mass to its initial position (Hooke's law). This force, $F_2 = -fx$, where x is the displacement from the equilibrium position (in m) and f is the force constant of the spring (in N/m), causes the mass to vibrate, i.e. to produce an harmonic motion (periodic motion).

Solving the Newton's second law of motion, $F = ma$ (where m is the mass and a its acceleration), for this simple case of a single point mass conneted to a spring obeying Hooke's law, or the equivalent Lagrange's equation of motion, $\frac{d}{dt}\left(\frac{dT}{d\dot{x}_i}\right) + \frac{dV}{dx_i} = 0$ (where $T = \frac{1}{2}m\dot{x}^2$ and $V = \frac{1}{2}fx^2$ are the kinetic and potential energies of a spring, respectively, the x_i are any set of cartesian displacement coordinates and the dot denotes the derivate with respect to time):

$$ma = -fx \qquad \text{or} \qquad m\frac{d^2x}{dt^2} + fx = 0 \qquad \text{or} \qquad m\ddot{x} + fx = 0 \tag{5.1}$$

where $\ddot{x}$ reperesents the second derivative of x with respect to time, it is determined that the displacement of the single point mass particle is given by

$$\boldsymbol{x = A\ cos\ (2\pi\nu t + \varepsilon)} \tag{5.2}$$

which describes an harmonic movement of maximum displacement or amplitude A, phase constant, ε, and frequency, ν; t represents time, in seconds. The frequency, in s^{-1} (also known as Hz), is given by:

$$\nu = \frac{1}{2\pi}\sqrt{\frac{f}{m}} \tag{5.3}$$

For a system with N point masses particles, such as a molecule with N atoms, calculation of the displacement of all the N masses is significantly more complicate. Lagrange equation is applied, which requires to find the expressions for T and V.

For a molecule with N atoms, the total kinetic energy is given by (a sum of the kinetic energy of all the atoms, in a three-dimensional space[34]):

$$2T = \sum_{i=1}^{3N} m_i \dot{x}_i^{\,2} \tag{5.4}$$

which can be simplified using mass-weighted cartesian coordinates $q_i = \sqrt{m_i}x_i$[35] to:

$$2T = \sum_{i=1}^{3N} \dot{q}_i^{\,2} \tag{5.5}$$

[34] The coordinates are labeled in such a way that x_1, x_2, x_3 are the coordinates, x, y and z respectively, of the first atom, whereas x_4, x_5 and x_6 are the coordinates for the second atom, and so forth.

[35] These coordinates are labeled in such a way that $q_1 = \sqrt{m_1}x_1$, $q_2 = \sqrt{m_1}x_2$, $q_3 = \sqrt{m_1}x_3$, $q_4 = \sqrt{m_2}x_4$, $q_5 = \sqrt{m_2}x_5$, and so forth ($m_i = m_1$ to $i = 1, 2, 3$; $m_i = m_2$ to $i = 4, 5, 6$, and so on).

where $\dot{q}_i$ reperesents the first derivative of q_i with respect to time.

In addition, when using mass-weighted coordinates all the amplitudes are properly adjusted to the different masses of the point particles, as the amplitude is dependent of the mass.

Regarding the potential energy, it is known that it is a complex function of the geometry of the system, i.e. that it changes continually with the mass-weighted cartesian coordinates (q_i). For a molecule with N atoms, in which the atoms present small displacements from the equilibrium position, the total potential energy can be described by a Taylor series as:

$$V = V_0 + \sum_{i=1}^{3N} \left(\frac{dV}{dq_i}\right)_0 q_i + \frac{1}{2} \sum_{i=1}^{3N} \sum_{j=1}^{3N} \left(\frac{d^2V}{dq_i\, dq_j}\right)_0 q_i q_j + \ldots \quad (5.6)$$

where the derivates are evaluated at $q_i = 0$, i.e. at the equilibrium position. This expansion can be simplified to:

$$2V = \sum_{i=1}^{3N} \sum_{j=1}^{3N} \left(\frac{d^2V}{dq_i\, dq_j}\right)_0 q_i q_j \; = \sum_{i=1}^{3N} \sum_{j=1}^{3N} f_{ij}\, q_i q_j \quad (5.7)$$

with $f_{ij} = \left(\frac{d^2V}{dq_i\, dq_j}\right)_0$, since the constant V_0, the potential energy of the equilibrium position, can be taken as zero, the term with the first derivative can also be taken as zero because at equilibrium the potential energy corresponds to a minimum, hence $\left(\frac{dV}{dq_i}\right)_0 = 0$, and the higher expansion terms are ignored as it is assumed that atoms present small displacements from the equilibrium position [172-175].

From equations 5.5 and 5.7, and taking the required derivates ($\frac{d}{dt}\left(\frac{dT}{d\dot{q}_i}\right)$ and $\frac{dV}{dq_i}$), Lagrange's equation is written as:

$$\ddot{q}_i + \sum_{j=1}^{3N} f_{ij} q_j = 0 \quad (5.8)$$

which is a short form of the $3N$ simultaneous differential equations, with index i running from 1 to $3N$. $\ddot{q}_i$ reperesents the second derivative of q_i with respect to time. The solutions of these simultaneous differential equations are functions of the harmonic oscillator [173-175]:

$$q_i = A_i \cos\,(2\pi\nu t + \varepsilon) \quad (5.9)$$

The frequency v is given by:

$$\nu = \frac{1}{2\pi}\sqrt{\frac{f}{\mu}} \quad (5.10)$$

where μ is the reduced mass ($\frac{1}{\mu} = \frac{1}{m_1} + \frac{1}{m_2} + \cdots + \frac{1}{m_i}$).

Combining equations 6.8 and 6.9 it is obtained:

$$\sum_{j=1}^{3N} f_{ij} A_j - (2\pi\nu_i)^2 A_i = 0 \qquad (5.11)$$

which can be re-writen as:

$$\sum_{j=1}^{3N} (f_{ij} - \lambda\delta_{ij}) A_j = 0 \qquad (5.12)$$

where $\lambda = (2\pi\nu)^2$ and δ_{ij} is the Kronecker symbol ($\delta_{ij} = 1$ if $i = j$; $\delta_{ij} = 0$ if $i \neq j$).

This equation is a short form of $3N$ simultaneous homogeneous linear equations of unknown A_j, whose solutions will be different from the trivial solution ($A_j = 0$ with $j = 1,2,\ldots,3N$, which has no interest since it implies that all atoms are at rest) when:

$$\left| f_{ij} - \lambda\delta_{ij} \right| = 0 \qquad (5.13)$$

which is known as the *vibrational secular equation* and has a $3N$ order. The solution of this equation gives, unambiguously, the values of the vibrational frequencies of the system, ν_i, since $\lambda_i = (2\pi\nu_i)^2$. However, from these $3N$ values, only 3*N*-6 or 3*N*-5 present a frequency different from zero, which correspond to *vibrational degrees of freedom*. The 6 or 5 values which present a frequency equal to zero correspond to the *translational* and *rotational degrees of freedom* [173].

Unfortunately, because the amplitude and the frequency of a vibrational system are unrelated, the amplitudes, A_i, are not determined unequivocally. Nevertheless, for a particular solution λ_k:

$$q_i = A_{i\mathrm{k}} \cos\,(2\pi\nu_k t + \varepsilon_k) \qquad i = 1, 2, \ldots., 3N \qquad (5.14)$$

that shows that in a given vibrational mode k, all the atoms involved are vibrating around the equilibrium position in phase (ϵ_{k}) and with the same frequency ν_{k}, but with different amplitudes, $A_{i\mathrm{k}}$. This type of vibrational mode is designed as *normal mode of vibration* and the frequency that is associated to it, is referred to as *fundamental* or *normal* frequency [123,174,175].

However, because the $3N$ equations 6.8 are simultaneous differential, the sum of two or more of the solutions 6.14 are also a solution:

$$q_i = \sum_{i=1}^{3N} A_{i\mathrm{k}} \cos\,(2\pi\nu_k t + \varepsilon_k) \qquad i = 1, 2, \ldots., 3N \qquad (5.15)$$

This indicates that each mass-weighted coordinate, q_i, is associated to more than one frequency ν_k, i.e. to more than one normal mode and therefore, it occurs overlapping between several modes. This occurs because the potential energy in mass-weighted coordinates (equation 6.7) presents cross terms.

It is therefore necessary to establish a new set of coordinates that allow each coordinate to be associated with only one of the $3N-6$ normal vibrational modes. These are the *normal coordinates* Q_k, defined from mass-weighted cartesian coordinates as:

$$Q_k = \sum_{i=1}^{3N} l'_{ik} q_i \tag{5.16}$$

Each normal coordinate Q_k is a linear combination of the coordinates q_i, which represent the movements of the atoms within a molecule relative to the equilibrium position[36]. The coefficients l'_{ik} ensures that each normal coordinate is associated with only one normal vibration mode, hence the number of degrees of freedom corresponds to the number of modes of motion [(175)].

In a normal coordinate space, kinetic and potential energies can be written as:

$$2T = \sum_{k=1}^{3N-6} \dot{Q}_k^{\,2} \tag{5.17}$$

$$2V = \sum_{k=1}^{3N-6} \lambda_k Q_k^{\,2} \tag{5.18}$$

which combined with Lagrange's equation result in:

$$\ddot{Q}_k + \lambda_k Q_k = 0 \tag{5.19}$$

The solutions to this equation are given by:

$$Q_k = Q_{ik} \cos\,(2\pi\nu_k t + \varepsilon_k) \qquad i = 1, 2, \ldots, N \tag{5.20}$$

Each normal coordinate Q_k describes how each atom i is displaced from the equilibrium position during the associated normal mode k, and consists in a displacement vector for each atom as shown in Figure 5.1 and Figure 5.3 Reversing the arrows, it is represented the opposite phase of the same vibration.

Each normal mode acts as a harmonic oscillator, independent of any other normal mode.

Classification of the normal vibrational modes

In general the vibrational modes can be classified as *stretching modes* (ν), which involve change of the bond length and *bending modes*, which involve change of bond angle. Bending modes are further classified as *in-plane bending* (δ), also called *deformation*, when one or more angles are changed, or as *out-of-plane bending* (π), when one atom oscillates relatively to the plane made by three neighbour atoms. To some characteristic bending modes special descriptive names were given: *scissoring* - in-plane symmetric bending mode, *wagging* (ρ_w) - out-of-plane bending, *twisting* (ρ_t) - out-of-plane bending and *rocking* (ρ_r) - in-

[36] With the mass-weighted coordinates, three displacement vectors are placed in each atom, with origin at the equilibrium position.

plane bending. Figure 5.3 shows the normal vibrational modes of a methylene group when attached to a molecule. The only bending in four-membered ring systems (Figure 5.4) is referred to as *ring puckering* mode, as it resembles 'puckering' of the ring framework [176].

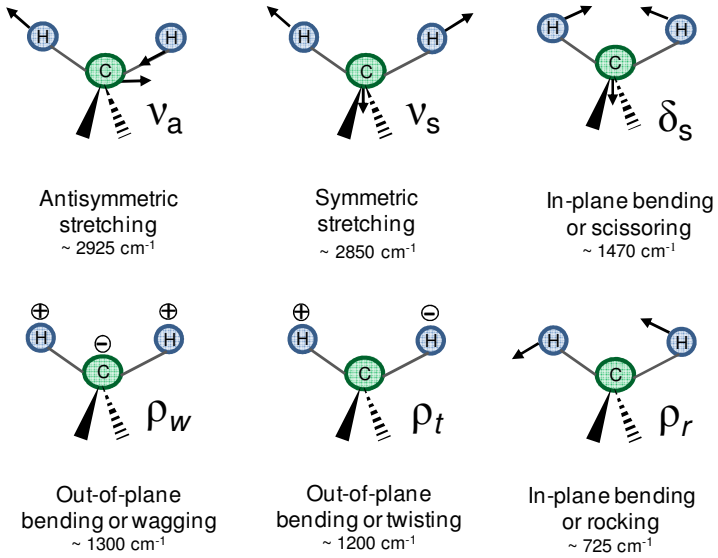

Figure 5.3 Approximate form of the normal modes of a methylene (CH_2) group when attached to a molecule and respective frequencies. The + and - signals indicate upward and downward motion in the plane of the paper, respectively (adapted from *Nakamoto K.* [175], *Schrader B.* [177] and *Shurvell HF.* [178]).

When any symmetry exists in a molecule (such as the plane of symmetry that passes, vertically, through the carbon atom in Figure 5.3) the vibrational modes will reflect that symmetry. If the symmetry properties are preserved during the vibration (which, for the referred symmetry plane, means that the bonds are still mirror like), the vibrations are classified as *in-phase* or *symmetric* (s). If, otherwise, the symmetry properties are not preserved during the vibration, the vibrations are classified as *out-of-phase* or *antisymmetric*[37] modes (a) [123,175]. The particular case of the symmetric expansions and contractions of the bonds in cyclic and tethaedrical compounds are referred to as *breathing* [176].

Numbering of the normal modes is conventionally made by ordering the modes by descending symmetry, the totally symmetric modes at the top of the list. Modes of the same symmetry are ordered by decreasing energy. Generally, for vibrations involving the same atoms, stretching modes have higher energy than the bending modes and antisymmetric stretching modes have higher energy than the symmetric modes [180].

[37] Antisymmetric modes are often also referred as "asymmetric". However, currently, this term is not considered correct [179].

Whenever two or more vibrational modes present approximately the same frequency, either as a result of symmetry of the molecule (the motion they describe is identical) or simply accidently, these are said to be *degenerate*.

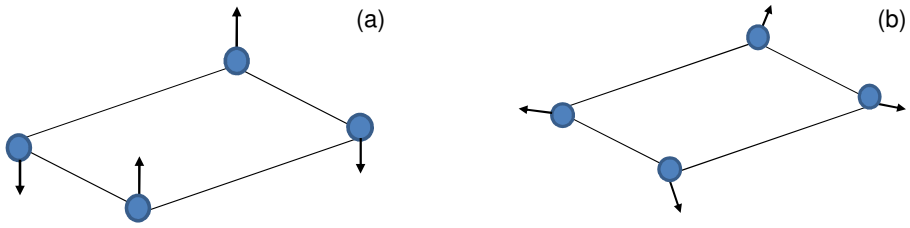

Figure 5.4 (a) Puckering and (b) breating modes of a four-membered ring (adapted from *Sathyanarayana DN.* [176]).

5.1.2 Quantum mechanics (QM) approach

Although classical mechanics describes molecular vibrational frequencies, according to it, an harmonic oscillator (a bond) may vibrate with any amplitude, i.e. it can posses any amount of energy, even zero (at rest), what is not actually correct. Quantum mechanics, instead, predict that molecules have only definite energy states, i.e. they can only lose or gain restricted amounts of energy. Therefore, to fully understand vibrational spectroscopy both classical and quantum mechanics are necessary [123,181].

In contrast to macroscopic particles for which the classical mechanics can determine exactly the position and velocity (or momenta), i.e. the state of the system, for microscopic scale particles (atoms, molecules, nuclei), due to their reduced mass, the act of the measurement itself perturbes their position or momentum in such a way, that these two quantities cannot be determined simultaneously (*Heisenberg's uncertainty principle*). As direct consequence of this uncertainty, quantum mechanics expresses microscopic particles as if they are spreading through space like a wave, and gives their position as a probability density of finding the particle at a given location in space.

The state of quantum-mechanical system is described by a state function ($\boldsymbol{\Psi}_{x,t}$), called wavefunction, which is a function of time and space coordinates of the particles of the system, and contains all the information about the particles, such as position, momentum, energy, etc. The possible $\boldsymbol{\Psi}_{x,t}$ and the energy of the system are found solving the (time-dependent) *Schrödinger equation* [174,180,181]:

$$-\frac{\hbar}{2m}\frac{d^2\boldsymbol{\Psi}_{x,t}}{dx^2} + V_{x,t}\boldsymbol{\Psi}_{x,t} = -\frac{\hbar}{i}\frac{d\boldsymbol{\Psi}_{x,t}}{dt} \qquad (5.21)$$

where $\hbar = \frac{h}{2\pi}$ and $i = \sqrt{-1}$. The probability density is given by $|\mathbf{\Psi}|^2$.

To characterize a stationary system, such as an isolated atom or molecule, whose potential energy is independent of the time, we start assuming that wavefunction $\mathbf{\Psi}_{x,t}$ can be separated into two independent functions of position and time:

$$\mathbf{\Psi}_{x,t} \equiv \Psi_x \cdot \phi_t \tag{5.22}$$

thus, a *time-independent Schrödinger equation* can be written, which for a one-particle, one-dimensional system is [181]:

$$-\frac{\hbar}{2m}\frac{d^2\Psi_x}{dx^2} + V_x\Psi_x = E\Psi_x \tag{5.23}$$

This equation can be written in the more compact form,

$$\hat{H}\Psi_x = E\Psi_x \tag{5.24}$$

where $\hat{H}$ is the Hamilton operator or *Hamiltonian* ($\hat{H} = \hat{T} + \hat{V}$, where $\hat{T}$ and $\hat{V}$ are the operators of the kinetic and potential energy, respectively). Each function Ψ_x and the corresponding energy are called eigenfunctions and eigenvalues of the Hamilton operator, respectively [174,180,181].

To solve *Schrödinger equation*, even for the simplest case of a diatomic molecule, several approximations are employed. To a first approximation, it is assumed that nuclei and electrons are pontual masses. Secondly, because an electron possesses a much smaller mass than the nuclei, hence, moves faster than the nuclei - appearing that the nuclei is stationary, the electronic and nuclear motion can be treated separately, i.e. the total wavefunction of a molecule can be separated into an electronic wavefunction and nuclear wavefunction (*Born-Oppenheimer approximation*).

For such cases, the total nuclear wavefunction of a molecule can then be separated into electronic, vibrational and rotational wavefunctions (neglecting nuclear spin) [172,174]:

$$\Psi = \psi_{elec} \cdot \psi_{vib} \cdot \psi_{rot} \tag{5.25}$$

and consequently, the corresponding energies are additive:

$$E = E_{elec} + E_{vib} + E_{rot} \tag{5.26}$$

Within the limits of the perturbation theory, these contributions can be calculated independently to a good degree of accuracy [181,182]. Therefore, the vibrational *Schrödinger equation* can be expressed as:

$$\widehat{H}_{vib}\Psi_{vib} = E_{vib}\Psi_{vib} \tag{5.27}$$

Using the expressions for T and V based in the normal coordinates Q_k (equations 6.17 and 6.18), the vibrational Hamiltonian assumes the form [172]:

$$\widehat{H} = -\frac{\hbar}{2}\sum_{k=1}^{3N-6}\frac{d^2}{dQ_k{}^2} + \frac{1}{2}\sum_{k=1}^{3N-6}\lambda_k Q_k{}^2 \tag{5.28}$$

and the total vibrational *Schrödinger equation* is*:*

$$-\frac{\hbar}{2}\sum_{k=1}^{3N-6}\frac{d^2\psi_{vib}}{dQ_k{}^2} + \frac{1}{2}\sum_{k=1}^{3N-6}\lambda_k Q_k{}^2\,\psi_{vib} = E_{vib}\psi_{vib} \tag{5.29}$$

where E_{vib} is the total vibrational energy. Since the normal coordinates Q_k are independent of each other, the total vibrational wavefunction can be separated into $3N-6$ wavefunctions, each associated with a single normal coordinate:

$$\psi_{vib} = \psi_1(Q_1)\cdot\psi_2(Q_2)\cdot\ldots\cdot\psi_{3N-6}(Q_{3N-6}) \tag{5.30}$$

and so, $3N-6$ equations of the form:

$$-\frac{\hbar}{2}\frac{d^2\psi_k}{dQ_k{}^2} + \frac{1}{2}\lambda_k Q_k{}^2\psi_k(Q_k) = E_k\psi_k(Q_k) \tag{5.31}$$

are obtained. These are time-independent Schrödinger equations for the harmonic oscillator model, and their eigenvalues are:

$$E_k = \left(v_k + \frac{1}{2}\right)h\nu_k \qquad \begin{matrix} k = 1, 2, \ldots, 3\text{N-}6 \\ v_k = 0, 1, 2, \ldots \end{matrix} \tag{5.32}$$

where, v_k is vibrational quantum number associated to the normal vibrational mode k, h is the Planck's constant (6.626 x 10^{-34} J s) and ν_k is the classical vibrational frequency, described by equation 6.3. This means that the harmonic oscillator can possess only discrete energy values and vibrate only with discrete amplitude, contrary to the classical idea. Any molecule (or ion) can only exist in definite energy states, called *stationary states*, in which it will remain indefinitely, unless some external factor, such as exposition to electromagnetic radiation, intervenes. Then, a molecule (or ion) may absorb or emit a photon of frequency ν and make a *transition* to another stationary state, as long as $h\nu$ matches the difference in energy between the two states.

Stationary states differ in energy and in the amplitude of the oscillation. The lowest energy state (v_k = 0, $E = \frac{1}{2}h\nu_k$) is called *fundamental* or *ground state* and corresponds to the normal frequency of the classic mechanics. Stationary states of higher energy are called *excited*

states. Because, under normal conditions, most of the population is in the level $v_k = 0$[38] and according to the harmonic-oscillator selection rule only those transitions corresponding to $\Delta v_k = \pm 1$ are allowed, the main transitions are $v_k = 0 \rightarrow 1$, which are referred to as *fundamental transitions* [181]. Transitions starting from excited states, which are observed as *hot bands*, can also occur as long as they obey the harmonic oscillator selection rule, such as the transition $v_k = 1 \rightarrow 2$. However, as their name points out, these transitions only become more intense and observable, with the increasing of temperature, as the population of the excited states increases with the increase of temperature.

Experimentally, one finds deviations from the harmonic oscillator model, since bands forbidden by the harmonic oscillator approximation are observed and oposite to the predicted series of equally spaced and never ending vibrational levels, a molecule actually presents a finite number of vibrational levels and once the vibrational energy exceeds the dissociation energy, D_e, the molecule dissociates [176,181]. This occurs because bonds in real molecules do not act as a harmonic oscillator, but rather as anharmonic vibrators, since the force needed to compress a bond by a definite distance is larger than the force required to stretch it [123].

A correction term is then introduced in equation 6.32 to account for anharmonicity:

$$E_k = \left(v_k + \frac{1}{2}\right) h\nu_k - \left(v_k + \frac{1}{2}\right)^2 h\chi_k\nu_k \qquad \begin{matrix} k = 1, 2, ..., 3\text{N-6} \\ v_k = 0, 1, 2, ... \end{matrix} \tag{5.33}$$

where χ_k is the *anharmonicity constant*.

Due to anharmonicity, the harmonic oscillator selection rule is relaxed and bands caused by transitions that involve the variation of a single vibrational quantum number by $\Delta v_k > 1$, named *overtones* and bands caused by transitions that involve the variation of two or more vibrational quantum numbers at the same time by $\Delta v_k \geq 1$ and $\Delta v_l \geq 1$ (where k and l represent two different modes), named *combination*, become allowed. *Overtones* bands occur when a single photon excites a single mode beyond $\Delta v_k = 1$; the transition $v = 0 \rightarrow 2$, referred to as the *first overtone* has a frequency of approximately twice that of the fundamental transition, $2\nu_1$, the transition $v = 0 \rightarrow 3$, referred to as the *second overtone*, has approximately three times the frequency of that of the fundamental transition, $3\nu_1$, and so on. *Combination bands* occur when a single photon excites more than one vibration, fundamental or overtone, producing bands with frequencies approximately to the sum or

[38] According to Boltzman distribution, at room temperature (and for relatively light molecules), the population of the higher energetic states is normally lower than that of the ground state [181]. As the intensity of each transition is proportional to the population of the energy level from which the transition originates, the intensity of the transitions originated in the ground state are most intense.

difference of the involved vibrations, for example, $2\nu_1 + \nu_2$; $\nu_1 + \nu_3$ or $3\nu_2 + \nu_1$. Generally, overtones and combination bands are much weaker than the fundamental modes from which they derived [180,182,183].

Because anharmonicity lowers the spacing between adjacent vibrational levels as v increases, hot bands, overtones and combinations present a frequency below the expected value [174].

Although, infrared and Raman spectroscopy are both vibrational spectroscopic techniques, the mechanism of interaction of radiation with matter is different for each technique, thus complementary vibrational information may be acquired. A brief introduction to both techniques will be given.

5.2 Infrared spectroscopy

Infrared radiation is insufficient to cause electronic transitions, but it has enough energy to induce vibrational and rotational transitions in the ground electronic state.

When a sample is illuminated with infrared radiation (which contains a continuous range of frequencies), those frequencies of the infrared radiation that coincide exactly with vibration frequencies of the sample are selectively absorbed, decreasing the intensity of the beam that passes through the sample (for each frequency) from $I_0(\nu)$ to $I(\nu)$ (Figure 5.5 and 5.6a).

Figure 5.5 Simplified scheme of the infrared absorption mechanism (adapted from *Ferraro JR, et al.* [163]).

Two ways are commonly used to express how much light is absorbed by the sample. Either as the percentage of incident radiation that is transmitted by the sample, percentage transmittance, $T\ (\%)$:

$$T\ (\%) = \frac{I}{I_0} \times 100 \tag{5.34}$$

or as the fraction of the incident radiation that is absorbed by the sample, absorbance, A:

$$A = \log \frac{I_0}{I} \tag{5.35}$$

Because according to Beer-Lambert law, absorbance is linearly related to the concentration, c, of the sample:

$$A = \varepsilon l c \tag{5.36}$$

where ε is the molecular absorption coefficient (L mol^{-1} cm^{-1}), and l and c are the pathlenght (cm) and the concentration (mol L^{-1}) of the sample, respectively, IR spectroscopy can be used for quantitative analysis [(163)].

The graphic plot of the measured absorbance, A (or % transmittance, T) at each frequency, originates an *Infrared spectrum* (Figure 5.6b). However, because in vibrational spectroscopy the reciprocal of the wavelength, called wavenumber $\tilde{\nu}$ ($\tilde{\nu} = 1/\lambda$, in cm^{-1}) rather than the frequency ν ($\nu = c/\lambda$, in cycle/s) is used to characterize the electromagnetic radiation, IR spectra are generally a graphic representation of absorbance (or % transmittance) *vs*. wavenumbers.

Because frequency and wavenumber only differ by c, the velocity of light ($\tilde{\nu} = \nu/c$), it is not unusual to refered to the wavenumber as the vibrational frequency.

5.3 Normal Raman spectroscopy

Raman spectroscopy differently from infrared spectroscopy does not observe light absorbed/transmitted by a sample, but rather the light that is inelasticly scattered by the sample.

Scattering can be understood as an absorption-emission concerted process, i.e. the absorption of one photon of the incoming radiation is accompanied by simultaneous emission of one photon in a different direction, with no measurable time delay between the two events[39]. With absorption the molecule arises to a highly energetic non-stationary state (is not a solution of the Schrödinger equation), normally designed as virtual state, from which it will tend to move on to one of its stationary states, emitting a photon with a different direction from the exciting one [(181)].

[39] Although, in order to become clearer, it is normally referred that emission takes place after absorption, the opposite order, emission followed by the absorption can occur [(184)].

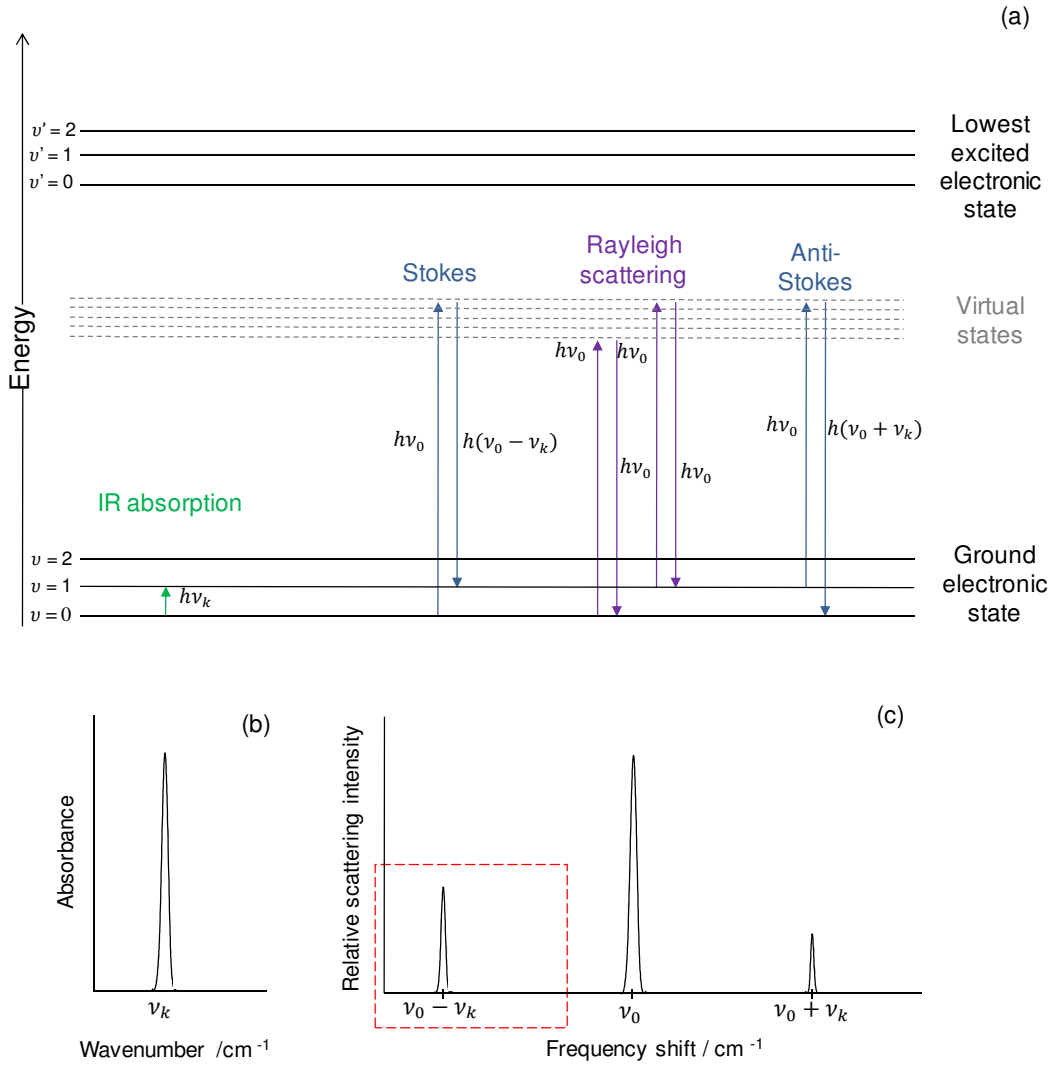

Figure 5.6 (a) Energy level diagram illustrating the energetic transitions induced by infrared absorption, and Raman and Rayleigh scattering in a diatomic molecule (single vibration mode). (b) Infrared spectrum and (c) Raman and Rayleigh scattering simplified spectrum (the red dash square represents the usual Raman spectra). Figure adapted from *Nakamoto K.* [175] and *Keresztury G.* [185] (not to scale).

When monochromatic radiation of frequency ν_0 is incident on a molecular system, most scattered photons will have the same energy of the incident photon (elastic scattering), the scattering process being known as Rayleigh scattering. However, during the interaction process, as observed and published by C.V. Raman in 1928[40], the excitation photon can lose

[40] C.V. Raman (with K.S. Krishnan) was the first one to observe and publish this inelastic scattering phenomenon in liquids, in 1928. These two Indian physicists observed that a small fraction of the radiation scattered by certain molecules presented a different wavelength from that of the incident beam, and that the shifts in wavelength were independent of the wavelength of excitation, but rather, depend upon the chemical structure of the molecules responsible for the scattering, more precisely on the vibrational (and/or rotational) motions, just like in infrared spectroscopy.

part of its energy to the molecule, or gain part of the energy of the molecule (inelastic scattering), the scattering process being known as *Raman scattering* (Figure 5.7). Although the Raman scattering is much weaker than the Rayleigh scattering (about 10^{-3}) it is observed if a strong excitation source, such as a laser[41] is used [186].

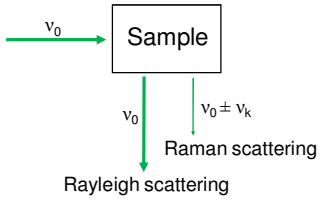

Figure 5.7 Simplified scheme of the Raman scattering mechanism (adapted from *Ferraro JR, et al.* [163]).

It is observed that the excitation photon, ν_0, losses part of its energy to the molecule, and creates a scattered photon with frequency $\nu = \nu_0 - \nu_k$, where ν_k corresponds to the frequency associated to a vibrational transition, when the molecule is initially at its ground state (the most probable situation according Boltzman distribution). Otherwise, the excitation photon, ν_0, gains part of the energy of the molecule and creates a scattered photon with frequency $\nu = \nu_0 + \nu_k$, when the molecule is initially in an excited state (Figure 5.6a).

Consequently, for each scattering event three bands appear in the spectrum of the scattered light, a dominant band (Rayleigh line) with the same frequency of the exciting radiation (ν_0) and two bands equally shifted from this dominant band, one to the negative frequency side ($\nu = \nu_0 - \nu_k$) that for historical reasons is referred to as Stokes band and other to the positive frequency side ($\nu = \nu_0 + \nu_k$) referred to as anti-Stokes band [181].

In practice, because Raman frequencies are measured relatively to the excitation source, frequency shifts, the origin of the abscissa scale in the Raman spectrum can be placed at the position of the excitation frequency, ν_0, and instead of a frequency shift ($\nu_0 \pm \nu_k$) (Figure 5.6b), a frequency ($\pm\nu_k$) is used. Furthermore, as Stokes and anti-Stokes bands provide precisely the same molecular information, only the most intense part of the spectrum, Stoke's, is generally recorded, with the dispense of the negative sign. The *Raman spectrum* is generally a plot of intensity of scattered light versus wavenumber (Figure 5.6c, red dash square).

In normal Raman spectroscopy the frequency of the excitation radiation is chosen to be far apart from the frequency of any electronic absorption band, since when (intentionally or

[41] LASER is the acronym of "Light Amplification by Stimulated Emission of Radiation".

not) the frequency of the excitation source is near or exactly the same of an electronic transition, resonance and/or fluorescence effects can occur. While Resonance (and pre-resonance) Raman spectra can be very useful for identification (since special features are enhanced), fluorescence is a hazard to Raman analysis. Due to its strong intensity, fluorescence emission swamps the weaker Raman scattering (typically only about 10^{-6} of the intensity of the incident radiation [163,186]) making spectra acquisition seriously difficult.

Because Raman scattering efficiency depends on the fourth power of the frequency of the light being scattered, ν^4, highly quality spectra are acquired when higher frequency light is used as excitation. Unfortunately, because the laser used in Raman spectroscopy is invariably focussed to a very bright spot, large transfers of energy can occur if the sample is capable of absorbing the laser radiation. This can causes sample heating and consequently, in severe cases, burning and/or decomposition [187]. Nevertheless, several procedures, such as reduction of the laser power, changing of the laser wavelength, defocusing the laser beam on the samples, cooling the sample and rotating the sample, can be used to reduce laser absorption [163].

5.4 Infrared and Raman activity

Depending on the symmetry of the molecules, some vibrational transitions are only *allowed* or *active* in the IR spectra, only active in the Raman spectra or active in both spectra. Vibrational transitions which are not active are *forbidden* or *inactive* in one or in both spectra.

A vibrational mode is theoretically infrared *allowed* or *active*, originating a band in the IR spectra, if the electric dipole moment of the molecule changes in the course of the vibration mode. Vibrations that produce the largest variation of electric dipole moment, i.e. vibrations involving polar bonds such as O–H, N–H, C=O, are the ones that exhibit the most intense infrared bands; the largest the electric dipole moment variation with the vibration mode, the strongest the correspondent IR band [188].

A vibrational mode is theoretically Raman *allowed* or *active*, originating a band in the Raman spectra, if the *polarizability* of the molecule changes in the course of the vibration mode. When a molecule is exposed to an electric field it suffers distortion, as electrons and nuclei are forced to move in oppose directions and an induced electric dipole moment, P, proportional to the molecular polarizability and to the electric field strength ($P = \alpha E$) is developed. Generally, vibrations involving symmetrical bonds, such as C=C, C–C, and S–S exhibit the most intense Raman bands, since these involve the largest variation of the

polarizability; the largest the polarizability variation with the vibration mode, the strongest the correspondent Raman band.

For centrosymmetric molecules, i.e. molecules which have a centre of symmetry, the *rule of mutual exclusion* applies - the vibrational modes which are symmetric with respect to an inversion through the center of symmetry are Raman active but IR inactive, while the vibrational modes which are antisymmetric with respect to an inversion through the center of symmetry are Raman inactive but IR active. This relationship is useful for discerning if the molecule under study has a center of symmetry and demonstrates the complementary nature of IR and Raman spectroscopies best of all [181,189].

Because different selection rules are applied to IR and Raman spectroscopies, the IR and Raman spectra of the same sample may present significant differences. Figure 5.8 presents the IR and Raman spectra of the inorganic pigment malachite, $[Cu_2(CO_3)_2(OH)_2]$, illustrating the similarities and differences that can occur between these two types of vibrational spectra. Because the vibrational modes of the three involved groups, OH, CO_3^{2-} and CuO, are infrared and Raman active, the IR and Raman spectra for this pigment are very similar, both in number and position of the bands (due to the cut-off of the equipment, there is no IR information below 650 cm^{-1}). However, some differences are seen, for example, the OH stretching modes 3405/3334 (IR) 3386/3317 (R) are much more intense in the IR spectrum [190,191], because as referred before, when allowed, vibrations involving polar bonds present more intense bands in the IR spectrum than in the Raman spectrum.

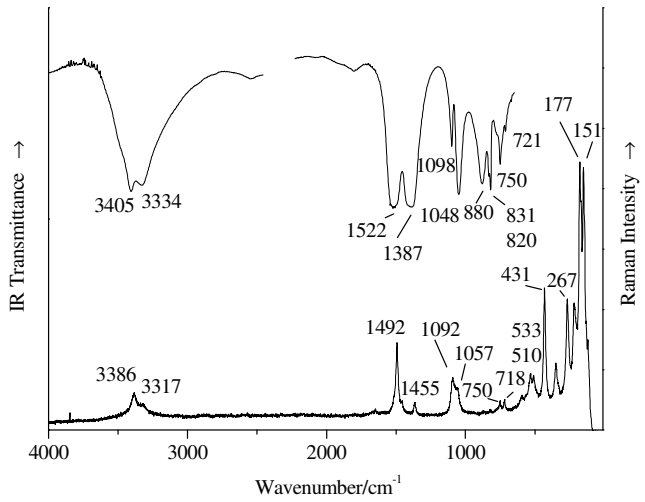

Figure 5.8 Infrared (top) and Raman (bottom) spectra of malachite.

Due to the complementary of IR and Raman spectroscopies, both techniques are needed to achieve complete structural information.

5.5 Interpretation of vibrational spectra

Interpreting a vibrational spectrum consists in the assignment of each band of the spectrum to a vibrational mode (CM) or to the transition associated to that mode (QM), which is not straightforward even for simple molecules. According to the model of the harmonic oscillator, 3*N*-6 (3*N*-5) normal vibrational modes or fundamental transitions are expected. However, there are a high number of factors that can influency the number of bands and the vibrational frequencies, adding complexity to the interpretation.

Normal Coordinate Analysis (NCA) is the most accurate method for the interpretation of a spectrum. This complex method calculates the normal coordinates (describe the type of vibrational motion) of molecules (or ions) and the respective bands in the vibrational spectra, both frequencies and intensities. However, an accurate *a priori* knowledge of force constants, equilibrium geometry and atomic masses and the existence of experimental frequencies is a prerequisite [175,182].

For small molecules, because the number of normal modes is reduced and the force constants can be reliably calculated with (6.2), the interpretation of the spectra based in NCA is relatively simple, but for polyatomic molecules, as the number of atoms and the complexity of the normal vibrations increases, calculations become burdensome. Fortunately, a large number of computer programs have become available, making it possible to calculate normal modes for larger molecules, even those that are inactive or inaccessible with infrared and Raman spectra [176]. The programs, starting from a trial set of force constants, generates frequencies, compares them with experimental ones and refine the force constant until the difference between the calculated and the experimental spectra is minimal as possible. It is important to refer that the calculated values are harmonic, while the experimental ones are essentially anharmonic [192].

As already referred, depending on the symmetry of the molecules, some normal vibrational are *allowed* while others are *forbidden*, therefore, for molecules with some symmetry or part of molecules with symmetry, it is possible to predict theoretically which vibration modes will be allowed, i.e. the number of bands to expect, without the complex calculations of NCA. Combining *Molecular Symmetry* (symmetry properties), *Group Theory* (a branch of mathematics) and Quantum Mechanics, spectra are qualitatively determined.

The symmetry of a molecule (or part of a molecule) is expressed by *symmetry elements* present in it, such as mirror planes or rotation axes, which relate equivalent part of the molecule to each other. Therefore, only under a certain set of *symmetry operations*, such as rotation, reflection, inversion, etc., directly related to the symmetry elements present in the molecule, will the molecule be invariant, i.e. will retain its original configuration or move into a new orientation equivalent to the original one [193].

Because each set of symmetry operations posses the properties of a mathematical group it is called point group[42]. Based on the symmetry elements present in the molecule, which can be found using systematic procedure, such as flow charts, it is possible to assign any molecule to a point group [163,180,193].

Each point group can have different representations, which are listed under a *character table* available, most commonly as appendices in relevant books. Because normal coordinates form the basis for one of such representations[43], they can be classified into symmetry species of a point group and their activity determinate by inspection of the respective character table: a vibration is Infrared active if it belongs to the same symmetry specie of at least one of the components of the electric dipole moment μ_i (x, y, z), while a vibration is Raman active if it belongs to the same symmetry specie of, at least, one of the components of the molecular polarizability tensor α_{ij} $(xy, xz, yz, x^2, y^2, z^2)$ - these are the *General Vibrational Selection Rules* [175,180].

Because this approach does not determine frequency and intensity of the bands, the number of bands determined to be active may not correspond to the number observed in real spectra as described below (5.5.2).

Although *Normal Coordinate Analysis* and *Molecular Symmetry* with *Group Theory* allow the interpretation of vibrational spectra, these two approaches are quite complex for most routine qualitative and quantitative purposes. A much simpler semi-empiric approach, *Functional Group Analysis*, is generally used, even though complete assignment is not possible.

5.5.1 Functional Group Analysis

From observation of the vibrational spectra of a large number of compounds, throughout the years, it was verified that, several groups of atoms, were relatively insensitive to the rest of the molecule, originating characteristic bands in a relatively narrow range of wavenumbers (frequencies), called *group frequencies*[44] or *characteristic frequencies*.

Although most or all the atoms in the molecule are vibrating in each normal mode, certain normal modes can be considered as involving mainly the motion of a small group of atoms - *functional group* (the other atoms vibrating only slightly), whose frequency is almost exclusively dependent on the magnitude of the force constant. The most known functional groups are those present in organic molecules, such as hydroxyl (O-H), carbonyl (C=O) and

[42] So named because at least one point, the center of mass, is invariant to all operations of the group.
[43] μ_i and α_{ij} also form the basis for one of such representations.
[44] We recall that in vibrational spectroscopy, the term frequency is commonly used to refer to wavenumber ($\tilde{\nu}$), and that the two terms are used interchangeably. Therefore, although called a group frequency it is in fact a group wavenumber.

nitriles (C≡N). Table 5.1 presents the wavenumber range of the stretching vibrations of some organic functional groups.

Table 5.1 Characteristic wavenumber ranges of the stretching vibrations of some organic functional groups.

Functional group	Wavenumbers / cm^{-1}
O-H	3700-3000
N-H	3520-3280
C≡N	2260-2130
C=C	1900-1500
C=O	1840-1630
C=N	1690-1610
C-Cl	850-550
C-Br	700-500
C-I	600-465

Adapted from *Shrader B.* [177] and *Shurvell HF.* [178]

Although the group frequency occurs in a relatively narrow wavenumber range, because the value of the force constant depends on the electronic structure of the vibrating bond, which may be slightly perturbed by different side groups, the group frequencies wavenumber range for each specific class of compounds is even narrower. For example, all the molecules containing a carbonyl group (C=O) present a stretching band at about 1840-1630[45] cm^{-1}, but the precise wavenumber region depends of whether the carbonyl group is included in an ester, aldehyde, ketone, carboxylic acid, etc. (Table 5.2).

Table 5.2 Narrower wavenumber ranges of the stretching vibrations of carbonyl groups of some classes of compounds.

Class of compoud	Wavenumber / cm^{-1}
Ester	1750 - 1740
Aldehyde	1740 - 1720
Ketone	1720 - 1700
Carboxylic acid	1710 - 1690
2º Amide	1680 - 1630

Adapted from *Shurvell HF.* [178]

[45] If metal carbonyls and the salts of carboxylic acids are included, this region is extended to 2200-1350 cm^{-1} [178].

Because the binding forces within polyatomic ions (covalent bonds) that constitute the inorganic compounds are significantly stronger than the forces binding the ion to the rest of the structure, polyatomic ions, such as carbonates (CO_3^{2-}), sulfates (SO_4^{2-}) and phosphates (PO_4^{3-}) can also be treated as functional groups. Table 5.3 presents the main infrared wavenumber ranges for some inorganic polyatomic ions.

Table 5.3 Main IR wavenumber ranges of some common inorganic ions.

Ion	Wavenumber / cm^{-1}
Carbonate	1490-1410, 880-860
Sulfate	1130-1080, 680-610
Phosphate	1100-1000
Silicate	1100-900

Adapted from *Bellamy LJ.* [194]

Based in the group frequencies values, which are well documented and can easily be found in the *group frequency tables*, *charts* and devoted books [175,177,178,188,194-196], the spectrum of the "unknown" is, in first place, visually examined in order to assign most characteristic bands and rapidly identify the class of compound (carbonate, acetate, sulfate, aldehyde, etc.). The same importance must be given to either the presence as to the absence of bands. Knowing the class of compound, the spectrum of the "unknown" is then compared with *reference spectra* of compounds belonging to that class, paying attention both to position, intensity and shape of the bands.

Comparison is done against spectra of published Atlas (printed libraries) and reference papers and books, or using computer search programs, which selected from digital databases the spectra that most closely match that of the "unknown". A perfect match between the "unknown" spectrum and a reference spectrum is a confident proof of its identity.

Because spectra depend of the experimental set-up conditions and physical state of the sample, is highly recommended to compare spectra acquired under the same conditions. Therefore, often there is the need to acquire reference spectra of samples for each particular study.

For complex samples, it might be necessary to use the complementarity of other analytical techniques. A previous knowledge of the compound's origin, such as its elemental composition facilitates the vibrational analysis.

5.5.2 Factors affecting the vibrational spectra

There are a high number of factors that can increase or reduce the number of bands regarding the 3*N*-6 (3*N*-5) number predicted from the harmonic oscillator model, produce shifts in the vibrational frequency or change the appearance (shape and symmetry) of the bands, adding complexity to the interpretation of the spectra, but at the same time providing an unambiguous fingerprint for any particular molecule.

Anharmonicity, Fermi resonance, vibronic coupling, splitting of degenerate frequencies by lowering of the symmetry, intermolecular interactions, factor group splitting (in crystals), physical state and temperature increase are some of the factors that can led to an increase of the number of bands [188].

As referred before, because bonds in real molecules act as anharmonic vibrators, *overtone* and *combination* transitions become allowed (as long as they obey the selection rules) and the respective bands can be observed in the vibrational spectra. Nonetheless, overtone and combination bands are generally much weaker than the fundamental modes from which they derived, not being always observed.

When two vibrational modes have approximately the same energy (accidental degeneracy) and the same symmetry, *Fermi resonance* can occur, producing two close bands, when only one was expected. The two bands, which are referred as *Fermi doublet*, present approximately the same intensity and a frequency slightly below and slightly above the expected value. Because often the energy of an overtone or combination is very close to that of a fundamental, this interaction is more commonly for these cases [178].

When adjacent bonds, vibrating in the same plane are accidentally degenerate, there can be a mixture of the modes and no longer can the bands be assigned to a single mode. This interaction is called *vibronic coupling* and as result, in-phase and out-of-phase combinations of the vibrations will appear.

When two or more vibrational modes are physically indistinguishable in space, such as the bending modes of a linear XY_2molecule (like CO_2), Figure 5.9, they are referred as degenerate by symmetry, in the presented case as doubly degenerated modes. Degenerated modes are characterized for present the same frequency, i.e. appear as a single band in the IR and Raman spectra. Whenever the symmetry of the group is lowered, the initially degenerated modes may become different and consequently, present different frequencies, increasing the number of bands.

Due to intermolecular interactions, symmetry can be lowered causing splitting of degenerate modes and the formation of new species, such as dimmers, which involve the formation of new bonds, can originate new bands. As will be presented below, in the particular case of crystals, due to the lowering of symmetry, factor group splitting and lattice

vibrations, the number of bands can be larger than the number of bands of spectra of other physical states.

Since the population of the excited states increases with temperature, raising the temperature, transitions starting from excited states become more intense and the respective *hot bands* can become observable.

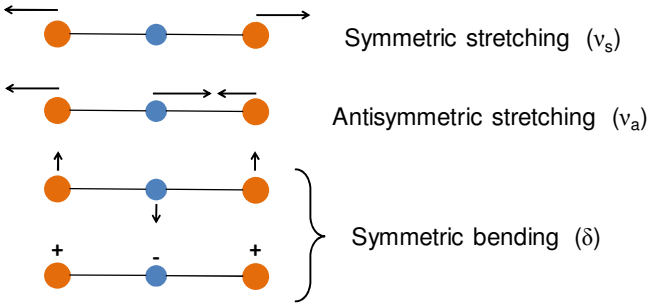

Figure 5.9 The normal modes of vibration of a linear XY_2molecule (like CO_2). The + and - signals indicate upward and downward motion in the plane of the paper, respectively. The upper symmetric bending occurs in the plane of the paper (just like the two stretching modes), while the bottom symmetric bending occurs at right angles to the plane of the paper.

On the other way, vibrations forbidden by selection rules, weak intensity of the bands, accidental degeneracy, degeneracy by symmetry, cut-off of the equipment and poor quality of the spectra can cause a reduction of the number of bands relatively to the 3*N*-6 (3*N*-5) number predicted from the harmonic oscillator model.

As already presented in 6.4, depending on the symmetry of the molecules, some vibrations are allowed, while others are forbidden. When the vibration is allowed, the respective band can be identified or not, depending on its intensity - weak bands may not be identified. However, if forbidden, no band will be identified.

When accidentally or by symmetry two or more vibrational modes are degenerated, the respective bands cannot be resolved in the spectra of the liquid and solid phases. Instead, the spectra present broad bands, which are an overlap of the several not resolved bands.

The cut-off that the equipment presents, especially in IR spectroscopy, where often the lower limit is 650 - 450 cm^{-1}, does not allow the detection of bands occurring at lower wavenumbers, such as bonds involving heavy metals. In Raman spectroscopy, the cut-off is not a drawback, since it is normal to go down to wavenumbers such as 100 - 50 cm^{-1}.

Spectra quality is in fact a very important parameter in spectra interpretation, since poor quality: either very low or very high intensity, low signal-to-noise ratio, low resolution or sloping baseline, can produce not only a reduction of the number of bands, but also changes in the shape, frequency and relative intensity of some of the bands, making difficult the

comparison with reference spectra. In Raman spectroscopy, fluorescence, which is several times more intense than the Raman scattering, is often responsible for a high sloping baseline that completely or almost swamps the Raman signal from the sample.

Temperature, indutive/resonance effects, steric effects, intermolecular interactions and physical state of the sample (gas, liquid, solid) contribute to the form, intensity and position of the bands.

Lowering of the temperature usually makes the bands sharper and at the same time shifts their frequencies to higher values; inductive and resonance effects, because they change the distribution of the electrons in the molecule, are responsible for the raise and decrease of the expected frequencies, respectively. Inductive effects raise the frequency as a result of the displacement of the electron cloud towards the adjacent more electronegative group, resonance effects decrease the frequency as delocalized structures are formed; when the functional group is part of a ring, due to steric effects, as the angle strain increases (i.e. the ring becomes smaller), the frequency also increases; Intermolecular interactions produce changes of the force constant, and therefore shifts in the frequency. In particular, polar solvents, through solvent-solute interactions, such as hydrogen bonding, can cause significant shifts of group frequencies and broadening of bands [178,188,196].

5.5.3 Vibrations in crystals

Interpretation of a spectrum of a solid state sample, specially crystals, where molecules (or ions) have well defined positions (sites in the *lattice*) and intermolecular interactions become important, is somewhat more complex that for isolated molecules (or ions).

A crystal can be seen as a three-dimensional regularly repeating of a 'structural motif' the *unit cell* that is itself composed by a number of molecules (atoms, ions). By convenience, the pattern produced is generally expressed in terms of an array of imaginary points located at the position of the molecules (atoms, ions), called the *crystal lattice*, which may be regarded as a sort of framework or skeleton of the crystal. A crystal can then be considered to have a total of 3NZ degrees of freedom, which combine to form 3NZ vibrational modes, where Z is the number of unit cells and N the number of atoms in each unit cell [163,197].

Because intramolecular bonds (covalent bonds) are normally stronger than the intermolecular ones (van der Walls forces, electrostatic interactions and hydrogen bonds), molecules (ions) in a crystal keep their individuality and can be approximately treated as isolated entities (Local Symmetry). In fact, their spectra are quite similar to the spectra of the same molecules in the gaseous, liquid or matriz-isolated state.

However, due to the intermolecular interactions that exist, different restrictions are imposed to their vibrational modes and consequently, the symmetry of the molecule is

generally lower in the crystalline state (Site Symmetry) than in the gaseous (isolated) state. This reduction of symmetry (due to the disappearance of some symmetry elements) may cause splitting of the degenerate vibrations and band shifting, may activate inactive vibrations, etc, producing a spectrum with some unique features, very useful for identification purposes.

Additional complexity to the spectra of crystals arises from the fact that when the unit cell contains more than one chemically equivalent molecule (ions), these can couple. As a result, the bands seen for the molecule in the free state can be splitted into as many components as the molecules in the unit cell and the frequency shifted. This intermolecular coupling is called *factor group* splitting or *Davydov* splitting [163,198].

Site Group Analysis, which is based in the site symmetry, provides an adequate interpretation of the internal vibrational modes (depend only of the molecule/ion). However it neglects the coupling of vibrations between neighbouring molecules (ions).

Since molecules (ions) are bonded to neighbouring molecules (ions) in each unit cell and, each unit cell is bonded to neighbouring unit cells, displacement of one or more atoms from their equilibrium site position, even by a small amount, causes the displacement of neighbouring atoms, giving rise to waveform vibrations that propagate through the entire lattice, called *lattice vibrations* or *phonons*[46].

The waveform vibrations are divided in two branches: *acoustic* and *optical*, depending of the motion. The *acoustic branch* represents the modes where the molecules (atoms) in each unit cell are vibrating in the same direction. This motion corresponds to an overall translation of the unit cell as a whole (*acoustic vibrations*), consequently, in a three-dimensional lattice there are three acoustic modes. The *optic branch* represents the modes where the molecules (atoms) in each unit cell are vibrating in opposite directions (the center of mass of the unit cell remaining unshifted). Depending on the direction of the displacement of the molecules (ions) relatively to their equilibrium site position, the lattice modes are further classified as *longitudinal* (LO and LA) if the vibration (displacement) is formed along the direction of propagation, or as *transverse* (TO and TA) if the vibration is formed at right angles to the direction of propagation [163,199]. Figure 5.10 schematically represents the wave motion that can occur in an infinite unidimensional diatomic lattice. Various wave motions are associated to each of the branches presented, as result of the different phases of motion between consecutive cells[47].

[46] In analogy with the photon of the electromagnetic wave, since the energy of the lattice vibrations is also quantized.
[47] An elucidative demo can be seen in internet [200].

Since Z is very large, a crystal has a huge number of vibrations. However, fortunately, the observed IR and Raman spectra are relatively simple because: (i) the radiation used in IR and Raman spectroscopy has much longer wavelengths than the dimensions of the unit cell (thousands of Ångströns *vs.* several Ångströns) hence, only the vibrational modes in which neighbouring unit cells vibrate in phase are observed, (ii) only the frequencies of the optical modes are detected in IR and Raman spectroscopy. The frequency of the acoustic modes are very low, occurring in sonic and ultrasonic region, and hence its name [123,163].

As referred before, 3 out of the 3NZ modes are acoustic (translations of the unit cell as a whole) hence, do not appear in the IR and Raman spectra. This leaves 3NZ-3 optical modes, which are grouped in Z(3N-6) internal modes (depend only of the molecule/ion) and 6Z-3 *lattice modes*[48] or *external modes*. The *lattice modes* are further classified as 3Z *rotatory lattice* modes (also known *librations*) and 3Z-3 *translatory lattice* modes, which result of the 'frizzed' rotational and translational degrees of freedom that a molecule presents when isolated, respectively [175,176,197]. A complete interpretation of the spectra of samples in the solid state is obtained using the *Factor Group Analysis*.

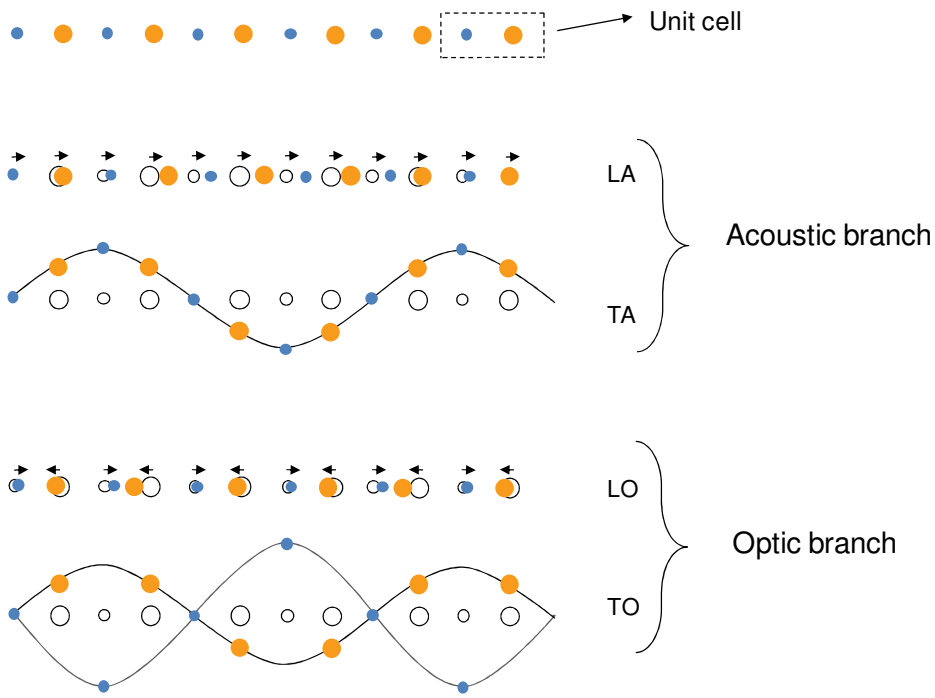

Figure 5.10 Wave motion for an infinite one-dimensional diatomic chain (adapted from *Ferraro JR, et al.* [163] and *Franke K, et al.* [199]).

[48] External vibrations only.

Rotatory and translatory lattice modes generally occur below 300 cm^{-1} (intermolecular forces are weaker than intramolecular), a region normally not used for most current IR analyses (which are in the mid-infrared region, MIR), but easily obtained by Raman. However, for molecules (ions) with flexible bonds and/or containing heavy atoms, internal vibrations can have such low frequencies that occur in the same region of the lattice modes, making difficult the band assignment. Assignment of the lattice modes is particularly important when interpreting the spectra of ionic crystals, semiconductors and metals [123].

Spectra of crystals are also affected by the existence of imperfections in the crystal lattice. If imperfections, such as the presence of impurities and vacancies exist, an additional broadening of the Raman bands is verified. In particular, the Raman spectra of amorphous materials are characterized by very broad features [186].

5.6 Infrared and Raman microscopies

Infrared microscopy (μ-IR) is known since about late 1940s, early 1950s. In fact, the first IR microscope was commercialized in 1953: a Perkin-Elmer Model 85. However, it was not until mid-1980s, when the well established interferometric spectrometers were combined with the microscopes, that it had become widespread. During the 1908s and 1990s there were improvements in the development of micro-sampling accessories and more sensitive detectors, but the fundamental design features of current IR microscopes are still mainly those present in the Perkin-Elmer Model 85 [112,113].

Ramam microscopy (μ-R) (also known as Raman microprobe) was developed in the mid-1970s, but for many years was not widespread as a result of its high cost, low sensitivity and large sized equipment. Since the early-1990s, with the employment of charge-couple device detectors (CCD), which provide much higher sensitivity levels and holographic notch filters, which efficiently block the undesirable excitation light, Raman microscopes became low-cost, highly efficient, benchtop and therefore, more available [201-203].

Nowadays, both techniques are routine techniques in a large number of laboratories, since they provide molecular information using a smaller amount of sample than the conventional IR and Raman spectroscopies, and also provide information not obtained by conventional techniques, such as stratigraphic analysis and depth profile.

5.6.1 Instrumentation

The design of an IR or Raman microscopy assembly is obtained introducing a compound microscope in the bulk vibrational instrumentation. It consists basically in an excitation source, a compound microscope, a spectrometer, a detector and a PC. This last, allows the

control of the measurements quality, the functions of the spectrometer and the digital acquisition of the spectra. Figure 5.11 shows an Infrared microscopy assembly (interferometer configuration), while Figure 5.12 shows a dispersive configuration of a Raman microscopy assembly (the equipments that have been used in this study).

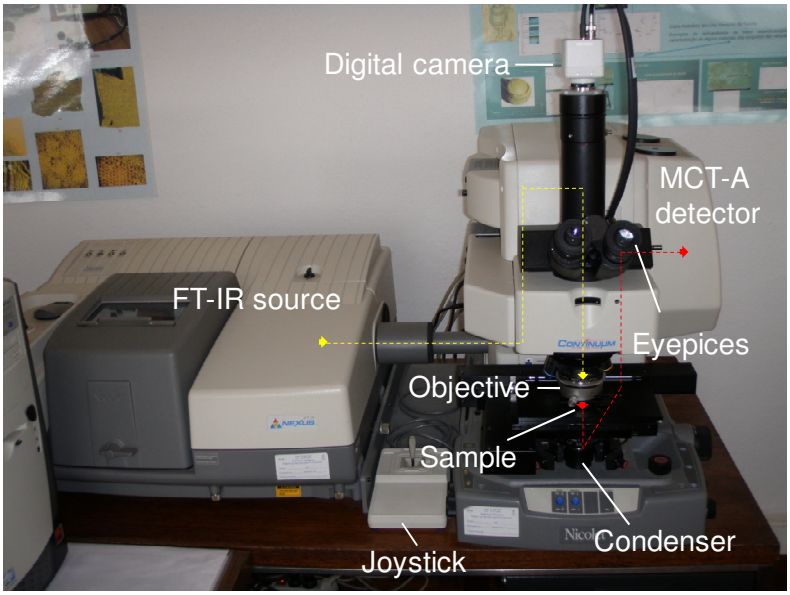

Figure 5.11 FT-IR microspectrometer (Nicolet, LCRJF laboratory). Modulated broad-band IR light from a Michelson interferometer is focused onto the sample with a Cassegrainian objective. Light transmitted by the sample is collected by a Cassegrainian condenser and subsequently focused onto a MCT-A detector.

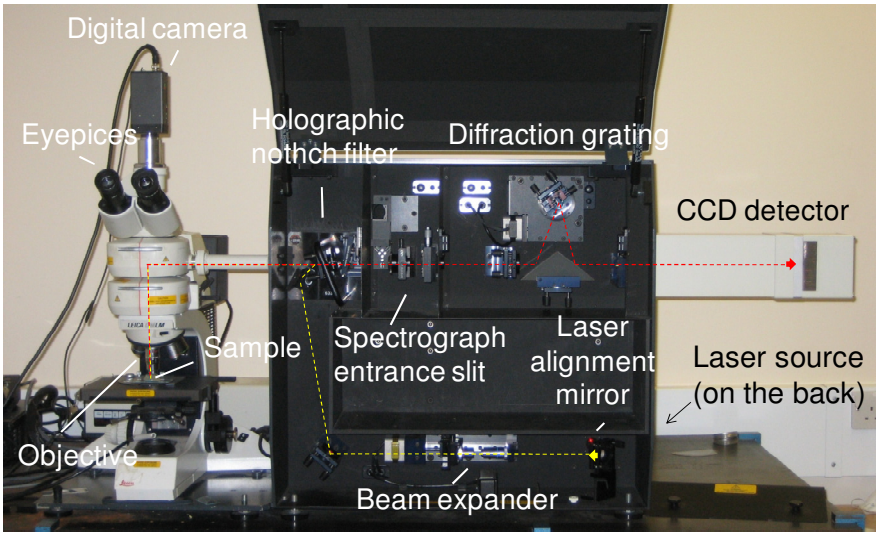

Figure 5.12 Raman microspectrograph (Renishaw, UCL laboratory). A laser source is focused onto the sample with an ordinary objective. Light reflected by the sample is collected by the same objective, passed through a holographic filter, following through a spectrograph and subsequently focused onto a CCD detector.

Exciting source

For μ-IR, radiation is normally emitted by a broadband source, such as silicon-carbide rod (known as Globar) or quartz lamps [143], while different laser excitation lines raging from UV to NIR can be used as excitation source for μ-R. However, for dispersive μ-R the most common are the visible wavelengths 488 and 514 nm from the argon ion laser, 632.8 nm from the He-Ne laser and about 780 nm from a diode laser, and the near-infrared wavelength 1064 nm from the Nd-YAG laser, the most common for FT-Ramam microscopy. Choice of the laser source is a very important parameter in μ-R since scattering efficiency (proportional to ν^4), spot size (and therefore resolution), fluorescence and sample damage, all depend of the excitation wavelength [204].

In order to observe and align the sample or area of interest within the IR/laser beam, white radiation, parfocal and collinear with the IR/laser radiation is also present in both microscopes [113].

Microscope lenses (condenser and objective)

Because glass (used in optical microscopy) is opaque to mid-infrared radiation, reflecting optics and Cassegrain lens (or mirrors, of the proper configuration) have to be used as optical elements in μ-IR. Unfortunately, Cassegrain optics differ from conventional lenses in a way that equation (5.1) is no longer the most suitable. For these optics the diameter of the Airy disk is reduced from $1.22\ \lambda/NA$ to $1.0\ \lambda/NA$, what reduces the energy on the focal plane of the Airy disk (from 84% to 49%) and increases greatly the energy in the first ring (from 7% to 44%) - information coming from the first disk has to be considered. Typically, Cassegrain optics present a numerical aperture (NA) of 0.6, with magnifications of 6x and 15x, allowing the use of accessories that require a moderate working distance, such as diamond compression cells (the complete assembly), anvil cells and slide-on ATR (Attenuated Total Internal Reflection) attachment. Higher magnification, 32x (NA 0.65) can also be found, however, at the expense of working distance (8 mm *vs*. 15 mm) and with not such a significant gain in NA [113].

IR microscopes are mainly reflecting microscopes, in which the light from the source is focused on the sample by the objective (lens above the sample stage[49]) and the light transmitted by the sample is recollimated by the condenser (in reflection methods, such as ATR, light is collected by the objective) [205,206]. There are also some models in which transmitted light is supplied from the condenser [82].

[49] According to OM, *condenser* is used to refer the lens that focus the light in the sample and *objective* is the lens that forms the primary magnified inverted image of the sample. However, in μ-IR, often, *objective* is used to refer the lens above the sample stage, while *condenser* is used to refer the lens below the sample stage.

Since μ-R routinely uses visible wavelengths lasers as excitation source, conventional glass optics, lenses and windows can be used, without any reduction in sensitivity [207]. When near-infrared wavelengths are used, reflecting optics or similar must be employed. Microscope objectives used for μ-R generally have magnifications of 5x, 20x, 50x and 100x. Regarding the numerical aperture, for light absorbing samples, maximum Raman signal is obtained using the highest numerical aperture as possible, but for transparent or translucent samples the choice of the correct numerical aperture is more complex [208].

Spectral analysers

Spectral analysers can be of two types: dispersive (scanning monochromators, spectrographs) or nondispersive (where the interferometric are the most common).

In a scanning monochromator or spectrograph, the beam of polychromatic radiation enters the device through a narrow slit and is separated into individual components by a prism (where light is dispersed due to the different index of refraction of the different wavelengths), a grating (where light is diffracted) or a combination of both. A series of images of the entrance slit is produced, each spatially dispersed as function of the wavenumber.

Scanning monochromators then employ an exit slit positioned in the plane of the spectral images, to isolate a narrow portion of the images of the entrance slit. Rotating the prism or the grating, successive images passes through the exit slit into the detector. Because only a small fraction of wavelengths coming from the sample are analysed at any given time, the efficiency of scanning monochromators is inherently reduced. In a spectrograph, which only differs from scanning monochromator in the exit section, since there is no exit slit, when combined with a position-sensitive detector, a portion of the spectral images are directly focused onto the detector. In this way a spectrograph simultaneously measure the entire spectrum or a major section of it, being more efficient than the scanning monochromator [209-211].

The interferometric spectrometers, also referred to as Fourier transform (FT) spectrometers because this mathematical process is necessary to transform the interferograms into spectra, all the wavelengths of the polychromatic radiation are simultaneously processed and detected. Most commercial Fourier-transform spectrometers are based in the Michelson interferometer. The IR radiation from a broad band source is directed to a beamsplitter that divides the light between two beams with optical paths that can be changed. These two beams strike mirrors that reflect them back to the beamsplitter, where they are recombined and create interference. In a typical interferometer one mirror remains fixed, while the other retreats from the beamsplitter at constant speed. When the

paths of the two beams are equal, the two beams are in phase. At every other position of the moving mirror, the beams are out of phase and create a repeating interference pattern, which is a sum of cosine waves for all the wavelengths. This modulated beam passes then through the sample and hits the detector, producing an interferogram, which is a plot of the intensity *vs.* optical path difference. Through a FT, the interferogram can be converted into a single beam spectrum, whose resolution is determined by the distance that the moving mirror travelled.

Because in an interferometer the device that controls the entrance of the size of the source and the angles of the light going through the spectrometer is a circular aperture (Jacquinot stop) instead of a slit, for a given resolution, the optical throughput can be significantly higher than that obtained with a dispersive spectrometer. This results in a substantial gain in energy at the detector, which translates to higher signals (better sensibility) and improved signal-to-noise ratio (S/N) or a faster recording speed [50]. This is the Jacquinot (or throughput) advantage. A second advantage of interferometers over dispersive spectrometers is the fact that as all the wavelengths of light entering the device are simultaneously detected, there is an improvement in the S/N per unit time[51]. This is known as the Fellgett (or multiplex) advantage. The third advantage (Connes advantage) is the higher accuracy of the frequency scale, as a result of an internal He-Ne laser. This advantage allows spectra to be perfectly superimposed and co-added, not requiring the need for external calibration [(209-211)].

μ-IR uses almost exclusively FT spectrometers, while in μ-R both dispersive as FT spectrometers are used. However, for the analysis of small samples and mapping applications, where high spatial resolution is required, dispersive Raman instruments are generally more sensitive and well-suited than FT-Raman [(202,207,210)]. The Jacquinot advantage is reduced as the entrance aperture of the interferometer is reduced to a pinhole and, if the instrument is shot-noise limited (i.e. the noise level increases with the square root of the total light flux entering in the detector), the fact that all wavelengths are entering simultaneously at the device (Fellgett advantage) can become a disadvantage [(210,212,213)].

Detectors

When analysing micro samples there is the need for high sensitivity and speed. In μ-IR these two parameters are best met when using an IR sensitive mercury cadmium telluride

[50] In practice, however, the aperture size depends of the resolution, the wavelength range, the detector type and a few other factors and when its size is reduced, for example, for area isolation, the Jacquinot advantage is not so significative.

[51] This advantage applies only if the performance of the instrument is limited by detector noise, i.e. noise is independent of the power of the radiation incident on the detector, as is the case of Infrared spectroscopy.

(HgCdTe - MCT) detector. This is a photon detector (the electrons are excited directly by the absorption of radiation) that has to be cooled to the liquid nitrogen temperature (77 K) in order to avoid excitation of electrons by thermal motion. Unfortunately, this detector has two serious drawbacks, firstly it does not cover the entire IR range because there is a minimum energy to excite an electron and secondly, it has a wavelength-dependent response [211,214]. Detector size is also an important parameter, since for FT-IR, the largest source of noise is the detector and the noise of the detector is directly proportional to its area. The area of the detector should be as reduced as possible, ensuring that is not smaller than the sample's image. Sizes ranges from 25 x 25 µm to 4000 x 4000 µm, but as compromise between several factors, the standard size is 250 x 250 µm [112,113].

For µ-R, a thermoelectrically cooled charge-coupled device (CCD) detector is generally used when employing visible excitation lasers. This is a two-dimensional silicon-based semiconductor arranged as an array of photosensitive elements that presents a high quantum efficiency and sensitivity in a wide wavelength range [163]. For NIR measurements, liquid nitrogen cooled Ge and InGaAs photodiode-array detectors are generally employed, since CCD perform less adequately in the near infrared that in the visible [210].

Because Raman signal is extremely low compared with the intensity of the excitation radiation, which is reflected and/or diffuse scattered by the sample, these have to be removed from the whole optical system using a narrow-band holographic notch filter specific to the laser photon energy (or using a series of monochromator and narrow slits).

5.6.2 Spatial and spectral resolution

Spatial resolution

When the sample size is very small and/or only part of the sample is to be analysed, a *confocal* microscopic arrangement is desirable. Unlike a conventional widefield microscope, where the entire field of view is uniformly illuminated and observed, the confocal arrengement isolates the light originated from a small sample or a small area of the sample and efficiently eleminates information coming from outside the area of interest [201,205,215].

In µ-IR, confocality is obtained using one or two variable size field stops, commonly referred to as apertures. Because IR sources are extended sources that overfill the aperture of the optic, when a single aperture is used, this should be placed before the sample. However, optimum spatial resolution[52] is obtained if a dual aperturing (second aperture after

[52] In vibrational microscopy the spatial resolution, also referred to as least resolvable separation (LRS), is defined as the ability to measure the spectrum of a point or area of interest without significant contamination information from neighboring areas.

the sample) is employed. The aperture before the sample restricts the infrared beam to match the size of the aperture, while the aperture after the sample restricts radiation reaching the detector to that being transmitted from an area matching the size of the aperture [206,215].

Although, in theory these masking apertures define the area of analysis, it is known that beyond a certain point the aperture itself will cause light to be distributed into neighbouring regions. If the aperture dimension are of the order of, or smaller than, the wavelength of the radiation, diffraction effects will occur; some of the radiation will bend around the defined masking area and impinge on the surrounding area. Consequently, light from outside the aperture will be also collected and the acquired spectrum will contain, not only information regarding the area of interest, but also information from neighbouring areas.

According to *Nishikida K.* [216], the smallest area to be isolated in an IR microscope employing a dual confocal aperture and Cassegrainian optics is diffraction limit to λ/NA x λ/NA μm^2. Which, for a mid-infrared range of 4000-650 cm^{-1} (2.5-15.4 µm) and employed 0.58 NA objective/condenser, corresponds to the minimum area of 4 x 4 μm^2 for 4000 cm^{-1} and 27 x 27 μm^2 for 650 cm^{-1}. If the aperture is reduced in the attempt to analyse areas with a thickness smaller than 27 µm, information from adjacent areas will also be collected [206].

However, the minimum area is not only diffraction-limited. In fact, due to the properties of conventional thermal source and sensitivity of the detector, generally the minimum area is larger than the diffraction limit.

Conventional IR thermal source are extended sources and typically, the diameter of the image of the source that is formed at the sample plane by the objective is ~300-1000 µm, much larger than the area of interest. Therefore, in order to restrict the area of the sample to be illuminated, an aperture is employed. Unfortunately, because these sources are also not very bright, when the apertures are introduced and worst, when their size is reduced so as to analyse only the area of interest, the energy throughput that reaches the detector is significantly reduced. Since in FT-IR set-up the largest source of noise is the detector, with the noise being directly proportional to the square root of the active area of the detector, also the signal-to-noise ratio (S/N) is significantly reduced [113,206,217-220]. If the sample's image is less than the area of the detector, because the outer portions of the detector are not being utilized to collect IR energy, but still contribute to the noise, sensitivity decreases and the spectra will present a poor quality [112].

The ultimate limit of area size is the result of a combination between the diffraction effects, source brightness and detector response, the typical value for a conventional IR thermal source ranging between 20-100 µm [83,87,206,216,218,219,221].

For most conventional Raman microscopes without futher modification, due to the zero dimensions of the laser source, the spatial resolution is diffraction-limited by the objective lens according to equation 4.1, and a 1 μm is commonly achievable with visible radiation [10,143,203,204,208].

The choice of the wavelength of the laser excitation line and the NA of the objective has a high impact on the spot size and thererefore, on the spatial resolution, the highest the numerical aperture and the shortest the wavelength, the better the spatial resolution [208].

However, a confocal arrangement is desirable when there is a need to minimize the depth resolution, allowing an excellent discrimination against a strong scatterer or a fluorescence matrix. For samples with some transparency, confocality also allows depth profiling, i.e. the selective analysis at different dephts of the sample. Using the confocal arrangement a sampling volume of ca. 2 μm^3 is achievable [201].

The confocal arrangement can be achived using, either a pinhole aperture that has often been installed at the back focal plane of the microscope, or combining the spectrograph entrance slit with the active area of the CCD detector [201,204].

In the first approach, a pinhole is placed on the optical axis/ at the image back plane of the microscope, blocking the size of the sample image. The pinhole (that ranges in size from 100-500 μm) has the effect of eliminating light originating from the out-of-focus regions of the sample, enancing spatial resolution, in the focal plane (xy directions) and especially, above and below the focal plane (the z direction). Performance is futher improved when another pinhole is incorporated in the incident laser beam optics, in order to remove speckle and diffracted light and achived a clean focus. Unfortunately, this set-up has some drabacks, since the use of pinholes rejects a significant amount of the Raman photons of interest, reducing dramatically the overall efficiency (measurement of the spectra more difficult) and unwanted diffraction effects may begin to occur [207,222]. The use of small pinholes (< 100 μm) must then be balanced agains these disadvantages.

If the μ-R system is equipped with a stigmatic monochromator and a CCD detector, another efficient and simpler (time-consuming optical aligment of small pinholes is not necessary) confocal arrangement is achivable, which combines the spectrograph entrance slit and the active area of the CCD detector. In this arrangement (the one existing in the equipment used in this work, Figure 5.12) the entrance slit of the spectrograph works as one physical aperture, restricting the light that enters in the spectrograph. Besides, because a 2D CCD detector collects spectral data in the direction perpendicular to the entrance slit of the spectrograph and spatial information in the direction parallel to the entrance slit, information from out of focus regions can be further eliminated restricting the active area of the CCD

detector in the dimension containing the spatial information, i.e. the image height dimension [201,202,204].

Spectral resolution

The ability to distinguish closely spaced peaks or bands in a spectrum is referred to as *spectral resolution*. The higher the spectral resolution, the higher the number of peaks or bands that are isolated, and consequently the easier it is to compare the spectrum with reference spectra. A high spectral resolution is particularly important when peaks/band of several compounds occur at near wavenumbers.

Spectral resolution is a fairly complex function of the inherent linewidth of the vibrational transition being probed, the source linewidth and the spectrometer/detector resolution [223] and is expressed as the spacing between the wavenumbers being collected. The lower the spacing, the higher the resolution and *vice versa* (4 cm^{-1} is a better resolution that an 8 cm^{-1}).

For instance when a spectrum is acquired with 4 cm^{-1}, bands with a spacing bellow this value will appear as a single broad band, i.e. they will not be resolved.

Unfortunately, other conditions being constant, resolution and S/N are usually traded off parameters - when resolution is improved S/N is decreased. As resolution increases, more resolution elements are measured by scan, i.e. the measurement time per resolution element is reduced, and consequently, signal is deteriorated. In addition, the relationship between resolution and S/N is complicated by the fact that the optical throughput decreases as the spectral resolution improves. In order to achieve high spectral resolution, either the slit width of the grating in the dispersive spectrometer or the Jacquinot stop in the Fourier transform spectrometer must be set small. This reduction in the throughput results in an additional decrease in the S/N [224,225].

Generally, μ-R studies present a higher spectral resolution than μ-IR studies, 1 cm^{-1} against 4 cm^{-1}, respectively [10,183].

6 Infrared and Raman microscopy analysis

The vibrational spectrum of a molecule is considered to be a unique physical property and is characteristic of the molecule.

J. Coates

This chapter presents and discusses the results of the analysis of the paintings' samples obtained by Infrared and Raman microscopy (μ-IR and μ-R). Further, it compares the efficiency of both techniques for component identification in complex mixtures.

The results obtained by each technique are presented separately, μ-IR followed by μ-R, in accordance with chronological order of analysis, organized by functional group and presented by alphabetic order with reference to the samples (Table 3.1, Appendix D) from which the spectra were obtained. It should be noted that it is often very difficult, if not impossible, to distinguish between the mineral and synthetic forms of many compounds by μ-IR and μ-R. Hence, compounds will be normally identified by their chemical name if it not known whether they are synthetic or mineral.The main difficulties found in the identification of the compounds are also described. The relative intensities and shape of the bands are reported on the right side of their wavenumbers as vw (very weak), w (weak), m (medium), s (strong), vs (very strong), sh (shoulder) and br (broad).

The identification of the compounds contained in the samples by μ-IR and μ-R was based on comparison of the spectrum of the unknown with spectra from reference samples obtained in-house employing the same equipment and conditions[53], or culled from published scientific papers, books internet and spectral libraries. Whenever known, the assignment of the bands is also indicated. Search programs were not used because most libraries of reference spectra are mainly composed by spectra of pure materials, being ineffective in the analysis of spectra from complex samples as the ones under analysis.

Since the assignment of broad bands is not straightforward, differences relatively to reference spectra can be found.

The reference samples used were: *Celadonite*, Akaky River, Cyprus, obtained from Dr. R. Siddall, Geology Department, UCL, London; *chrome orange*, Winsor & Newton (~1880), obtained from Dr. L. Burgio, the Victoria & Albert Museum, London; *Glauconite*, Oystershell Hill, United Kingdom, from Mr. A. Hart and Mr. M. Rumsey, Natural History Museum, London; *strontium yellow*, AP. Fitzpatrick, London, *Anatase*, Alfa Aesar; *manganese oxide* ($Mn^{IV}O_2$), Aldrich, *Rutile*, Sigma Aldrich; *Quartz*, Alfa; *carmine*, Sigma Chemical Co., *lead (II) sulfate*, Aldrich; *Malachite* (reference 1), *lead antimonate yellow* synthesized in the Department of Chemistry of the UCL; obtained from Dr. Robin J.H: Clark, Chemistry Department, ULC, London; *chrome yellow*, Fluka, *zinc yellow*, Ferrario Color, *viridian*, Winsor & Newton, *vert Émeraude*, Lefranc, *ivory black*, Winsor & Newton and *noir d'ivory* (ivory black), Lefranc, *Malachite* (reference 2), Zaire, *Goethite*, Cercal, Portugal, *Hematite*, Atlas Mountains, Morocco, *Magnetite*, Alvito, Portugal, *cerussite*, Tsumed, Namibia, *lead white*, synthesized in the Laboratório de Conservação e Restauro José de Figueiredo, obtained from Laboratório de Conservação e Restauro José de Figueiredo.

[53] In μ-R, the laser beam, the power and the number of scans can be different from sample to sample. The rest of the experimental conditions were kept.

6.1 Infrared microscopy

6.1.1 Experimental conditions

Samples

150 samples, removed from the 23 paintings under analysis (Table 3.2, Appendix D), were prepared as thin sections as described in section 3.2.2 and analysed by μ-IR.

Since the study of micro samples may cause some misinterpretations and the preparation and analysis of thin sections is a difficult task, more than one thin section was analysed for each sample. In total, 843 spectra were acquired and interpreted. Representative spectra of the compounds that were identified and major difficulties found in their identification will be presented.

Experimental set-up

Infrared analysis was carried out using a Nicolet NEXUS spectrometer coupled to a Nicolet CONTINUμM infrared microscope. The spectrometer has a Ge-on-KBr beamsplitter and an EverGlo infrared source. The IR microscope is equipped with an x15 (NA 0.58) Infinity corrected Reflachromat objective and condenser pair and is fitted with a 250 x 250 μm^2 Nicolet mercury-cadmium-telluride (MCT-A) detector, cooled with liquid nitrogen (working range of 4000-650 cm^{-1}).

Thin sections and reference samples (a few particles) were compressed in a Thermo Spectra-Tech μSample Plan micro compression diamond cell (which consists in two flat type IIA diamond windows of 2 mm diameter compress against each other, using a metallic support shown in Figure 6.1 and analysed in transmission mode, placing only one part of the cell on the stage of the microscope. The area of analysis of the sample was defined by the double aperture contained in the microscope. A total of 256 scans were acquired and averaged, with a spectral resolution of 4 cm^{-1}, using a 1.8988 cm/s scanning mirror velocity. Happ-Genzel apodization and Mertz phase correction were implemented. Computer control, data acquisition, data processing and band assignment were achieved through Thermo Electron's OMNIC software. No spectral processing, other than removal of the carbon dioxide bands, was performed.

Spectra will be presented in the percentage transmittance format, which provides the best dynamic range for both weak and intense bands in qualitative analysis [226].

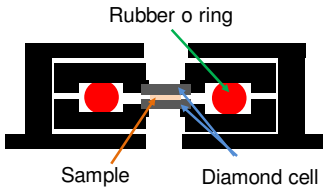

Figure 6.1 Representation of a transversal cut of the Thermo Spectra-Tech µSample Plan micro compression diamond cell set-up.

6.1.2 Results and discussion

µ-IR was able to identify a large number of compounds, summarized inTable 6.1, which also shows their distribution through the 23 paintings. However, several difficulties were found during the samples' preparation, analysis and interpretation of the respective IR spectra. Since these difficulties somehow restrict the efficiency of µ-IR to accomplish the objective of this study, they will be described below.

6.1.2.1 Difficulties in sample's preparation and analysis

The preparation of thin sections proved to be a serious drawback to µ-IR, especially for samples composed by more than 4 layers. Crumbing upon microtome cutting and loss of a large part of the sample, generally, the inner layers, were frequent. Moreover, since thin sections tend to curl, when trying to flatten them, the sample often skipped from the medium (Figure 6.2). Consequently and, although several thin slices were prepared for each sample, it was very difficult to have a thin section with the complete cross section sequence.

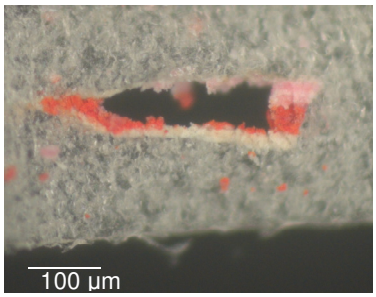

Figure 6.2 Unsuccessful thin section of sample **W3**, viewed under reflected light.

Regarding the difficulties of the analysis of the samples, the main difficulty consisted in the individual analysis of each layer, for which, four main factors contributed, namely depth colour reduction, irregular division of the sample by the two parts of the diamond cell and diffraction effects/infrared source size and brightness.

Thin sections were compressed in a micro compression diamond cell in order to improve the quality of acquired spectra (avoid saturation of the most intense bands[54]) and, at the same time, increase the area of each layer by expansion. However, compression makes it very difficult, or even impossible, to distinguish adjacent layers. The compression of the sample causes the decrease of its thickness, particle size and the average depth to which radiation penetrates before being scattered. Consequently, an apparent loss of colour of some of the layers occurred [49,82,227] and differentiation between layers and/or determination of the sample orientation become very difficult.

Often, an irregular division of the thin section between the two parts of the diamond cell was verified, making stratigraphic analysis more difficult. When after compression the two parts of the cell were separated, portions of the sample remained in one part of the cell, while the rest remained in the other part. This caused difficulties, both to establish the stratigraphic order and to provide enough area of each layer for analysis.

Moreover, diffraction effects, which seriously limit the spatial resolution, together with the intrinsic characteristics of the IR radiation (poor brightness and finite source size) made the analysis of thin layers very difficult or even impossible. In order to analyse isolated layers with small thickness, the dual aperture size had to be reduced so as to analyse an area below 50 x 50 μm^2. In these conditions, poor quality spectra (weak bands and S/N), with bands assigned to compounds from adjacent layers were acquired.

Due to the described difficulties found in layer differentiation and analysis, more than one layer were often analysed simultaneously.

6.1.2.2 Interpretation of the infrared spectra

Except for the ground layers that proved to be composed by simple mixtures, the interpretation of most of the infrared spectra required a careful analysis. Due to the complex mixture of compounds present in each layer, the respective spectra exhibit a large number of bands, most of the times overlapped and even merged into broad envelopes.

A detailed interpretation of the IR spectra of the compounds found in the samples analysed by μ-IR, organized by functional groups and presented by alphabetic order is presented below. As mentioned before, the main difficulties to IR spectra interpretation are also emphasized.

[54] Although this procedure was taken, saturation was observed for some samples.

Table 6.1 Compounds* identified by µ-IR in Pousão's paintings

	Paintings																						
	Early			French			Italian															Final	
Compounds	A	B	C	D	E	F	G	H	I	J	K	L	M	N	O	P	Q	R	S	T	U	V	W
Arsenites																							
Emerald green								●			●	●										●	
Carbonates																							
Calcium carbonate - calcite form			●		●	●			●		●			●	●	●							
Lead white	●	●	●	●	●	●	●	●	●	●	●	●	●	●	●	●	●	●	●	●	●	●	●
Lead carbonate		●	●	●	●	●		●	●		●			●	●	●		●	●	●	●		●
Chromates																							
Chrome orange															●								
Chrome yellow	●		●					●											●		?		
Strontium yellow			●	●													●						
Zinc yellow								●			●			●	●								
Cyanides																							
Chrome green																			●		●		
Prussian blue				●	●	●			●		●	●		●			●		●	●	●		●
Oxides and Oxyhydroxides																							
Viridian						●		●	●											●			
Phosphates																							
Bone/ivory black	?	●		●			●			●	?						●						
Silicates																							
Celadonite					●				●														●
Kaolin/Kaolinite	●	●		●		●	●		●		●		?		?	●			●	●	●		●
Quartz	●	●		●	●	●	●		●		●		●				●		●				
Sulfates																							
Barium sulfate					●	?	●	●	●	?	●								●	●	●		
Brochantite								●															
Gypsum	●				●	●	●	?	?	?	●	●					●		?				

A - *Casa rústica de Campanhã*, **B** - *O mendigo Lapita*, **C** - *Paisagem - Abertura da Rua Alexandre Herculano*, **D** - *Jardim de Luxemburgo (estudo)*, **E** - *Aldeia de St. Sauves*, **F** - *Paisagem de St. Sauves*, **G** - *Cansada (Cachopa de Capri)*, **H** - *Casas brancas de Capri*, **I** - *Cecília*, **J** - *Escadas de um pardieiro - Roma*, **K** - *Esperando o sucesso*, **L** - *Fachada de casa soterrada - Roma*, **M** - *Miragem de Nápoles*, **N** - *Portão*, **O** - *Rapariga de Anacapri*, **P** - *Rua de Roma*, **Q** - *Senhora vestida de preto*, **R** - *Janela das persianas azuis*, **S** - *Mulher da água*, **T** - *Paisagem de Anacapri*, **U** - *Rapariga deitada no tronco de uma árvore*, **V** - *Cais de Barcelona* and **W** - *Flores Campestres*.

* Pigments are in blue, while extenders, associated compounds or impurities are in green

? Probable identification

Arsenites

Emerald green, copper acetoarsenite, $Cu(CH_3COO)_2.3Cu(AsO_2)$, was generally easily identified by the simultaneous presence of the band at 1558-1557(vs) due the acetate antisymmetric stretching mode and a doublet at 820-818(s) and 771-769(s) cm^{-1}, probably due to the As-O symmetric and antisymmetric stretching modes, respectively (Figure 6.3a andFigure **6.5**Ab) [178,195,228,229]. The acetate symmetric stretching mode occurring at 1455(m) [178,230] was also identified in some of the samples; however, since it has been often masked by the carbonate antisymmetric stretching band at ~1430-1400 cm^{-1} (Figure 6.3b) that mode was not very useful for identification purposes.

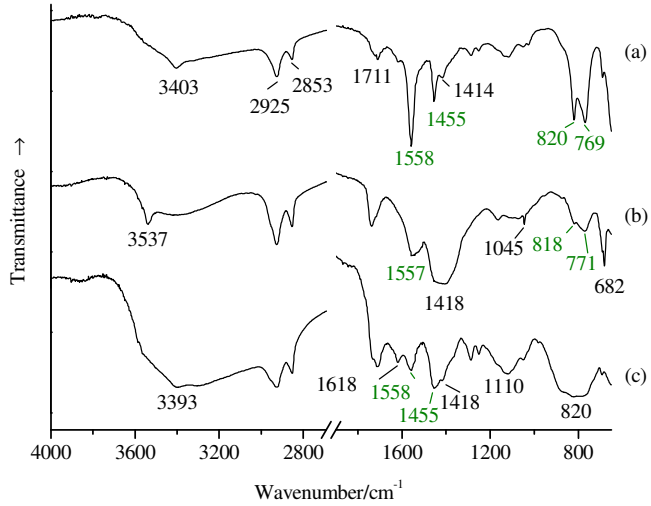

Figure 6.3 Infrared spectra of: (a) layer 5 of sample **H8**, identified as a mixture of emerald green and lead white in oil, (b) layer 1 of sample **V1**, identified as a mixture of lead white and emerald green in oil, and (c) layers 3-5 of sample **H8**, identified as a mixture of emerald green, a chromate salt, a carbonate compound and a sulfate or silicate compound in oil.

If a compound with bands occurring at similar wavenumbers to those of the emerald green doublet, such as a chromate pigment, is present in a large amount, as shown in the spectrum presented in Figure 6.3c, band masking occurs and the identification of emerald green becomes more dubious. In this spectrum, the simultaneous presence of bands at 1558 and 1455 cm^{-1} clearly suggests the presence of a copper acetate; however since other copper acetate compounds, such as verdigris $(Cu(CH_3COO)_2.H_2O$, $[Cu(CH_3COO)_2].x[Cu(OH)_2].yH_2O$ and other compositions [231,232]) can also be found in paintings [233], it is not sure that emerald green is the copper acetate. Presence of emerald green was confirmed because the layers under analysis (3-5 of sample **H8**) include the layer whose spectrum is presented in Figure 6.3a.

Carbonates

Carbonates are very important constituents of Pousão samples, since almost every spectrum presents a very intense and broad band at about 1430-1400 cm^{-1}, arising from the antisymmetric stretching vibration of the carbonate ion, CO_3^{2-} (Figure 6.4) [175,234].

In fact, these compounds are present in such a high concentration, that even though a diamond compression cell was used, the 1400 cm^{-1} band was very often saturated (Figure 6.4a), preventing the determination of its true absorption wavenumber and consequently making difficult the identification of the carbonate compound. Nevertheless, thanks to diagnostic bands, calcium carbonate - calcite form (2515, 1794, 876 and 713 cm^{-1}, Figure 6.4b), lead carbonate (1052 and 838 cm^{-1}, Figure 6.4c) and lead white (3538, 1045 and 682 cm^{-1}, Figure 6.4d), were identified, even when mixed together, like in the spectrum presented in Figure 6.4a.

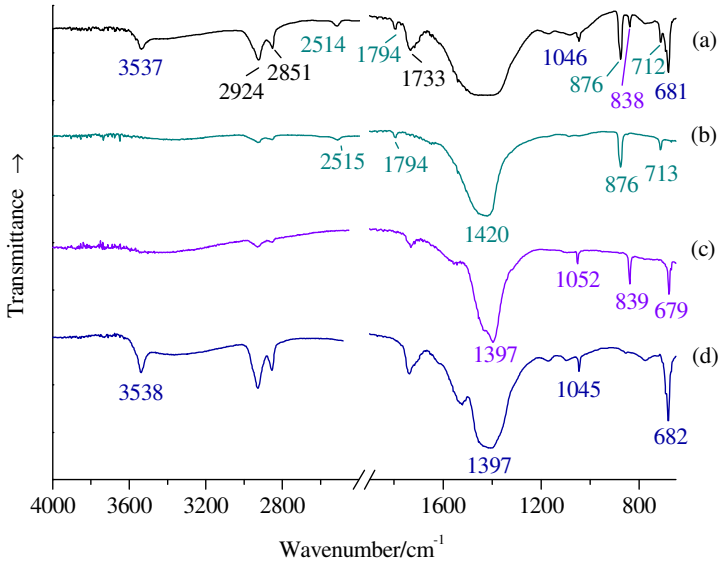

Figure 6.4 Infrared spectra of: (a) ground layer of sample **O2**, identified as a mixture of lead white, lead carbonate and calcium carbonate - calcite form in oil, (b) layer 1 of sample **F1**, identified as calcium carbonate – calcite form in oil, (c) layer 1 of sample **E6**, identified as lead carbonate in oil and (c) layers 3 and 4 of sample **J2**, identified as a mixture of lead white and lead carboxylates in oil.

Calcium carbonate - calcite form, $CaCO_3$, characterized by an infrared spectrum with absorption bands occurring at 2515-2514(w), 1794(m), 1420(vs), 876(s) and 713(m) cm^{-1} (Figure 6.4b) was identified in the paintings [235,236]. Occurring at wavenumbers where no other compound, specially lead white, appears to absorb, the bands 2515 and 1794 cm^{-1} assigned to combination modes of carbonate ion ($2\upsilon_2+\upsilon_4$ and $\upsilon_1+\upsilon_4$, respectively) [237] and the band at 876 cm^{-1} assigned to the out-of-plane bending mode of carbonate ion were the

most important bands to the identification of this compound [236,238]. The bands at 1420 and 713 cm^{-1} are assigned to the antisymmetric stretching and to the in-plane bending of the carbonate ion, respectively [175,234].

When present in small amounts, identification of this compound was very difficult since the weak combination bands disappear and except for the band occurring at 875 cm^{-1}, all the other bands are masked by those of lead white, a major component of the samples.

Lead carbonate, $PbCO_3$, geologically known as cerussite, was identified by its infrared bands occurring at 1398(vs) and 1052(s), due to the antisymmetric and symmetric stretching modes, respectively, and 838(s) and 678(s) cm^{-1}, due to the out-of-plane and in-plane bending modes of the carbonate ion, respectively (Figure 6.4c) [175,239].

Normally, present in a low concentration relatively to lead white (Figure 6.5Aa shows one of the few exceptions), lead carbonate was frequently difficult to identify with certainty because only the bending band at 838 cm^{-1} was visible, Figure 6.5Bb.

Identification should never be based on the presence of a single band, since other compounds can produce similar bands. However, as few other compounds have strong absorptions in this region (an example is celadonite Figure 6.13 and Figure **6.14**) [221] the existence of a band at 838 cm^{-1} in the spectra strongly suggests the presence of lead carbonate in the samples.

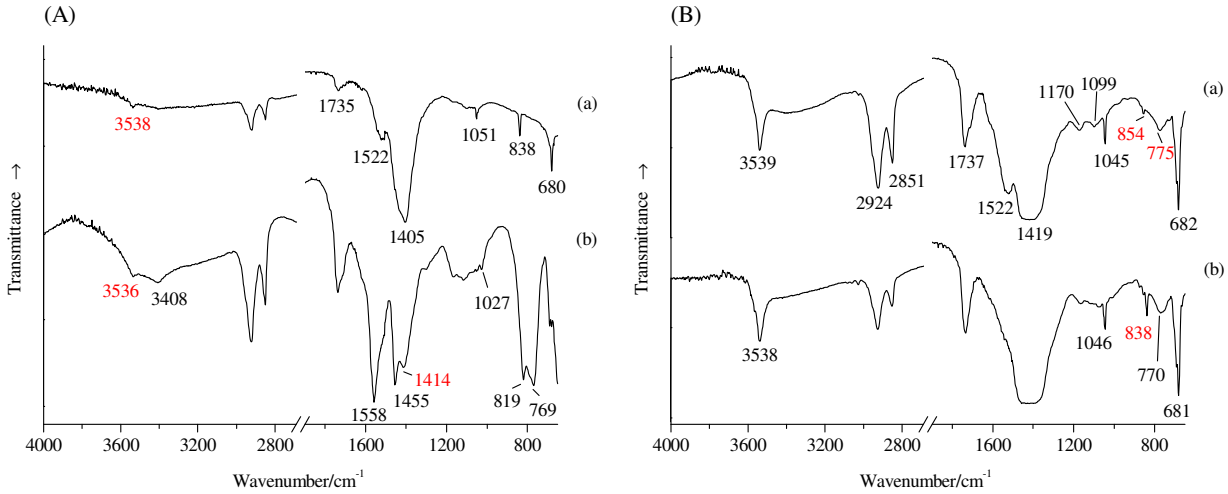

Figure 6.5 Infrared spectra of: (A)(a) the layer 2 of sample **E6**, identified as a mixture of lead carbonate, lead white and lead carboxylates in oil, and (b) sample **H2**, identified as a mixture of emerald green and lead white in oil; (B)(a) the layer 1 of sample **I2**, identified as a mixture of lead white and lead carboxylates in oil, and (b) the ground layer of sample **W1**, identified as a mixture of lead white and lead carbonate in oil.

Lead white, basic lead carbonate, $2PbCO_3.Pb(OH)_2$ is a very important synthesized pigment, and was identified in almost every sample layer thanks to its very intense and characteristic infrared spectrum with bands at about 3539-3537(w), 1420-1397(vs), 1045(s), 854(vw), 777-770(m) and 682-681(s) cm^{-1} (Figure 6.4a,d and Figure 6.5).

The band at 3539-3537 cm^{-1}, due to the superposition of the symmetric and antisymmetric hydroxyl stretching modes, was extremely helpful for the identification of this pigment when present in small quantities and/or mixed with compounds with overlapping bands, such as lead carbonate (Figure 6.5Aa) and emerald green (Figure 6.5Ab). In the spectra presented in Figure 6.5A, only the band at 3538(6) cm^{-1} accounts for the existence of lead white, the rest of the bands being due to lead carbonate and lead carboxylates or emerald green.

The bands at 1406 and 1045 cm^{-1} are due, to the antisymmetric and symmetric stretching modes of the carbonate ion, respectively, and the band at 683 cm^{-1} is due to the in-plane bending mode of the carbonate ion [175,239]. The bands at 854 and 777 cm^{-1}, attributed to the out-of-plane bending mode of the carbonate ion and to the in-plane bending mode of PbOH (tentative assignment) [175,239], respectively, are not normally referred, due to their weak intensity. However, whenever lead white spectrum is saturated (Figure 6.5Ba) the intensity of these two bands significantly increases, what can mislead to the suspicion of the presence of other compound.

Chromates

Among the yellow, orange and red pigments present in the samples, μ-IR was able to identify only the chromate pigments, which are characterized for presenting one to several intense bands between 960 and 700 cm^{-1}, assigned to the antisymmetric and symmetric stretching modes of the chromate ion, CrO_4^{2-} (Figure 6.6), as result of lift of degenerate vibrations in the crystalline host. Figure 6.6 presents, side by side, spectra of the chromate pigments identified in the samples and the spectra of reference pigments.

Chrome orange, basic lead chromate, $PbO.PbCrO_4$, isostructural with the mineral phoenicochroite (Figure 6.32) [51] exhibits a single, broad and poorly defined band at about 852-847(vs) cm^{-1} due to the chromate antisymmetric stretching mode [240] (Figure 6.6Aa and Ba), while **chrome yellow**, lead chromate, $PbCrO_4$, which occurs naturally as crocoite, presents a doublet at about 849-848(s) and 832-819(s) cm^{-1} (and sometimes two shoulders on both the low and high wavenumber sides [241]), due to the antisymmetric and symmetric stretching modes, respectively (Figure 6.6Ab and Bb) [242].

Strontium yellow, strontium chromate, $SrCrO_4$ presents three bands at about 913(s), 876-874(m) and 845-844(s) cm^{-1} (Figure 6.6Ac and Bc), while **zinc yellow** (a complex zinc

potassium chromate, see below) presents four bands at 951-947(m), 878-877(vs), 808-803(m) and 719-715(w) cm^{-1} (Figure 6.6Ad and Bd) [26,238,242,243].

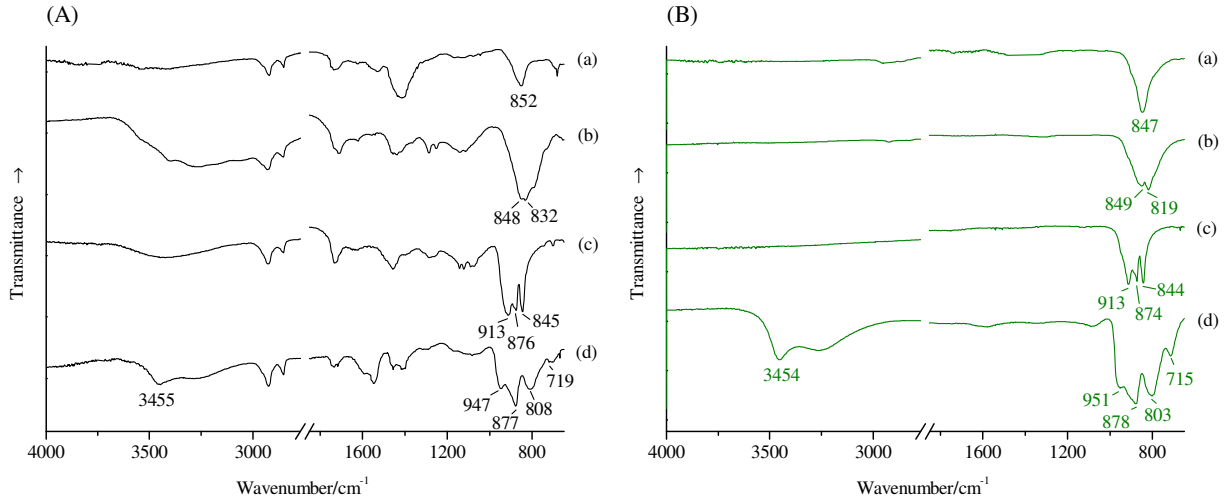

Figure 6.6 Infrared spectra of: (A)(a) layer 2 of sample **O3**, identified as chrome orange in oil, (b) layer 5 of sample **H8**, identified as chrome yellow in oil, (c) the layer 1 of sample **Q5**, identified as strontium yellow in oil and (d) the layer 2 of sample **N5**, identified as zinc yellow in oil; (B) reference samples: (a) chrome orange, (b) chrome yellow, (c) strontium yellow, and (d) zinc yellow.

Although zinc yellow is accepted to be a complex zinc potassium chromate of approximated composition $K_2O.4ZnCrO_4.3H_2O$ [242], different chemical compositions of zinc chromate have been sold under this name, such as anhydrous zinc chromate, which is used as a corrosion-inhibiting primer on aircraft parts made of aluminium or magnesium. This would not constitute a problem, if these different zinc chromate compounds did not exhibit similar mid-infrared spectra (Table 6.2) and consequently could not be distinguished by IR spectroscopy.

Table 6.2 presents the wavenumbers of the IR bands of different zinc chromate compounds found in references, namely, anhydrous zinc chromate ($ZnCrO_4$) [244], hydrated zinc chromate ($ZnCrO_4.7H_2O$) [241], basic potassium zinc chromate ($K_2CrO_4.3ZnCrO_4.Zn(OH)_2$) [245], $K_2O.4ZnCrO4.3H_2O$ and the wavenumbers of our reference sample of zinc potassium chromate, whose composition was confirmed by μ-XRD (Figure 7.34, $K_2Zn_4O(CrO_4)_4.3H_2O$ being equivalent to the empirical formula $K_2O.4ZnCrO_4.3H_2O$ [242]). The similarities in band number and position among these compounds are clearly visible.

Table 6.2 Overview of the IR band position of several zinc chromate compounds

$ZnCrO_4$ [244]	$ZnCrO_4.7H_2O$ [241]	$K_2CrO_4.3ZnCrO_4.Zn(OH)_2$ [245]	$K_2O.4ZnCrO_4.3H_2O$ [242]	$K_2Zn_4O(CrO_4)_4.3H_2O$ *
	3450(s, b)			3454(m)
				3265(m)
	2700(w, b)			
	1218-1185(m)			
	1090(s)			
	1055-1050(sh)			
945(s, sh)		950(s, b)	955(s)	951(s, sh)
938(vs)	942-940(s, sh)			
	875(s)	875(s, b)	880(s)	878(vs)
850(m)				
			815(s)	
818(s)	810-795(vs, b)	800(s, vb)		803(vs)
	720-715(m, b)	718(w, vb)	715(w)	715(m)

References are presented between parentheses; * Values obtained in this study

Although in some cases these orange and yellow pigments were easily distinguished, as shown in Figure 6.6A, serious difficulties were often found for their identification or to distinguish one from another, like shown in Figure 6.7.

Whenever the spectrum is saturated (Figure 6.7Aa), the identification of the chromate(s) is compromised, since the exact wavenumbers of the band(s) are uncertain.

When two or more chromate pigments are mixed together, due to overlapping of the bands, only one of them was generally identified; in general, the one with more bands. That is the case of the layer 7 of sample **C2** whose spectrum is shown in Figure 6.7Ab, where although a mixture of chrome yellow and strontium yellow is present (identified by μ-R), only strontium yellow was identified. Strontium yellow and zinc yellow were the most easily identified chromate pigments.

When the chromate pigment is present as a minor component in the mixture, the coincidence of band position among some other compounds and the chromate pigments can originate some difficulties. That is the case of the band at 912 cm^{-1} present in the kaolin, the band at 875 cm^{-1} present in calcium carbonate - calcite form, the band at 855 cm^{-1} present in lead white (this band has a medium intensity when the spectrum is saturated), the band at 838 cm^{-1} present in lead carbonate and the doublet at 820/771 cm^{-1}, present in emerald green. Two examples of these difficulties are presented in the spectra shown in Figure 6.7Ac and Ba: in the spectrum (Ac) the band at 912 cm^{-1} from kaolin can be confused with a strontium yellow band, although only chrome yellow is present (confirmed by μ-R) and in the spectrum (Ba) the strong emerald green doublet at 820/773 cm^{-1} masks the zinc yellow bands at 815 and 715 cm^{-1} (zinc yellow presence was confirmed by μ-R).

Because the spectra of chrome orange and chrome yellow are so similar, is very difficult, or even impossible, to distinguish one form another in a mixture were the pigment is present as a minor component.

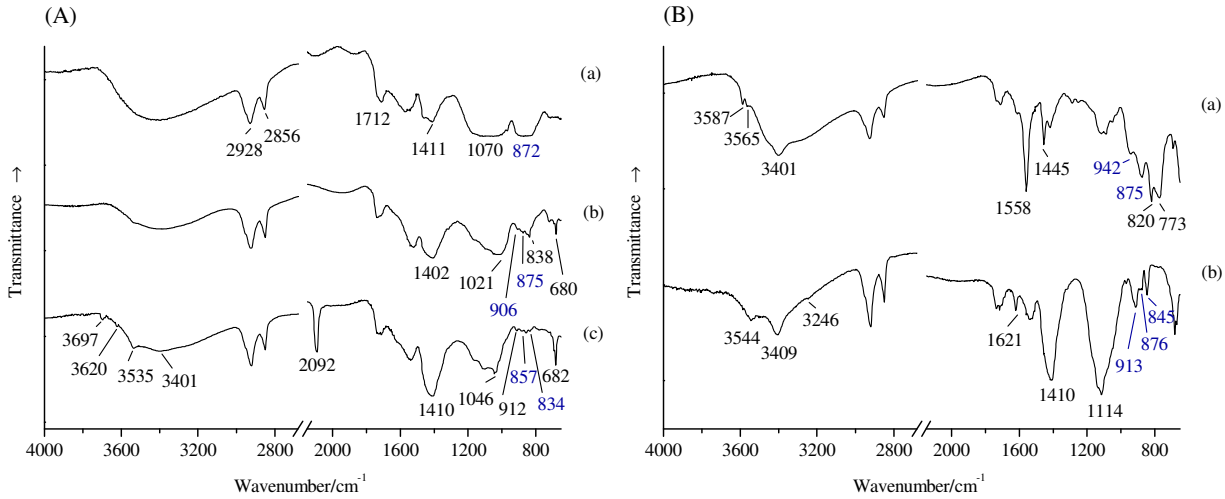

Figure 6.7 Infrared spectrum of: (A)(a) layers 3 and 4 of sample **C2**, identified as a mixture of a carbonate, a silicate or sulfate compound and a chromate compound in oil, (b) layer 7 of sample **C2**, identified as a mixture of a silicate or sulfate compound, strontium yellow and lead carbonate in oil, and (c) layer 3 of sample **U1**, identified as a mixture of lead white, kaolin, chrome green (Prussian blue with chrome yellow) in oil; (B)(a) layer 4 of sample **H8**, identified as a mixture of emerald green, brochantite and zinc yellow in oil, and (b) sample **Q8**, identified as a mixture of lead white, lead carboxylates, gypsum and strontium yellow in oil.

It is worth noting that, although it has been reported that when mixed with a high content of sulfate compounds the identification of these yellow and orange pigments would be difficult [(26)], the high content of gypsum in some of the samples was not an impediment to strontium yellow identification, as shown in the spectrum presented in Figure 6.7Bb.

Cyanides

Chrome green, a pigment produced by the intimate mixture of very fine particles of chrome yellow and Prussian blue (see below) was identified by the simultaneous detection of its two constituents (Figure 6.8a). However, except for a very few cases, this pigment was normally difficult to identify by μ-IR. Firstly, because, the identification of chrome yellow in a mixture is very difficult (due to overlapping); secondly, because IR spectroscopy seems to present a relatively weaker sensitivity to chrome yellow (about 5 times weaker) than to Prussian blue [(246)], leading to the wrong supposition that the yellow pigment is absent. That is the case of the spectrum presented in the Figure 6.8b, the spectrum of the green layer 3 of

sample **U9**, where only the band due to Prussian blue is easily identified. The bands of chrome yellow (easily identified by μ-R) are so weak in this IR spectrum that they can be assigned to lead white, the major component of the layer.

The fact that chrome green was often extended with kaolin (Figure 6.7Ac), barium sulfate or calcium sulfate dihydrate [26,246], difficulted even further the identification of this pigment.

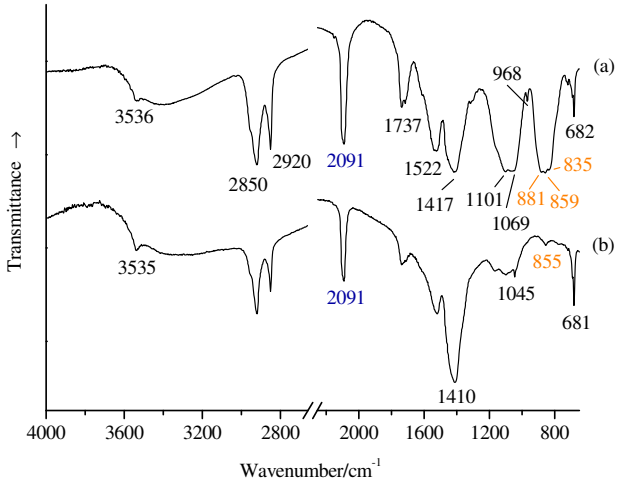

Figure 6.8 Infrared spectra of: (a) layer 3 of sample **S2**, identified as a mixture of chrome green, lead white, lead carboxylates and a sulfate/silicate compound in oil, and (b) the layer 3 of sample **U9**, identified as a mixture of Prussian blue, lead white, lead carboxylates and maybe chrome yellow in oil.

Prussian blue, iron^{III} hexacyanoferrate^{II}, $Fe_4[Fe(CN)_6]_3.14\text{-}16H_2O$ was the only blue pigment identified by μ-IR. This pigment is characterized for producing a very intense band at 2096-2090 cm^{-1} (Figure 6.9a and b), arising from the C≡N (more exactly, Fe^{II}–C≡N–Fe^{III} [195]) stretching vibration of the ferrocyanide ion ($Fe(CN)_6^{4-}$), a region where no other art material seems to absorb [245,247].

Due to its great tinting strength, Prussian blue has normally been used by painters in relatively small quantities but apparently this would constitute a problem to its identification by IR spectroscopy, since it has been reported by *Newman R.* [26], this technique presents a high sensitivity for the identification of this blue pigment - down to about 5%. Unfortunately, we verified that referred high sensitivity is not always present, since for some of the samples with a concentration probably above 5% (as it was ofent identified by μ-R) this pigment could not be identified by μ-IR. For example, although the presence of Prussian blue in the layers 2 and 3 of the sample **K3** was easily confirmed by μ-R, its identification by μ-IR (Figure 6.9c) was very uncertain, and the pigment would probably be referred to as not present.

The painting samples under analysis are very complex pigment mixtures, constituted by a high content of highly absorbing components, such as lead white, for which, the limit of 5% is probably no longer valid.

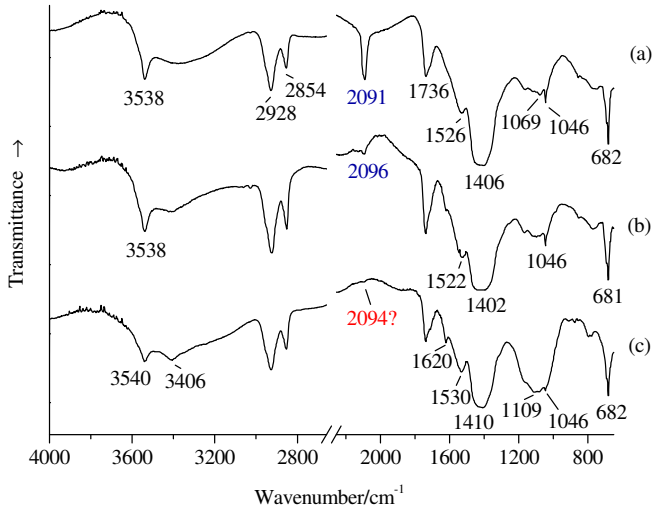

Figure 6.9 Infrared spectra of: (a) layer 2 of sample **U4**, identified as a mixture of lead white, lead carboxylates and Prussian blue in oil, (b) layer 3 of sample **L2**, identified as a mixture of lead white, lead carboxylates and Prussian blue in oil, and (c) layers 2 and 3 of sample **K3**, identified as a mixture of lead white, lead carboxylates, and maybe calcium sulfate dihydrate and Prussian blue in oil.

Oxides and Oxyhydroxides

Viridian (Guignet's green/ Pannetier's green/ Mittler's green), a transparent green pigment first synthesized during the 19th century [85], was identified in the samples thanks to its characteristic bands occurring at about 1064 and 793 cm^{-1} [248,249], which have not yet been assigned.

Known to be a hydrated chromium^{III} oxide with composition $Cr_2O_3.2H_2O$ [26,85,90], this pigments was not expected to produce any mid-infrared bands except for water vibrations, since the characteristic bands of the Cr-O modes occur in the far infrared region (FIR), outside the wavenumber range of our detector. However, in the spectra acquired during the analysis of some green layers (Figure 6.10a and b) bending mode of water ca. 1635 cm^{-1} was not observed (which can also result from overlapping of other bands) and instead, two unique mid-infrared bands at 1064 and 793 cm^{-1} are exhibited. The mid-IR reference spectra of this pigment (Figure 6.10c and d) are very similar to the spectra acquired during the analysis of the painting's samples.

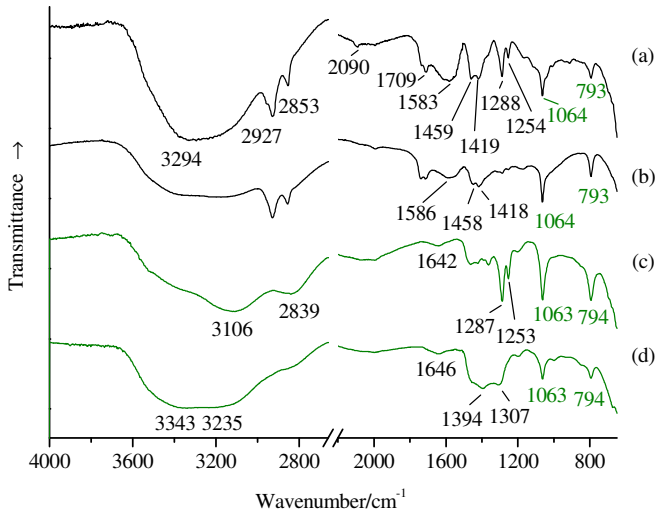

Figure 6.10 Infrared spectra of: (a) layers 3-5 of sample **F6**, identified as a mixture of Prussian blue, viridian and carboxylates in oil, (b) layer 3 of sample **T3**, identified as viridian in oil, (c) reference sample of viridian (viridian - W&N) and (d) reference sample of viridian (vert émeraude - Lefranc).

In order to obtain a more complete spectrum and determine viridian's composition, the reference sample of viridian from Windsor & Newton was analysed using a FT-IR equipment capable of reaching lower wavenumbers. The acquired spectrum is presented in Figure 6.11.

It is known that both lattice water (water molecules trapped in the crystalline lattice) and coordinate water originate, besides strong hydroxyl stretching bands between 3550 and 3200 cm^{-1}, also exhibits a HOH bending mode (nondissociated water) at 1650-1580 cm^{-1} [195,250,251]. As shown in Figure 6.11, the intensity of this band, which occurs at about 1635 cm^{-1}, is very reduced when compared with other bands of the spectrum, suggesting that only a small amount of water is in fact present, probably a small amount of loosely adsorbed water.

Hydroxo complexes, instead, although also producing the strong hydroxyl stretching bands between 3550 and 3200 cm^{-1}, do not exhibit the HOH bending mode near 1600 cm^{-1}, but rather a MOH bending mode below 1200 cm^{-1} [195]. Since the synthesis of viridian generally consists in calcinating a dichromate compound (for example, $K_2Cr_2O_7$) whit boric acid (H_3BO_3) and the subsequent hydrolysis during the washing for removal of residual reagents [85], it is possible that dissociated water, rather than nondissociated water, is bonded to the metal.

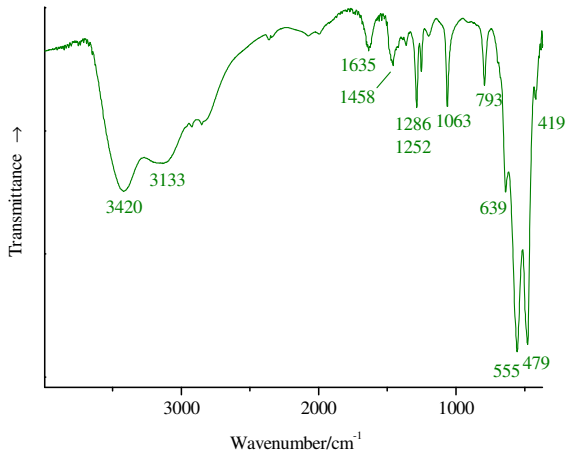

Figure 6.11 Infrared spectra of the reference sample of viridian (viridian - W&N) (Nicolet 6700 spectrometer fitted with a DTGS detector, 4 cm^{-1} resolution, 128 scans).

A search through the existing works about viridian and chromium oxides, hydroxides and oxyhydroxides was conducted and it was found that other compositions have been assigned to viridian, namely $Cr_2O(OH)_4$ [248,252] (which is equivalent to $Cr_2O_3.2H_2O$), $Cr_2O(OH)$ [253], $Cr_4O_3(OH)_6$ [254], $Cr(OH)_3.xH_2O$, α-CrOOH and γ-CrOOH [248,255], or even $Cr_2O_3.(xH_2O)$-Cr_3BO_6 [256]. Unfortunately, the number of published spectra of these compounds, especially of the three CrOOH polymorphic structures is very reduced and not always in agreement, what does not allow a comparison to be made [255,257,258]. Nevertheless, it was noticed that the two bands of viridian at about 555 and 479 cm^{-1} and even the shoulder at 639 cm^{-1}, are closely to those present in $Cr(OH)_3.xH_2O$ compounds [255,258,259].

In order to identify the form(s) present in viridian, XRD analysis was employed. However, due to its disordered structure, it was very difficult to obtain a good diffractogram and no conclusion was obtained.

Phosphates, silicates and sulfates

Phosphates, silicates and sulfates produce IR spectra showing a very intense band at about 1030-1000 cm^{-1}, 1100-900 cm^{-1} and 1130-1080 cm^{-1} [194], respectively, with probable overlapping when they co-exist in a mixture. This fact not only restricts the usefulness of the IR spectra for differentiation of compounds inside each functional group, like previously showed for carbonates, but also for differentiation among compounds belonging to these three functional groups. We will present separately the phosphates, silicates and sulfates identified in the samples, preceded by the most representative difficulties in their differentiation.

Phosphates

Bone/ivory black - Although bone and ivory have compositional and structural differences, which account for the different properties of these materials, their overall composition is very similar: an organic matrix mainly composed by cross-linked collagen protein (type I collagen) and a mineral phase, whose major component is biological apatite (anhydrous apatite in bone and a hydroxylapatite in ivory)[55]. When heated at high-temperatures, to form bone and ivory black pigments, the differentiation between these materials becomes even more difficult [85,260-263].

As shown in Figure 6.12, bone/ivory black is identified by IR bands assigned to its inorganic content (the apatite), which occur at 3569-3567(w), due to the hydroxyl stretching modes, 1455(w) and 1416(w), due to the splitting of the antisymmetric stretching mode of the carbonate group, 1120-1089(w) and 1040-1035(vs), due to the splitting of the antisymmetric stretching mode of the phosphate group, 962 cm^{-1}, due to the symmetric stretching mode of the phosphate group and 874 cm^{-1}, due to the bending out-of-plane of the carbonate group [260,261,263,264].

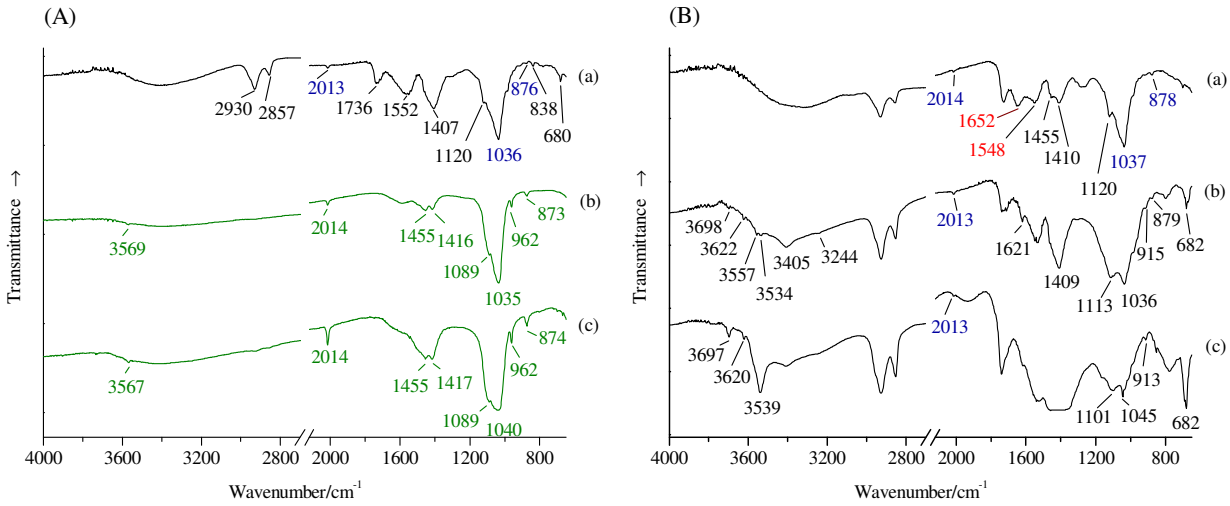

Figure 6.12 Infrared spectra of: (A)(a) layer 2 of sample **B4**, identified as a mixture of bone/ivory black, lead carbonate, lead carboxylates in oil, (b) reference sample of bone/ivory black (Lefranc), and (c) reference sample of bone/ivory black (Winsor & Newton); (B)(a) layer 2 of sample **J3**, identified as bone/ivory black with a fraction of a proteinaceous material, (b) layers 2 and 3 of sample **G4**, identified as a mixture of lead white, lead carboxylates, gypsum, kaolin and bone/ivory black in oil, and (c) layer 2 of sample **G3**, identified as a mixture of lead white, lead carboxylates, kaolin and bone/ivory black in oil.

[55] The exact structure of the mineral apatite is not well defined because substitutions in the mineral apatite lattice can occur [262].

Bands assignable to the organic matrix (probably a residual collagen material), which occur at 1652 and 1548 cm^{-1}, the amide I and amide II bands, respectively, were identified very rarely (Figure 6.12Ba) [260,262]. The weak band at 2013 cm^{-1}, which has not yet been assigned, seems to be very characteristic of this black pigment [265] and was extremely useful for its identification.

Identification of bone/ivory black was compromised whenever present in a relatively low concentration, and/or when a significant amount of silicates and/or sulfates was present. That is the case of the two spectra presented in Figure 6.12Bb and c. In the first spectrum (Figure 6.12Bb) the band at 1036 cm^{-1} can be assigned both to bone/ivory black and to kaolin, a component identified in the layer (3968, 3622, 1113 and 915 cm^{-1}), and the band at 879 cm^{-1} can be assigned to bone/ivory black and to a carbonate compound in low amount, for example, calcium carbonate - calcite form. Identification of this black pigment was possibly due to the presence of the weak band at 2013 cm^{-1}. In the second spectrum (Figure 6.12Bc) no band besides the 2013 cm^{-1} can be assigned to bone/ivory black.

Silicates

Characterized for producing strong absorption band(s) within a relatively narrow wavenumber interval (1100-900 cm^{-1}, due predominantly to the antisymmetric stretching vibration of the SiO_4 units) the differentiation between silicate compounds, especially in a mixture, can be very difficult [175,266,267]. Diagnostic bands, in particular those due to the hydroxyl stretching modes (3800-3500 cm^{-1}), which are sensitive to the clay structure and crystallinity, are extremely helpful for their identification [267-269].

Celadonite, one of the two main green colouring agents of green earth, the other being glauconite, was identified in three paintings. Because celadonite (approximate chemical composition $K(Mg,Fe^{2+})(Fe^{3+},Al)[Si_4O_{10}](OH)_2$) and glauconite (approximate chemical composition $(K,Na,Ca)(Fe^{3+},Al,Mg)_2(Si,Al)_4O_{10}(OH)_2$) present similar chemical composition and crystal structure [270,271], their differentiation by some analytical techniques such as elemental and thermal analysis and X-ray diffraction, can be seriously difficult. However, IR spectroscopy is able to differentiate between these two minerals with relatively facility (Figure 6.13) [250,272].

Celadonite, a well crystallized mineral of volcanic origin produces an IR spectrum (Figure 6.13*a*) with sharp and well-defined bands at 3601(w), 3578(w), 3557(m) and 3533(w) cm^{-1}, due to hydroxyl stretching modes at 1113(m) cm^{-1}, due to the stretching of apical Si-O, 1076(m), 977(vs) and 960(vs) cm^{-1}, due to antisymmetric stretching of equatorial Si-O, and at 839(w) and 800(m) cm^{-1} [26,250,272-275].

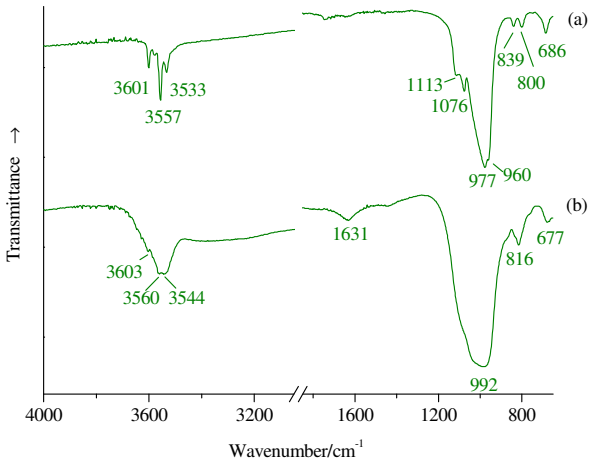

Figure 6.13 Infrared spectra of reference samples of: (a) celadonite and (b) glauconite.

Glauconite[56], on the other hand, gradually formed from sedimentary minerals after deposition, shows a great composition variety, presenting an irregular structure and, consequently, an IR spectrum (Figure 6.13b) with broader and diffuser bands than celadonite [(26,268,272,274)]. In contrast to the three sharp hydroxyl stretching bands of celadonite, glauconite exhibits three broad and week bands at 3603, 3560 and 3544 cm^{-1} and, due to the higher aluminium substitution in the silicate tetrahedra in glauconite (10-16 % vs. 2-6% [(250)]), the four medium to strong intensity bands in the celadonite spectrum, from the Si-O modes (1113-960 cm^{-1}), are broaden into just one band at about 992 cm^{-1} in the glauconite spectrum [(272)]. An additional band is seen in the spectrum presented in Figure 6.13b, occurring at 1631(w) cm^{-1} due to the hydroxyl bending mode.

In the presence of carbonates and carboxylates (see below), generally the major components of the painting samples under analysis, celadonite identification is easily done, provided it is present in a relatively significant amount (Figure 6.14A). As seen in Figure 6.14Aa and Ab, except for the bands at 3533 cm^{-1} that can be assigned both to celadonite and lead white and at 838 cm^{-1} that can be assigned both to celadonite and lead carbonate, most of the celadonite bands (in blue) are easily identified.

However, if celadonite is present in a relatively small amount, or if the sample contains a significant amount of compounds whose bands overlap with those of celadonite, as is the case of the spectra presented in Figure 6.14B, its identification is compromised. The spectrum shown in Figure 6.14Ba that was obtained from the same layer as the spectrum shown in Figure 6.14Ab, but from a different thin-section, demonstrates that, even if there is

[56] In fact glauconite is the name given to a series of minerals, although it is/can be used as a mineral name species too.

no significant band overlapping between carbonates (or carboxylates) and celadonite, if celadonite is present in a relatively small amount, its identification can be difficult.

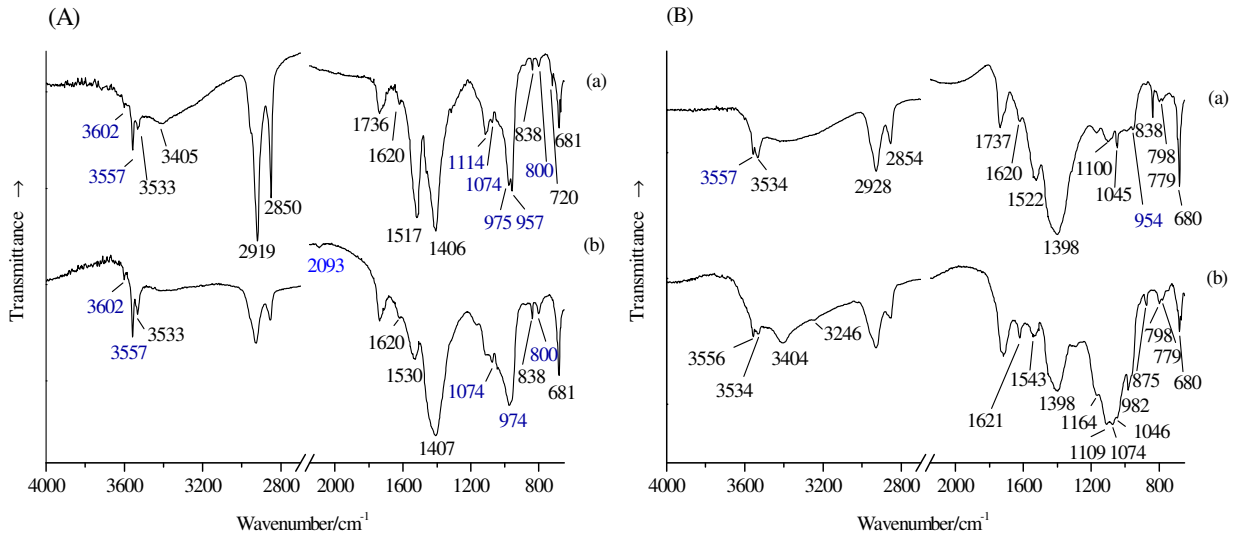

Figure 6.14 Infrared spectra of: (A)(a) sample **E4** (all layers), identified as a mixture of lead white, celadonite and maybe lead carbonate and (b) the layer 3 of sample **E7**, identified as a mixture of lead white, lead carboxylates, celadonite and Prussian blue in oil; (B)(a) layer 3 of sample **E7** (from a different thin section than spectrum Ab), identified as a mixture of lead white, lead carboxylates, lead carbonate, quartz and celadonite in oil, and (b) layer 2 of sample **I4**, identified as a mixture of lead white, lead carboxylates, quartz and maybe barium sulfate, calcium carbonate – calcite form, and gypsum and/or celadonite in oil.

Due to band overlapping between celadonite and gypsum (see below), especially in complex mixtures, it can be very difficult to identify which of these two compounds is present or even, if both are present. For example, in the spectrum shown in Figure 6.14Bb, the hydroxyl stretching band at 3556 cm^{-1} can be assigned to both celadonite and gypsum, the hydroxyl stretching band at 3534 cm^{-1} can be assigned to both celadonite and lead white (whose presence is confirmed by other bands) and the band at 3246 cm^{-1} can be assigned to gypsum. As no further bands assignable to celadonite or gypsum are visible in the spectrum due to masking by the strong sulfate/silicate stretching modes (1164-982 cm^{-1}), there is no certain if celadonite, gypsum, or both, are present. Other compounds present in this complex mixture are lead white, lead carboxylates, quartz, and maybe barium sulfate (982 cm^{-1}) and calcium carbonate - calcite form (875 cm^{-1}).

Kaolin is the name given to the subgroup of dioctahedral 1:1 phyllosilicates, which includes kaolinite, dickite, nacrite and halloysite, clay minerals with identical chemical composition ($Al_2[Si_2O_5](OH)_4$) and identical structure of the individual layers, differing only in

layer stacking arrangement [267]. Due to these similarities the IR spectra of these four clay minerals are quite similar and consequently, somewhat difficult to differentiate [267]. Nevertheless, since different hydroxyl stretching patterns are produced, due to the different hydrogen bonding among the layers, differentiation among these four clay minerals is still possible.

The hydroxyl stretching region of kaolinite is characterized by exhibiting four bands at about 3698, 3668, 3654 and 3621 cm^{-1} (Figure 6.15a), of dickite and nacrite are by three bands at about 3704, 3654 and 3621 cm^{-1}, 3700, 3648 and 3629 cm^{-1}, respectively, and of halloysite by only two bands at about 3695 and 3620 cm^{-1} [269,276,277]. Although the hydroxyl stretching bands of these kaolin minerals differ both in number and position, whenever these bands are weak, like in the spectra shown in Figure 6.15b and c, or when a mixture of these minerals is present, their differentiation is very difficult. Nevertheless, as in dickite and nacrite the bands at *ca.* 3654 and 3648 cm^{-1}, respectively, have a higher intensity than the band at 3700 cm^{-1}, whenever this band at 3700 cm^{-1} occurs, it is expected that the bands at 3654(dickite) or 3648(nacrite) cm^{-1} also occur. Because this band was not identified in any of the acquired spectra, the presence of these two kaolin polytypes was excluded.

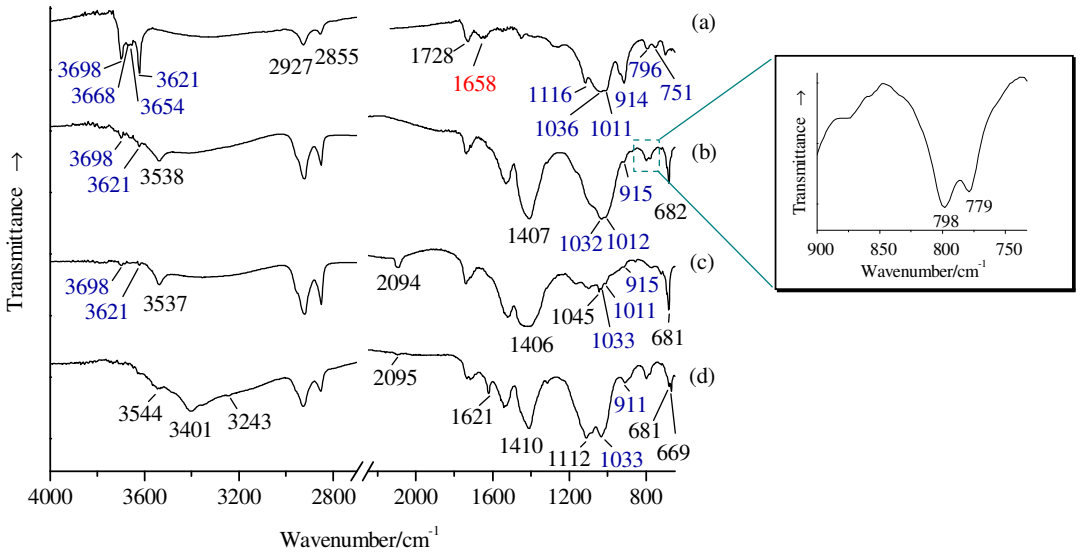

Figure 6.15 Infrared spectra of: (a) layer 1 of sample **T2**, identified as kaolinite in a proteinaceous binder, (b) the layer 2 of sample **G2**, identified as a mixture of lead white, lead carboxylates, quartz and kaolin in oil, (c) the layers 2-4 of sample **U13**, identified as a mixture of lead white, lead carboxylates, Prussian blue and kaolin in oil, and (d) the layers 5-8 of sample **K9**, identified as a mixture of lead white, lead carboxylates, gypsum, quartz and maybe kaolin in oil. The inset presents the enlargement of the quartz's doublet.

Unfortunately, the differentiation between kaolinite and halloysite is not so easy, since weak kaolinite spectra normally present only its two most intense bands that coincide with the two bands of halloysite [269,277]. Consequently, in the spectra where only the two bands at about 3698 and 3621 cm^{-1} are visible, like in Figure 6.15*b* and *c*, it is not possible to know whether kaolinite or halloysite, or even a mixture of the two, since these minerals often occur together [269], is present. So, in these cases, the mineral compound is referred to as kaolin [57].

It is important to refer that in a few spectra, although bands assignable to kaolin minerals, such as the intense Si-O stretching band at 1033 cm^{-1} and the hydroxyl bending (Al_2OH) band at 911 cm^{-1} were present, the characteristic hydroxyl stretching bands were not visible (Figure 6.15d), probably due to masking by other compounds. In these cases, identification of kaolin was impossible, since there are other compounds (silicates, sulfates and phosphates) absorbing at similar wavenumbers. In the particular case of the spectrum presented in Figure 6.15d, the bands at 1033 and 911 cm^{-1} are in fact due to kaolin, whose presence was confirmed analysing another thin-section from the same sample.

Kaolinite**,** a particular clay mineral of the kaolin group, also known as china clay, was identified with confidence in the samples where it was the major component. The spectrum presented in Figure 6.15a, showing the four hydroxyl bands of this mineral, 3698(m), 3668(w), 3654(w) and 3621(m) cm^{-1} is representative of one of those samples. The first three bands arise from the stretching of the inner-surface (or outer) hydroxyl groups, while the last one arises from the stretching of the inner hydroxyl groups (OH groups located inside the layer, laying between the tetrahedral and octahedral sheets). Other bands of kaolinite occur at 1116(m) cm^{-1}, arising from the stretching of apical Si-O (perpendicular to SiO_4 tetrahedral sheet), at 1036-1031(vs) cm^{-1} and 1012(vs) cm^{-1}, arising from the antisymmetric stretching of equatorial Si-O bonds (in-plane), at 936 and 914 cm^{-1}, arising from the Al_2OH bending modes of inner-surface and inner OH groups, respectively, and at 795 and 755 cm^{-1}, arising from hydroxyl translational modes (due to the flexing of the O-Si-O framework) [250,266,267,279-281].

α-Quartz, silicon dioxide (SiO_2), the low temperature silica polymorph, was easily identified in a large number of paintings due to its characteristic doublet at ca. 798 and 779 cm^{-1} (Figure 6.15b, insert), arising from the Si-O-Si bending mode, characteristic of the "ring" structure found in quartz, in which the silicate tetrahedra are joined together to form rings.

[57] Although intercalation methods have been developed to differentiate kaolinite and halloysite, even when mixed together [266,278], these methods are not suitable for the samples under analysis, which are very complex.

The most intense band of its spectrum, 1084-1079 cm^{-1}, arising from the SiO_4 antisymmetric stretching (Figure 6.19Bb) was normally masked by other compounds [250,268,282].

Identification of quartz in the samples by this technique was expected, because quartz is the most abundant mineral in earth's crust, hence frequently occurs associated with other minerals [250], and because infrared spectroscopy is capable of detect quartz even when present in almost trace amounts [268]. However, in the presence of significant amounts of orange or yellow chromate pigments its identification is seriously compromised, as the major absorption bands of the chromate compounds can mask the quartz doublet.

Sulfates

Barium sulfate, $BaSO_4$, which occurs naturally as barite, was identified by its infrared spectra with bands at about 1174(s), 1113(sh), 1083(s) and 984(m) cm^{-1} (Figure 6.16). The first three bands are due to the split of the triply degenerate antisymmetric stretching mode of the sulfate ion, while the last band is due to the symmetrical stretching mode [245,283,284].

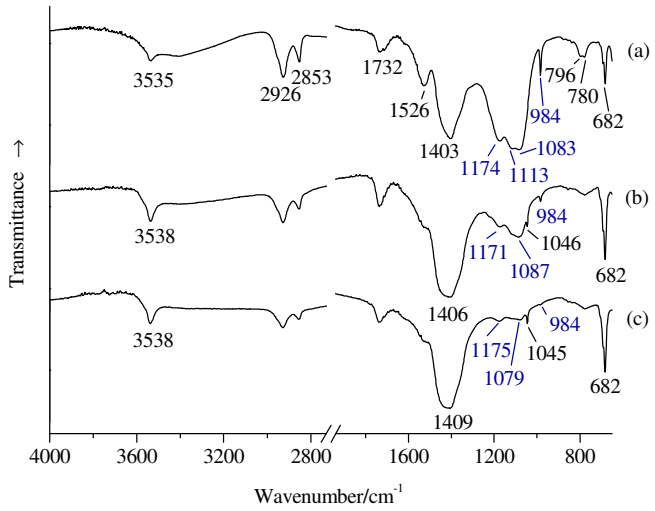

Figure 6.16 Infrared spectra of: (a) layers 1 and 2 of sample **I1**, identified as a mixture of barium sulfate, lead white, lead carboxylates and quartz in oil, (b) ground layer of sample **G4**, identified as a mixture of barium sulfate, lead white and lead carboxylates in oil, and (c) ground layer of sample **H4**, identified as a mixture of lead white, lead carboxylates and maybe barium sulfate in oil.

Like expected, as the relatively concentration of barium sulfate decreases, Figure 6.16 (a trough c), its identification becomes more difficult. While in the first two spectra barium sulfate is easily identified, in spectrum (c) it is done with some doubt, since its more intense bands (between 1174-1083 cm^{-1}) are masked or mislead with the bands resulting from the triglyceride ester linkage of the drying oil binder, which due to aging, lost their characteristic

maple leaf pattern (1239, 1170 and 1101 cm^{-1}) and exhibit instead only two bands of almost the same intensity at about 1166 and 1092 cm^{-1} [285]. Albeit very weak, the characteristic band at 984 cm^{-1} raised the suspicion of the presence of barium sulfate, which was confirmed by μ-R.

Brochantite - The green basic copper^{II} sulfate, $Cu_4(SO_4)(OH)_6$, naturally occurring as brochantite, was identified in sample **H8**, thanks to its characteristic doublet at 3587(m) and 3565(m) cm^{-1}, arising from the hydroxyl stretching modes and to the bands at 1115(m) and 1096(m) cm^{-1}, due to the sulfate antisymmetric stretching mode (Figure 6.17). Other bands of this compound occur at 3400 cm^{-1}, due to hydroxyl stretching mode at 986(sh) due to the sulfate symmetric stretching mode, and at 945(w) and 873(m), due to hydroxyl librations [175,250,283,286,287].

Because the synthetic and the natural (brochantite) forms of basic copper^{II} sulfate present identical vibrational spectra, they cannot be distinguished [287]. Nevertheless, as brochantite is a common impurity of malachite, a basic copper^{II} carbonate mineral with composition $Cu_2CO_3(OH)_2$ [288], the occurrence of the basic copper^{II} sulfate associated with malachite indicates that its origin is natural. In this sample **H8**, malachite itself was not identified suggesting that basic copper^{II} sulfate is present in the synthetic form. However, by μ-R (Figure 6.31Aa), malachite was, in fact, identified in this same sample, suggesting that it is brochantite that is present.

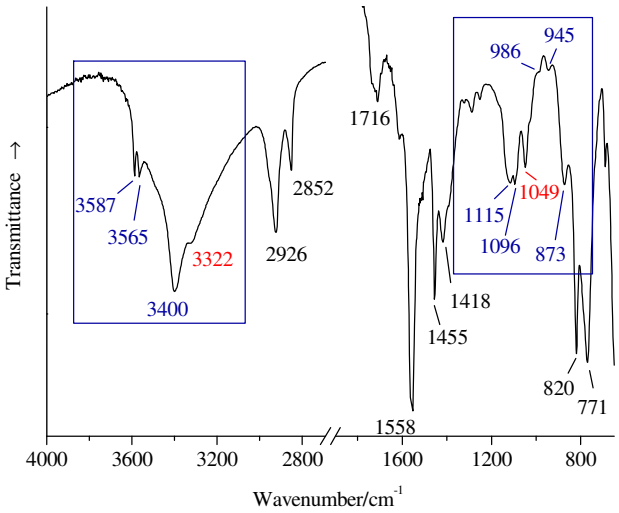

Figure 6.17 Infrared spectrum of layers 4 and 5 of sample **H8** identified as a mixture of brochantite (bands assigned in blue), emerald green and lead white in oil.

Due to its intense and characteristic bands occurring at 3400(s) and 3320(s), due to hydroxyl stretching mode, 1500(vs) and 1400(vs), due to the carbonate antisymmetric

stretching mode, 1095(m), due to carbonate symmetric stretching mode, 1045(vs) and 875(m), due to hydroxyl out-of-plane bending, 820(m) due to carbonate out-of-plane bending mode and 748(m) [190] malachite is generally easily identified by IR spectroscopy. However, because the other components of the sample, brochantite, emerald green and possibly lead white (as the band at 1418 cm^{-1} can account for the existence of lead white) present bands at similar wavenumbers to those of malachite, malachite's bands were masked and its identification was not possible.

We may question if the bands at 3322 and 1049 cm^{-1} (in red), not assignable to any other pigment, and the band at 1418 cm^{-1} (Figure 6.17), cannot be due to malachite [190,191], but still identification is very doubtfully.

Gypsum, calcium sulfate dihydrated, $CaSO_4.2H_2O$, also known as terra alba was identified (Figure 6.18A) thanks to the its characteristic IR bands arising from the lattice water (hydrogen bonded) vibrational modes, namely four overlapped bands at about 3552-3538(m), 3494-3484(vw), 3410-3408(s) and 3248-3244(w) cm^{-1} (forming a leaf pattern), where the the first three bands arise from the antisymmetric and symmetric stretching modes of water molecules and the last arises from the first overtone of the water bending mode, and two bands at 1687(w) and 1621-1618(m) cm^{-1}, due to the O-H-O bending mode of water molecules. The reason for the existence of two bands due to antisymmetric stretching modes bending modes and two bands for beding modes is the existence of factor-group plitting, as a consequence of the presence of two water molecules in the spectroscopic unit cell of gypsum [250,289,290].

Bands arising from the vibrational modes of the sulfate ion occur at 1137-1134(vs) and 1117-1111(vs) cm^{-1} (antisymmetric stretching mode) and 670 cm^{-1} (antisymmetric bending mode). The symmetric stretching which is expected to occur at 1004 cm^{-1} was not visible [283,291].

Although in the two spectra presented in Figure 6.18A, gypsum is easily identified, for most part of the spectra, since the concentration of gypsum in the layers is relative low, its identification was normally uncertain, as exemplified in the representative spectra shown in Figure 6.18*B*. In the first spectrum (Figure 6.18Ba), gypsum is still easily identified by the hydroxyl bands occurring at 3544, 3410 and 1620 cm^{-1} and to the sulfate antisymmetric stretching band at 1117 cm^{-1}. In the other two spectra (Figure 6.18Bc and d), although the presence of gypsum is possible, it is very uncertain. Besides, the absence of the bands at 3244 and 1687 cm^{-1} (also seen in the first spectrum), the band at 3552-3544 cm^{-1} is masked by the hydroxyl stretching band of lead white occurring at about 3538 cm^{-1} and the bands arising from the stretching of the sulfate ion are easily masked by (or confused with) bands

from other sulfate or silicate compounds. Only the existence of the bands at 3409 and 1620 - 1618 cm^{-1} suggests the presence of gypsum, but, as these bands can also be present in other compounds containing interlayer or loosely adsorbed water (for example, Copiapite $(Fe^{2+},Mg)Fe_4^{3+}[(OH)I(SO_4)_3]_2.20H_2O$ [250]), they cannot be used to rule out gypsum presence.

Nevertheless, although the bands at 3409, 1620 and 1112 cm^{-1} in the spectrum shown in Figure 6.18Bb have low intensity, because bands assigned to other sulfate or silicate compounds are not visible, gypsum is probably present in the sample.

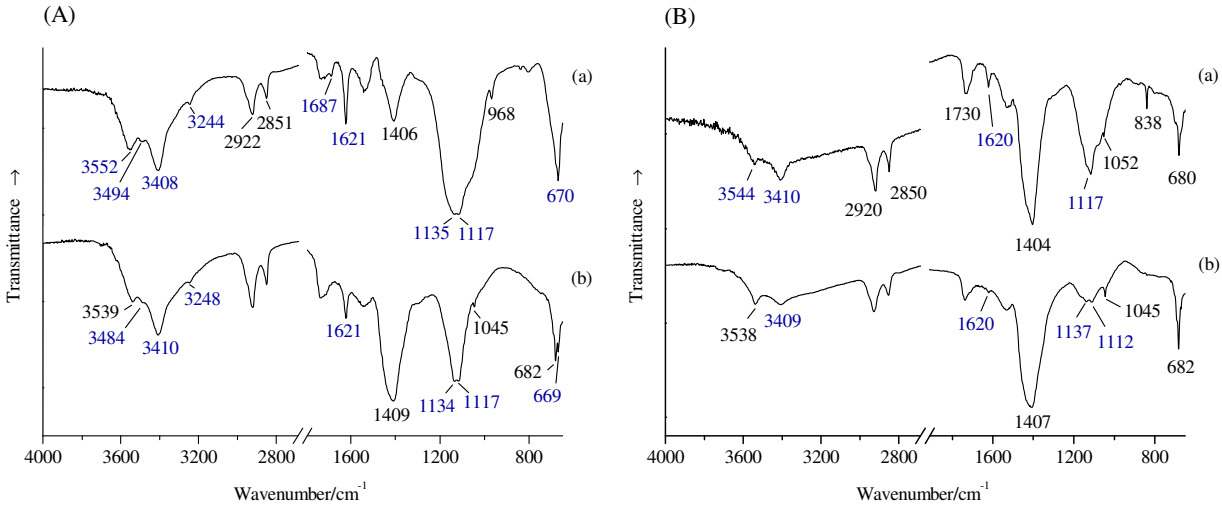

Figure 6.18 Infrared spectra of: (A) (a) layer 3 of sample **F3**, identified as a mixture of gypsum, lead carbonate, lead carboxylates in oil, and (b) layer 2 of sample **A2**, identified as a mixture of lead white, lead carboxylates and gypsum in oil; (B) (a) layer 1 of sample **E6**, identified as a mixture of lead carbonate, lead carboxylates and maybe lead white and gypsum in oil, and (b) layers 2-6 of sample **A4**, identified as a mixture of lead white and maybe gypsum in oil.

Difficulties in distinguishing phosphates, silicates and sulfates

Because the most intense band in the infrared spectrum of phosphates, silicates and sulfates occurs in the same wavenumbers, distinguishing these compounds one from another can be seriously compromised and in some cases it is only possible to conclude that a sulfate or a silicate is probably present (Figure 6.19A), or that a silicate or a phosphate is probably present (Figure 6.19B).

Figure 6.19A presents three spectra showing the difficulties to distinguish sulfate from silicate compounds, while Figure 6.19B presents three spectra showing the difficulties to distinguish silicate from phosphate compounds.

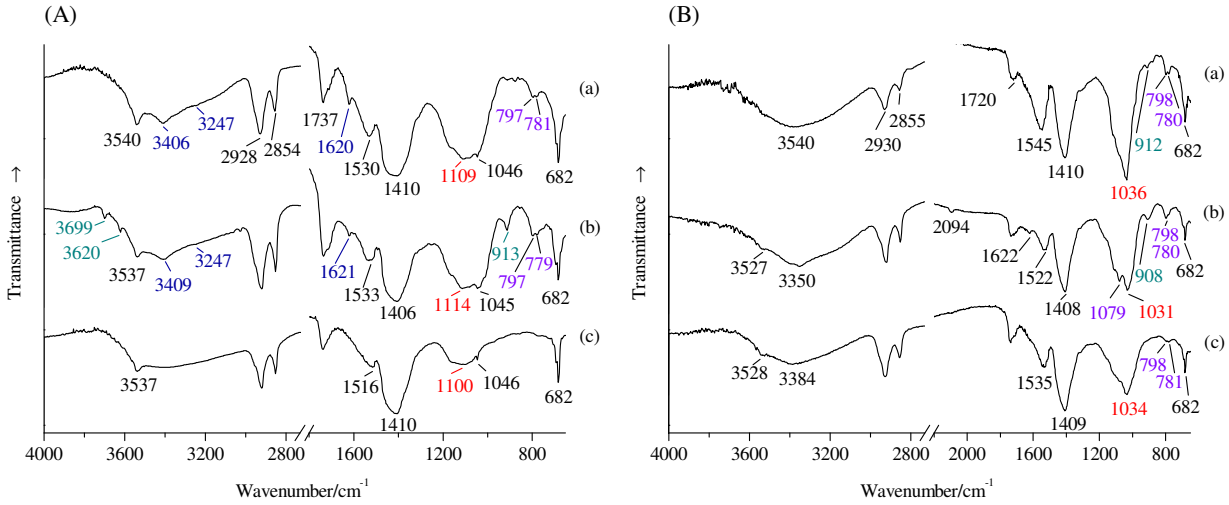

Figure 6.19 Infrared spectra of: (A)(a) layer 1 of sample **K3**, identified as a mixture of lead white, lead carboxylates, quartz and a sulfate/silicate compound (probably gypsum) in oil, (b) layers 2 and 3 of sample **I6**, identified as a mixture of lead white, lead carboxylates, quartz, kaolin and maybe gypsum in oil, and (c) layer 4 of sample **W4**, identified as a mixture of lead white, lead carboxylates and a sulfate/silicate compound in oil; (B)(a) layer 2 of sample **B2**, identified as a mixture of lead white, lead carboxylates, quartz and a silicate/phosphate compound in oil, (b) layers 2 and 3 of sample **K11**, identified as a mixture of lead white, lead carboxylates, quartz, Prussian blue and a silicate/phosphate compound in oil, and (c) layer 4 of sample **K12**, identified as a mixture of lead white, lead carboxylates, quartz and a silicate/phosphate compound in oil.

The three spectra of Figure 6.19A are characterized by intense and broad bands between 1200 and 1000 cm^{-1}, whose origin is difficult to assign with certain. Although a very similar pattern is present in the two first spectra (Figure 6.19Aa and Ab), they have the contribution from different compounds: quartz (796 and 781 cm^{-1}) and probably gypsum (3406, 3247 and 1620 cm^{-1}) in the first spectrum (Figure 6.19Aa) and kaolin (3699, 3620 and 913 cm^{-1}), quartz (797 and 779 cm^{-1}) and probably gypsum (3409, 3247 and 1621 cm^{-1}) in second spectrum (Figure 6.19*Ab*). Due to the broad envelope these bands, the existence of other(s) silicate(s) or sulfate(s) must not be excluded. In the third spectrum (Figure 6.19Ac) as there are no diagnostic bands, the origin of the band at 1100 cm^{-1} is not ruled out, the possible conclusion being that a silicate or/and a sulfate compound(s) may be present.

In a similar way, the three spectra of Figure 6.19B are characterized by the presence of an intense band at 1036-1031 cm^{-1}, difficult to assign due to lack of diagnostic bands. In the first two spectra (Figure 6.19Ba and Bb) the small band at 912-908 cm^{-1} suggest the presence of kaolin, but as there is no signal of the hydroxyl stretching bands of this compound, the assignment of the band at 1030 cm^{-1} to kaolin is not sure.

As showed in Figure 6.12, also bone/ivory black presents a very intense band at 1040-1035 cm^{-1}, but again, no diagnostic band of this compound, such as the characteristic band at 2014 cm^{-1} is present in any of the three spectra. Consequently, the origin of the band at 1036-1031 cm^{-1} is not identified, and the only possible conclusion is that a silicate or/and a phosphate compound(s) may be present.

Figure 6.20 demonstrates another difficulty found in the identification of the bands occurring in the silicate wavenumbers. As can be seen in Figure 6.20A, the spectra (a) and (b) presented a weak to medium band at 1026 and 1009 cm^{-1}, respectively, while the spectrum (c) a very intense band at 1010 cm^{-1}. The position of the band seems very low for sulfates and even for phosphates, being probably due to a silicate. In fact, there is a silicate blue pigment, ultramarine blue or lazurite (the former is the synthetic phase and the last is the naturally occurring phase), $Na_8[Al_6Si_6O_{24}]S_n$, whose IR spectrum presents a strong and broad band between 1150-950 cm^{-1} (Figure 6.20Ba), assigned to the stretching modes in the tetrahedral Si-O units that make-up the skeleton [25,268,292], whose presence in the samples would explain the existence of the above referred band.

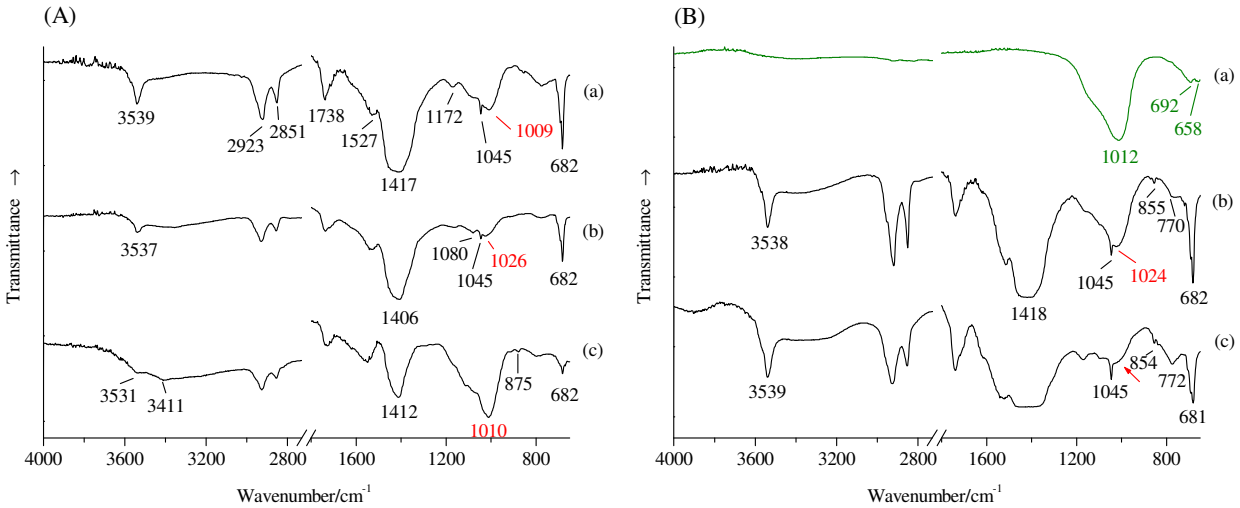

Figure 6.20 Infrared spectra of: (A)(a) layers 2-5 of sample **H1**, identified as a mixture of lead white, lead carboxylates and a silicate compound in oil, (b) sample **J4**, identified as a mixture of lead white, lead carboxylates and a silicate compound in oil, and (c) sample **M1**, identified as a mixture of lead white, lead carboxylates and a silicate compound in oil; (B)(a) reference sample of ultramarine blue (Winsor & Newton), (b) sample **T1**, identified as a mixture of lead white, lead carboxylates and a silicate compound in oil, and (c) layer 2 of sample **S1**, identified as a mixture of lead white and lead carboxylates in oil.

However, as shown in the IR spectra of two layers with a significant amount of ultramarine blue (μ-R results indicate this as the only/major blue pigment of the layers), Figure 6.20Bb

and Bc, the identification of this blue pigment by μ-IR in the samples under analysis is not straightforward. While in the spectrum of sample **T1**, a silicate band is visible, even if not allowing the identification the silicate compound, in the spectrum of the layer 2 of sample **S1**, the silicate band occurs only as a shorder. Therefore, although we can suspect that the bands marked in red in the spectra of Figure 6.20A are due to ultramarine blue, other silicate compounds can be responsible for these bands.

Other compounds

Binder

Detection and identification of the binder by IR spectroscopy is not a simple task, since a binder is itself a complex mixture of closely related compounds normally not resolved by IR. Furthermore, the presence of pigments and extenders, generally in a larger percentage than the binder, significantly masks its IR spectrum below 1500 cm^{-1} [221,293]. Notwithstanding, in general the spectra exhibit well resolved spectral features that allow the identification of the binder class [285], as an oil, wax, resin, gum or proteinaceous material [293].

The presence, in most of the spectra, of bands at about 2929(m) and 2854(m) cm^{-1}, assigned to the asymmetric and symmetric stretching modes of CH_2 groups, respectively, at 1729(w) cm^{-1}, assigned to the carbonyl stretching mode and at about 1166 and 1092 cm^{-1}, due to the triglyceride ester linkage, indicated that the binder was a drying oil [285]. The existence of lead soaps originated from the saponification of fatty esters of the oil medium with lead containing pigments, corroborated this identification [294].

Exceptions to the drying oil were found in i) the ground layer of the samples **T2**, **W4** and **W7**, which proved to be from restoration areas (see next chapter) and ii) in the ground layer of the painting ***F***.

The existence of a band at 1658-1652 cm^{-1}, assigned to the amide I band and the bands at 2927, 2855 and 1728 cm^{-1}, due to unsaturated fatty esters, in the spectra of the ground layer of the samples **T2** (Figure 6.15a), **W4** and **W7**, suggest that the binder is either egg yolk (egg yolk contains these two groups) or a mixture of a proteinaceous material with a drying oil, such as egg-oil or animal glue-oil emulsion [285,294,295]. However, in accordance with the restoration record, the binder used in the masses to fill the lacunae, was animal glue, hence the presence of bands due to unsaturated fatty esters in the spectrum of the ground layer of the restoration samples is probably due to infiltration of the drying oil used as binder in the above layers.

As shown in Figure 6.21a, in some of the spectra of the ground layer of painting ***F*** which is composed by calcium carbonate - calcite form (2513, 1795, 1417(saturated), 876 and 713 cm^{-1}), the existence of the two bands at 3363 and 1652 cm^{-1}, assignable to a proteinaceous

material, and of three bands at 2919, 2850 and 1716 cm^{-1}, assignable to unsaturated fatty esters suggest that the binder is either egg yolk, egg-oil emulsion or animal glue-oil emulsion.

However, since on other spectra of the same ground layer (in another samples), there is no signal of the existence of proteinaceous material, only bands assigned to an oil medium being visible (Figure 6.21b), it is concluded that, either i) the binder is a mixture of an drying oil with a proteinaceous material (egg or animal glue) – painting layers in which the binder is glue the amount of binder is generally relatively very low [71], what would explain the low content in proteinaceous material, or ii) the proteinaceous material comes from the sizing of the canvas, being this the most probable explanation.

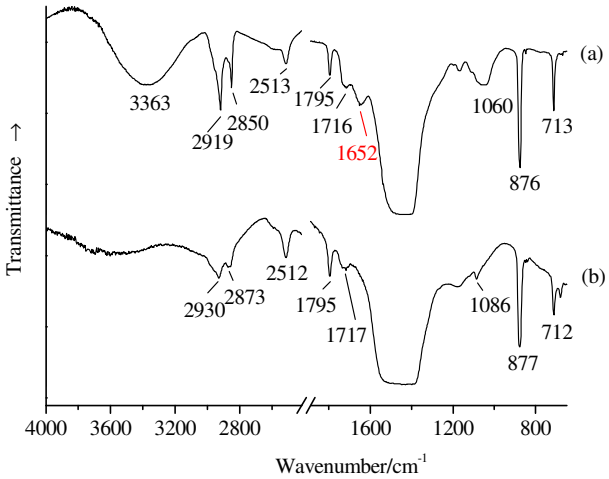

Figure 6.21 Infrared spectra of: (a) ground layer 1 of sample **F1**, identified as calcium carbonate--calcite form and proteinaceous material, (b) ground layer 1 of sample **F5**, identified as calcium carbonate-calcite form in oil.

Metal carboxylate salts (soaps)

Most of the spectra exhibiting the characteristic bands of lead white (and lead carbonate) also presented a broad, medium to weak band at ~1545-1510 cm^{-1}, probably due to the antisymmetric stretching mode of the carboxylate ion (COO^-) of the lead carboxylate salts (lead fatty acid soaps), produced by the reaction of the free fatty acids of the drying oil with lead pigments [178,285,296-298]. The symmetric stretching mode of the lead carboxylate which occurs at ~1419 cm^{-1} is masked by the intense and broad band due to the carbonate antisymmetric stretching mode of lead white (and lead carbonate).

Similar to lead, also copper, potassium, zinc and cobalt-containing compounds are known to form metal carboxylates, whose carboxylate antisymmetric stretching band occurs at about 1585 cm^{-1}, 1566-1560 cm^{-1}, 1548-1540 cm^{-1}, and 1542 cm^{-1}, respectively [298-299]. As band

position is very similar for some of these carboxylates, it is very difficult to determine by IR analysis only which metal carboxylate have been formed, even more, when mixtures of metal carboxylates are likely to be present.

Although in most of the spectra the antisymmetric stretching band of the carboxylate ion, is probably mainly due to lead carboxylates, the existence of other metal carboxylates cannot be excluded. In fact, in a few spectra, a significant position's shift or a difference in the band intensity of the COO^- antisymmetric stretching band relatively to the CO_3^{2-} antisymmetric stretching/COO^- symmetric stretching bands was observed, suggesting the presence of different metal carboxylates as shown in the cases referred below:

The wavenumbers of the broad band at about 1586-1583 cm^{-1} identified in the spectra of the green layer of samples **F6** (Figure 6.10a), **T3** (Figure 6.10b) and **T7** (Figure 6.22a) suggest the presence of a copper carboxylate. However, while in sample **F6** the presence a copper compound (emerald green) could be the reason for the formation of copper carboxylates, sample **T7** does not contain copper (SEM/EDS analysis, Figure 7.30) hence, does not presents copper carboxylates. The presence of copper carboxylates in sample **T3** was not evaluated.

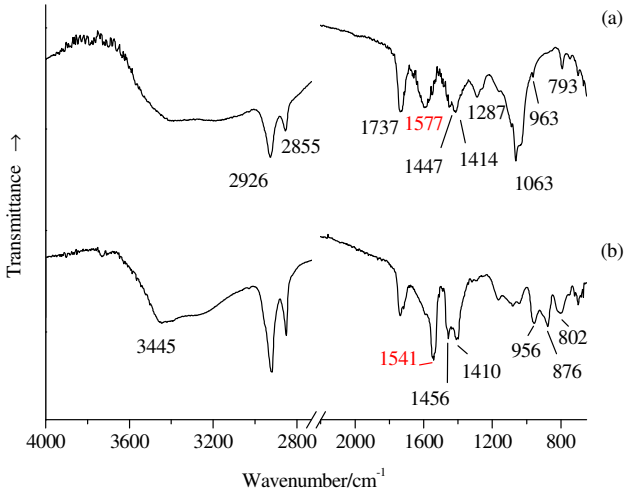

Figure 6.22 Infrared spectra of: (a) layer 2 of sample **T7** identified as a mixture of viridian and metal carboxylate(s) in oil and (b) layer 2 of sample **N2**, identified as a mixture of zinc yellow, a carbonate compound and metal carboxylate(s) in oil.

b) The spectra of the paint layers of samples **N2**, **N3** and **N5** present an unusual highly intense carboxylate antisymmetric stretching band, occurring at 1541 cm^{-1}, suggesting a particularly high amount of carboxylates relatively to the rest of the samples (Figure 6.22b is a representative spectra of the three samples). The band's wavenumber suggest either lead carboxylates, zinc carboxylates, cobalt carboxylates, or a mixture of these. Since lead white

is present in the layer, lead carboxylates are also probably present, but due to the high relatively intensity of the band, zinc or cobalt carboxylates are likely present. Because zinc yellow is present in the layers under analysis (956, 876 and 802 cm^{-1}) in the samples **N2** and **N5** (result confirmed by μ-R), while zinc and cobalt were identified by SEM/EDS in the sample **N3** (Figure 7.21b), it appears that the unusual high intensity of the antisymmetric stretching band of the carboxylate is probably due to the presence of both lead and zinc carboxylates[58].

c) The spectrum of sample **E4** presents a high intense carboxylate band at about 1517 cm^{-1} (Figure 6.14Aa). Because lead white is present in the sample, lead carboxylates probably contribute to this band, but the reason for such a high intensity is not known.

Polysaccharide material

Although the presence of red to pink semi-transparent pigments similar to lake pigments was easily visualized by OM in several samples, their identification by μ-IR was somewhat impossible. Figure 6.23 presents the μ-IR spectra of four red layers mainly composed by such pigments.

Unexpectedly, the overall spectra pattern is quite similar for spectra (a), (b) and (c): a very intense and broad band in the hydroxyl stretching region (3393-3370 cm^{-1}) and three bands at about 1153, 1081 and 1024 cm^{-1}, with a distinct pattern resembling the one of a natural polysaccharide material, such as starch, suggesting that starch is a major component of the layers mainly composed by red lake pigments. The two weak bands at 930 and 859 cm^{-1} (Figure 6.23b) are characteristic of starch and the bands at 1635 and 1412 cm^{-1} can also account for the existence of the polysaccharide material (the reffered bands are marked at pink) [87,300].

Lake pigments are chelate complexes of dyes and metal cations [301], prepared by co-precipitation/adsorption of the organic dyestuff with/onto an inorganic substrate. Although the organic dyestuff is rich in infrared absorption bands, lake pigments normally present a very low dyestuff content [302] (as expected as already expected) thus, the bands due to the dyestuff were not visible, making the identification of the lake pigment difficult.

Regarding the inorganic substrate, which was normally an amorphous and highly variable inert compound formed by the reaction between potash alum (potassium aluminium sulfate, $KAl(SO_4)_2.12H_2O$) and an alkali (a solution of potassium or sodium carbonate), but also calcium carbonate - calcite form, barium sulfate, kaolin, zinc oxide and tin salts [303-305], there

[58] Due to its basic character, zinc is known for reacting with oil in a more pronounced manner than lead, thus, zinc pigments readily react with fatty acids to form zinc soaps [296].

is also no indication about is composition. In the spectrum presented in Figure 6.23d, lead white is easily identified, in but it is probably from an adjacent layer (as result of diffraction effects).

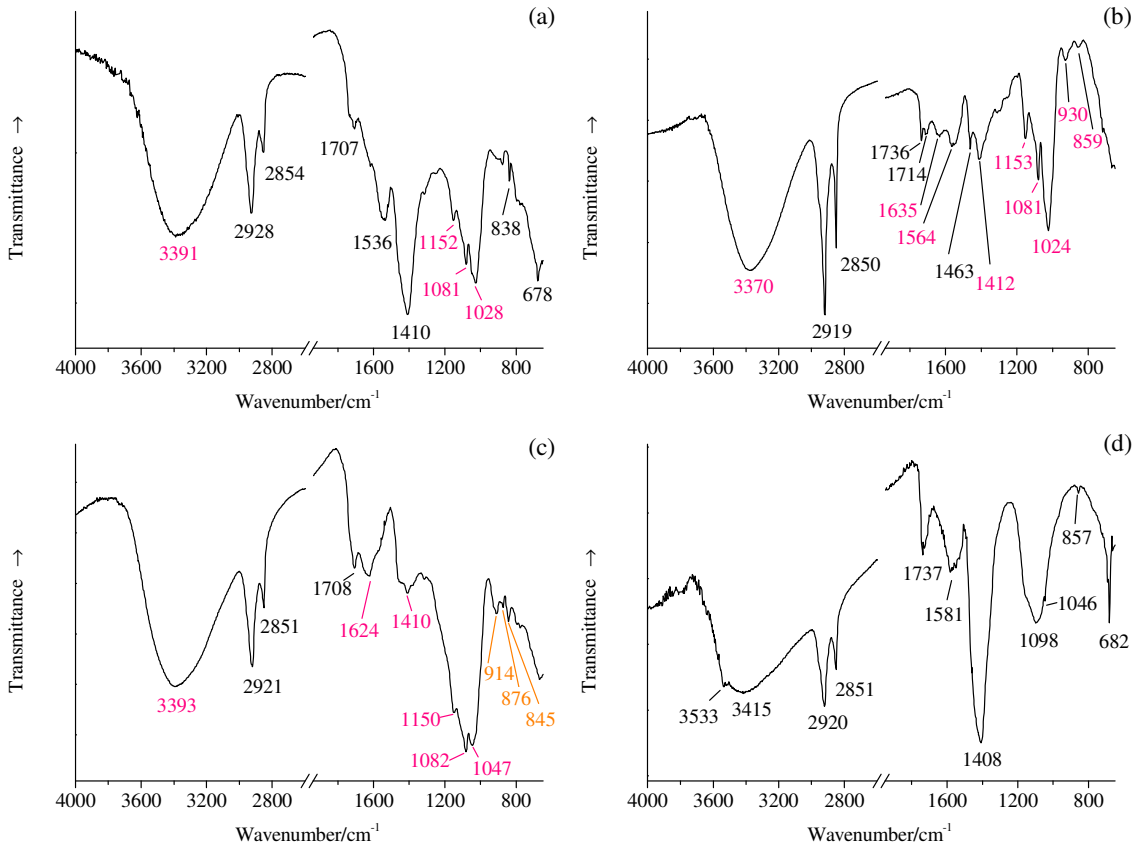

Figure 6.23 Infrared spectra of: (a) layers 3 and 4 of sample **E5**, identified as a mixture of lead carbonate, lead carboxylates and a polysaccharide material (probably starch), (b) layer 3 of sample **F4**, identified as a polysaccharide material (probably starch) and maybe wax, (c) layer 2 of sample **Q5**, identified as a polysaccharide material (probably starch) and strontium yellow, and (d) layers 2 and 3 of sample **W4**, identified as lead white and a sulfate/silicate compound or polysaccharide material.

By the 19th century the most important sources of red dyestuff for artists' pigments were madder root and cochineal insects [85,90,136]. Because cochineal lake pigments were found to often contain polysaccharide material (starch in some cases) [293,303-305] we can suspect that the lake pigment with a polysaccharide material content (Figure 6.23a-c) is cochineal lake, but further characterization is required, even because oftenly two lake pigments were mixed to obtain the desired colour [136].

The fact that no resin bands were identified suggests that resin, often added in a little amount to enhance the translucency of the lake pigments, does not seem to have been

added to these lake pigments. Instead, the presence of bands assignable to wax (Figure 6.23*b*): very strong C-H stretching bands at 2919 and 2850 cm^{-1}, arising from the large number of CH_2 groups and a band at 1463 cm^{-1}, arising from the CH_2 bending mode [87,177], suggest that wax was added to this red lake layer.

Resin

Bands assignable to the inclusion resin were identified in some of the spectra (Figure 6.24a). Because the overall resin spectrum is very characteristic, it is easily identifiable. Although, inclusion resin has a very intense infrared spectrum (Figure 6.24b), there were no significant cases where overlapping of the sample bands by those of the resin made the sample components identification impossible.

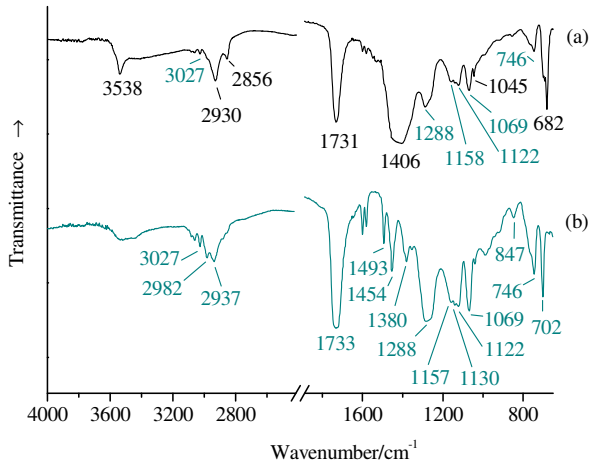

Figure 6.24 Infrared spectra of: (a) sample **R4**, identified as lead white and the embedding resin, and (b) the embedding resin.

Size

Size, diluted glue, used to prepare the support, was identified when analysing the samples **T3**, **U1**, **U7** and **U8** (Figure 6.25). Besides identification of bands assignable to the glue (Figure 6.25a) [295] in some cases, also the bands assignable to the cellulose [306] of the canvas fibbers, 1376, 1159, 1087,1061, 1037 and 898 cm^{-1}, were identified (Figure 6.25b and c).

Unknown compound 1

As presented in Figure 6.26, an unknown pattern with bands occurring at 1002 - 994m, 957w, 899 - 896m, 878m and 835 cm^{-1}, was identified in the spectra of the blue layers of samples **I3**, **R1**, and **R8**. Unfortunately, no assignment of these bands to a specific compound was possible, since no reference spectra exhibited these bands. Still, as cerulean

blue, a cobalt stannate pigment ($CoO.nSnO_2$) was identified by μ-XRD in sample **I3**, and by SEM/EDS in the samples **R1** and **R8**, it is possible that there is a connection between the existence of these bands and the presence of this pigment. Although not presented, the spectra of the blue layers of sample **R4** presented the same unknown pattern.

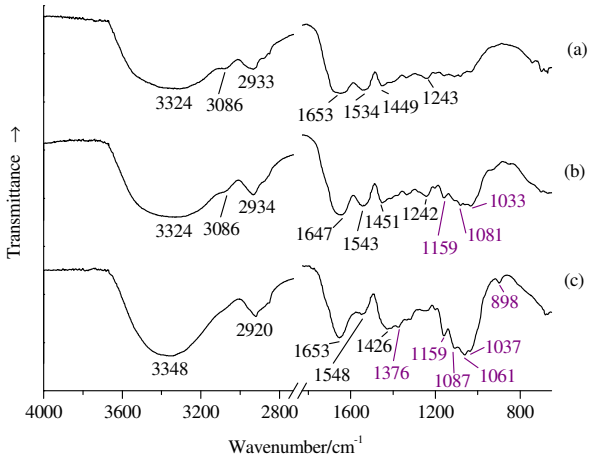

Figure 6.25 Infrared spectra of size layers: (a) layer 1 of sample **U7**, identified as animal glue, (b) layers 1 and 2 of sample **T3**, identified as animal glue and a polysaccharide material (probably cellulose, wavenumbers in purple), and (c) layer 1 of sample **U1**, identified as cellulose (wavenumbers in purple) and animal glue.

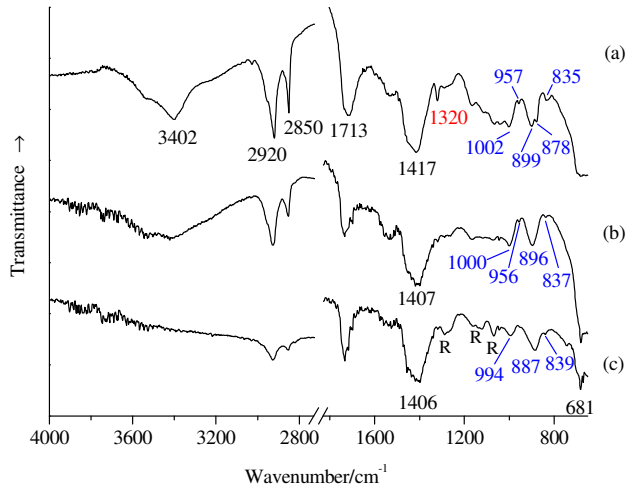

Figure 6.26 Infrared spectra of: (a) layer 2 of the sample **I3**, identified as a carbonate, lead carboxylates and unknown compound 1 in oil, (b) layers 2 -3 of sample **R1**, identified as lead white, lead carboxylates and unknown compound 1 in oil, (c) sample **R8**, identified as lead white, lead carboxylates, inclusion resin (R) and unknown compound 1 in oil.

6.2 Raman microscopy analysis

6.2.1 Experimental conditions

Samples

Having three different types of samples available, namely bulk samples (without any preparation), cross sections (used for OM) and thin sections (prepared for µ-IR), an initial test was made in order to determine which sample preparation method was the most suitable to conduct the Raman stratigraphic analysis. The results indicated that cross-sectioned samples were the most suitable. While bulk samples and thin sections, being very fragile, had to be handled with care and correctly positioned using a needle or a scalpel, cross sections, presenting a high mechanic resistance and a reasonable size, were easily handled. Moreover, while curling of thin sections made their analysis almost impossible, and the irregular shape of bulk samples made the analysis of their internal layers extremely difficult, cross sections, presenting all layers of the sample at the same focal plane and at a high contrast of colour (due to the polished surface), made the focusing of the laser over each pigment grain really easy.

Based on these results, the µ-R analysis of the 150 samples was conducted using the cross sections prepared for OM (see section 3.2.1. for sample preparation), the only exception being sample **O3**. In fact, the small size of sample **O3** did not allow the preparation of a cross section. The analysis of this sample was limited to the top and bottom surfaces (Figure D89).

Since when studding micro samples, homogeneity becomes an important consideration, because an impurity can be erroneously identified as sampling material, several similar coloured grains in each layer were analysed. In total, more than 2000 Raman spectra were acquired and analysed.

Experimental set-up

Raman spectra were recorded with a spectral resolution of 1 cm^{-1} using a Renishaw System 1000 Raman spectrometer coupled to a Leica MDLM optical microscope (x10 ocular), bands being reported to within an uncertainty of ± 1 cm^{-1}. The spectrometer is equipped with a holographic notch filter, a dispersive grating of 1800 grooves mm^{-1}, a 20 µm slit width and a thermoelectrically cooled charge-coupled device (CCD) detector operating at -70 °C. The excitation source was a He-Ne (632.8 nm) Renishaw laser, an argon-ion (514.5 nm) Spectra-Physics (Model 263C/Model 165) for analysis of reference sample of celadonite and glauconite, which was daily aligned through the several optical components; the intensity

of the signal adjust (using the 520.5 cm^{-1} line of a silicon wafer); and the diffraction grating of the spectrograph calibrated by reference to the emission lines of an absolute standard, a Neon lamp.

Laser beam was focused onto each pigment grain (with the help of cross-wires) using an x100 Olympus objective (NA 0.95), or an x50 Leica objective (NA 0.75) for some of the reference samples. Power at the sample's surface was controlled using neutral density filters with optical throughputs of 1, 10, 25, 50 and 100%, leading to a power at the sample surface between 0.02 and 2 mW (Table 6.3), measured with an Ando AQ 2150 Optical Multimeter. The number of scans accumulated and averaged to produce each presented spectrum is indicated in their caption.

Computer control and data acquisition were performed using the GRAMS/32 software package (Galactic Industries Corporation, USA) operating on a standard PC. Band assignment and graphic construction were performed using ORIGIN 6.0 software. No spectral processing other than removal of sharp spikes (attributed to cosmic rays - low level events, hitting the detector[59]), was performed.

Table 6.3 He-Ne laser (632.8 nm) power at the sample surface.

	Objective	
	x 50	x 100
100%	2.00 mW	0.63 mW
50%	1.00 mW	0.32 mW
25%	0.41 mW	0.13 mW
10%	0.25 mW	0.10 mW
1%	0.03 mW	0.02 mW

6.2.2 Results and discussion

In order to avoid degradation during analysis, the laser line 632.8 nm was employed. We verified that this laser line, besides being the most suitable for the analysis of yellow to red coloured pigments, since laser induced alteration of these pigments was minimized, it was also quite suitable for the analysis of blue to green and black coloured pigments. In fact, no improvement was verified when analysing blue to green and black coloured pigment particles using the 514 nm laser line, thus the entire analysis was undertaken using the 632.8 nm laser line.

[59] Sharp spikes can also be a result of "hot pixels". Sometimes the response of a certain pixel or row of pixel in a CCD detector can be significantly higher that its neighbours, such pixels are known as "hot pixels". However, while cosmic rays are manifested randomly, "hot pixels" appear continuously at the same wavenumbers.

Initially, we were using a 50x objective, the higher magnification objective available in the microscope, which proved to be very insufficient for the analysis of the samples. Although the spatial resolution is 1.0 and the approximate depth resolution is 1.6, using this objective only a very small number of pigments were identified and their spectra were dominated by fluorescence. By changing to a 100x objective (NA 0.95), for which the spatial resolution is 0.8 and the approximate depth resolution is 1.0, visualisation of individual pigment grains and focusing of the laser beam on each grain was possible, and its identification was easily conducted.

Table 6.4 summarizes the compounds identified in the samples and their distribution through the 23 paintings. As done for μ-IR, a detailed interpretation of the Raman spectra of the compounds found in the samples, organized by functional group, presented by alphabetic order and referred to the samples from which the spectra were obtained (Appendix D) is outlined. In particular, due to the high number of oxides and oxyhidroxides, these compounds were further grouped my metal. The main difficulties found in the interpretation of the Raman spectra are also emphatized.

Table 6.4 Compounds* identified by μ-R in Pousão's paintings

	Paintings																						
	Earlier			French			Italian															Final	
Compounds	A	B	C	D	E	F	G	H	I	J	K	L	M	N	O	P	Q	R	S	T	U	V	W
Arsenites																							
Emerald green						•		•			•	•							•			•	
Scheele's green								•			•												
Carbonates																							
Calcium carbonate - calcite form			•		•	•	•		•		•			•	•	•	•	?	•				
Lead carbonate	•	•	•	•	•	•	•	•	•		•		•	•	•	•			•	•	•		•
Lead white	•	•	•	•	•	•	•	•	•	•	•	•	•	•	•	•	•	•	•	•	•	•	•
Malachite								•															
Chromates																							
Chrome orange	•		•	•	•	•	•		•	•	•	•	•	•	•	•		•	?		•		
Chrome yellow	•		•	•	•	•		•	•		•	•		•	•	•	•	•	•	•			•
Strontium yellow	•	•	•	•							•						•						
Zinc yellow					•	•		•			•	•	•	•						•		•	
Cyanides																							
Chrome green								•											•		•		•
Prussian blue				•	•	•			•	•	•	•		•					•	•	•	•	•

(*continued overleaf*)

Table 6.4 (*continued*)

Compounds	Paintings																						
	Earlier			French			Italian															Final	
	A	B	C	D	E	F	G	H	I	J	K	L	M	N	O	P	Q	R	S	T	U	V	W
Oxides and Oxyhydroxides																							
Anatase	•										•		•	•									
Brookite											•												
Cobalt blue	•		•		?	?	•	•	•		•		?		?	?		?		?		?	
Cobalt oxide								•															
Iron^{III} oxide	•	•	•	•	•		•	•	•	•	•	•	•	•		•		•	•	•	•	•	•
Iron^{III} oxyhydroxide				•	•		•		•	•	•	•	•	•			•		•		•	•	•
Lead^{II,IV} oxide			•																	•			
Lead antimonate yellow					•	•			•	?	•	•					•		•	•			
Rosiaite					•	•			•		•								•				
Rutile											•	•			•								
Tetragonal lead^{IV} oxide [a]					•					•	•												
Viridian				•	•	•		•	•			•								•			•
Zinc white																							•
Silicates																							
Celadonite					•				•														
Kaolinite																				•			•
Quartz			•				•				•											•	
Ultramarine blue	•		•		•	•	•	•	•	•	•	•		•	•	•			•	•	•	•	•
Sulfates																							
Barium sulfate					•	•	•	•	•	•	•		•		•		•		•	•	•		
Basic lead sulfate					•	?			•		•						•						
Brochantite								•															
Lead sulfate			?		•	?			•	?	•	?				•	?		•	?			?
Sulfides																							
Cadmium red										•										•			•
Cadmium yellow			?				?	?			•		•								•	?	
Copper^{II} sulfide																			•	•			
Mercury^{II} sulfide	•		•	•	•	•	•	•	•	•	•	•	•	•	•	•	•	•	•	•	•	•	•
Realgar/parealgar				•			•	•															•
Other pigments [b]																							
Carbon-based black	•	•	•	•	•	•	•	•	•	•	•	•	•	•	•	•	•	•	•	•	•	•	•
Cochineal lake	•		•	•	•	•		•	•	•	•	•		•		•	•	•	•	•	•	•	•
Madder lake																•							•

A - *Casa rústica de Campanhã*, **B** - *O mendigo Lapita*, **C** - *Paisagem - Abertura da Rua Alexandre Herculano*, **D** - *Jardim de Luxemburgo (estudo)*, **E** - *Aldeia de St. Sauves*, **F** - *Paisagem de St. Sauves*, **G** - *Cansada (Cachopa de Capri)*, **H** - *Casas brancas de Capri*, **I** - *Cecília*, **J** - *Escadas de um pardieiro - Roma*, **K** - *Esperando o sucesso*, **I** - *Fachada de casa soterrada - Roma*, **M** - *Miragem de Nápoles*, **N** - *Portão*, **O** - *Rapariga de Anacapri*, **P** - *Rua de Roma*, **Q** - *Senhora vestida de preto*, **R** - *Janela das persianas azuis*, **S** - *Mulher da água*, **T** - *Paisagem de Anacapri*, **U** - *Rapariga deitada no tronco de uma árvore*, **V** - *Cais de Barcelona* and **W** - *Flores Campestres.*

* Pigments are in blue, while extenders, associated compounds or impurities are in green
? Propable identification
[a] By identification of the laser induced formed orthorhombic lead^{II} oxide
[b] Pigments that do not belong to a specific functional group

Arsenites

Emerald green, Schweinfurt green[60], copper acetoarsenite, $Cu(CH_3COO)_2.3Cu(AsO_2)_2$ was identified by its characteristic Raman bands at 2926(m) and 2853(w), due to C-H antisymmetric and symmetric stretching modes, respectively, 1556(w) and 1439(m), due to COO^- antisymmetric and symmetric stretching modes, respectively, 1354(w), due to methyl symmetric bending mode, 949(s), due to C-C symmetric stretching, 684(m), due to COO^- in-plane bending mode, 489(s), due to in-plane COO^- rocking mode and 833(m), 758(m), 537(s), 430(s), 368(s), 323(s), 292(s), 241(vs), 215(s), 173(s), 152(s), 119(w) and 106(vw) cm^{-1} (Figure 6.27) [230,307-310]. As shown in the three representative spectra of Figure 6.27A, although a common pattern is observed in the spectra, the relative intensity of some of the bands, especially those below 300 cm^{-1}, can be quite different.

When emerald green is present in a low amount and mixed with other pigments (Figure 6.27B), only four bands, namely 950, 240, 215 and 174 cm^{-1} (in green), were observed.

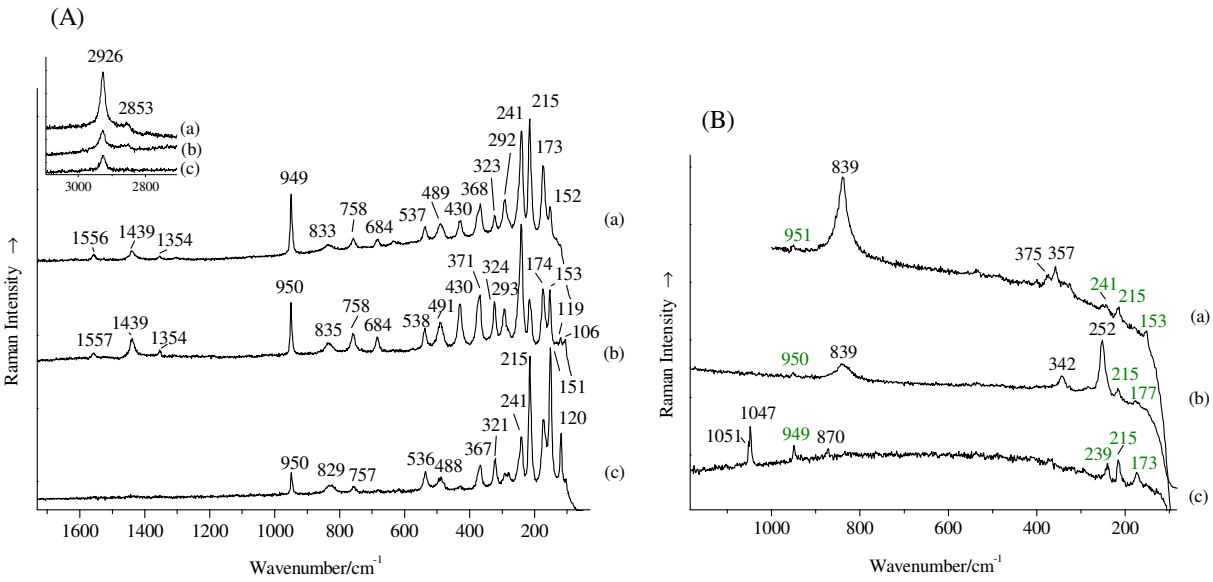

Figure 6.27 Raman spectra of: (A) green pigment grains from: (a) layer 4 of sample **H8** (40 scans, 0.63 mW) (b) layer 5 of sample **H2** (12 scans, 0.63 mW) and (c) layer 2 of sample **H7** (5 scans, 0.63 mW), all identified as emerald green; (B)(a) ground of layer 5 of sample **H2**, identified as a mixture of emerald green with chrome yellow (8 scans, 0.63 mW), (b) ground of layer 1 of sample **L3**, identified as a mixture of emerald green emerald green with chrome yellow and vermilion (4 scans, 0.63 mW), and (c) ground of layer 2 of sample **H7**, identified as a mixture of emerald green emerald green with lead white (5 scans, 0.63 mW).

[60] Emerald green is both copper acetate and copper arsenite, but will be present together with the other arsenite compounds, rather than in the acetate group.

Scheele's green was identified by its Raman bands at 950(w), 780(m), 659(w), 540(w), 497(m), 446(w), 424(vw), 370(vs), 275(m), 238(w), 215(vw), 204(vw), 192(vw), 183(vw), 152(vw-sh) and 135(s) cm^{-1} (Figure 6.28a) [252,308].

This green pigment is known to be a copper^{II} arsenite, but its composition is not known with certainty. Although $CuHAsO_3$ [90,311] and $Cu(AsO_2)_2$ [228,252,308] are the most referred compositions, other compounds, like $CuO.As_2O_3$, $2CuO.As_2O_3.2H_2O$, $3CuO.As_2O_3.2H_2O$, $Cu_3(AsO_3)_2.3H_2O$, $CuAsO_2$ and $CuAs_2O_4$, seem to make also part of this pigment composition [85].

Comparing the Raman spectrum of Scheele's green with the one of emerald green ($Cu(CH_3COO)_2.3Cu(AsO_2)_2$) (Figure 6.27A), it is observed that there are no bands in common between these two pigments, raising doubts about $Cu(AsO_2)_2$ being the composition of Scheele's green. Instead, when compared with the Raman spectrum of a reference sample of arsenolite, As_2O_3 (cubic phase) downloaded from RRUFF^{TM} Project library (Figure 6.28b), which exhibits bands at 780(m), 560(s), 470(m), 370(vs), 268(vs) and 183(m) cm^{-1} [312-313], several similarities are observed, suggesting that the composition of the Scheele's green under analysis is probably one (or more than one) of the three referred compositions that contain As_2O_3 ($CuO.As_2O_3$, $2CuO.As_2O_3.2H_2O$ and $3CuO.As_2O_3.2H_2O$).

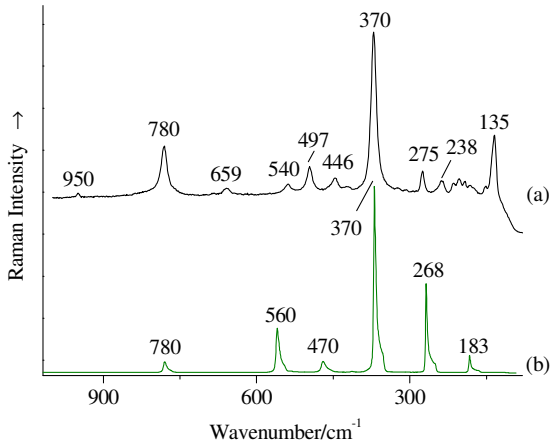

Figure 6.28 Raman spectrum of: (a) green-grey pigment grain of layer 3 from sample **H2**, identified the as Scheele's green (40 scans, 0.63 mW) and (b) arsenolite (ID R050383) downloaded from RRUFF^{TM} Project library [314] (532 nm excitation line).

Carbonates

Calcium carbonate-calcite form, $CaCO_3$, the thermodynamically most stable polymorph of calcium carbonate, was identified by the characteristic Raman bands occurring at 1086(s), 713(w), 282(m) and 156(vw) cm^{-1} (Figure 6.29). The first band arises from the symmetric

stretching mode of the carbonate ion, the second from the in-plane bending mode of the carbonate ion and the last two from lattice modes [126,237].

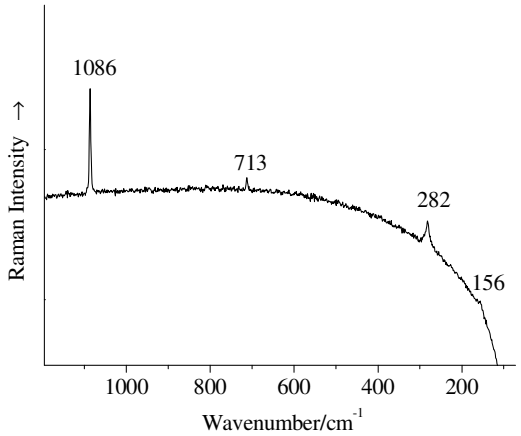

Figure 6.29 Raman spectrum of a brownish particle of layer 1 of sample **K13** (5 scans, 0.63 mW), identified as calcium carbonate - calcite form.

Lead carbonate, $PbCO_3$, and **lead white** or basic lead carbonate, $Pb_3(OH)_2(CO_3)_2$ two white lead carbonates, were identified by the strongest feature of their Raman spectrum, a single band at 1053(s) cm^{-1} and a doublet of bands at 1051(m) and 1048(s) cm^{-1}, respectively, arising from the symmetric stretching mode of the CO_3^{2-} ion (Figure 6.30). The factor-group splitting of the symmetric stretching mode in lead white arises from the existence of carbonate ions in, at least, two different sites [126,239].

Although, like found by μ-IR analysis, **lead white** and **lead carbonate** are common components of the samples and both are good Raman scatterers [239], producing intense Raman spectra, their identification in the samples by μ-R was somehow compromised. Normally, their spectra presented very high fluorescence and low quality, when compared with the spectra acquired from other compounds, probably due to the oil medium and/or to the presence of lead carboxylates[61] [315]. This difficulty has also been verified by *Aibéo CL, et al.* [56] during the analysis of ground layers of 19th and 20th century paintings.

Besides, visualization and consequent focusing of the laser line on the small white grains in coloured layers is not easy and differentiation between lead white and lead carbonate is equally not easy, as the band at 1053-1051 cm^{-1} exists for the two compounds. So, lead white and a mixture of lead white with lead carbonate can be easily confused.

[61] Its is known that in oil paintings, the particles of lead white are completely enveloped by the organic binding medium [315] and since lead carboxylates (which have an organic content) were identified by μ-IR as being present in the samples, probably both can be responsible for the fluorescence background.

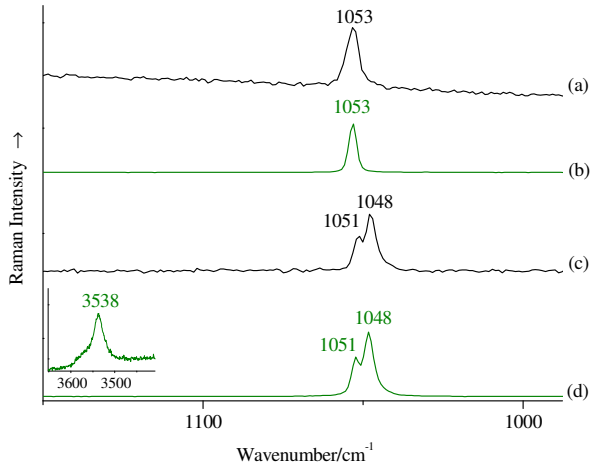

Figure 6.30 Raman spectra of: (a) white ground of layer 2 of sample **P1**, identified as lead carbonate (20 scans, 0.63 mW), (b) lead carbonate reference sample (10 scans, 2.00 mW), (c) a big white pigment grain of layer 2 of sample **H7**, identified as lead white (6 scans, 0.63 mW) and (d) lead white reference sample, the inset presents the hydroxyl band (12 scans, 2.00 mW).

Malachite, the naturally occurring form of basic copper^{II} carbonate, $Cu_2CO_3(OH)_2$, was identified by its Raman bands occurring at 1492(vs) and 1365(w) cm^{-1}, due to the carbonate antisymmetric stretching mode, 1096(m) and 1057(m) cm^{-1}, due to the carbonate symmetric stretching mode, 749(w) and 717(w) cm^{-1}, due to the carbonate in-plane bending mode and 596(w), 533(m), 508(m), 431(vs), 350(m), 267(vs), 217(m), 177(vs), 167(vs), 152(s), 142(m), 130(w) 119(w) cm^{-1}, due to the lattice modes (Figure 6.31Aa) [191,308].

In Figure 6.31, the spectra of two reference samples of malachite are also presented (in green). Both spectra show significant differences in the region of the lattice modes (different number of bands and different relative intensities). Nevertheless, as the rest of the spectra of both reference samples is identical, identification of this pigment is generally easy.

It is worth noting that the two bands occurring at 3386-3380 and 3321-3316 cm^{-1} (hydroxyl stretching region) in the two reference samples of malachite present a significantly different position regarding those acquired by *Frost RL., et al.* [191], which occurred at 3468 and 3386 cm^{-1} (633 nm). The reason for this difference is not known.

Basic copper^{II} carbonate exists both in a natural, malachite, and a synthetic form, **green verditer** or **green bice**, which cannot be distinguished by vibrational spectroscopy. However, because: i) the synthetic form, although relatively inexpensive, seems to have been rejected as an artists' pigment since the 18th century, apparently due to its pale colour [316], ii) the mineral form is very abundant and iii) brochantite (Figure 6.57), an associated mineral of malachite, was identified in the same samples were basic copper^{II} carbonate was identified, it can be concluded that the mineral form was probably the one used by Pousão.

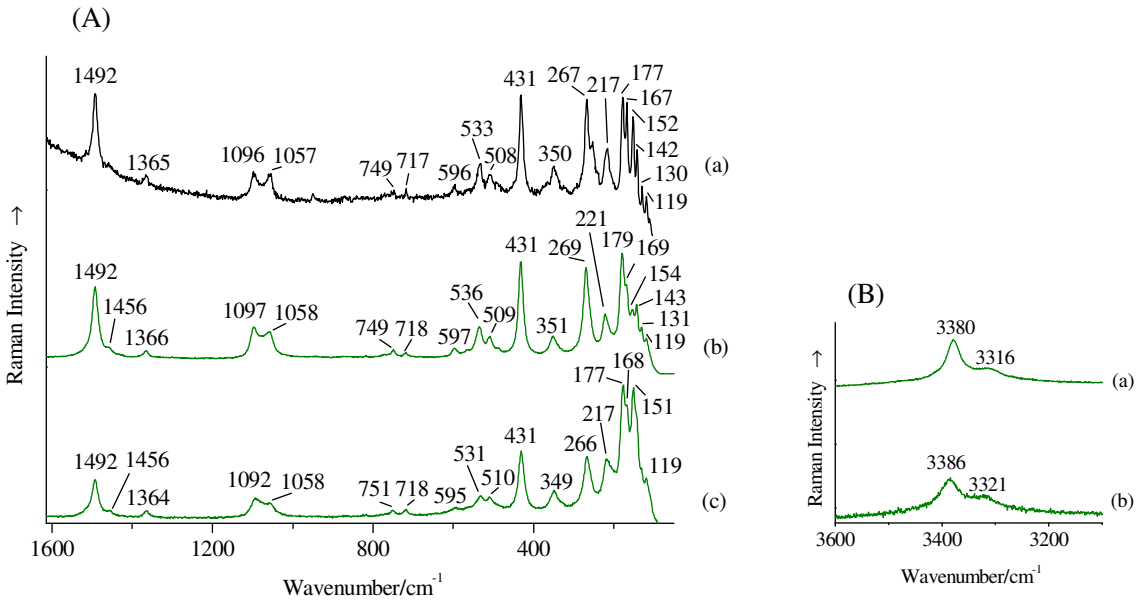

Figure 6.31 Raman spectra of: (A)(a) dark green pigment grain of layer 4 of sample **H8** (15 scans, 0.63 mW), identified as malachite, (b) malachite reference sample 1 (80 scans, 2.00 mW) and (c) malachite reference sample 2 (20 scans, 1.00 mW); (B) hydroxyl stretching region of: (a) spectrum (Ab) and (b) spectrum (Ac).

Chromates

Chrome orange, lead chromate^{VI} oxide also known as basic lead chromate, (Pb_2OCrO_4 or most commonly PbCrO4. PbO) is the most abundant orange pigment in the samples. This pigment was identified by its intense Raman bands occurring at 846(s), 836(s), 824(vs), 380(m), 354(vw), 341(m), 322(w) and 145(m) cm^{-1} (Figure 6.32a).

Initially, some difficulties and doubts regarding the identification of this pigment were raised because: i) two different formulae ($PbCrO_4$.PbO and $PbCrO_4.Pb(OH)_2$) have been given for it; ii) there were discrepancies among the published data and iii) none of the published reference spectra of chrome orange entirely match the spectra acquired in our analyse. A Raman spectrum with a very intense band at 828-824 cm^{-1} in the CrO_4^{2-} stretching region, a doublet in the CrO_4^{2-} bending region at 359/341 and a band at 151-149 cm^{-1} either due to lattice modes or to P-O modes, was attributed to the $PbCrO_4$.PbO composition [126,308], while a Raman spectrum with three bands at 849-845, 838 and 826-824 in the CrO_4^{2-} stretching region, four bands in the CrO_4^{2-} bending region at 382-379, 356-355, 343-341 and 324-323, with no report of a band in the 150 cm^{-1} region was attributed both to the $PbCrO_4$.PbO [240] and to the $PbCrO_4.Pb(OH)_2$ compositions [156].

Except for the band occurring at 150 cm^{-1}, not present in the published spectra probably due to the cut-off, our spectra are very similar to the spectra presented in the references

Roncaglia DI, et al. [240] and *Castro K, et al.* [156]. But still remains the doubt about the right chemical composition of the orange pigments present in the Pousão samples. Since some yellow-red pigments, such as lead antimonate yellow ($Pb_2Sb_2O_7$) and litharge (PbO) also exhibit a strong Raman band in the 150 cm^{-1} region, remains also the doubt that the orange pigment under analyse is a mixture of chrome orange with one of these pigments or chrome orange.

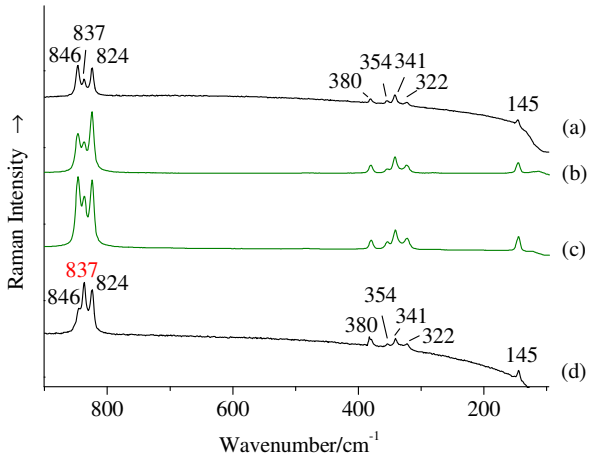

Figure 6.32 Raman spectra of: (a) orange pigment grains of the white ground layer 3 of sample **C5**, identified as chrome orange (2 scans, 0.10 mW), (b) chrome orange reference sample (Winsor and Newton) (10 scans, 0.13 mW), (c) phoenicochroite reference sample (10 scans, 0.41 mW) and (d) orange pigment grain of sample **K10**, identified as chrome orange maybe mixed with chrome yellow (5 scans, 0.13 mW).

In order to clarify this matter, a reference sample of chrome orange and another of the mineral phoenicochroite (Pb_2OCrO_4) [317-318], whose composition had been confirmed by μ-XRD, were analysed by μ-R, the spectra being presented in Figure 6.32b and c, respectively. As clearly demonstrated in Figure 6.32a-c, identical Raman spectra are produced by the orange pigment under analysis, the chrome orange reference sample and the phoenicrocoite reference sample, indicating that the orange pigment under analysis is chrome orange only, an isostructural with the mineral phoenicochroite. This result confirms the analysis of *Pollack and Feller* that in 1976 referred that there was no structurally bound hydroxyl group present in this pigment [85]. The relative intensities of the bands in the stretching region do often differ, probably as a result of different grain orientations. The reason(s) why reference spectra presented in the references *Bell IM, et al.* [308] and *Burgio L, et al.* [126], which are identical between them (probably deriving from the same bulck sample), is different from the spectra by us acquired is(are) not known.

There is no evidence that this orange pigment contains lead sulfate, considered to be commonly present in the purest grades of chrome orange [85].

Because the only stretching band[62] of chrome yellow at 837 cm^{-1} occurs at about the same wavenumber than one of the three stretching bands of chrome orange, a mixture of these two pigments is difficult to identify, and when the amount of chrome yellow is relatively low, most probably, only chrome orange will be identified. In the spectrum presented in Figure 6.32d, where chrome orange is immediately identified, the relative high intensity of the 837 cm^{-1} band, which in chrome orange is normally lower than the other two stretching bands (Figure 6.32a-c), leads to the suspicion that chrome yellow is also present.

Chrome yellow, $PbCrO_4$ was identified by its Raman bands at 838(vs), 357(s), 399(w), 375(m), 336(w), 324(vw) and 135(w) cm^{-1} (Figure 6.33a), **strontium yellow**, $SrCrO_4$ by its Raman bands at 929(vw), 926(vw), 915(m), 893(vs), 865(vs), 859(sh), 430(vw), 425(vw), 402(m), 374(m), 348(m) and 338(m) cm^{-1} (Figure 6.33b), and **zinc yellow**, a complex zinc (potassium) chromate with the approximate composition $K_2O.4ZnCrO_4.3H_2O$ [242] by its Raman bands at 941(s), 893(m), 872(vs), 773(m), 409(m), 376(w), 358(m), 343(m), 170(vw), 143(vw) and 113(vw) cm^{-1} (Figure 6.33c) [126,308].

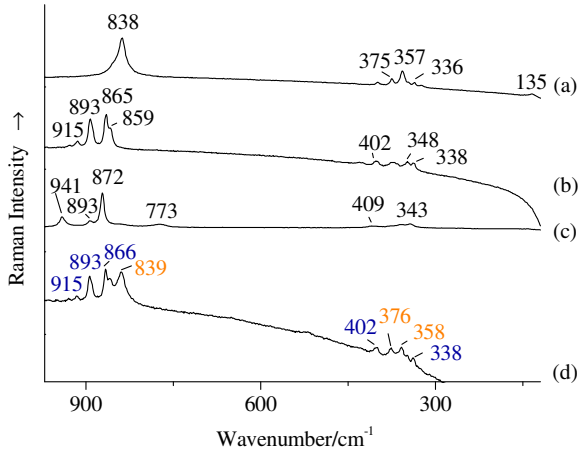

Figure 6.33 Raman spectra of: (a) yellow pigment grains of layer 3 of sample **E4**, identified as chrome yellow (3 scans, 0.63 mW), (b) brownish pigment grain of layer 2 of sample **D1**, identified as strontium yellow (15 scans, 0.63 mW), (c) green ground of layer 6 of sample **H2**, identified as zinc yellow (5 scans, 0.63 mW) and (d) a yellow-white pigment grain of layer 2 of sample **Q2**, identified as a mixture of chrome yellow (wavenumbers in orange) and strontium yellow (wavenumbers in blue) (4 scans, 0.32 mW).

[62] The antisymmetric stretching band is weaker than the symmetric band and is not resolved from the last one.

The bands at high wavenumbers are due to the CrO_4^{2-} ion antisymmetric and symmetric stretching modes, while the bands between 500 and 300 cm^{-1} are due to the bending modes of the same ion and the band at 135 cm^{-1} to lattice modes [175,319,320].

Unlike in the μ-IR analysis, mixtures of these pigments (either true mixtures or the proximity between pigment grains) were also easily identified, as shown in the spectrum presented in Figure 6.33d, which corresponds to a mixture of strontium yellow with chrome yellow.

Cyanides

Chrome green - One of the most known mixed pigments, which consists in a mixture of chrome yellow (Figure 6.33) with Prussian blue (see below), was identified in some of the samples, since the green colour that seemed to be due to a single pigment yield both chrome yellow and Prussian blue characteristic bands (Figure 6.34a).

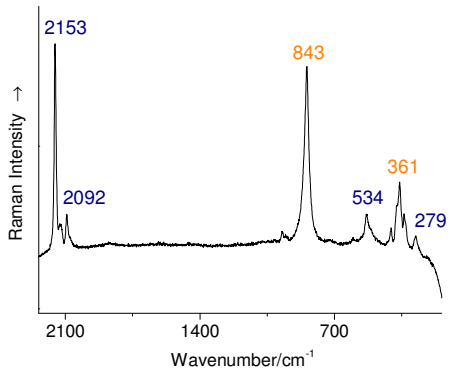

Figure 6.34 Raman spectra of the green ground of layer 2 of sample **S2**, identified as chrome green (25 scans, 0.32 mW). Prussian blue bands are in blue, while chrome yellow bands are in orange.

Prussian blue, iron^{III} hexacyanoferrate^{II}, $Fe_4[Fe(CN)_6]_3.14\text{-}16H_2O$ was identified by its Raman bands at 2153(vs), 2092(m), 949(vw), 532(m) and 280(m) cm^{-1} (Figure 6.35a) [126,321]. The two bands at higher wavenumbers are due to the C≡N stretching modes in the hexacyanoferrate ion ($Fe(CN)_6^{4-}$), and the bands at 532 and 280 cm^{-1} are probably due to the Fe–C stretching and Fe–CN deformation modes, respectively [195].

Whenever the noise and the background are high or the pigment concentration is low, only the two C≡N stretching bands at 2153 and 2092 cm^{-1} are observed (Figure 6.35b and c). Nevertheless, as no other compound seems to present bands at these wavenumbers, these two bands allow the identification of this pigment in a mixture, like for example, in the background of layer 2 of sample **I5**, whose spectrum is presented in Figure 6.35*c*, where a mixture of Prussian blue and ultramarine blue (Figure 6.54*)* was identified.

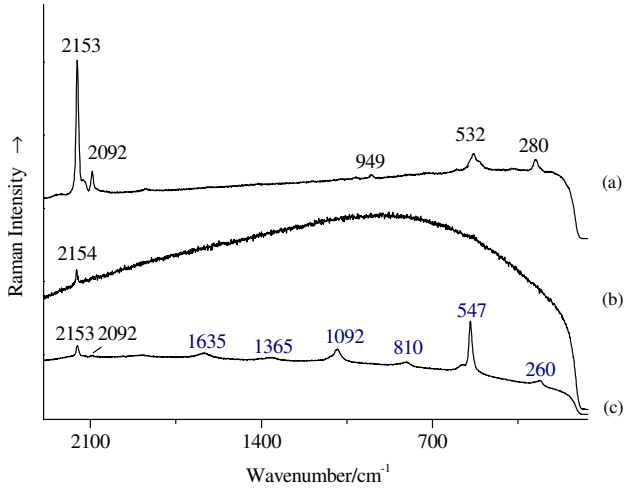

Figure 6.35 Raman spectra of: (a) a dark blue particle of layer 2 of sample **S7**, identified as Prussian blue (16 scans, 0.32 mW), (b) a blue particle of layer 1 of sample **I5**, identified as Prussian blue (1 scan, 0.32 mW) and (c) the blue background of layer 2 of sample **I5**, identified as a mixture of Prussian blue and ultramarine blue (band wavenumbers in blue) (2 scans, 0.63 mW).

Oxides and Oxyhydroxides

Chromium oxide

Viridian, a green pigment firstly synthesized during the 19th century [85], also known as Guignet's green, was identified by its Raman spectrum with bands occurring at 781(vw), 487(m) and 265(m) cm^{-1} (Figure 6.36) [248,308]. Whenever the intensity of the referred bands is weak, either due to high fluorescence background or due to a low amount of this pigment, its identification becomes more difficult, as can be seen in the Figure 6.36a.

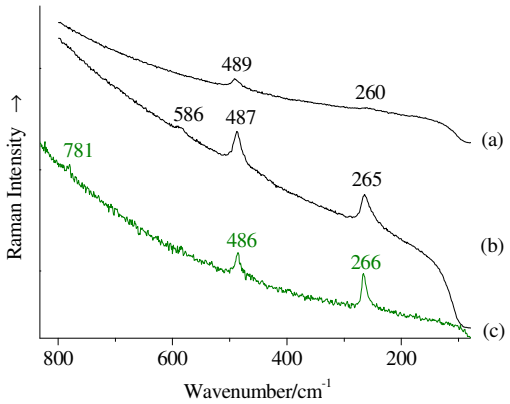

Figure 6.36 Raman spectra of: (a) green-bluish pigment grain of the green layer 4 of sample **H8**, identified as viridian (20 scans, 0.63 mW), (b) green pigment grain of the green layer 2 from sample **I7**, identified as viridian (50 scans, 0.63 mW) and (c) reference sample of viridian (Winsor & Newton) (10 scans, 0.10 mW).

As referred before (μ-IR analysis), although the composition of this pigment is normally described as hydrated chromium^{III} oxide, $Cr_2O_3.2H_2O$, we think it is more porbably an hydroxide or oxyhydroxide.

Cobalt oxides

Cobalt blue, cobalt aluminate, $CoAl_2O_4$ or commonly $CoO.Al_2O_3$ [322], was identified by its two Raman bands at 517(w) and 200(w) cm^{-1} (Figure 6.37*Aa*) [308,321]. However, as the Raman spectrum of this pigment was at best very weak and in some cases impossible to acquire, its identification was often difficult and ambiguous (Figure 6.37Ab), and its presence had to be confirmed by SEM/EDS (Figure 7.9a).

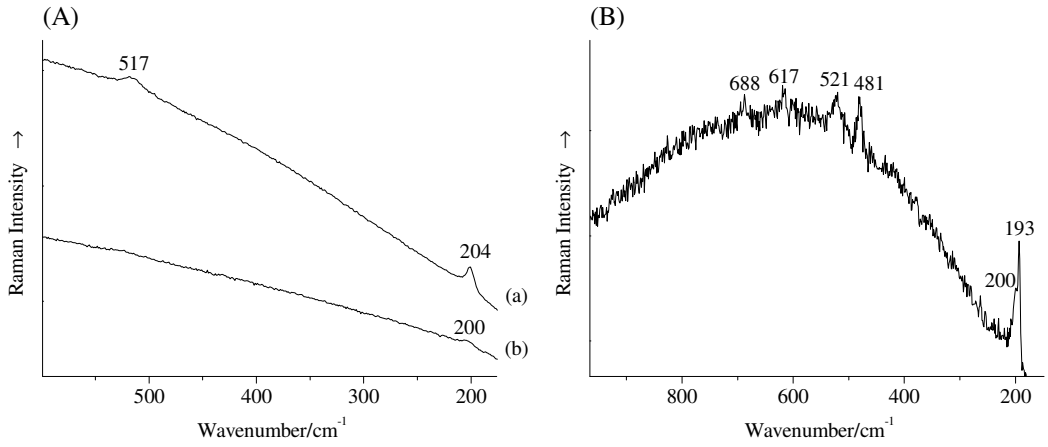

Figure 6.37 Raman spectra of: (A)(a) blue pigment grains of layer 3 of sample **H5**, identified as cobalt blue (13 scans, 0.63 mW) and (b) blue ground of layer 2 of sample **A3**, probably cobalt blue (7 scans, 0.63 mW); (B) black particle of layer 2 of sample **H7**, identified as cobalt oxide (10 scans, 0.13 mW).

Cobalt oxide, Co_3O_4, a cobalt oxide with cubic spinel structure was identified, in sample **H7**, by its characteristic Raman spectrum (Figure 6.37*B*) that exhibits five bands at 688(w), 617(w), 521(m), 481(m), 200(sh) and 193(s) cm^{-1} [323,324]. This grey/black compound that seems to have never been used as an artistic pigment, except for one report [324], is probably present as an impurity.

Iron oxides and oxyhydroxides

Iron^{III} oxyhydroxide, α-FeOOH, also known by the name of the mineral with the same composition, goethite, or by the name of its synthetic form, Mars yellow, was identified by its Raman spectrum (Figure 6.38) revealing bands at 549(w), 478(w), 389(m), 298(m), 244(w) and 203(vw) cm^{-1} [126,308,325].

Although the background of the spectra for the iron oxyhydroxide grains present in the samples was normally very intense, identification against the spectrum of a reference sample (Figure 6.38b) was still possible.

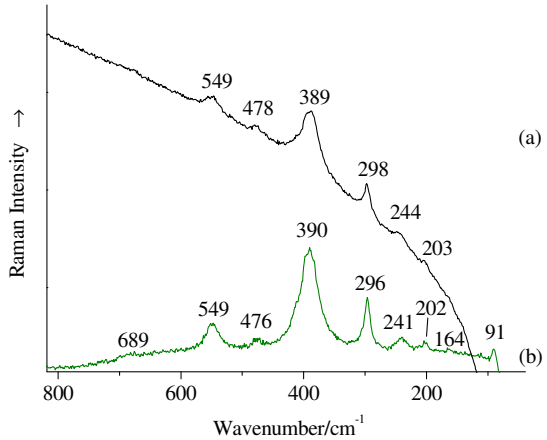

Figure 6.38 Raman spectra of: (a) yellow-brownish pigment grains of layer 3 of sample **E5**, identified as iron^{III} oxyhydroxide (23 scans, 0.63 mW) and (b) goethite reference sample (10 scans, 0.13 mW).

Iron^{III} oxide, α-Fe_2O_3, commonly known as, the equivalent mineral hematite, or the synthetic equivalent Mars red, was identified by its Raman bands occurring at 1320(s), 612(s), 496(m), 411(s), 296(sh), 291(vs), 244(m) and 225(vs) cm^{-1} (Figure 6.39a and b) [126,325,326].

As shown in Figure 6.39b, some pigment grains presented, associated with the iron^{III} oxide spectrum, a relative intense band at ca. 660 cm^{-1} (sometimes more intense than the adjacent 610 cm^{-1} iron^{III} oxide band). Unfortunately there has been no consensus in the assignment of these band, which has been assigned to iron^{III} oxide/hematite [327-329] magnetite (Fe_3O_4) [158,325,330-332], or even, wrongly, to kaolinite [333].

Because magnetite can be transformed into hematite naturally or under the laser line [325,334], the band at 660 cm^{-1} has often been assigned to trace residual magnetite in hematite [158,325,330-332]. However, the assignment of this band to the Raman forbidden longitudinal-optical phonon (LO) of iron^{III} oxide, which is observed in samples with some amount of disorder [327-329], such iron oxide produced by dehydration of goethite below 900ºC or whetered hematite [85,329], seems more correct. Raman scattering of hematite is much larger that Raman scattering of magnetite, so, a very small amount of hematite produces intense hematite bands in the Raman spectrum of magnetite, while, the existence of bands of residual magnetite in the hematite spectrum seems improbable [328,329,334,335]. Furthermore, the Raman spectrum of magnetite is characterized by an intense band at 670 cm^{-1} rather than at 660 cm^{-1} [326,336].

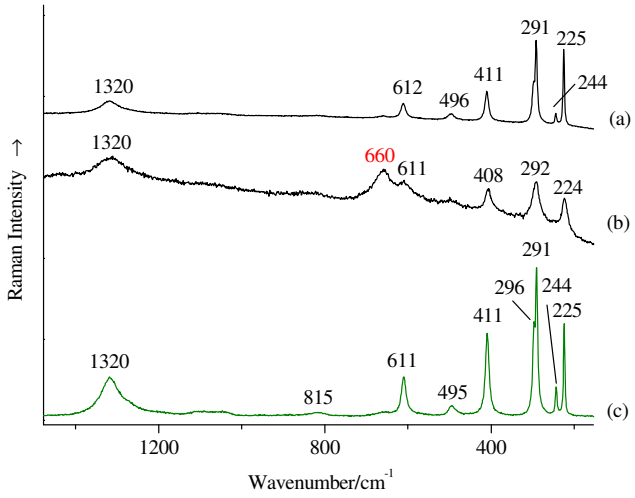

Figure 6.39 Raman spectra of: (a) red pigments grains of the reddish layer 4 of sample **K7**, identified as hematite (10 scans, 0.13 mW), (b) big brown particle of the brown layer 7 of sample **K9**, identified as hematite (17 scans, 0.32 mW) and (c) hematite reference sample (3 scans, 0.63 mW).

Another possibility, for the presence of the 660 cm^{-1} band, not referred before, is the existence of manganese oxides/oxyhydroxides, since these compounds, especially the black MnO_2 minerals, were added (at 6-15 wt%) to iron oxide/oxyhydroxide in order to produce Umber pigments [333,337,338].

Due to their opacity and thermal absorption, manganese oxides/oxyhydroxides are greatly unstable under the laser line, leading to the formation of new phases or amorphous material [339,340] and although they are generally known by their low Raman activity [339] a very good Raman spectrum was aquired for a synthetic sample of MnO_2 with the 632.8 nm laser line, Figure 6.40 [339,340].

Reference sample of Umber and Sienna pigments should be studied in order to check this hypothesis, and also to determine if the pigments containing manganese oxides can be distinguished from those pigments not containing manganese oxides by Raman spectroscopy.

Although the band at ~1320 cm^{-1} has been most of the times ascribed to two-magnon scattering (magnetic scattering) [325,326], it seems that this band is not due to magnetic scattering, but rather to an overtone of a Raman-forbidden LO near 660 cm^{-1}, while the two-magnon scattering appears to occur as a weak and broad band at ca. 1525 cm^{-1} [327,341].

We call the attention to the fact that significant differences can be found between Raman spectra of iron oxide, such as different relative intensity, broadening and shift of the bands, as a result of crystal orientation, Fe/Al substitution and doping [326]. We also want to refer that,

although goethite and hematite were often identified in the same layer, there was no signal that hematite was produced by laser-induced transformation of goethite; no intermediate structures between hematite and goethite have been identified [340].

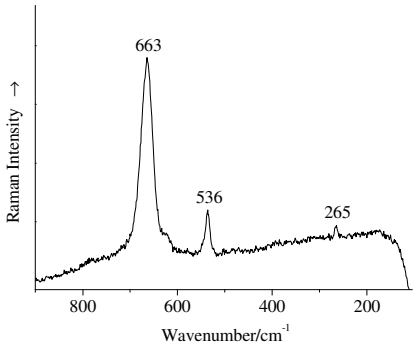

Figure 6.40 Raman spectrum of the reference sample of manganese oxide (30 scans, 2.00 mW).

Lead oxides

Lead antimonate yellow, also wrongly referred to as Naples yellow, since this name has been used to describe a shade of colour rather that the lead antimonate yellow itself [342], was identified in a large number of samples, although in some cases with difficulty. This synthetic yellow pigment (one of the oldest), is prepared calcinating mixtures of lead and antimony oxides or salts, at high temperatures [342,343] [63].

Ideally, its chemical composition is $Pb_2Sb_2O_7$, isostructural with the anhydrous analogue of the mineral bindheimite. However, depending on the nature of the reagents, the ratios of the reagents, the time and temperature of the calcination and the presence of flux agents, more than one phase $Pb^{II}_{y}Sb^{V}_{2-x}O_7$ (where $2 \leq y \leq 3$ and $0 \leq x \leq 1$) and/or by-products, such as $PbSb_2O_6$, $Pb_{3+x}Sb_2O_{8+x}$ and lead sulfates, can be formed [342-349]. As a consequence, its identification by Raman spectroscopy and by other techniques has involved several doubts.

Owing to the existence of different phases of lead antimonate yellow, the strongest band of its Raman spectrum, which is due to the lattice Pb-O stretching mode, can occur in the range 147-124 cm^{-1}, rather that at 146 cm^{-1} as expected (Table 6.5 and Figure 6.41a-d) and with different intensities[64], making difficult its distinction from other lead-oxide-based yellow pigments (litharge, massicot, lead-tin yellow type I, lead-tin yellow type II, lead-tin-antimony) whose spectra exhibit a similar band (between 150 and 120 cm^{-1}). Other characteristic

[63] There is a large number of recipes to produce lead antimonate yellow, most of which are uncertain to the nature of the reagents (their historical names are unclear) and vague with respect to the temperature and time of the reaction. In fact, some will not yield lead antimonate at all [342,343].

[64] We found that the exposition of a standard sample to the 632.8 nm laser line did not produce any shift or changed the relative intensity of this band, hence, cannot be the cause for this change.

Raman bands of lead antimonate yellow occur at 511(m), 343(w), 320(w) and 293(w) cm^{-1} (Figure 6.41a-d and Table 6.5) [350-354].

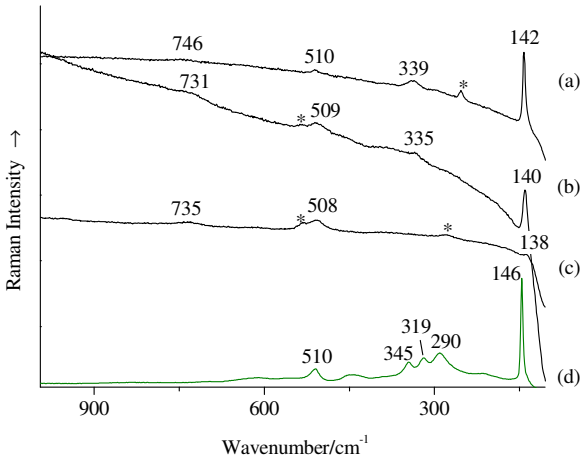

Figure 6.41 Raman spectra of: (a) yellow pigment grain of the sample **Q6** (5 scans, 0.63 mW), (b) yellow-green pigment grain of layer 2 of sample **S7** (15 scans, 0.63 mW), (c) yellow pigment grain of layer 2 of sample **S7** (10 scans, 0.63 mW), identified as lead antimonate yellow, and (d) reference sample of lead antimonate yellow (4 scans, 0.41 mW) (identity confirmed by μ-XRD and SEM/EDS). * marks the 253 cm^{-1} vermilion band in spectrum (a), and the 532 and 280 cm^{-1} bands of Prussian blue in the spectra (b) and (c).

Table 6.5 Raman band positions of lead antimonate yellow

Sendova M, *et al.* (354)	Bouchard M, *et al.* (353)	This work		Rosi F, *et al.* (348) [a]	Guineau B. (344)	Clark RJH, *et al.* (345)	Sakellariou K, *et al.* (351)	de Lucas MCM, *et al.* (352)	Coulomban P, *et al.* (350)
		reference	paintings						
785 nm	632.8 nm	632.8 nm		532.0 nm	514.5 nm	514.5 nm	514.5 nm	514.5 nm	457.9, 514.5 nm
	960								
	702(w)			807					
				655	639(w)			645-642(vw)	
	599(m)								
507(m)	508(s)	510(m)	517-508(m)	513(m-s)	513(m)	513(wm)	510(s)	513(s)	510(m)
				490					
	449(m)	445(w)		460(vw)	455(m)	464(m)	450(w)	461-458(w)	450(m)
								392(vw)	
338(m)	336(s)	345(m)	344-335(w)		332(s)	343(s)	333(w)	337	330(m)
	318(s)	319(s)		320					
	285(s)	290(s)	309-290(w)				290(w)[c]	306	
				235(m-s) [b]	242(w)				
	200(m)			200(w-m) [b]				205-203(vw)	
138(s)	145(vs)	146(vs)	143-127(w-vs)	107-120s	141(vs)	147(vs)	135-124(vs)	135(vs)	145-130(vs)
						76(s)			

References are presented between parentheses
[a] not all the bands are always present (varying with the reagent stoichiometry)
[b] wavenumbers deduced from the publised spectrum

Because lead-tin yellow type I has a characteristic band of medium-to-strong intensity at about 196 cm^{-1}, not present in the spectrum of lead antimonate yellow and litharge, massicot and lead-tin yellow type II do not have a band at ca. 510 cm^{-1}, present in the spectrum of lead antimonate yellow, it is possible to distinguish between lead antimonate yellow and these four lead-oxide-based pigments. However, as the Raman spectra of lead-tin-antimony oxide ($Pb_2Sn_xSb_{2-x}O_{7-x/2}$) [347,355,356] is essentially the same as that of lead antimonate yellow, the use of a complementary technique becomes mandatory, thus, SEM/EDS and μ-XRD analysis were carried out on six and four of the cross-sections, respectively, for which the yellow pigment was previously identified by μ-R. No tin was identified by the SEM/EDS analysis (in any of the six samples), only antimony and lead (Figure 7.14b), suggesting the presence of lead antimonate yellow, which was confirmed by μ-XRD analysis.

As shown in the spectra presented in the Figure 6.42, lead sulfate (Figure 6.42A) and, more rarely, basic lead sulfate (Figure 6.42B), were found associated with lead antimonate yellow (a result confirmed by μ-XRD analysis). As the Raman spectrum of lead antimonate yellow and basic lead sulfate (see below) have the 147 cm^{-1} band in common, distinction between a mixture of lead antimonate yellow with lead sulfate and a mixture of lead antimonate yellow with basic lead was often very difficult (Figure 6.59). It is known that lead antimonate yellow was often sold containing considerable amounts of basic lead sulfate (and also of silica, rutile, barium sulfate and carbonates), but there is no report for the existence of lead sulfate [342].

An hypothesis to the existence of the lead sulfates associated with lead antimonate yellow (that needs to be confirmed) is the use of Sb_2S_3 as the antimony containing reagent instead of an antimony oxide, since it was verified that when Sb_2S_3 was used as a starting material in the synthesis of lead tin-antimony yellow, lead sulfate and/or basic lead sulfate (and rosiaite) were produced [347].

As presented in Figure 6.43a, $PbSb_2O_6$, also known as rosiaite, the analogous pale yellow/colourless mineral [357], was identified in some of the samples where lead antimonate was present, always associated with lead sulfate. This compound is characterized by a Raman spectrum presenting a very strong band at 656 cm^{-1}, with other less intense bands at 729, 526, 506, 451, 314, 296, 255, 211, 191 cm^{-1} (Figure 6.43b).

The presence of $PbSb_2O_6$ on sample **S5** was confirmed by μ-XRD analysis, together with lead sulfate, lead carbonate, lead white and Sb_2O_4. This last compound, Sb_2O_4 ($Sb^{III}Sb^{V}O_4$)

also known as cervantite, the analogous mineral, is also a by-product of lead antimonate synthesis [343]; however, it has not been identified by μ-R[65].

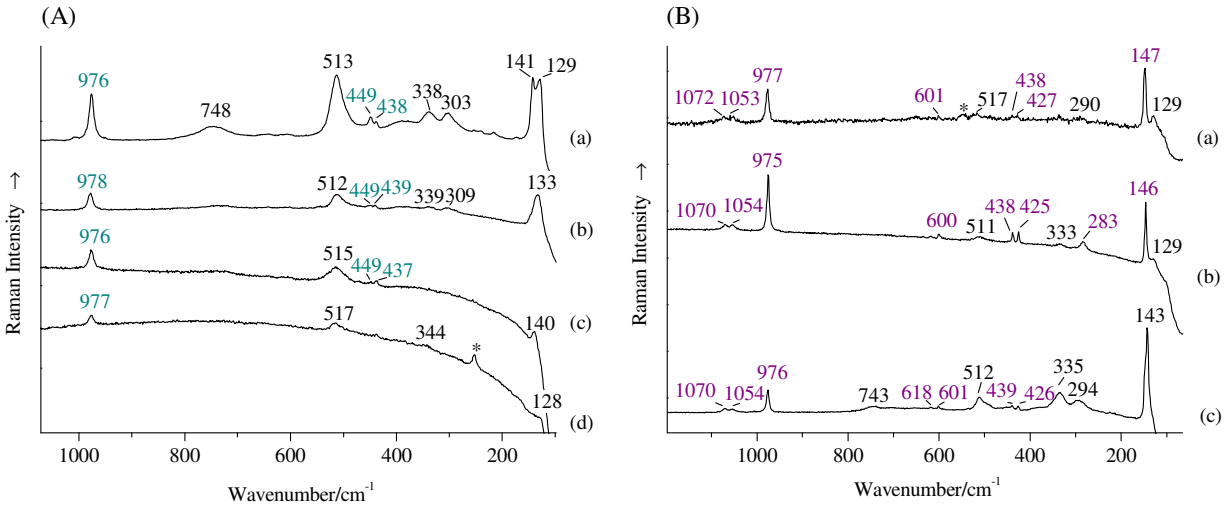

Figure 6.42 (A) Raman spectra identified as a mixture of lead antimonate yellow with lead sulfate (wavenumbers in blue): (a) yellow pigment grain of layer 5 of sample **K4** (12 scans, 0.63 mW), (b) yellow-greenish pigment grain of layer 6 of sample **K7** (10 scans, 0.63 mW), (c) yellow pigment grain of layer 2 of sample **S5** (16 scans, 0.63 mW), and (d) yellow pigment grain of layer 3 of sample **T1** (6 scans, 0.63 mW); * marks the 253 cm^{-1} vermilion band; (B) Raman spectra identified as a mixture of lead antimonate yellow with basic lead sulfate (wavenumbers in purple): (a) yellow-greenish pigment grain of layer 6 of sample **K7** (4 scans, 0.10 mW), (b) yellow-greenish pigment grain of layer 6 of sample **K7** (10 scans, 0.63 mW) and (c) yellow pigment grain of layer 5 of sample **K4** (10 scans, 0.13 mW); * marks ultramarine blue.

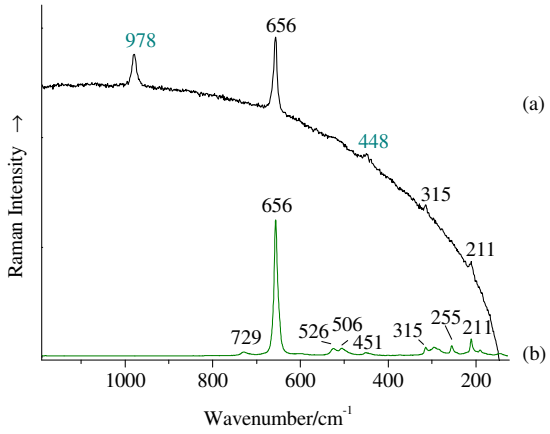

Figure 6.43 Raman spectrum of: (a) yellow-greenish pigment grain of layer 4 from the sample **I1**, identified as a mixture of $PbSb_2O_6$ and lead sulfate (10 scans, 0.63 mW) and (b) rosiaite (ID R070384) downloaded from RRUFF™ Project library [314] (532 nm excitation line).

[65] Sb_2O_4 Raman bands occur at 453(m), 398(m), 263(m) and 193(vs) cm^{-1} [358].

It is worth noting that, when $PbSb_2O_6$ is present in the samples (band at 655 cm^{-1}), the identification of lead antimonate yellow is more difficult, as can be seen in Figure 6.44Ab and Bb. The background in these spectra is more sloping, and consequently, the P-O band 127 cm^{-1} is weaker or, even not observed.

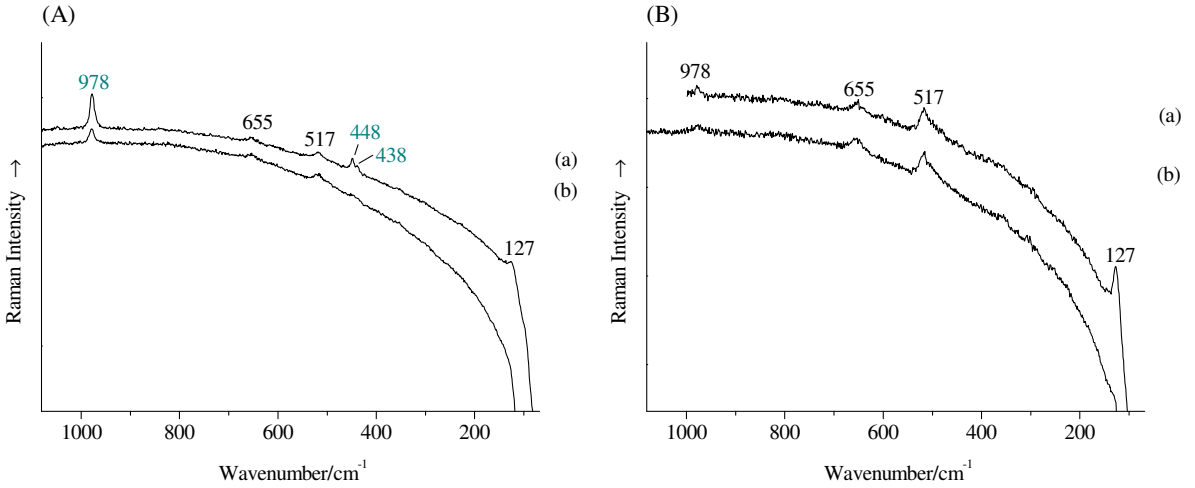

Figure 6.44 Raman spectra of: (A)(a) white pigment grain of layer 3 of sample **E4** (10 scans, 0.63 mW) and (b) yellow pigment grain of layer 4 of sample **E4** (10 scans, 0.63 mW); (B)(a) yellow pigment grain of layer 3 of sample **K14** (5 scans, 0.63 mW) and (b) yellow pigment grain of layer 2 of sample **K14** (4 scans, 0.63 mW).

Lead^{II,IV} oxide, Pb_3O_4 ($Pb^{II}_2Pb^{IV}O_4$), known as minium, its mineral equivalent, and as red lead (synthetic form), was identified by its Raman spectrum with bands at 549(vs), 481(w), 391(m), 314(w), 225(m), 151(m) and 121(vs) cm^{-1} (Figure 6.45) [308,359].

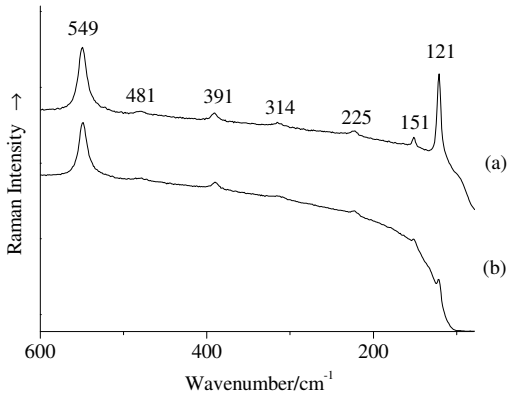

Figure 6.45 Raman spectra of: (a) yellow-orange pigment of layer 3 of sample **T4** (8 scans, 0.13 mW) and (b) orange-red pigment grain of layer 2 of sample **C5** (2 scans, 0.13 mW), both identified as lead^{II,IV} oxide.

Although the spectrum is normally characterized by two very intense bands at 549 and 121 cm^{-1}, assigned to a stretching of the Pb^{IV}-O bond and to the coupling of the angular deformations of the O-Pb^{IV}-O and O-Pb^{II}-O bonds, respectively, with the other five bands having a lower intensity [359] (Figure 6.45a), it was also found that the band at 121 cm^{-1}, can present a very low intensity (Figure 6.45b) [360,361], probably due to some amount of the high sloping and curved background. This feature associated with a high noise and a low amount of the pigment, can make very difficult the distinction between $lead^{II, IV}$ oxide and ultramarine blue, which also has an intense band at 550 cm^{-1} (Figure 6.54).

Tetragonal $lead^{IV}$ oxide, PbO_2, also known as plattnerite, the analogous mineral, was identified based in the presupposition that it was laser degradated during analysis, producing orthorhombic $lead^{II}$ oxide.

Orthorhombic $lead^{II}$ oxide, also known as massicot, the analogous mineral, was identified in the samples when analysing black grains, rather than when analysing yellow grain as it would be expected. Figure 6.46A presents two of the spectra acquired during the analysis of the small black pigment grains[66] of layer 2 of sample **K4** (Figure 6.47). The upper spectrum (Figure 6.46Aa) is characteristic of orthorhombic $lead^{II}$ oxide, with bands observed at 383(w), 287(m) and 142(s) cm^{-1}, but the bottom spectrum (Figure 6.46Ab) presents broader red-shift bands, occurring at 279(w) and 138(s) cm^{-1} characteristic of the spectrum acquired when orthorhombic $lead^{II}$ oxide is formed during laser-induced degradation of other lead oxides, namely PbO_2 (black), Pb_3O_4 (red) and tetragonal PbO (red) [126,362].

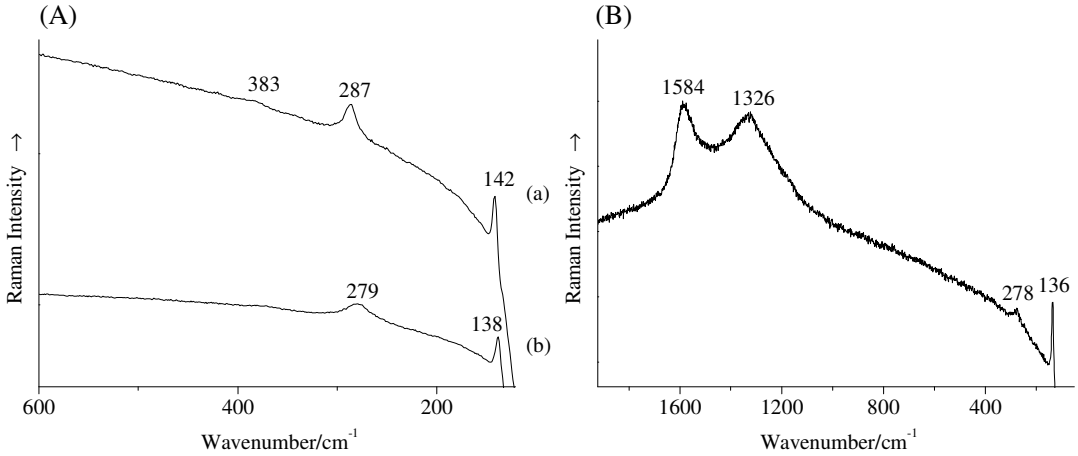

Figure 6.46 Raman spectra of: (A) black pigment grains of layer 2 of sample **K4**: (a) (16 scans, 0.13 mW) and (b) (4 scans, 0.63 mW), identified as orthorhombic $lead^{II}$ oxide; and (B) black pigment grain of layer 3 of sample **E7** (2 scans, 0.63 mW) identified as carbon-based blak and orthorhombic $lead^{II}$ oxide.

[66] Carbon-based black pigments where also present in this layer, but having a significantly larger size.

As can be seen in the images of the black pigment grains (Figure 6.47) before and after the acquisition of the spectrum exhibited in Figure 6.46Ab, alteration of the black pigment is clear, which lead us to suppose that orthorhombic lead^{II} oxide is probably present as a result of the transformation of back PbO_2 (tetragonal lead^{IV} oxide) under the laser line, even though, the maximum power used (0.63 mW), was not expected to be enough to induce this transformation [362].

Tetragonal lead^{IV} oxide also is a brown-black compound that absorbs most of the incident and scattered radiation, being very unstable under the laser line [362,363].

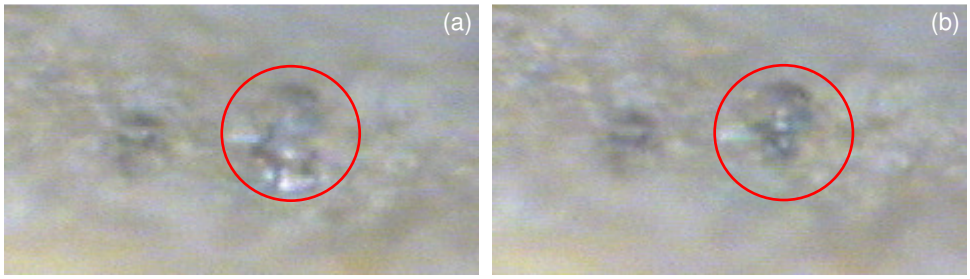

Figure 6.47 The black pigments of the brown layer 2 from sample **K4** visualised under the microscope of the Raman equipment (x1000): (a) before and (b) after acquisition of the spectrum of Figure 6.46Ab.

The spectrum in Figure 6.46B was acquired during the analysis of a black pigment grain of the blue layer 2 of sample **E7**. Besides exhibiting the two bands characteristic of a carbon-based black material, 1584(vs) and 1326(vs) cm^{-1} (Figure 6.64), the spectrum also presents the orthorhombic lead^{II} oxide shifted bands, 278(w) and 136(s) cm^{-1}. In this case, these bands can be both due to transformation of black PbO_2 under the laser line or to the presence of orthorhombic lead^{II} oxide that, when exposed to high laser light power, does present a shift of its characteristic Raman bands [362]. A similar spectrum was also identified in the sample **J2**.

Titanium oxides

Titanium^{IV} dioxide - Anatase, brookite and rutile, the three most commonly encountered crystalline polymorphs of titanium^{IV} dioxide, TiO_2, were identified in the samples.

Rutile yields the less intense Raman spectrum of the three (one order of magnitude weaker than the other two polymorphs) with bands at 608(m), 447(m), 236(m) and 141(w) cm^{-1} (Figure 6.48a), **anatase** exhibits characteristic Raman bands at 638(m), 513(m), 395(m) 195(vw) and 141(vs) cm^{-1} (Figure 6.48b), while **brookite** is characterized by a relatively complex spectrum, in accordance with its lower crystal symmetry, displaying Raman bands

at 637(m), 583(w), 544(w), 500(w), 462(w), 412(w), 366(m), 319(s), 285(w), 246(m), 213(m), 193(w), 152(vs), 148(sh) and 124(sh) cm^{-1} (Figure 6.48c) [126,364-366].

Although these compounds occur naturally, there is no firm evidence that they have ever been used as an artists' pigment before the 20th century [336] when their industrial manufacture processes were developed [367]. Because brookite is very difficult to produce, it has had no value in the TiO_2 pigment industry [70].

Except for layer 2 of sample **L3**, which has a high rutile content, the TiO_2 polymorphs occurred in the samples simply as trace components, probably due to the presence of an earth pigment (ex., $iron^{III}$ oxide, $iron^{III}$ oxyhydroxide), since these compounds are common accessory minerals in many sedimentary and metamorphic rock types [158,326,336,340,368,369]. These compounds are known by their extremely intense Raman response, even when present in trace amounts, as a result of the high polarizability of the Ti atom [336,370].

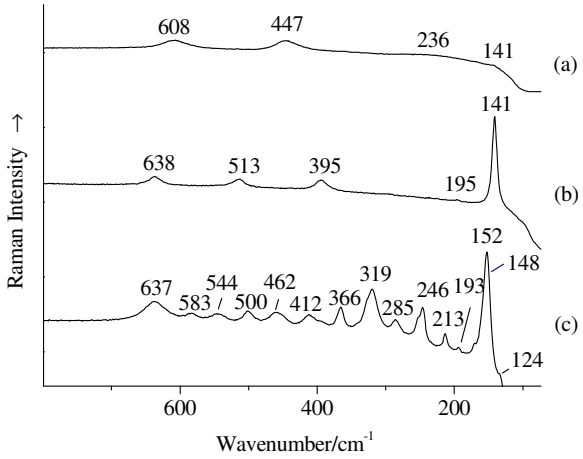

Figure 6.48 Raman spectra of: (a) white pigment grains of layer 2 of sample **L3**, identified as rutile (5 scans, 0.63 mW), (b) the yellowish pigments grains of layer 4 of sample **K7**, identified as anatase (5 scans, 0.13 mW), and (c) white pigment grain of layer 3 of sample **K3**, identified as brookite (5 scans, 0.32 mW).

Zinc oxides

Zinc white, $zinc^{II}$ oxide, ZnO, a white pigment also known as Chinese white was identified by μ-R only on two samples of the painting ***Flores Campestres*** (**W5** and **W8**), which proved to have been removed from restorations areas (see chapter 7). However, as presented in Appendix A and chapter 7, this pigment was identified in other samples by means of microchemical tests (1984) and μ-XRD and SEM/EDS.

The difficulty of μ-R for the identification of this pigment, a poor Raman scatterer, is easily illustrated by the weak intensity of the spectrum presented in Figure 6.49a which, despite the collection of 272 scans, exhibits only the 438 cm^{-1} band (Figure 6.49b) [126,371]. Even the

ultramarine blue band (549 cm^{-1}), which is present in a relatively lower amount, is more intense than the zinc oxide band.

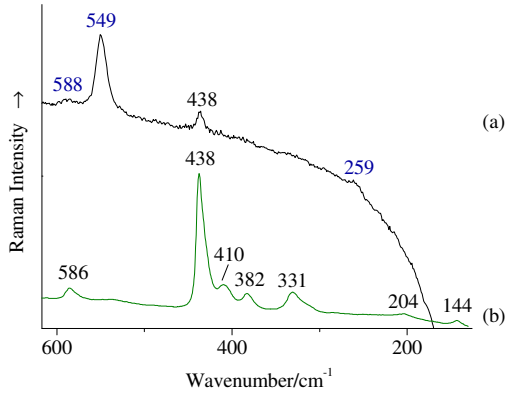

Figure 6.49 Raman spectrum of: (a) the ground of layer 2 from the sample **W5**, identified as a mixture of zinc white and ultramarine blue (wavenumbers in blue) (272 scans, 0.63 mW) and (b) synthetic zinc oxide (ID R060027) downloaded from RRUFF™ Project library [314] (532 nm excitation line, 150 mW).

Silicates

Celadonite, a green clay mineral of approximate chemical composition $K(Mg,Fe^{2+})(Fe^{3+},Al)[Si_4O_{10}](OH)_2$ [270], was identified, in two paintings, by comparison with a Raman spectrum of a reference sample, Figure 6.50A.

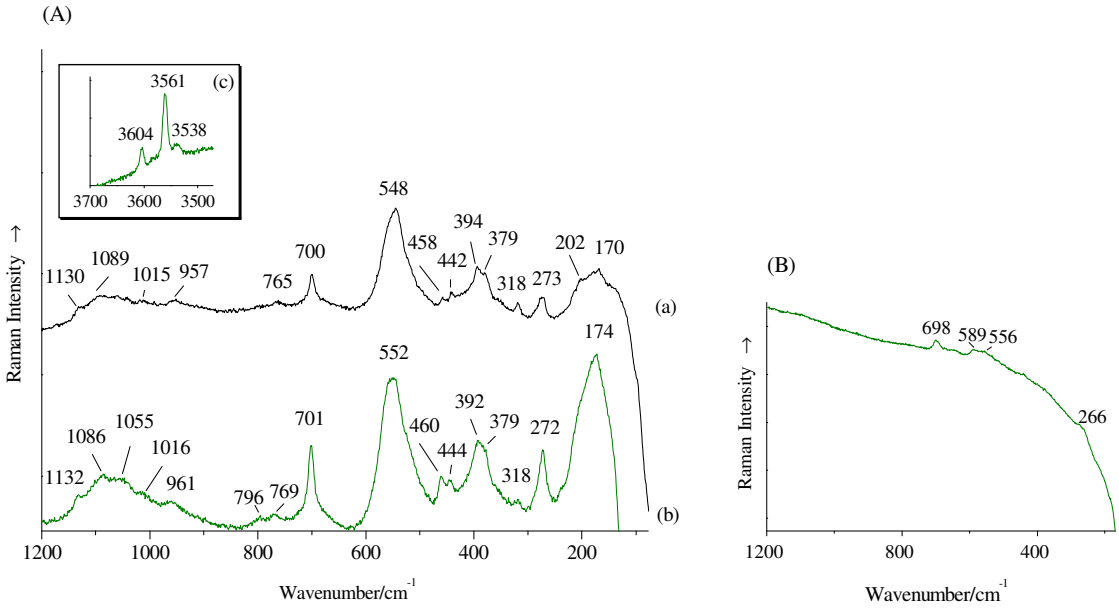

Figure 6.50 Raman spectra of: (A) (a) green pigment grain of the green layer 3 of sample **E4** (50 scans, 0.63 mW), (b) celadonite reference sample (100 scans, 0.63 mW) and (c) hydroxyl stretching region of spectrum (b); (B) glauconite reference sample (80 scans, 0.63 mW).

Celadonite together with glauconite, a clay mineral with approximate chemical composition $(K,Na,Ca)(Fe^{3+},Al,Mg)_2(Si,Al)_4O_{10}(OH)_2$ [270,271], are the two main green colouring agents of "green earth"- a green mineral pigment used since antiquity - others being cronstedtite and chlorite. Celadonite is a well crystallized mineral of volcanic origin, while glauconite (series name) is formed gradually from sedimentary minerals after deposition and consequently can vary widely in composition [272,372]. Although these two mica group minerals are formed under different geological conditions (celadonite in vesicular cavities or fractures in volcanic rocks and glauconite in sandstones and marls deposited as marine sediments)[67] [274], they are very similar chemically and structurally, what leads to difficulties to their distinction, even by XDR analysis [272,250].

As shown before, IR spectroscopy was able to differentiate these two minerals with relatively facility, but at the time this study was made[68], there were some discrepancies between the published data regarding the ability of Raman spectroscopy to distinguish these two minerals, not allowing a conclusion to be drawn. While the Raman spectra attributed to celadonite were generally very similar (the differences they presented are now known to be due to different laser excitations) [306,372,373], the Raman spectrum attributed to glauconite was either reported as identical to that of celadonite [374,375], suggesting that differentiation between the two was impossible, or as having an intense band at c. 590 cm^{-1} [372].

To clarify this matter, a reference sample of celadonite (Akaki River, Cyprus) and a reference sample of glauconite (Oystershell Hill, UK), whose identification was confirmed by μ-IR analysis (Figure 6.13) [250,274], were analysed by μ-R. As shown in Figure 6.50A, the spectra acquired for the celadonite reference sample and for the green pigment particles of the painting samples are very similar, and match those reported elsewhere [360,372,373], while the spectrum of the glauconite reference sample (Figure 6.50B) is very different from the one of celadonite. Characteristic bands of celadonite occur at 3604(m), 3561(s), 3538(w), 1132(w), 1086(w), 1055(w), 1016(sh), 961(w), 796(vw), 769(vw), 701(m), 552(s), 460(w), 444(w), 392(m), 379(m), 318(w), 272(m) and 174(s) cm^{-1}, while glauconite exhibits a very weak Raman spectrum with bands occurring at 698(w), 589(vw), 556(vw) and 266(vw) cm^{-1}. The bands above 3500 cm^{-1} are due to hydroxyl stretching modes, the bands between 1140 and 360 cm^{-1} are mainly due to Si-O and Al-O stretching modes and Si-O-Si, Si-O-Al, Al-O-Al bending modes, the specific attribution is not known for certain, and the bands below 360 cm^{-1} are mainly due to lattice modes [376,377].

[67] Mixtures of these two minerals can only be artificial as they do not occur naturally.

[68] Recently an important study, using several reference samples of celadonite and glauconite and three different excitation sources, has been published [275].

The reference samples of celadonite and glauconite were also analysed using the 514.5 nm excitation laser line, the most suitable to the study green pigments. As can be seen in Figure 6.51, celadonite spectrum presents some differences relatively to the spectrum acquired with the 632.8 nm excitation line (Figure 6.50), both in relative band intensity and in band position, with bands occurring at 3604(m), 3582(w), 3566(s) and 3538(w), 1135(w), 1072(w), 963(w), 800(vw), 770(vw), 703(s), 552(s), 459(w), 397(m), 360(m), 320(w), 274(m), 241(vw) and 218(w) cm^{-1}. Glauconite spectrum is better defined spectrum that the one acquired with the 632.8 nm laser line, bands being detected at 3611(vw), 3568(vw), 701(w), 592(m) and 266(vw) cm^{-1}. Again, the spectra of celadonite and glauconite are quite distinct, allowing the distinction from one another.

It is worth mentioning that, as reported by *Ospitali F, et al.* [275], small differences can occur between reference samples of celadonite or glauconite under the same laser excitation, probably due to the presence of associated minerals.

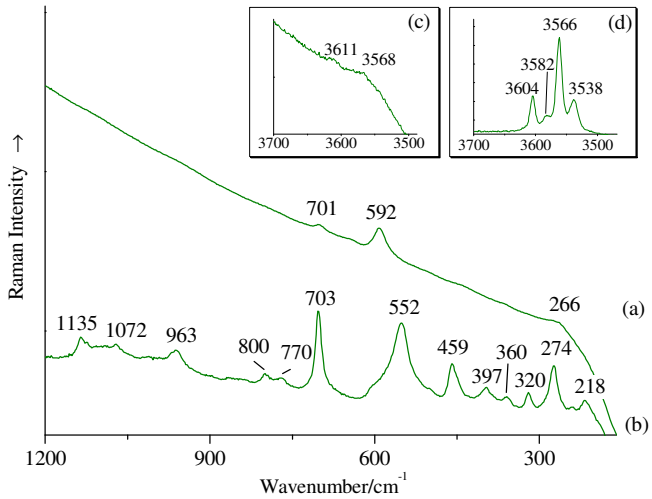

Figure 6.51 Raman spectra of: (a) glauconite reference sample (300 scans, 0.9 mW) and (b) celadonite reference sample (100 scans, 0.9 mW) obtained using the argon-ion excitation line. The insets (c) and (d) are the hydroxyl stretching region of the spectra presented in (a) and (b), respectively.

Kaolinite, $Al_2[Si_2O_5](OH)_4$ a naturally occurring inorganic polymer from the kaolin group was identified by a very weak Raman spectrum (100 scans were necessary) presenting only three, out of the four hydroxyl stretching bands characteristics of this compound, 3695(w) and 3652(vw) cm^{-1}, due to the stretching modes of the inner-surface hydroxyl groups and 3620(w) cm^{-1}, due to the stretching mode of the inner hydroxyl group (Figure 6.52). The fourth band, not observed, occurs at 3678-3668 cm^{-1} and is also due to stretching modes of the inner-surface hydroxyl groups [267,276,280].

Like referred in μ-IR analysis, kaolinite is one of the kaolin polytypes, others being dickite, nacrite and halloysite. Although the kaolin polytypes differ only in the layer stacking arrangement, different hydrogen bonds are formed in each one, and consequently different hydroxyl stretching patterns are presented in each spectrum, allowing their differentiation. Kaolinite is characterized for exhibiting four bands, while dickite and nacrite exhibit three bands (ca. 3707, 3641 and 3623 cm^{-1}, and 3708, 3644 and 3624 cm^{-1}, respectively) and halloysite only two bands (ca. 3702 and 3627-3624 cm^{-1}) [276,278,279]. Dickite and nacrite are easily distinguished from kaolinite because both present a moderate band at 3641 and 3644 cm^{-1}, respectively, while kaolinite only has weak bands at these wavenumbers. Because no band was identified at 3644-3641 cm^{-1}, the presence of dickite and nacrite was excluded. However, because in the weak kaolinite spectrum the two weak bands at 3654-3650 and 3692-3684 cm^{-1} may not be observed, and a similar spectrum to that of halloysite is produced (two bands only), the distinction between kaolinite and halloysite is not so easy, even though, kaolinite bands seem to occur at lower wavenumbers than those of halloysite.

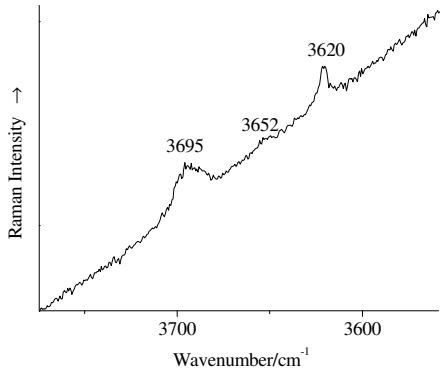

Figure 6.52 Raman spectrum of the white of layer 1 of sample **T2**, identified as kaolinite (100 scans, 0.63 mW).

Unlike to the μ-IR results, where kaolin was identified in a large number of samples, only kaolinite was identified by μ-R analysis and, only in the samples where it was the main compound. Kaolin compounds, like other clay minerals, are usually weak Raman scatterers due to the high ionic character of the Si-O bonding (about 50%), so the lack of Raman signal arising from kaolin (kaolinite) in the samples under analysis, which present an admixture with other compounds, is not surprising [268,280,336,370]. The fact that a proteinaceous material (high fluorescent material in Raman spectroscopy) is mixed with kaolinite (μ-IR result) probably contributed to the acquisition of poor quality spectra.

Another important fact is that no TiO_2 polymorph, normally associated with specific natural sources of kaolinite was detected associated with kaolinite [366,370,379].

α-quartz, trigonal SiO_2, a natural silica polymorph very abundant in Earth's continental crust, was detected on four paintings by way of its characteristic Raman band at 464(m) cm^{-1}, arising from the symmetric bending mode of the Si-O-Si (SiO_4 tetrahedra). In only a few cases was the band at 209(w) cm^{-1} also visible (Figure 6.53) [282,336,380].

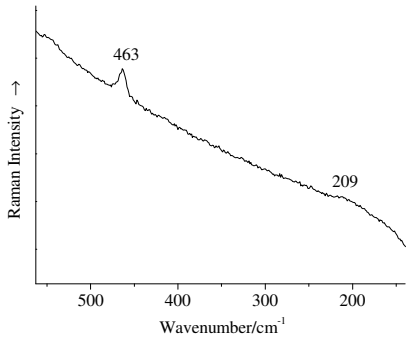

Figure 6.53 Raman spectrum of a whitish pigment grain of sample **V1**, identified as α-quartz (10 scans, 0.63 mW).

Ultramarine blue (lazurite), an aluminosilicate with composition $Na_8[Al_6Si_6O_{24}]S_n$, was identified by its characteristic resonance Raman spectrum of the S_3^- (and S_2^-) ions entrapped in the aluminosilicate matrix (Figure 6.54).

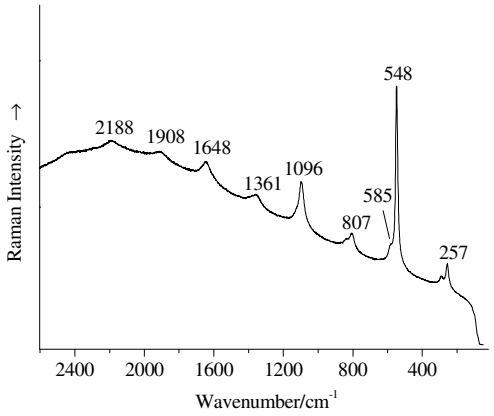

Figure 6.54 Raman spectrum of the blue pigment grains of layer 2 of sample **S1**, identified as ultramarine blue (5 scans, 0.63 mW).

As the exciting line 632.8 nm lies within the envelope of the lowest electronic band of ultramarine blue (a very broad band with a maximum at *ca.* 610 nm) a resonance Raman spectrum is obtained [381]. This spectrum is characterized by; i) the enhancement of the intensity of the totally symmetric fundamental vibration band (ν_1) of the S_3^- ions at 548 cm^{-1}; ii) the occurrence of high-intensity overtone progression bands of this fundamental ($n\nu_1$), respectively, 2188(w) ($4\nu_1$), 1648(m) ($3\nu_1$) and 1096(s) ($2\nu_1$) cm^{-1} and iii) the occurrence of a

progression of combination bands ($\nu_2+n\nu_1$) of the stretching mode (ν_1) with the bending mode (ν_2) that occurs at 257(m) cm^{-1}, respectively, 1908(w) ($\nu_2+3\nu_1$), 1361(m) ($\nu_2+2\nu_1$) and 807(m) ($\nu_2+\nu_1$) cm^{-1} [381,382].

The entrapped S_2^- ions in ultramarine blue are also known for producing a resonance Raman spectrum; however, as the used laser line falls outside of the envelope of its electronic band, only the totally symmetric fundamental band of this ion, which occurs at 585(w-sh) cm^{-1} is detected [381].

Sulfates

Barium sulfate, $BaSO_4$, also known as barium white and barite was identified by its characteristic Raman bands at 988(vs) cm^{-1}, due to the symmetric stretching mode of the SO_4^{2-} ion, 617(w) cm^{-1}, due to the antisymmetric bending mode and a doublet at 463(w) and 453(w) cm^{-1}, due to the symmetric bending mode (Figure 6.55) in a large number of samples [126,175,283,308].

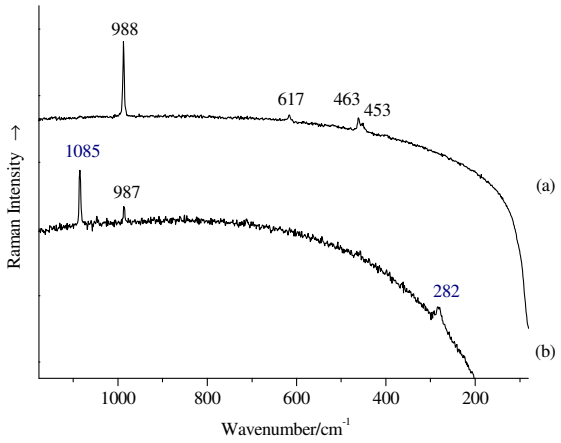

Figure 6.55 Raman spectra of: (a) a white particle of layer 1 of sample **K13**, identified as barium sulfate (5 scans, 0.63 mW) and (b) a brownish particle of layer 1 of the sample **K12**, identified as a mixture of barium sulfate and calcium carbonate - calcite form (band wavenumbers in blue) (5 scans, 0.63 mW).

Basic lead sulfate, $PbSO_4.PbO$ (Pb_2OSO_4), which occurs naturally as lanarkite, was identified by its characteristic Raman bands occurring at 1070(m), 1055(m), 976(vs), 619(w), 601(w), 439(m), 426(m), 334(m), 284(m) and 147(vs) cm^{-1} (Figure 6.56a) [383-385]. The doublet at 1070 and 1055 cm^{-1} is due to the antisymmetric stretching mode of the SO_4^{2-} ion, the band at 976 cm^{-1} is due to the symmetric stretching mode of the SO_4^{2-} ion, the doublet at 619 and 601 cm^{-1} is due to the antisymmetric bending mode of the SO_4^{2-} ion, the doublet at 439 and

426 cm^{-1} is due to the symmetric bending mode of the SO_4^{2-} ion and the bands at 334, 284 and 147 are due to PbO modes. Unfortunately, due to spectrometric cut-off limitations, the band at 147 cm^{-1} has not always been reported [383-385] and doubts were raised about the nature of this band. In order to confirm the presence of an intense band in those wavenumbers in lanarkite spectrum, a reference sample of that mineral was analysed by μ-R (Figure 6.56b).

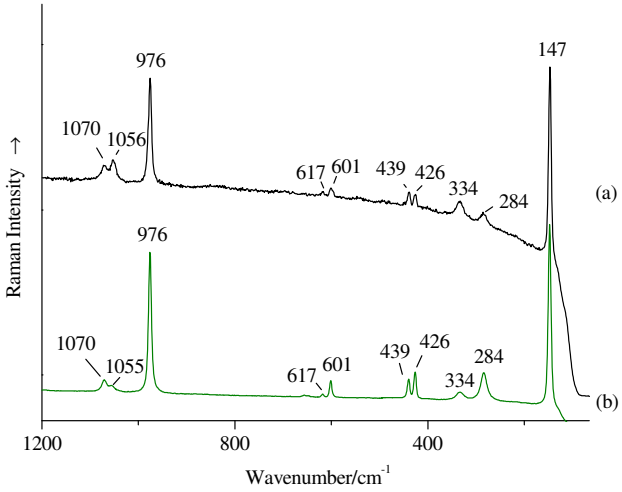

Figure 6.56 Raman spectra of: (a) a grey particle of layer 5 of sample **K12**, identified as basic lead sulfate (10 scans, 0.63 mW) and (b) lanarkite reference sample (35 scans, 2.00 mW).

Brochantite, the natural form of basic copper^{II} sulfate $Cu_4(OH)_6(SO_4)$, was identified in sample **H8** by its Raman bands at 3586(m), 3562(m) and 3393(m) cm^{-1}, due to the hydroxyl stretching modes, 973(s) cm^{-1}, due to the sulfate symmetric stretching, 623(w), 611(w) and 595(w) cm^{-1}, due to the sulfate antisymmetric bending mode and 482(w), 452(vw) and 393(w) cm^{-1}, due to the sulfate symmetric bending mode and to Cu-O stretching modes (assignment is difficult due to overlapping), and 195(vw) and 154(vw) cm^{-1} probably due to lattice modes Figure 6.57 [154,287]. This compound was identified associated with malachite.

Lead sulfate, $PbSO_4$, which occurs naturally as anglesite, was identified by its Raman bands occurring at 978(m), 449(w) and 438(w) (a doublet) cm^{-1} (Figure 6.59a and b). The first band is due to the symmetric stretching mode of the SO_4^{2-} ion, while the doublet is due to the symmetric bending mode of the SO_4^{2-} ion [383,385].

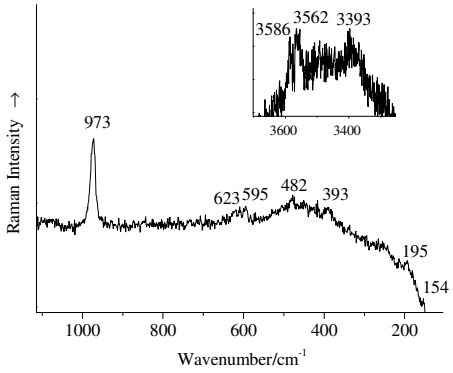

Figure 6.57 Raman spectrum of the green-whitish background of layer 4 of sample **H8**, identified as brochantite (25 scans, 0.63 mW), the inset shows the hydroxyl region.

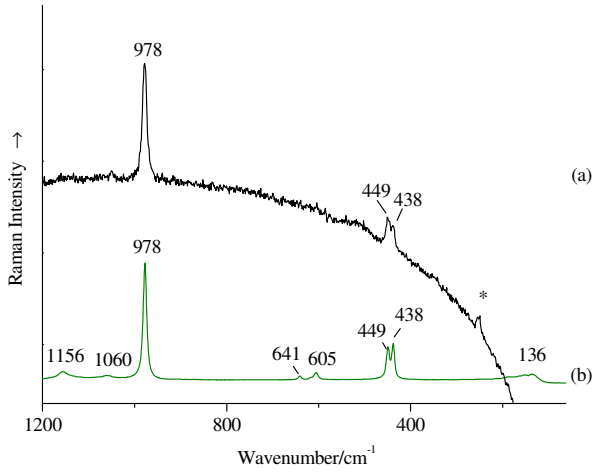

Figure 6.58 Raman spectra of: (a) a grey particle of layer 5 of sample **I7**, identified as lead sulfate (5 scans, 0.63 mW), the * marks a vermilion band and (b) lead sulfate reference sample (3 scans, 0.63 mW).

The fact that lead sulfate and basic lead sulfate have some bands in common, can constitute a problem for their identification, especially when mixed with lead antimonate yellow (see Figure 6.41), which has the band at 147 cm^{-1} in common with the basic compound. It is possible to distinguish one from another through the shift of the doublet produced by symmetric bending mode of the SO_4^{2-} ion, which occurs at 438/449 for lead sulfate and 426/439 for basic lead sulfate, and also through the existence of the doublet 1055/1070 in the basic compound, due to the antisymmetric stretching mode of the SO_4^{2-} ion. However, when the spectrum has weak bands, the doublet(s) is(are) not observed, as shown in Figure 6.59, and it is not possible to distinguish these two lead sulfates by μ-R.

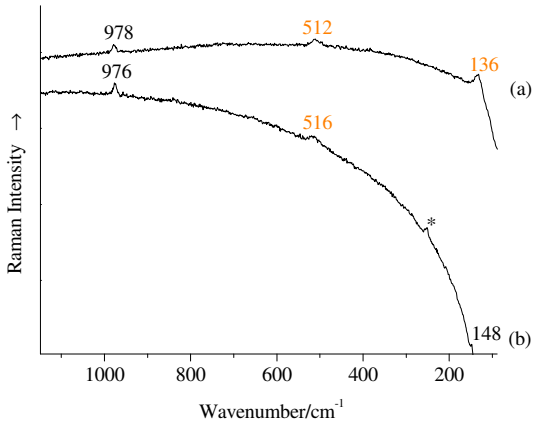

Figure 6.59 Raman spectra of: (a) yellow-greenish ground of the green layer 6 of sample **K7**, identified as a mixture of lead antimonate yellow (wavenumbers at orange) with probably lead sulfate (6 scans, 0.13 mW), and (b) green ground of the green layer 2 of sample **I4**, identified as a mixture of lead antimonate yellow (wavenumber at orange) with lead sulfate or basic lead sulfate and vermilion (wavenumber at red) (15 scans, 0.63 mW).

Sulfides

Cadmium red, cadmium sulfide-selenide (CdS_xSe_{1-x}), was identified by its characteristic Raman spectrum, which simultaneously presents two optical fundamental phonons (LO), CdS-type and CdSe-type and their overtones and combination modes. Bands occur at 590(m) ($2LO_{CdS}$), 489(w) ($LO_{CdSe}+LO_{CdS}$), 295(s) (LO_{CdS}) and 195(m) (LO_{CdSe}) cm^{-1}, Figure 6.60a [386,387].

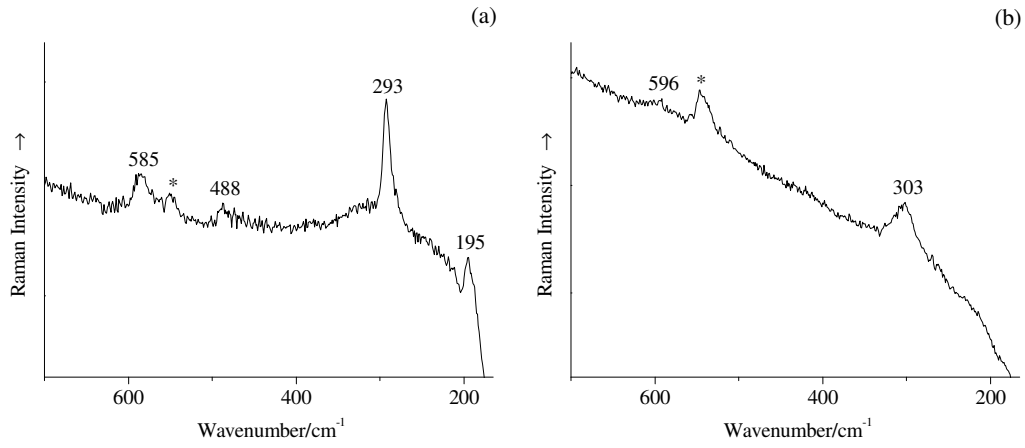

Figure 6.60 Raman spectra of: (a) red pigment grain of layer 2 of sample **W5**, identified as cadmium red (10 scans, 0.63 mW) and (b) pigment of layer 2 of sample **U10**, identified as cadmium yellow (18 scans, 0.63 mW); * marks a band probably due to ultramarine.

Being a mixing system (and not CdS and CdSe separate particles) the Raman bands of this compound present a composition-dependence shift [386,388], what accounts for the existence of different published reference spectra (578(m), 283(s), 210(w) cm^{-1}) [389] [69].

Cadmium yellow, cadmium sulfide, CdS, was identified as being the palest yellow pigment present on the paintings. Its Raman spectrum is characterized by two weak bands[70] at 303 and 596 cm^{-1}, corresponding to the longitudinal optical phonon mode (LO) and its first overtone (2LO), respectively (Figure 6.60b) [308,390,391]. Unfortunately, the spectra acquired in the analysis of pigment were at best very weak and SEM/EDS analysis had to be used for confirmation (Figure 7.7). One of the reasons for such a weak Raman spectrum can be the fact that an amorphous form seems to occur together with the crystalline form of cadmium sulfide, since reduction of the ordered structure of a compound results into the broadening of the bands and consequent reduction of their intensity [85].

Copper^{II} sulfide - Black-brownish particles present in the samples **S1** and **T1** were identified as copper^{II} sulfide, CuS, by way of the Raman bands at 473(s), 264(m) and 140(w) cm^{-1} (Figure 6.61a) [314,392].

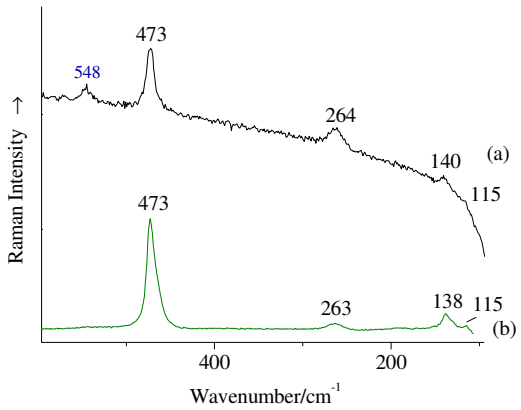

Figure 6.61 Raman spectrum of: (a) brown grain of layer 2 from the sample **T1**, identified as copper sulfide (10 scans, 0.32 mW); the band at 548 cm^{-1} is due to ultramarine blue and (b) covellite (ID R060306) downloaded from RRUFF™ Project library [314] (532 nm excitation line, 150 mW).

Although the analogue mineral, covellite, has been known since 1832 [393], there is only, very recent, report of its use as a pigment [394]. Instead, the presence of this compound in the samples is probably due to a reaction between a sulfur-containing pigment, ultramarine blue

[69] In nanocrystal this compound does also have a size-dependence shift [387].

[70] In fact, this pigment exhibits a characteristic resonance Raman spectrum; however, because the energy of the excitation laser line that was used (632.8 nm - 1.96 eV) is lower than its band gap (~2.5 eV in bulk material at room temperature), no resonance effect is produced [308,390,391].

(present in the two samples) and a copper-containing one, emerald green (a few grains still remain in the first sample) [228]. The fact that some emerald green grains did not react, has been reported previously [395].

Mercury^{II} sulfide - The highly intense orange/red pigments seen all over the cross sections were identified as mercury^{II} sulfide, HgS, commonly known as *vermilion* (synthetic form) or *cinnabar* (mineral form). These two forms, indistinguishable by Raman spectroscopy, exhibit a characteristic intense Raman spectrum with bands occurring at 342(m), 283(w) and 252(vs) cm^{-1} (Figure 6.62) [126,308].

This pigment has such a good response to Raman analysis that, even when present in a small concentration, it was easily identified. Although this was an advantage for its identification, it makes it difficult the identification of other pigments with worse response, such as goethite, whose bands are masked by those of mercury^{II} sulfide.

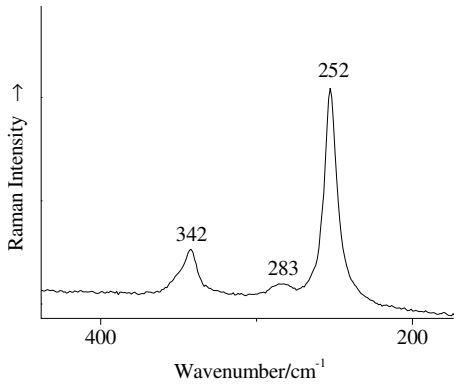

Figure 6.62 Raman spectrum of a red pigment of layer 3 of the sample **K7**, identified as mercury^{II} sulfide (1 scan, 0.13 mW).

Realgar and χ-phase/pararealgar

The mineral realgar, tetra-arsenic^{II} tetrasulfide (α-As_4S_4), was identified in sample **G4** by its Raman spectrum (Figure 6.63Aa) with bands occurring at 367(vw), 353(vs), 342(s) and 326(w), due to As-S stretching modes, 220(s), due to As-As-S bending mode, 192(s) and 182(vs), due to As-As stretching and As-S-As bending mode, respectively, 171(vw), due to As-As stretching mode and 166(vw) and 143(w) cm^{-1}, due to As-As-S bending mode. The weak band at 235 cm^{-1} suggests that some alteration into pararealgar is already occurring as this band is not present in the reference sample of realgar (Figure 6.63Ba), but a doublet at these wavenumbers is present in the reference sample of pararealgar (Figure 6.63Bb) [396-398].

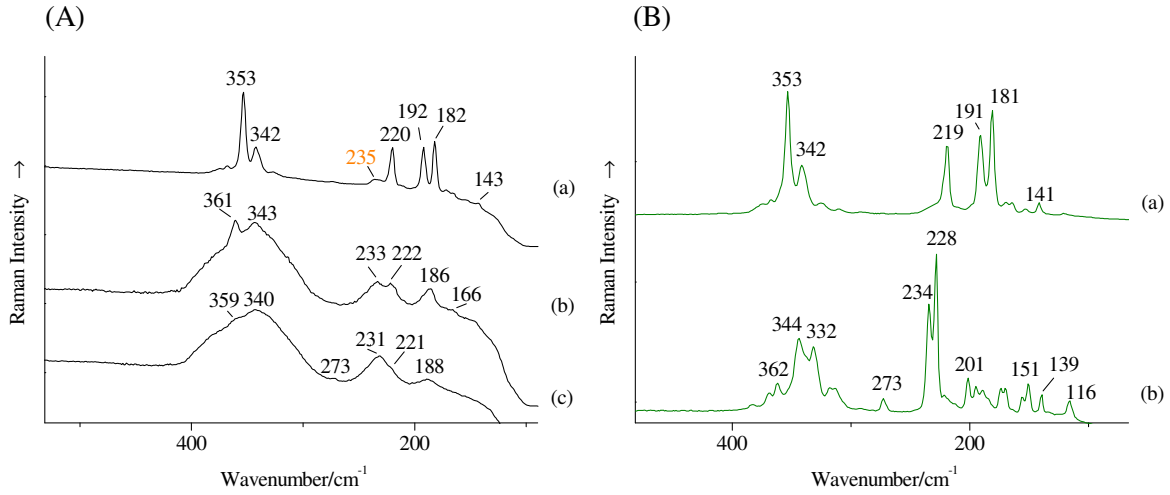

Figure 6.63 (A) Raman spectra of: (a) orange/coral pigment grain of layer 2 of sample **G4**, identified as realgar (4 scans, 0.10 mW), and (b) coral pigment grain of layer 2 of sample **G4** (2 scans, 0.13 mW) and (c) coral pigment grain of layer 1 of sample **H1** (18 scans, 0.10 mW), identified as χ-phase and/or mixture of χ-phase and pararealgar; (B) Raman spectra of: (a) realgar reference sample and (d) pararealgar reference sample, both provided by *Burgio L.* [398].

In the other samples, the pigment grains with an orange-coral colour were identified as **χ-phase** [397] or a mixture of **χ-phase** and **pararealgar** [399], the spectra being characterized for exhibiting bands at 361(s)-359(sh), 343-340(vs), 273(vw), 233-231(s), 222(s)-221(sh), 188-186(w), 166(vw) and 143(vw) cm^{-1} (Figure 6.63Ab and c). These spectra are identical to the spectra presented by *Chaplin et al.* [400] and similar to the spectra of χ-phase [397] and mixture of χ-phase and pararealgar [399], although presenting broader bands.

Pararealgar is a low symmetry, light-induced polymorph of both the As_4S_4 α-phase (realgar) and the β-phase (low-temperature and high-temperature phases, respectively), while the χ-phase, also a light-induced phase, seems to be a precursor to pararealgar [399,401]. According to *Bonazzi et al.* [397], the χ-phase can be considered as an expanded, less-ordered β-phase, leading to broader Raman bands than the β-phase.

It is known that the realgar when exposed to light, either sunlight or laser light, transforms into pararealgar and/or χ-phase, with different rates of the transformation, depending of the wavelength of the light to which realgar is exposed [396,399,401,402]. To determine if the transformation of realgar into the mixture of χ-phase and pararealgar, identified in the samples, occurred due to exposure to sunlight (either before or after use by Pousão) or to laser light is very difficult.

We must refer that pararealgar is not the final degradation product of realgar, but only an intermediate, as the continuous photo-degradation of realgar leads to the formation of arsenolite (As_4O_6), a colourless/white compound [399,402].

Other pigments

Since carbon-base black pigments and lake pigments do not belong to any functional group, they will be presented under the group *other pigments*.

Carbon-based black

The majority of the brown/black pigments gave rise to a Raman spectrum (Figure 6.64) with two distinct broad bands at ca. 1590(vs) and 1340(vs) cm^{-1}, characteristic of poorly organized carbonaceous material. The first band is commonly known as the *G band,* while the second band is called the *D1 band* (the defect band). Both bands are assigned to lattice vibrations in the plane of graphite-like rings. However, while the *G band* is always active, the *D1 band*, resulting from disordered allowed zone-edge mode, becomes active only with the decrease in symmetry at the edges of the planes [403-406]. Both bands broaden with increasing disorder, while the *D1 band* grows in intensity with increasing disorder [404]. Figure 6.64 shows how both position and relative intensity of the *G* and *D1* bands are highly variable.

Poorly organized or amorphous carbon is the characteristic component of the carbon-based black pigments, i.e. pigments produced by the combustion of hydrocarbons, often referred to as carbon black, lamp black, charcoal, bone black and ivory black, depending of the starting material [85].

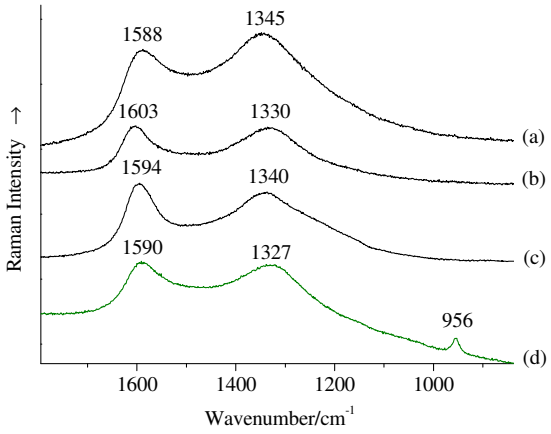

Figure 6.64 Raman spectra of carbon-based black pigments from: (a) the grey layer 3 of sample **J1** (15 scans, 0.63 mW), (b) the brown layer 2 of sample **G4** (3 scans, 0.13 mW), and (c) the blue layer 2 of sample **D1** (6 scans, 0.32 mW); (d) Raman spectrum of a reference sample of ivory black from Windsor & Newton (40 scans, 1.00 mW).

Different parameters of the Raman spectrum, such as band position, intensity ratio and area ratio have been used to estimate the carbonaceous materials degree of organization [405,407]. However, no tentative assignment to any of the several disordered carbon-based black pigments was done since; i) analysis was conducted in polished cross sections and polishing can induce the formation of new defects; ii) as a result of its opacity, carbonaceous material can suffer laser-induced heating, causing the shift of the G band position and iii) there is different baseline definition between the spectra, that consequently cannot be compared [405].

The inexistence of a band at ca. 960 cm^{-1} assignable to the symmetric stretching mode of phosphate ion, present in the reference spectrum of bone/ivory black (Figure 6.64d), seems to indicate that neither bone nor ivory black pigments were used in the paintings. However, bone/ivory black pigment was identified by μ-IR (Figure 6.12A) and confirmed by SEM/EDS (Figure 7.8) in some of the samples, indicating that μ-R presents some difficulties in the identification of the phosphate band when the black pigment is present in a mixture.

Although bone black and ivory black have a different starting material, bone and ivory, respectively, they have an identical composition and consequently are practically indistinguishable. The band at ca. 960 cm^{-1} accounts for the present of the inorganic component of bones and ivory, apatite and hydroxylapatite, respectively [260,261,263].

These results clearly show that the identification of the black pigments by μ-R is not always feasible. Although distinction between organized carbon-based black materials (e.g. graphite), disordered carbon-based materials (e.g. charcoal) and inks is easily accomplished, the distinction between different types of disordered carbon-based materials can be very difficult, especially when the carbonaceous material is present in a complex pigment mixture. Whenever, differentiation is necessary, a complementary technique such as IR, PIXE [407] or LIBS [28,408] should be employed.

Cochineal and mader lake pigments

High fluorescence of these compounds is normally a problem for Raman analysis [136,409]. However, reasonable intensities and signal/noise ratios were obtained, allowing the identification of **cochineal** and **madder lake pigments**. Lake pigments are chelate complexes of dyes and metal cations, made by (co-)precipitation of a coloured dyestuff onto the substrate (an inorganic base material) [301,303].

Cochineal lake, a lake pigment based in the red dyestuff removed from the body of the female insect *Dactylopius coccus*, whose main colouring component is carminic acid,

$C_{22}O_{13}H_{20}$ [85,303], was identified by its Raman spectrum with bands occurring at 1525(vw), 1483(m), 1418(m), 1315(s), 1303(s), 1185(w), 1253(w), 1222(w) and 1105(m) cm^{-1} (Figure 6.65Aa).

As can be seen in Figure 6.65A, the spectrum of cochineal lake present in the samples is very similar to the one exhibited by a reference sample of cochineal carmine (C.I. 75470), which consists in a calcium-aluminium lake of carminic acid (Figure 6.65Ab) [126,410]. However, no bands possibly assignable to inorganic compounds often used as substrate and/or additives, such as alum (potassium aluminium sulfate), sodium/potassium carbonate, chalk, barium sulfate, kaolin and zinc oxide were identified [303]. Starch, which was identified by µ-IR in the samples mainly composed by red lake pigments (Figure 6.23), was not identified by µ-R.

Madder lake, alizarin dye, was identified by its Raman bands at 1648(w), 1521(vw-sh), 1480(s), 1356(vw-sh), 1327(s), 1291(m), 1218(vw), 1185(vw), 1164(vw), 903(vw), 843(w), 655(w) and 484(w) cm^{-1} (Figure 6.65B) [126,344,409]. Madder is a dyestuff derived from the roots of various plants of the Rubiaceae family and is characterized by the presence of a series of active anthraquinone components, the mainly being alizarin, $C_{14}H_8O_4$, and purpurin, $C_{14}H_8O_5$, others are, for example, pseudopurpurin, quinizarin, morindone, xanthopurpurin and rubiadin [85,409].

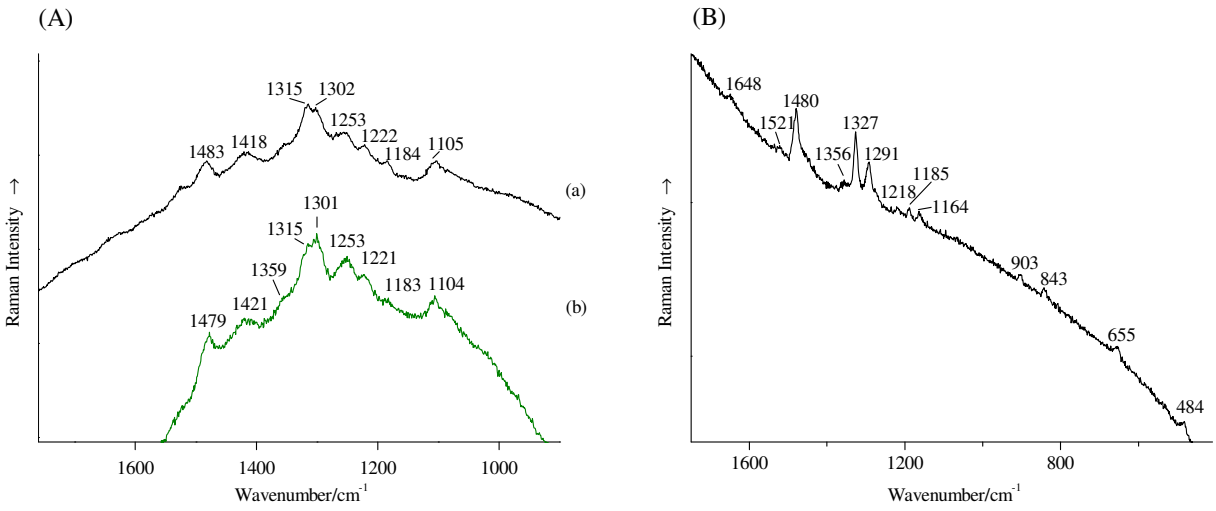

Figure 6.65 Raman spectra of: (A)(a) red lake pigments of layer 2 of sample **Q5**, identified as cochineal lake (47 scans, 0.13 mW) and (b) carmine reference sample (372 scans, 0.02 mW); (B) purple pigment grain of layer 2 of sample **W6**, identified as madder lake (20 scans, 0.63 mW).

Other compounds

Aluminium oxide/ water-slurry Alumina - Very often, a very intense doublet at 1403 and 1374 cm^{-1} (Figure 6.66), was observed associated with the Raman spectrum of the pigment under analysis. This doublet occurs at approximately the same wavenumbers of the ruby's main fluorescence lines, the R-lines[71], which at atmospheric pressure occur at 1398 and 1367 cm^{-1} (wavelength 692.7 and 694.2 nm, respectively) (411-413). Ruby is a gemstone with corundum form (corundum is the naturally occurring crystalline form of aluminium oxide (α-Al_2O_3)) in which a small fraction of the Al^{3+} ions were replaced by Cr^{3+} ions. Clearly, the detection of this doublet in the samples is not due to the presence of ruby, but rather, to the presence of particles of the α-Al_2O_3, (which must have Cr^{3+} ions, of unknown origin), used for polishing the samples, as confirmed by the analysis of the slurry used for polishing.

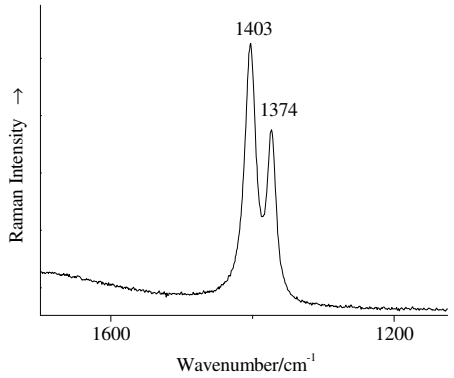

Figure 6.66 Raman spectra of a greenish grain of layer 4 of sample **H8**, identified as alumina water-slurry used for polishing (1 scans, 0.63 mW).

Black ink - Often, when analysing black and purple points in the samples, a spectrum with bands occurring at 1540(s), 1450(m), 1400(w), 1337(s), 1267(m), 1188(w), 1156(vw), 959(w) and 749(s) cm^{-1} (Figure 6.67a), which proved to be identical to the spectrum of a reference sample of a black permanent pen's ink used to label the samples (Figure 6.67b), was acquired. Apparently, the ink used to labelled the samples did not fix well to the resin, and was transferred during storage (samples were stored all together in a bag) and/or during handling.

Silicon carbide - Residue of silicon carbide, SiC, used as abrasive for grinding the surface of the samples, was identified in one sample. Its Raman spectrum exhibits bands at 965 cm^{-1}, 795, 786 and 766 cm^{-1} (Figure 6.68) (414).

[71] The ruby R lines have been used for many years to pressure calibration in high-pressure diamond-anvil cells.

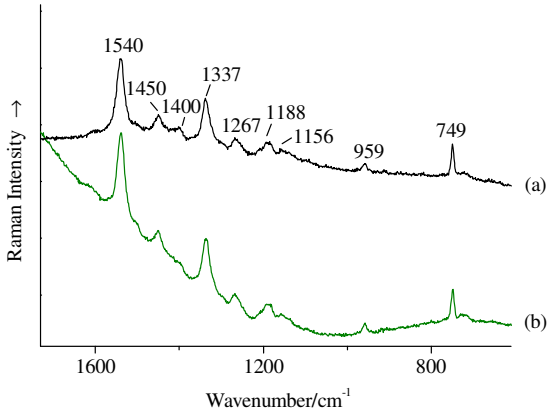

Figure 6.67 Raman spectra of: (a) black particle of layer 1 of sample **P1** (2 scans, 0.13 mW) and (b) black ink reference sample (5 scans, 0.32 mW).

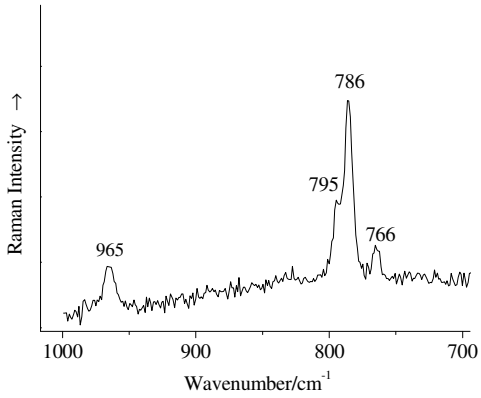

Figure 6.68 Raman spectra of a white grain of layer 2 of sample **E6**, identified as silicon carbide used for the grinding (7 scans, 0.32 mW).

Unknown compound 2

Sporadically, when analysing brown and black pigment grains a weak spectrum with one single band occurring between 682 and 610 cm^{-1}, as represented in the spectra of Figure 6.69, was acquired. The band position and its morphology strongly suggest the presence of a manganese, iron or mixed oxide/oxyhydroxide; however, the assignment to a particular compound is very difficult. Firstly, because iron, but specially manganese, can constitute a large number of oxides whose structure can be very complex, involving solid solutions, stacking faults and intergrowth sequences of structural variants [334,336,415]. Secondly, since both iron and manganese oxides are good absorbers of the laser radiation, band position shift or alteration of the sample composition can occur during the analysis [334,339,340], what leads to, the fact that there is a significant discrepancy among the published Raman spectra of these compounds [339,340,416].

The weak intensity of the spectra can be due to the presence of the compound in only trace amounts or to a weak Raman response. In fact, the Raman spectra of manganese oxides are generally very weak, even for well-crystallized compounds [416].

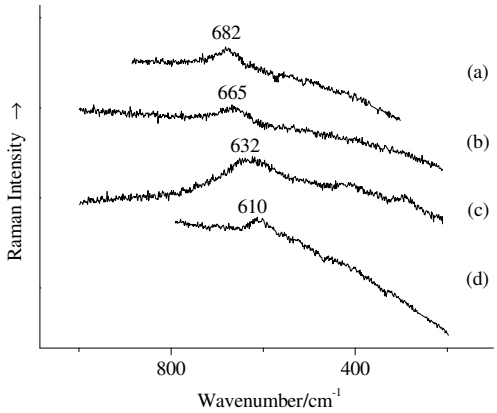

Figure 6.69 Raman spectra of: (a) brown pigment of layer 2 of sample **U13** (15 scans, 0.32 mW), (b) black pigment of layer 2 of sample **P1** (3 scans, 0.32 mW), (c) black pigment of layer 2 of sample **P2** (13 scans, 0.32 mW) and (d) brown pigment of layer 2 of sample **H1** (10 scans, 0.63 mW).

Unknown compound 3

In samples **F6**, **K3**, **S5** and **S7** it was identified the presence of a compound whose Raman spectrum exhibits two strong bands at 460 and 640 cm^{-1} (Figure 6.70). This unknown compounds seems to be related to the presence of lead antimonate yellow as it was also be detected by *Rosi et al.* [349] in the ancient ceramics containing antimonite pigments.

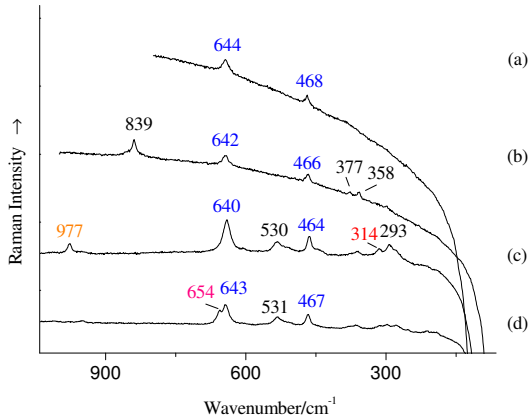

Figure 6.70 Raman spectra of: (a) white pigment of layer 2 of sample **K3** (4 scans, 0.32 mW), (b) white pigment of layer 4 of sample **F3** (8 scans, 0.32 mW) (wavenumbers in black are due to chrome yellow), (c) grey pigment of layer 2 of sample **S7** (20 scans, 0.63 mW) (wavenumbers: in orange is due to lead sulfate; in black are due to Prussian blue; in red is an unknown compound) and (d) white pigment of layer 2 of sample **S5** (22 scans, 0.63 mW) (wavenumber in pink are from rosiaite and the wavenumbers in black are from Prussian blue).

6.3 Infrared microscopy *vs.* Raman microscopy

Based on different interaction mechanisms between light and matter, μ-IR and μ-R present different advantages and limitations for the characterization of the oil paintings' samples under analysis.

Due to the high complexity of these samples, which are made up of several layers with a widely-range width, each composed by a complex pigment mixture, the current study offers an opportunity to assess the advantages and difficulties of these two vibrational techniques for the analysis of oil paintings.

In what follows, major advantages and difficulties of μ-IR and μ-R concerning sample preparation, spectra acquisition and spectra interpretation detected along this study will be addressed.

6.3.1 Sample preparation

As mentioned in section 2.2.2, sample preparation is a decisive step in any type of analysis, since it is tailored to the sample, the analytical technique and the purpose of analysis. Especially when dealing with micro samples, sample preparation can be a limiting factor, since it will strongly affect the quality of the results.

One of the main objectives of this study is to identify the pigments and dyes present in each layer of the samples of Pousão's oil paintings. However, the reduced size, complexity and heterogeneity of the samples hampered or made the removal and individual analysis of small fractions (particle samples) of each layer very difficult. Instead, samples had to be prepared and analysed as layered samples: thin sections (μ-IR) and cross sections (μ-R).

In the case of μ-IR, the samples had to be prepared as thin sections, so as to let the light be transmitted through them in the more convenient transmission mode. Although at the price of more sample preparation time, since the thin section require the microtoming of the cross sections, transmitted μ-IR is the method of choice in most cases, and the primary method for layered samples. In fact, the transmission method provides good quality spectra without artefacts, allows a reduction of the area of analysis, and the possible presence of surface imperfections or topography difference does not cause any constrain, as it was verified for the reflection methods [82,118].

Unfortunately, for the samples under analysis the preparation of thin sections proved to be very demanding, time-consuming and was not always successful, since during microtoming a large part of the samples was lost. Thus, it is considered that the sample preparation turned out to be quite a handicap for the μ-IR analysis.

In the case of μ-R the cross sections previously prepared for the OM analysis proved to be rather suitable. In order to determine the number, thickness, sequence and interaction of the layers that constitute the samples, the OM analysis is always performed at the beginning of any study in this field. Therefore, the fact that the μ-R analysis could be performed in the same samples prepared for OM constitutes a major advantage. No more sample and sample preparation time were required.

Although some published studies [293,417] refer that the polishing of the resin during the cross sections preparation leaves an irregular layer of resin over the sample, thus causing fluorescence, most pigment particles in the samples under study produced a good Raman signal and no fluorescence.

6.3.2 Spectra acquisition

Both μ-IR and μ-R are able to produce a spectrum in just a few seconds. However, in the cases where signal to noise is low, the compound has a low signal, or fluorescence is high, increased acquisition times might be necessary for both techniques. In this study acquisition times were 1 minute for μ-IR and up to 5 hours for μ-R.

Although a confocal system, making used of restringing apertures, was employed in the μ-IR analysis, the spatial resolution obtained with this technique was always much lower than the one achieved with μ-R. Employing a globar IR source, a common 250 μm x 250 μm MCT-A detector and a 0.58 NA objective/condenser, the spatial resolution was set to 50 μm. Below this value, poor-quality spectra, which in addition contain information from the neighbouring layers or embedding resin[72], were collected. Consequently, often μ-IR involved the analysis of an area larger than the area of paint layers, not allowing the individual analysis of each layer.

μ-R proved to have a good spatial resolution. For a 632.8 nm laser source and a NA 0.95 objective, the spot diameter of the source on an opaque sample is diffraction limited to 0.8 μm and the approximate depth resolution is about 1 μm [202,203,418]. This good spatial resolution allowed to focus the laser line on each pigment/compound grain and analyse each one individually, excluding the interference from nearby compounds.

In the μ-IR analysis, it was often difficult to attribute a certain pigment/compound to a particular layer, by comparison with the OM images, since samples were analysed as thin sections. Firstly, because the thin sections are prepared using a fragment of the bulk sample

[72] Although the embedding resin exhibit strong absorptions of their own, no significant problems with the embedding resin were found.

different from the one used for the preparation of the cross sections for OM, the stratigraphy of the thin section can be somewhat different from the one of the cross section. Secondly, since thin sections are very thin, a diminution of the depth of colour relatively to the one of the cross sections occurs; and, as their surface is not polished, the image under the IR microscope was not sharp, making the differentiation among layers difficult. Thirdly, because in order to produce good quality IR spectra and increase the layer area to improve the spatial resolution, thin sections were squeezed between diamond cells. This compression procedure led to an odd distribution of the sample through the two diamond cells and even to the alteration of the well-defined structure of the stratigraphy.

Unlike μ-IR, in the case of μ-R it was very easy to attribute a pigment/compound particle to a particular layer by comparison with the OM images, since the samples were the same cross sections analysed by OM.

Due to the fact that the high sensitive MCT-A detector used for μ-IR analysis presents a lower cut-off at 650 cm^{-1}, the identification of a large number of pigments/compounds exhibiting mainly/only infrared bands bellow that wavenumber[73] was very difficult/impossible. Unlike μ-IR, μ-R allowed the identification of most of the inorganic pigments/compounds, since it is possible to acquire the entire vibrational spectrum with a single instrument, accessing wavenumbers even below 200 cm^{-1}[74]. For example, while cobalt blue and iron$^{(III)}$ oxide were identified by μ-R, they were not identified by μ-IR because the IR bands of these pigments, 665, 558 and 512 cm^{-1} (cobalt blue) [238,420] and 579 and 483 cm^{-1} (iron$^{(III)}$ oxide) [249,421] occur below 650 cm^{-1}. This constitutes another major advantage of μ-R over μ-IR for pigment identification.

Obviously, μ-R also has some limitations, namely the occurrence of fluorescence and chemical alteration/degradation of the samples under the laser line, although they were almost successfully avoided in the current study.

Fluorescence, which can be caused by impurities, binder, organic compounds, etc., constitutes a serious drawback of μ-R, as its emission is often several orders of magnitude more intense than the Raman signal, partially or totally masking the Raman spectrum and

[73] Some pigments absorb even bellow the wavenumber range accesssible to the common mid-infrared DTGS detector (cutt off 350 cm^{-1}); for those, far-infrared setups are required.

[74] Raman spectrometers are able to range from 4000 to about 100 cm^{-1} .The lower limit depends of the notch filter, since the cut-off edge of the filter is often not sharp enough to prevent rejection of Raman photons very near the excitation line, within 75-100 cm^{-1} [419].

hampering identification[75]. However, in the current study, fluorescence did not constitute a significant problem in general, as the use of the 100x objective allowed for the distinction between most of the pigment grains and the binder fluorescence matrix. Nevertheless, red lake pigments (cochineal lake and madder lake), cobalt pigments (cobalt blue and cerulean blue) and cadmium pigments (yellow and red) were normally accompanied by fluorescence, which often did not permitt their identification. A case in point was cerulean blue, whose Raman spectrum was always completely masked by an intense fluorescence background which hampered its identification by
μ-R. At any rate this pigment was identified by SEM/EDS and μ-XRD (see chapter 7).

The chemical alteration/degradation caused by absortion of the incident laser line by some of the samples was avoided by employing the 632.8 nm line. With this line only some irrelevant dark particles suffered alteration during the Raman analysis. Therefore, as long as there is no laser induced alteration/degradation of the samples' components, μ-R is considered a non-destructive technique, as poved by the fact that cross sections were further analysed by SEM/EDS and FM.

Due to the lower energy values of the IR radiation, fluorescence or degradation during the μ-IR analysis did not constitute a problem. However, as it is very dififcult to recover the squezeed thin sections from the compression cell and use them for further analysis, μ-IR is considered a destructive technique, even if it has been classified as non-destructive [(118)].

Another disadvantage of μ-R which cannot be avoided is the requirement of calibration of the spectrometer/spectrograph in the dispersive set-ups on a daily or even an hourly basis. An unskilled user may induce calibration errors that will make spectra matching difficult. It is worth recalling that the dispersive set-ups are more suitable for microscopic analysis than the FT set-ups (see page 90). Unlike μ-R, in μ-IR no such errors are likely to occur, since FT spectrometers are always employed and the calibration is performed by the instrument itself.

6.3.3 Interpretation of the spectra

For both techniques, the interpretation of the spectra was in general based on the comparison of the acquired spectra with those kept in databases or reference works.

However, the interpretation of the IR spectra was more complex and time-consuming. This was due to the fact that in μ-IR a larger number of compounds are simultaneously analysed, since what is under analysis is an area rather than isolated grains. Each

[75] As fluorescence is laser wavelength dependent this problem can be overcome in many cases by using near-infrared (NIR) excitation wavelengths (e.g Nd/YAG - yttrium aluminium garnet), with the cost of significant loss in spatial resolution and scattering intensity [(33)].

compound may produce a large number of bands, usually quite broad and tending to overlap and merge into broad envelops, obviously making the spectra interpretation quite complex.

As another consequence of being an area analysis, the compounds in minor or trace amounts were generally overshadowed by the main components [26,118,422]. In this study, since lead white (a major component of the samples) shows a high response to IR analysis, the identification of other compounds contained in the samples was made very difficult, if not impossible, depending on their concentrations and respective band positions.

Unlike the μ-IR spectra, the μ-R spectra were much simpler and easy to interpret, since they exhibited a smaller number and narrower bands [10]. This was due to the fact that, as the laser line is focused on individual particles, in general a single compound is analysed each time. Moreover, under the normal Raman spectroscopy conditions, overtone and combination bands are generally not observed.

6.4 Conclusions

To establish Pousão's palette, 153 samples prepared from 23 paintings by Pousão were analysed by the vibrational spectroscopic techniques μ-IR and μ-R. In total, more than 800 IR spectra and 2000 Raman spectra were acquired and interpreted.

Although providing the same type of information, those techniques have different selection rules, since they are based on different mechanisms of interaction of light with matter, and offer different advantages and limitations for the analysis of oil paintings' samples.

Table 6.6 summarizes the compounds (pigments, extenders and/or associated compounds) identified by μ-IR and μ-R in Pousão's paintings and clearly shows that both techniques were successful for this purpose.

μ-IR proved to be more suitable for the identification of extenders and/or associated compounds (associated with the mineral form of the pigment or a result of the synthesis process), such as gypsum, calcite, kaolin and quartz, than for the identification of pigments. The only exceptions were lead white, the main white pigment in the samples, and bone/ivory black. Frequently, lead white was more easily identified by μ-IR than by μ-R and bone/ivory black was always only identified by μ-IR, as both pigments have several characteristic and intense, mid-infrared bands above 650 cm^{-1}. Within the 18 compounds[76] identified by μ-IR, 11 were pigments.

[76] Excluding compounds presented under the section named *other compounds*.

Table 6.6 Compounds* identified by μ-IR and μ-R in Pousão's paintings

Compound	μ-IR	μ-R
Arsenites		
Emerald green	•	•
Scheele's green		•
Carbonates		
Calcium carbonate - calcite form	•	•
Lead carbonate	•	•
Lead white	•	•
Malachite		•
Chromates		
Chrome orange	•	•
Chrome yellow	•	•
Strontium yellow	•	•
Zinc yellow	•	•
Cyanides		
Chrome green	•	•
Prussian blue	•	•
Oxides and Oxyhydroxides		
Anatase		•
Brookite		•
Cobalt blue		•
Cobalt oxide		•
Iron^{III} oxide		•
Iron^{III} oxyhydroxide		•
Lead^{II,IV} oxide		•
Lead antimonate yellow		•
Tetragonal lead^{IV} oxide [a]		•
Rosiaite		•
Rutile		•
Viridian	•	•
Zinc white		•
Phosphates		
Bone/ivory black	•	
Silicates		
Celadonite	•	•
Kaolin	•	•
Quartz	•	•
Ultramarine blue		•
Sulfates		
Barium sulfate	•	•
Basic lead sulfate		•
Brochantite	•	•
Gypsum	•	
Lead sulfate		•
Sulfides		
Cadmium red [b]		•
Cadmium yellow		•
Copper^{II} sulfide		•
Realgar/pararealgar		•
Mercury^{II} sulfide		•
Red lake pigments		
Other pigments		
Carbon-based black		•
Cochineal lake		•
Madder lake		•

* Pigments are in blue, while extenders, associated compounds or impurities are in green
[a] By identification of the laser induced formed orthorhombic lead^{II} oxide
[a] Its presence is due to a conservation intervention

In general, μ-IR is more suitable for the identification of organic compounds, since their analysis by μ-R is often hindered by fluorescence. In particular, μ-IR allowed for a quick identification of the type of binding medium, without requiring sample solubilisation, volatilization or ionization, as other techniques do [118,135].

The major limitations of μ-IR were: i) the demanding preparation of the thin sections, not always well succeeded; ii) the poor quality and the complexity of the IR spectra containing information from neighbouring layers or embedding resin, when areas smaller than 50 x 50 μm^2 were isolated and analysed and iii) the cut-off of the MCT-A detector, which hampered the detection of a large number of pigments with IR bands below 650 cm^{-1}.

Unlike μ-IR, μ-R proved to be more suitable for the identification of pigments – which in fact, constitute one of the main objectives of this study – than for the identification of extenders and/or associated compounds. Within the 41 compounds[76] identified by μ-R, 25 were pigments.

The accessibility to the low-wavenumber region of the vibrational spectrum (<500 cm^{-1}), the high spatial and spectral resolutions and its non-destructiveness made μ-R more suitable than μ-IR for pigment identification in the samples under study

Since the extenders and/or associated compounds contained in the samples are mainly silicates, aluminosilicates or clay minerals (for example, kaolin) and the Si-O bonding exhibits a high ionic character (about 50%) [268,280,370], μ-R showed some difficulties for their identification. As consequence of the virtually zero polarizability change occurring during the vibrational modes of ionic bonds, the corresponding Raman bands were very weak [336,370]. Moreover, probably due to an iron-rich content [379,414], their Raman spectra were frequently accompanied by an intense fluorescence background, hampering their identification. At any rate, the identification of those compounds does not constitute an objective of this study.

The major limitation of μ-R was the high fluorescence presented by some of the particles under analysis, which hampered their identification. Although laser induced alteration during analysis was also observed, this occurred only for a few irrelevant black particles, whose identification was possible, through the identification of the degradation product [33].

Finally, one might question whether it is worth performing μ-IR analysis of thin sections when performing μ-R analysis of the cross sections and whether the results provided by the conventional FT-IR analysis using KBr pellets (much more simple to prepare than the thin sections) combined with the results from μ-R, would not provide the same level of information than the μ-IR results combined with μ-R results.

In spite of the above mentioned limitations of μ-IR, the amount of information obtained by this technique is always greater than the one obtained by conventional IR analysis. Firstly, because, when using conventional IR, unless each layer can be sampled and individually analysed, the stratigraphy of the sample is completely destroyed and it is no longer possible to attribute each compound to a specific layer. Secondly, since several compounds would be simultaneously analysed, those compounds with lower concentration would probably be overshadowed by others with higher concentration.

In the current study the usefulness of μ-IR was relatively small, since one of the main aims is to establish Pousão's palette and the paintings under analysis contain lead white as major white pigment, both in ground and paint layers, which could also be identified by μ-R. However, it is important to stress that the use of μ-IR will surely be very useful [122,157,423] for studies in which ground layer(s) and/or paint layers are mainly composed by gypsum, kaolin, etc., such as polychrome sculptures and altarpieces, wall paintings and panel paintings.

7 SEM/EDS, μ-XRD and FM analysis

Led by a new paradigm, scientists adopt new instruments and look in new places.

T. S. Kuhn

This chapter presents the results of the analysis of some of Pousão paintings' samples obtained by scanning electron microscopy with energy-dispersive X-ray spectrometry (SEM/EDS), X-ray microdiffraction (μ-XRD) and fluorescence microscopy (FM). Additionaly, it discusses their limitations and compares the results with those previously obtained by the microchemical tests.

7.1 Introduction

As reported before in chapter 6, µ-IR and µ-R proved to be able to identify a large number of pigments, extenders, associated compounds and even impurities, but, some questions still remain, essentialy due to the experimental cut-off of the infrared detector at 650 cm^{-1} and to the weak Raman response and /or fluorescence of some compounds.

Since characterization of Pousão's palette is one of the major objectives of this study, the auxiliary techniques, scanning electron microscopy with energy-dispersive X-ray spectrometry (SEM/EDS), micro X-ray diffraction (µ-XRD) and fluorescence microscopy (FM) were employed in order to answer the questions and provide a more complete study. µ-XRD and SEM/EDS were used to confirm the presence of compounds whose vibrational spectrum was weak or inexistent (for example, cadmium yellow) or to verify the presence of pigments that were supposed to exist but provided no vibrational answer (for example, zinc white). FM, not as rigorous as the two previous techniques, was used to easily and quickly confirm or exclude the presence of madder lake and zinc white, pigments with significant auto-fluorescence.

To provide quicker and more accurate results, the analysis by these three auxiliary techniques was undertaken with the support of specialised technicians.

A brief introduction to these three techniques is provided bellow. Additional information can be found in specialized publications [95,103-107,110,145].

7.1.1 Scanning electron microscopy with energy-dispersive X-ray spectrometry (SEM/EDS)

Optical microscopy is generally capable of resolving the pigment particles found in historical paintings, because these were hand-ground and normally vary in size between 1-10 µm. However, with the industrialisation in the 19th century, a large number of pigments were no longer hand-grounded but, instead, machine-grinded, producing much smaller pigments particles (0.1-0.5 µm), so small and scattering light so efficiently, that can barely be resolved by the optical microscope [21,89]. In such cases, where high resolution is required, a microscopic technique using radiation with lower wavelength than the visible light must be employed, since the lower the wavelength of the incident radiation, the highest the resolution. The most commonly used technique is electron microscopy, either scanning electron microscopy (SEM) or transmission electron microscopy (TEM), that employs as incident radiation a beam of highly energetic electrons, with wavelengths that can go down to 0.01 nm.

The excellent resolution and high magnifications obtained with electron microscopy, in particular SEM, which is regularly applied for the examination of cross-sections, allows not

only the analysis of these smaller pigment grains, but also the study of the deterioration processes never considered by the painter [21]. Although SEM is also used for morphology examination of pigments and samples, the main used of SEM is the identification of the elemental composition of pigments in samples [3], because nowadays most scanning electron microscopes are coupled to one (or more) x-ray spectrometer that detects the X-rays emitted when the electron beam interacts with the sample's surface (SEM/EDS).

Setup

By heating a tungsten filament, electrons are produced and accelerating them across a huge potential difference, an electron beam is produced, which is usually focused on the sample using electromagnetic fields (lenses cannot focus electrons).

When the electron beam hits the sample, a large number of interactions can occur between the incident electrons and the atoms of the sample. Among these interactions, the production of secondary and backscattered electrons is used to produce electronic images of the sample surface, while the production of X-rays is used for the elemental/chemical analysis of the sample [105].

An important requisite of electron microscope is the fact that the sample's surface must be electrically conducting. When the sample surface is not electrically conducting, it will tend to become negatively charged during analysis, causing repletion with deviation of the beam electrons from its normal path and consequent distortion of the image and artifacts. Besides, degradation caused by beam heating or radiation damage of a sample can also occur. To make the sample surface electrically conducting, a thin coat layer of a conducting material, such as gold or carbon is usually deposited over its surface. Since the coating will absorb the X-rays emitted from the sample and will also emit its own characteristic X-rays, the coating should be as thin as possible, be of as low atomic weight as possible and must not contain any element which might be of interest, i.e. carbon coatings should not be used if we are interest in detected carbon in the sample [105,110].

Electronic images

As the name of the technique indicates (SEM), the produced images are scanning images, sequentially built up, pixel by pixel and line by line. The electron beam is scanned across the surface of the specimen in a motion similar to a television camera, while the detector counts the number of electrons (secondary or backscattered) given off from each point on the surface. The resultant image, an enlarged monochromatic image of specimen, is

displayed on a computer screen and can be stored as a digital image, which can easily be operated in any image software.

There are two types of electronic images, secondary electron and backscattered electrons images.

Secondary electron images are images produced by the secondary electrons, i.e. electrons that escape from the specimen with less than 100 eV (low energetic electrons). Because these electrons present a small sampling volume, Figure 7.1, (the detected secondary electrons signal are originated in a region that is little larger than the incident beam's diameter) they can originate a better spatial resolution than other signals and produce images where the contrast is associated to the topography of the sample.

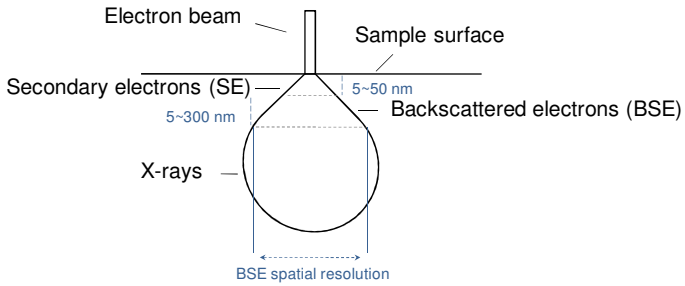

Figure 7.1 The interaction volume and the regions from which secondary electrons, backscattered electrons and X-rays can be detected (adapted from *Goodhew PJ, et al.* [105] and *Leng Y.* [110]).

Backscattered electrons images are images produced by the backscattered electrons, i.e. incident electrons that after a few collisions inside the sample emerge at its surface. Although their penetration in the sample is generally limited to a fraction of a micrometer, it is larger than the penetration of the secondary electrons, Figure 7.1, hence they yield information at a worse spatial resolution. However, as the backscattered electron coefficient, i.e. the number of backscattered electrons emitted from the specimen is strongly dependent of the atomic number, backscattered electrons produce atomic number contrast image. The different chemical elements are represented by various shades of grey, the heaviest elements appear with a bright colour while the lightest with a dark one. Care must be taken as the contrast from adjacent elements is quite small, and consequently the resolution between phases with similar atomic number may be very poor.

Backscattered electrons are usually not as numerous as the secondary electrons, but the improvement in backscattered detectors during the past few years, greatly increased the use of this image mode, particularly when used in conjunction with energy dispersive X-ray analysis.

Elemental analysis

During the interaction of the electron beam with the sample, X-rays characteristic of the atoms present in the sample are produced, allowing the qualitative and/or quantitative elemental analyse of the sample.

Whenever atoms are hit by energetic photons or particles, such as the electrons of the electron beam, an electron is ejected from an inner shell (K, L or M) of the atom, living a vacancy and the atom in an excited state, highly energetic and unstable. In order to relax to its fundamental energy state, an electron from an outer shell immediately fills the electron vacancy and the excess of energy is released as a photon. Because the energy of the photon corresponds to the difference between the two electronic states, it is highly characteristic of that atom.

Although in a large atom there is a large number of possible electron transitions, each one leading to an X-ray of a unique wavelength; the K series lines are the most frequently used for analysis, followed by the L series lines, which are used to identify high atomic number atoms, since the energy necessary to excite the K series of lines of these atoms is extremely high and not always achievable.

Because X-rays energies (or wavelengths) of almost all known elements have been precisely measured and can be easily found in any book dealing with X-ray spectrometry, coupling an X-ray detector to the electron microscope is possible to perform an elemental analysis. However, light elements are particularly difficult to detect, since the X-rays that they produced are easily absorbed by the sample and by the detector's window [105].

There are two types of systems for elemental analysis, the wavelength dispersive spectrometer and the energy dispersive spectrometer. The wavelength dispersive spectrometer (WDS) can determine very accurately the position of a single X-ray line (resolving closely spaced lines), thus identifying a wider range of elements that the energy dispersive spectrometer (EDS). Although presenting some loss of precision and resolution relatively to WSD, EDS system quickly gained importance due to the fact that it much less expensive than WSD and can collected X-rays of all energies simultaneously, allowing a qualitative analysis in just a few seconds to minutes [105,110].

Environmental scanning electron microscopy

Because electrons are strongly scattered off by anything that gets on the way and the electron source is easily contaminated, a moderately high vacuum is used in conventional SEM in order to allow electrons to travel unhindered [105,424]. This imposed several restrictions to the sample under analysis. The samples had to be clean, dry and electrically conductive. Conductivity is obtained by coating the sample surface with a conductive coating as above

described; while wet and/or oily samples are dehydrated or cleaned previous to analyse to avoid sample destruction and image artifacts [103,110].

Over the past years, scanning electron microscope which can operate in a range of pressures (from high vacuum to pressures capable to avoid dehydration), temperatures (up to 1500 ºC, since the environmental secondary detector is insensitive to heat) and gas composition, i.e. environmental scanning electron microscope (ESEM), have been developed overcoming the problems found for the conventional SEM [424].

Working at poor vacuum, conductive coating is not a requirement as any possible charge accumulation is dissipated by the gas inside the sample compartment, which is a good conductor; drying out of water or the volatilization of oily films does not occurs immediately, not affecting image quality, thus, wet, dirty, oily samples can be analysed without any previous cleaning or preparation/modification as occurs for conventional SEM [103,105,110,424,425].

Besides sample imaging, X-ray microanalysis is also possible with ESEM. However, at high pressures there is generally a loss of spatial resolution, due to the scattering of the primary electron beam in the presence of the gas molecules, named “beam skirting”. Due to the presence of the gas, the electrons are scattered out from the primary beam, forming a low profile skirt around the primary beam, hence, significant contributions from areas outside the focus of the primary beam do occur, imposing several limitations to X-ray microanalysis [424-426].

7.1.2 Micro X-ray diffraction (μ-XRD)

X-ray diffraction is a classic, accurate technique of molecular structure determination, which has been extensively applied in conservation/restoration, to identify pigments, corrosion products, metallic alloys, ceramic materials, pollution slats, and minerals. This technique is based in the diffraction of an incident X-ray beam by the reticular plans of a crystalline material and identification is performed comparing the results with reference files.

Whenever a wave finds an obstacle or a hole of dimensions comparable to its wavelength, diffraction occurs: sound waves (λ of the order of 1 m) are diffracted by macroscopic objects, light waves (λ of the order of 500 nm) are diffracted by narrow slits [427] and X-rays (λ of the order of 0.01-10 nm) are diffracted by crystals [428].

A crystal can be defined as a solid composed by atoms, molecules, groups of atoms, group of molecules or ions arranged in a three-dimensional periodic pattern, i.e. the regularly repeating of a ‘structural motif’. The pattern adopted is generally expressed in terms of an

array of imaginary points, which have a fixed relation in space to the atoms, called the *lattice*, which may be regarded as a sort of framework or skeleton of the crystal.

When a monochromatic X-ray beam[77] of wavelength λ falls on a crystal, a small fraction of it will collide with electrons in the atoms that constitute the crystal and will be elastically scattered (has the same wavelength/frequency of the incident beam) in all directions [106]. For some directions, the scattered rays will be out of phase and they will interfere destructively, giving a smaller amplitude, or even cancel, but for other directions the scattered rays will be in phase and they will interfere constructively, giving greater amplitude. Consequently, a pattern of varying intensity, called diffraction pattern, is produced.

Since a crystal presents a regular array of obstacles (the atoms) we can think of each plane of obstacles as a slit-type diffraction grating (for the X-rays), i.e. the waves scattered from that given plane will only add constructively if the 'reflection' angle equals the incident angle (θ) [428]. However, as the crystal is a three-dimensional structure and the X-ray will penetrate the crystal, we must consider the scattering from many sets of planes (Figure 7.2).

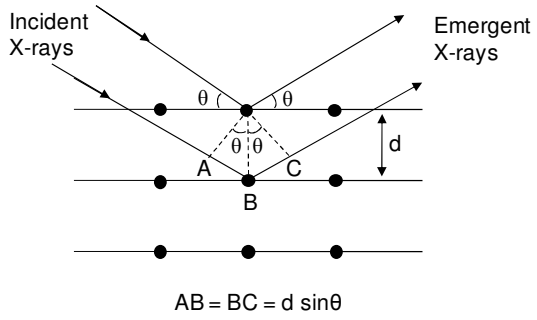

Figure 7.2 X-ray diffraction between adjacent Bragg planes (adapted from *FishbanePM, et al.* [428]).

From geometric calculations it is possible to determine that constructive interference of the waves scattered by two adjacent d spaced planes occurs only when the path difference between the two waves (AB + BC = $2d\ sin\theta$) is an integral multiple of the X-ray's wavelength ($n\lambda$) [106,428], that is, constructive interfere will occur only when the incident angle satisfies the equation known as Bragg's law:

$$2d\ sin\theta = n\lambda \tag{7.1}$$

[77] As referred for SEM/EDS, X-rays can be produced by the interaction of accelerated electrons with matter. Monochromatic X-ray beams are produced by X-ray tubes, where accelerated electrons hit a target surface, producing X-rays characteristics of that surface. A filter system is them employed to filter in the most intense line (Kα, for the copper target surface) and filter out continuous X-rays and other less intense characteristic lines.

where d is the interplanar spacing (the distance between the crystallographic planes), θ the incidence angle, n an integer number (n=1, 2, 3, …) and λ the wavelength of the incidence radiation.

Because the position and intensity of the diffracted beams will depend of the arrangements of the atoms (molecules or ions) in space and of some other atomic properties (in the case of X-rays, especially of the atomic number of the atoms), each diffraction pattern is unique and characteristic of a specific compound and can be used for identification purposes.

The most widely used X-ray diffraction method for artwork compounds identification is still the powder method [(3)], which requires the reduction of the sample to a homogeneous powder. This preparation ensures that there are many crystallites randomly oriented and consequently, that some of them will always be oriented so as to satisfy the Bragg condition. However, this procedure, besides destroying the sample's stratigraphy also, requires a significant amount of sample, being non-viable for the study of most artworks.

Thanks to technologic developments, nowadays it is possible to perform X-ray diffraction analysis of a small area of a sample or object in a non-destructive or even *in-situ* mode, using a conventional laboratory X-ray source[78]. It is the so called micro X-ray diffraction analysis (μ-XRD) and this method basically consists in the use of a collimating capillary that reduces and focus the diverging X-ray beam to a small spot beam at the sample surface with diameter as small as tens of micrometers. The sample fragments without any preparation, cross sections, thin sections [(108,429,430)] and even art objects of reduced size are placed over the equipment stage, the X-ray beam is focused in a small area of interest and the respective diffractogram is collect.

7.1.3 Fluorescence microscopy (FM)

When observed under ultraviolet (UV) light, some materials/compounds exhibit very characteristic auto-fluorescence [(3)] than can be used to support identification purposes. The examination of artists' materials using ultraviolet fluorescence microscopy has been used to help in pigment identification (for example, zinc white and madder exhibit unique visible fluorescence), to provide clues regarding the binder (oil, protein or modern synthetic resin), to help the distinction of layers and particles that appear similar under visible light and to identify retouchings and overpaints (for example, traditional drying oils fluoresce more

[78] The high brilliant synchrotron radiation sources used in the Synchrotron X-ray microdiffraction (SR μ-XRD) are known for allowing the analysis of smaller areas in reasonable time, with a high precision and accuracy. However, due to their huge size, synchrotron sources are of limited availability.

strongly as they age, consequently, retouch/restoration/overpaint layers appear darker than old paint layers when viewed under ultraviolet light) [78,145,431].

Nonfluorescent compounds can also be visible and therefore detectable under UV light if previously tagged with a fluorescent dye or fluorochrome.

Fluorescence is a type of luminescence process in which electronic excited-state atoms, ions, or molecules (promoted by absorb a photon) spontaneous and rapidly drop to a lower electronic state, releasing a photon with a lower energy (longer wavelength) than the absorbed one; being the exceeding energy released in the form of molecular vibrations or heat. Because the absorption and the following emission events occur almost simultaneously, fluorescence stops when the exciting source is turned off.

A fluorescence microscope, in reflection mode (Figure 7.3), which provides a high-contrast efficient imaging that the transmission mode, consists basically in: an UV, violet or blue bright light source; an objective that acts both as condenser, converging the excitation light on the sample, and as objective, collecting the light reflected by the sample and forming an image of the sample in the image plane; and a *fluorescence filter set* also referred to as *fluorescence filter cube* (due to its shape), composed by three essential filters – excitation filter, dichroic mirror and emission filter. The excitation filter acts as a barrier to wavelengths from the source, selectively transmitting a band of short wavelengths. The dichroic mirror (or beam splitter) reflects the selected wavelengths towards the objective (which focused them on the sample) and transmits the fluorescent light emitted by the sample towards the eyepieces or digital camera. It also directs any excitation light reflected by the sample back toward the source. Finally, the emission filter transmits the visible light wavelengths emitted by fluorescence, while blocking any residual excitation light [110-145].

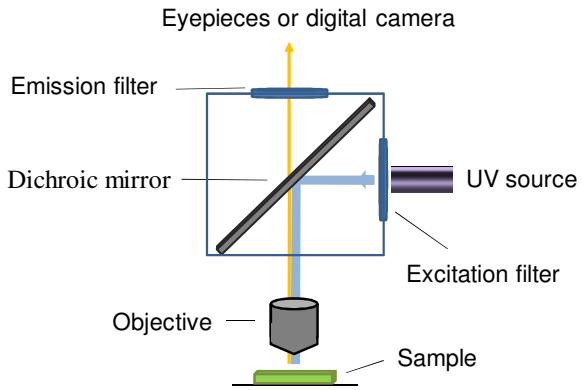

Figure 7.3 Schematic diagram of the configuration of a reflected light fluorescence microscope, in which the filters are arranged in a fluorescence filter cube (adapted from *Murphy DB.* [145]).

7.2 Experimental Conditions

7.2.1 SEM/EDS

Sample preparation

The SEM/EDS analysis was conducted using the cross-sectioned samples prepared for OM and used for µ-R. Table 7.1 indicates the samples (32) analysed by this technique in two different equipments (see below). Due to the low conductivity of the samples, the surface of all the cross sections had to be covered with a thin film of carbon. In the case of the cross sections analyzed in the Hitachi S-2400, in order to place several samples into the sample chamber at the same time, bulk of the excess resin block was removed with a cutting saw, causing some crakes.

Table 7.1 Samples analysed by SEM/EDS

	Painting	Samples	
		Philips XL30	Hitachi S-2400
A	*Casa Rústica de Campanhã*	-	A3
B	*O mendigo Lapita*	-	B3
C	*Paisagem - Abertura da Rua Alexandre Herculano*	-	C4
D	*Jardim de Luxemburgo (estudo)*	-	D2
E	*Aldeia de St. Sauves*	-	E1
F	*Paisagem de St. Sauves*	F1, F5	F6
G	*Cansada (Cachopa de Capri)*	-	-
H	*Casas brancas de Capri*	H1, H5	-
I	*Cecília*	I1	I7
J	*Escadas de um pardieiro - Roma*	J2	-
K	*Esperando o sucesso*	K7	-
L	*Fachada de casa soterrada - Roma*	L3	-
M	*Mirágem de Nápoles*	M1	-
N	*Portão*	-	N3
O	*Rapariga de Anacapri*	-	O1
P	*Rua de Roma*	-	P1
Q	*Senhora vestida de preto*	Q5, Q6	Q4
R	*Janela das persianas azuis*	R8	R1
S	*Mulher da água*	S5, S7	S2
T	*Paisagem de Anacapri*	T2	T4, T7
U	*Rapariga deitada no tronco de uma árvore*	-	-
V	*Cais de Barcelona*	-	V3
W	*Flores campestres*	W4	-

Experimental set-up

The SEM/EDS analysis was carried out using two different equipments in two different laboratories. The first apparatus, owned by the Archaeology Department of ULC, London, was a Philips XL30 environment scanning electron microscope (ESEM) operating at high

vacuum, coupled to an Oxford INCA energy dispersive X-ray spectrometer (EDS). The electron source is a tungsten filament and the accelerated voltage was set to 20 kV. The second apparatus, owned by the Departamento de Materiais of UTL-IST, Lisbon, was a Hitachi S-2400 scanning electron microscope (SEM), coupled to a Rontec energy dispersive X-ray spectrometer (EDS). The electron source is a tungsten filament and the accelerated voltage was set to 25 kV.

7.2.2 µ-XRD

Sample preparation

The µ-XRD analysis was conducted using the bulk samples (samples without any preparation). Table 7.2 indicates the samples analysed by this technique (24). Among them, 9 were also analysed by SEM/EDS.

Table 7.2 Samples analysed by µ-XRD

	Painting	Samples
A	*Casa Rústica de Campanhã*	A1, A4
B	*O mendigo Lapita*	B1, B3
C	*Paisagem - Abertura da Rua Alexandre Herculano*	-
D	*Jardim de Luxemburgo (estudo)*	-
E	*Aldeia de St. Sauves*	-
F	*Paisagem de St. Sauves*	-
G	*Cansada (Cachopa de Capri)*	-
H	*Casas brancas de Capri*	H4, H8
I	*Cecília*	I1, I3
J	*Escadas de um pardieiro - Roma*	J2
K	*Esperando o sucesso*	K5, K7
L	*Fachada de casa soterrada - Roma*	L3
M	*Mirágem de Nápoles*	-
N	*Portão*	N5
O	*Rapariga de Anacapri*	-
P	*Rua de Roma*	-
Q	*Senhora vestida de preto*	Q5
R	*Janela das persianas azuis*	-
S	*Mulher da água*	S1, S2, S5, S7
T	*Paisagem de Anacapri*	T2
U	*Rapariga deitada no tronco de uma árvore*	-
V	*Cais de Barcelona*	V3
W	*Flores campestres*	W1, W2, W4, W7

Experimental set-up

The µ-XRD analysis was carried out using a Bruker D8 DISCOVER diffractometer equipped with Cu Kα radiation, a Göbel mirror assembly and a GADDS detector, owned by the LCRJF, Instituto dos Museus, Lisbon. The angular range (2θ) was scanned from 6.2 to

71.6° at a step size of 0.02° and the working voltage and current were, respectively, 40 kV and 40 mA. To allow the analysis of relatively small areas of interest in the samples, a 1-mm-diameter pinhole collimator was used. Different acquisition times were used, depending of the sample. The diffractograms were background subtracted and analysed using Bruker EVA software. Phases were identified by comparison with the Joint Committee on Powder Diffraction Standards – International Centre for Diffraction Data (JCPDS-ICDD) database files.

7.2.3 FM

Sample preparation

The FM analysis was conducted using the cross-sectioned samples prepared for OM and used for μ-R and SEM/EDS. Table 7.3 indicates the samples (9) analysed by this technique. Among these, 4 were also analysed by SEM/EDS and another 4 by μ-XRD.

Table 7.3 Samples analysed by FM

	Painting	Samples
A	*Casa Rústica de Campanhã*	-
B	*O mendigo Lapita*	-
C	*Paisagem - Abertura da Rua Alexandre Herculano*	C2
D	*Jardim de Luxemburgo (estudo)*	-
E	*Aldeia de St. Sauves*	-
F	*Paisagem de St. Sauves*	F1, F4
G	*Cansada (Cachopa de Capri)*	G3
H	*Casas brancas de Capri*	-
I	*Cecília*	-
J	*Escadas de um pardieiro - Roma*	J2
K	*Esperando o sucesso*	K7
L	*Fachada de casa soterrada - Roma*	-
M	*Mirágem de Nápoles*	-
N	*Portão*	N5
O	*Rapariga de Anacapri*	-
P	*Rua de Roma*	-
Q	*Senhora vestida de preto*	Q5
R	*Janela das persianas azuis*	-
S	*Mulher da água*	-
T	*Paisagem de Anacapri*	-
U	*Rapariga deitada no tronco de uma árvore*	-
V	*Cais de Barcelona*	-
W	*Flores campestres*	W3

Experimental set-up

The FM analysis was carried out using a Leitz Laborlux 12 ME microscope fitted with a filter system A cube (UV excitation range, exciting filter BP 340-380) or a filter system I 2/3 cube (excitation filter BP 450-480), at Victoria and Albert Museum, London.

7.3 Results and discussion

As previously referred, SEM/EDS, µ-XRD and FM were employed in order to, either confirm, or clarify the results of the vibrational analysis. Depending on the doubts, one, two or even the three auxiliary techniques were employed. Results will be presented and discussed by pigment and/or question.

Whenever the auxiliary techniques were used to corroborate results obtained µ-IR and/or µ-R these are described as “comfirmed”, while whenever the auxiliary techniques allow the identification of a compound not identified by the vibrational techniques, the results are described as “identified”. However, since SEM/EDS only provides elemental composition, not allowing to the distinction between compounds with similar elemental composition, the identification based on this technique must be done cautiously.

Photomicrographs of the samples to which reference is made, but are not presented, can be found in Appendix D. Backscattered images of all the samples analysed by SEM/EDS can be found in Appendix E. JCPDS-ICDD files of the main phases identified by µ-XRD are presented in figure’s caption.

Restoration samples

During the analysis by OM, µ-IR and µ-R, three samples showed a different behaviour from all the others: samples **T2** (Figure 7.4a) from ***Paisagem de Anacapri***, **W4** (Figure 7.4b) and **W7** from ***Flores Campestres*** (Figure D150). Unexpectedly, only kaolinite was detected in the ground layer of these three samples, whereas in all other samples the ground layer is mainly composed by lead white. This raised some questions about their origin, and the suspicion that they migh have been removed from restoration areas. Both SEM/EDS and µ-XRD were employed to confirm the origin of the samples.

The backscattered images of samples **T2** and **W4** (Figure 7.4c and d) clearly shows kaolin sharps particles in the layer 1, while its SEM/EDS elemental analysis detects aluminium, silicium, oxygen and potassium, elements present in kaolin and no lead at all was detected (Figure 7.5a).

The analysis of the upper layer(s) of these samples by SEM/EDS and µ-XRD is in accordance with the results of µ-IR and µ-R: no lead white, only zinc white (Figure 7.5b-c andFigure **7.6**).

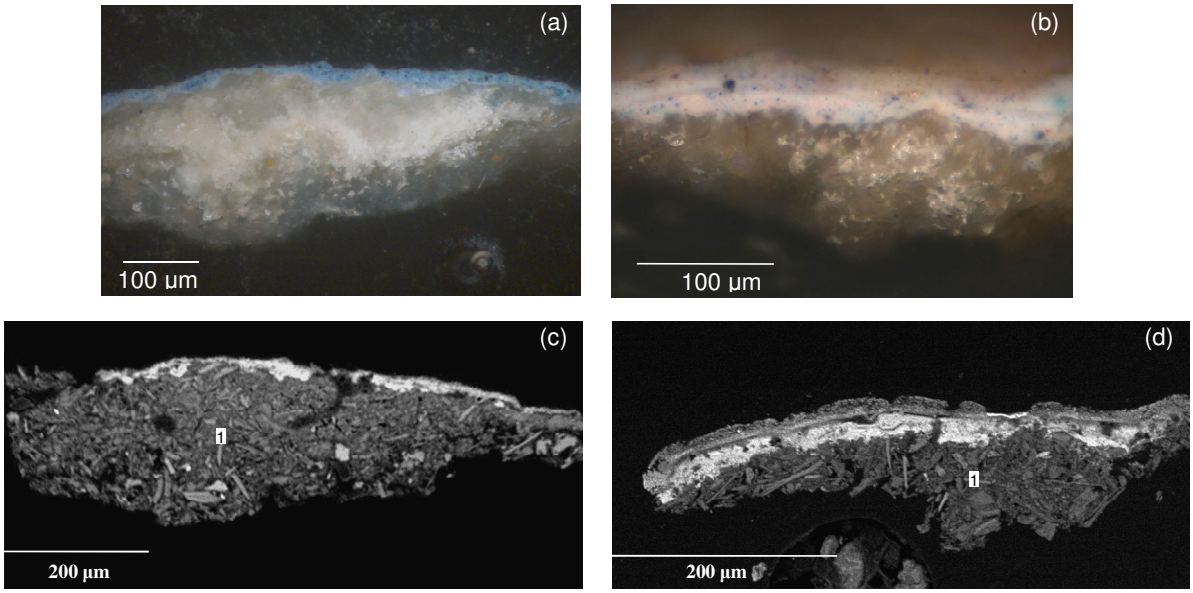

Figure 7.4 Cross section of the samples: (a) **T2** and (b) **W4** under reflected light. Backscattered images of the samples: (c) **T2** and (d) **W4**.

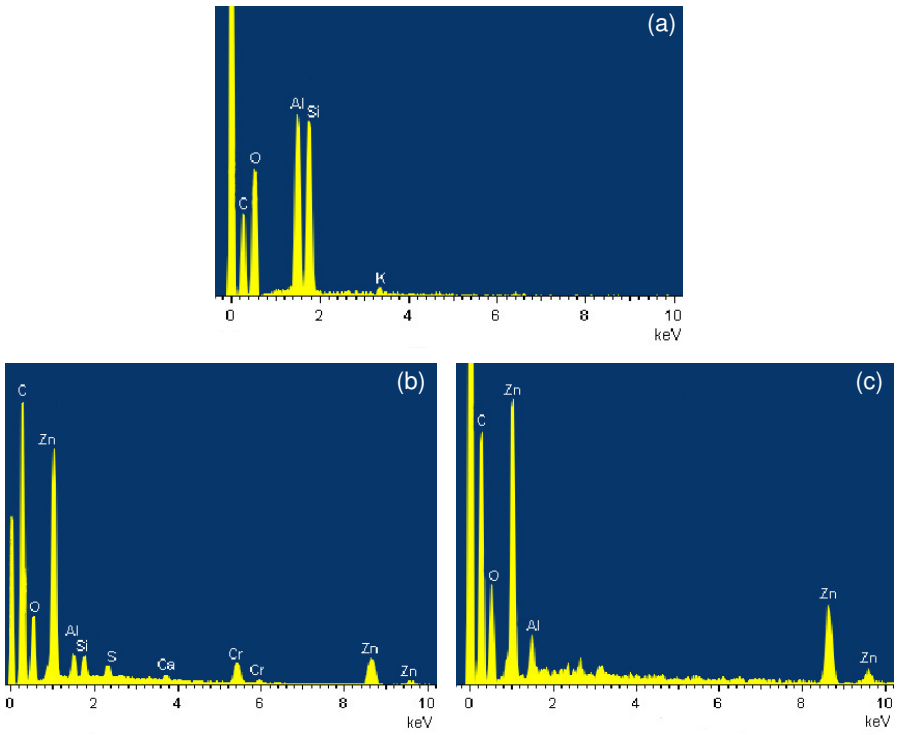

Figure 7.5 SEM/EDS spectra of: (a) white layer 1 of sample **W4**, (b) blue layer 2 of sample **T2** and (c) grey layer 3 of the sample **W4**.

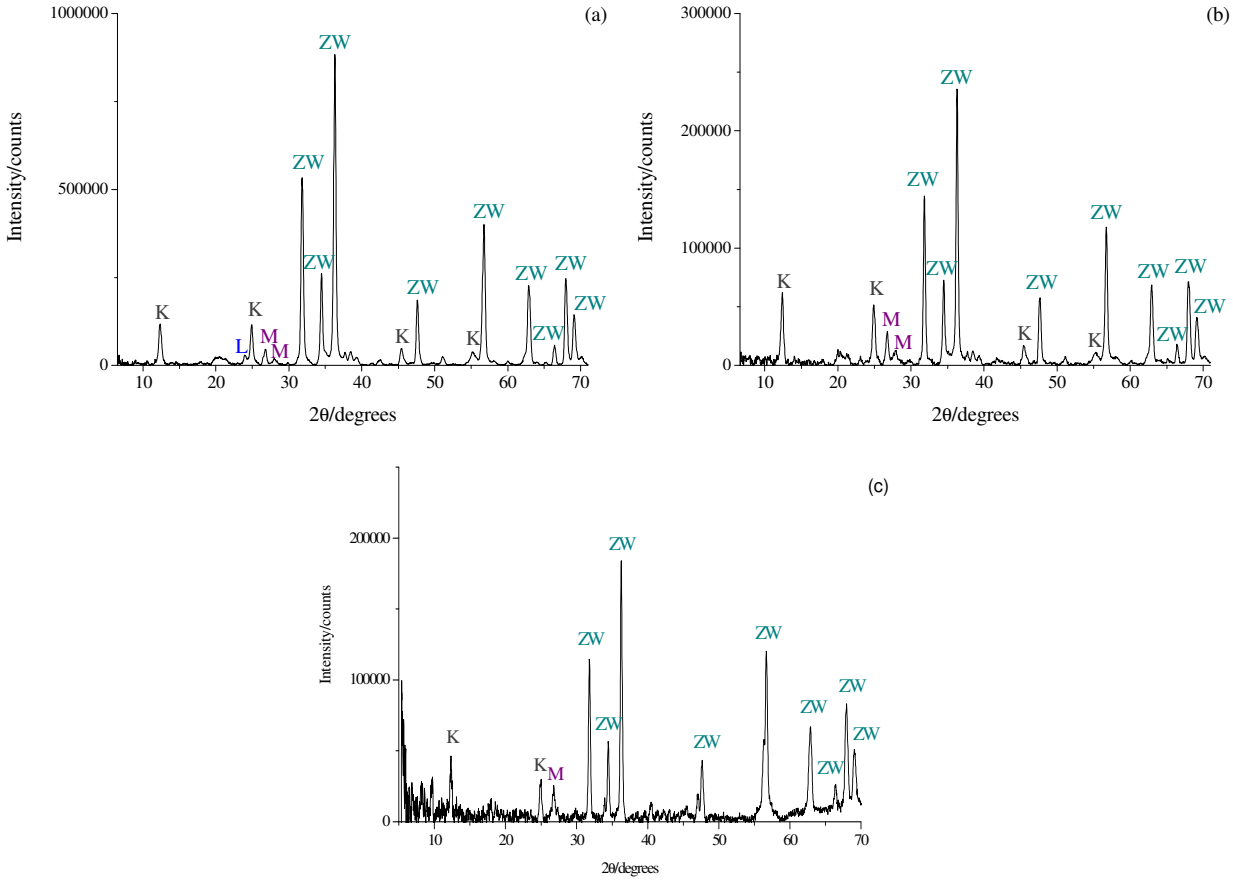

Figure 7.6 X-ray diffraction pattern of: (a) the blue layer 2 of sample **T2,** (b) the grey layer 3 of sample **W4** and (c) the grey layer 3 of sample **W7**. Phase abbreviations: K- kaolinite (JCPDS 080-0885), L-Lazurite-C (JCPDS 046-0103), M-muscovite ((a) JCPDS 006-0263; (b) 082-0576) and ZW-zinc white ((a) JCPDS 036-1451; (b) 005-0664).

The records of the intervention carried out in 1984 (at LCRJF), referred that, both ***Paisagem de Anacapri*** as ***Flores Campestres*** were retouched, and that a mixture of kaolinite with animal glue was normally used to fill lacunae. Moreover, by then, due to its toxicity, lead white had been fully replaced by other white pigments, hence would not have been used by restorators.

Based on these records and the above presented results, it can be conclude that samples **T2**, **W4** and **W7** are from restorations areas, rather than from the original painting. Therefore, these samples will not be considered for further analysis.

Cadmium yellow

As illustrated in Figure 6.60b, the identification of cadmium yellow (cadmium sulfide), CdS, by μ-R was normally very difficult, since, at best, a very weak spectrum was acquired and most of the times it was not possible to acquire a spectrum at all. Besides, since its IR bands occur bellow 650 cm^{-1} [432], its identification by μ-IR was not possible.

SEM/EDS was purposely used to confirm the presence of this yellow pigment in some of the samples [79]. In other samples, this pigment was identified by chance, when the presence of other compounds was being confirmed. This was the case of sample **F6**, which was analysed by SEM/EDS to confirm the existence of emerald green and viridian.

In sample **F6**, two yellow pigments, namely chrome yellow and zinc yellow, had been identified by μ-R and apparently no other yellow pigment was present. However, the acquisition of a SEM/EDS spectrum for the yellow pigment grains of green layer 2 exhibiting only the peaks of cadmium and sulfur (Figure 7.7) allowed the identification of this pigment with quite certainty.

Because cadmium yellow was mixed with two yellow and a blue pigment (Prussian blue), the three with very good Raman responses, its weak Raman signal was masked.

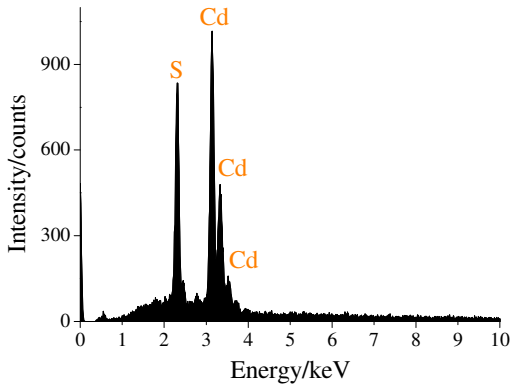

Figure 7.7 SEM/EDS spectrum of the yellow pigments of green layer 2 from sample **F6**, identifying cadmium yellow.

Cadmium yellow was confirmed by SEM/EDS in the paintings: ***Miragem de Nápoles*** (**M3**) and ***Cais de Barcelona*** (**V3**), and identified in the paintings: ***Paisagem de St. Sauves*** (**F6**), ***Fachada de casa soterrada - Roma*** (**L3**), ***Portão*** (**N3**), ***Mulher da água*** (**S2**) and ***Paisagem Anacapri*** (**T7**).

[79] μ-XRD was not employed due to the reduced size of the cadmium yellow pigment grains present in the samples and to their apparently low amount.

Carbon-based black pigments

As referred in the previous chapter, μ-R analysis of the carbon-based black pigments provided different results from those obtained by μ-IR. While μ-R identified only a carbon-based black material, μ-IR was able to go further and identify, in the samples where the pigment was present in a large amount, the carbon-based black material as the bone/ivory black pigment.

The differentiation between carbon-based black pigments by SEM/EDS elemental analysis is normally very difficult because these pigments are mainly composed by carbon if not only composed by carbon. However, because bone and ivory black pigments, prepared by charring waste ivory or bone, respectively, contain also phosphorous, calcium, oxygen and even magnesium, and black pigments with an argillaceous content, such as graphite and black chalk, contain also silicon and aluminium (potassium, iron and titanium can also be present) [407], differentiation can be possible. For example, SEM/EDS elemental analysis of the black layer of sample **Q4** (Figure 7.8) indicates a high phosphorus and calcium content, characteristic of bone/ivory black pigments, in agreement with the μ-IR result.

A relatively high amount of silicon is also visible (Figure 7.8b), suggesting that another black pigment, possibly one with an argillaceous content, is also present. The existence of an argillaceous (may produced high fluorescence) carbon-based black pigment in sample **Q4** could explain why μ-R was able to identify the phosphate band in the reference sample of bone/ivory black (Figure 6.64d) but was not able to do it in this and other painting's samples.

The identification of cobalt and tin, suggest that the blue pigment particles, not identified neither by μ-R nor be μ-IR are cerulean blue, while the identification of lead, suggest that lead white not identified either by μ-R or by μ-IR, is probably also present.

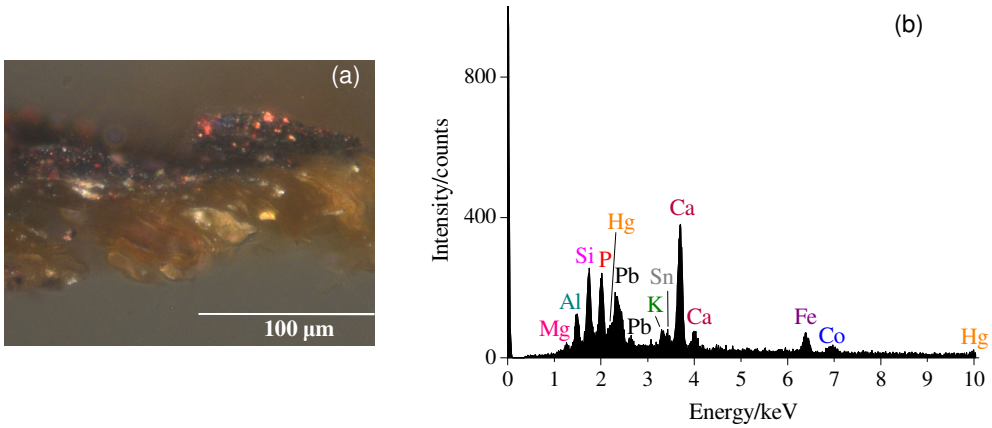

Figure 7.8 (a) Cross section of sample **Q4** under reflected light and (b) SEM/EDS spectrum of the black layer of sample **Q4**.

Cobalt blue and cerulean blue

Similarly to what happened with cadmium yellow, also the identification of cobalt blue (cobalt aluminate), $CoAl_2O_4$ was very difficult by μ-R, since the Raman spectra of this pigment were, at best, very weak (Figure 6.37). In those worst cases, Prussian and ultramarine blue, which exhibits a good Raman response, were excluded, but the presence of other blue pigments, such as smalt and cerulean blue had to be questioned. Because cobalt blue IR bands occur at 665, 558 and 512 cm^{-1} [238,420], near and below the detector's cut-off (650 cm^{-1}), this pigment was not identified by μ-IR in any of the samples.

Due to the general amorphous nature of cobalt blue, μ-XRD analysis is unfruitful to its identification. Consequently, only SEM/EDS analysis was used to confirm, and even, identify the presence of this pigment. Cobalt blue was confirmed/identified by the simultaneous detection of aluminium and cobalt, when these elements could not be attributed to any other compound, as illustrated in the spectrum of the blue pigments of the upper layer of the sample **R1** (Figure 7.9b). The high content of lead is probably due to lead white which was identified in this sample by the vibrational techniques.

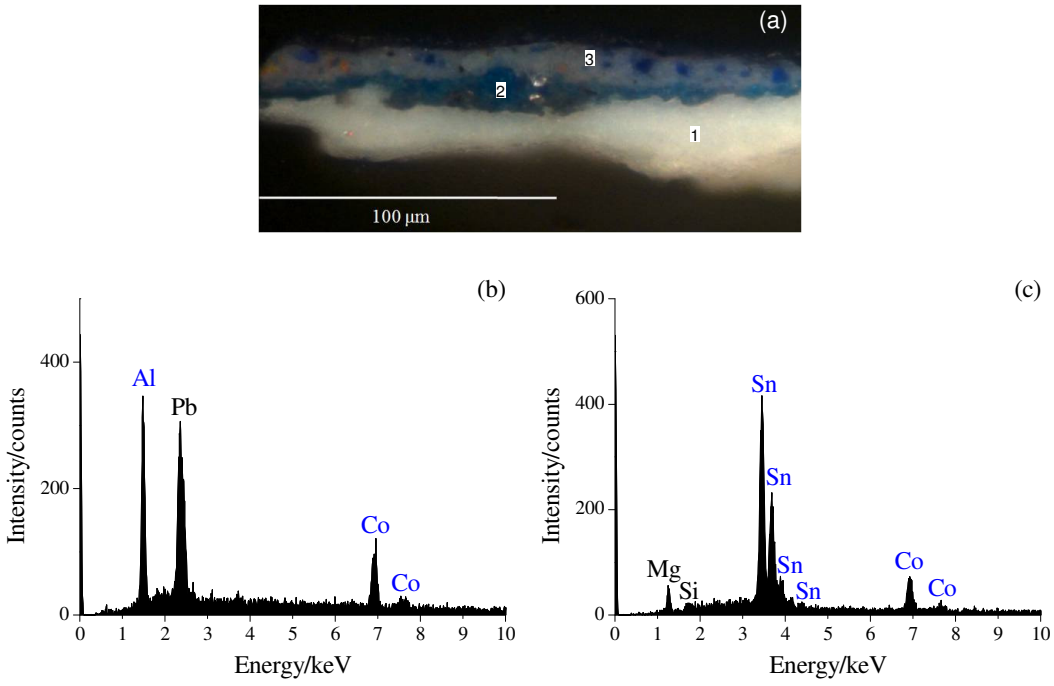

Figure 7.9 (a) Cross section of sample **R1** under reflected light; SEM/EDS spectra of the blue pigments of: (b) blue layer 3 of sample **R1** and (c) layer 2 of sample **R1**.

Cobalt blue was confirmed by SEM/EDS in the paintings: ***Casas brancas de Capri*** (**H5**), ***Cecília*** (**I1**, **I7**), ***Rua de Roma*** (**P1**), ***Paisagem de Anacapri*** (**T4**), and identified by SEM/EDS in the paintings: ***Casa Rústica de Campanhã*** (**A3**), ***Estátua do jardim de***

Luxemburgo (estudo) (**D2**), ***Aldeia de St. Sauves*** (**E1**), ***Paisagem de St. Sauves*** (**F5**), ***Portão*** (**N3**), ***Rapariga de Anacapri*** (**O1**), ***Senhora vestida de Preto*** (**Q6**) and ***Janela das persianas azuis*** (**R1**).

Unexpectedly, during the analysis of some of the samples by SEM/EDS and μ-XRD, in order to confirm the presence of suspicious pigments, another cobalt pigment, cerulean blue (cobalt stannate), $CoO.nSnO_2$, was identified. For example, the SEM/EDS spectrum of the blue pigments of the blue layer 2 of the sample **R1**, (Figure 7.9c) allowed the identification of cerulean blue by the simultaneous detection of tin and cobalt which could not be attributed to any other compound. And because cerulean blue is a crystalline phase (unlike cobalt blue) it was identified also by μ-XRD, as shown in the diffractogram of the blue layer 2 from the sample **I3**, Figure 7.10 (peaks **CB**).

Because the IR bands of this pigment occur below the detector's cut-off [249], its detection by μ-IR was not possible. However, the fact that no Raman signal from this pigment, known to produce a relative intense Raman spectrum [56,308], was acquired in any of the studied samples was very surprising and inexplicable.

Cerulean blue was identified by SEM/EDS in the paintings: ***Rapariga de Anacapri*** (**O1**), ***Senhora vestida de preto*** (**Q4, Q5**) and ***Janela das persianas azuis*** (**R1**, **R8**) and identified by μ-XRD in the painting ***Cecília*** (**I3**).

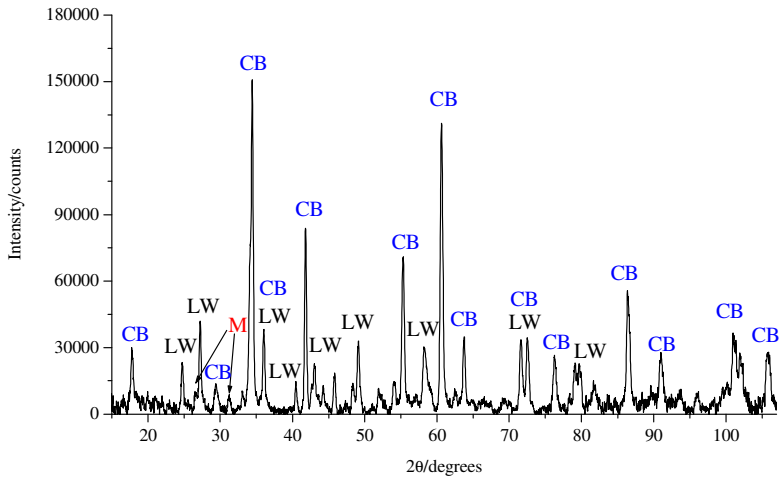

Figure 7.10 X-ray diffraction pattern of the blue layer 2 from the sample **I3**. Phase abbreviations: CB-cerulean blue (JCPDS 029-0514), LW-lead white (JCPDS 010-0401, 013-0131) and M-mercury^{II} sulfide (JCPDS 006-0256).

Copper pigment

As we can see in Figure 7.11a, the green layer of the sample **V3** is relatively thick and apparently contains a few green and yellow grain particles; neither μ-R nor μ-IR were able to identify the existing pigment(s). A high fluorescence background was obtained in the μ-R analysis, probably due to a high organic content, and, the IR acquired spectrum only exhibited bands of lead white, the major compound of the two lower layers, because it was not possible to analyse this green layer independently.

Both SEM/EDS and μ-XRD analysis were used specially in order to identify the green pigment(s) of the layer, since this(these) is(are) the responsible for the colour of the layer. Unfortunately, μ-XRD analysis only identified lead white, lead carbonate and quartz, giving no information regarding the coloured pigments. The SEM/EDS analysis, although producing a low intensity spectrum (Figure 7.11b) probably due to a high organic content, was able to provide elemental information about the green layer. Several elements were identified: aluminium, silicon, lead, potassium, calcium, barium, iron, zinc and especially copper, suggesting that a copper pigment is present.

Since no arsenic was identified, emerald green ($Cu(CH_3COO)_2.3Cu(AsO_2)_2$) and Scheele's green ($CuHAsO_3$) are excluded hypotheses. Possible copper-based pigments are still, malachite ($Cu_2CO_3(OH)_2$), brochantite ($Cu_4(OH)_6(SO_4)$), azurite ($Cu_3(OH)_2(CO_3)_2$) (mixed with a yellow pigment to produce green), and most probably, verdigris or copper resinate, two copper pigments that have a high organic content.

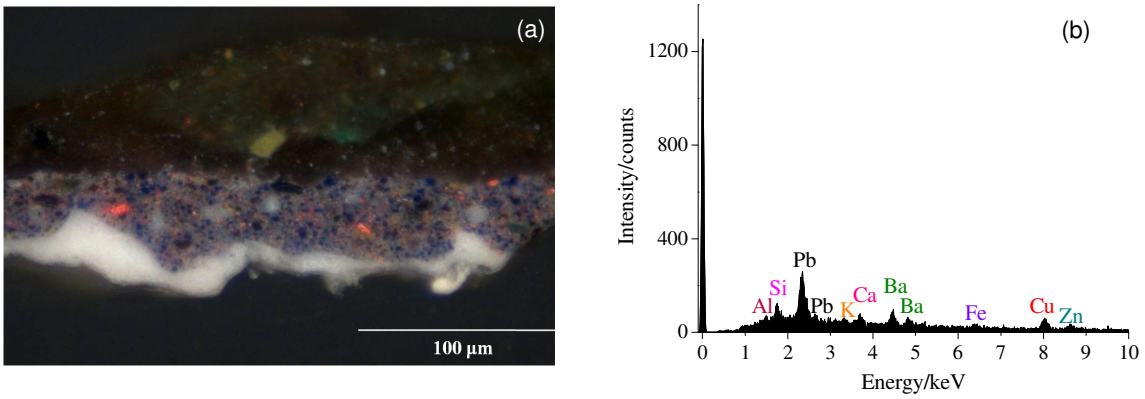

Figure 7.11 (a) Cross section of sample **V3** under reflected light and (b) SEM/EDS spectrum of the green layer 3 of this sample.

Lead antimonate yellow and associated compounds

As referred in chapter 6, the identification of lead antimonate yellow ($Pb^{II}_{y}Sb^{V}_{2-x}O_7$, where $2 \leq y \leq 3$ and $0 \leq x \leq 1$) by μ-R showed several difficulties, especially, concerning its differentiation from lead-tin-antimony yellow ($Pb_2Sn_xSb_{2-x}O_{7-x/2}$), that seems to have a very similar Raman spectrum. IR spectrum of this pigment is characterized by an intense band at about 670 cm^{-1} and other weaker bands bellow the detector's cut-off (650 cm^{-1}) [249,351,432]. However, probably due to a relative reduced amount, this pigment was not identified by μ-IR in any of the samples.

Therefore, μ-XRD and SEM/EDS were employed to corroborate the identity of the lead antimonate yellow reference sample (Figure 7.12) and to confirm the presence of this yellow pigment in the samples **I1**, **I3**, **S5**, **S7** by μ-XRD and in the samples **I1**, **I7**, **K7**, **Q6**, **S5**, **S7** by SEM/EDS.

Although, both lead antimony yellow and lead-tin-antimony yellow (even lead-tin yellow type II) have a cubic pyrochlore-type crystal structure, their different cell size (lead antimonate yellow < lead tin-antimony yellow < lead-tin yellow type II) allows their distinction by XRD [347]. As shown in Figure 7.12, the identity of the reference sample of lead antimonate yellow was confirmed.

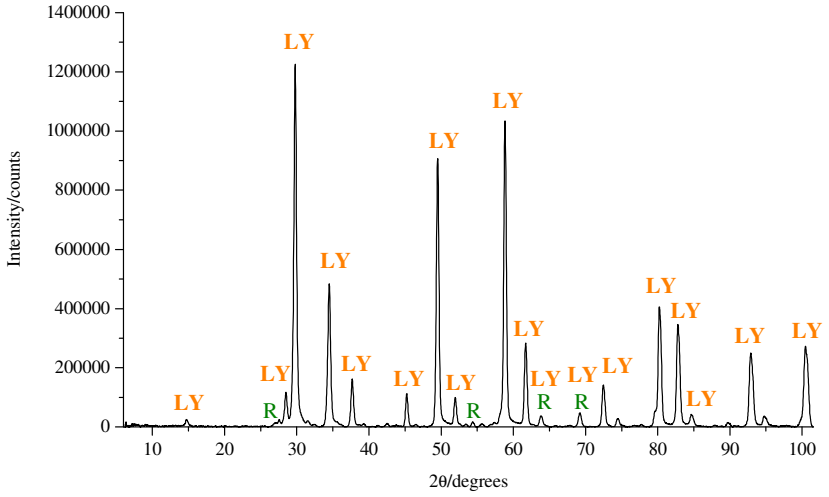

Figure 7.12 X-ray diffraction pattern of the reference sample of lead antimonate yellow. Phase abbreviations: LY-lead antimonate yellow (JCPDS 074-1354, 042-1355) and R-titanium oxide-rutile form (JCPDS 021-1276).

Lead antimonate yellow was also easily identified by μ-XRD in the four samples, matching the bindheimite synthetic phase (JCPDS: 18-0687) with a cell size a = 10.47 Å, while lead-tin-antimony yellow has a cell size of ca. 10.56 Å or a bimodal size 10.55-10.57 Å and 10.46-

10.51 [347,348]. Figure 7.13 presents the diffractograms of two of the samples where lead antimonate yellow was identified (lines are marked with **LY**).

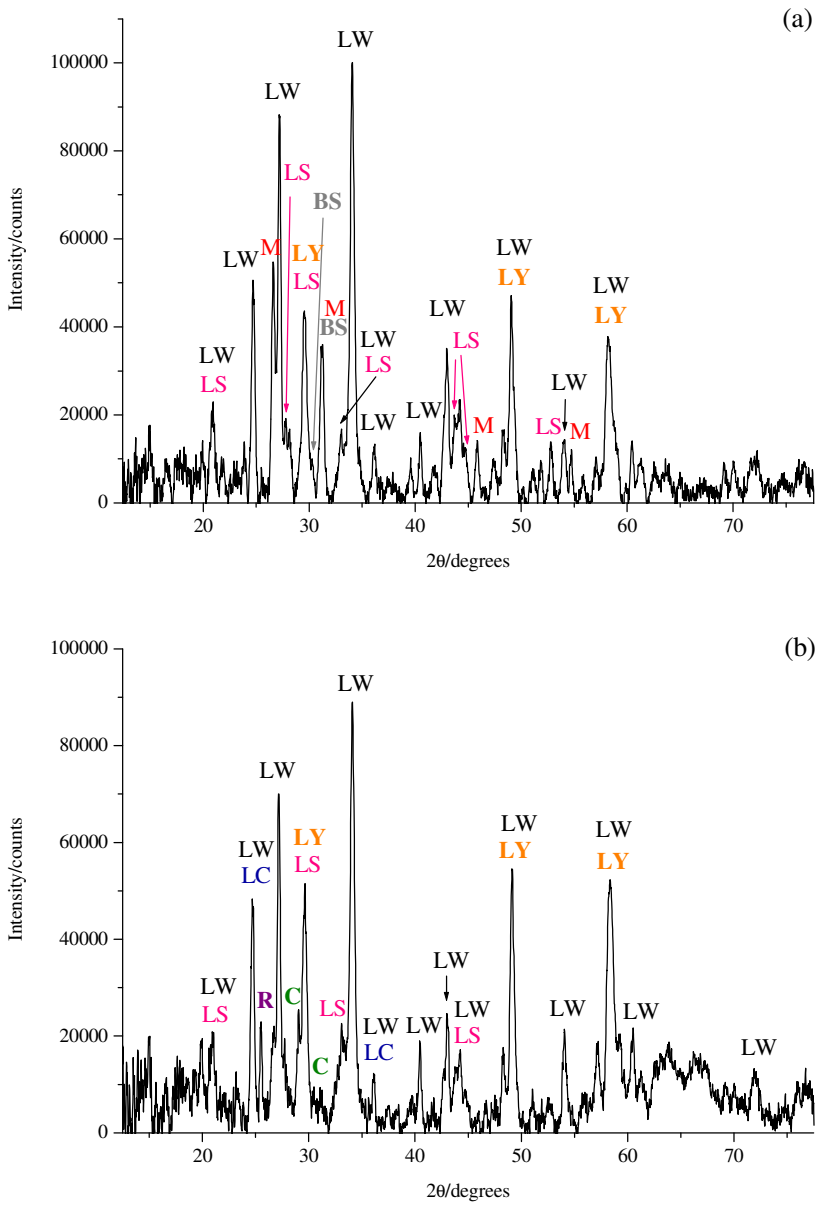

Figure 7.13 X-ray diffraction pattern of: (a) layers 4 and 5 of sample **I1**, and (b) layer (2) of sample **S5**. Phase abbreviations: LW- lead white (JCPDS 013-0131, 010-0401), LS-lead sulfate (JCPDS 036-1461), M-mercury^{II} sulfide (JCPDS 080-2192), BS-basic lead sulfate (JCPDS 018-0702), LY-lead antimonate yellow (JCPDS 018-0687), LC-lead carbonate (JCPDS 047-1734), R-rosiaite (JCPDS 049-1867), and C-cervantite (JCPDS 011-0694).

The SEM/EDS spectra of the yellow pigment grains under question only exhibit peaks due to lead and antimony, as shown in the spectrum in Figure 7.14b, obtained during the analysis

of sample **I7** (Figure 7.14a), confirming the presence of lead antimonate yellow and excluding the presence of other lead pigments.

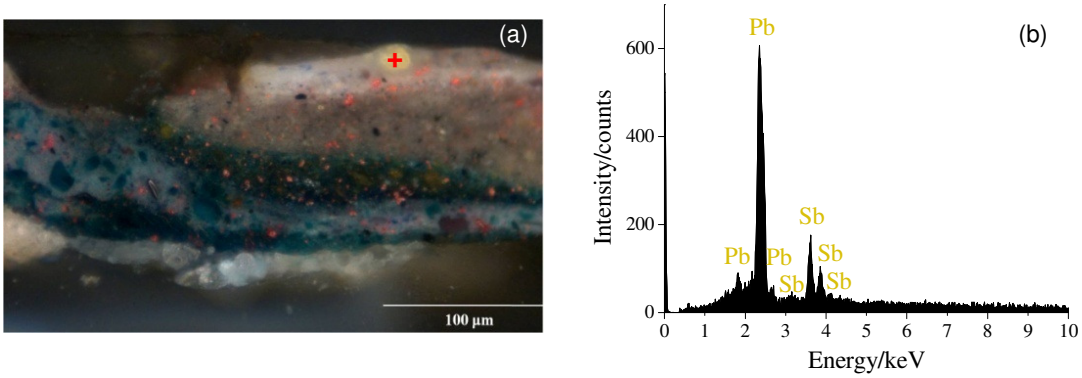

Figure 7.14 (a) Cross section of sample **I7** viewed under reflected light and (b) SEM/EDS spectrum of the yellow pigment marked with a red cross in (a).

The presence of lead antimonate yellow was confirmed by µ-XRD in the paintings: ***Cecília*** (**I1**, **I3**) and ***Mulher da água*** (**S5**, **S7**) and by SEM/EDS in the paintings: ***Cecília*** (**I1**, **I7**), ***Esperando o sucesso*** (**K7**), ***Senhora vestida de preto*** (**Q6**) and ***Mulher da água*** (**S5**, **S7**).

Also referred, in chapter 6 was the fact that lead sulfate, basic lead sulfate and rosiaite seem to have been found associated with lead antimonate yellow. Unfortunately, because the M_α line of lead (2.34 keV) and K_α line of sulfur (2.31 keV) overlap, it is very difficult to identify sulfur when lead is present, and consequently impossible to confirm the presence of lead sulfate ($PbSO_4$) and basic lead sulfate ($PbSO_4.PbO$) by SEM/EDS. Because rosiaite composition ($PbSb_2O_6$) has the same elements as lead antimonate yellow (Pb, Sb and O), its identification by SEM/EDS was also impossible.

Although, a significant number of lines overlaped making the assignement of the diffractograms very complex, still, it was possible to confirme by µ-XRD, the presence of lead sulfate (in samples **I1**, **S5** and **S7**), lines marked with **BS**, and basic lead sulfate (in sample **I1**), lines marked with **LS**, associated with lead antimonate yellow.

As can be seen in Figure 7.13b, rosiaite ($PbSb_2O_6$) and cervantite (Sb_2O_4), marked with **R** and **C**, respectively [343,346,347], were identified in the blue layer 2 of sample **S5**, together with lead antimonate yellow, lead sulfate and lead white, confirming the µ-R results and suggesting that these phases are probably associated with the synthesis method of lead antimonate yellow[80].

[80] There is a large number of recipes, most of which are uncertain to the nature of the reagents and vague with respect to the temperature and time of the reaction. Depending on these factors, more than one phase $Pb^{II}_{y}Sb^{V}_{2-x}O_7$ (where $2\leq y\leq 3$ and $0\leq x\leq 1$) and/or by-products can be formed [342-347].

Red lake pigments

The identification of the red glazing pigments by vibrational microscopic techniques proved to be very difficult, as only a polysaccharide material (starch), probably used as extender, was identified by μ-IR and the μ-R spectra of these red particles were characterized by a very intense fluorescence background that sometimes hampered their identification. Still, μ-R was able to identify cochineal lake pigment in nineteen paintings and madder lake pigment in two paintings.

Examination of the cross section of sample **W3** under visible light (Figure 7.15a) strongly suggest the presence of madder; however, only lead white and mercury^{II} sulfide were identified by μ-R and lead white and a silicate or sulfate compound by μ-IR. In order to easily and quickly confirm the presence of madder lake pigment, which is characterized for producing an intense and very unique bright orange colour [295,431], FM was employed. As shown in Figure 7.15b, madder lake pigment is present in the sample.

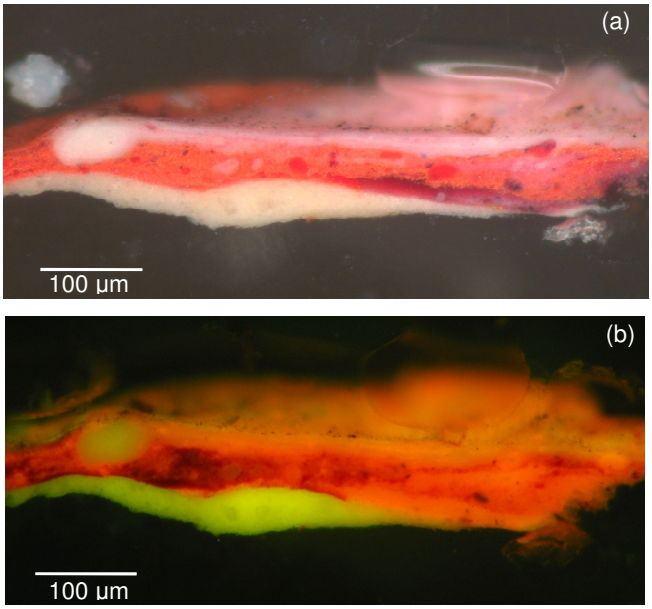

Figure 7.15 Cross section of the sample **W3** viewed under: (a) reflected light and (b) ultraviolet light (I 2/3 cube).

The red colour of the large red layer of samples **F4** (Figure 7.16a) and **Q5** (Figure 7.16b) was identified by μ-R to be mainly due to cochineal lake. However, because cochineal lake was often mixed with madder lake [136], these two samples were examined by FM to check for the presence of madder lake pigment. By looking at the cross sections of these two samples under UV light (Figure 7.16c andFigure 7.16d, respectively), no orange fluorescence characteristic of madder lake was observed, excluding its presence.

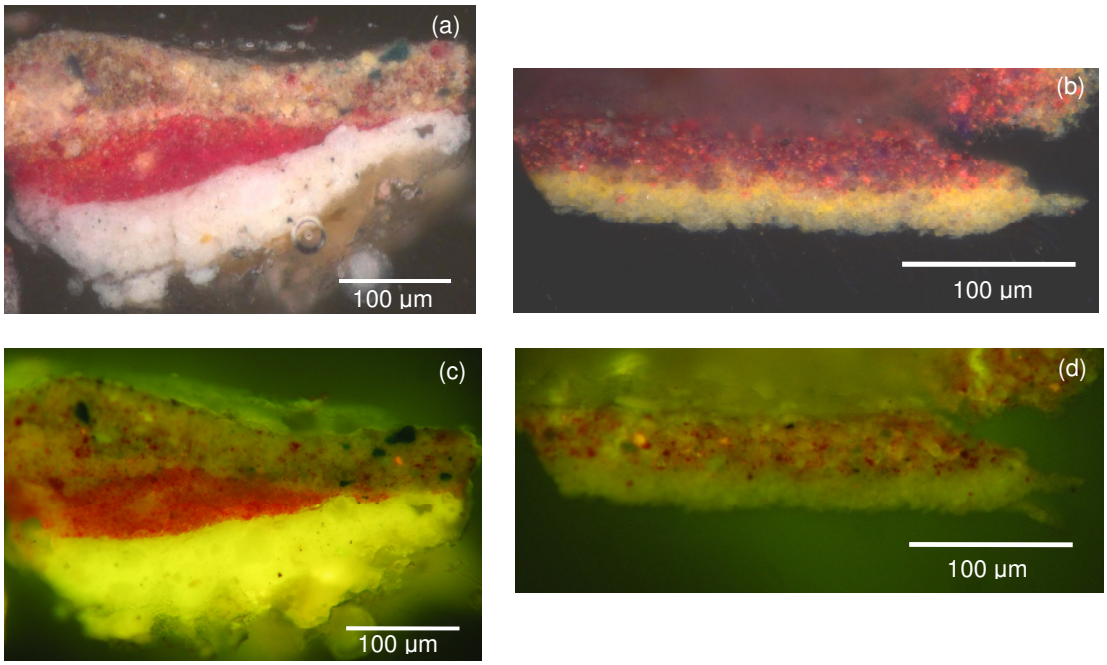

Figure 7.16 Cross-section of the sample (a) **F4** and (b) **Q5** viewed under reflected light; cross-section of the sample (c) **F4** and (d) **R5** viewed under ultraviolet light (I 2/3 cube).

Lake pigments are synthesized by co-precipitation/adsorption of a coloured dyestuff with/onto a substrate, which is an inorganic material [301,303] that influences the properties of the pigment, such as its colour and permanence [304]. However, neither of the two vibrational techniques was able to provide information regarding this inorganic material.

Therefore, in order to obtain information regarding the substrate and how the pigment was prepared, the elemental composition of the red lake pigments of samples **F6** and **Q5** was determined by SEM/EDS [304].

The analysis of the red lake pigment grains (marked with a red circle) of sample **F6** (Figure 7.17, indicates that these are mainly composed by aluminium, sulfur and potassium (Figure 7.17b-d), suggesting that potash alum, potassium aluminium sulfate, $AlK(SO_4)_2.12H_2O$, the most common ingredient to form the substrate, was used. The relatively high sulfur content (the contribution from cadmium yellow is very small) suggests that the substrate was done following a common 19th method in which the dyestuff and the alum are mixed first and the alkali added after, generally leading to incorporation of sulfate ions in the pigment [304]. The other identified elements are due to other pigments present in the sample; cadmium (spectrum a) from cadmium yellow, strontium and lead (spectrum c) from strontium yellow, and lead (spectrum d) from lead white.

The elemental analysis of the red layer 2 of sample **Q5** indicates a different composition (Figure 7.18). Besides aluminium and sulfur, silicon (in a high amount), tin, cobalt and mercury were also identified. Mercury is probably due to mercury^{II} sulfide (HgS) identified by

μ-R, while cobalt can be associated to cobalt blue ($CoAl_2O_4$) and/or to cerulean blue ($CoO.nSnO_2$).

Although a polysaccharide material was identified by μ-IR in the two samples, apparently no tin is present in the red lake pigments of sample **F6**, and the tin identified in sample **R5** can be due to the presence of cerulean blue. Consequently, the presence of the tin-containing cochineal variety that is known to have been extended with starch [305] cannot be ruled out.

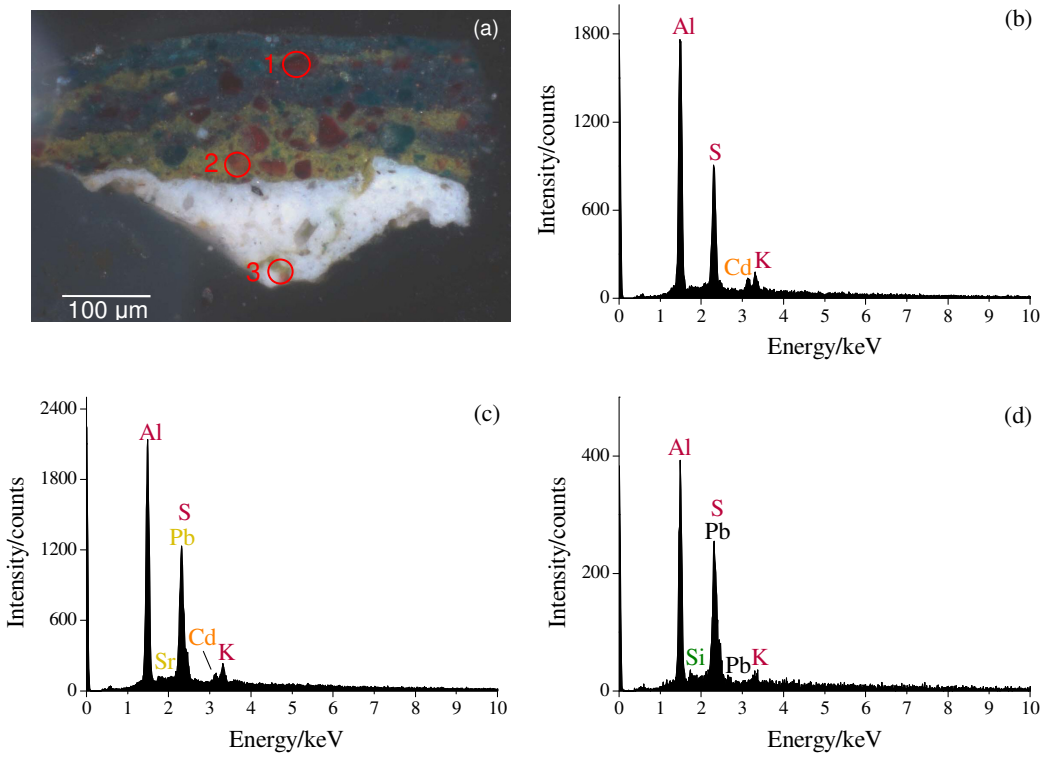

Figure 7.17 (a) Cross section of sample **F6** under reflected light; SEM/EDS spectra of the marked red pigments: (b) point 1, (c) point 2 and (d) point 3.

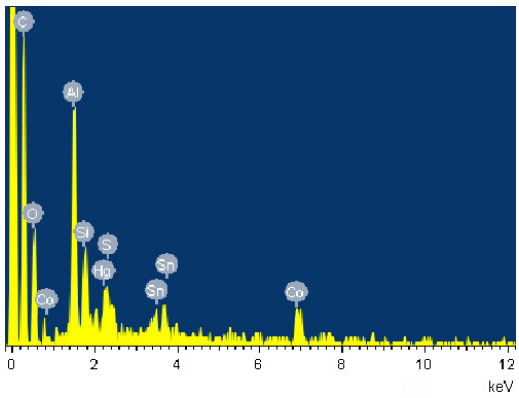

Figure 7.18 SEM/EDS spectrum of the red layer of sample **Q5** (Figure 7.16b).

The identification of the red lake pigment grains, by μ-R, as cochineal lake, was obtained by comparison with the spectra of a cochineal carmine reference sample, known to have calcium in its composition. However, no calcium was identified by SEM/EDS[81] for the cochineal lake particles present in the samples **F6** and **Q5**. This result suggests that μ-R is not able to differentiate between lake pigments of the same dyestuff with slightly different substrates.

Rutile

The identification of rutile, anatase and brookite in the samples by μ-R, was not unexpected, since these titanium oxide polymorphs are excellent scatterers and usually are easily identified by this technique, even when present in trace quantities. However, the identification by μ-R of only rutile in the white layer of sample **L3** marked with a red cross (Figure 7.19A), and no other compound such as aluminosilicates, with which rutile occurs naturally, was odd. Even more, because this compound has only been used as a white pigment since 1920s[82]. Contradictorily, μ-IR results point to a high lead white content in this layer. Both μ-XRD and SEM/EDS were used to clarify this issue.

The SEM/EDS analysis (Figure 7.19Ba-c) of the white layer of sample **L3** supported the μ-R results. Although, other elements, mainly aluminium and silicium, probably due to the existence of an aluminosilicate, were identified, the presence of titanium, in a large amount relatively to the other elements (Figure 7.19Ba) and not only as a trace compound, was confirmed. On the other side μ-XRD analysis does not support the μ-R results, but rather the μ-IR results. The diffractogram of the white layer (Figure 7.20) only identifies lead white and lead carbonate, with no signal of rutile or of any aluminosilicate compound.

Since μ-R and SEM/EDS analysis were performed in the cross sections prepared for OM, while μ-IR and μ-XRD analysis were performed in different sample fragments, the most plausible conclusion to this inconsistency is that sample **L3** has three layers, a white ground layer 1 composed by lead white and lead carbonate (similar to the other samples of the same painting), a green layer 2 composed by emerald green, viridian, mercury^{II} sulfide, iron^{III} oxide, iron^{III} oxyhydroxide, chrome yellow, zinc yellow and lead white, and a post Pousão white layer 3 composed by rutile and aluminosilicate compound.

[81] If calcium is present, it is in a very low concentration, not allowing it to be discernible from the background.

[82] It was not until 1920s that an economical method of purifying the metal oxide was established, and consequently, only since then was titanium white been commercialized. Due to the non hazardous, strong and opaque white, rutile form quickly became the most popular white pigment amongst artists [433,434].

The fact that in the sample prepared for OM (also used for μ-R and SEM/EDS) the white ground layer 1 is below the resin surface, made its analysis by μ-R and SEM/EDS impossible.

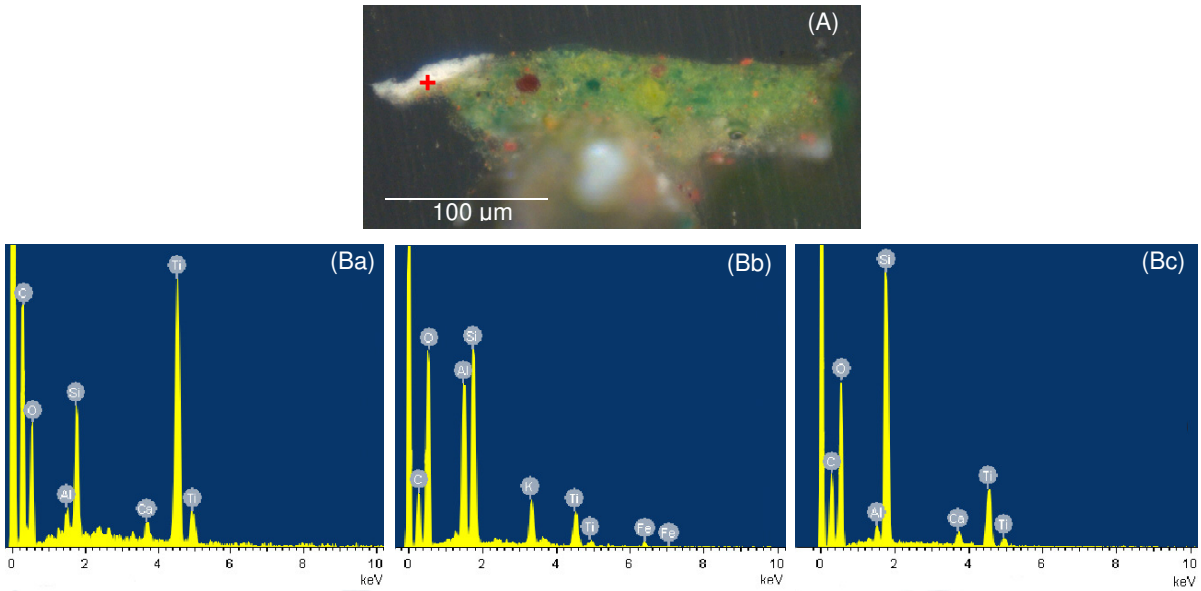

Figure 7.19 (A) Cross section of sample **L3** under reflected light; (B) SEM/EDS spectra of the white layer 2 of sample **L3**: (a) area analysis[83], (b) point analysis and (c) point analysis.

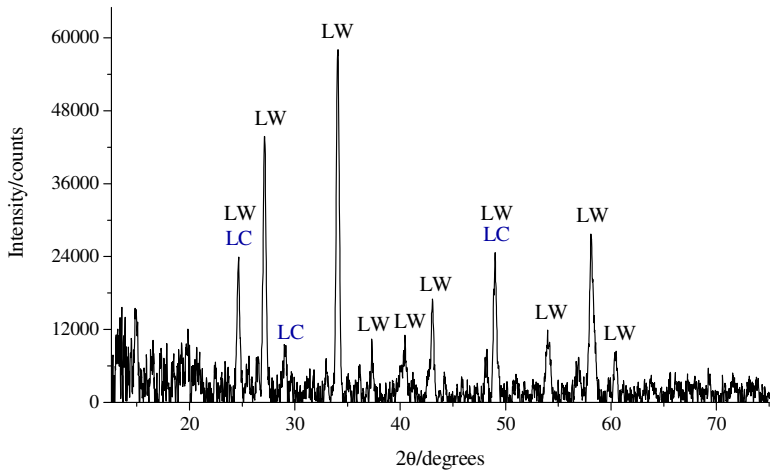

Figure 7.20 X-ray diffraction pattern of the white layer 1 from the sample **L3**. Phase abbreviations: LW-lead white (JCPDS 010-0401, 013-0131) and LC-lead carbonate (JCPDS 047-1734).

[83] In an area analysis, the spectrum presented is the average of the elements identified in that area.

Zinc white

While the results of the study performed in 1984 (Appendix A) indicated the presence of zinc white in four of the paintings under analysis in this study (***Paisagem - Abertura da Rua Alexandre Herculano***, ***Cansada (Cachopa de Capri)***, ***Esperando o Sucesso*** and ***Portão***), this white pigment was identified by μ-R only in the samples that proved to have been removed from restoration areas.

Since the characteristic IR bands of this pigment occur at wavenumbers below the cut-off of the equipment [249,432], its identification by μ-IR was impossible. However, becuase μ-R apparently has no limitation for the identification of zinc white, its detection by this technique in the referrered paintings should have occurred, but it was not the case.

SEM/EDS, μ-XRD and FM were employed to verify the existence of the zinc white in the referred paintings and a few others. The main results are presented below, organized in two groups: the first group is formed by the samples having both lead white and zinc white (a zinc content, for the samples that were analysed by SEM/EDS) and the second group is formed by the samples having a paint layer with high zinc content and no lead white.

First group

To this first group belong the samples **B3**, **I7**, **N3**, **N5**, **S1** and **V3**, characterized by having lead white in conjunction with a significant zinc content, which seems to be due to zinc white in the samples analysed by μ-XRD.

As an example, SEM/EDS analysis of the blue layer 2 of sample **N3** (Figure 7.21) clearly identifies the simultaneous presence of zinc and lead, and the μ-XRD analysis of layers 2 and 3 of the sample **B3** (Figure 7.22) identifies simultaneously zinc white, lead white and lead carbonate.

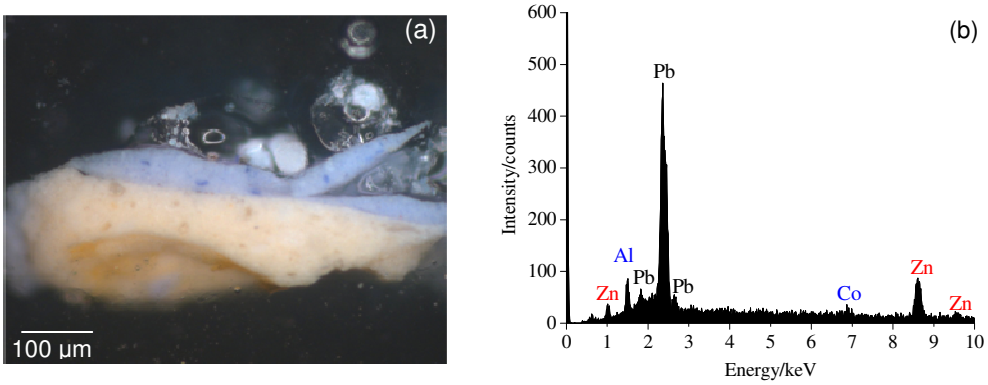

Figure 7.21 a) Cross section of sample **N3** viewed under reflected light and (b) SEM/EDS spectrum of the blue layer 2 from sample **N3**.

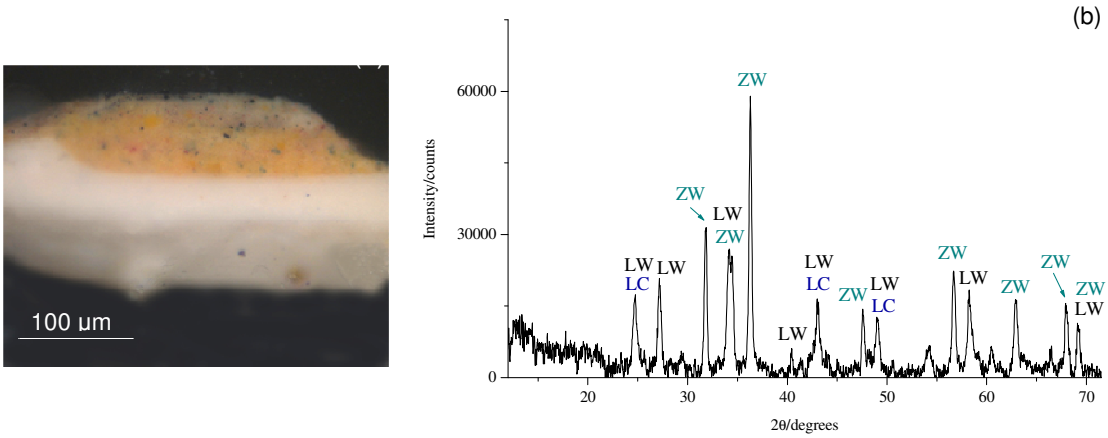

Figure 7.22 (a) Cross section of sample **B3** viewed under reflected light and (b) X-ray diffraction pattern of the layers 2 and 3 from the sample **B3**. Phase abbreviations: LW-lead white (JCPDS 010-0401, 013-0131), LC-lead carbonate (JCPDS 047-1734) and ZW-zinc white (JCPDS 036-1451).

Although, in general, the results of SEM/EDS and µ-XRD were in agreement, this was not the case for sample **B3** (Figure 7.22 and Figure 7.23). While the µ-XRD analysis of the yellow layer 2 and the grey layer 3 of this sample, as above referred, allowed the identification of zinc white, lead white and lead carbonate, zinc (and therefore, zinc white) was not identified in any of those layers by SEM/EDS (Figure 7.23, SEM/EDS spectrum of the yellow layer 2 is identical to this spectrum). This divergence between results not clearly understood.

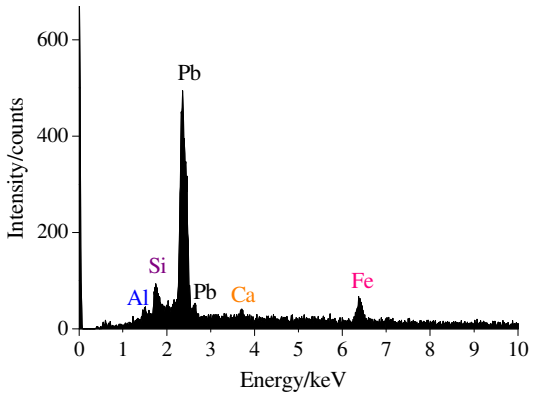

Figure 7.23 SEM/EDS spectrum of the grey layer 3 from the sample **B3**.

The results of the study carried out in 1984 indicated, in particular, the presence of zinc white in the ground layer of three paintings by Pousão, two of them now under study: ***Esperando o Sucesso*** and ***Portão***, suggesting that these two paintings are somewhat different from the remaining.

The µ-XRD analysis of sample **K5** and the SEM/EDS, µ-XRD and FM analysis of sample **K7**, both from ***Esperando o Sucesso*** confirmed the µ-IR and µ-R results, which showed that

the ground layer of these two samples is mainly composed by lead white, barium sulfate and calcium carbonate - calcite form, with no zinc white (see e.g. Figure 7.24). No signal of the strong yellow-green fluorescence of zinc white when observed under UV light [431] is seen in Figure 7.24b, zinc was not detected by SEM/EDS analysis (Figure 7.24c) and μ-XRD did not identify zinc white (Figure 7.24d).

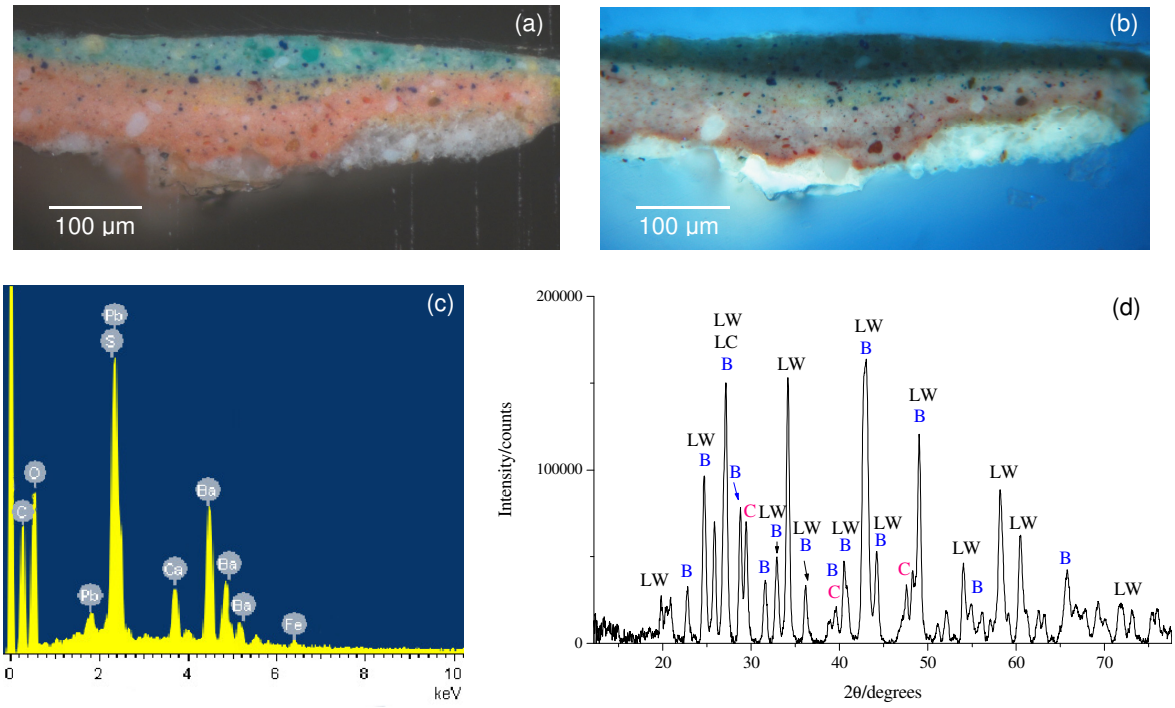

Figure 7.24 Cross-section of the sample **K7** viewed under: (a) reflected light and (b) ultraviolet light (A cube); (c) SEM/EDS spectrum and (b) XRD pattern of the ground layer from sample **K7**. Phase abbreviations: LW-lead white (JCPDS 010-0401, 013-0131), B-barium sulfate (JCPDS 024-1035) and C-calcium carbonate - calcite form (JCPDS 005-0586).

The case of the painting ***Portão***, was not so simple. While the SEM/EDS analysis of the ground layer of the sample **N3** (Figure 7.21a) was in agreement with the results obtained by μ-IR and μ-R, which only identified, lead white, lead carbonate and calcium carbonate-calcite form (Figure 7.25a), the μ-XRD analysis of the ground layer of the sample **N5**[84] clearly indicates also the presence of zinc white (Figure 7.25b).

In order to easily and quickly confirm the presence of zinc white, FM was employed. As shown in Figure 7.26, zinc white is, in fact, present in the sample, since the 'sparky' yellow-green fluorescence that characterises zinc white when observed under UV light [431] is clearly observed; however, zinc white is present only on the paint layers and not on the ground layer.

[84] The size of the sample **N3** was not enough for the μ-XRD analysis.

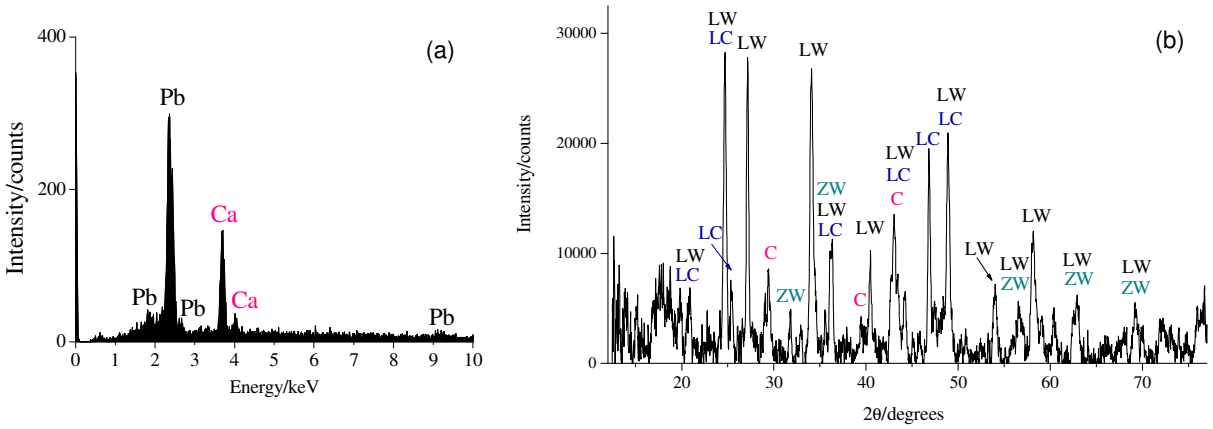

Figure 7.25 (a) SEM/EDS spectrum of the ground layer of sample **N3** and (b) X-ray diffraction pattern of the ground layer of the sample **N5**. Phase abbreviations: LW-lead white (JCPDS 013-0131), LC-lead carbonate (JCPDS 047-1734), C-calcium carbonate-calcite form (JCPDS 005-0586) and ZW-Zinc white (JCPDS 036-1451).

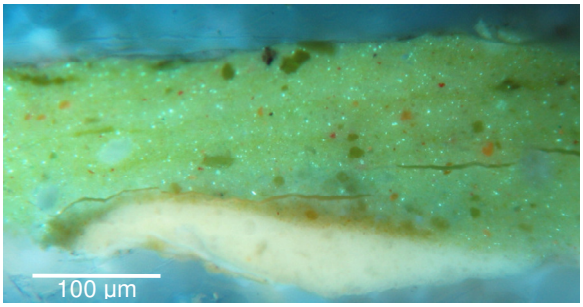

Figure 7.26 Cross-section of the sample **N5** viewed under ultraviolet light (A cube).

Since due to the large X-ray beam diameter and to the X-ray penetration, when analysing the ground layer of sample **N5**, the paint layer, which has zinc white, might also have been analysed, leading to an erroneous result that zinc white is in the ground layer, the ground layer of a another sample from the same painting, sample **N2**, was also analysed by µ-XRD.

As shown in Figure 7.27, only lead white was identified by µ-XRD in the ground layer of sample **N2**, being in agreement with the results obtained by µ-IR and µ-R, SEM/EDS and FM.

These results show that zinc white is not present on the ground layer of the paintings ***Esperando o Sucesso*** and ***Portão***.

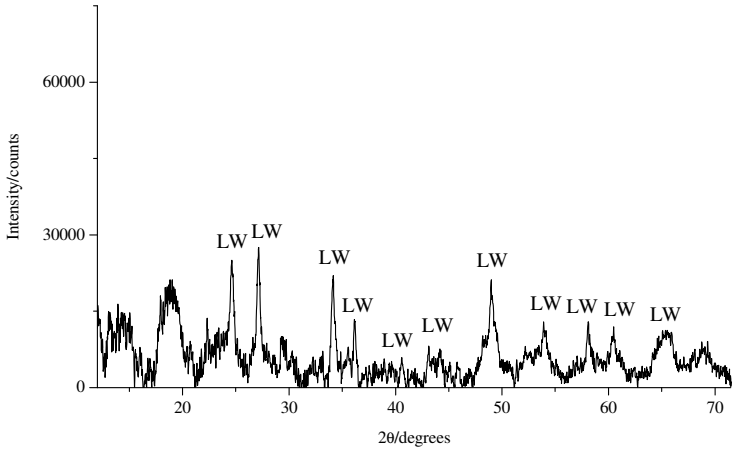

Figure 7.27 X-ray diffraction pattern of the ground layer of the sample **N2**. Phase abbreviations: LW-lead white (JCPDS 013-0131, 010-0401).

The nonexistence of zinc white in the ground layer was confirmed by μ-XRD for the samples **K5** and **K7** (***Esperando o Sucesso***), **H4 (*Casas Brancas de Capri***), **S2** (***Mulher da água***) and **W1** and **W2** (***Flores campestres***), and by FM for the samples **C2** (***Paisagem - Abertura da Rua Alexandre Herculano***) and **G3** (***Cansada (Cachopa de Capri)***).

The fact that neither μ-R[85] nor SEM/EDS allowed the identification of zinc white when μ-XRD and FM clearly showed its presence, illustrates the importance of the use of these last two techniques for the identification of this pigment.

Second group

To this group belong the samples **F1**, **J2** and **T7** (Figure 7.28a-c), characterized by having a paint layer (marked with a red cross) with a high zinc content (possibly zinc white) and no lead white.

Unexpectedly, when analysing these three samples by μ-IR and μ-R, one paint layer of each sample (blue layer 5, grey layer 4 and green layer 2, respectively) provided no signal of lead white, a very common pigment in Pousão's layers, raising questions about the layers' origin. In their backscattered images (Figure 7.28d-f), the suspicious layers are easily distinguished from the others, since they present a darker colour, the rest of the layers appearing much lighter coloured[86]. The elemental analysis indicated that while the light layers are mainly composed by lead (probably from lead white) and do not have zinc, the

[85] As already referred, the IR bands of zinc white occur below the cut-off of the detector employed in μ-IR.

[86] The lower layer of sample **F1** is only composed by calcium carbonate-calcite form, what explains its different colour from the right above layers.

layers marked with a red cross are characterized by a high zinc content and the apparent absence of lead[87], Figure 7.29 and Figure 7.30.

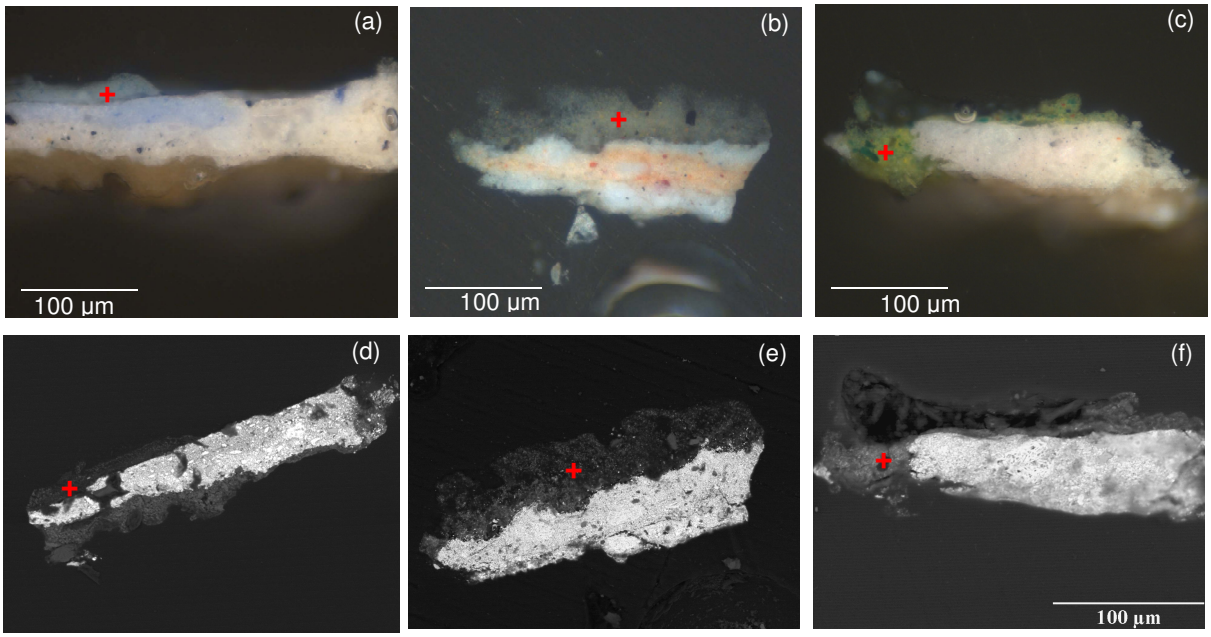

Figure 7.28 Cross section of the samples: (a) **F1**, (b) **J2**, and (c) **T7**, under reflected light. SEM backscattered image of the samples: (d) **F1**, (e) **J2**, and (f) **T7**.

In the sample **T7** from ***Paisagem Anacapri***, the SEM/EDS elemental analysis of the green layer 2 shows that besides the large amount of Zn (Figure 7.30), there is also a significant amount of Cr, what could suggest the presence of zinc yellow (approximate composition $K_2O.4ZnCrO_4.3H_2O$). However, this yellow pigment, which normally is a very good Raman scatterer, was not identified by µ-R. Instead, the chromium content was identified by µ-R to be due to green pigment viridian. The simultaneous presence of cadmium and sulfur suggested that the yellow pigment present in the layer, which was not able to be identified neither by µ-R or µ-IR, is cadmium yellow (CdS).

Although the absence of lead white in this layer is unusual for samples under analysis[88], there is no pigment in this layer that suggests that it was not applied by Pousão. In fact, the other green sample of this painting, sample **T3**, looks very similar to **T7** when observed by OM, and when analysed by µ-R and µ-IR indicated more or less the same composition. Zinc is present in this sample either due to zinc white or to another zinc compound, such as zinc sulfide (present in lithopone – zinc sulfide + barium sulfate), zinc sulfate (present in sulfopone – zinc sulfate + calcium sulfide) and zinc carbonate [(85,435)].

[87] If lead exits it must be in a very low concentration that did not allowed it to be discernible from the background.
[88] Because sulfur and lead lines overlap, it is difficult to detect low amounts of lead in the presence of high sulfur content. Consequently, it is hard to assure that lead is really absent from this layer.

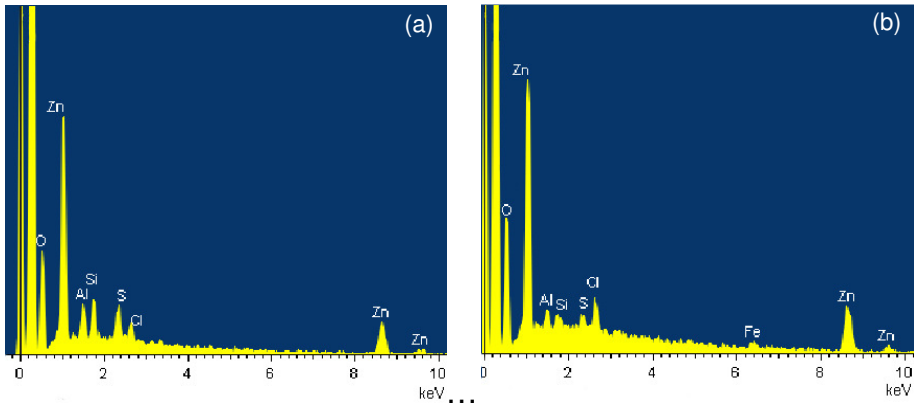

Figure 7.29 SEM/EDS spectra of: (a) an area of the blue layer 5 of sample **F1** and (b) an area of the grey layer 4 of sample **J2**.

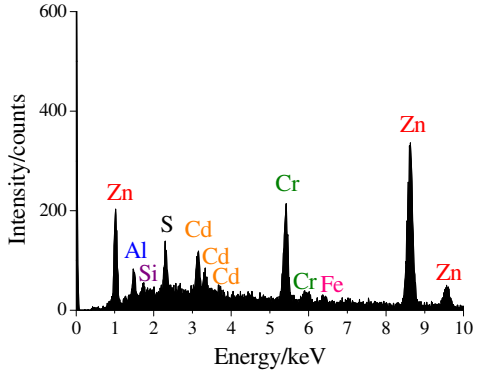

Figure 7.30 SEM/EDS spectrum of an area of the green layer 2 of sample **T7**.

A different scenario occurs for samples **F1** and **J2**, since no other element common to Pousão's pigments was identified in the blue layer 5 of sample **F1** and the grey layer 4 of sample **J2**. In order to check for the presence of zinc white in these two samples, FM was employed (Figure 7.31 and Figure 7.32). The cross section of sample **J2** presented in Figure 7.32 is different from the one presented in Figure 7.28b because it was acquired after the SEM/EDS analysis, hence, the sample had to be polished to remove the carbon deposit, what caused the loss of some of the layers.

When viewed under UV light, the blue layer 5 of sample **F1** from ***Paisagem St. Sauves*** appears to have a different morphology (less compact) relatively to the other layers (Figure 7.31b), suggesting that this layer belongs to a later intervention; the brownish layer 4 (only seen under visible reflected light) probably being remain dirty varnish or simply dirty. However, apparently no zinc white is present in this layer, as the "sparkle" look that zinc white presents under UV light (see Figure 7.26) was not observed.

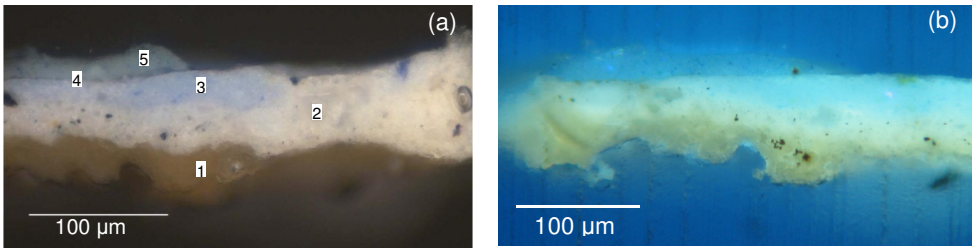

Figure 7.31 Cross section of the sample **F1** viewed under: (a) reflected light and (b) ultraviolet light (A cube).

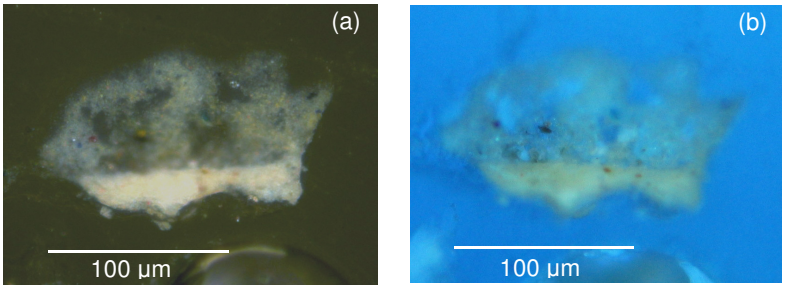

Figure 7.32 Cross section of the sample **J2** viewed under: (a) reflected light and (b) ultraviolet light (A cube).

The same was verified for sample **J2** from ***Escadas de um pardieiro***. Although the grey layer 4 proved to have a high zinc content, apparently it is not due to zinc white, since no fluorescence is observed (Figure 7.32b). A result corroborated by µ-XRD, which identified only lead white and lead carbonate when analysing this layer (Figure 7.33). However, these compounds are probably from the underneath layers, since none of them was identified by µ-IR and µ-R in the layer in question.

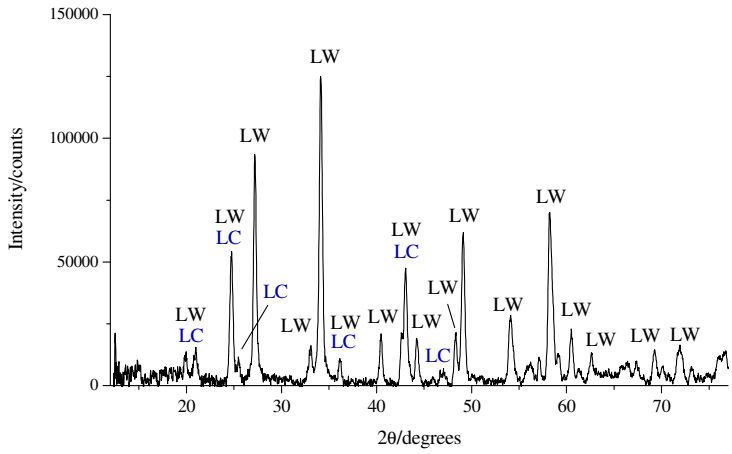

Figure 7.33 X-ray diffraction pattern of the grey layer 4 from the sample **J2**. Phase abbreviations: LW-lead white (JCPDS 010-0401, 013-0131) and LC-lead carbonate (JCPDS 076-2056).

The fact that the pigment cadmium red, only commercialized since 1910 [85], was identified, by μ-R, in the grey layer 4 indicates that it could not have been applied by Pousão, who died in 1884. Therefore, this layer can be a result of the conservation intervention carried out in 1984 or due to paint transference from a frame.

In both samples **F1** and **J2** zinc is probably due to the presence another zinc compound, rather than zinc white, such as zinc sulfide (present in lithopone – zinc sulfide + barium sulfate), zinc sulfate (present in sulfopone – zinc sulfate + calcium sulfide) and zinc carbonate [85,435].

Zinc white was identified in the paint layers of the paintings ***O mendigo Lapita*** (**B3**), ***Portão*** (**N3**) and ***Mulher da água*** (**S1**), by μ-XRD, and ***Portão*** (**N3**) by FM. Besides, SEM/EDS also suggest its presence in the paint layers of the paintings ***Cecília*** (**I7**), ***Paisagem de Anacapri*** (**T7**) and ***Cais de Barcelona*** (**V3**).

Zinc yellow

Zinc yellow is known to have been sold under different chemical compositions, but it is the approximated complex zinc potassium chromate composition, $K_2O.4ZnCrO_4.3H_2O$ [242] the one generally accepted as correct.

μ-XRD analysis of the reference sample of zinc yellow (Figure 7.34) indicated that it was mainly composed by $K_2Zn_4O(CrO_4)_4.3H_2O$/ $4ZnCrO_4.K_2O.3H_2O$ (JCPDS 08-0202), identical to the formula above, and SEM/EDS analysis of the zinc yellow pigment grains of samples **K7** and **L3** (Figure 7.35) which identified zinc, chromium, potassium and oxygen, seem to corroborate this hypothesis.

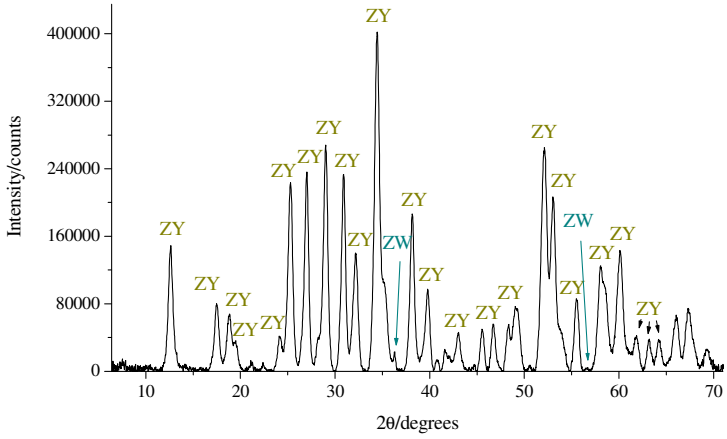

Figure 7.34 X-ray diffraction pattern of the reference sample of zinc yellow. Phase abbreviations: ZY-zinc yellow (JCPDS 08-0202) and ZW-zinc white (JCPDS 036-1451).

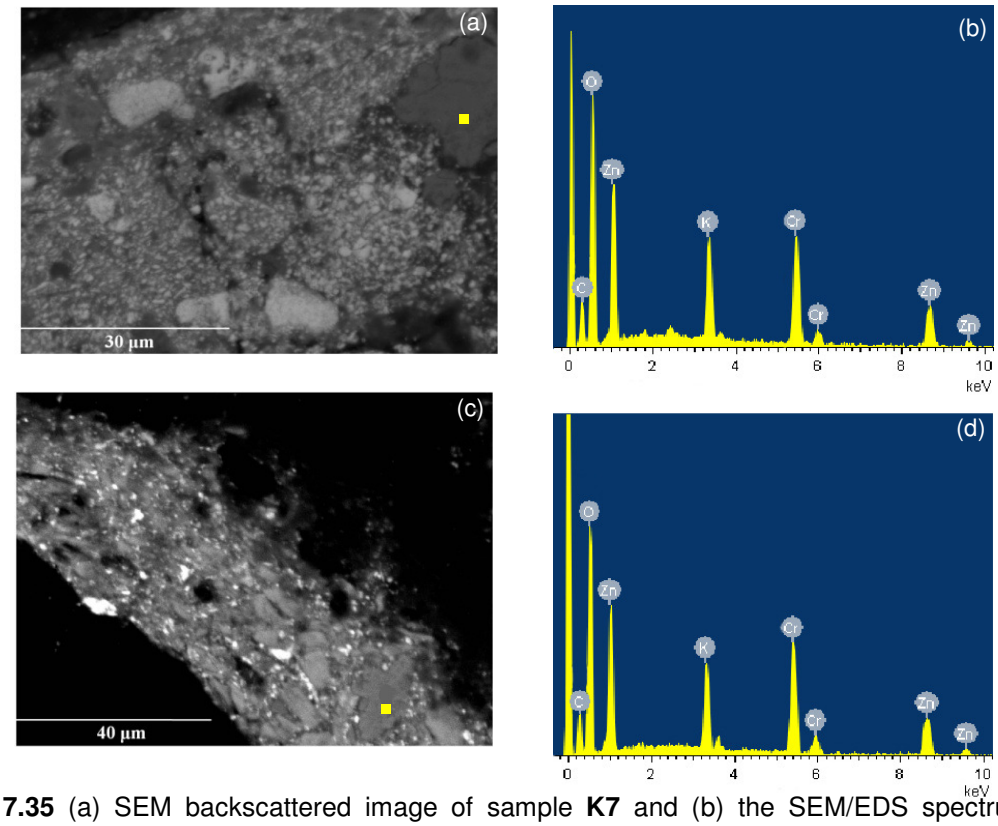

Figure 7.35 (a) SEM backscattered image of sample **K7** and (b) the SEM/EDS spectrum of the marked yellow pigment; (c) SEM backscattered image of **L3** and (d) the SEM/EDS spectrum of the marked yellow pigment.

However, when analysing the green layer 4 of sample **H8** by µ-XRD (Figure 7.36) a different zinc yellow phase, $4ZnO.CrO_3.3H_2O$ (JCPDS 011-0275), with no potassium was identified.

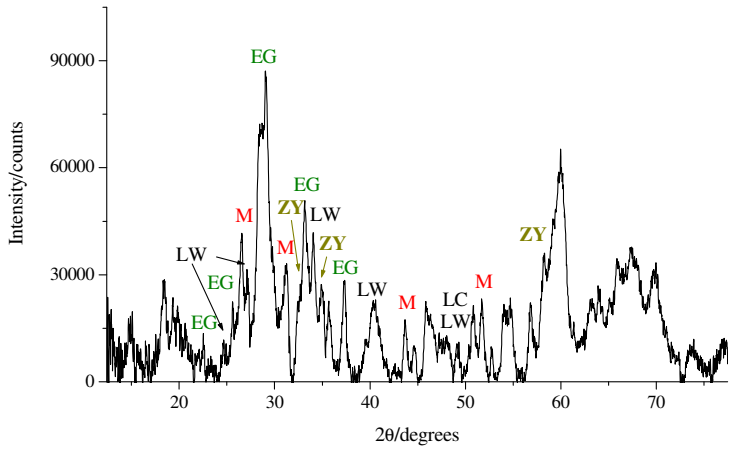

Figure 7.36 X-ray diffraction pattern of the green layer 4 from the sample **H8**. Phase abbreviations: LW-lead white (JCPDS 013-0131, 010-0401), LC-lead carbonate (JCPDS 047-1734), EG-emerald

green (JCPDS 031-0448), M-mercury^{II} sulfide (JCPDS 080-2192) and ZY-zinc yellow (JCPDS 011-0275).

As referred before, the distinction of the different possible compositions of zinc yellow by IR seemed to be very difficult, if not impossible. The same is now verified for RS, since the Raman spectrum of the yellow grains of sample **H8** (and on all other painting samples) is identical to that of the reference sample of zinc yellow (Figure 7.37).

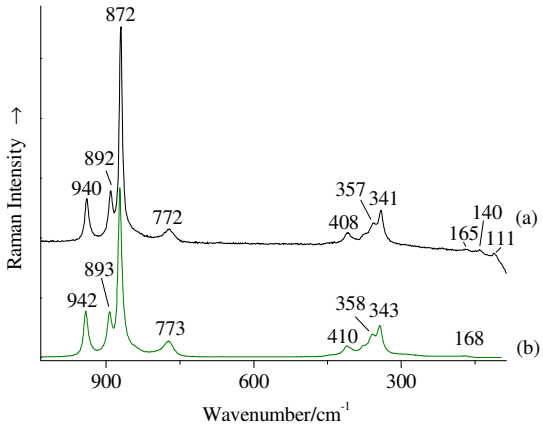

Figure 7.37 Raman spectra of: (a) yellow pigment grains of the green layer 4 of sample **H8**, identified as zinc yellow (5 scans, 0.63 mW) and (b) zinc yellow reference sample (Ferrario Colours) (1 scans, 0.13 mW). See experimental conditions on the previous chapter.

7.4 SEM/EDS, μ-XRD and FM advantages and limitations

Over the past decades, the use of analytical techniques for research in conservation science has expanded notably and nowadays an extensive range of analytical techniques are made available for this purpose. However, when carrying out a scientific study of an artwork it can be difficult to select the best analytical approach, since the risk to produce poor quality or to duplicate results, to waste time, funds and even to destroy the priceless samples is high. Therefore, particularly in this field, where no test analyses are allowed, a prior knowledge of the strengths and weaknesses of each analytical technique is very important.
In what follows, the major advantages and difficulties of SEM/EDS, μ-XRD and FM found along this study for the analysis of oil paintings are presented.

SEM/EDS

The elemental analysis provided by SEM/EDS was very helpful to clarify some questions which remained after the μ-IR and μ-R analysis, since this technique provides the elemental composition of the pigment grains and of small areas of the samples.

In the current study, SEM/EDS allowed to: i) confirm and/or identify the presence of cobalt blue and cadmium yellow, two pigments that could not be identified either by μ-R or by μ -IR (IR bands occur below 650 cm^{-1}), ii) confirm that lead antimonite yellow and not lead-tin-antimony yellow was present in the samples and iii) identify zinc white and cerulean blue, two pigments that could not be identified either by μ-R or by μ -IR (IR bands below 650 cm^{-1}).

Unfortunately, SEM/EDS does not provide information regarding how the elements are linked, and so, does not allow for the distinction between: i) polymorphs[89], such as anatase and rutile (TiO_2) or calcite and aragonite ($CaCO_3$), ii) compounds with identical elemental composition, such as malachite ($Cu_2CO_3(OH)_2$) and azurite ($Cu_3CO_2(OH)_2$) or red lead (Pb_3O_4) and massicot (PbO) and iii) mixtures of compounds that led to the presence of the same elements, such as $CaSO_4$ + $PbCO_3$ and $CaCO_3$ + $PbSO_4$. Therefore, for identification purposes, especially, when analysing complex samples, such as those under study, SEM/EDS must be used in conjunction with more specific techniques, since a wrong interpretation may be easily performed.

Since an energy dispersive spectrometer was employed, it was possible to acquire a full elemental spectrum, i.e. to identify all the elements[90] of the sampling point/area in just a few seconds. However, the use of this type of spectrometer can also constitute a drawback to this technique. Using this spectrometer it was very difficult to distinguish close together lines, such as the lead and sulfur lines, which make it very difficult or even impossible to identify lead sulfate ($PbSO_4$) in a mixture with lead antimonate yellow (approximately $Pb_2Sb_2O_7$), as identified by μ-R and μ-XRD. In such cases, a wavelength dispersive spectrometer is more suitable.

The SEM/EDS analysis required samples to be covered with a thin film of carbon, thus samples have to be polished previously to any other analysis. Since the removal of the carbon layer for further uses of the sample may change its stratigraphy, causing layers to disappear and/or new layers to appear, this technique is considered to be destructive.

μ-XRD

Based on the distinct diffraction pattern that each particular crystal structure gives rise to, μ-XRD allows for an exact determination of the composition of samples with only a few micrograms and in a non-destructive way, since the grounding procedure, normally associated with powder XRD, is not performed.

[89] Compounds with identical chemical compositions but different crystalline forms.

[90] Lower abundance elements might not be detected and elements with atomic number below the atomic number of Na are not detected.

In the current study, μ-XRD was important for: i) identification of zinc white, which proved to be a poor Raman scatterer, but has a high X-ray absorption coefficient [436], ii) identification of cerulean blue, a light blue pigment that produced an intense fluorescence background hampering its identification by μ-R, iii) confirmation of the presence of lead sulphate, basic lead sulphate and rosiaite and iv) identification of cervantite as associated phase of lead antimonate yellow.

However, μ-XRD presents several limitations and some of them very restringing. The first one is that amorphous or poorly crystalline phases are very difficult or impossible to identify, since μ-XRD is based on the crystalline structure. For instance, the amorphous pigments viridian and cobalt blue were identified by μ-R, but could not be identified by μ-XRD. A second limitation is its low immunity to interference. For instance, the co-existence of a significant content of an amorphous phase can seriously difficult the identification of the crystalline phases, since the background is swamped, peaks are less visible; and compounds with low X-ray absorption coefficients may be difficult to identify in the presence of others with higher X-ray absorption coefficients [436,437]. Since lead white, the main component of almost all the samples, has a high X-ray absorption coefficient, the diffractograms were generally dominated by the peaks of this pigment, seriously constraining the identification of other existing compounds, especially those present in lower concentrations. A third limitation of μ-XRD is the requirement of larger acquisition periods, since, as samples were not grounded and no sample stage rotator was used, preferential orientation of the crystals in the sample can occur, making identification more difficult.

The fourth limitation of this technique is the fact that the analysis of the samples was not always straightforward, since a suitable area for analysis should be, preferably, large (minimum 1 mm, which is the diameter of the collimator) and flat. Samples were adjusted in order to find a suitable area for analysis, but most of the times the analysis was confined to the top and bottom layers. In some cases, due to the low spatial resolution of the technique (ca. 1000 μm) more than one layer was simultaneously analysed.

Finally, the high fluorescence of the iron-containing compounds under Cu Kα radiation, such as iron^{III} oxides and oxyhydroxides and Prussian blue, inhibited the identification of these pigments.

Since, the μ-XRD analysis was conducted using the bulk samples, without any preparation, this technique is considered to be non-destructive.

FM

The characteristic auto-fluorescence that some materials/compounds exhibit when observed under ultraviolet light can be used to easily, quickly and relatively inexpensively, support identification purposes and access the samples' characterization.

In the current study, FM was valuable to: i) identify madder lake in a sample where, neither µ-IR, nor µ-R provided any information about this red lake pigment, ii) confirm the absence of madder lake in samples with layers mainly composed by cochineal lake pigment, since often these two pigment were mixed together, iii) identify or confirm the absence of zinc white.

However, some misinterpretations can occur [304,431]. Especially in complex mixtures, a different fluorescence behaviour from the one expected may be observed. This is due to the fact the characteristic fluorescence of a specific compound can be changed by the response of other compounds or by photobleaching (loss of the ability to fluoresce as result of continuously exposure to excitation radiation). Therefore, the results of this technique should always be carefully interpreted and, preferably, in conjunction with those obtained by other techniques.

Although not detected in the current study, another drawback of this technique is the possible fading of some organic pigments and dyes, due to the release of energy in the form of heat and not in the form of fluorescence. Thus, minimisation of the time under UV light is recommended.

Since, no degradation/alteration in the samples was observed, this technique is considered to be non-destructive.

Comparison among µ-IR, µ-R, SEM/EDS, µ-XRD and FM

A comprehensive evaluation of µ-IR and µ-R and of the auxiliary techniques for the analysis of the samples of Pousão's oil paintings was separately carried out in sections 6.3 and above, respectively. Therefore, only a brief comparison among all these techniques together will be outlined in this section.

µ-R, FM and SEM/EDS did not require sample preparation, since the analysis by these techniques was performed over the cross sections previously prepared for OM. This not only saved sample and time, but also simplified the comparison of the results obtained by those techniques with the OM results. Nevertheless, as SEM/EDS samples' images are in black and white, the results obtained by this technique were more difficult to compare with the OM results than the ones obtained by µ-R and FM.

Although, like the above techniques, μ-XRD did not require sample preparation, as the analysis was conducted over the bulk samples, the comparison of the results obtained by this technique with the ones obtained by the other techniques was not always easy, since in general only the upper and lower layers of the samples were analysed

Similar to μ-XRD, the μ-IR results were often difficult to compare with the ones obtained by the other techniques, since the procedures used for the preparation and analyse of the thin sections can cause alterations of its stratigraphy relatively to the one of the cross sections analysed by OM, μ-R, SEM/EDS and FM. Those procedures are time- and sample-consuming and constitute a serious handicap of the μ-IR technique.

As to the analysis time, except for μ-XRD, which required several hours, if not days of data acquisition, SEM/EDS required a few minutes for vacuum establisment inside the sample's chamber, μ-R required from a few minutes to five hours, depending on the samples, μ-IR always required one minute and FM was able to produce results in a few seconds.

μ-IR, μ-R and μ-XRD are highly specific techniques, allowing for the exact determination of the compounds present in the samples. However, μ-XRD is limited to the analysis of crystalline ordered compounds and μ-IR only permits the identification of compounds exhibiting IR bands above 650 cm^{-1}. Unlike these techniques, FM has low specificity and must be used with caution, since only a few compounds fluoresce and fluorescence emission can be altered by the presence of other compounds or by the observation conditions. Although SEM/EDS is highly specific for chemical elements, it has no specificity for the identification of compounds.

SEM/EDS is the technique with the highest spatial resolution, approximately 0.002 μm, allowing for the individual analysis of each particle in the samples. μ-R and FM also have good spatial resolutions, approximately 1 μm and 0.2-0.5 μm, respectively, which allow for the individual analysis of most pigments grains in the samples. However when the pigments were machine grounded and the dimensions of the grains were lower than the spatial resolution, such as was the case of cadmium yellow, the pigments particles could not be resolved.

μ-IR and μ-XRD were the analytical techniques with the lowest spatial resolution, approximately 50 μm and 1000 μm, respectively. These low spatial resolutions not only did not permit the analysis of individual grains but also sometimes did not even allow for the individual analysis of each layer of the samples.

Among these five techniques, μ-IR was considered to be the most destructive, because after compression of the thin sections in the diamond cells, the recovery of the thin sections for further analysis was impossible.

Liwewise μ-IR, SEM/EDS was considered a destructive technique since the removal of the carbon layer required for further analyses, may cause alterations in the samples' stratigraphy.

μ-R, μ-XRD and FM were considered to be non-destructive techniques. In fact, the chemical alteration/degradation of some samples during the μ-R analysis as result of the laser being focused on a very bright spot, only occurred for a few and irrelevant black particles.

Although each technique proved to be useful at different stages of the current study, and the combination of all the results offered a significant insight into the composition of Pousão's paintings, μ-R demonstrated to be the best effective technique for pigment identification in the studied samples.

7.5 Comphreensive identification

SEM/EDS, μ-XRD and FM were used as auxiliary techniques to the μ-IR and μ-R analysis, confirming uncertain identifications and identifying unidentified compounds. Combining the results of these five analytical techniques it is possible to summarize the composition of the samples under analysis as presented in Table 7.4.

Table 7.4 Compounds* identified by μ-IR, μ-R, SEM/EDS, μ-XRD and FM in Pousão's paintings

Compounds	Paintings																						
	Earlier			French			Italian															Final	
	A	B	C	D	E	F	G	H	I	J	K	L	M	N	O	P	Q	R	S	T	U	V	W
Arsenites																							
Emerald green						•		•			•	•							•			•	
Scheele's green								•			•												
Carbonates																							
Calcium carbonate - calcite form			•		•	•	•		•		•			•	•	•	•	?	•				
Lead carbonate	•	•	•	•	•	•	•	•	•	•	•	•	•	•	•	•		•	•	•	•	•	•
Lead white	•	•	•	•	•	•	•	•	•	•	•	•	•	•	•	•	•	•	•	•	•	•	•
Malachite								•															
Chromates																							
Chrome orange	•		•	•	•	•	•		•	•	•	•	•	•	•	•		•	?		•		
Chrome yellow	•		•	•	•	•		•	•		•	•		•	•	•	•	•	•	•	?		•
Strontium yellow	•	•	•	•							•						•						
Zinc yellow					•	•		•			•	•	•	•	•					•		•	
Cyanides																							
Chrome green								•											•		•		•
Prussian blue				•	•	•			•	•	•	•		•			•		•	•	•	•	•
Oxides and Oxyhydroxides																							
Anatase	•										•		•	•									
Brookite											•												
Cerulean blue									•						•		•	•					
Cervantite																			•				
Cobalt blue	•		•	•	•	•	•	•	•		•		?	•	•	•	•	•		•		?	
Cobalt oxide								•															
Iron^{III} oxide	•	•	•	•	•		•	•	•	•	•	•	•	•		•		•	•	•	•	•	•
Iron^{III} oxyhydroxide				•	•		•		•	•	•	•	•	•			•		•		•	•	•
Lead^{II,IV} oxide			•																	•			
Lead antimonate yellow					•	•			•	?	•	•					•		•	•			
Rosiaite					•	•			•		•								•				
Rutile											•	•			•								
Tetragonal lead^{IV} oxide [a]					•					•	•												
Viridian				•	•	•		•	•			•								•			•
Zinc white		•							?					•					•	?		?	
Phosphates																							
Bone/ivory black	?	•		•			•			•	?						•						
Silicates																							
Celadonite					•				•														•
Kaolin	•	•		•		•	•		•		•		?		?	•			•	•	•		•
Quartz	•	•	•	•	•	•	•		•		•		•				•		•			•	
Ultramarine blue	•		•		•	•	•	•	•	•	•	•		•	•	•			•	•	•	•	•

(*continued overleaf*)

Table 7.4 (*continued*)

Compounds	Paintings																						
	Earlier			French			Italian															Final	
	A	B	C	D	E	F	G	H	I	J	K	L	M	N	O	P	Q	R	S	T	U	V	W
Sulfates																							
Barium sulfate					•	•	•	•	•	•	•		•		•		•		•	•	•		
Basic lead sulfate					•	?			•		•						•						
Brochantite								•															
Gypsum	•				•	•	•	?	?	?	•	•					•		?				
Lead sulfate			?		•	?			•	?	•	?				•	?		•	?			?
Sulfides																							
Cadmium red [b]										•										•			•
Cadmium yellow			?			•	?	?			•	•	•	•					•	•	•	•	
Copper[II] sulfide																			•	•			
Mercury[II] sulfide	•		•	•	•	•	•	•	•	•	•	•	•	•	•	•	•	•	•	•	•	•	•
Realgar/parealgar				•			•	•															•
Other pigments [c]																							
Carbon-based black	•	•	•	•	•	•	•	•	•	•	•	•	•	•	•	•	•	•	•	•	•	•	•
Cochineal lake	•		•	•	•	•		•	•	•	•	•		•		•	•	•	•	•	•	•	•
Madder lake																•							•

A - *Casa rústica de Campanhã*, **B** - *O mendigo Lapita*, **C** - *Paisagem - Abertura da Rua Alexandre Herculano*, **D** - *Jardim de Luxemburgo (estudo)*, **E** - *Aldeia de St. Sauves*, **F** - *Paisagem de St. Sauves*, **G** - *Cansada (Cachopa de Capri)*, **H** - *Casas brancas de Capri*, **I** - *Cecília*, **J** - *Escadas de um pardieiro - Roma*, **K** - *Esperando o sucesso*, **L** - *Fachada de casa soterrada - Roma*, **M** - *Miragem de Nápoles*, **N** - *Portão*, **O** - *Rapariga de Anacapri*, **P** - *Rua de Roma*, **Q** - *Senhora vestida de preto*, **R** - *Janela das persianas azuis*, **S** - *Mulher da água*, **T** - *Paisagem de Anacapri*, **U** - *Rapariga deitada no tronco de uma árvore*, **V** - *Cais de Barcelona* and **W** - *Flores Campestres.*

* Pigments are in blue, while extenders, associated compounds or impurities are in green
? Propable identification
[a] by identification of the laser induced formed orthorhombic lead[II] oxide
[b] This pigments is due to a conservation intervention. Therefore, will not be used for futher considerations.
[c] pigments that do not belong to a specific functional group

7.6 Microchemical results *vs.* current study results

As already mentioned, in 1984 some of the paintings were sampled and their pigments identified by microchemical analysis. Since this former study was conducted almost thirty years ago, when examination and analytical techniques had not yet reached today's level of development/information, it was expected that the current study would provide additional information. Table 7.5 summarizes the results of the 1984 study and the results of the current study, only for the paintings analysed in 1984.

The comparison of the results allows for three major conclusions to. First, as expected, a much larger number of pigments were identified in the current study (19 *vs.* 26), especially the yellow and orange pigments. While chrome orange, lead antimonate yellow, strontium

yellow and zinc yellow had not been identified in 1984, they were easily identified in the current study. Importantly, cochineal lake, easily identified in almost all the paintings by μ-R, had not been identified by the microchemical analysis.

Second, according to the results presented in Table 7.5, microchemical analysis seems to present a higher selectivity for the identification of zinc white than the multi-technique approach used in this study. While in 1984 zinc white was identified in the ground layer of two paintings (***K*** and ***N***) and in the paint layers of three paintings (***C***, ***G*** and ***N***), in the current study, zinc white was only identified in the paint layer of painting ***N***.

However neither μ-XRD, which had a high and accurate response to zinc white nor FM, which easily identified this pigment even in low amounts (Figure 7.26) were able to identify zinc white[91] in the ground layer of paintings ***K*** and ***N***. This raises some questions regarding the microchemical results.

The microchemical analysis is basically an elemental analysis, in which by chemical reaction with an added reagent a visible phenomenon is produced. Therefore, tests employed for the zinc white identification were able to identify only the presence of the zinc, and not the presence of zinc compounds. Additional tests were necessary to eliminate other possibilities, such as zinc sulfide (present in lithopone – zinc sulfide + barium sulfate), zinc sulfate (present in sulfopone - zinc sulfate + calcium sulfide), zinc carbonate and zinc yellow [(85,435)].

Due to the complex nature of the samples under study and to the low specificity of this technique, the microchemical analysis was probably very complex and fraught with uncertainty and their results must be used carefully.

Finally, copper resinate and cobalt green, two green pigments identified by the microchemical tests in sample **C2** and samples **N2** and ***U*1**, respectively, were not identified by μ-IR or by μ-R. FM was used to analyse sample **C2,** but no insight into the existence of copper resinate was possible. No other auxiliary techniques were employed in the analysis of these three samples.

[91] Identification of zinc white by μ-IR was impossible due to the detector's cut-off; identification by μ-R, except for the restoration samples, was not possible as well; SEM/EDS presented some not understand difficulties in identifying zinc in some of the samples.

Table 7.5 Pigments identified in Pousão's paintings*: 1984 study and current study

	1984								Now							
	Early	Italian						Final	Early	Italian						Final
Pigments	**C**	**G**	**K**	**N**	**O**	**Q**	**U**	**W**	**C**	**G**	**K**	**N**	**O**	**Q**	**U**	**W**
Ground																
Lead white	•	•	•	•	•	•	•	•	•	•	•	•	•	•	•	•
Zinc white			•	•												
Bone/ivory black						•										
Carbon-based black									•	•	•	•			•	•
$Iron^{III}$ oxide									•		•				•	
$Iron^{III}$ oxyhydroxide											•					
$Mercury^{II}$ sulfide								•								•
Ultramarine blue																•
White																
Lead white	•	•	•	•	•	•	•	•	•	•	•	•	•	•	•	•
Zinc white	•	•		•								•				
Yellow and orange																
Cadmium yellow	•	•	•					•	?	?	•	•			•	
Chrome orange									•	•	•	•	•		•	
Chrome yellow	•			•					•		•	•	•	•	?	•
$Iron^{III}$ oxyhydroxide	•	•	•			•				•	•	•		•	•	•
Lead antimonate yellow											•			•		
Strontium yellow									•		•			•		
Zinc yellow											•	•	•			
Red																
Cochineal lake									•		•	•		•	•	•
$Iron^{III}$ oxide	•	•	•	•			•		•	•	•	•			•	•
Madder lake								•								•
$Mercury^{II}$ sulfide	•	•	•	•	•	•		•	•	•	•	•	•	•	•	•
Realgar/parealgar										•						•
Green																
Celadonite														•		•
Chrome green	•	•		•			•	•							•	•
Cobalt green				•			•									
Copper resinate	•															
Emerald green	•		•								•					
Scheele's green											•					
Viridian								•			•					•

(*continued overleaf*)

Table 7.5 *(continued)*

	1984								Now							
	Early	Italian						Final	Early	Italian						Final
Pigments	**C**	**G**	**K**	**N**	**O**	**Q**	**U**	**W**	**C**	**G**	**K**	**N**	**O**	**Q**	**U**	**W**
Blue																
Cerulean blue													•	•	•	
Cobalt blue	•	•	•	•			•		•	•	•	•	•	•	•	
Prussian blue	•		•	•			•				•	•			•	•
Ultramarine blue									•	•	•	•	•		•	•
Black																
Bone/ivory black		•	•			•				•				•		
Vegetable carbon-based black	•						•	•								
Carbon-based black									•	•	•	•	•	•	•	•

C - Paisagem - Abertura da Rua Alexandre Herculano, **G** - Cansada (Cachopa de Capri), **K** - Esperando o sucesso, **N** – Portão, **O** - Rapariga de Anacapri, **Q** - Senhora vestida de preto, **U** - Rapariga deitada no tronco de uma árvore, **W** - Flores campestres

* Only the paintings analised in 1984
? Probable identification

7.7 Conclusions

Since the identification of all the compounds present in the samples of Pousão's paintings by μ-IR and μ-R was not always possible or conclusive, SEM/EDS, μ-XRD and FM were used as auxiliary analytical tools.

The results of the analysis by these techniques proved to be valuable and a good contribution to increasing the knowledge about Pousão's samples. In particular, the presence of lead antimonate yellow was confirmed by SEM/EDS and μ-XRD, while by μ-R its identification was often somewhat uncertain. Further, the pigments cadmium yellow, cobalt blue, zinc white, cerulean blue and madder lake were identified by SEM/EDS, μ-XRD and FM in all the samples where the vibrational techniques failed their identification.

In spite of having chosen these auxiliary techniques to solve specific problems to which it was supposed they would provide the answers, some questions remained and even new ones arose, since , like μ-IR and μ-R, they also have their own limitations.

However, this study clearly highlighted the importance of a multi-technique approach when analysing complex samples and clearly demonstrated the superiority of μ-R for pigment identification over the other analytical techniques.

8 Pousão's palette and painting technique

There are many ways of enjoying paintings; each aspect of a work has its own individual appeal. [...] A close study of an artist's technique – the particular diversity and order which he or she has employed to achieve a given image – will enhance the appreciation of both painter and painting.

A. Bowness

This chapter reports the most important findings on Pousão's palette and technique. An overall discussion of the analytical results presented in the previous chapters is undertaken. Additionally, a comparison of the final results with art history information about easel paintings and data culled from studies on other painters is sketched out.

Some questions always crop up as to a painter's work: what materials and technique(s) did the painter use? Was he influenced by any specific painter or movement? Although in some cases, significant answers can be obtained from existing ordering notes, diaries, painter's letters, reviews and comments by the artists, etc. Only a scientific research of the artist's work allows an exactly insight into the technique and the materials he used.

In the case of Pousão, as no other source of information seems to exist, the scientific analysis of the paintings was the only way of achieving an insight into its work. As described before by employing a multi-technique approach, which included, OM, μ-IR, μ-R, μ-XRD, SEM/EDS and FM, 150 samples removed from 23 paintings by Pousão, belonging to the Museu Nacional Soares do Reis (Appendix B), were analysed.

The examination of the paintings and the analysis of their samples, by the various techniques, besides the characterization of Pousão's palette, revealed special features related to the painting technique, such as the paint layer structure, the way in which the composition evolved and other materials that were employed, major conclusions being presented below.

However, because the paintings under analysis generally were in a good state of preservation, samples were removed mainly from the edges concealed by the frames and, in a few cases, from the surface cracks (Appendix B), not being possible to collect, either samples from all the existing pictorial elements, or as many samples as it would be desirable to fully understand the construction of each different pictorial element.

8.1 Support and ground layer

8.1.1 Support

Approximately, the same number of wood panel and canvas supported paintings were studied (Table 8.1) and, in general, the wood panel support presented smaller dimensions that the canvas.

Comparing the dimensions of the wood panels, it is visible that five of the paintings, ***Jardim de Luxemburgo (estudo)***, ***Fachada de casa soterrada - Roma***, ***Miragem de Nápoles***, ***Rua de Roma*** and ***Cais de Barcelona***, have approximately the same dimensions (16.5 x 10 cm), corresponding to approximately half of the painting ***Escadas de um pardieiro - Roma*** (16.0 x 22.2 cm). It seems that Pousão bought wood panels having the dimensions of the painting ***Escadas de um pardieiro - Roma*** that he divided in two. The slightly different dimensions are due to the paring of the panels.

Regarding the other wood panels, it is difficult to say if they were bought or were made from reused wood.

Table 8.1 Supports and dimensions of the paintings

		Painting	Period	Dimensions[a] /cm
wood panel	D	*Jardim de Luxemburgo (estudo)*	French	16.5 x 9.0
	L	*Fachada de casa soterrada - Roma*	Italian	9.9 x 16.5
	M	*Miragem de Nápoles*	Italian	9.7 x 16.3
	P	*Rua de Roma*	Italian	16.5 x 9.9
	V	*Cais de Barcelona*	Final	16.5 x 10.0
	J	*Escadas de um pardieiro - Roma*	Italian	16.0 x 22.2
	A	*Casa rústica de Campanhã*	Early	20.2 x 12.8
	B	*O mendigo Lapita*	Early	23.5 x 14.2
	Q	*Senhora vestida de preto*	Italian	28.3 x 18.4
	R	*Janela das persianas azuis*	Italian	28.5 x 25.0
	E	*Aldeia de St. Sauves*	French	46.0 x 37.8
canvas	O	*Rapariga de Anacapri*	Italian	18.5 x 13.8
	N	*Portão*[b]	Italian	29.2 x 21.2
	W	*Flores campestres*	Final	30.0 x 22.5
	F	*Paisagem de St. Sauves*	French	46.0 x 65.5
	I	*Cecília*	Italian	82.3 x 57.2
	C	*Paisagem - Abertura da Rua Alexandre Herculano*	Early	68.8 x 122.4
	U	*Rapariga deitada no tronco de uma árvore*	Italian	73.5 x 115.5
	H	*Casas brancas de Capri*	Italian	70.5 x 141.0
	T	*Paisagem de Anacapri*	Italian	70.5 x 140.5
	G	*Cansada (Cachopa de Capri)*	Italian	130.5 x 81.5
	K	*Esperando o sucesso*	Italian	131.5 x 83.5
	S	*Mulher da água*	Italian	144.0 x 135.5

[a] height x width; [b] canvas on an auxiliary paper support

When comparing canvas paintings dimensions, two sets of paintings present approximate dimensions: two landscape paintings - ***Casas brancas de Capri*** and ***Paisagem de Anacapri*** - and two portrait paintings - ***Cansada (Cachopa de Capri)*** and ***Esperando o sucesso***, suggesting that they have the same origin.

Comparing the dimensions of the canvas paintings with those presented by ready-stretched canvas standard 19th century formats from Lefranc & Company and Bourgeois [(90)], while no exact matches occurred, very good approximations were found for four paintings and the 'marine' format from Bourgeois, namely ***Paisagem de St. Sauves*** with the No. 15 (65 x 46 cm^2), ***Rapariga deitada no tronco de uma árvore*** with the No. 50 (116 x 73 cm), and ***Cansada (Cachopa de Capri)*** and ***Esperando o sucesso*** with the No. 60 (130 x 81).

8.1.2 Ground layer

The examination of the paintings and the visualization of the cross sections under the optical microscope indicated that an opaque white ground layer was generally used. Exceptions were found in ***Jardim do Luxemburgo*** and ***Senhora vestida de preto*** (Figure 8.1), both wood panel paintings, where no ground layer is present and ***Paisagem de St. Sauves*** where there is a calcium carbonate - calcite form in oil ground layer and a white lead in oil *imprimitura*.

The opaque white ground is generally a single white ground layer of variable thickness, but in the painting ***Paisagem - Abertura da Rua Alexandre Herculano***, three ground layers of slightly different opacity were used.

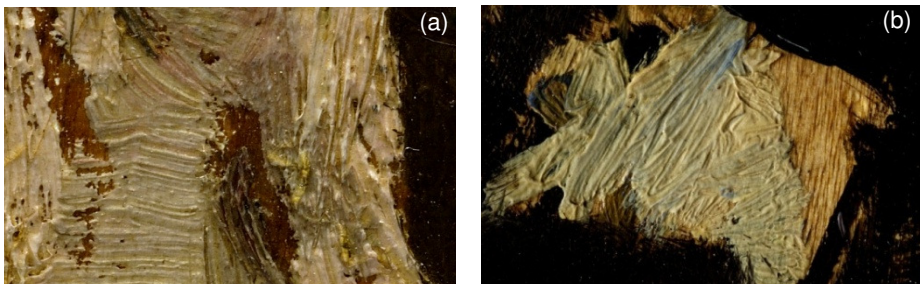

Figure 8.1 Detail of the paintings: (a) ***Jardim de Luxemburgo (estudo)*** and (b) ***Senhora vestida de preto***, showing the wood panel support. Photo: LCRJF.

The analysis of the ground layer(s) indicate that it is mainly constituted by lead white in oil medium. In the canvas paintings lead white is, most of the times, extended with barium sulfate, calcium carbonate - calcite form, or both, while in the wood panel paintings (marked with pink in Table 8.2) a purest grade of lead white seems to have been used. Although the wood panels seem to have been bought, the ground layer they present was probably applied by Pousão since commercially prepared grounds of lead white were normally extended with other white pigments/extenders, such as kaolin, barium sulfate, calcium carbonate - calcite form and so on [90,315], which were not identified.

No stamps or labels from the supplier exist in the back of the canvases, making difficult to ascertain if the canvases were bought ready-primed or unprimed. This absence can be due to the conservation intervention of 1984, since some of the canvases were relined at that time.

Commercially primed canvases were generally pre-primed and then stretched, leaving the tacking margins/edges covered with the ground layer. However, the painting ***Mulher da Água*** (Figure 8.2) exhibits a canvas not entirely primed, indicating that it was prepared after being stretched, probably by Pousão. The painting ***Cecília*** was also not entirely primed.

Table 8.2 Pigments and extenders identified in the ground layers of the paintings

	Paintings																							
	Early			French			Italian																Final	
Compounds	**A**	**B**	**C**	**D**	**E**	**F**	**G**	**H**	**I**	**J**	**K**	**L**	**M**	**N**	**O**	**P**	**Q**	**R**	**S**	**T**	**U**	**V**	**W**
White pigments and extenders																							
Lead white	•	•	•[a]		•	•[a]	•	•	•	•	•	•	•	•[a]	•[a]	•		•	•[a]	•	•	•	•[a]
Barium sulfate						•	•	•	•		•									•	•		
Calcium carbonate - calcite form			•			•[b]					•				•				?				
Coloured pigments																							
Carbon-based black	•	•	•			•	•	•	•	•	•			•		•		•	•	•	•		•
Iron^{III} oxyhydroxide											•								•				
Iron^{III} oxide			•								•								•	•	•		
Ultramarine blue																			?				•
Mercury^{II} sulfide																•							•
Zinc yellow					•																		

A - *Casa rústica de Campanhã*, **B** - *O mendigo Lapita*, **C** - *Paisagem - Abertura da Rua Alexandre Herculano*, **D** - *Jardim de Luxemburgo (estudo)*, **E** - *Aldeia de St. Sauves*, **F** - *Paisagem de St. Sauves*, **G** - *Cansada (Cachopa de Capri)*, **H** - *Casas brancas de Capri*, **I** - *Cecília*, **J** - *Escadas de um pardieiro - Roma*, **K** - *Esperando o sucesso*, **I** - *Fachada de casa soterrada - Roma*, **M** - *Miragem de Nápoles*, **N** - *Portão*, **O** - *Rapariga de Anacapri*, **P** - *Rua de Roma*, **Q** - *Senhora vestida de preto*, **R** - *Janela das persianas azuis*, **S** - *Mulher da água*, **T** - *Paisagem de Anacapri*, **U** - *Rapariga deitada no tronco de uma árvore*, **V** - *Cais de Barcelona* and **W** - *Flores Campestres.*

[a] Lead carbonate is also present
[b] The only component of ground layer. The others compounds are present in the *imprimitura*.

Figure 8.2 Back-side of the painting ***Mulher da água***, showing the canvas stretched over the wooden frame (stretcher). Photo: LCRJF.

The painting ***Paisagem de St. Sauves*** has a rather unusual preparation: a brownish ground layer constituted by calcium carbonate - calcite form and a proteinaceous binder, over which a white *imprimitura* (or a second ground layer) constituted by lead white, barium sulfate and an oil binder was applied. Looking at the cross section of the sample **F2** (Figure 8.3), it seems that the *imprimitura* was applied while the ground layer was not completely dry, suggesting that both were applied by the same person (Pousão, the merchants or a

craftsman). The use of a ground layer of calcium carbonate or gypsum with animal glue for panel paintings in Europe, is very common since early medieval times; however, the use of ready-primed canvas with this ground was less common [69,235,438].

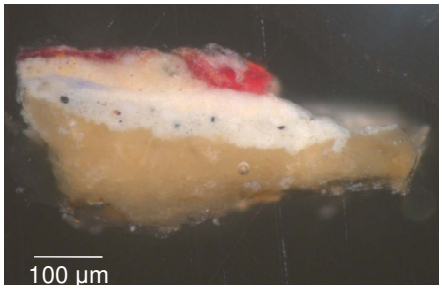

Figure 8.3 Cross section of sample **F2**, viewed under reflected light.

There seems to be no alteration on the ground layer's colour throughout the four periods under study. Carbon-based black and ochres were added in a low amount to tone the white and/or to accelerate the drying [69] , being not characteristic of a single period. Ultramarine blue, mercury^{II} sulfide and zinc yellow particles were also identified in four paintings (***Aldeia de St. Sauves***, ***Rua de Roma***, ***Mulher da água*** and ***Flores Campestres***), apparently not due to transference from the upper paint layer. The ultramarine blue, for example, can have been added to counteract the yellowing of the oil medium [89].

8.2 Painting technique

8.2.1 Underdrawing

The examination of the painting's surface reveals that in some of them, major areas and elements of the composition, such as sky, landscape, architecture and principal figures were outlined with a black line, before painting. Sometimes it appears a pencil line, such as for example, the black lines used to define the tree logs, in the upper right corner of ***Rapariga deitada no tronco de uma árvore*** (Figure 8.4a), while other times it seems more like a carbon-based black stroke, such as the lines used to define the woman in ***Mulher da água*** (Figure 8.4b). The underdrawing seems to have served only as a rough indication of composition.

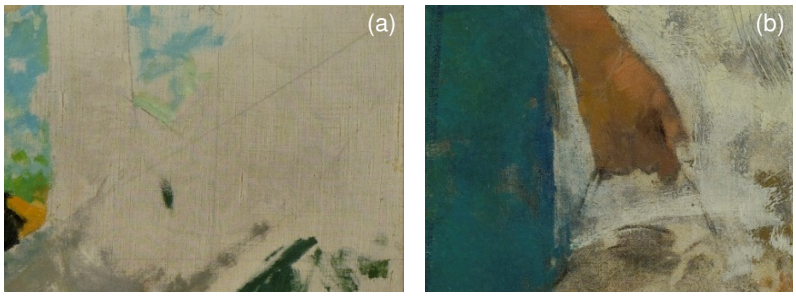

Figure 8.4 Detail of the painting: (a) ***Rapariga deitada no tronco de uma árvore***, showing the black underdrawing pencil line used to define the tree logs and (b) ***Mulher da água***, showing the carbon-based black strokes used to define the hand and jug. Photo: LCRJF.

8.2.2 Outlining

Long continuous strokes of blue, black and brown were used to outline some elements during the paint construction. For example, there is a blue stroke defining the cactus in the lower right corner of ***Casas brancas de Capri*** (Figure 8.5a), the cloths of the woman in ***Mulher da água*** and the roof of ***Janela das persianas azuis***, while there is brownish stroke defining the tree log of ***Rapariga deitada no tronco de uma árvore*** (Figure 8.5b).

Figure 8.5 Detail of the painting: (a) ***Casas brancas de Capri***, showing the blue outline of the cactus; (b) ***Mulher da água***, showing the blue outline of the woman's cloth; ***Janela das persianas azuis***, showing the blue outline of the roof; and (c) ***Rapariga deitada no tronco de uma árvore***, showing the brown outline to adjust the tree log dimensions. Photo: LCRJF.

The unfinished state of ***Mulher da água*** makes it possible to see that a grey-black wash (water-based of carbon black) was applied to the reserve areas, as is the case of the earthen pot seen in detail in Figure 8.6.

Figure 8.6 Detail of the painting ***Mulher da água***, showing the reserve for the earthen pot done with a grey-black wash. Photo: LCRJF.

Another particular detail is the existence of a black pencil line dividing the areas of the sky and the sea in ***Paisagem de Anacapri*** (Figure 8.7), which was drawn after the tree vegetation was painted.

Figure 8.7 Detail of the painting ***Paisagem de Anacapri***, showing the black pencil line drawn over the paint layer. Photo: LCRJF.

8.2.3 Paint structure

In general, paint layers were applied after the ground layer had dried. However, in a few cases, the ground layer was not completely dry and some pigment particles appeared dispersed through the ground layer. In the same way, an organized and clear division between the paint layers is normally present, indicating that the complex colour blending of each layer was done on the palette before being applied in the painting, and that subsequent adjustments to the composition were done after the lower layer had dried. However, wet-in-wet work, blending or half blending the colours on the canvas was also identified, especially in the vegetation and ground areas, such as in foreground - left side of ***Casas brancas de Capri*** (Figure 8.8) and in the small figures.

Regarding the number of layers, it varies significantly, even across a single painting (1 to 10). For example, in the painting ***Cecília***, while the blue of the skirt is made of a single blue layer (**I5,** Figure D50), the black of the pedestal is made of six layers with very different hues (Figure 8.9). This sample exhibits one of the cases where an underpaint with a contrasting colour, is used in order to modify the precise hue of the final layer. Other examples of sample presenting an underpaint with a contrasting colour are samples **I7** and **K6** (Figures D52 and

D63). As what concerns the paint layer thickness, layers ranging from 4 to 358 µm were identified.

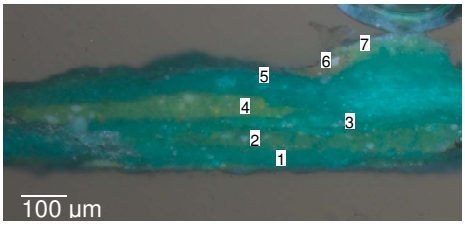

Figure 8.8 Cross section of sample **H2** viewed under reflected light: the dark green layers 1, 3 and 5 are composed by emerald green, Scheele's green, lead white, chrome yellow, mercury^{II} sulfide and carbon-based black, the light green layers 2, 4 and 7 are composed by chrome green, emerald green, zinc yellow, lead white and mercury^{II} sulfide, and the brown layer 6 is composed by chrome yellow, emerald green and maybe cadmium yellow.

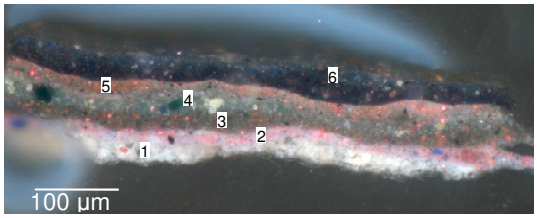

Figure 8.9 Cross section of sample **I1** viewed under reflected light: the white ground layer 1 is composed by lead white (extended with barium sulfate), the pink layer 2 is composed by lead white (with lead carbonate), mercury^{II} sulfide, iron^{III} oxide, cochineal lake, ultramarine blue and carbon-based black, the brown layer 3 is composed by iron^{III} oxide, mercury^{II} sulfide, chrome orange, ultramarine and viridian, the green layer 4 is composed by celadonite, mercury^{II} sulfide, lead antimonate yellow (with basic lead sufate) and carbon-based black, the pink layer 5 is composed by mercury^{II} sulfide, cochineal lake, lead white, iron^{III} oxyhydroxide, ultramarine blue and carbon-based black; the black layer 6 is composed by ultramarine blue, chrome yellow, vermilion, iron^{III} oxyhydroxide and carbon-based black.

8.2.4 Palette

In accordance with the results of the sample's analysis presented in the previous chapters, 26 pigments were identified in the paint layers, distributed by painting as shown in Table 8.3. As summarized in this table, it seems that Pousão's selection of pigments is more or less fixed, not varying with of the type support (wood panel or canvas) or the painting period. Generally, each painting has a large number of yellows and orange pigments, three reds and two/three blues pigments.

Also important is the fact that Pousão made a great use of the 19th century pigments, especially of the yellow chromates, the cobalt-based blue pigments, ultramarine blue and

viridian. The use of individual pigments, including some very brief remarks on their historical background is described in more detail below.

Often, pigments exist both in natural as in a synthetic form. Some natural forms were and still are economical viable, such as ochres, green earths, etc., while others were replaced by cheapest synthetic forms, such as ultramarine blue that replaced lazurite.

Unfortunately, due to the enormous complexity of the samples under analysis and to the fact that Infrared and Raman spectroscopies and X-ray diffraction exhibit the same spectrum/diffractogram for both the natural and the synthetic forms, it is almost impossible to ascertain which form was used. Being so, compounds will be referred to by some of their most common/commercial names.

White pigments

Clearly ***lead white/basic lead carbonate*** ($2PbCO_3.Pb(OH)_2$) is the most important pigment of Pousão's palette, being present in every painting and in almost every layer. In some paintings it was identified associated with ***lead carbonate/cerussite*** ($PbCO_3$), which is probably due to the synthesis process of lead white, which basically consists in the corrosion of a sheet of metallic lead to exposition to acetic acid (vinegar) vapour in the presence of carbon dioxide, where it can be a product [315,439-441]. Hydrocerussite, the natural form of lead white is a relatively rare mineral, while cerussite, the natural form of lead carbonate is very abundant. However, there is no record of their use as white pigments [315].

Zinc white/zinc oxide (ZnO) has been used as a white pigment since its introduction in the 18th century, when considerable concern about lead poisoning arose, and a substitute for lead white was looked for [90]. However, due to its relatively poor hiding power, poor dry ability and high cost, was not extensively used as an artist' pigment, prior to the second quarter of the nineteenth century, when improvements were made [85,442]. Zinc white was identified in conjunction with a great concentration of lead white in two paintings. Apparently there is no reason for Pousão to have mixed these two white pigments, but it is known that manufacturer used zinc white as lightening agent of various pigments [85,90].

Table 8.3 Pousão's palette

	Paintings																						
	Earlier			French			Italian															Final	
Compounds	A	B	C	D	E	F	G	H	I	J	K	L	M	N	O	P	Q	R	S	T	U	V	W
White																							
Lead white	•	•	•	•	•	•	•	•	•	•	•	•	•	•	•	•	•	•	•	•	•	•	•
Zinc white		•							?					•					•	?		?	
Yellow and orange																							
Cadmium yellow			?			•	?	?			•	•	•	•					•	•	•	•	
Chrome orange	•		•	•	•	•	•		•	•	•	•	•	•	•	•		•	?		•		
Chrome yellow	•		•	•	•	•		•	•		•	•		•	•	•	•	•	•	•	?		•
Iron^{III} oxyhydroxide				•	•		•		•	•	•	•	•	•			•		•		•	•	•
Lead antimonate yellow					•	•			•	?	•	•					•		•	•			
Strontium yellow	•	•	•	•							•						•						
Zinc yellow					•	•		•			•	•	•	•	•					•		•	
Red and brown																							
Cochineal lake	•		•	•	•	•		•	•	•	•	•		•		•	•	•	•	•	•	•	•
Iron^{III} oxide	•	•	•	•	•		•	•	•	•	•	•	•	•		•		•	•	•	•	•	•
Madder lake																•							•
Mercury^{II} sulfide	•		•	•	•	•	•	•	•	•	•	•	•	•	•	•	•	•	•	•	•	•	•
Realgar/parealgar				•			•	•															•
Green																							
Celadonite					•				•														•
Chrome green								•											•		•		•
Emerald green						•		•			•	•							•			•	
Malachite								•															
Scheele's green								•			•												
Viridian				•	•	•		•	•			•								•			•
Blue																							
Cerulean blue									•						•		•	•					
Cobalt blue	•		•	•	•	•	•	•	•		•		?	•	•	•	•	•		•		?	
Prussian blue				•	•	•			•	•	•	•		•			•		•	•	•	•	•
Ultramarine blue	•		•		•	•	•	•	•	•	•	•		•	•	•			•	•	•	•	•
Black																							
Bone/ivory black	?	•		•			•			•	?						•						
Carbon-based black	•	•	•	•	•	•	•	•	•	•	•	•	•	•	•	•	•	•	•	•	•	•	•

A - *Casa rústica de Campanhã*, **B** - *O mendigo Lapita*, **C** - *Paisagem - Abertura da Rua Alexandre Herculano*, **D** - *Jardim de Luxemburgo (estudo)*, **E** - *Aldeia de St. Sauves*, **F** - *Paisagem de St. Sauves*, **G** - *Cansada (Cachopa de Capri)*, **H** - *Casas brancas de Capri*, **I** - *Cecília*, **J** - *Escadas de um pardieiro - Roma*, **K** - *Esperando o sucesso*, **l** - *Fachada de casa soterrada - Roma*, **M** - *Miragem de Nápoles*, **N** - *Portão*, **O** - *Rapariga de Anacapri*, **P** - *Rua de Roma*, **Q** - *Senhora vestida de preto*, **R** - *Janela das persianas azuis*, **S** - *Mulher da água*, **T** - *Paisagem de Anacapri*, **U** - *Rapariga deitada no tronco de uma árvore*, **V** - *Cais de Barcelona* and **W** - *Flores Campestres.*

? Propable identification

Yellow and orange pigments

Seven yellow to orange pigments were identified: chrome yellow, chrome orange, strontium yellow, zinc yellow, cadmium yellow, iron^{III} oxyhydroxide and lead antimonate yellow. The existence of a relatively large number of yellows in a palette is not unusual, since it is very difficult to modify its colour by mixing it with other pigments (except for lightening with the addition of a white pigment) [438].

Strontium yellow ($SrCrO_4$), ***zinc yellow*** (approximately $K_2O.4ZnCrO_4.3H_2O$), and especially, ***chrome yellow*** ($PbCrO_4$) and ***chrome orange*** (PbCrO4. PbO) are presented in a large number of samples. Although chromate pigments were known for their tendency to darken, because they presented a good covering power and an economical price, they were popular pigments until the 1990's [434]. Chrome orange, the first pure, intense and opaque orange pigment to become available to painters [90]was significantly used by Pousão, like, for example, in ***Casa rústica de Campanhã*** (Figure 8.10).

Cadmium yellow/cadmium sulfide (CdS), a rarely available and highly cost pigment (four times the price of the chromes [438]), was identified in green, brown and even blue layers, but not in the yellow ones. Although cadmium yellow has two mineral equivalents, the commoner greenockite and hawleyite, there is no evidence that they were ever used as a pigment [85]. The commercialization of this pigment in large scale started in 1840-1850 and two principal types of the pigment did exist: the pure form and the lithopone variety that consists in the precipitation of CdS with barium sulfate. There is no signal of the existence of the lithopone variety in the paintings.

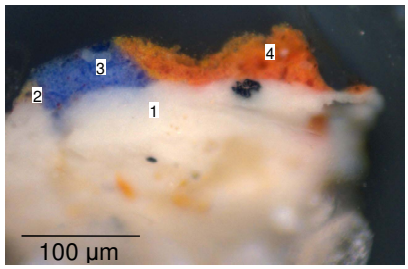

Figure 8.10 Cross section of sample **A3** viewed under reflected light: the white ground layer 1 is composed by lead white with carbon-based black and ultramarine blue; the brown layer 2 is composed by lead white, mercury^{II} sulfide and chrome yellow, the blue layer 3 is composed by lead white, cobalt blue, iron^{III} oxide and cochineal lake, and the orange layer 4 is composed by chrome orange, chrome yellow, iron^{III} oxide, lead white and carbon-based black.

Iron^{III} oxyhydroxide/goethite/Mars yellow (α-FeOOH), ranging in colour from yellow to brownish, was identified in layers of all hues, but it seems that it was in the samples removed from the brown areas that it was more important. In the 19th century, both the natural and the

synthetic forms of iron oxides, designed as Mars colours, were available, but the simultaneous identification of natural compounds such as kaolin, quartz and calcium carbonate - calcite form in the same layers, suggest that the natural form was used.

Lead antimonate yellow (approximately $Pb_2Sb_2O_7$), a pigment that had been lost and rediscovered several times [342] was identified on nine paintings. Associated with this pigment were identified *basic lead sulfate/lanarkite* ($PbO.PbSO_4$), *lead sulfate/anglesite* ($PbSO_4$), *rosiaite* ($PbSb_2O_6$) and *cervantite* (Sb_2O_4). Although *basic lead sulfate* has been used as a white pigment since 1870[92] [12,85,337] and *lead sulfate* was sold in bottles until 1830, under the name *Flemish white* [85,315,443], it seems that these compounds were not used intently to be white pigments, but are rather present as extenders, or as by-products of the synthesis of lead antimonate yellow [441], rosiaite and cervantite (rarely identified) are known by-products of the synthesis of lead antimonate yellow [343]. There is no evidence that bindheimite, the natural form of this pigment was ever used as an artists' pigment [342].

Red and brownish pigments

Six red and brownish pigments were identified: mercury^{II} sulfide, iron^{III} oxide, cochineal lake, madder lake, realgar and χ-phase/pararealgar.

Mercury^{II} sufide/vermilion/cinnabar (HgS), ***iron^{III} oxide/hematite/Mars red*** (α-Fe_2O_3) and ***cochineal lake*** are very common pigments in the samples, either to warm layers of any colour or to produce orange, pink, red and brown layers.

During the 19th century, both cinnabar (the natural form of mercury^{II} sulfide), used as a pigment since ancient times, and vermilion (the synthetic form of mercury^{II} sulfide), known since the 8th century [444], were available from French colour suppliers at about the same price [90] so, either one or both forms could have been used by Pousão. In the same way, both the natural (hematite) and the synthetic forms (Mars red) of iron^{III} oxide were available, and could have been used. However, as also referred for iron^{III} oxyhydroxide/goethite, the simultaneous identification of natural compounds such as kaolin, quartz, gypsum and calcium carbonate - calcite form, which normally occur associated with the mineral form, suggest that the natural form, hematite, was the used.

Cochineal lake is largely the most important of the lake pigments used by Pousão, while ***madder lake*** was identified only in two paintings. Due to their intensity of hue and colour saturation, traditional lake pigments were an important part of the painters' palette [438]. And by the 19th century, cochineal and madder pigments became the preferred artists' lake

[92] Under different names, e.g. *white lead (basic sulfate)*, *white lead (sulfate*, *sublimed white lead* and *Maxwell Lyte lead white*).

pigment, while lac and kermes are barely mentioned [136,445], so its preference in detriment of the other lake pigments is understandable.

Realgar (α-As_4S_4) and ***χ-phase/pararealgar*** were identified in five samples (**D2**, **G4**, **H1**, **H8**, **W5**), but only in the sample **H1** (Figure 8.11), removed from the brown ground in the bottom of the painting ***Casas brancas de Capri***, it was a major pigment.

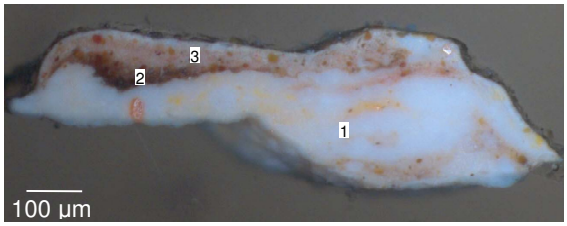

Figure 8.11 Cross section of sample **H1** viewed under reflected light: the white layer 1 is composed by lead white, realgar, iron^{III} oxide, cadmium yellow and carbon based black; the brown layer 2 is composed by iron^{III} oxide, mercury^{II} sulfide and carbon-based black and the brown layer 3 is composed by lead white, mercury^{II} sulfide, iron^{III} oxide, cadmium yellow and carbon-based black.

Blue pigments

Four blue pigments are present in the samples: cerulean blue, cobalt blue, Prussian blue and ultramarine blue.

Cobalt blue ($CoAl_2O_4$), characterized for a pure blue hue, a highly stability and the ability of accelerating the drying of the oil medium, can be considered a very important pigment in Pousão's palette, as it was chosen to provide colour to the sky (Figure 8.12) and sea in most of the paintings.

Cerulean blue ($CoO.nSnO_2$), whose hue is slightly greenish that cobalt blue was identified in four paintings, most of the times together with cobalt blue [90]. These two cobalt-based pigments are the most expensive of the four blue pigments [90,321].

Although ***Prussian blue*** ($Fe_4[Fe(CN)_6]_3.14\text{-}16H_2O$), a synthetic pigment introduced in the early 1700s [85], is present in a large number of paintings, only in a few of the samples under analysis was it the pigment providing the blue hue to the layers. It was generally used to warm some beige and brown layers, or mixed with yellow pigments to provide a green hue.

In a similar way, there were only few where ***Ultramarine blue*** ($Na_8[Al_6Si_6O_{24}]S_n$), the synthetic equivalent of the mineral lazurite, was responsible for the colour of the blue layers. Two of these samples were removed from sky, and a third from the sea.

The current study does not allow the distinction between the natural form of this pigment, lazurite and its synthetic equivalent, ultramarine blue, synthesised on a large scale since 1828 [381,446]. Nevertheless, since lazurite was and still is, much more expensive than

ultramarine blue, and this pigment was used most of the times, to warm other hues, the synthetic form is probably the one that is present.

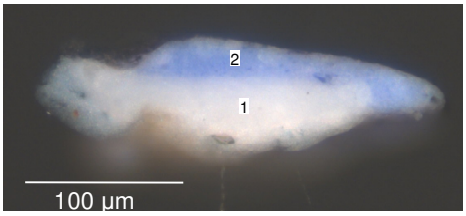

Figure 8.12 Cross section of sample **M2** viewed under reflected light: the white ground layer 1 is composed by lead white and carbon-based black and the blue layer 2 is composed by cobalt blue and lead white.

Purple pigments

None of the purple pigments introduced during the 19th century, such as cobalt violet (either $Mg_2Co(AsO_4)_2$ or $Co_3(PO_4)_2$) or manganese violet ($(NH_4)_2Mn_2(P_2O_7)_2$) [85], were identified in any painting. Instead, mixtures of inorganic blue pigments with organic reds were identified in the purple coloured layers. For example, in the sample **T4** from ***Paisagem de Anacapri*** (Figure 8.13), the purple layer 2 was obtained mixing cobalt blue with cochineal lake, while the purple layer 3 was obtained mixing cochineal lake with ultramarine blue. In sample **W5** (Figure D148) from ***Flores campestres***, the purple particles present in the green layer 2 were identified as a mixture of Prussian blue with madder lake.

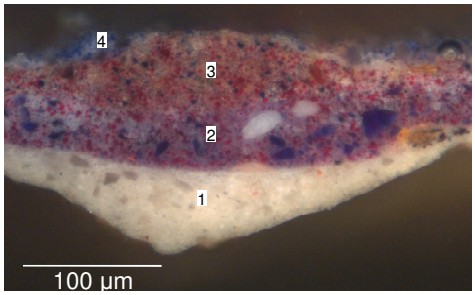

Figure 8.13 Cross section of sample **T4** viewed under reflected light: the white ground layer 1 is composed by lead white (extended with barium sulfate), iron^{III} oxide and carbon-based black; the purple layer 2 is composed by lead white, cobalt blue, cochineal lake, mercury^{II} sulfide and carbon-based black, the brown layer 3 is composed by ultramarine blue, cochineal lake, zinc yellow, lead white and carbon-based black and the blue layer 4 is composed by ultramarine blue, lead white, zinc yellow, mercury^{II} sulfide and carbon-based black.

Green pigments

Six green pigments were identified: celadonite, chrome green, emerald green, malaquite and viridian. Green paint mixtures, such as ultramarine blue with chrome yellow and Prussian blue with cadmium yellow seems to also exist.

Viridian and ***emerald green*** are apparently the most common single green pigments used for the green areas, viridian for deep shades and emerald green for light shades, being the simultaneous presence of both also very common. ***Viridian***, a bluish-green transparent pigment, firstly manufactured in 1838 by Pannetier and patented by Guignet in 1859, was almost twice as expensive as emerald green what apparently did not constitute a problem for Pousão [447]. ***Emerald green*** ($Cu(CH_3COO)_2.3Cu(AsO_2)_2$), a blue-green shining colour, was firstly synthesized in 1814 when trying to improve ***Scheele's green*** ($CuHAsO_3$), a very popular green pigment at the time [85,447]. Scheele's green was identified in two of the paintings, in a low amount and associated with emerald green, being probably an impurity of emerald green. Due to their high toxicity, emerald green and Scheele's green were removed from the artists' palette in the 1960's [228].

Celadonite (approximately $K(Mg,Fe^{2+})(Fe^{3+},Al)[Si_4O_{10}](OH)_2$), a less abundant and relatively expensive mineral used for green earth pigments was identified in the paintings ***Aldeia de St. Sauves***, ***Cecília*** e ***Flores Campestres***, normally mixed with other green pigments. Figure 8.14 shows the cross section of the sample **E7** removed from the tree leafs of ***Aldeia de St. Sauves***, whose green shade is provided by celadonite and viridian.

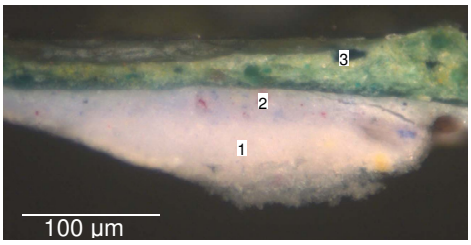

Figure 8.14 Cross section of sample **E7** viewed under reflected light: the white ground layer 1 by lead white and zinc yellow, the blue layer 2 is composed by cobalt blue, zinc yellow, cochineal lake and carbon-based black and the green layer 3 is composed by celadonite, viridian, lead white (with lead carbonate), chrome yellow, chrome orange and Prussian blue.

Malachite ($Cu_2CO_3(OH)_2$) was identified in a single sample, **H8**, which was removed from the dark green hue of the cactus in the lower left corner of the painting ***Casas brancas de Capri***. Associated with malachite was identified ***brochantite*** ($Cu_4(OH)_6(SO_4)$).

Chrome green, a mixture of Prussian blue with chrome yellow that could have been bought already prepared under the name Brunswick was identified in the paintings ***Casas***

Brancas de Capri, ***Mulher da água***, ***Rapariga deitada no tronco de uma árvore*** and ***Flores Campestres***.

Other green paint mixtures were also identified; namely ultramarine blue with chrome yellow, which provided the green hue of the green layers of sample **C2** (Figure D11) (no green pigment was identified), and Prussian blue with cadmium yellow, which was used to achieve the light green hue of the green layers 2 and 4 of sample **F6** (Figure D32) and the green hue of the green layers of sample **U13** (Figure D138).

Black pigments

Carbon-based black pigments are common in Pousão paintings and in very dark layers. For example, in layer 2 of sample **G4** from ***Cansada (Cachopa de Capri)*** (Figure 8.15) the carbon-based black pigment was identified as ***bone/ivory black***, a pigment produced by calcination of bones and/or ivory. Unfortunately, in layers with a reduced number of carbon-based black particles, it was not possible to distinguish between bone/ivory black and vegetable carbon-based black.

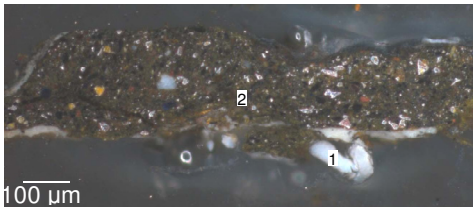

Figure 8.15 Cross section of sample **G4** viewed under reflected light: the white ground layer 1 is composed by lead white (extended with barium sulfate) and the brown layer 2 is composed by bone/ivory black, iron^{III} oxide, mercury^{II} sulfide, realgar and χ-phase/pararealgar, cadmium yellow, cobalt blue and lead white.

8.2.5 Main painting elements

Based on the pigment identification (Table 8.3) it is possible to systematize the build-up method of each particular element of the composition as presented bellow:

Sky

Sky was generally executed applying over the ground layer, a single blue layer, as in ***Casa Rústica***, ***Paisagem - Abertura da Rua Alexandre Herculano***, ***Casas Brancas de Capri***, ***Portão***, ***Mulher da água***, ***Paisagem de Anacapri*** and ***Cais de Barcelona***, or two blue layers, as in ***Aldeia St. Sauves***, ***Paisagem St. Sauves***, ***Rua de Roma***. Except for the paintings ***Mulher da água*** and ***Paisagem de Anacapri***, where ultramarine blue and lead

white are the main components, a mixture mainly composed by cobalt blue and lead white is responsible for the layer colour. Figure 8.16 shows the cross section of the sample **C1**, removed from the sky of ***Paisagem - Abertura da Rua Alexandre Herculano***.

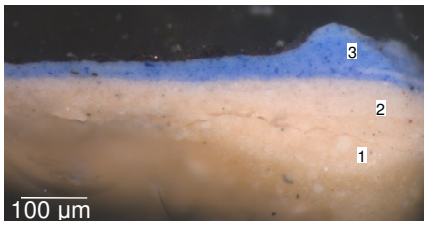

Figure 8.16 Cross section of sample **C1** viewed under reflected light: the white ground layers 1 and 2 are composed by lead white (with lead carbonate and extended with calcium carbonate - calcite form, iron^{III} oxide and carbon-based black and the blue layer 3 is composed by lead white (with lead carbonate), cobalt blue and carbon-based black.

Sea (water)

Only three[93] samples from sea (water) areas were analysed, namely **H5** from ***Casas brancas de Capri***, **M2** from ***Miragem de Nápoles*** and **V1** from ***Cais de Barcelona***. In the two wood panel paintings (***Miragem de Nápoles*** and ***Cais de Barcelona***) a single blue layer is present, mainly composed by lead white and cobalt blue in **M2** and lead white, ultramarine blue and emerald green in **V1**. In the sample from the canvas painting, **H5** (Figure 8.17), a more complex structure, consisting of five well defined blue layers, mainly composed by lead white and cobalt blue, is present.

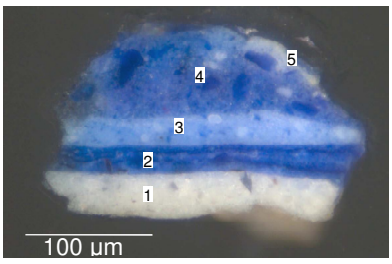

Figure 8.17 Cross section of sample **H5** viewed under reflected light: the white ground layer is composed by lead white (extended with barium sulfate) and carbon-based black, the blue layer 2 is composed by lead white and cobalt blue, the blue layer 3 is composed by lead white, cobalt blue and mercury^{II} sulfide, the blue layer 4 is composed by lead white and cobalt blue and the white layer 5 is composed by lead white.

[93] The sample removed from the sea of ***Paisagem de Anacapri*** proved to come from a restoration area.

Other blue elements/areas

The blue of the wall in ***Estátua do Jardim de Luxemburgo*** (sample **D2**) and ***Janela das persianas azuis*** (samples **R2** and **R3**) are mainly composed by cobalt blue and lead white. The bluish-green of the chair in ***Cecília*** (sample **I3**) and the background of ***Rapariga de Anacapri*** (sample **O1**) is mainly composed by cerulean blue with lead white and the bluish-grey background of ***Senhora vestida de preto*** (sample **Q6**) is a mixture of lead white, cobalt blue, mercury^{II} sulfide, iron^{III} oxyhydroxide, lead antimonate yellow and carbon-based black.

Vegetation

Foliage of the trees, cactus and ground vegetation are very complex and composed by variable pigment mixtures in which the green hue is normally obtained by the simultaneous use of more than one type of green pigment and/or green mixture.

Of particular interest is the fact that, in contrast to what would be expect, the dark hue of the cactus, in the lower left corner of ***Casas brancas de Capri*** (layers 4 and 5 of sample **H8**), was not merely built with a darker shade (obtained adding dark pigments) of the adjacent light colour (layer 2 of sample **H7**), nor applying a dark layer over the lightest one. Instead, the dark hue was built up in a applying two darker green layers with a more complex pigment mixture suggesting that, for Pousão, different shades meant different colours (Figure 8.18a and b).

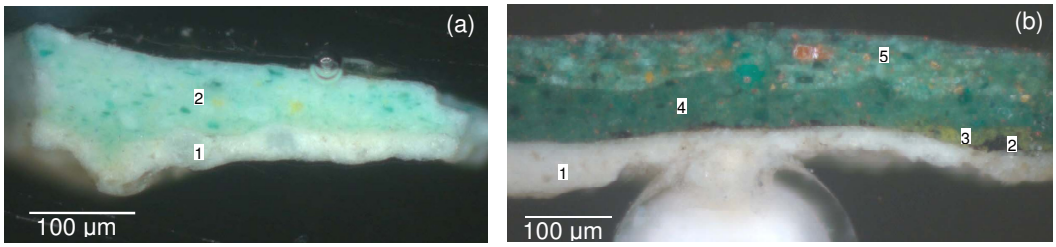

Figure 8.18 (a) Cross section of the sample **H7** viewed under reflected light: the white ground layer 1 is composed by lead white (extended with barium sulfate) and carbon-based black and the green layer 2 is composed by lead white, emerald green, chrome yellow, zinc yellow and cochineal lake; (b) Cross section of the sample **H8** viewed under reflected light: the white ground layer 1 is composed by lead white (extended with barium white) and carbon-based black, the brown layer 2 is composed by carbon-based black, the light green layer 3 is composed by ultramarine blue, chrome yellow, zinc yellow and carbon-based black, the green layer 4 is composed by malachite (with brochantite), emerald green, viridian, realgar, mercury^{II} sulfide and zinc yellow and the green layer 5 is composed by emerald green, viridian, malachite, lead white, chrome yellow, zinc yellow, realgar, vermilion, cobalt blue and carbon-based black.

Flesh areas

Because only two samples from flesh areas were analysed, namely sample **I6**, from the hand of ***Cecília*** and sample **S6**, from the hand of ***Mulher da água***, and further, ***Mulher da água*** is an unfinished painting, is very difficult to draw any conclusion regarding the flesh tone.

8.2.6 Binder

Due to the high complexity of the samples and to the intrinsic limitations of the analytical technique, μ-IR, although the binder was identified as a drying oil, it was not possible to specify which drying oil(s) was/were used. However, thanks to a parallel study carried out at LCRJF, in which the samples were analysed by gas chromatography combined with mass spectrometry (GC/MS)[94], it was possible to conclude that linseed oil is present in the dark areas and ground layers, while walnut oil, which yellows less [(72,448)], is present in the lighter areas such as in the sky.

These results might suggest a careful selection of the drying oil by Pousão and his concern regarding the discoloration of the painting. However, since from 1860 on, nearly all the artists used tube paint (which already contain oil and even driers) due to their convenience and easy acquisition, painters were no longer to absolutely choose the oil to paint with[95 (74)], hence, it was difficult to attribute the choice of the oil medium to Pousão.

8.2.7 Extenders, associated compounds/impurities and degradation compounds

Extenders and associated compounds/impurities are not generally included in the painter's palette, since they were not intentionally used as colouring materials. However, these compounds may indicate unique manufacturers or particular geographic areas of mineral compounds, being in fact closely linked to the palette. Therefore, it was decided to include in this chapter the extenders, the associated compounds/impurities and even the degradation compounds identified in the samples under analysis (Table 7.4) and some brief remarks on their origin and historical background.

Unfortunately, due to the high complexity of the samples, it was very difficult to relate any of such compounds to a specific pigment, except for degradation compounds.

[94] Unpublished.

[95] Oil and/or diluents were added to paints during painting.

Extenders

Calcium carbonate – calcite form ($CaCO_3$), the most common mineral form of calcium carbonate[96], has been used as an extender since early medieval times [(235)], while ***barium sulfate*** ($BaSO_4$) came into significant use as an extender only in the beginning of the 19th century (both in the synthetic as in the natural forms) [(284)].

Associated compounds/impurities

Kaolin ($Al_2[Si_2O_5](OH)_4$), ***gypsum*** ($CaSO_4.2H_2O$) and ***quartz*** (SiO_2) are compounds commonly associated with earth pigments such as iron oxides, which can contain a relatively low percentage of the colouring compound and a high percentage of clay silica and feldspar minerals. Quartz is very abundant in Earth's surface while kaolin commonly occurs with goethite [(338)]. However, kaolin was also extensively employed as an extender, for example, of chrome green and chrome yellow [(90)].

Anatase, rutile and brookite, the three polymorphic forms of titanium^{IV} dioxide (TiO_2), which were identified only as trace compounds, are most probably also associated to the presence of mineral compounds.

Brochantite ($Cu_4(OH)_6SO_4$) was identified in the same sample were basic copper^{II} carbonate was identified, indicating that malachite is the form that is present.

Lead carbonate ($PbCO_3$), known geologically as cerussite, was identified in most part of the paintings. Although this white compound, both in the synthetic and mineral form, has been used as a pigment [(85)], it is probably present in the painting's samples as a by-product of the lead white, since it is known that it is formed during the process of converting metallic lead into lead white [(315,449)].

Tetragonal lead^{IV} oxide, also known as plattnerite was identified in three paintings. However, its identification is uncertain since it was based in the supposition that it was laser degradated during analysis, producing lead^{II} oxide (known as massicot) a yellow pigment. This compound occurs naturally in lead ores and is formed by alteration of other lead based compounds [(85)]. Its presence might be associated to lead white.

Lead^{II,IV} oxide (Pb_3O_4) was identified as a single grain in only two samples (**C4** and **T4**), suggesting that it is present as an impurity. In fact, although its mineral form, minium, has been used since antiquity, this pigment was not very popular during the 19th century [(450)].

Lead sulfate ($PbSO_4$), ***basic lead sulfate*** ($PbSO_4.PbO$), ***rosiaite*** ($PbSb_2O_6$) and ***cervantite*** (Sb_2O_4) are most probably present in the painting's samples as by-products of the

[96] Aragonite and vaterite are two less common polymorphic forms of calcium carbonate.

synthesis of lead antimonate yellow. In fact, most of the times, they were identified in association with that yellow pigment.

Cobalt oxide (Co_3O_4) was identified in only one sample **H7**. This grey/black compound that except for one report [324], seems to have never been used as an artistic pigment, is probably present as an impurity.

Degradation compounds

Copper^{II} sulfide (CuS), which was identified in samples **S1** and **T1** seems to result from the reaction between ultramarine blue (sulfur-containing pigment) and emerald green (copper-containing pigment) [228,395]. Although the analogue mineral of this compound, covellite, has been known since 1832 [393], there is only one recent report of its use as a pigment [394].

8.2.8 Surface texture

In terms of brushwork, generally the wood panel paintings present a larger use of texture than the canvas. Wood panels were worked mainly with thick impastoed brushstrokes, painted sketchily, with the end of the brush (to draw in the wet paint), a spatula and even fingers. An example is shown in a detail of ***O mendigo Lapita*** (**B**) presented in Figure 8.19a.

Figure 8.19 Detail of the painting: (a) ***O mendigo lapita*** and (b) ***Cansada (Cachopa de Capri)***. Photo: LCRJF.

Canvas paintings texture shows a correlation with the type of work. Portraits, such as ***Cecília*** (***I***), ***Esperando o sucesso*** (***K***) and ***Cansada (cachopa de Capri)*** (***G***) (Figure 8.19b) were executed with almost invisible brushstrokes and with such a minute rendering that they are almost photographic in appearance, while landscape paintings present, both smooth and

textured areas. Smooth surfaces are present in the sky, sea, architectural elements and even some vegetation elements, while more or less impastoed brushstrokes are present in the large ground and vegetation areas, such as the foreground of ***Aldeia de St. Sauves***, ***Paisagem de St. Sauves*** and ***Casas brancas de Capri*** (left side). Small personages were generally also sketched in impastoed brushstrokes (Figure 8.20).

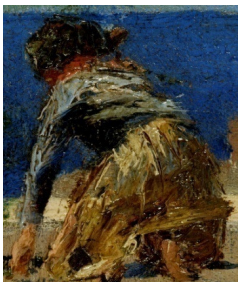

Figure 8.20 Detail of the painting ***Casas brancas de Capri***. Photo: LCRJF.

8.2.9 Alterations to the original composition

The examination of the paintings and cross sections suggests that no significant alteration to the original composition were made. This was confirmed by the X-radiography analysis done in some of the paintings. However, an intriguing area is seen in the painting ***Paisagem - Abertura da Rua Alexandre Herculano*** (Figure 8.21) below the muzzle of the ox (inside the red box), where there are apparently visible reserved areas for the eyes and mouth of the ox. Although the observed pattern inside the red box can be simply a coincidence, it can also be a result of a change in the ox position, since with the aging of the binding medium, transparency of the paint layers increases and often alterations to composition become visible. Unfortunately, there are no X-radiographies of this painting, hence it is not possible to check if the position of the ox was ever changed.

Figure 8.21 Detail of the painting ***Paisagem - Abertura da Rua Alexandre Herculano***. Photo: LCRJF.

In the painting ***Aldeia de St. Sauves***, a drying crack pattern, not seen in any other painting, is present in the green of the tree leaves (Figure 8.22). This usually occurs when the underlying paint is still wet while the surface paint had dried, or when a large amount of binding medium and a low concentration of pigments are used. Looking at the cross section of the sample **E7** (Figure 8.14), which was removed from this area, it seems that the blue layer was already dried when the green was applied (well defined layers) indicating that the drying crack pattern was produced by a relatively large amount of binding medium.

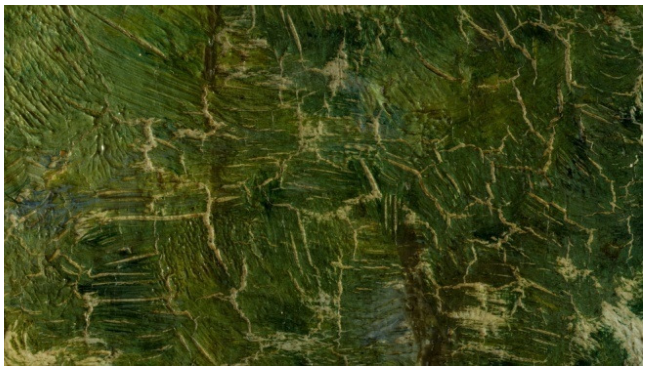

Figure 8.22 Detail of the painting ***Aldeia de St. Sauves***, showing the cracking pattern of the tree foliage. Photo: LCRJF.

8.3 Conservation state assessment of the paintings

A work is only capable of expressing its message when its physical existence is assured. Consequently, paintings were checked for signs of deterioration and the results of the analysis of the paintings' materials discussed in terms of their potential impact on the condition and appearance of the paintings.

Lead carboxylate (soaps) and protrusions

Metal carboxylates (or metals soaps) were identified in most of the samples (chapter 6), mainly as a result of the reaction between the oil binding medium and lead white. Even though, metal carboxylate salts can contribute to durability of the oil paints, it is known that they can agglomerate into lumps (or inclusions) and, in a further stage, form protrusions in the paint surface [73,285,296].

A careful visual examination of the painting surface and the examination of the cross-sections by OM and SEM did not show any signal of the formation of inclusions and/or protrusions. Instead, metal carboxylates seem to be uniformly distributed through the layers, as normally found for mature aged oil medium [36,285].

It has been proved that the formation of the agglomerates is normally associated not to lead white but to other lead-based pigments such as lead-tin yellows or red lead, which were not identified[97]. However, as the film ages, the formation of inclusions in samples where lead soaps are uniformly distributed can be favourable [296]. Variable relative humidity conditions or introduction of water during restoration treatments can be enough for inclusion formation since moisture is thought to play an important role in this process [449,451].

Another fact of concern is the presence of lead antimonate yellow in some of the samples, a lead-based pigment for which, up to date, there is no study regarding the possible formation of protrusions. A continuous observation of the painting surface in all the paintings is desirable in order to detect and control this process.

Darkening/fading of the pigments and incompatibilities

Darkening/fading of the pigments and incompatibilities among them were verified to assess possible contributions to past and future change in appearance of the paintings. Significant changes in colour in the past, due to pigment alteration are not noticeable and future alterations are not likely since incompatibilities were not identified. For example, although lead compounds are known to be unstable in proximity to sulfide pigments, such as mercury^{II} sulfide or realgar, forming lead^{II} sulfide/galena (PbS) and to atmospheric pollutants, forming by oxidation lead^{IV} oxide/plattnerite (PbO_2) [362,363,452], no signal of such alterations of lead white was observed; significant change in colour of the yellow chromate pigments, known by their instability to light, was not evident; cadmium yellow (CdS), known to be incompatible with lead and copper based pigments (especially with emerald green), leading to discoloration by the formation of copper and lead sulfides [85], has apparently suffered no alteration. Copper sulfide was, in fact, identified in two samples, not of as an alteration of cadmium yellow, but rather, as result of an alteration of emerald green by reaction with ultramarine blue. Nevertheless, because copper sulfide is present in such a low amount, no colour change was produced due to its formation.

The impact of the increased transparency of the paint with time, apparently, is not a significant issue, since paint layers contain a little amount of medium and are often applied thickly.

[97] At least lead-tin yellow was not identified and red lead was identified only as an impurity.

8.4 Conclusions

The examination of the paintings under study and the analysis of their samples by six analytical techniques allowed a closer insight into Pousão's palette and technique. Special features, such as the materials and the way the paintings evolved, were identified.

As regards the support, the wood panel paintings (half of the number of the paintings under study) are, generally, smaller than the canvas paintings. The fact that some of the paintings have similar dimensions suggests that they share the same source. For instance, the paintings ***Jardim de Luxemburgo (estudo)***, ***Fachada de casa soterrada - Roma***, ***Miragem de Nápoles***, ***Rua de Roma*** and ***Cais de Barcelona***, all of them with similar dimensions (about 16.5 x 10 cm), seem to have been prepared cutting in half a wood panel with similar dimensions to the painting ***Escadas de um pardieiro - Roma*** (16.0 x 22.2 cm).

The ground layer(s) are, in general, composed by lead white in oil medium. A pure white lead grade in wood panel paintings and a grade extended with barium sulfate, calcium carbonate-calcite form, or both in the case of canvas paintings, are present. Exceptions are the paintings ***Jardim de Luxemburgo (estudo)*** and ***Senhora vestida de preto***, two wood panel paintings with no ground layer, and ***Paisagem de St. Sauves***, a canvas painting with a ground layer constituted by calcium carbonate-calcite form in oil medium and an *imprimitura* constituted by lead white in oil medium.

The fact that no stamps or marks from the supplier were visible in any of the paintings, made it difficult to establish whether these were bought ready-primed or were primed by Pousão. However, the fact that wood panels present a pure grade of lead white in the ground layer suggests that these were primed by Pousão. Commercial ready-primed supports normally presented ground layers of lead white extended with other white pigments/extenders, such as kaolin, barium sulfate and calcium carbonate - calcite form.

As far as the paint layers and the artist's technique are concerned the following conclusions can be drawn: i) the existence of underdrawing and outlining was detected, ii) the paint layers were executed in different ways, even across the same painting; while some were added after the previous one had already dried (major areas of sky and architecture of canvas paintings), others were painted wet-in-wet, blending, or half blending the colours (vegetation areas and small figures), iii) the paint layers vary significantly, both in number (1 to 10) and thickness (4 to 358 µm), iv) each paint layer is generally composed by a very complex mixture of pigments.

Pousão's palette is composed by 26 pigments, distributed by painting as shown in Table 8.3. Pousão was very fortunate to live through a period of great discovery and technical

development in artists' pigments and he made fully use of it, using new pigments such as cobalt blue, chrome yellow and viridian. However, more traditional pigments, such as ochre pigments or bone/ivory black, were also used.

Comparing the palette and technique used in the different periods of his life and in the canvas and wood panel supports, it appears that both of them did not differ significantly, making it difficult to define Pousão's practices. However, comparing the dimensions and surface texture of the paintings, it seems that the paintings can be divided in two groups: i) refined paintings or refined paintings to be, all of them painted on canvas (except ***Aldeia de St. Sauves***, which was painted on wood panel) and ii) sketches, all of them painted on wood panels (with the above mentioned exception).

On observing all the paintings, it is clear that the canvas paintings were painted with a highest degree of care and finalization relatively to the wood panel paintings, which seem to have been painted more freely. It is worth noting that, being a student on a scholarship, Pousão had regularly to present paintings at the Academia Portuense de Belas Artes and that canvas paintings with a relatively smooth surface and high degree of 'finish' were favoured in the academic circles and exhibitions. In fact, some of these finished paintings, such as ***Cansada (Cachopa de Capri)*** and ***Casas brancas de Capri***, have preparatory drawings and/or painted studies [(20)], indicating that a meticulous academic planning was present in the refined paintings. The canvas paintings ***Mulher da água***, **Portão**, ***Rapariga de Anacapri***, ***Paisagem de Anacapri***, ***Rapariga deitada no tronco da árvore*** and ***Flores campestres*** are unfinished paintings, whose conclusion would most probably lead to the clear and finished degree of the other canvas paintings. The wood panel paintings generally present a sense of immediacy and spontaneity commonly associated with sketches or certain types of Impressionist works.

Although the current study is so far the most complete one about Pousão's palette, results cannot be generalized to the entire Pousão's *oeuvre*, since, due to the good conservation state of the paintings, sampling was normally limited to the edges, hence it is uncertain whether the entire range of pigments has been identified. Furthermore, other important paintings by this painter have not been studied.

9 Final conclusions and suggestions for future work

The beauty, mystery, joy, and inspired observation of the human spirit that paintings evoke result from a complex of intuitive and cognitive choices made by the artist.

W. S. Taft and J. W. Mayer

This chapter summarizes the major conclusions of the current work, concerning either the samples or the employed analytical techniques and lines up some suggestions and guidelines for future work.

9.1 Final conclusions

The research work described in this thesis has two main objectives: i) to establish Pousão's palette – constructing a database for future comparison – and to access the conservation state of the paintings; ii) to evaluate the Raman microscopy (μ-R) efficiency for pigment identification in oil paintings' cross sections and to compare it with the infrared microscopy (μ-R) efficiency for the same purpose.

As to the first main objective, the following conclusions can be drawn. The examination and detailed analysis of 23 paintings by Henrique Pousão allowed to conclude that his palette (only taking the analysed paintings into account) is comprised by 26 pigments; no dyes were identified. Some of the pigments are more traditional pigments, namely iron^{III} oxide, iron^{III} oxyhydroxide, celadonite, malachite, lead antimonate yellow, bone/ivory black, carbon-based black, realgar/pararealgar, mercury^{II} sulfide, cochineal and madder lakes, lead white and Prussian blue, while others are 19th century pigments, namely cobalt blue, cerulean blue, ultramarine blue, chrome yellow, chrome orange, strontium yellow, zinc yellow, cadmium yellow, viridian, emerald green, Scheele's green, chrome green and zinc white.

The characterization of the paintings' structure was also achieved. In general, paintings are characterized by presenting a lead white ground layer (with 3 exceptions), over which one paint layer, such as in sky areas and up to 10 paint layers, such as vegetation areas, were applied. Paint layers, with thickness ranging from 4 to 358 μm, were normally constituted by a complex mixture of pigments and were normally applied after the ground layer or previous paint layers had dried.

Apparently, the paintings are in good state of conservation. They do not show ruptures, detachments or protrusions or any signal of pigment fading. However, as the painting ***Portão*** presents a relatively high amount of metal carboxylates (metal soaps) in some areas, continuous observation of this painting is recommended in order to control the possible formation of metal protrusions.

As regards the second main objective of this thesis, μ-R proved to be, among the six used techniques (OM, μ-IR, μ-R, SEM/EDS, μ-XRD and FM), the most suitable technique for pigment identification on micro, complex, multi-layered samples. Attributes, such as high specificity and reproducibility, good sensitivity, high spectral (ca. 1 cm^{-1}) and spatial (ca. 1 μm) resolutions, relatively low cost, short acquisition time, and non-destructiveness, made μ-R very successful for the referred purpose.

Like μ-R, μ-IR is highly specific and reproducible, offers good sensitivity, relatively low cost and short acquisition time. However, its lower spectral resolution (ca. 4 cm^{-1}) makes the interpretation of spectra difficult and its lower spatial resolution (ca. 50 μm) makes it difficult to individual analyse each layer. Moreover, μ-IR has some other severe limitations: i) demanding and time-consuming preparation of thin sections, ii) the need of their compression in a diamond cell, which makes this technique destructive and iii) the cut-off of the detector (650 cm^{-1}), which hampers the identification of most inorganic pigments, making it less suitable than μ-R for the above referred purpose.

Nevertheless, for studies with different purposes, μ-IR can be very useful in identifying compounds for which μ-R presents difficulties, such as binding medium, varnish, aluminosilicates and clay materials.

Optical microscopy (OM) is the basic and mandatory first approach for the characterization of cross sections, since a reasonable comprenhensive understanding of the painting structure is essential in order to derive the maximum information from the other analytical techniques that will be applied. By examinating the cross-sectioned samples under reflected visible light, it was possible to: i) identify the painting technique, ii) determine the number and thickness of layers, iii) determine the colour of the pigments, iv) reveal the existence of reworks (*pentimenti*), v) provide support to the evaluation of the conservation state of the paintings and vi) identify possible unrepresentative samples, such as those removed from restoration areas.

Fluorescence microscopy (FM), like OM, is valuable for the characterization of the sample structure. Because varnishes layers are fluorescent under UV, this technique can be use to reveal reworks and conservation interventions. Moreover, since some pigments are also fluorescent under UV light, this technique can may be used as a first, fast and inexpensive approach for pigment identification, in particular of zinc white and lake pigments.

The elemental analytical technique, SEM-EDS, is valuable for clarifying particular questions relative to elemental composition such as the distinction between cobalt blue ($CoAl_2O_4$) and cerulean blue ($CoO.nSnO_2$) and the identification of pigments whose fluorescence inhibited the analysis by μ-R. However, it is worth noting that this technique should not be used by itself, especially for the analysis of complex samples, as there is a high risk of producing misleading interpretations.

μ-XRD is valuable for the identification of sample components, as it determines the exact phase composition. In particular, this technique is priceless for the identification of zinc white, which presents a high X-ray absorption coefficient, but proved to be difficult to be detected by SEM/EDS and μ-R. Unfortunately, this technique is not suitable for the identification of amorphous or less ordered compounds, leaving some pigments unidentified, such as cobalt

blue. Moreover, the μ-XRD analysis is commonly restricted to upper and lower layers and very time-consuming, since often several hours, if not days are required for data acquisition.

Only by employing a multi-technique approach was it possible to obtain the maximum information about the complex mixtures elaborated by Pousão. Each used analytical technique proved to be useful at different stages of the current study giving additional information and complementing the one previously obtained. However, although complete identification was laboriously sought for some compounds remained unidentified.

This research was intended to provide art historians, conservators/restorators and art scientists with a comprehensive database of Pousão's materials and technique, which can be used for future reference purposes, such as authentication, understanding of the context in which the paintings were created and assessment of future preservation/conservation interventions.

In addition, due to the complex nature of the samples, the current research constitutes a source of information regarding the advantages and disadvantages of some of the most used analytical techniques for pigment analysis, assessing the selection of the most appropriate technique(s) for future studies.

9.2 Sugestions for future work

The following questions and hypotheses were raised during this study. They certainly deserve further investigation and provide topics for future research.

1) To complete Pousão's palette

In the current study, 23 paintings by Pousão were analysed and the respective palette was established. However, although being a study of considerable scope, it represents only part of Pousão's work, and therefore should be further pursued.

In order to fully establish Pousão's palette, other paintings should be analysed, whenever possible, for example, during intervention conservations. Then, it will be more accurate to determine if a pigment is or is not consistent with Pousão's palette.

2) Comparison with other 19th century painters

The extent to which Pousão's technique evolved as a result of his own experimentation or of the influence of the contemporary painting manuals, painters and teachers is not clear. A comparative study of the Pousão's materials and technique with those used by his teachers,

such as António Costa, Yvon and Cabanel, and Portuguese, French, Italian and even Spanish 19th century painters, such as Marques de Oliveira, Silva Porto, Corot, Cabanel, Cabianca, Sernes and Pradilla would be interesting and perhaps could indicate to what extent Pousão's technique was a product of his training or the influence from other painters.

3) Sulfate compounds associated to lead antimonate yellow

Results of the current study suggested that lead sulfate, and more rarely basic lead sulfate, rosiaite, cervantite and others unknown are present in the sample associated with lead antimonate yellow. It is known that lead antimonate yellow was often sold containing considerable amounts of basic lead sulfate (and also silica, rutile, barium sulfate and carbonates), but there is no report for the existence of lead sulfate [342].

The presence of these lead sulfates and oxides in lead antimonate yellow may be caused by the use of Sb_2S_3 instead of an antimony oxide, in the synthesis method of the yellow pigments. It has been found that, when using Sb_2S_3 as starting material in the synthesis of lead tin-antimony yellow, a pigment closely related to lead antimonate yellow, lead sulfate rosiaite and/or basic lead sulfate was produced [347,348].

Studies must be conducted to confirm this hypothesis and clarify the origin of the two sulfate compounds.

4) Umber and Sienna pigments

During analysis by µ-R some pigment grains presented a relative intense band at ca. 660 cm^{-1}, associated with the $iron^{III}$ oxide spectrum,. Although this band has been assigned to either $iron^{III}$ oxide or magnetite (Fe_3O_4) it can also be due to the presence of manganese oxides/oxyhydroxides, since these compounds, especially the black MnO_2 minerals, were added (at 5-20 wt%) to iron oxide/oxyhydroxide in order to produce Umber pigments [85,338].

It would be interesting to analyse reference samples of Umber and even Sienna pigments (manganese oxides/oxyhydroxides < 5%) by Raman spectroscopy, in order to confirm the hypothesis of the 660 cm^{-1} band being due to the existence of manganese oxides/oxyhydroxides and verify if Umber and Sienna pigments can be distinguished from the ochre pigments not having manganese oxides.

5) Viridian

Known to be a hydrated $chromium^{III}$ oxide with composition $Cr_2O_3.2H_2O$ [85,248], viridian's IR spectra seems to point instead to a hydroxo compound. While the bending mode of water at ca. 1635 cm^{-1} is not present, the strong hydroxyl stretching bands between 3550 and 3200

cm^{-1} were observed. Further investigation should be carried out in order to clarify this pigment's composition.

6) Zinc yellow

During the current study it was found that apparently neither µ-IR nor µ-R, wre able to distinguish among different zinc chromate compounds (zinc yellow). It would be interesting to analyse different chemical compositions of zinc chromate (whose identity had been previously determined by XRD) by IR and Raman and assess if it possible to distinguish among zinc chromate compounds based on their vibrational spectra.

7) Zinc white identification by µ-XRD

The main analytical techniques of this study, µ-IR and µ-R, proved to be unable to identify zinc white in the samples of Pousão's paintings. It would be worth analysing a representative number of samples by XRD, which has a high and accurate response to zinc white, and evaluate the importance of this white pigment in Pousão's palette.

References

1. Winter J. Overview. In: Sackler NAS Colloquium. Scientific Examination of Art: Modern Techniques in Conservation and Analysis. Proceedings of the National Academy of Sciences; 2003 March 19-21; Washinton D. C. Washington, D. C.: The National Academic Press; 2005.

2. Piqué F. Science for the conservation of wall paintings. The Getty Newsletter [serial online] 2005 [cited 2010 Oct 01]; 20(2):[1 screen]. Available from: URL:http://www.getty.edu/conservation/publications/newsletters/20_2/news_in_cons2.html

3. Stuart BH. Analytical techniques in materials conservation. Chichester: John Wiley & Sons; 2007.

4. Sackler NAS Colloquium. Scientific Examination of Art: Modern Techniques in Conservation and Analysis. Proceedings of the National Academy of Sciences; 2003 March 19-21; Washinton D. C. Washington, D. C.: The National Academic Press; 2005.

5. Dorge V, Howlett FC, editors. Painted Wood: History and Conservation. Proceedings of the symposium of Williamsburg; 1994 Nov 11-14; Virginia, USA. Los Angeles: The Getty Conservation Institute; 1998.

6. Craddock P. Scientific investigation of copies, fakes and forgeries. Oxford: Elsevier; 2009.

7. Leonard B. Warhol Foundation Accused of Defacing Art. Chourthouse News Services. [Online]. 2010 Jan 19 [cited 2010 Oct 01]; [1 screen]. Available from: URL:http://www.courthousenews.com/2010/01/19/23814.htm

8. Grann D. The Mark of a Masterpiece. The man who keeps finding famous fingerprints on uncelebrated works of art. The New Yorker [serial online] 2010 Jul [cited 2010 Oct 01]. Available from: URL: http://www.newyorker.com/reporting/2010/07/12/100712fa_fact_grann

9. Spoto G, Torrisi A, Contino A. Probing archaeological and artistic solid materials by spatially resolved analytical techniques. Chem Soc Rev. 2000;29:429-39.

10. Clark RJH. Raman microscopy as a structural and analytical tool in the fields of art and archaeology. J Mol Struct 2007;834-836:74-80.

11. Mayer W, Stanley TJ, James W. The Science of Paintings. New York: Springer-Verlag; 2000.

12. González MLG. Exámen Científico aplicado a la conservación de obras de arte. 1st ed. Madrid: Instituto de conservatión y restauración de bienes culturales (España); 1994.

13. Matteini M, Moles A. Scienza e restauro, Metodi di indagine. 6th ed. Florença: Nardini Editore; 2002.

14. Mairinger F, Schreiner M. New methods of chemical analysis - a tool for the conservator. In: Brommelle NS, Thomson G, editors. Preprints of the contributions to the 9th IIC International Congress: Science and technology in the service of conservation; 1982 Sep 3-9; Washington. London: International Institute for Conservation of Historic and Artistic Works; 1982. p. 5-15.

15. Baer NS, Low MJD. Advances in scientific instrumentation for conservation: an overview. In: Brommelle NS, Thomson G, editors. Preprints of the contributions to the 9th IIC International Congress: Science and technology in the service of conservation; 1982 Sep 3-9; Washington. London: International Institute for Conservation of Historic and Artistic Works; 1982. p. 1-4.

16. Creagh DC. The characterization of artefacts of cultural heritage significance using physical techniques. Radiat Phys Chem 2005;74:426-42.

17. Boutine JL. The modern museum. In: Bradley D, Creach D, editors. Physical techniques in the study of art, archaeology and cultural heritage. 1st ed. Oxford: Elsevier; 2006, p. 1-39. (vol. 1).

18. Doménech-Carbó MT. Novel analytical methods for characterising binding media and protective coatings in artworks. Anal Chem 2008;621:109-39.

19. Mantler M, Schreiner M. X-Ray fluorescence spectrometry in art and archaeology. X-ray spectrom 2000;29:3-17.

20. Rodrigues A. Henrique Pousão. Lisboa: Edições Inapa; 2004. (Pintores Portugueses).

21. Townsend JH. Microscopy and paintings. Microscopy and Analysis. 1994;39:11-3.

22. Karapanagiotis I, Valianou L, Daniilia S, Chryssoulakis Y. Organic dyes in Byzantine and post-Byzantine icons from Chalkidiki (Greece). J Cult Herit. 2007;8:294-8.

23. Blanc R, Espejo T, López-Montes A, Torres D, Crovetto G, Navalón A, et al. Sampling and identification of natural dyes in historical maps and drawings by liquid chromatography with diode-array detection. J Chromatogr A. 2006;1122:105-13.

24. Mazzeo R, Joseph E, Minguzzi V, Grillini G, Baraldi P, Prandstraller D. Scientific investigations of the Tokhung-Ri tomb mural paintings (408 A.D.) of the Koguryo era, Democratic People's Republic of Korea. J Raman Spectrosc. 2006;37:1086-97.

25. Zorba T, Pavlidou E, Stanojlovic M, Bikiaris D, Paraskevopoulos KM, Nikolic V, et al. Technique and palette of XIIIth century painting in the monastery of Mileseva. Appl Phys A Mater Sci Process. 2006;83:719-25.

26. Newman R. Some applications of infrared spectrosocpy in the examination of painting materials. J Am Inst Conserv. 1980;19:42-62.

27. Osticioli I, Mendes NFC, Nevin A, Gil FPSC, Becucci M, Castelluci E. Analysis of natural and artificial ultramarine blue pigments using laser induced breakdown and pulsed Raman spectroscopy, statistical analysis and light microscopy. Spectrochim Acta A. 2009;73:525-31.

28. Burgio L, Clark RJH, Stratoudaki T, Doulgeridis M, Anglos D. Pigment identification in painted artworks: a dual analytical approach employing laser-induced breakdown spectroscopy and Raman microscopy. Appl Spectrosc. 2000;54:463-69.

29. Denker A, Opitz-Coutureau J. Paintings-high-energy protons detected pigments and paint layers. Nucl Instrum Methods Phys Res B. 2004;213:677-82.

30. Grassi N, Migliori A, Mandò PA, del Castillo, HC. Differential PIXE measurements for the stratigraphic analysis of the painting Madonna dei fusi by Leonardo da Vinci. X-ray Spectrom. 2005;34:306-9.

31. Bussotti L, Carboncini MP, Castellucci E, Giuntini L, Mandò PA. Identification of pigments in a fourteenth-century miniature by combined micro-Raman and PIXE spectroscopic techniques. Stud Conserv. 1997;42:83-92.

32. Burgio L, Clark RJH, Sheldon L, Smith GD. Pigment identification by spectroscopic means: evidence consistent with the attribution of the painting Young Woman Seated at a Virginal to Vermeer. Anal Chem 2005;77:1261-67.

33. Clark RJH. Pigment identification by spectroscopic means: an arts/science interface. C R Chim. 2002;5:7-20.

34. Vandenabeele P, Edwards HGM, Moens L. A decade of Raman spectroscopy in art and archaeology. Chem Rev 2007;107:675-86.

35. Favaro M, Vigato PA, Andreotti A, Colombini MP. La Medusa by Caravaggio: characterisation of the painting technique and evaluation of the state of conservation. J Cult Herit 2005;6:295-305.

36. Keune K, Boon JJ. Imaging secondary ion mass spectrometry of a paint cross Ssection taken from an early netherlandish painting by Rogier van der Weyden. Anal Chem 2004;76:1374-85.

37. Tognazzi A, Lapucci R, Martini S, Leone G, Magnani A, Rossi C. TOF-SIMS characterization of pigments and binders in 'the Martyrdomof St. Catherine', in Zejtun (Malta). Surf Interface Anal. 2010; (in press).

38. van Ham R, van Vaeck L, Adams F, Adriaens A. Feasibility of analyzing molecular pigments in paint layers using TOF S–SIMS. Anal Bioanal Chem. 2005;383:991–7.

39. Villa CA, Ciliberto E. Copper resinate: an XPS study of degradation. Appl Phys A Mater Sci Process. 2006;83:699-703.

40. Clark RJH, Curri L, Henshaw GS, Laganara C. Characterization of brown–black and blue pigments in glazed pottery fragments from Castel Fiorentino (Foggia, Italy) by Raman microscopy, X-ray powder difractometry and X-ray photoelectron spectroscopy. J Raman Spectrosc. 1997;28:105-9.

41. James BJ, Cameron R, Baskcomb C. Selected area XPS analysis for identification of pigment compounds in microscopic paint flakes. Res Lett Mater Sci 2008; 247053.

42. Parras-Guijarro D, Montejo-Gámez M, Ramos-Martos N, Sánchez A. Analysis of pigments and coverings by X-ray diffraction (XRD) and micro Raman spectroscopy (MRS) in the cemetery of Tutugi (Galera, Granada, Spain) and the settlement convento 2 (Montemayor, Córdoba, Spain). Spectrochim Acta A. 2006;64:1133-41.

43. Herrera LK, Cotte M, Jimenez de Haro MC, Duran A, Justo A, Perez-Rodriguez JL. Characterization of iron oxide-based pigments by synchrotron-based micro X-ray diffraction. Appl Clay Sci. 2008;42:57-62.

44. Ferrero JL, Roldán C, Juanes D, Rollano E, Morera C. Analysis of pigments from Spanish works of art using a portable EDXRF spectrometer. X-ray Spectrom. 2002;31:441-7.

45. Klockenkämper R, von Bohlen A, Moens L. Analysis of pigments and inks on oil paintings and historical manuscripts using total reflection X-ray fluorescence spectrometry. X-ray Spectrom. 2000;29:119-129.

46. Gil M, Carvalho ML, Seruya A, Ribeiro I, Alves P, Guilherme A, et al. Pigment characterization and state of conservation of an 18th century fresco in the Convent of S. António dos Capuchos (Estremoz). X-ray Spectrom. 2008;37:328-337.

47. Harkins TR, Harris JT, Shreve OD. Identification of pigments in paint products by infrared spectroscopy. Anal Chem. 1959;31:541-5.

48. Casadio F, Toniolo L. The analysis of polychrome works of art: 40 years of infrared spectroscopic investigations. J Cult Herit. 2001;2:71-8.

49. Best SP, Clark RJH, Withnall R. Non-destructive pigment analysis of artefacts by Raman microscopy. Endeavour. 1992;16:66-73.

50. Ortega-Avilés M, Vandenabeele P, Tenorio D, Murrilo G, Jiménez-Reyes M, Gutiérrez N. Spectroscopic investigation of a 'Virgin of Sorrows' canvas painting: A multi-method approach. Anal Chim Acta. 2005;550:164-172.

51. Correia AM, Clark RJH, Ribeiro MIM, Duarte MLTS. Pigment study by Raman microscopy of 23 paitings by the Portuguese artist Henrique Pousão (1959-1884). J Raman Spectrosc. 2007;38:1390-1405.

52. Vandenabeele P, Verpoort F, Moens L. Non-destructive analysis of paintings using Fourier transform Raman spectroscopy with fiber optics. J Raman Spectrosc. 2001;32:263-9.

53. Burgio L, Clark RJH, Theodoraki K. Raman microscopy of Greek icons: identification of unusual pigments. Spectrochim Acta A. 2003;59:2371-89.

54. Ricci C, Borgia I, Brunetti BG, Miliani C, Sgamellotti A, Seccaroni C, et al. The Perugino's palette: integration of an extended in situ XRF study by Raman spectroscopy. J Raman Spectrosc 2004;35:616-21.

55. Ropret P, Centeno SA, Bukovec P. Raman identification of yellow synthetic organic pigments in modern and contemporary paintings: Reference spectra and case studies. Spectrochim Acta A. 2008;69:486-97.

56. Aibéo CL, Goffin S, Schalm O, van der Snickt G, Laquière N, Eyskens P, et al. Micro-Raman analysis for the identification of pigments from the 19th and 20th century paintings. J Raman Spectrosc.2008., Vol. 39, pp. 1091-1098.

57. Lau D, Villis C, Furman S, Livett M. Multispectral and hyperspectral image analysis of elemental and micro-Raman maps of cross-sections from a 16th century painting. Anal Chim Acta 2008;610:15-24.

58. Ropret P, Miliani C, Centeno SA, Tavzes Č, Rosi F. Advances in Raman mapping of works of art. J Raman Spectrosc 2010 (in press)

59. Lopes FF. Breve memória sobre a vida e arte de Henrique Pousão. Lisboa: Seara Nova; 1946.

60. de Figueiredo M. O pintor Henrique Pousão. Círculo Dr. José de Figueiredo; 1942.

61. da Silva JJS. Alocução proferida no dia 1 de Abril de 1984, data oficial do inicio das «Comemorações do 1º Centenário da morte do pintor Henrique Pousão», na praça da Républica, junto do monumento do artista. In: Henrique Pousão 1859-1884 - textos das alocuções proferidas durante as comemorações do 1º centenário da morte do pintor; 1984; Vila Viçosa. Vila Viçosa: Câmara Municipal de Vila Viçosa; 1984. p. 11-20. (II Série dos Cadernos Culturais da Câmara Municipal de Vila Viçosa).

62. Lemos MA. Pousão e o Naturalismo. In: Henrique Pousão 1859-1884 - textos das alocuções proferidas durante as comemorações do 1º centenário da morte do pintor; 1984; Vila Viçosa. Vila Viçosa: Câmara Municipal de Vila Viçosa; 1984. p. 35-54. (II Série dos Cadernos Culturais da Câmara Municipal de Vila Viçosa).

63. Lopes FF. Cartas de Henrique Pousão e excertos de outras cartas e escritos que se lhe referem. Lisboa: Portugália Editora, 1946.

64. Varela A. Henrique Pousão - No seu verismo sem compromisso. In: Revista e Boletim da Academia Nacional de Belas Artes, nº13-14. Lisboa: Academia Nacional de Belas Artes; 1959.

65. Gomes A. Pousão e a historiografia da arte. In: Henrique Pousão 1859-1884 - textos das alocuções proferidas durante as comemorações do 1º centenário da morte do pintor; 1984; Vila Viçosa. Vila Viçosa: Câmara Municipal de Vila Viçosa; 1984. p. 63-68. (II Série dos Cadernos Culturais da Câmara Municipal de Vila Viçosa).

66. da Silva JJS. Henrique Pousão - considerações à volta do seu centenário. In: Henrique Pousão 1859-1884 - textos das alocuções proferidas durante as comemorações do 1º centenário da morte do pintor; 1984; Vila Viçosa. Vila Viçosa: Câmara Municipal de Vila Viçosa; 1984. p. 21-30. (II Série dos Cadernos Culturais da Câmara Municipal de Vila Viçosa).

67. Gombrich EH. The Story of Art. 16th ed. London: Phaidon, 2005.

68. Bomford D. Pocket Guides: Conservation of paintings. London: The National Gallery, 2005.

69. van Hout N. Meaning and development of the ground layer in the seventeenth century paintings. In: Hermes E, Ouwerkerk A, Costaras N, editores. Looking Through Paintings - The study of painting techniques and materials in support of art historical research. Baar: de Prom; 1998. pp. 199-225.

70. Buxbaum G, Pfaff G, editors. Industrial Inorganic Pigments. Third, Completly Revised and Extended Edition. 3rd ed. Weinheim: Wiley-VCH; 2005.

71. Newman R. Tempera and other nondrying-oil media. In: Dorge V, Howlett FC, editores. Painted wood: History and Conservation - Proceedings of a symposium organized by the Wooden Artefacts Group of the American Institute for Conservation of Historic and Artistic Works; 1994 Nov 11-14; Williansburg, Virginia. Los Angeles: The Getty Institute for Conservation; 1999. p. 33-63.

72. Hommes ME. Painters' methods to prevent colour changes described in sexteenth to early eighteenth century sources on oil painting techniques. In: Hermes E, Ouwerkerk A, Costaras N, editores. Looking Through Paintings - The study of painting techniques and materials in support of art historical research. Baar: de Prom; 1998. pp. 91-132.

73. Erhardt D. Paints based on drying-oil media. In: Dorge V, Howlett FC, editores. Painted wood: History and Conservation - Proceedings of a symposium organized by the Wooden Artefacts Group of the American Institute for Conservation of Historic and Artistic Works; 1994 Nov 11-14; Williansburg, Virginia. Los Angeles: The Getty Institute for Conservation; 1999. p. 17-32.

74. Townsend JH. The materials used by British oil painters throughout the nineteenth century. Rev Conserv 2002;3:46-55.

75. Clarke M. The analysis of medieval European manuscripts. Rev Conserv 2001;2:3-17.

76. Cruz AJ. A pintura de Columbano segundo as suas caixas de tintas e pincéis. Conservar Património 2005;1:5-19.

77. Nadolny J. The first century of published scientific analyses of the materials of historical painting and polychromy, circa 1780-1880. Rev Conserv 2003;4:39-51.

78. Khandekar N. Preparation of cross-sections from easel painting. Rev Conserv 2003;4:52-63.

79. American Institute for conservation of historic and artistic works. Code of ethics and guidelines for practice. [Online] 2010 [cited 210 Oct 01]; [2 screens] Available from: URL:http://www.conservationus.org/index.cfm?fuseaction=page.viewPage&PageID=858&d:\CFusionMX7\verity\Data\dummy.txt

80. Derrick MR. Infrared Microspectroscopy in the Analysis of Cultural Artifacts. In: Humecki HJ, editor. Practical Guide to Infrared Microspectroscopy. New York: Marcel Dekker; 1995. p. 287-322. (Practical spectroscopy series; vol 19).

81. Martin JS. Microscopic examination and analysis of the structure and composition of paint and varnish layers. In: Dorge V, Howlett FC, editores. Painted wood: History and Conservation - Proceedings of a symposium organized by the Wooden Artefacts Group of the American Institute for Conservation of Historic and Artistic Works; 1994 Nov 11-14; Williansburg, Virginia. Los Angeles: The Getty Institute for Conservation; 1999. p. 64-79.

82. Reffner JA, Martoglio PA. Uniting Microscopy and Spectroscopy. Humecki HJ, editor. Practical Guide to Infrared Microspectroscopy. New York: Marcel Dekker; 1995. p. 41-84. (Practical spectroscopy series; vol 19).

83. van der Weerd J, Heeren RMA, Boon JJ. Preparation methods and accessories for the infrared spectroscopic analysis of multi-layer paint films. Stud Conserv 2004;49:193-210.

84. Farrell E. Pigments and media. Techniques in paint analysis. Moss RW, editor. Paint in America: The colour of historical buildings. New York: John Wiley & Sons; 1994.

85. Eastaugh N, Walsh V, Chaplin T, Siddall R. Pigment Compendium, A Dictionary of Historical Pigments. Oxford: Elsevier Butterworth-Heinemann; 2004.

86. Cabral JMP. Exame Científico de pinturas de cavalete. Fundação Calouste Gulbenkian. 1995 Feb. Available from: URL: http://zircon.dcsa.fct.unl.pt/dspace/handle/123456789/214

87. Derrick MR, Stulik D, Landry JM. Infrared spectroscopy in conservation science. Los Angeles: The Getty Conservation Institute; 1999. (Scientific tools for conservation).

88. Twonsend JH. The characterisation of nineteenth century paint. In: Tenhent NH, editor. Conservation Science in the UK. Preprints of the meeting held in Glasgow; 1993 May, pp. 33-35.

89. Townsend JH, Keune K. Microscopical techniques applied to traditional paintings. infocu. 2006;1:54-65.

90. Bomford D, Kirby J, Leighton J, Roy A. Art in the Making - Impressionism. New Haven: National Gallery Publications; 1990.

91. Calligaro T. Photodetectors at «Le Louvre» X-ray, γ-ray and visible spectrometries applied to art and archaeology issues. International Conference «New Developments in Photodetection»; 2002 Jun17-21; Beune.
Available from: ndip.in2p3.fr/beaune02/sessions/calligaro.pdf

92. Pigments through the Ages [Online]. [cited 2010 Apr 12]; Available from: URL: http://www.webexhibits.org/pigments/intro/look.html.

93. Calligaro T, Dran JC, Klein M. Application of photo-detection to art and archaeology at the C2RMF. Nucl Instrum Methods Phys Res A 2003;504:213-21.

94. Gargano M, Ludwig N, Poldi G. A new methodology for comparing IR reflectographic systems. Infrared Phys Tech 2007;49:249-53.

95. Cullity BD. Elements of X-ray Diffraction. 2nd ed. London: Addison-Wesley Publishing Company; 1978.

96. Moioli P, Seccaroni C. Analysis of art objects using a portable X-ray fluorescence spectrometer. X-ray Spectrom 2000;29:48-52.

97. Neelmeijer C, Brissaud I., Calligaro T, Demortier G, Hautojärvi A, Mäder M, et al. Paintings - a challenge for XRF and PIXE analysis. X-ray Spectrom. 2000;29:101-110.

98. Dik J, Janssens K, van der Snick G, van der Loeff L, Rickers K, Cotte M. Visualization of a lost painting by Vincent van Gogh using synchrotron radiation based X-ray. Anal chem 2008;80:6436-42.

99. de Viguerie L, Beck L, Salomon J, Pichon L, Walter P. Composition of Renaissance paint layers: simultaneous particle induced x-ray emission and backscattering spectrometry. Anal Chem 2009;81:7960-7966.

100. Smith GD, Clark RJH. Raman microscopy in art history and conservation science. Rev Conserv 2001;2:96-110.

101. Siddall R. "Not a day without a line drawn": Pigments and painting techniques of Roman artists. Infocus 2006;2:19-31.

102. Townsed JH. Themomicroscopy applied to painting materials from the late 18th and 19th centuries. Thermochim Acta. 2000;365:79-84.

103. Goldstein JI, Newbury DE, Joy DC, Lyman CE, Echlin P, Lifshin E, et al. Scanning electron microscopy and X-ray microanalysis. 3rd ed. New York: Springer; 2003.

104. Reimer L. Scanning electron microscopy: Physics of image formation and microanalysis. 2nd ed. New York: Springer; 1998.

105. Goodhew PJ, Humphreys J, Beanland R. Electron microscopy and analysis. 3rd ed. London: Taylor & Francis; 2001.

106. Warren BE. X-ray Diffraction. New York: Dover; 1990.

107. Suryanarayana C, Norton MG. X-Ray Diffraction: A practical approach. New York: Plenum Press; 1998.

108. Grunwaldová V, Bezdička P, Kotulánová E, Grygar T, Hradilová J, Hradil D. News in using of powder X-ray microdiffraction for identification of paint layers in artworks. In: EPDIC 10. European Powder Diffraction Conference 10; 2006 Sep 1-4; Geneva, Switzerland.

109. Welcomme E, Walter P, Bleuet P, Hodeau JL, Dooryhee E, Martinetto P, et al. Classification of lead white pigments using synchrotron radiation micro X-ray diffraction. Appl Phys A Mater Sci Process 2007;89:825-32.

110. Leng Y. Materials Characterization: Introduction to microscopic and spectroscopic methods. Singapore: John Wiley & Sons (Asia) Pte Ltd; 2008.

111. Spragg RA. IR spectroscopy sample preparation methods. In: Lindon JC, Tranter GE, Holmes JL, editors. Encyclopedia of Spectroscopy and Spectrometry. New York: Academic Press; 1999. vol 2 p. 1058-1066.

112. Katon JE. Infrared microspectroscopy. A review of fundamentals and applications. Micron 1996;27:303-14.

113. Sommer AJ. Mid-infrared transmission microspectroscopy. In: Chalmers JM, Griffiths PR, editors. Handbook of Vibrational Spectroscopy. Chichester: John Wiley & Sons Ltd.; 2002.

114. Rosenzweig B, Carretti E, Picollo M, Baglioni P, Dei L. Use of mid-infrared fiber-optic reflectance spectroscopy (FORS) to evaluate efficacy of nanostructured systems in wall painting conservation. Appl Phys A Mater Sci Process 2006;83:669-73.

115. Bacci M, Fabbri M, Picollo M, Porcinai S. Non-invasive fibre optic Fourier transform-infrared reflectance spectroscopy on painted layers. Identification of materials by means of principal component analysis and Mahalanobis distance. Anal Chim Acta 2001;446:15-21.

116. Ploeger R, Scalarone D, Chiantore O. Non-invasive characterisation of binding media on painted glass magic lantern plates using mid-infrared fibre-optic reflectance spectroscopy. J Cult Herit 2010;11:35-41.

117. Bruni S, Cariati F, Casasio F, Toniolo L. Spectrochemical characterization by micro-FTIR spectroscopy of blue pigments in different polychrome works of art. Vib Spectrosc 1999;20:15-25.

118. Ryland SG. Infrared Microspectroscopy of Forensic Paint Evidence. In: Humecki HJ, editor. Practical Guide to Infrared Microspectroscopy. New York: Marcel Dekker; 1995. p. 163-243. (Practical spectroscopy series; vol 19).

119. Miller LM, Smith RJ. Synchrotrons versus globars, point-detectors versus focal plane arrays: Selecting the best source and detector for specific infrared microspectroscopy and imaging applications. Vib Spectrosc 2005;38:237-240.

120. Slavadó N, Butí S, Tobin MJ, Pantos E, Prag AJNW, Pradell T. Advantages of the use of SR-FTIR microspectroscopy: applications to Cultural Heritage. Anal Chem 2005;77:3444-51.

121. Reffner JA, Martoglio PA. Fourier transform infrared microscopical analysis with synchrotron radiation: The microscope optics and system performance (invited). Rev Sci Instrum 1995;66:1298-1302.

122. Salvadó N, Butí S, Pantos E, Bahrami F, Labrador A, Pradell T. The use of combined synchrotron radiation micro FT-IR and XRD for the characterization of Romanesque wall paintings. Appl Phys A Mater Sci Process 2008;90:67-73.

123. Schrader B. General survey of vibrational spectroscopy. In: Schrader B, editor. Infrared and Raman Spectroscopy: Methods and Applications. Cambridge: VCH; 1995. p. 7-61.

124. Ruiz-Moreno S, Pérez-Pueyo R, Gabaldón A, Soneira M, Sandalinas C. Raman laser fibre optic strategy for non-destructive pigment analysis. Identification of a new yellow pigment (Pb, Sn, Sb) from the Italian XVII century painting. J Cult Herit. 2003;4:309s-13s.

125. Vandenabeele P, Tate J, Moens L. Non-destructive analysis of museum objects by fibre-optic Raman spectroscopy. Anal Bioanal Chem 2007;387:813-9.

126. Burgio L, Clark RJH. Library of FT-Raman spectra of pigments, minerals, pigment media and varnishes, and supplement to existing library of Raman spectra of pigments with visible excitation. Spectrochim Acta A 2001;57:1491-1521.

127. Schulte F, Brzezinka K, Lutzenberger K, Stege H. Raman spectroscopy of synthethic organic pigments used in the 20th century works of art. J Raman Spectrosc 2008;39:1455-63.

128. Vandenabeele P, Wehling B, Moens L, Edwards H, De Reu M, van Hooydonk G. Analysis with micro-Raman spectroscopy of natural organic binding media and varnishes used in art. Anal Chim Acta 2000;407:261-274.

129. Skoog DA, Holler FJ, Nieman TA. Principles of Instrumental Analysis. 5th ed. London: Sauders College Publishing; 1998.

130. Burinsky DJ. Mass Spectrometry. In: Ahuja S, Jespersen N, editors. Modern Instrumental Analysis. Oxford: Elsevier; 2006., p. 319-396. (Comprehensive analytical chemistry; vol 47)

131. Vallance SL. Applications of chromatography in art conservation: techniques used for the analysis and identification of proteinaceous and gum binding media. Analyst 1997;122:75R-81R.

132. Cappitelli F. THM-GCMS and FTIR for the study of binding media in Yellow Islands by Jackson Pollock and Break Point by Fiona Banner. J Anal Appl Pyrolysis 2004;71:405-15.

133. Andreotti A, Bonaduce I, Colombini MP, Gautier G, Modugno F, Ribechini E. Combined GC/MS analytical procedure for the characterization of glycerolipid, waxy, resinous, and proteinaceous materials in a unique paint microsample. Anal Chem 2006;78:4490-4500.

134. Doménech-Carbó MT, Osete-Cortina L, Cañizares JC, Bolívar-Galiano F, Romero-Noguera J, Fernández-Vivas MA, et al. Study of the microbiodegradation of terpenoid resin-based varnishes from easel painting using pyrolysis–gas chromatography–mass spectrometry and gas chromatography–mass spectrometry. Anal Bioanal Chem 2006;385:1265-80.

135. Doménech-Carbó MT, Kuckova S, Cañizares JC, Osete-Cortina L. Study of the influencing effect of pigments on the photoageing of terpenoid resins used as pictorial media. J Chromatogr A 2006;1121:248-58.

136. Kirby J, White R. The identification of red lake pigment dystuffs and a discussion of their use. Nat Gall Tech Bull. 1996;17:56-80.

137. Halpine SM. An improved dye and lake pigment analysis method for high-performance liquid chromatography and diode-array detector. Stud Conserv 1996;41:76-94.

138. Maguregui MI, Alonso RM, Barandiaran M, Jimenez RM, García N. Micellar electrokinetic chromatography method for the determination of several natural red dystuff and lake pigments used in art work. J Chromatogr A 2007;1154:429-36.

139. Reedy TJ, Reedy CL. Statistical Analysis in Art Conservation Research. Marina del Rey: The Getty Conservation Institute; 1988. (Research in conservation; vol 1).

140. San Andres M, Baez MI, Baldonedo JL, Barba C. Transmission electron microscopy applied to the study of works of art: sample preparation methodology and possible techniques. J Microsc 1997;188:42-50.

141. Davidson MW, Abramowitz M. Optical Microscopy. In: Hornak J, editor. Encyclopedia of Imaging Science and Technology. New York: Wiley-Interscience; 2002. vol 2 p. 1106-1141.

142. Pallister DM, Morris MD. Fundamentals of light microscopy. In: Morris MD, editor. Microscopic and spectroscopic imaging of chemical state. New York: Marcel Dekker; 1995. p. 1-19. (Practical spectroscopy series; vol 16).

143. Colarusso P, Kidder LH, Levin IW, Lewis EN. Raman and Infrared Microspectroscopy. In: Lindon JC, Tranter GE, Holmes JL, editors. Encyclopedia of Spectroscopy and Spectrometry. New York: Academic Press; 1999. vol 3 p. 1945-54.

144. Clarke AR, Eberhardt CN. Microscope techniques for materials science. Cambridge: Woodhead Publishing Limited; 2002.

145. Murphy DB. Fundamentals of light microscopy and electronic imaging. New York: Wiley-Liss; 2001.

146. Martin SJ. Microscopic examination and analysis of the structure and composition of paint and varnish layers. In: Dorge V, Howlett FC, editores. Painted wood: History and Conservation - Proceedings of a symposium organized by the Wooden Artefacts Group of the American Institute for Conservation of Historic and Artistic Works; 1994 Nov 11-14; Williansburg, Virginia. Los Angeles: The Getty Institute for Conservation; 1999. p. 64-79.

147. Plester J. Cross-section and chemical analysis of paint samples. Stud Conserv 1956;2:110-57.

148. Edwards HGM, Farwell DW, Rozenberg S. Raman spectroscopic study of red pigment and fresco fragments from King Herod's Palace at Jericho. J Raman Spectrosc 1999;30:361-6.

149. Liem NQ, Sagon G, Quang VX, Tan HV Colomban P. Raman study of the microstructure, composition and processing of ancient Vietnamese (proto)porcelains and celadons(13-16th centuries). J Raman Spectrosc 2000;31:933-42.

150. Schrader B, Schulz H, Andreev GN, Klump HH, Sawatzli J. Non-destructive NIR-FT-Raman spectroscopy of plant and animal tissues, of food and works of art. Talanta 2000;53:35-45.

151. Castro K, Rodríguez-Laso MD, Fernández LA, Madariaga JM. Fourier transform Raman spectroscopic study of pigments present in decorative wallpapers of the middle nineteenth century from the Santa Isabel actory (Vitoria, Basque Country, Spain). J Raman Spectrosc 2002;33:17-25.

152. Zuo J, Zhao X, Wu R, Du G, Xu C, Wang C. Analysis of the pigments on painted pottery figurines from the Han Dynasty's Yangling Tombs by Raman microscopy. J Raman Spectrosc 2003;34:121-5.

153. Jurado-López A, Demko O, Clark RJH, Jacobs D. Analysis of the palette of a precious 16th century illuminated Turkish manuscript by Raman microscopy. J Raman Spectrosc 2004;35:119-24.

154. Hayez V, Guillaume J, Hubin A, Terryn H. Micro-Raman spectroscopy for the study of corrosion products on copper alloys: setting up of a reference database and studying works of art. J Raman Spectrosc 2004;35:732-8.

155. Robinet L, Eremin K, del Arco BC, Gibson LT. A Raman spectroscopic study of pollution-induced glass deterioration. J Raman Spectrosc 2004;35:662-70.

156. Castro K, Vandenabeele P, Rodríguez-Laso MD, Moens L, Madariaga JM. Micro-Raman analysis of coloured lithographs. Anal Bioanal Chem 2004;379:674-83.

157. Pérez-Alonso M, Castro K, Álvarez M, Madariaga JM. Scientific analysis versus restorer's expertise for diagnosis prior to a restoration process: the case of Santa Maria Church (Hermo, Asturias, North of Spain). Anal Chim Acta 2004;524:379-89.

158. Striova J, Lofrumento C, Zoppi A, Castellucci EM. Prehistoric Anasazi ceramics studied by micro-Raman spectroscopy. J Raman Spectrosc 2006;37:1139-45.

159. Chaplin TD, Clark RJH, McKay A, Pugh S. Raman spectroscopic analysis of selected astronomical and cartographic folios from the early 13th century Islamic 'Book of Curiosities of the Sciences and Marvels for the Eyes'. J Raman Spectrosc 2006;37:867-77.

160. Schrader B, editor. Infrared and Raman Spectroscopy: Methods and applications. New York: VCH, 1995.

161. Lindon JC, Tranter GE, Holmes JL, editors. Encyclopedia of Spectroscopy and Spectrometry. New York: Academic Press; 1999.

162. Chalmers JM, Griffiths PR, editors. Handbook of Vibrational Spectroscopy. Chichester: John Wiley & Sons Ltd.; 2002.

163. Ferraro JR, Nakamoto , Brown CW. Introductory Raman Spectroscopy. 2nd ed. New York: Elsevier, 2003.

164. Messerschmidt RG, Harthcock MA, editors. Infrared Microspectroscopy: theory and applications. New York: Marcel Dekker, 1988.

165. Humecki HJ, editor. Practical Guide to Infrared Microspectroscopy. New York: Marcel Dekker; 1995. (Practical spectroscopy series; vol 19).

166. Turrel G, Corset J, editors. Raman Microscopy: Developments and Applications. London: Elsevier, 1996.

167. Launer PJ. Regularities in the infrared absorption spectra of silicate minerals. Am Mineral 1952;37:764-784.

168. Chesters MA. High-resolution electron energy loss spectroscopy. In: Chalmers JM, Griffiths PR, editors. Handbook of Vibrational Spectroscopy. Chichester: John Wiley & Sons Ltd.; 2002.

169. Hipps KW, Mazer U. Inelastic electron tunneling spectroscopy. In: Chalmers JM, Griffiths PR, editors. Handbook of Vibrational Spectroscopy. Chichester: John Wiley & Sons Ltd.; 2002.

170. Shepard N. The historical development of experimental techniques in Vibrational Spectroscopy. In: Chalmers JM, Griffiths PR, editors. Handbook of Vibrational Spectroscopy. Chichester: John Wiley & Sons Ltd.; 2002.

171. Parker SF. Inelastic neutron scattering. In: Chalmers JM, Griffiths PR, editors. Handbook of Vibrational Spectroscopy. Chichester: John Wiley & Sons Ltd.; 2002.

172. Levine IN. Molecular Spectroscopy. New York: John Wiley & Sons: 1975.

173. Duarte MLTD. Aplicações da Espectroscopia de Raman à Química estructural. Dissertação apresentada à Faculdade de Ciências da Universidade de Lisboa para obtenção do grau de Doutor. Faculdade de Ciências da Universidade de Lisboa; 1981.

174. Diem M. Introduction to modern vibrational spectroscopy. New York: John Wiley & Sons; 1993.

175. Nakamoto K. Infrared and Raman Spectra of Inorganic and Coordination Compounds. Part A: Theory and Applications in Inorganic Chemistry. 5th ed. New York: John Wiley & Sons; 1997.

176. Sathyanarayana DN. Vibrational Spectroscopy: Theory and applications. New Delhy: New age International Publishers; 2005.

177. Schrader B. Vibrational spectroscopy of different classes and state compounds: Organic substances. In: Schrader B, editor. Infrared and Raman Spectroscopy: Methods and applications. New York: VCH, 1995. p. 189-222.

178. Shurvell HF, Spectra-Structure correlations in the Mid- and Far-infrared. In: Chalmers JM, Griffiths PR, editors. Handbook of Vibrational Spectroscopy. Chichester: John Wiley & Sons Ltd.; 2002.

179. Bertie JE. Glossary of terms used in vibrational spectroscopy. In: Chalmers JM, Griffiths PR, editors. Handbook of Vibrational Spectroscopy. Chichester: John Wiley & Sons Ltd.; 2002.

180. Harris DC, Bertolucci MD. Symmetry and spectroscopy: An introduction to vibrational and electronic spectroscopy. New York: Oxford University Press; 1978.

181. Levine IN. *Physical Chemistry.* 4th ed. Singapore: McGRAW-HILL; 1995.

182. Groner P. Normal Coordinate Analysis. In: Chalmers JM, Griffiths PR, editors. Handbook of Vibrational Spectroscopy. Chichester: John Wiley & Sons Ltd.; 2002.

183. Griffiths PR. Introduction to Vibrational Spectroscopy. In: Chalmers JM, Griffiths PR, editors. Handbook of Vibrational Spectroscopy. Chichester: John Wiley & Sons Ltd.; 2002.

184. Andrews DL. Rayleigh scattering and Raman Effect, Theory. In: Lindon JC, Tranter GE, Holmes JL, editors. Encyclopedia of Spectroscopy and Spectrometry. New York: Academic Press; 1999. vol 3 p. 1993-2000.

185. Keresztury G. Raman Spectroscopy: Theory. In: Chalmers JM, Griffiths PR, editors. Handbook of Vibrational Spectroscopy. Chichester: John Wiley & Sons Ltd.; 2002.

186. Turrell G. The Raman Effect. In: Turrel G, Corset J, editors. Raman Microscopy: Developments and Applications. London: Elsevier, 1996.

187. Hendra JP. Sampling considerations for Raman Spectroscopy. In: Chalmers JM, Griffiths PR, editors. Handbook of Vibrational Spectroscopy. Chichester: John Wiley & Sons Ltd.; 2002.

188. Mayo DW, Miller FA, Hannah RW. Course notes on the interpretation of infrared and Raman spectra. New Jersey: John Wiley & Sons; 2003.

189. Tasumi M, Sakamoto A, Hieda T, Torii H. Use of Group Theory for band assignment and structure correlation. In: Chalmers JM, Griffiths PR, editors. Handbook of Vibrational Spectroscopy. Chichester: John Wiley & Sons Ltd.; 2002.

190. Goldsmith JA, Ross SD. The infra-red spectra of azurite and malachite. Spectrochim Acta A 1968;24:2131-7.

191. Frost RL, Martens WN, Rintoul L, Mahmutagic E, Kloprogge JT. Raman spectroscopic study of azurite and malachite at 298 and 77 K. J Raman Spectrosc 2002;33:252-9.

192. Steele D. Infrared Spectroscopy: Theory. In: Chalmers JM, Griffiths PR, editors. Handbook of Vibrational Spectroscopy. Chichester: John Wiley & Sons Ltd.; 2002.

193. Kettle SFA. Symmetry and Structure. New York: John Wiley & Sons; 1985.

194. Bellamy LJ. The infrared Spectra of Complex Molecules. 3rd ed. London: Chapman and Hall Ltd; 1975.

195. Nakamoto K. Infrared and Raman Spectra of Inorganic and Coordination Compounds. Part B: Applications in Coordination, Organometallic, and Bioinorganic Chemistry. 5th ed. New York: John Wiley & Sons, Inc.; 1997.

196. Edwards HGM. Spectra-structure correlations in Raman Spectroscopy. In: Chalmers JM, Griffiths PR, editors. Handbook of Vibrational Spectroscopy. Chichester: John Wiley & Sons Ltd.; 2002.

197. Bougeard D. Crystals. In: Schrader B, editor. Infrared and Raman Spectroscopy: Methods and applications. New York: VCH, 1995. p. 314-323.

198. Pettinari C, Santini C. IR and Raman Spectroscopy of Inorganic, Coordination and Organometallic Compounds. In: Lindon JC, Tranter GE, Holmes JL, editors. Encyclopedia of Spectroscopy and Spectrometry. New York: Academic Press; 1999. vol 2 p. 1021-34.

199. Frank K, Pascual JI. Experimentalphysik IV - Struktur der Materie [Online]. 2009 [cited 2010 Oct 01]. Available from:
URL: http://users.physik.fu-berlin.de/~pascual/Vorlesung/SS09/index.htm (lattice vibrations)

200. Lee MA, Schmidt KE. Java Phonon Applet: Transverse Optical and Acoustic Phonon Dispersion [Online]. 2000 Jul 01 [cited 2010 Oct 01]. Available from:
URL: http://fermi.la.asu.edu/ccli/applets/phonon/phonon.html

201. Williams KPJ, Pitt GD, Smith BJE, Whitley A, Batchelder DN, Hayward IP. Use of a Rapid Scanning Stigmatic Raman Imaging Spectrograph in the Industrial Environment. J Raman Spectrosc 1994;25:131-8.

202. Barbillat J, Dhamelincourt P, Delhaye M, da Silva E. Raman Confocal Microprobing, Imaging and Fiber-Optic Remote Sensing: a Further Step in Molecular Analysis. J Raman Spectrosc 1994;25:3-11.

203. Turrell G, Delhaye M, Dhamelincourt P. Characteristics of Raman Microscopy. In: Turrel G, Corset J, editors. Raman Microscopy: Developments and Applications. London: Elsevier, 1996. p. 27-49.

204. Fredericks PM. Depth Profiling by Microspectroscopy. In: Chalmers JM, Griffiths PR, editors. Handbook of Vibrational Spectroscopy. Chichester: John Wiley & Sons Ltd.; 2002.

205. Schiering DW, Tague TJ, Reffner JA, Vogel SH. A dua confocal aperturing microscope for IR microspectrometry. Analusis 2000;28:46-52. Available from:
URL:http://analusis.edpsciences.org/index.php?option=article&access=standard&Itemid=129&url=/articles/analusis/pdf/2000/01/schiering.pdf.

206. Sommer AJ, Katon JE. Diffraction-induced stray light in Infrared Microspectroscopy and its effect on spatial resolution. Appl Spectrosc 1991;45:1633-40.

207. Williams KPJ, Batchelder DN. Raman microscopy - Spectroscopy and direct two-dimensional imaging. Spectrosc Eur 1994;6:19-26.

208. inVia Raman microscope: Objective lens options. Technology note SPD/PN/088. 2006 Dec. 1.2.

209. Hendra P, Jones C, Warnes G. Fourier Transform Raman Spectroscopy - Instrumentation and Chemical Applications. Chichester: Ellis Horwood; 1991.

210. Delhaye M, Barbillat J, Aubard J, Bridoux M, da Silva E. Instrumentation. In: Turrel G, Corset J, editors. Raman Microscopy: Developments and Applications. London: Elsevier, 1996. p. 51-173.

211. Spragg RA. IR Spectrometers. In: Lindon JC, Tranter GE, Holmes JL, editors. Encyclopedia of Spectroscopy and Spectrometry. New York: Academic Press; 1999. vol 2 p. 1048-1057.

212. Bowei BT, Chase DB, Lewis IR, Griffiths PR. Anomalies and artifacts in Raman spectroscopy. In: Chalmers JM, Griffiths PR, editors. Handbook of Vibrational Spectroscopy. Chichester: John Wiley & Sons Ltd.; 2002.

213. Chase B. Fourier Transform Near-infrared Raman Spectroscopy. In: Chalmers JM, Griffiths PR, editors. Handbook of Vibrational Spectroscopy. Chichester: John Wiley & Sons Ltd.; 2002.

214. Henry C. The stable world of FT-IR. Anal Chem 1998;70:273A-6A.

215. Messerschmidt RG. Minimizing Optical Nonlinearities in Infrared Microspectroscopy. In: Humecki HJ, editor. Practical Guide to Infrared Microspectroscopy. New York: Marcel Dekker; 1995. p. 3-39. (Practical spectroscopy series; vol 19).

216. Nishikida K. Spatial Resolution in Infrared Microscopy and Imaging. Thermo Scientific Application Note 2007;50717.

217. Martin MC. How to use a Synchrotron for IR microscopy. R&D Magazine 2000 May: 105.

218. McIntosh LM, Jackson M. Ex vivo vibrational spectroscopy imaging. In: Chalmers JM, Griffiths PR, editors. Handbook of Vibrational Spectroscopy. Chichester: John Wiley & Sons Ltd.; 2002.

219. Miller LM, Dumas P. Chemical imaging of biological tissue with synchrotron infrared light. Biochim Biophys Acta Biomembr 2006;1758:846-57.

220. Holman HY, Martin MC. Synchrotron radiation infrared spectromicroscopy: a non-invasive molecular probe for biogeochemical processes. Adv Agron 2006;90:79-127.

221. Langley A, Burnstock A. The analysis of layered paint samples from modern paintings using FTIR microscopy. In: Grattan D, edition. Preprints of ICOM, 12th triennial meeting Committee for Conservation; 1999 Aug 29-Sep 03; Lyon, France. London: James & James;1999 vol. 1, pp. 234-241.

222. Schaeberle MD, Morris HR, Turner II J.F, Treado PJ. Raman Chemical Imaging Spectroscopy. Anal Chem 1999;71:175A-81A.

223. Pan M, Benner RE, Smith LM. Continuous lasers for Raman Spectrometry. In: Chalmers JM, Griffiths PR, editors. Handbook of Vibrational Spectroscopy. Chichester: John Wiley & Sons Ltd.; 2002.

224. Low MJD, Baer NS. Application of infrared Fourier transform spctroscopy to problems in conservation. Stud Conserv 1977;22:116-28.

225. Buijs H. Incandescent sources for Mid- and Far-infrared spectroscopy. In: Chalmers JM, Griffiths PR, editors. Handbook of Vibrational Spectroscopy. Chichester: John Wiley & Sons Ltd.; 2002.

226. Coates J. Interpretation of infrared spectra, a practical approach. In: Meyers RA, editor. Encyclopedia of Analytical Chemistry. Chichester: John Wiley & Sons; 2000. p. 10815-10837.

227. Edwards HGM. Art works studied using IR and Raman spectroscopy. In: Lindon JC, Tranter GE, Holmes JL, editors. Encyclopedia of Spectroscopy and Spectrometry. New York: Academic Press; 1999. vol 1 p. 2-17.

228. Fiedler I, Bayard M. Emerald green and Scheele's green. In: FitzHugh EW, editor. Artists' Pigments. A Handbook of their History and Characteristics. Oxford: National Gallery: Washington and Oxford University Press, 1997. vol. 3 p. 219-71.

229. Frost RL, Bahfenne S. Raman spectroscopic study of the arsenite minerals leiteite $ZnAs_2O_4$, reinerite $Zn_3(AsO_3)$ and cafarsite $Ca_5(Ti,Fe,Mn)_7(AsO_3)_{12}$·4H2O. J Raman Spectrosc 2010;41:325-328.

230. Ito K, Bernstein HJ. The vibrational spectra of the formate, acetate, and oxalate ions. Can J Chem 1956;34:170-178.

231. Chaplin TD, Clark RJH, Scott DA. Study by Raman microscopy of nine variants of the green-blue pigment verdigris. J Raman Spectrosc 2006;37:223-9.

232. Scott DA, Taniguchi Y, Koseto E. The verisimilitude of verdigris: a review of the copper carboxylates. Rev Conserv 2001;2:73-91.

233. Kuhn H. Verdigris and copper resinate. Stud Conserv 1970;15:12-36.

234. Adler HH, Kerr PF. Infrared absorption frequency trends for anhydrous normal carbonates. Am Mineral 1963;48:124-37.

235. Gettens RJ, FitzHugh EW, Feller RL. Calcium carbonate whites. In: Roy A, editor. Artists' Pigments. A Handbook of their History and Characteristics. Oxford: National Gallery: Washington and Oxford University Press; 1993. vol. 2 p. 203-26.

236. Matsuda Y, Tsukada M. Identification of calcium carbonate contained as body in modern paints by FTIR spectroscopy. In: Postprints of IRUG meeting; 1995 Sep 12-13; London, UK. London: Victoria & Albert Museum; 1998 p. 25-33.

237. Gunasekaran S, Anbalagan G. Spectroscopic characterization of natural calcite minerals. Spectrochim Acta A 2007;68:656-64.

238. Learner TJS. Analysis of Modern Paints. Los Angeles: The Getty Conservation Institute; 2004.

239. Brooker MH, Sunder S, Taylor P, Lopata VJ. Infrared and Raman spectra and X-ray diffraction studies of solid lead(II) carbonates. Can J Chem 1983;61:494-502.

240. Roncaglia DI, Botto IL, Baran EJ. Vibrational spectrum of Pb_2CrO_5. J Mater Sci Lett. 1985;4:1427-8.

241. Gadsden JA. Infrared spectra of minerals and related inorganic compounds. London: Butterworths; 1975.

242. Kühn H, Curran M. Chrome yellow and other chromate pigments. In: Feller RL, editor. Artists' Pigments. A Handbook of their History and Characteristics. Cambridge: National Gallery: Washington and Cambridge University Press; 1986. vol. 1 p. 187-217.

243. Doyle WP, Eddy P. Infra-red spectra of chromates(V) of calcium, strontium and barium. Spectrochim Acta A 1967;23:1903-7.

244. Cord PP, Courtine P, Pannetier G. Spectres de vibration des chromates et des molybdates des métaux divalents de la première serie de transition. Spectrochim Acta A 1972;28:1601-13.

245. Nyquist RA, Kagel RO. Infrared Spectra of Inorganic Compounds (3800-45 cm^{-1}). New York: Academic Press Inc.; 1973.

246. Desnica V, Furic K, Hochleitner B, Mantler M. A comparative analysis of five chrome green pigments based on different spectroscopic techniques. Spectrochim Acta B 2003;58:681-7.

247. Berrie BH. Prussian blue. In: FitzHugh EW, editor. Artists' Pigments. A Handbook of their History and Characteristics. Oxford: National Gallery: Washington and Oxford University Press, 1997. vol. 3 p. 191-217.

248. Newman R. Chromium Oxide Greens: Chromium oxide and hydrated chromium oxide. In: FitzHugh EW, editor. Artists' Pigments. A Handbook of their History and Characteristics. Oxford: National Gallery: Washington and Oxford University Press, 1997. vol. 3 p. 273-293.

249. Silva CE, Silva LP, Edwards HGM, de Oliveira LFC. Diffuse reflection FTIR spectral database of dyes and pigments. Anal Bioanal Chem 2006;386:2183-91.

250. van der Marel HW, Beutelspacher H. Atlas of Infrared spectroscopy of Clay Minerals and their Admixtures. Amsterdam: Elsevier; 1976.

251. Falk M. The frequency of the O-H-O bending fundamental in solids and liquids. Spectrochim Acta 1984;40A:43-48.

252. Castro K, Pérez-Alonso M, Rodríguez-Laso MD, Fernández LA, Madariaga JM. Online FT-Raman and dispersive Raman spectra database of artists' materials (e-VISART database). Anal Bioanal Chem 2005;382:248-58.

253. Nassau K. The physics and chemistry of color: the 15 mechanisms. In: Shevell SK, editor. The science of color. New York: Elsevier, 2003. p. 247-280.

254. Wöhler L, Becker W. Colour and composition of Guignet's green. Zeitsch. angew. Chem. 1908;21:1600-6.

255. Saraswat IP, Vajpei AC. Characterization of chromium oxide hydrated gel. J Mater Sci Lett 1984;3:515-7.

256. Zumbuehl S, Scherrer NC, Berger A, Eggenberger A. Early Viridian pigment composition - characterisation of a (hydrated) chromium oxide borate pigment. Stud Conserv 2009;54:149-59.

257. Livinstone A, Jackson B, Davidson PJ. Grimaldiite, CrOOH, a second occurrence, from the Hiaca Mine, Colquechaca, Bolivia. Mineral Mag 1984;48:560-2.

258. Aoki Y, Habazaki H, Konno H. Interconversion between Rare-Earth Metal(III) Chromates(V) and Low-Crystalline Phases by Reduction with Methanol and Oxidation in Air. Chem Mater 2003;15:2419-28.

259. Ratnasamy P, Léonard AJ. Structural Evolution of Chromia. J Phys Chem 1972;76:1838-43.

260. Godfrey IM, Ghisalberti EL, Beng EW, Byrne LT, Richardson GW. The analysis of ivory from a marine environment. Stud Conserv 2002;47:29-44.

261. Pasteris JD, Wopenka B, Freeman JJ, Rogers K, Valsami-Jones E, van der Houwen JAM, et al. Lack of OH in nanocrystalline apatite as fuction of degree of atomic order: implications for bone and biomaterials. Biomaterials 2004;25:229-38.

262. Ruppel ME, Burr DB, Miller LM. Chemical makeup of microdamaged bone differs from undamaged bone. Bone 2006;39:318-24.

263. Wang L, Fan H, Liu J, Dan H, Ye Q, Deng M. Infrared spectroscopic study of modern and ancient ivory from sites at Jinsha and Sanxingdui, China. Mineral Mag 2007;71:509-18.

264. Brophy GP, Nash JT. Compositional, infrared, and X-ray analysis of fossil bone. Am Mineral 1968;53:445-54.

265. Vila A, Ferrer N, García JF. Chemical composition of contemporary black printing inks based on infrared spectroscopy: Basic information for the characterization and discrimination of artistic prints. Anal Chim Acta 2007;591:97-105.

266. Deng Y, White GB, Dixon JB. Effect of structural stress on the intercalation rate of Kaolinite. J Colloid Interface Sci 2002;250:379-93.

267. Madejová J. FTIR techniques in clay minerals studies. Vib Spectrosc 2003;31:1-10.

268. Milkey RG. Infrared spectra of some tectosilicates. Am Mineral 1960;45:990-1007.

269. Frost RL, Fredericks PM. Fourier transform Raman spectroscopy of kandite clays. Spectrochim Acta A 1993;49:667-74.

270. Rieder M, Cavazzini G, D' Yakonov YS, Frank-Kamenetskii VA, Gottardi G, Guggenheim S, et al. Nomenclature of the micas. Can Mineral 1998;36:905-12.

271. Anthony JW, Bideaux RA, Bladh KW, Nichols MC. Glauconite. In: Handbook of Mineralogy. Tucson Arizona: Mineral Data Publishing; 2001. vol 2.

272. Grissom CA. A literature search for a pigment study. In: Preprints of the ICOM Committee for Conservation 4th Triennial Meeting; 1975 Oct 13-18; Venice, Italy. Paris: International Council of Museums;1975. p. 75/21/5-1 - 75/21/5-7.

273. Velde B. Infrared spectra of synthetic micas in the series muscovite - MgAl celadonite. Am Mineral 1978;63:343-9.

274. Grisson CA. Green Earth. In: Feller RL, editor. Artists' Pigments. A Handbook of their History and Characteristics. Cambridge: National Gallery: Washington and Cambridge University Press; 1986. vol. 1 p. 141-167.

275. Ospitali F, Bersani D, Di Lonardo G, Lottici PP. "Green earths": vibrational and elemental characterization of glauconites, celadonites and historical pigments. J Raman Spectrosc 2008;39:1066-73.

276. Frost RL. Fourier transform Raman spectroscopy of kaolinite, dickite and halloysite. Clays Clay Miner 1995;43:191-5.

277. Cruz MDR. Genesis and evolution of the kaolin-group minerals during the diagenesis and the beginning of metamorphism. In: Nieto F, Jiménez-Millán J, editors. Diagenesis and Low-Temperature Metamorphism. Theory, Methods and Regional Aspects. Seminarios de la Sociedad Española de Mineralogia. Jaén: Sociedad Española de Mineralogia; 2007. vol. 3 p. 41-52. Available from: URL:http://www.ehu.es/sem/revista/seminarios.htm

278. Frost RL, Van Der Gaast SJ, Zbik M, Kloprogge JT, Paroz GN. Birdwood kaolinite: a highly ordered kaolinite that is difficult to intercalate - an XRD, SEM and Raman spectroscopic study. Appl Clay Sci 2002;20:177-187.

279. Frost RL, Tran TH, Rintoul L, Kristof J. Raman microscopy of dickite, kaolinite and their intercalates. Analyst 1998;123:611-6.

280. Frost RL, Fredericks PM, Kloprogge JT, Hope GA. Raman spectroscopy of kaolinites using different excitation wavelengths. J Raman Spectrosc 2001;32:657-63.

281. Balan E, Saitta AM, Mauri F, Calas G. First-principles modeling of the infrared spectrum of kaolinite. Am Mineral 2001;86:1321-30.

282. Williams Q. Infrared, Raman and optical spectroscopy of earth materials. In: Ahrens TJ, editor. Mineral physics and crystallography: a handbook of physical constants. Washington: American Geophysical Union., 1995. p. 291-302.

283. Adler HH, Kerr PF. Variations in infrared spectra, molecular symmetry and syte symmetry of sulfate minerals. Am Mineral 1965;50:132-47.

284. Feller RL. Barium sulfate - natural and synthetic. In: Feller RL, editor. Artists' pigments. A handbook of their History and characteristics. Cambridge: National Gallery: Washington and Cambridge University Press; 1986. vol. 1 p. 47-64.

285. Meilunas RJ, Bentsen JG, Steinberg A. Analysis of aged paint binders by FTIR Spectroscopy. Stud Conserv 1990;35:33-51.

286. Schmidt M, Lutz HD. Hydrogen bonding in basic copper salts: a spectroscopic study of malachite, $Cu_2(OH)_2CO_3$ and brochantite, $Cu_4(OH)_6SO_4$. Phys Chem Miner 1993;20:27-32.

287. Makreski P, Jovanovski G, Dimitrovska S. Minerals from Macedonia: XIV. Identification of some sulphate minerals by vibrational (infrared and Raman) spectroscopy. Vib Spectrosc 2005;39:229-39.

288. Bersani D, Antonioli G, Lottici PP, Casoli A. Raman microspectrometric investigation of wall paintings in S. Giovanni Evangelista Abbey in Parma: a comparison between two artists of the 16th century. Spectrochim Acta A 2003;59:2409-17.

289. Seidl V, Knop O, Falk M. Infrared studies of water in crystalline hydrates: gypsum, $CaSO_4.2H_2O$. Can J Chem 1969;47:1361-8.

290. Knittle E, Phillips W, Williams Q. An infrared and Raman spectroscopic study of gypsum at high pressures. Phys Chem Miner 2001;28:630-40.

291. Anbalagan G, Mukundakumari S, Murugesan KS, Gunasekaran S. Infrared, optical absorption, and EPR spectroscopic studies on natural gypsum. Vib Spectrosc 2009;50:226-30.

292. Desnica V, Furic K, Schreiner M. Multianalytical characterisation of a variety of ultramarine pigments. e-PS 2004;1:15-21.

293. Plic J, White R. The application of FTIR-Microscopy to the analysis of paint binders in easel paintings. Nat Gall Tech Bull 1995;16:73-84.

294. Fiorin E, Vigato PA. Teodelinda's tales at Monza Cathedral: A physico-chemical diagnosis of the pictorial cycle. J Cult Herit 2007;8:13-25.

295. Brecoulaki H, Fiorin E, Vigato PA. The funerary klinai of tomb 1 from Amphipolis and a sarcophagus from ancient Tragilos, eastern Macedonia: a physico-chemical investigation on the painting materials. J Cult Herit 2006;7:301-11.

296. Higgitt C, Spring M, Saunders D. Pigment-medium intercations in oil paint films containing red lead or lead-tin yellow. Nat Gall Tech Bull 2003;24:75-95.

297. Plater MJ, de Silva B, Gelbrich T, Hursthouse MB, Higgitt CL, Saunders DR. The characterisation of lead fatty acid soaps in 'protrusions' in aged traditional oil paint. Polyhedron 2003;22:3171-9.

298. Robinet L, Corbeil M. The characterization of metal soaps. Stud Conserv 2003;48:23-40.

299. Spring M, Higgitt C, Saunders D. Investigation of Pigment-Medium intercation processes in oil containing degraded smalt. Nat Gall Tech Bull. 2005;26:56-69.

300. Regert M, Langlois J, Laval E, Le Hô AS, Pagès-Campagna S. Elucidation of moleculra and elementary composition of organic and inorganic substances involved in 19th century wax sculptures using an integrated analytical approach. Anal Chim Acta 2006;577:140-52.

301. Golikov V. The classification of coloured organic materials in painting and applied arts on the basis of natural dyes. In: Kirby J, editor. Dyes in History and Archaeology: Papers presented at the 18th meeting; 1999; Brussels, Belgium. Archetype Publications; 2002. p. 87-100.

302. Higgitt C, Kirby J, Spring M. Red lake pigments: linking analytical results to the recipes. In: Looking forward to the Past: Science and Heritage; 2006 Nov 28; London.

303. Schweppe H, Roosen-Runge H. Carmine - Cochineal Carmine and Kermes Carmine. In: Feller RL, editor. Artists' Pigments. A handbook of their History and characteristics. Cambridge: National Gallery: Washington and Cambridge University Press; 1986. vol. 1 p. 255-281.

304. Kirby J, Spring M, Higgitt C. The technology of red lake pigment manufacture: study of the dyestuff substrate. Nat Gall Tech Bull. 2005;26:71-87.

305. Kirby J. The reconstruction of late 19th-century French red lake pigments. In: Townsend JH, Stijnman A, Clarke M, editors. Art of the Past, sources and reconstruction. Proceedings of the 1st Symposium of the Art technological source research study group. 2004 Oct 14-15; Amsterdam. London: Archetype Publications; 2005. p. 69-77.

306. Choisy P, de la Chapelle A, Thomas D, Legoy MD. Non invasive techniques for the investigation of foxing stains on graphic art material. Restaurator 1997;18:131-52.

307. Mathey Y, Greig DR, Shriver DF. Variable-temperature Raman and infrared spectra of the copper acetate dimer $Cu_2(O_2CCH_3)_4(H_2O)_2$ and its derivates. Inorg Chem 1982;21:3409-13.

308. Bell IM, Clark RJH and Gibbs PJ. Raman spectroscopic library of natural and synthetic pigments (pre-~1850 AD). Spectrochim Acta A 1997;53:2159-79.

309. Frost RL, Kloprogge JT. Raman spectroscopy of the acetates of sodium, potassium and magnesium at liquid nitrogen temperature. J Mol Struct 2000;526:131-41.

310. Trentelman K, Stodulski L, Scott D, Back M, Stock S, Strahan D, et al. The characterization of a new pale blue corrosion product found on copper alloy artifacts. Stud Conserv. 2002;47:217-27.

311. Chasteen TG, Wiggli M, Bentley R. Of garlic, mice and Gmelin: the odor of trimethylarsine. Appl Organomet Chem 2002;16:281-6.

312. Flynn EJ, Solin SA, Papatheodorou GN. Vibrational excitations of As_2O_3. II. Crystalline phases. Phys Rev B: Solid State 1976;13:1752-8.

313. Gilliam SJ, Merrow CN, Kirkby SJ, Jensen JO, Zeroka D, Banerjee A. Raman spectroscopy of arsenolite: crystalline cubic As4O6. J Solid State Chem 2003;173:54-8.

314. Downs RT. The RRUFF Project: an integrated study of the chemistry, crystallography, Raman and infrared spectroscopy of minerals. In: Program and Abstracts of the 19th General Meeting of the International Mineralogical Association; 2006, Kobe, Japan. p. O03-13. Available from:URL:http://rruff.info/

315. Gettens RJ, Kühn H, Chase WT. Lead White. In: Roy A, editor. Artists' Pigments. A handbook of their History and characteristics. Oxford: National Gallery: Washington and Oxford University Press; 1993. vol. 2 p. 67-81.

316. Gettens RJ, FitzHugh EW. Malachite and Green Verditer. In: Roy A, editor. Artists' Pigments. A handbook of their History and characteristics. Oxford: National Gallery: Washington and Oxford University Press; 1993. vol. 2 p. 183-201.

317. Williams SA, McLean WJ, Anthony JW. A study of Phoenicochroite-its structure and properties. Am Mineral 1970;55:784-92.

318. Krivovichev SV, Burns PC. Chains of edge-sharing OPb_4 tetrahedra in the structure of $Pb_4O(VO_4)_2$ and in related minerals and inorganic compounds. Can Mineral 2003;41:951-8.

319. Baran EJ, Ferrer EG, Bueno I, Parada C. Vibrational Spectra of some double chromates of the type $LnK(CrO_4)_2$. J Raman Spectrosc 1990;21:27-30.

320. Frost R. Raman microscopy of selected chromate minerals. J Raman Spectrosc 2004;35:153-8.

321. Coupry C, Lautié A, Revault M, Dufilho J. Contribution of Raman spectroscopy to art and History. J Raman Spectrosc 1994;25:89-94.

322. Kock LD, De Waal D. Raman studies of the underglaze blue pigment on ceramic artefacts of the Ming dynasty and of unknown origins. J Raman Spectrosc 2007;38:1480-7.

323. Nan J, Yang Y, Lin Z. Raman spectroscopic study on the surface oxide layer of AB5-type metal hydride electrodes. Electrochim Acta 2001;46:1767-72.

324. Jiang J, Li L. Synthesis of sphere-like Co_3O_4 nanocrystals via a simple polyol route. Mater Lett 2007;61:4894-6.

325. de Faria DLA, Silva SV, de Oliveira MT. Raman microspectroscopy of some iron oxides and oxyhydroxides. J Raman Spectrosc 1997;28:873-8.

326. Froment F, Tournié A, Colomban P. Raman identification of natural red to yellow pigments: ochre and iron-containing ores. J Raman Spectrosc 2008;39:560-8.

327. Massey MJ, Baier U, Merlin R, Weber WH. Effects of pressure and isotopic substitution on the Raman spectrum of α-Fe_2O_3: Indentification of two-mangon scattering. Phys Rev B 1990;41:7822-7.

328. Bersani D, Lottici PP, Montenero A. Micro-Raman investigation of iron oxide films and powders produced by sol-gel syntheses. J Raman Spectrosc 1999;30:355-60.

329. de Faria DLA, Lopes FN. Heated goethite and natural hematite: can Raman spectroscopy be used to differentiate them?. Vib Spectrosc 2007;45:117-21.

330. Gasparov LV, Tanner DB, Romero DB, Berger H, Margaritondo G, Forró L. Infrared and Raman studies of the Verwey transitions in magnetite, Phys Rev B 2000;62:7939-7944.

331. van der Weerd J, Rehren T, Firth S, Clark RJH. Identification of iron oxide impurities in earliest industrial-scale processed platinum. Mater Characteriz 2004;53:63-70.

332. Chamritski I, Burns G. Infrared- and Raman-active phonons of magnetite, maghemite, and hematite: a computer simulation and spectroscopic study. J Phys Chem B 2005;109:4965-8.

333. Bikiaris D, Daniilia S, Sotiropoulou S, Katsimbiri O, Pavlidou E, Moutsatsou AP. et al. Ochre-differentiation through micro-Raman and micro-FTIR spectroscopies: application on wall paintings at Meteora and Mount Athos, Greece. Spectrochim Acta A 1999;56:3-18.

334. Shebanova ON, Lazor P. Raman study of magnetite (Fe_3O_4):laser-induced thermal effects and oxidation. J Raman Spectrosc 2003;34:845-852.

335. Shebanova ON. Lazor P. Raman spectroscopic study of magnetite ($FeFe_3O_4$): a new assignment for the vibrational spectrum. J Solid State Chem 2003;174:424-30.

336. Clark RJH, Wang Q, Correia A. Can the Raman spectrum of anatase in artwork and archaeology be used for dating purposes? Identification by Raman microscopy of anatase in

decorative coatings on Neolithic (Yangshao) pottery from Henan, China. J Archaeol Sci 2007;34:1787-93.

337. Gettens RJ, Stout GL. Painting Materials, A Short Encyclopaedia. New York: Dover Publications; 1966.

338. Hradil D, Grygar T, Hradilová J, Bezdička P. Clay and iron pigments in the history of painting. Appl Clay Sci 2003;22:223-236.

339. Julien CM, Massot M, Poisignon C. Lattice vibrations of manganese oxides – Part I. Periodic structures. Spectrochim Acta A 2004;60:689-700.

340. Ospitali F, Smith DC, Lorblanchet M. Preliminary investigation by Raman microscopy of prehistoric pigments in the wall-painted cave at Roucadour, Quercy, France. J Raman Spectrosc 2006;37:1063-71.

341. Ramirez MO, Krishnamurthi M, Denev S, Kumar A, Yang S, Chu Y, et al. Two-phonon coupling to the antiferromagnetic phase transition in multiferroic $BiFeO_3$. Condens Matter 2007; cond-mat.other arXiv:0712.0368v1. Available from: URL:http://arxiv.org/abs/0712.0368

342. Wainwright INM, Taylor JM, Harley RD. Lead Antimonate Yellow. In: Feller RL, editor. Artists' Pigments. A handbook of their History and characteristics. Cambridge: National Gallery: Washington and Cambridge University Press; 1986. vol. 1 p. 219-254.

343. Dik J, Hermens E, Peschar R, Schenk H. Early production recipes for lead antimonate yellow in Italian art. Archaeometry 2005;47:593-607.

344. Guineau B. L'étude des pigments par les moyens de la microspectrométrie Raman. In: Delamare F, Hackens T, Helly B, editors. PACT-17. Datation-Caractérisation des peintures pariétales et murales, European University Centre for Cultural Heritage; 1987, Ravello, p. 259–94.

345. Clark RJH, Cridland L, Kariuki BM, Harris KDM, Withnall R. Synthesis, structural characterization and Raman spectroscopy of the inorganic pigments Lead tin yellow types I and II and lead antimonite yellow: their identification on medieval paintings and manuscripts. J Chem Soc, Dalton Trans 1995: 2577-82.

346. Bultrini G, Fragalà I, Ingo GM, Lanza G. Characterisation and reproduction of yellow pigments used in central Italy for decorating ceramics during Renaissance. Appl Phys A Mater Sci Process 2006;83:557-65.

347. Hradil D, Grygar T, Hradilová J, Bezdička P, Grűwaldová V, Fogaš I, et al. Microanalytical identification of Pb-Sb-Sn yellow pigment in historical European paintings and its differentiation from lead tin and Naples yellows. J Cult Herit. 2007;8:377-86.

348. Rosi F, Manuali V, Miliani C, Brunetti BG, Sgamellotti A, Grygar T, et al. Raman scattering features of lead pyroantimonate compounds. Part I: XRD and Raman characterization of $Pb_2Sb_2O_7$ doped with tin and zinc. J Raman Spectrosc 2009;40:107-11.

349. Rosi F, Manuali V, Grygar T, Bezdicka P, Brunetti BG, Sgamellotti A, et al. Raman scattering features of lead pyroantimonate compounds: implication for the non-invasive identification of yellow pigments on ancient ceramics. Part II: In situ characterization of Renaissance plates by portable micro-Raman and XRF studies. J Raman Spectrosc 2010 (in press)

350. Colomban P, Sagon G, Faurel X. Differentiation of antique ceramics from the Raman spectra of their coloured glazes and paintings. J Raman Spectrosc 2001;32:351-60.

351. Sakellariou K, Miliani C, Morresi A, Ombelli M. Spectroscopic investigation of yellow majolica glazes. J Raman Spectrosc 2004;35:61-7.

352. de Lucas MCM, Moncada F, Rosen J. Micro-Raman study of red decorations in French faiences of the 18th and 19th centuries. J Raman Spectrosc 2006;37:1154-9.

353. Bouchard M, Smith DC, Carabatos-Nédelec C. An investigation of the feasibility of applying Raman microscopy for exploring stained glass. Spectrochim Acta A 2007;68:1101-13.

354. Sendova M, Zhelyaskov V, Scalera M, Gulliford C. Micro-Raman spectroscopy characterization of Della Robbia glazes. Archaeometry 2007;49:655-64.

355. Sandalinas C, Ruiz-Moreno S. Lead-tin-antimony yellow – Historical manufacture, molecular characterization and identification in seventeenth-century Italian paintings. Stud Conserv. 2004;49:41-52.

356. Sandalinas C, Ruiz-Moreno S, López-Gil A, Miralles J. Experimental confirmation by Raman spectroscopy of a Pb-Sn-Sb triple oxide yellow pigment in sixteenth-century Italian pottery. J Raman Spectrosc 2006;37:1146-53.

357. Jambor JL, Roberts AC. New mineral names. Am Mineral 1997;82:207-10.

358. Mestl G, Ruiz P, Delmon B, Knözinger H. In situ Raman spectroscopy characterization of 18O exchange in physical mixtures of antimony oxides and molybdenium oxide. J Phys Chem 1994;98:11283-92.

359. Vigoreux JP, Husson E, Calvarin G, Dao NQ. Etude par spectroscopié vibrationnelle des oxydes Pb_3O_4, $SnPb_2O_4$ et $SnPb(Pb_2O_4)_2$. Spectrochim Acta 1982;38A:393-8.

360. Daniilia S, Sotiropoulou S, Bikiaris D, Salpistis C, Karagiannis G, Chryssoulakis Y, et al. Panselinos' Byzantine wall paintings in the Protaton Church, Munt Athos, Greece: a technical examination. J Cult Herit. 2000;1:91-110.

361. Chaplin TD, Jurado-López A, Clark RJH, Beech DR. Identification by Raman microscopy of pigments on early postage stamps:distinction between original 1847 and 1858-1862, forged and reproduction postage stamps of Mauritius. J Raman Spectrosc 2004;35:600-4.

362. Burgio L, Clark RJH, Firth S. Raman spectroscopy as a means for the identification of plattnerite (PbO_2), of lead pigments and of their degradation products. Analyst 2001;126:222-7.

363. Smith GD, Derbyshire A, Clark RJH. In situ spectroscopic detection of lead sulphide on a blackened manuscript illumination by Raman microscopy. Stud Conserv. 2002;47;250-6.

364. Li J, Ishigaki T, Sun X. Anatase, Brookite, and Rutile Nanocrystals via Redox Reactions under Mild Hydrothermal Conditions: Phase-Selective Synthesis and Physicochemical Properties. J Phys Chem C 2007;111:4969-76.

365. Tompsett GA., Bowmaker GA, Cooney RP, Metson JB, Rodgers KA, Seakins JM. The Raman Spectrum of Brookite, TiO_2 (*Pbca*, $Z = 8$). J Raman Spectrosc 1995;26:57-62.

366. Murad E, Köster HM. Determination of the Ti speciation in commercial kaolins by Raman spectroscopy. Clay Miner 1999;34:479-85.

367. Laver M. Titanium dioxide whites. In: FitzHugh EW, editor. Artists' Pigments. A handbook of their History and characteristics. Oxford: National Gallery: Washington and Oxford University Press, 1997. vol. 3 p. 295-355.

368. Duval AR. Les prepartions colorees des tableaux de l'ecole Francaise des dix-septieme et dix-huitieme siecles. Stud Conserv. 1992:37;239-58.

369. Howard H. Pigments of English Medieval Wall painting. London: Archetype Publications; 2003.

370. Murad E. Identification of minor amounts of anatase in kaolins by Raman spectroscopy. Am Mineral 1997;82:203-6.

371. Alim KA, Fonoberov VA, Shamsa M, Balandin AA. Micro-Raman investigation of optical phonons in ZnO nanocrystals. J Appl Phys 2005;97:124313-1-124313-5.

372. Coupry C, Lautié A. Raman studies on surface of artefacts. Rev Met Paris 2001;9:789-93.

373. Damiani D, Gliozzo E, Memmi TI, Spangenberg JE. Pigments and Plasters Discovered in the House of Diana (*Cosa*, Grosseto, Italy): An integrated study between Art History, Archaeology and Scientific Analyses. Archaeometry 2003;45:341-54.

374. Baraldi P, Bonazzi A, Giordani N, Paccagnella F, Zannini P. Analytical characterization of roman plaster of the "Domus Farini" in Modena. Archaeometry 2006;48:481-99.

375. Baraldi P, Baraldi C, Curina R, Tassi L, Zannini P. A micro-Raman archaeometric approach to Raman wall paintings. Vib Spectrosc 2007;43:420-6.

376. Tlili A, Smith DC, Beny JM, Boyer H. A Raman microprobe study of natural micas. Mineral Mag 1989;53:165-79.

377. McKeown DA, Bell MI, Etz ES. Vibrational analysis of the dioctahedral mica: 2M1 muscovite. Am Mineral 1999;84:1041-8.

378. Shoval S, Yariv S, Michaelian KH, Boudeulle M, Panczer G. LO and TO crystal modes of the hydroxyl stretching vibrations in micro-Raman and infrared spectra of nacrite. Opt Mater. 2001;16:311-8.

379. Schroeder PA, Melear ND, Pruett RJ. Quantitative analysis of anatase in Georgia kaolins using Raman spectroscopy. Appl Clay Sci 2003;23:299-308.

380. Sato RK, McMillan PF. An infrared and Raman study of the isotopic species of α-Quartz. J Phys Chem 1987;91:3494-98.

381. Clark RJH, Franks ML. The resonance Raman spectrum of ultramarine blue. Chem Phys Lett 1975;34:69-72.

382. Colomban P. Lapis lazuli as unexpected blue pigment in Iranian Lâjvardina ceramics. J Raman Spectrosc 2003;34:420-3.

383. Trettenhahn GLJ, Nauer GE, Neckel A. Vibrational spectroscopy on the $PbO\text{-}PbSO_4$ system and some related compounds: Part 1. Fundamentals, infrared and Raman spectroscopy. Vib Spectrosc 1993;5:85-100.

384. Shapter JG, Brooker MH, Skinner WM. Observation of the oxidation of galena using Raman spectroscopy. Int J Miner Process 2000;60:199-211.

385. Batonneau Y, Brénard C, Laureyns J, Merlin JC. Microscopic and imaging Raman scattering study of PbS and its photo-oxidation products. J Raman Spectrosc 2000;31:1113-9.

386. Bischof T, Ivanda M, Lermann G, Materny A, Kiefer W, Kalus J. Linear and nonlinear Raman studies on CdS_xSe_{1-x} doped glasses. J Raman Spectrosc 1996;27:297-302.

387. Verma P, Gupta L, Abbi SC, Jain KP. Confinement effects on the electronic and vibronic properties of CdS0.65Se0.35 nanoparticles grown by thermal annealing. J Appl Phys 2000;88:4109-16.

388. Huber P, Karl H, Stritzker B. Combinatorial ion beam synthesis of CdSxSe1-x nanocrystals. Appl Surf Sci 2006;252:2497-2502.

389. Andrikopoulos KS, Daniilia S, Roussel B, Janssens K. In vitro validation of a mobile Raman-XRF micro-analytical instrument's capabilities on the diagnosis of Byzantine icons. J Raman Spectrosc 2006;37:1026-34.

390. Leite RCC, Porto SPS. Enhancement of Raman cross section in CdS due to resonant absorption. Phys Rev Lett 1996;17:10-2.

391. Lozada-Morales R, Zelaya-Angel O, Jiménez-Sandoval S, Torres-Delgado G. Extra Raman modes in CdS during cubic to hexagonal structural transformation. J Raman Spectrosc 2002;33:460-5.

392. Bouchard M, Smith DC. Catalogue of 45 reference Raman spectra of minerals concerning research in art or archaeology, especially on corroded metals and coloured glass. Spectrochim Acta A 2003;59:2247-66.

393. Covelitte. mindat.org. [Online]. 1993-2010 [cited 2010 Oct 01]. Available from: URL:http://www.mindat.org/min-1144.html

394. Jin P, Yao Z, Zhang M, Li Y, Xing H. A pigment (CuS) identified by micro-Raman spectroscopy on a Chinese funerary lacquer ware of West Han Dynasty. J Raman Spectrosc 2010;41:222-5.

395. Grim DM, Allison J. Laser desorption mass spectrometry as a tool for the analysis of colorants: the identification of pigments used in illuminated manuscripts. Archaeometry 2004;46:283-99.

396. Muniz-Miranda M, Sbrana G, Bonazzi P, Menchetti S, Pratesi G. Spectroscopic investigation and normal mode analysis of As_4S_4 polymorphs. Spectrochim Acta A 1996;52:1391-1401.

397. Bonazzi P, Menchetti S, Pratesi G, Muniz-Miranda M, Sbrana G. Light-induced variations in realgar and β- As_4S_4:X-ray diffraction and Raman studies. Am Mineral 1996;81:874-80.

398. Burgio L. Analysis of pigments on art objects by Raman microscopy and other techniques, PhD Thesis. University of London; 2000.

399. Trentelman K, Stodulski L, Pavlosky M. Characterization of pararealgar and other light-induced transformation products from realgar by Raman microspectroscopy. Anal Chem 1996;68:1755-61.

400. Chaplin TD, Clark RJH, Jacobs D, Jensen K, Smith GD. The Gutenberg Bibles: Analysis of the Illuminations and inks using Raman Spectroscopy. Anal Chem 2005;77:3611-22.

401. Douglass DL, Shing C, Wang G. The light-induced alteration of realgar to pararealgar. Am Mineral 1992;77:1266-74.

402. Daniels V, Leach B. The occurence and alteration of realgar on ancient Egyptian papyri. Stud Conserv. 2004;49:73-84.

403. Wang Y, Alsmeyer DC, McCreery RL. Raman Spectroscopy of carbon materials: structural basis of observed spectra. Chem Mater 1990;2:557-63.

404. Dhamelincourt P, Nakashima S. Applications to Materials Science. In: Turrel G, Corset J, editors. Raman Microscopy: Developments and Applications. London: Elsevier, 1996. p. 243-287.

405. Beyssac O, Goffé B, Petitet J, Froigneux E, Moreau M, Rouzaud J. On the characterization of disordered and heterogeneous carnonaceous materials by Raman spectroscopy. Spectrochim Acta A. 2003;59:2267-76.

406. Tyczkowski J, Kapica R, Łojewska J. Thin cobalt oxide films for catalysis deposited by plasma-enhamced metal-organic chemical vapor deposition. Thin Solid Films 2007;515:6590-5.

407. Pagès-Camagna S, Duval A, Guicharnuad H. Study of Gustave Moreau's black drawings: identification of the graphic materials by Raman microspectrometry and PIXE. J Raman Spectrosc 2004;35:628-632.

408. Mateo MP, Ctvrtnickova T, Nicolas G. Characterization of pigments used in painting by means of laser-induced plasma and attenuated total reflectance FTIR spectroscopy. Appl Surf Sci 2009;255:5172-6.

409. Whitney AV, Van Duyne RP, Casadio F. An innovative surface-enhamcement Raman spectroscopy (SERS) method for the identification of six historical red lakes and dyestuffs. J Raman Spectrosc 2006;37:993-1002.

410. Cañamares MV, Garcia-Ramos JV, Domingo C, Sanchez-Cortes S. Surface-enhanced Raman scattering study of the anthraquinone red pigment carminic acid. Vib Spectrosc 2006;40:161-7.

411. Jayaraman A. Diamond anvill cell and high-pressure physical investigations. Rev Mod Phys 1983;55:65-108.

412. Dao NQ, Delaigue L. Raman micro-spectrometry and its applications to the identification of inclusions in natural rubies. Analusis 2000;28:34-8.

413. Forman RA, Piermarini GJ, Barnett JD, Block S. Pressure measurement made by the utilization of ruby sharp-line luminescence. Science. 1972;176:284-5.

414. McMillan PF, Dubessy J, Hemley R. Applications in earth, planetary and environmental sciences. In: Turrel G, Corset J, editors. Raman Microscopy: Developments and Applications. London: Elsevier, 1996. p. 289-365.

415. Smith DC, Bouchard M, Lorblanchet M. An initial Raman microscopic investigation of Prehistoric rock art in caves of the Quercy district, S.W. France. J Raman Spectrosc 1999;30:347-54.

416. Julien C, Massot M, Rangan S, Lemal M, Guyomard D. Study of structural defects in γ-MnO_2 by Raman spectroscopy. J Raman Spectrosc 2002;33:223-8.

417. Macdonald AM, Rogerson CE, Vaughan AS, Wyeth P. Raman microspectroscopy interrogating 19th- and 20th-century painted trades union banners. In: Janaway R, Wyeth P, editors. Postprints first annual conference of the AHRC research Centre for textile conservation and textile studies, scientific analysis of ancient and historic textiles: informing preservation, display and interpretation. London: Archetype Publications; 2005. p. 222-229.

418. Derbyshire A, Withnall R. Pigment Analysis of Portrait Miniatures using Raman microscopy. J Raman Spectrosc 1999;30:185-8.

419. Smith GD, Clark RJH. Raman microscopy in archaeological science. J Archaeol Sci 2004;31:1137-60.

420. Lee GY, Ruy KH, Kim HG, Kim YY. The Preparation of Blue $CoAl_2O_4$ powders by the Malonate Method: The effect of the amount of Malonic acid used, the formation pathway of $CoAl_2O_4$ crystallites and the characteristics of the prepared powders. Bull Korean Chem Soc 2009;30:373-7.

421. Walter D. Characterization of synthetic hydrous hematite pigments. Thermochim Acta 2006;445:195-9.

422. Blanch AJ, Quinton JS, Lenehan CE, Pring A. Autocorrelation infrared analysis of mineralogical samples: The influence of user controllable experimental parameters. Anal Chim Acta. 2007;590:145-50.

423. Zieba-Palus J, Borusiewicz R. Examination of multilayer paint coats by the use of infrared, Raman and XRF spectroscopy for forensic purposes. J Mol Struct. 2006;792-793:286-92.

424. Stokes DJ. Principles and practice of Varaiable pressure/ Environmental Scanning Electron Microscopy (VP-ESEM). Chichester: John Wiley & Sons; 2008.

425. Danilatos GD. Environmetal Scanning Electron Microscopy and Microanalysis. Mikrochim Acta 1994;114-115:143-55.

426. Mansfield JF. X-ray microanalysis in the environmental SEM: a challenge or a contradiction? Mikrochim Acta 2000;132:137-43.

427. Atkins PW. The elements of Physical Chemistry. 2nd ed. Oxford: Oxford University Press; 1996.

428. Fishbane PM, Gasiorowicz S, Thornton ST. Physics for scientists and engineers. 2nd ed. London: Prentice Hall, 1996.

429. Šímová V, Bezdička P, Hradilova J, Hradil D, Grygar T. X-ray powder microdiffraction for routine analysis of paintings. Powder Diffr. 2005;20:224-9.

430. Švarcová S, Kotulanová E, Hradil D, Bezdička P. Laboratory powder X-ray microdiffraction – the use for pigments and secondary slats identification in frescos. In: ART2008. 9th International Conference on NDT of art; 2008 May 25-30; Jerusalem, Israel.

431. de La Rie ER. Ultraviolet radiation fluorescence of paint and varnish layers. In: van Schoute R, Verougstraete-Marcq H, editors. Scientific Examination of Easel Paintings, PACT, Journal of the European Study Group on Physical, Chemical and Mathematical Techniques Applied to Archaeology. 1986, vol. 13, pp. 91-108.

432. Vahur S, Teearu A, Leito I. ATR-FT-IR spectroscopy in the region of 550-230 cm^{-1} for identification of inorganic pigments. Spectrochim Acta A 2010;75;1061-72.

433. Titanium Dioxide Whites. Pigments through the Ages [Online]. [cited 2010 Oct 01]. Available from: URL:http://www.webexhibits.org/pigments/indiv/history/tiwhite.html

434. The history of Pigments. Windsor and Newton [Online]. [cited 2010 Oct 01]. Available from: URL: http://www.winsornewton.com/main.aspx?PageID=307

435. Casas AP, Llopis J. A spot test for zinc white. Stud Conserv. 2002;47:273-6.

436. Nel P, Lau D, Hay D, Wright N. Non-destructive micro-X-ray diffraction analysis of painted artefacts: Determination of detection limits for the chromium oxide-zinc oxide matrix. Nucl Instrum Methods Phys Res B 2006;251:489-95.

437. Fitz S. Identification of pigments in paintings with X-ray powder diffraction method – possibilities and limits. In: Preprints of 5th ICOM Committee for Conservation Triennial Meeting; 1978 Oct 1-8; Zagreb. Paris: International Council of Museums; 1978. pp. 78/20/7-1-78/20/7-6.

438. Kirby J, Stonor K, Roy A, Burnstock A, Grout R, White R. Seraut's Painting Practice: theory, development and technology. Nat Gall Tech Bull. 2003;24:4-37.

439. Bonford D, Roy A. Hogarth's 'Mariage à la Mode' and contemporary painting practices. Nat Gall Tech Bull. 1982;6:59-67.

440. Turgoose S. The corrosion of lead and tin before and after excavation. In: Miles G, Pollard S, editors. Lead and tin: studies in conservation and technology. United Kingdom Institute for Conservation, occasional paper nº 3; 1985. p. 15-26.

441. Black L, Allen GC. Nature of lead patination. Brit. Corros. J. 1999., Vol. 34, p. 192-7.

442. Kühn H. Zinc white. In: Feller RL, editor. Artists' Pigments. A handbook of their History and characteristics. Cambridge: National Gallery: Washington and Cambridge University Press; 1986. vol. 1 p. 169-186.

443. Winter J. "Lead white" in Japonese paintings. Stud Conserv 1981;26:89-101.

444. Gettens RJ, Feller RL, Chase WT. Vermilion and cinnabar. In: Roy A, editor. Artists' Pigments. A handbook of their History and characteristics. Oxford: National Gallery: Washington and Oxford University Press; 1993. vol. 2 p. 159-182.

445. Penny N, Spring M. Veronese's paintings in the National Gallery. Technique and materials: part I. Nat Gall Tech Bull. 1995;16:5-29.

446. Plester J. Ultramarine blue, natural and artificial. In: Roy A, editor. Artists' Pigments. A handbook of their History and characteristics. Oxford: National Gallery: Washington and Oxford University Press; 1993. vol. 2 p. 37-65.

447. Zieske F. An investigation of Paul Cézanne's Watercolors with emphasis on Emerald green. The American Institute for Conservation. The Book and Paper Group; 1995. vol. 14. Available from: URL: http://cool.conservation-us.org/coolaic/sg/bpg/annual/v14/bp14-09.html

448. O'Donoghue E, Romero R, Dik J. French Eighteenth-century painting techniques. Painting techniques: History, materials and studio techniques. Contributions to the IIC Dublin Congress; 1998 Sep 7-11; Dublin. p. 185-9.

449. Noble P, Boon JJ, Wadun J. Dissolution, Aggregation and Protusion – Lead soaps formation in 17th century grounds and paint layers. Art Matters. Zwolle: Waanders Printers; 2002.

450. FitzHugh EW. Read lead and minium. In: Feller RL, editor. Artists' Pigments. A handbook of their History and characteristics. Cambridge: National Gallery: Washington and Cambridge University Press; 1986. vol. 1 p.109-139.

451. Boon JJ, van der Weerd J, Keune K. Mechanical and chemical changes in Old Master painting: dissolution, metal soaps formation and remineralization processes in lead pigmented ground/intermediate paint layers of 17th century paintings. In: Vontobel R, editor. ICOM Committee for Conservation preprints, 13th Triennial Meeting, Rio de Janeiro. London: James & James; 2002. p. 401-6.

452. Burgio L, Clark RJH, Gibbs PJ. Pigment identification studies in situ of Javanese, Thai, Korean, Chinese and Uighur manuscripts by Raman microscopy. J Raman Spectrosc 1999;30:181-4.

Appendix A

Results of the microchemical tests undertaken in 1984

	Earlier	Italian						Final
Pigments	**C**	**G**	**K**	**N**	**O**	**Q**	**U**	**W**
Ground								
Bone/ivory black						•		
Lead white	•	•	•	•	•	•	•	•
Mercury^{II} sulfide						•		
Zinc white			•	•				
White								
Lead white	•	•	•	•	•	•	•	•
Zinc white	•	•		•				
Yellow								
Cadmium yellow	•	•	•					•
Chrome yellow	•			•				
Iron^{III} oxyhydroxide	•	•	•			•		
Red								
Iron^{III} oxide		•	•	•			•	
Madder lake								•
Mercury^{II} sulfide	•	•	•	•	•	•		•
Brown								
Ochre	•	•	•				•	
Umber		•						
Green								
Chrome green	•	•		•			•	•
Cobalt green				•			•	
Copper resinate	•							
Emerald green	•		•					
Viridian								•
Blue								
Cobalt blue	•	•	•	•			•	
Prussian blue	•		•	•			•	
Black								
Bone/ivory black		•	•			•		
Vegetable carbon-based black	•						•	•

C - Paisagem - Abertura da Rua Alexandre Herculano (MNSR Invº183), **G** - Cansada (Cachopa de Capri) (MNSR Invº 94), **K** - Esperando o sucesso (MNSR Invº 108), **N** - Portão (MNSR 117/71), **O** - Rapariga de Anacapri (MNSR 200), **Q** - Senhora vestida de preto (MNSR 114/39), **U** - Rapariga deitada num tronco de árvore (MNSR 86/88), **W** - Flores campestres (MNSR 117/96).

There are present only the results for the paintings currently under study.

Appendix B

Pousão paintings under analysis and sampling

Figure B1. ***Casa rústica de Campanhã*** **(*A*)**, 1880 (MNSR Invº 109). Oil on wood, 20.2 x 12.8 cm. Samples: **A1** - blue from the sky, **A2** - red from the balcony rail, **A3** - orange from the roof, **A4** - brown from the ground and **A5** - beige from the wall. Photo: LCRJF.

Figure B2. ***O mendigo Lapita* (*B*)**, 1880 (MNSR Invº 101). Oil on wood, 23.5 x 14.2 cm. Samples: **B1** - white from the wall, **B2** - brown-reddish from the ground, **B3** - light brown from the window frame and **B4** - black from the window. Photo: LCRJF.

Figure B3. ***Paisagem – Abertura da Rua Alexandre Herculano*** **(*C*)**, 1880 (MNSR Invº 183). Oil on canvas, 68.8 x 122.4 cm. Samples: **C1** - blue from the sky, **C2** - green from the trees, **C3** - light blue from the sky and **C4** - brown from the ground. Photo: LCRJF.

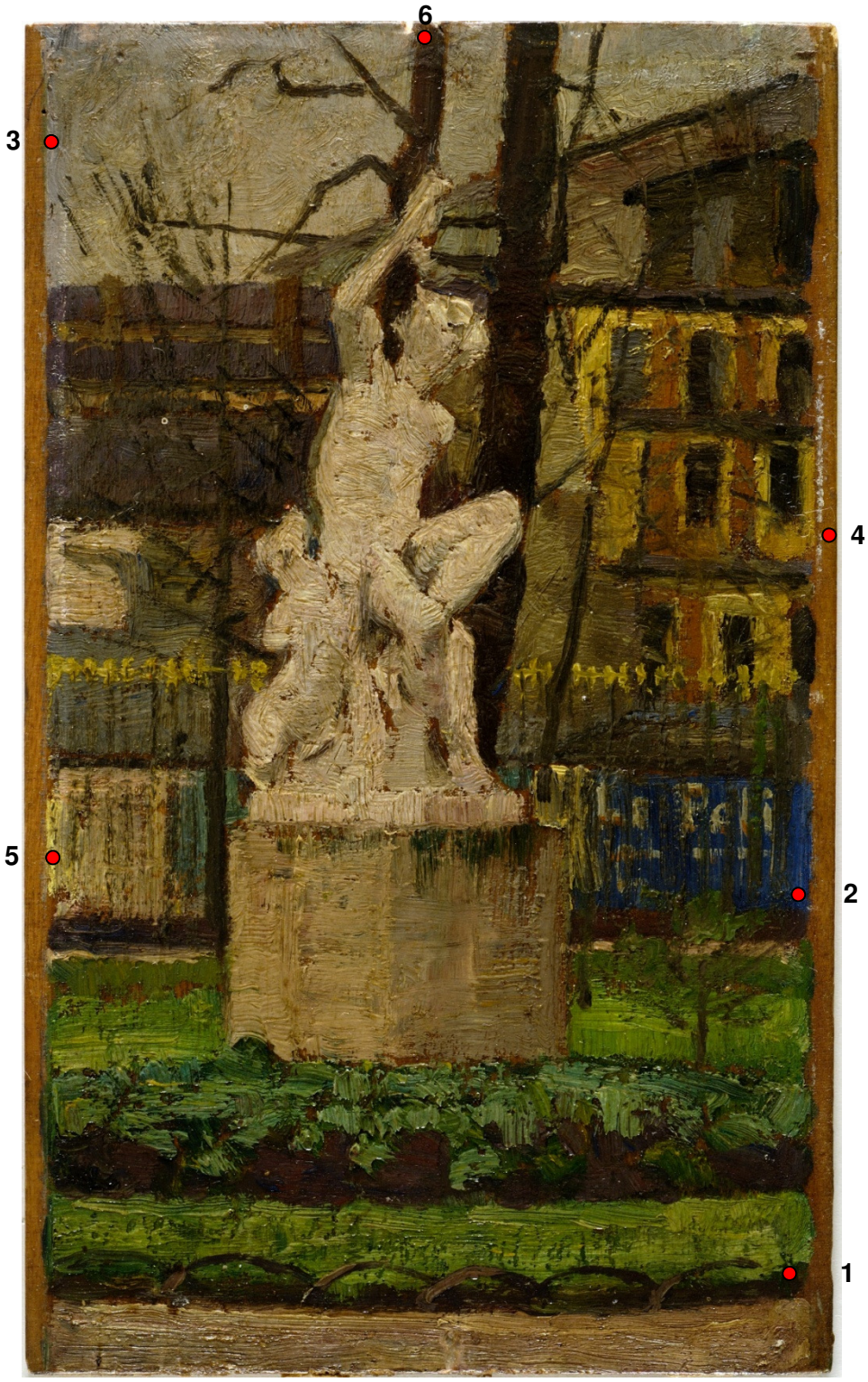

Figure B4. ***Jardim de Luxemburgo (estudo)*** **(*D*)**, 1880 (MNSR Invº 96/11). Oil on wood, 16.5 x 9.0 cm. Samples: **D1** - dark green from the grass, **D2** - blue from the wall, **D3** - blue from the sky, **D4** - yellow from the window, **D5** - beige from the wall and **D6** - brown from the tree bench. Photo: LCRJF.

Figure B5. ***Aldeia de St. Sauves*** **(*E*)**, 1881 (MNSR Invº 167). Oil on wood, 46.0 x 37.8 cm. Samples: **E1** - blue from the sky, **E2** - white from the cloud, **E3** - grey from the cloud, **E4** - green from the roof, **E5** - dark grey from the shadow, **E6** - brown from the ground and **E7** -dark green from the three foliage. Photo: LCRJF.

Figure B6. ***Paisagem de St. Sauves*** **(*F*)**, 1881 (MNSR Invº 158). Oil on canvas, 46.0 x 65.5 cm. Samples: **F1** - blue from the sky, **F2** - orange from the sky, **F3** - light green from the ground, **F4** - green from the ground, **F5** - dark blue from the sky and **F6** - dark green of the ground. Photo: LCRJF.

Figure B7. ***Cansada (Cachopa de Capri)*** **(*G*)**, 1882 (MNSR Invº 94). Oil on canvas, 130.5 x 81.5 cm. Samples: **G1** - white from the wall, **G2** - brown from the ground, **G3** - grey from the leaf and **G4** - green from the leaf. Photo: LCRJF.

Figure B8. ***Casas brancas de Capri*** **(*H*)**, 1882 (MNSR Invº 82). Oil on canvas, 70.5 x 141.0 cm. Samples: **H1** - brown from the ground, **H2 -** green from the bushes, **H3** - grey from the house wall, **H4** - blue from the sky, **H5** - blue from the sea, **H6** - white from the wall, **H7** - light green from the cactus, **H8** - dark green from the cactus and **H9** - ground layer. Photo: LCRJF.

Figure B9. ***Cecília* (*I*)**, 1882 (MNSR Invº 106). Oil on canvas, 82.3 x 57.2 cm. Samples: **I1** - black from the pedestal, **I2** - white from the kerchief, **I3** - blue from the chair, **I4** - green from the stripe, **I5** - dark blue from the skirt, **I6** - carnation from the finger, **I7** - grey from the pedestal and **I8** - yellow from the shroud. Photo: LCRJF.

Figure B10. ***Escadas de um pardieiro - Roma*** **(J)**, 1882 (MNSR Invº 83). Oil on wood, 16.0 x 22.2 cm. Samples: **J1** - grey from the wall, **J2** - beige from the ground, **J3** - dark brown from the door entrance and **J4** - brownish from the stone wall. Photo: LCRJF.

Figure B11. ***Esperando o Sucesso*** **(K)**, 1882 (MNSR Invº 108). Oil on canvas, 131.5 x 83.5 cm. Samples: **K1** - beige from the ground, **K2** - brown from the wood box, **K3** - yellow from the brush, **K4** - dark grey from the ground, **K5** - grey from canvas, **K6** - grey from the canvas, **K7** - green from the ground, **K8** - grey from the palette, **K9** - brown from the wood box, **K10** - beige from the ground, **K11** - dark green from the blanket, **K12** - white from the handkerchief, **K13** - grey from the canvas and **K14** - dark grey from the ground. Photo: LCRJF.

Figure B12. ***Fachada de casa soterrada - Roma*** **(*L*)**, 1882 (MNSR Invº 107/36). Oil on wood, 9.9 x 16.5 cm. Samples: **L1** - pink from the ground, **L2** - white from the wall, **L3** - green from the wall, **L4** - orange from the wall and **L5** - brown from the wall. Photo: LCRJF.

Figure B13. ***Miragem de Nápoles* (*M*)**, 1882 (MNSR Invº 91/49). Oil on wood, 9.8 x 16.5 cm. Samples: **M1** - brown from the ground, **M2** - blue from the water, **M3** - white, **M4** - beige from the wall and **M5** - orange from the wall. Photo: LCRJF.

Figure B14. ***Portão*** **(*N*)**, 1882 (MNSR Invº 117/71). Oil on canvas, 29.2 x 21.2 cm. Samples: **N1** - beige from the ground, **N2** - green from the trees, **N3** - blue from the sky, **N4** - beige from the wall and **N5** - green from the ground. Photo: LCRJF.

Figure B15. ***Rapariga de Anacapri*** **(*O*)**, 1882 (MNSR Invº 200). Oil on canvas, 18.5 x 13.8 cm. Samples: **O1** - blue from the background and **O2** - pink from the neckerchief and **O3** - red from the neckerchief. Photo: LCRJF.

Figure B16. ***Rua de Roma*** **(*P*)**, 1882 (MNSR Invº 96/24). Oil on wood, 16.5 x 9.9 cm. Samples: **P1** - blue from the sky, **P2** - brown from the roof, **P3** - grey from the ground, **P4** - white from the ground, **P5** - beige from the wall and **P6** - grey from the wall. Photo: LCRJF.

Figure B17. ***Senhora vestida de preto*** **(*Q*)**, 1882 (MNSR Invº 114/39). Oil on wood, 28.3 x 18.4 cm. Samples: **Q1** - black from the dress, **Q2** - yellow from the chair, **Q3** - yellow from the back, **Q4** - black from the dress, **Q5** - brown from the chair, **Q6** - grey from the back, **Q7** - red from the background and **Q8** - yellow from the back. Photo: LCRJF.

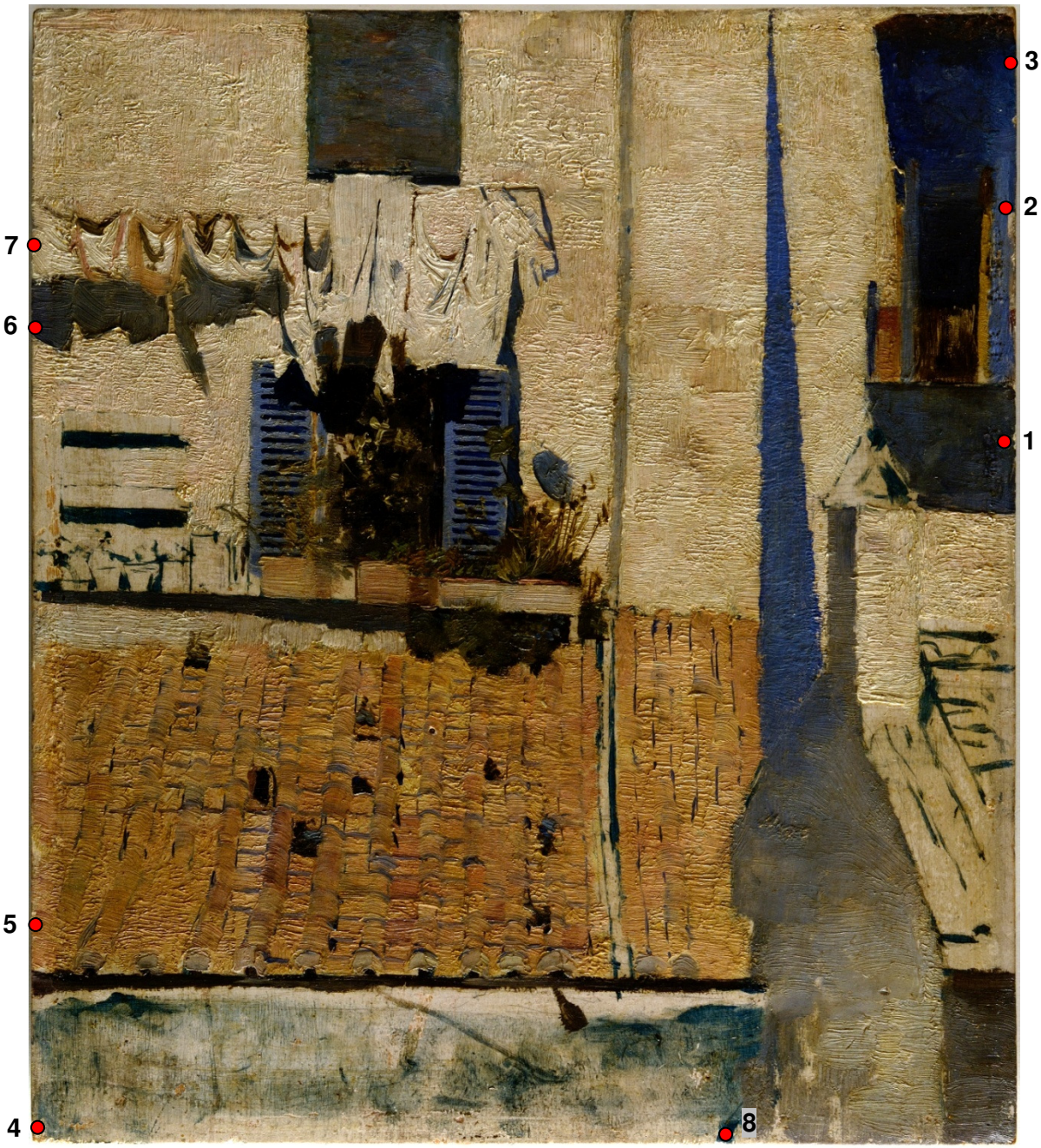

Figure B18. ***Janela das persianas azuis*** **(*R*)**, 1882-1883 (MNSR Invº 114/34). Oil on wood, 28.5 x 25.0 cm. Samples: **R1** - blue from the wall, **R2** - light blue from the wall, **R3** - dark blue from the wall, **R4** - greenish from the wall, **R5** - orange from the roof, **R6** - grey from the shadow of the clothes, **R7** - white from the clothes and **R8** - blue from the wall. Photo: LCRJF.

Figure B19. ***Mulher da água*** **(*S*)**, 1883 (MNSR Invº 115). Oil on canvas, 144.0 x 135.5 cm. Samples: **S1** - blue from the sky, **S2** - green from the bushes, **S3** - beige from the wall, **S4** - white from the kerchief, **S5** - blue from the blouse, **S6** - carnation from the hand and **S7** - blue from the skirt. Photo: LCRJF.

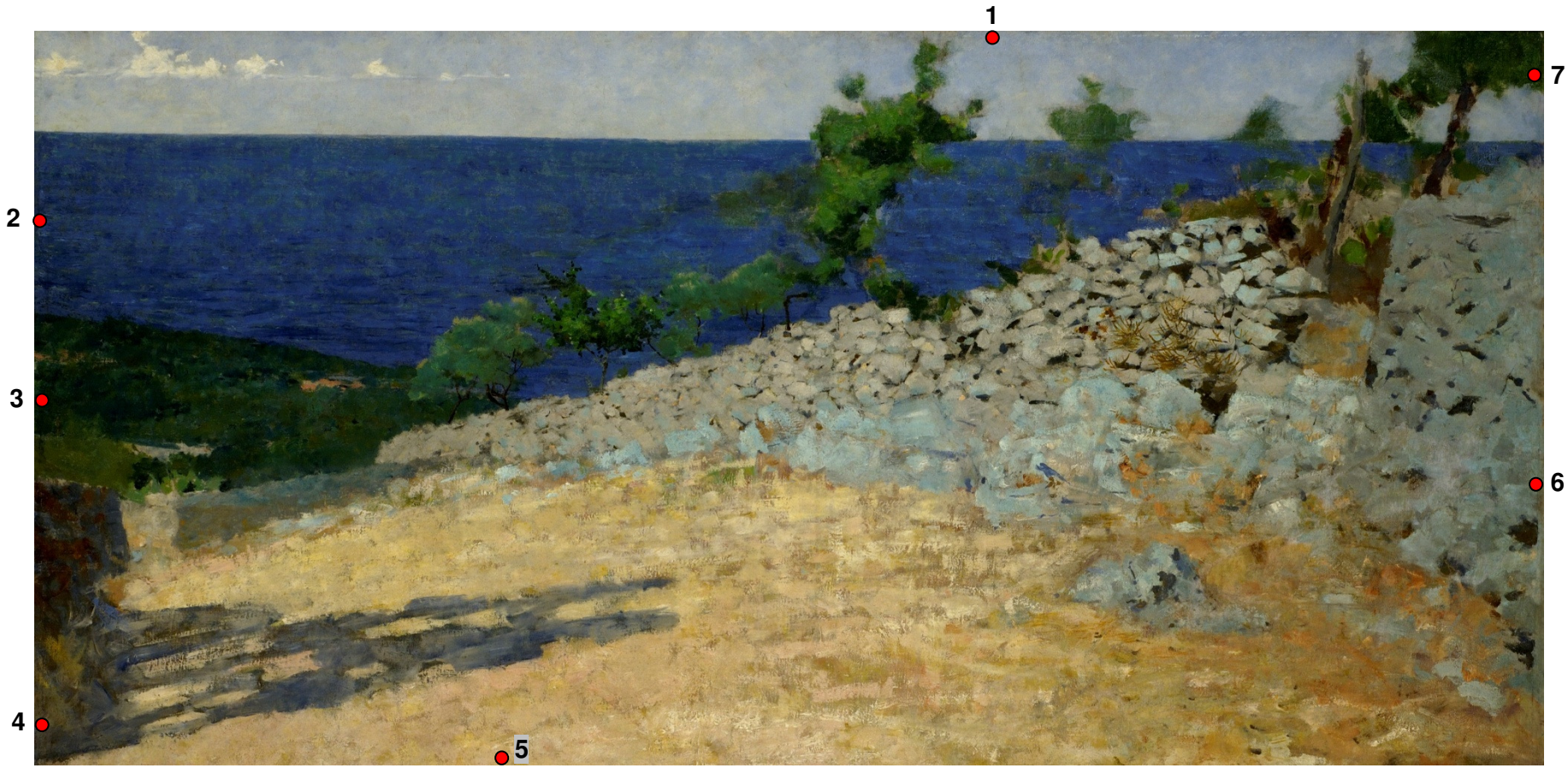

Figure B20. ***Paisagem de Anacapri* (*T*)**, 1883 (MNSR Invº 432). Oil on canvas, 70.5 x 140.5 cm. Samples: **T1** - blue from the sky, **T2** - blue from the sea, **T3** - green from the trees, **T4 -** grey from the shadow on the ground, **T5** - beige from the ground, **T6** - grey from the stone wall and **T7** - green from the tree. Photo: LCRJF.

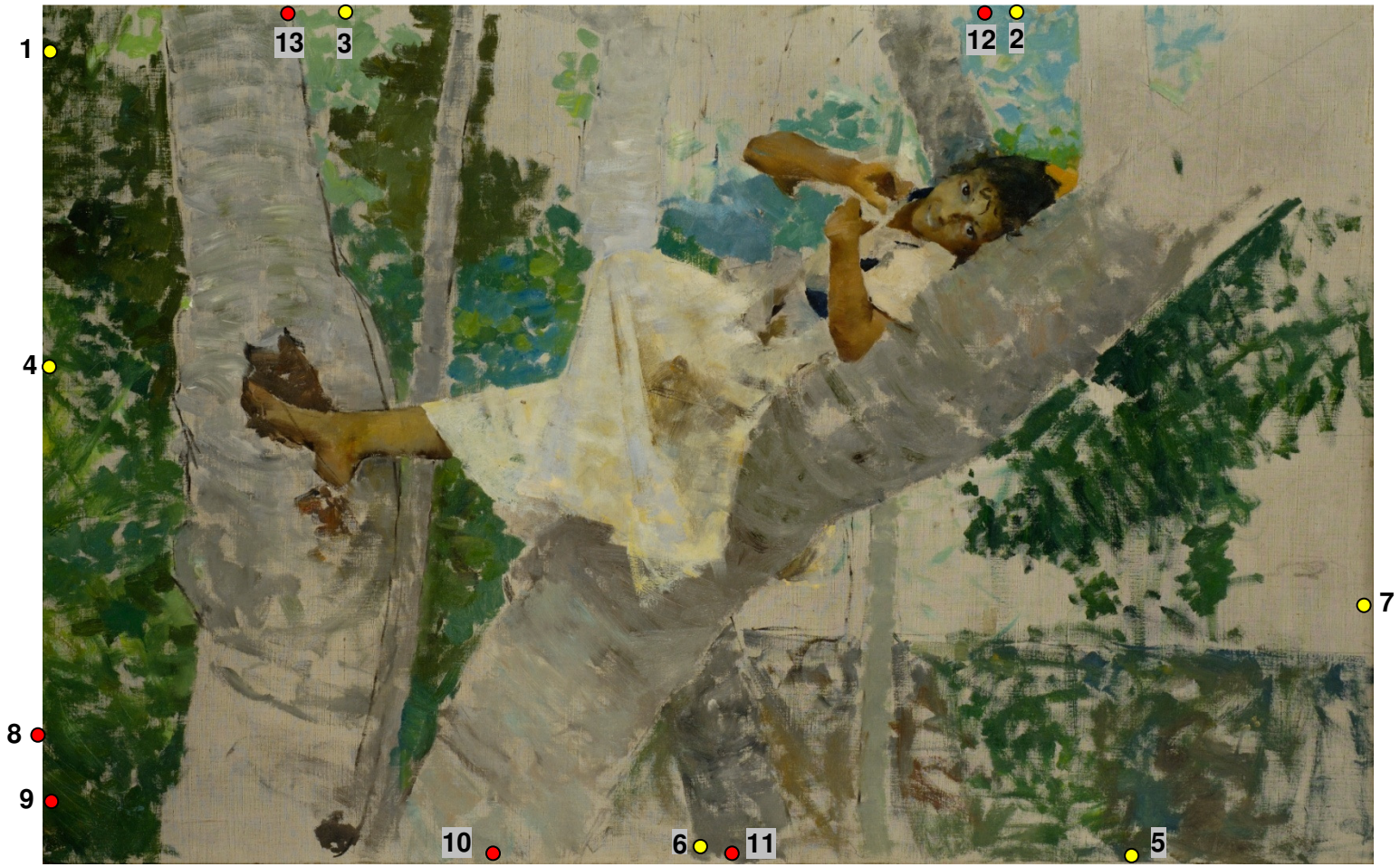

Figure B21. ***Rapariga deitada no tronco de uma árvore*** **(*U*)**, 1883 (MNSR Invº 86/88). Oil on canvas, 73.5 x 115.5 cm. Samples: **U1** - dark green from leafs, **U2** - light blue, **U3** - light green from leafs, **U4** - green from leafs, **U5** - grey, **U6** - background grey, **U7** - light grey from the back, **U8** - ground layer, **U9 -** green from leafs, **U10** - bluish from the tree bench, **U11** - grey from the tree bench, **U12 -** light blue and **U13 -** light green from leafs. Photo: LCRJF.

Figure B22. ***Cais de Barcelona* (*V*)**, 1883 (MNSR Invº 127/94). Oil on wood, 16.5 x 10.0 cm. Samples: **V1** - blue from the sea, **V2** - blue from the sky, **V3** - black from the boat, **V4** - beige from the ground and **V5** - brown from the crane. Photo: LCRJF.

Figure B23. ***Flores Campestres*** **(*W*)**, 1884 (MNSR Invº 117/96). Oil on canvas, 30.0 x 22.5 cm. Samples: **W1** - grey from the back, **W2** - green from the flowers, **W3** - red from the flower, **W4** - grey from the back, **W5** - green from the flowers, **W6** - red from the flower, and **W7** - light grey from the back. Photo: LCRJF.

Appendix C

Example of a sheet used for description of the sampling points

INSTITUTO PORTUGUÊS DE CONSERVAÇÃO E RESTAURO

Impresso

Colheita de amostras

P.Nº. ...13-06/E..... Data de entrada .....

Amostras	
Nº.	Descrição
1	tela
2	preto, fundo
3	branco, lenço
4	azul, cadeira
5	verde, risca manta
6	azul, saia
7	carnação, dedo
8	cinzento, penteado?
9	amarelo, risca manta
	11/07/2006

IMP.DEM.04

Appendix D

Samples viewed under reflected light

- Casa Rústica de Campanhã

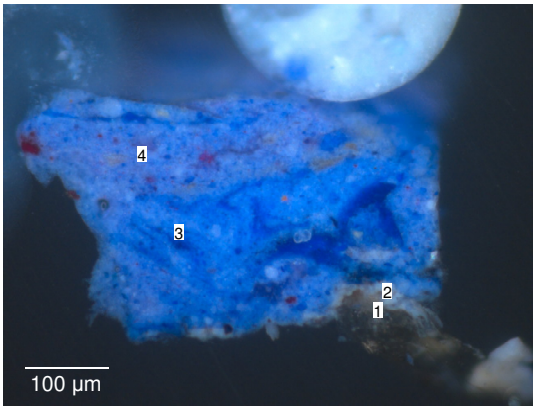

4 - blue paint layer (max. thickness 130 µm)
3 - blue paint layer (max. thickness 222 µm)
2 - white ground layer (max. thickness 14 µm)
1 - support

Figure D1. Cross section of sample **A1 -** blue from the sky of **Casa rústica de Campanhã**, viewed under reflected light.

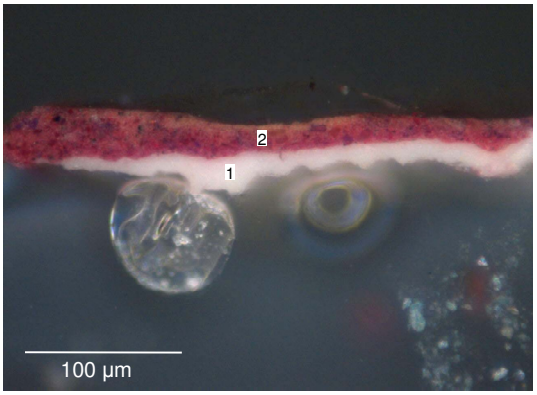

2 - red paint layer (max. thickness 38 µm)
1 - white ground layer (max. thickness 30 µm)

Figure D2. Cross section of sample **A2** - red from the balcony rail of **Casa rústica de Campanhã**, viewed under reflected light.

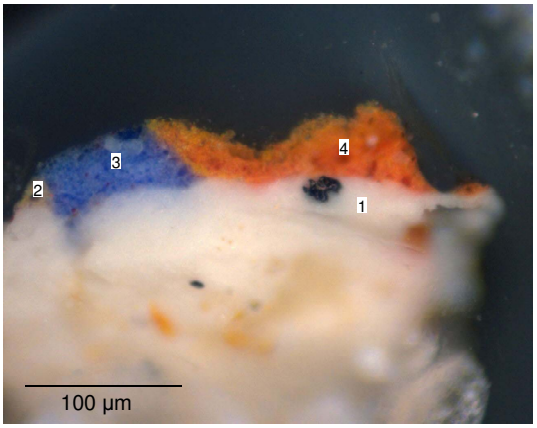

4 - orange paint layer (max. thickness 50 µm)
3 - blue paint layer (max. thickness 44 µm)
2 - brown paint layer (max. thickness 19 µm)
1 - white ground layer (max. thickness 88 µm)

Figure D3. Cross section of sample **A3** - orange from the roof of **Casa rústica de Campanhã**, viewed under reflected light.

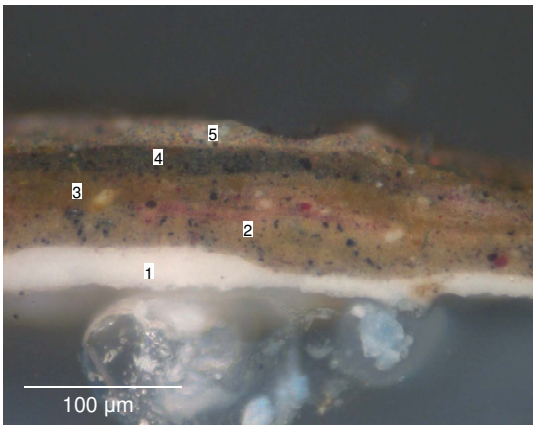

5 - brown paint layer (max. thickness 23 µm)
4 - black paint layer (max. thickness 20 µm)
3 - brown paint layer (max. thickness 33 µm)
2 - brown paint layer (max. thickness 42 µm)
1 - white ground layer (max. thickness 33 µm)

Figure D4. Cross section of sample **A4** - brown from the ground of **Casa rústica de Campanhã**, viewed under reflected light.

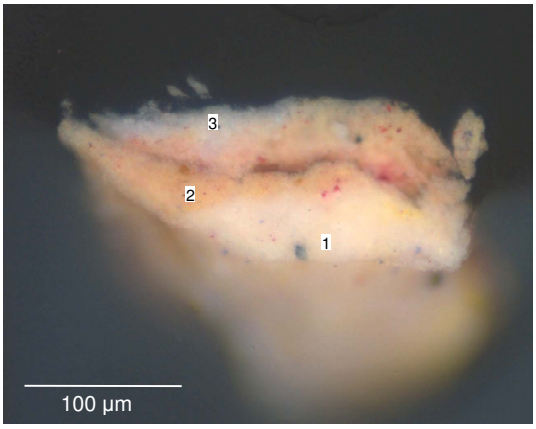

3 - beige paint layer (max. thickness 48 µm)
2 - orange paint layer (max. thickness 48 µm)
1 - beige paint layer (max. thickness 64 µm)

Figure D5. Cross section of sample **A5** - beige from the wall of **Casa rústica de Campanhã**, viewed under reflected light.

- O Mendigo Lapita

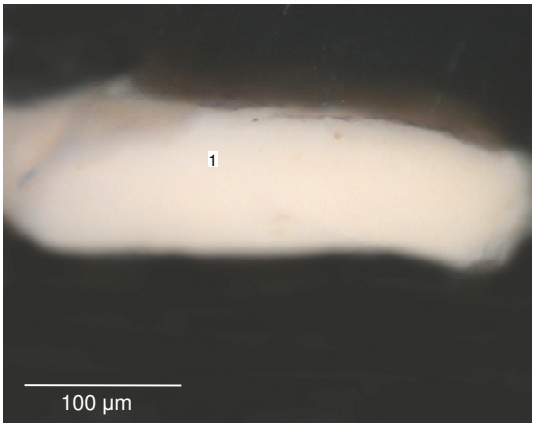

1 - white paint layer (max. thickness 120 µm)

Figure D6. Cross section of sample **B1** - white from the wall of **O mendigo Lapita**, viewed under reflected light.

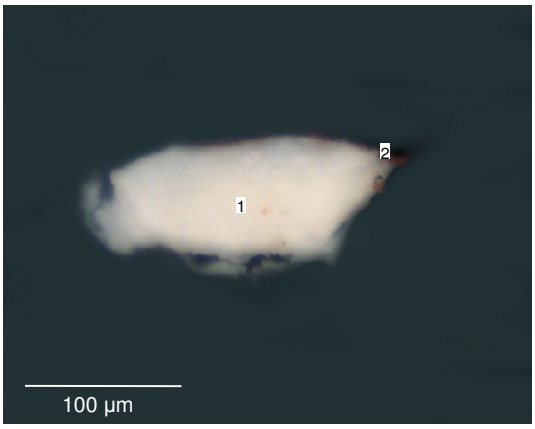

2 - reddish paint layer (max. thickness 6 µm)
1 - white ground layer (max. thickness 95 µm)

Figure D7. Cross section of sample **B2** - brown-reddish from the ground of **O mendigo Lapita**, viewed under reflected light.

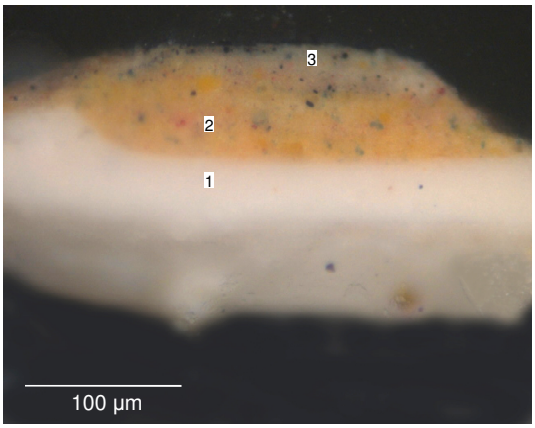

3 - grey paint layer (max. thickness 36 µm)
2 - yellow paint layer (max. thickness 65 µm)
1 - white ground layer (max. thickness 79 µm)

Figure D8. Cross section of sample **B3** - light brown from the window frame **O mendigo Lapita**, viewed under reflected light.

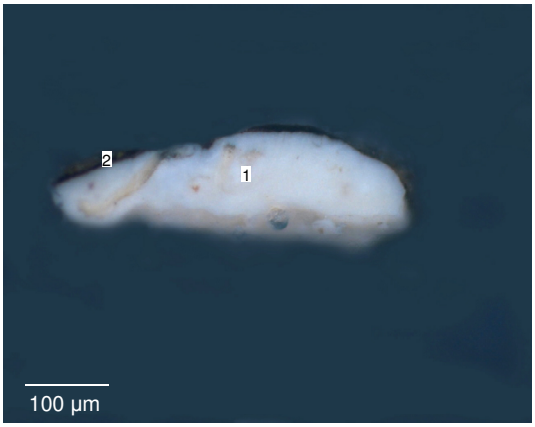

2 - black paint layer (max. thickness 11 µm)
1 - white ground layer (max. thickness 115 µm)

Figure D9. Cross section of sample **B4** - black from the window of **O mendigo Lapita**, viewed under reflected light.

- Paisagem – Abertura da Rua Alexandre Herculano

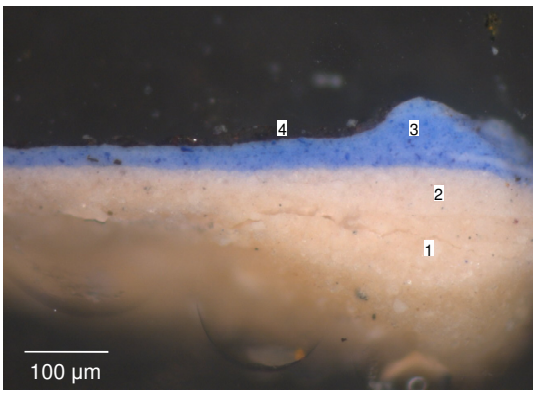

4 - varnish layer
3 - blue paint layer (max. thickness 107 µm)
2 - white ground layer (max. thickness 50 µm)
1 - white ground layer (max. thickness 100 µm)

Figure D10. Cross section of sample **C1** - blue from the sky of **Paisagem – Abertura da Rua Alexandre Herculano**, viewed under reflected light.

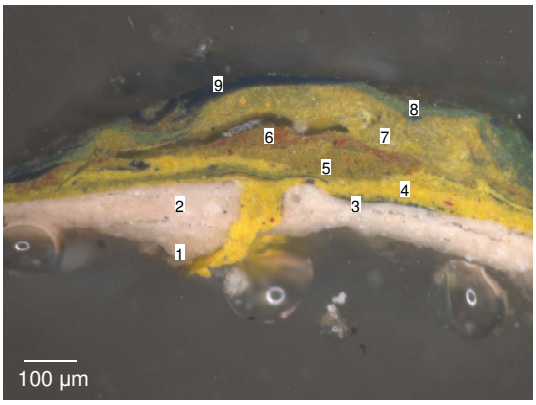

9 - green paint layer (max. thickness 20 µm)
8 - green paint layer (max. thickness 20 µm)
7 - greenish paint layer (max. thickness 126 µm)
6 - reddish paint layer (max. thickness 40 µm)
5 - brownish paint layer (max. thickness 50 µm)
4 - yellow paint layer (max. thickness 75 µm)
3 - green paint layer (max. thickness 26 µm)
2 - white ground layer (max. thickness 124 µm)
1 - white ground layer (max. thickness 62 µm)

Figure D11. Cross section of sample **C2**- green from the trees of **Paisagem – Abertura da Rua Alexandre Herculano**, viewed under reflected light.

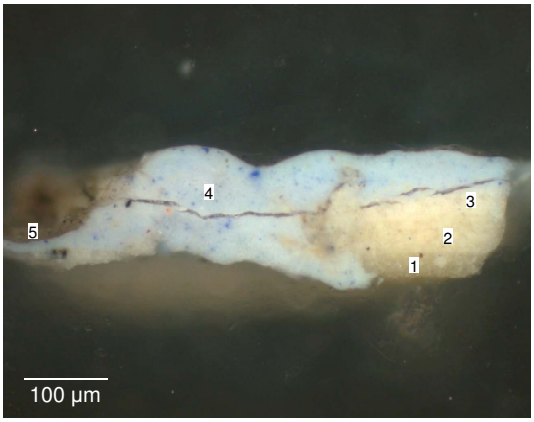

5 - varnish layer
4 - blue paint layer (max. thickness 173 µm)
3 - white ground layer (max. thickness 42 µm)
2 - white ground layer (max. thickness 51 µm)
1 - white ground layer (max. thickness 34 µm)

Figure D12. Cross section of sample **C3** - light blue from the sky of **Paisagem – Abertura da Rua Alexandre Herculano**, viewed under reflected light.

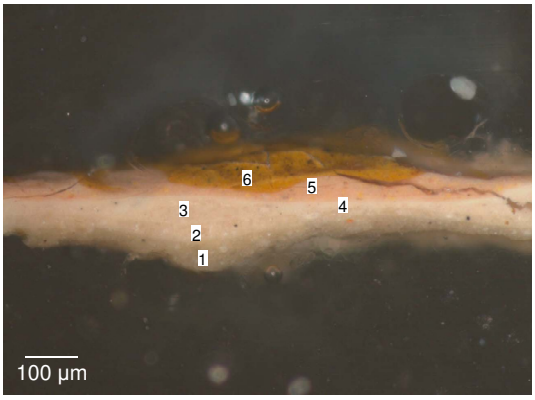

6 - yellow paint layer (max. thickness 30 µm)
5 - pinkish paint layer (max. thickness 64 µm)
4 - white paint layer (max. thickness 20 µm)
3 - white ground layer (max. thickness 57 µm)
2 - white ground layer (max. thickness 45 µm)
1 - white ground layer (max. thickness 75 µm)

Figure D13. Cross section of sample **C4** - brown from the ground of **Paisagem – Abertura da Rua Alexandre Herculano**, viewed under reflected light.

- Estátua do Jardim de Luxemburgo (estudo)

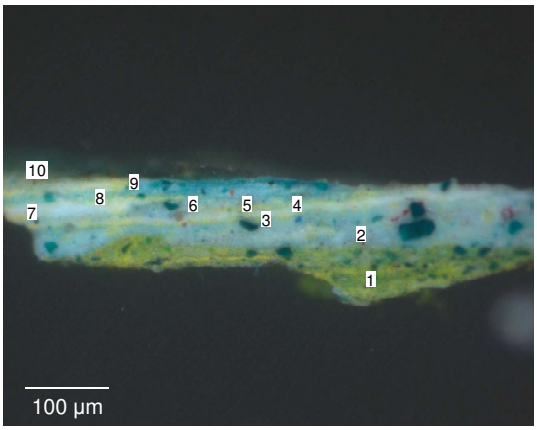

10 - yellow paint layer (max. thickness 17 µm)
9 - blue paint layer (max. thickness 25 µm)
8 - yellow paint layer (max. thickness 9 µm)
7 - white paint layer (max. thickness 16 µm)
6 - blue paint layer (max. thickness 19 µm)
5 - yellow paint layer (max. thickness 10 µm)
4 - white paint layer (max. thickness 12 µm)
3 - yellow paint layer (max. thickness 6 µm)
2 - blue paint layer (max. thickness 70 µm)
1 - green paint layer (max. thickness 87 µm)

Figure D14. Cross section of sample **D1** - dark green from the grass of **Estátua do Jardim de Luxemburgo (estudo)**, viewed under reflected light.

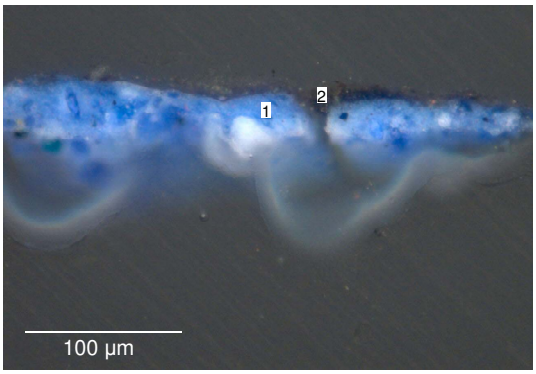

2 - black paint layer (max. thickness 12 µm)
1 - blue paint layer (max. thickness 45 µm)

Figure D15. Cross section of sample **D2** - blue from the wall of **Estátua do Jardim de Luxemburgo (estudo)**, viewed under reflected light.

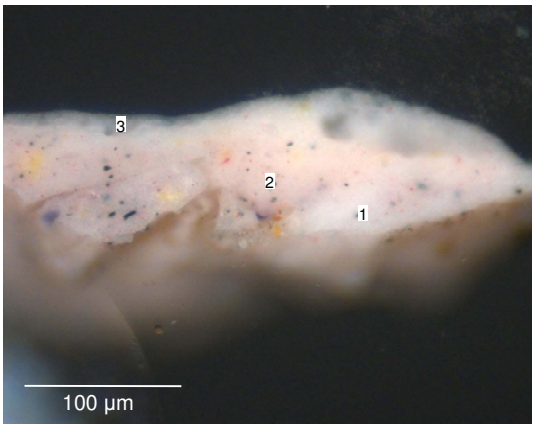

3 - white paint layer (max. thickness 105 µm)
2 - pink paint layer (max. thickness 72 µm)
1 - white paint layer (max. thickness 15 µm)

Figure D16. Cross section of sample **D3** - blue from the sky of **Estátua do Jardim de Luxemburgo (estudo)**, viewed under reflected light.

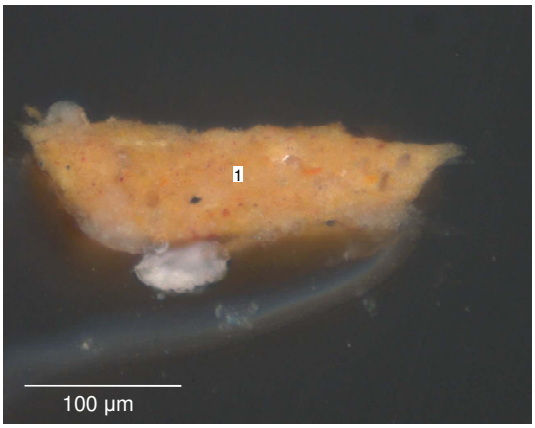

1 - orange paint layer (max. thickness 85 µm)

Figure D17. Cross section of sample **D4** - yellow from the window of **Estátua do Jardim de Luxemburgo (estudo)**, viewed under reflected light.

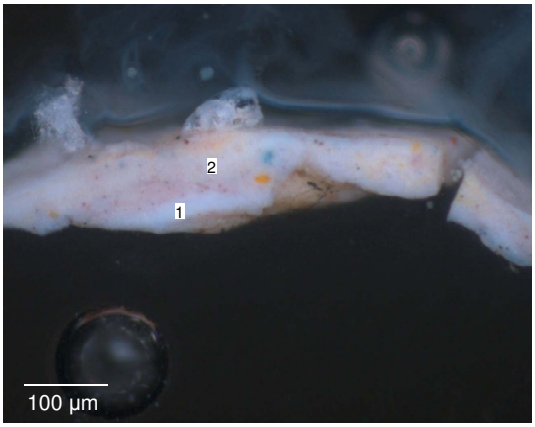

2 - beige paint layer (max. thickness 90 µm)
1 - white paint layer (max. thickness 26 µm)

Figure D18. Cross section of sample **D5** - beige from the wall of **Estátua do Jardim de Luxemburgo (estudo)**, viewed under reflected light.

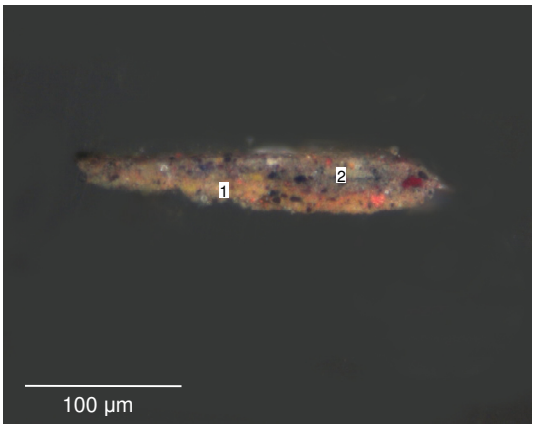

2 - grey paint layer (max. thickness 28 µm)
1 - brown paint layer (max. thickness 26 µm)

Figure D19. Cross section of sample **D6** - brown from the tree bench of **Estátua do Jardim de Luxemburgo (estudo)**, viewed under reflected light.

- Aldeia de St. Sauves

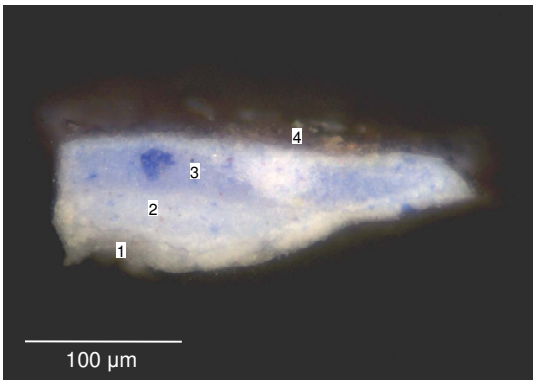

4 - varnish layer
3 - blue paint layer (max. thickness 45 µm)
2 - blue paint layer (max. thickness 35 µm)
1 - white ground layer (max. thickness 23 µm)

Figure D20. Cross section of sample **E1** - blue from the sky of **Aldeia de St. Sauves**, viewed under reflected light.

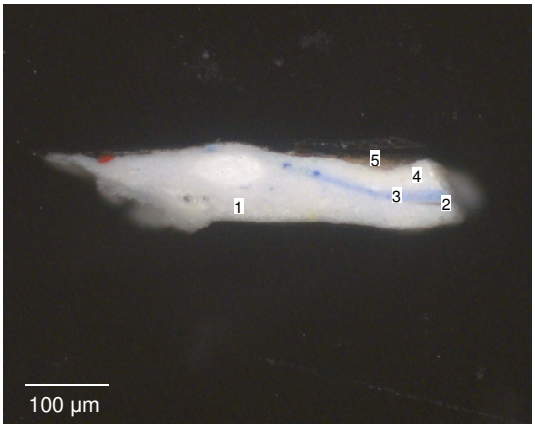

5 - varnish layer
4 - white paint layer (max. thickness 41 µm)
3 - blue paint layer (max. thickness 15 µm)
2 - brown paint layer (max. thickness 6 µm)
1 - white paint layer (max. thickness 98 µm)

Figure D21. Cross section of sample **E2** - white from the cloud of **Aldeia de St. Sauves**, viewed under reflected light.

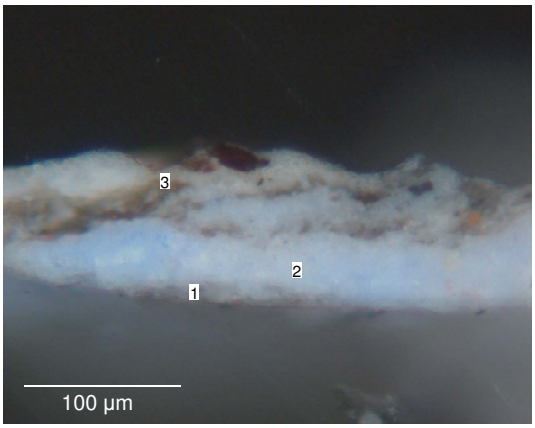

3 - brownish paint layer (max. thickness 66 µm)
2 - blue paint layer (max. thickness 55 µm)
1 - brownish paint layer (max. thickness 15 µm)

Figure D22. Cross section of sample **E3** - grey from the cloud of **Aldeia de St. Sauves**, viewed under reflected light.

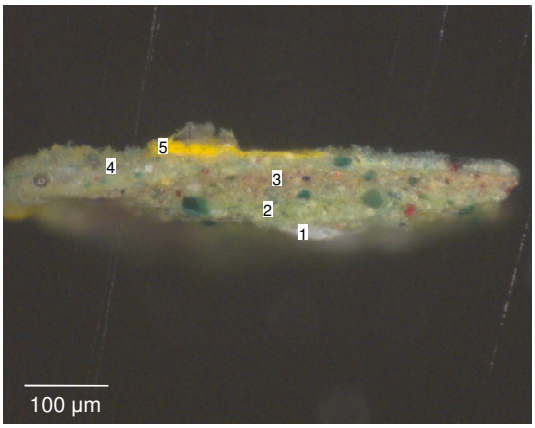

5 - yellow paint layer (max. thickness 20 µm)
4 - green paint layer (max. thickness 56 µm)
3 - brownish paint layer (max. thickness 39 µm)
2 - green paint layer (max. thickness 43 µm)
1 - white ground layer (max. thickness 21 µm)

Figure D23. Cross section of sample **E4** - green from the roof of **Aldeia de St. Sauves**, viewed under reflected light.

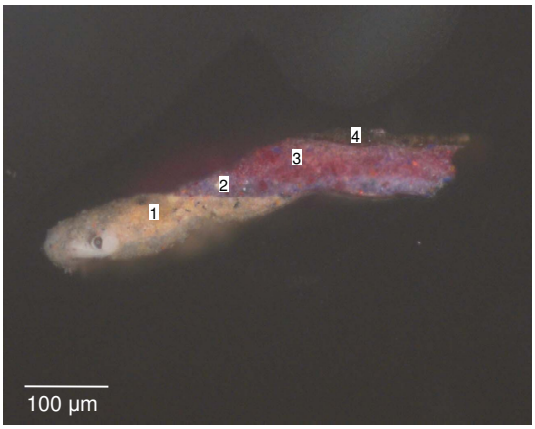

4 - brown paint layer (max. thickness 23 µm)
3 - purple paint layer (max. thickness 70 µm)
2 - purple paint layer (max. thickness 34 µm)
1 - beige paint layer (max. thickness 91 µm)

Figure D24. Cross section of sample **E5** - dark grey from the shadow of **Aldeia de St. Sauves**, viewed under reflected light.

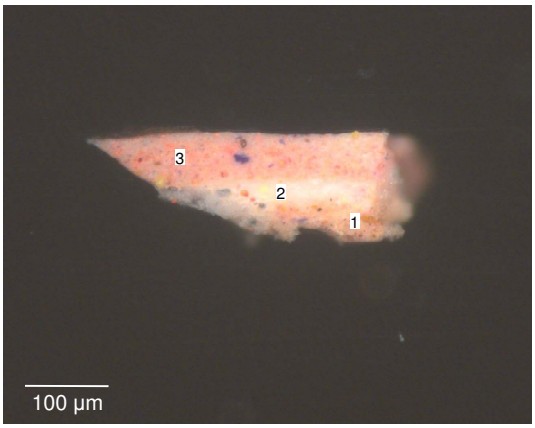

4 - varnish layer
3 - pinkish paint layer (max. thickness 68 µm)
2 - white paint layer (max. thickness 41 µm)
1 - brownish paint layer (max. thickness 51 µm)

Figure D25. Cross section of sample **E6** - brown from the ground of **Aldeia de St. Sauves**, viewed under reflected light.

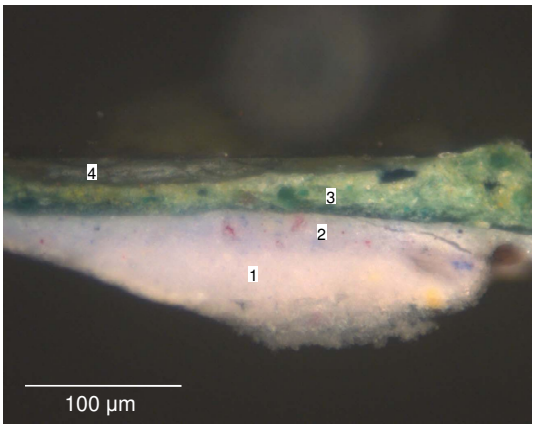

4 - varnish
3 - green paint layer (max. thickness 60 µm)
2 - blue paint layer (max. thickness 29 µm)
1 - white ground layer (max. thickness 65 µm)

Figure D26. Cross section of sample **E7** -dark green from the tree foliage of **Aldeia de St. Sauves**, viewed under reflected light.

- Paisagem de St. Sauves

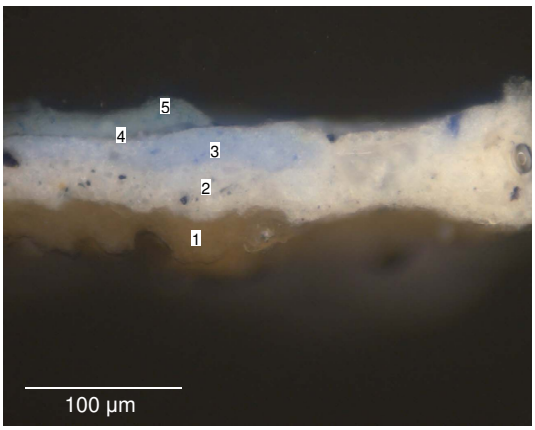

5 - blue paint layer (max. thickness 28 µm)
4 - brown layer (max. thickness 6 µm)
3 - blue paint layer (max. thickness 32 µm)
2 - white *imprimitura* (max. thickness 95 µm)
1 - brown ground layer (max. thickness 35 µm)

Figure D27. Cross section of sample **F1** - blue from the sky of **Paisagem de St. Sauves**, viewed under reflected light.

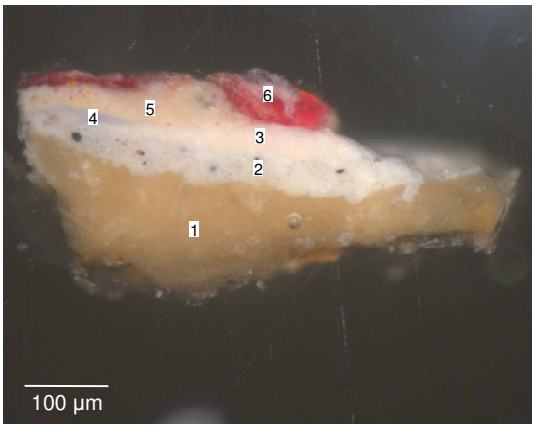

6 - red paint layer (max. thickness 60 µm)
5 - orange paint layer (max. thickness 59 µm)
4 - blue paint layer (max. thickness 16 µm)
3 - beige paint layer (max. thickness 47 µm)
2 - white *imprimitura* (max. thickness 61 µm)
1 - brown ground layer (max. thickness 173 µm)

Figure D28. Cross section of sample **F2** - orange from the sky of **Paisagem de St. Sauves**, viewed under reflected light.

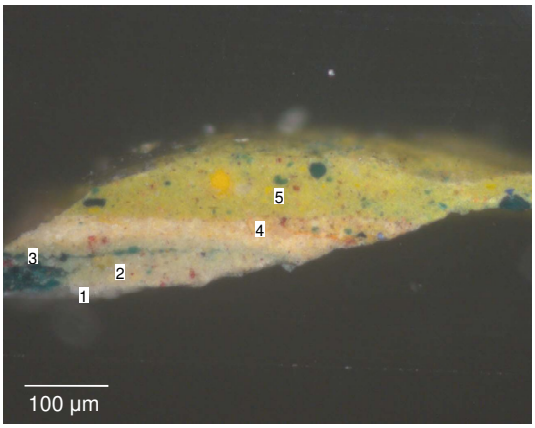

5 - green paint layer (max. thickness 102 µm)
4 - beige paint layer (max. thickness 60 µm)
3 - green paint layer (max. thickness 38 µm)
2 - green paint layer (max. thickness 51 µm)
1 - white paint layer (max. thickness 13 µm)

Figure D29. Cross section of sample **F3** - light green from the ground of **Paisagem de St. Sauves**, viewed under reflected light.

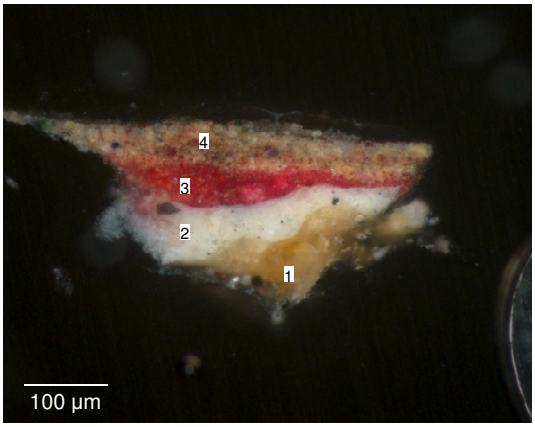

4 - brown paint layer (max. thickness 73 µm)
3 - red paint layer (max. thickness 69 µm)
2 - white *imprimitura* (max. thickness 78 µm)
1 - brown ground layer (max. thickness 74 µm)

Figure D30. Cross section of sample **F4** - green from the ground of **Paisagem de St. Sauves**, viewed under reflected light.

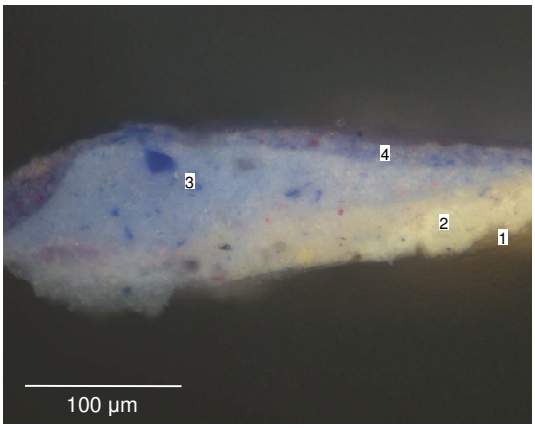

4 - purple paint layer (max. thickness 38 µm)
3 - blue paint layer (max. thickness 85 µm)
2 - white *imprimitura* (max. thickness 43 µm)
1 - brown ground layer (max. thickness 19 µm)

Figure D31. Cross section of sample **F5** - dark blue from the sky of **Paisagem de St. Sauves**), viewed under reflected light.

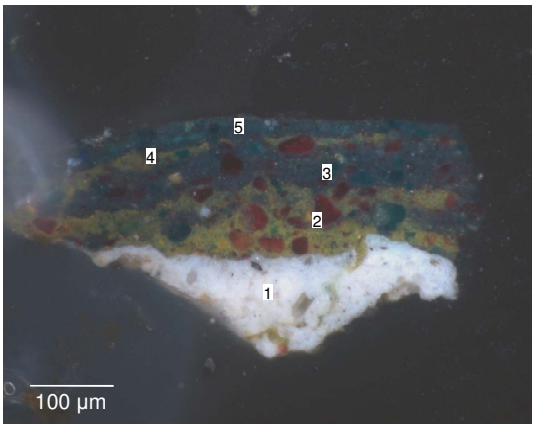

5 - green paint layer (max. thickness 33 µm)
4 - green paint layer (max. thickness 29 µm)
3 - green paint layer (max. thickness 70 µm)
2 - green paint layer (max. thickness 112 µm)
1 - white paint layer (max. thickness 143 µm)

Figure D32. Cross section of sample **F6** - dark green of the ground of **Paisagem de St. Sauves**, viewed under reflected light.

- Cansada (Cachopa de Capri)

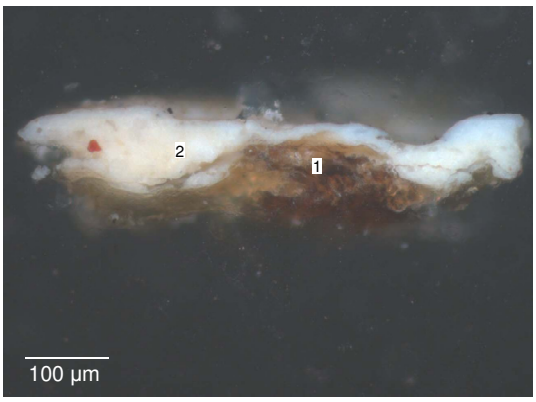

2 - white ground layer (max. thickness 120 µm)
1 - canvas fibbers

Figure D33. Cross section of sample **G1** - white from the wall of **Cansada (cachopa de Capri)**, viewed under reflected light.

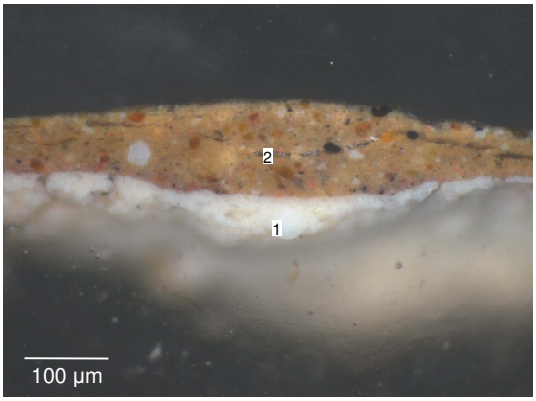

2 - brown paint layer (max. thickness 143 µm)
1 - white ground layer (max. thickness 62 µm)

Figure D34. Cross section of sample **G2** - brown from the ground of **Cansada (cachopa de Capri)**, viewed under reflected light.

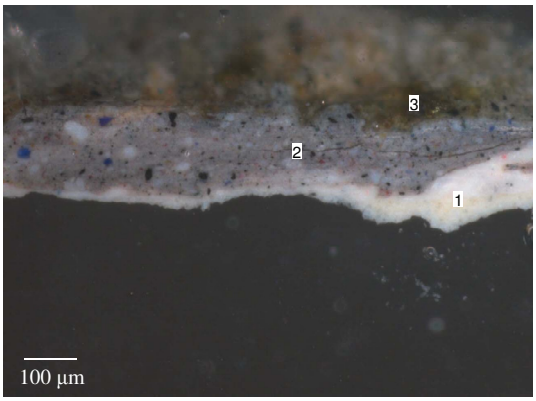

3 - varnish
2 - grey paint layer (max. thickness 200 µm)
1 - white ground layer (max. thickness 133 µm)

Figure D35. Cross section of sample **G3** - grey from the leaf of **Cansada (cachopa de Capri)**, viewed under reflected light.

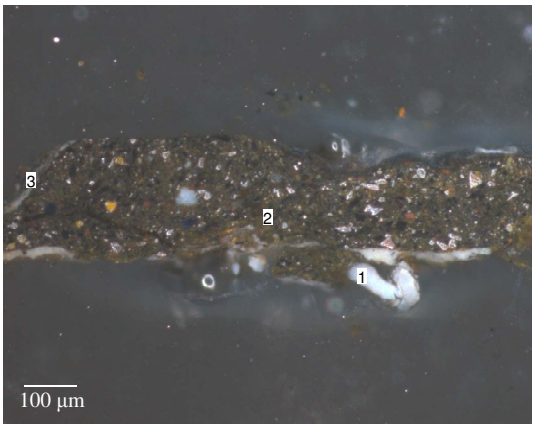

3 - white paint layer (max. thickness 26 µm)
2 - brown paint layer (max. thickness 282 µm)
1 - white ground layer (max. thickness 36 µm)

Figure D36. Cross section of sample **G4** - green from the leaf of **Cansada (cachopa de Capri)**, viewed under reflected light.

- Casas brancas de Capri

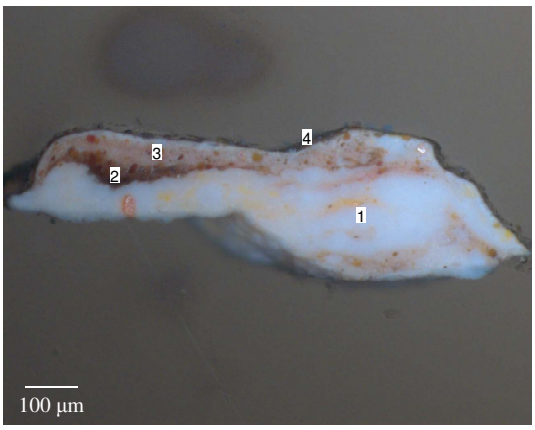

4 - varnish
3 - brown paint layer (max. thickness 77 µm)
2 - brown paint layer (max. thickness 43 µm)
1 - white paint layer (max. thickness 284 µm)

Figure D37. Cross section of sample **H1** - brown from the ground of **Casas brancas de Capri**, viewed under reflected light.

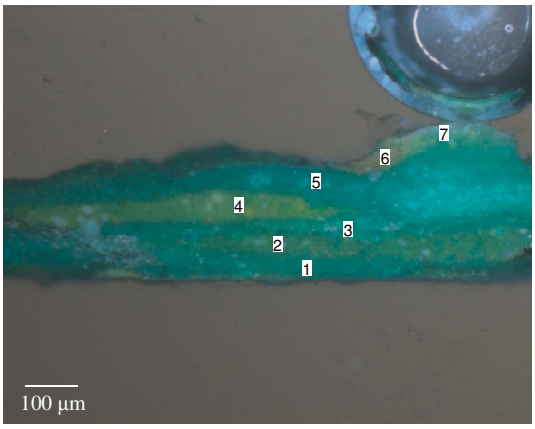

7 - green paint layer (max. thickness 53 µm)
6 - brown paint layer (max. thickness 49 µm)
5 - green paint layer (max. thickness 189 µm)
4 - green paint layer (max. thickness 68 µm)
3 - green paint layer (max. thickness 41 µm)
2 - green paint layer (max. thickness 45 µm)
1 - green paint layer (max. thickness 61 µm)

Figure D38. Cross section of sample **H2 -** green from the bushes of **Casas brancas de Capri**, viewed under reflected light.

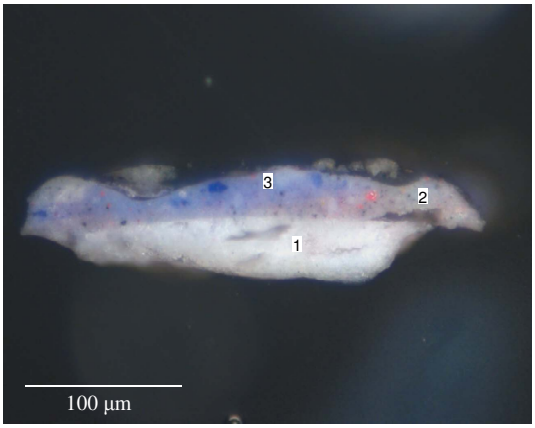

3 - blue paint layer (max. thickness 24 µm)
2 - grey paint layer (max. thickness 22 µm)
1 - white ground layer (max. thickness 48 µm)

Figure D39. Cross section of sample **H3** - grey from the house wall of **Casas brancas de Capri**, viewed under reflected light.

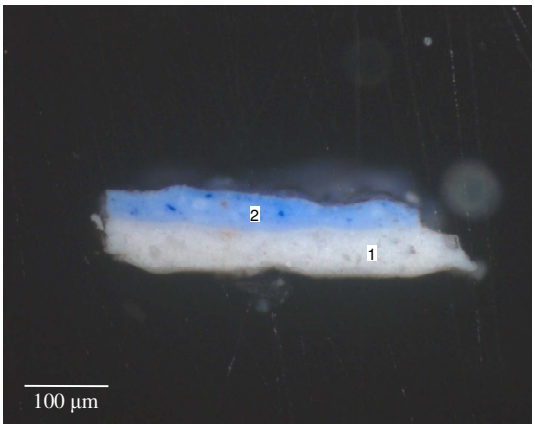

2 - blue paint layer (max. thickness 55 µm)
1 - white ground layer (max. thickness 72 µm)

Figure D40. Cross section of sample **H4** - blue from the sky of **Casas brancas de Capri**, viewed under reflected light.

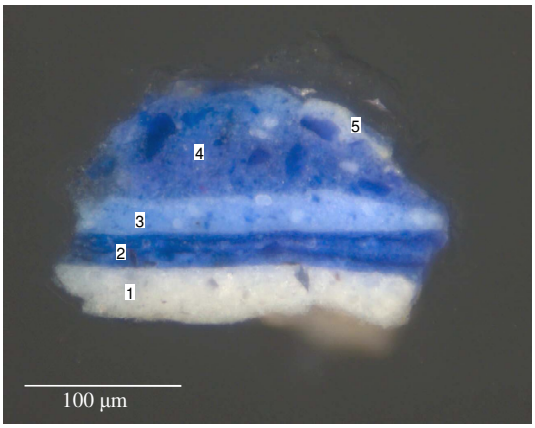

5 - blue paint layer (max. thickness 14 µm)
4 - blue paint layer (max. thickness 83 µm)
3 - blue paint layer (max. thickness 30 µm)
2 - blue paint layer (max. thickness 25 µm)
1 - white ground layer (max. thickness 46 µm)

Figure D41. Cross section of sample **H5** - blue from the sea of **Casas brancas de Capri**, viewed under reflected light.

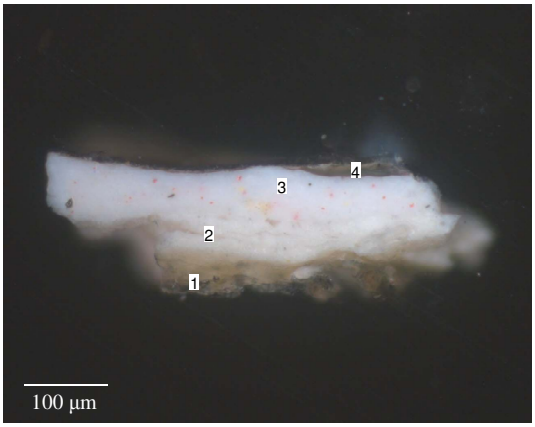

4 - varnish
3 - pink paint layer (max. thickness 82 µm)
2 - white ground layer (max. thickness 58 µm)
1 - size (max. thickness 51 µm)

Figure D42. Cross section of sample **H6** - white from the wall of **Casas brancas de Capri**, viewed under reflected light.

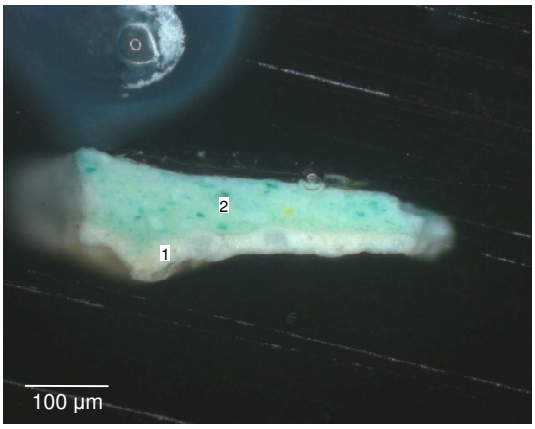

2 - green paint layer (max. thickness 118 µm)
1 - white ground layer (max. thickness 44 µm)

Figure D43. Cross section of sample **H7** - light green from the cactus of **Casas brancas de Capri**, viewed under reflected light.

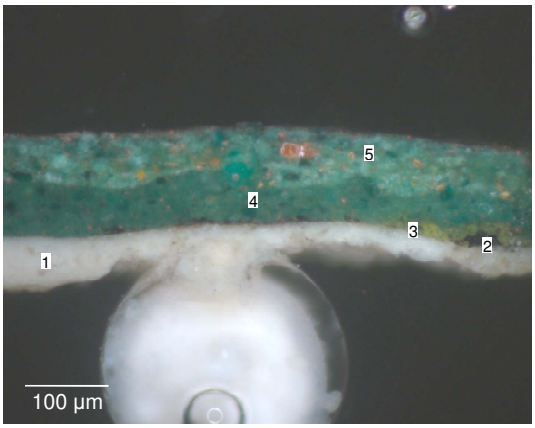

5 - green paint layer (max. thickness 91 µm)
4 - green paint layer (max. thickness 74 µm)
3 - green paint layer (max. thickness 21 µm)
2 - black paint layer (max. thickness 22 µm)
1 - white ground layer (max. thickness 74 µm)

Figure D44. Cross section of sample **H8** - dark green from the cactus of **Casas brancas de Capri**, viewed under reflected light.

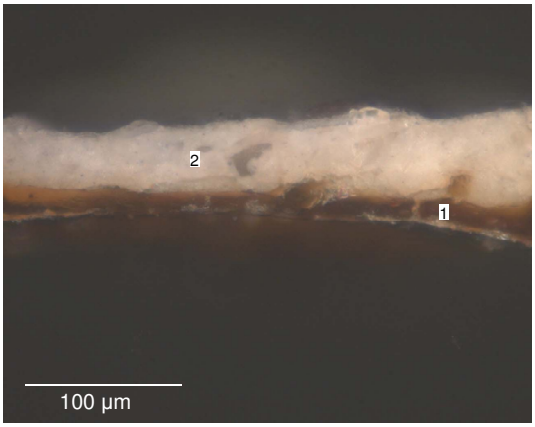

2 - white ground layer (max. thickness 66 µm)
1 - canvas (max. thickness 33 µm)

Figure D45. Cross section of sample **H9** - ground layer of **Casas brancas de Capri**, viewed under reflected light.

- Cecília

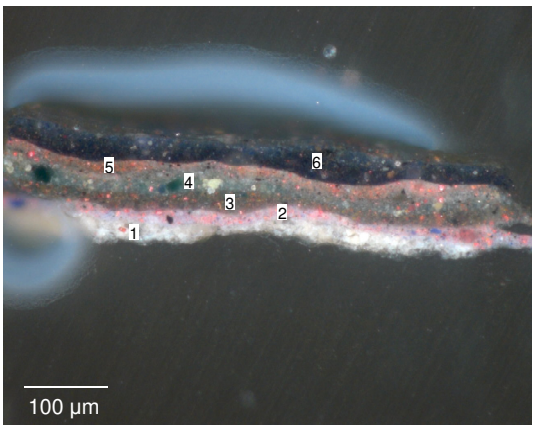

6 - black paint layer (max. thickness 38 µm)
5 - pink paint layer (max. thickness 19 µm)
4 - green paint layer (max. thickness 38 µm)
3 - brown paint layer (max. thickness 36 µm)
2 - pink paint layer (max. thickness 24 µm)
1 - white ground layer (max. thickness 38 µm)

Figure D46. Cross section of sample **I1** - black from the pedestal of **Cecília**, viewed under reflected light.

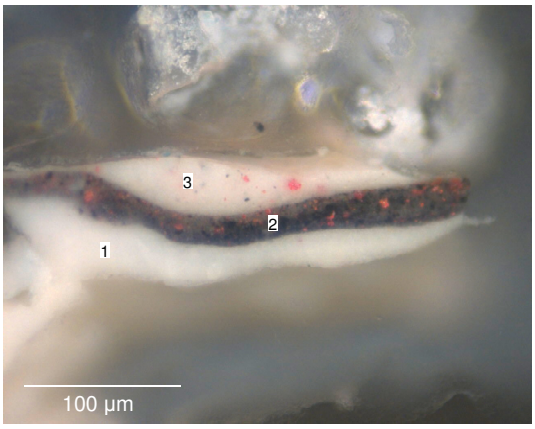

3 - pink paint layer (max. thickness 45 µm)
2 - brown paint layer (max. thickness 30 µm)
1 - white paint layer (max. thickness 58 µm)

Figure D47. Cross section of sample **I2** - white from the kerchief of **Cecília**, viewed under reflected light.

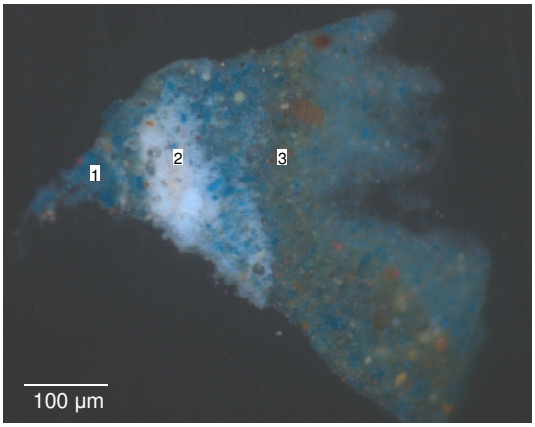

3 - blue paint layer (max. thickness 28 µm)
2 - white paint layer (max. thickness 22 µm)
1 - blue paint layer (max. thickness 75 µm)

Figure D48. Cross section of sample **I3** - blue from the chair of **Cecília**, viewed under reflected light.

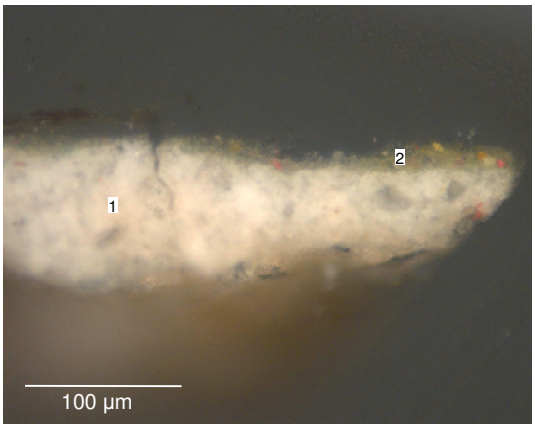

2 - green paint layer (max. thickness 19 µm)
1 - white ground layer (max. thickness 113 µm)

Figure D49. Cross section of sample **I4** - green from the stripe of **Cecília**, viewed under reflected light.

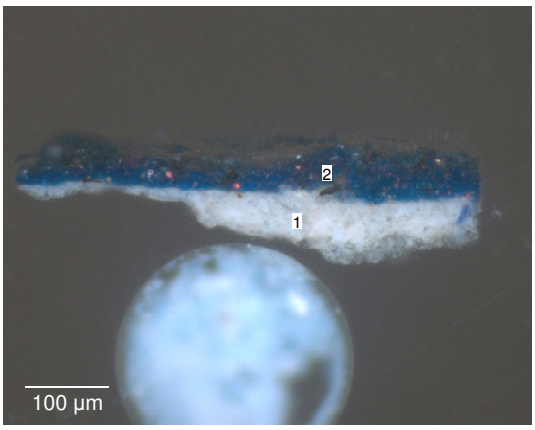

2 - blue paint layer (max. thickness 86 µm)
1 - white ground layer (max. thickness 97 µm)

Figure D50. Cross section of sample **I5** - dark blue from the skirt of **Cecília**, viewed under reflected light.

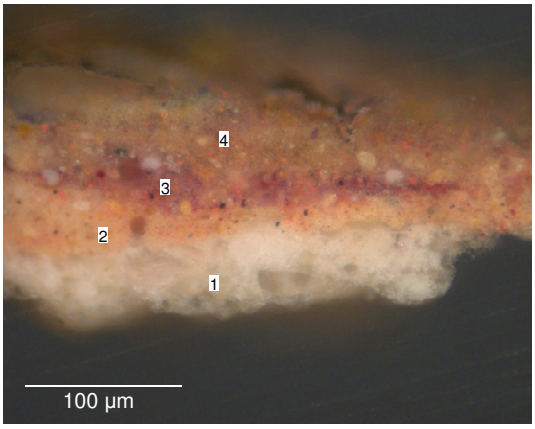

4 - beige paint layer (max. thickness 50 µm)
3 - reddish paint layer (max. thickness 41 µm)
2 - orange paint layer (max. thickness 50 µm)
1 - white ground layer (max. thickness 65 µm)

Figure D51. Cross section of sample **I6** - carnation from the finger of **Cecília**, viewed under reflected light.

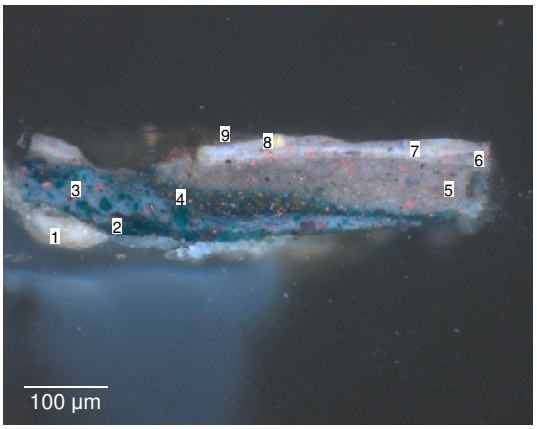

9 - varnish layer
8 - grey paint layer (max. thickness 8 µm)
7 - pink paint layer (max. thickness 8 µm)
6 - grey paint layer (max. thickness 15 µm)
5 - grey paint layer (max. thickness 73 µm)
4 - green paint layer (max. thickness 38 µm)
3 - blue paint layer (max. thickness 53 µm)
2 - blue paint layer (max. thickness 30 µm)
1 - white ground layer (max. thickness 54 µm)

Figure D52. Cross section of sample **I7** - grey from the pedestal of **Cecília**, viewed under reflected light.

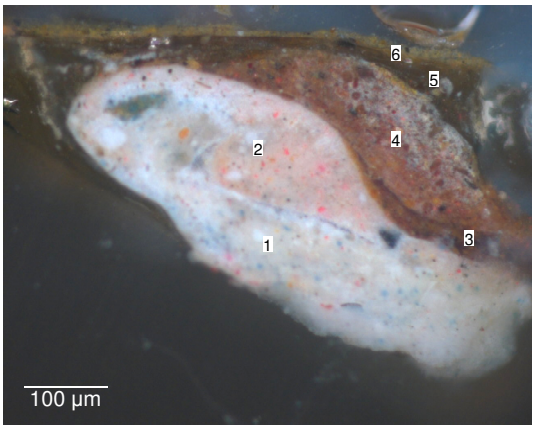

6 - yellow paint layer (max. thickness 14 µm)
5 - brown paint layer (max. thickness 69 µm)
4 - brown paint layer (max. thickness 157 µm)
3 - brown paint layer (max. thickness 34 µm)
2 - pink paint layer (max. thickness 163 µm)
1 - grey paint layer (max. thickness 174 µm)

Figure D53. Cross section of sample **I8** - yellow from the shroud of **Cecília**, viewed under reflected light.

- Escadas de um pardieiro - Roma

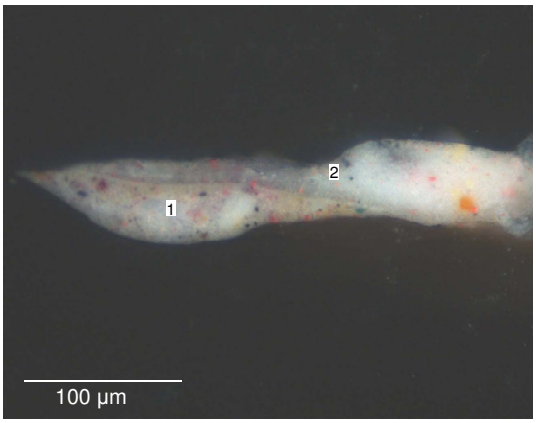

2 - grey paint layer (max. thickness 77 µm)
1 - grey ground layer (max. thickness 46 µm)

Figure D54. Cross section of sample **J1** - grey from the wall of **Escadas de um pardieiro - Roma**, viewed under reflected light.

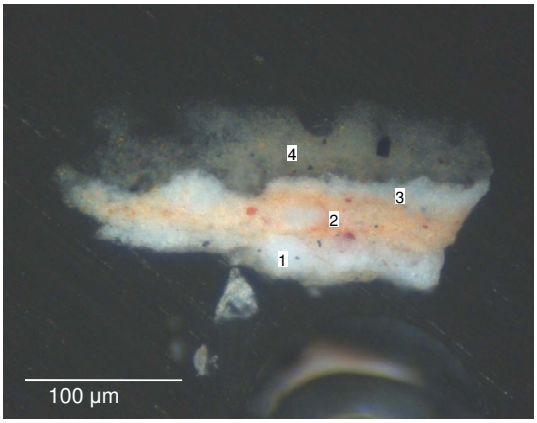

4 - green paint layer (max. thickness 58 µm)
3 - white paint layer (max. thickness 26 µm)
2 - orange paint layer (max. thickness 33 µm)
1 - white paint layer (max. thickness 26 µm)

Figure D55. Cross section of sample **J2** - beige from the ground of **Escadas de um pardieiro - Roma**, viewed under reflected light.

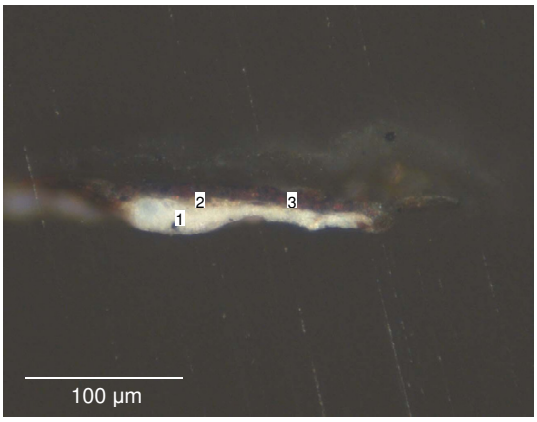

3 - brownish paint layer (max. thickness 15 µm)
2 - yellow paint layer (max. thickness 7 µm)
1 - white ground layer (max. thickness 28 µm)

Figure D56. Cross section of sample **J3** - dark brown from the door entrance of **Escadas de um pardieiro - Roma**, viewed under reflected light.

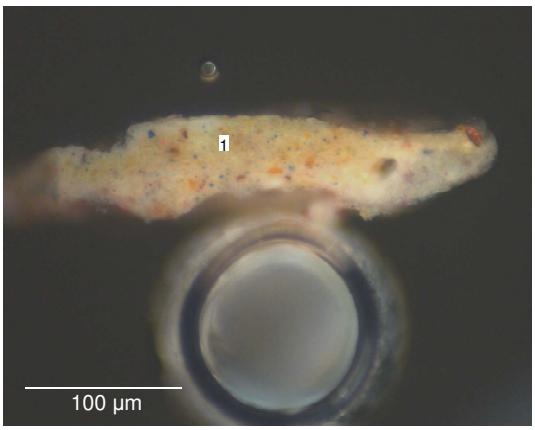

1 - beige paint layer (max. thickness 79 µm)

Figure D57. Cross section of sample **J4** - brownish from the stone wall of **Escadas de um pardieiro - Roma**, viewed under reflected light.

- Esperando o sucesso

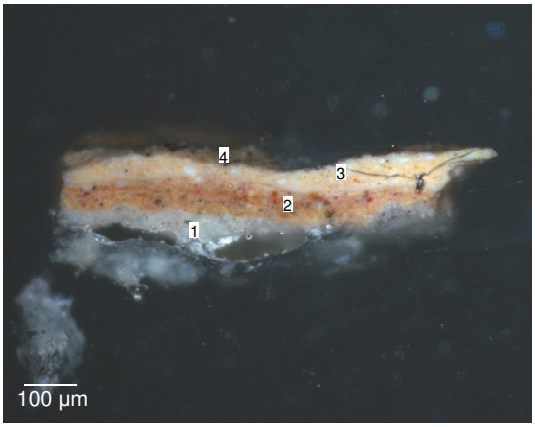

4 - varnish
3 - beige paint layer (max. thickness 80 µm)
2 - brown paint layer (max. thickness 82 µm)
1 - white ground layer (max. thickness 75 µm)

Figure D58. Cross section of the sample **K1** - beige from the ground of ***Esperando o sucesso***, viewed under reflected light.

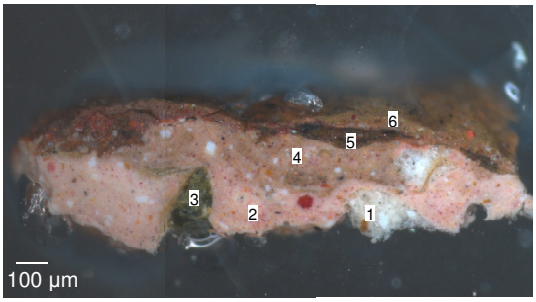

6 - brown paint layer (max. thickness 69 µm)
5 - brown paint layer (max. thickness 76 µm)
4 - brown paint layer (max. thickness 208 µm)
3 - green paint layer (max. thickness 25 µm)
2 - pink paint layer (max. thickness 269 µm)
1 - white ground layer (max. thickness 174 µm)

Figure D59. Cross section of the sample **K2** - brown from the wood box of ***Esperando o sucesso***, viewed under reflected light.

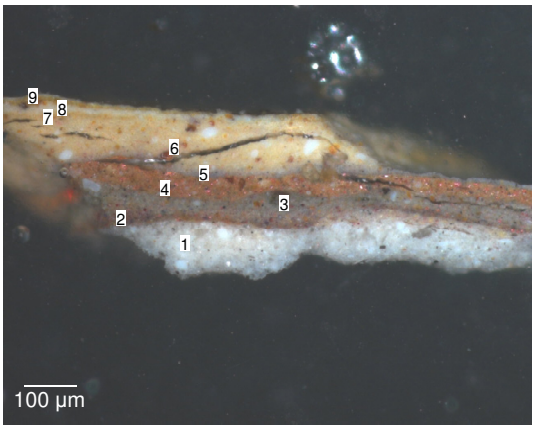

9 - yellow paint layer (max. thickness 26 µm)
8 - white paint layer (max. thickness 20 µm)
7 - yellow paint layer (max. thickness 19 µm)
6 - yellow paint layer (max. thickness 114 µm)
5 - grey paint layer (max. thickness 25 µm)
4 - brown paint layer (max. thickness 63 µm)
3 - grey paint layer (max. thickness 66 µm)
2 - brown paint layer (max. thickness 23 µm)
1 - white ground layer (max. thickness 124 µm)

Figure D60. Cross section of the sample **K3** - yellow from the brush of ***Esperando o sucesso***, viewed under reflected light.

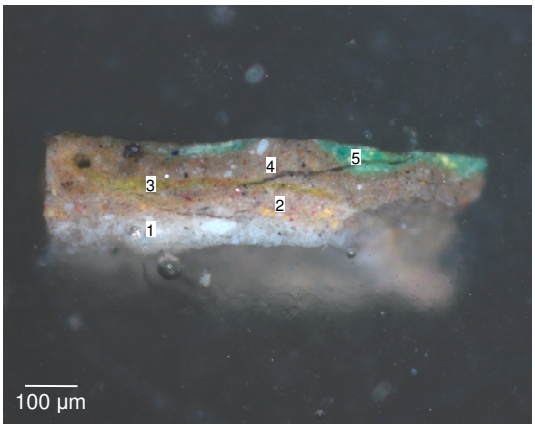

5 - green paint layer (max. thickness 66 µm)
4 - brown paint layer (max. thickness 81 µm)
3 - yellow paint layer (max. thickness 31 µm)
2 - brown paint layer (max. thickness 70 µm)
1 - white ground layer (max. thickness 103 µm)

Figure D61. Cross section of the sample **K4** - dark grey from the ground of ***Esperando o sucesso***, viewed under reflected light.

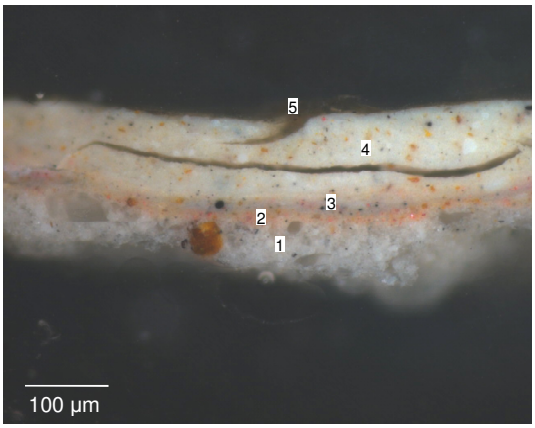

5 - varnish
4 - beige paint layer (max. thickness 122 µm)
3 - purple paint layer (max. thickness 32 µm)
2 - pink paint layer (max. thickness 27 µm)
1 - white ground layer (max. thickness 28 µm)

Figure D62. Cross section of the sample **K5** - grey from canvas of ***Esperando o sucesso***, viewed under reflected light.

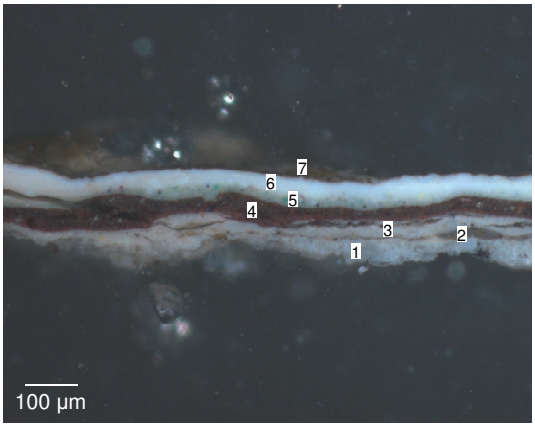

7 - varnish
6 - white paint layer (max. thickness 43 µm)
5 - greenish paint layer (max. thickness 32 µm)
4 - brwon paint layer (max. thickness 80 µm)
3 - white paint layer (max. thickness 48 µm)
2 - brown paint layer (max. thickness 28 µm)
1 - white ground layer (max. thickness 67 µm)

Figure D63. Cross section of the sample **K6** - grey from the canvas of ***Esperando o sucesso***, viewed under reflected light.

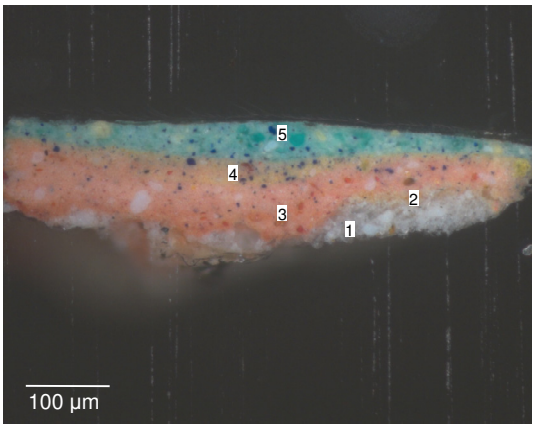

5 - green paint layer (max. thickness 57 µm)
4 - yellow paint layer (max. thickness 36 µm)
3 - reddish paint layer (max. thickness 83 µm)
2 - brownish paint layer (max. thickness 22 µm)
1 - white ground layer (max. thickness 48 µm)

Figure D64. Cross section of the sample **K7** - green from the ground of ***Esperando o sucesso***, viewed under reflected light.

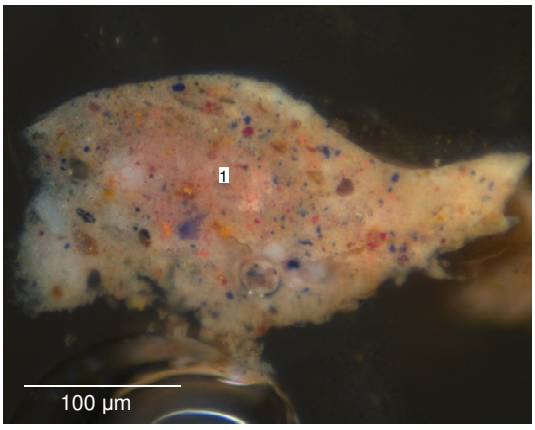

1 - beige paint layer (max. thickness 207 µm)

Figure D65. Cross section of the sample **K8** - grey from the palette of ***Esperando o sucesso***, viewed under reflected light.

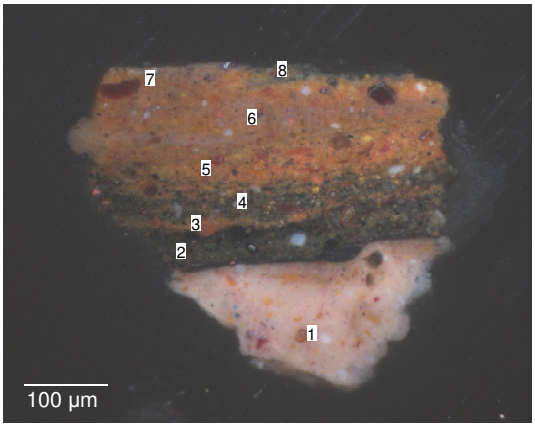

8 - green paint layer (max. thickness 18 µm)
7 - brown paint layer (max. thickness 94 µm)
6 - grey paint layer (max. thickness 23 µm)
5 - brown paint layer (max. thickness 61 µm)
4 - green paint layer (max. thickness 50 µm)
3 - brown paint layer (max. thickness 24 µm)
2 - green paint layer (max. thickness 78 µm)
1 - beige paint layer (max. thickness 184 µm)

Figure D66. Cross section of the sample **K9** - brown from the wood box of ***Esperando o sucesso***, viewed under reflected light.

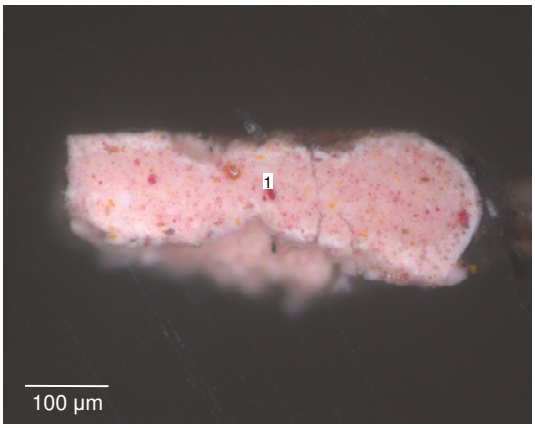

1 - pink paint layer (max. thickness 212 µm)

Figure D67. Cross section of the sample **K10** - beige from the ground of ***Esperando o sucesso***, viewed under reflected light.

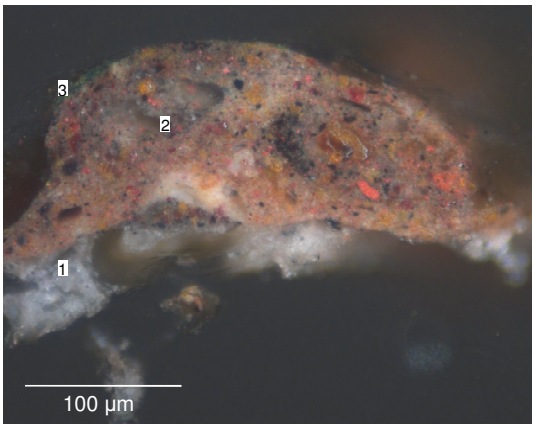

3 - green paint layer (max. thickness 7 µm)
2 - brown paint layer (max. thickness 148 µm)
1 - white ground layer (max. thickness 26 µm)

Figure D68. Cross section of the sample **K11** - dark green from the blanket of ***Esperando o sucesso***, viewed under reflected light.

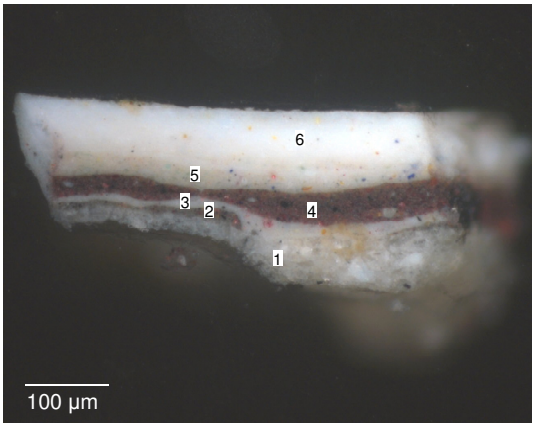

6 - white paint layer (max. thickness 96 µm)
5 - greenish paint layer (max. thickness 28 µm)
4 - brown paint layer (max. thickness 59 µm)
3 - white paint layer (max. thickness 30 µm)
2 - brown paint layer (max. thickness 17 µm)
1 - white ground layer (max. thickness 79 µm)

Figure D69. Cross section of the sample **K12** - white from the handkerchief of ***Esperando o sucesso***, viewed under reflected light.

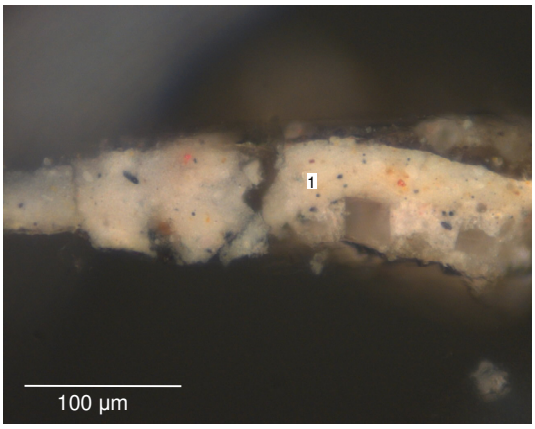

1 - white paint layer (max. thickness 86 µm)

Figure D70. Cross section of the sample **K13** - grey from the canvas of ***Esperando o sucesso***, viewed under reflected light.

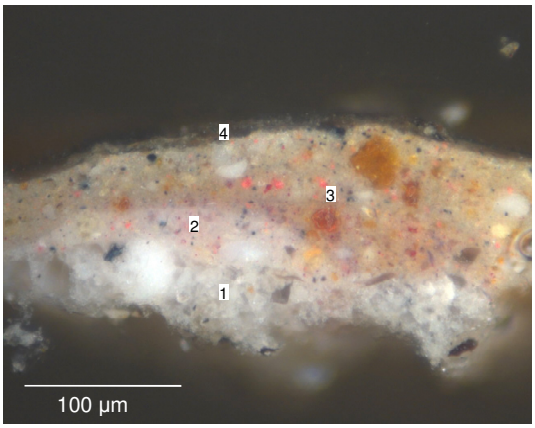

4 - varnish layer
3 - brown paint layer (max. thickness 118 µm)
2 - grey paint layer (max. thickness 36 µm)
1 - white ground layer (max. thickness 67 µm)

Figure D71. Cross section of the sample **K14** - dark grey from the ground of ***Esperando o sucesso***, viewed under reflected light.

- Fachada de porta soterrada - Roma

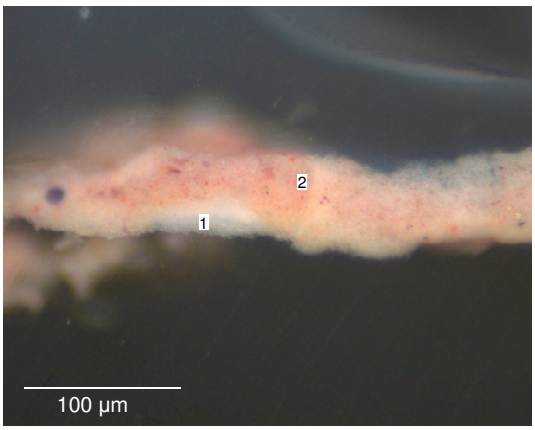

2 - pink paint layer (max. thickness 70µm)
1 - white ground layer (max. thickness 19 µm)

Figure D72. Cross section of the sample **L1** - pink from the ground of ***Fachada de porta soterrada - Roma***, viewed under reflected light.

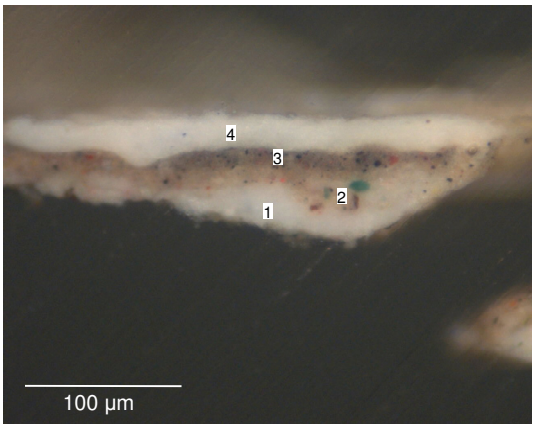

4 - white paint layer (max. thickness 44 µm)
3 - brown paint layer (max. thickness 17 µm)
2 - beige paint layer (max. thickness 33 µm)
1 - white ground layer (max. thickness 33 µm)

Figure D73. Cross section of the sample **L2** - white from the wall of ***Fachada de porta soterrada - Roma***, viewed under reflected light.

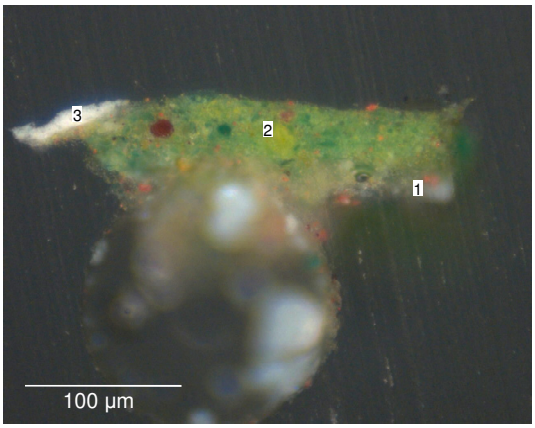

3 - white paint layer (max. thickness 14µm)
2 - green paint layer (max. thickness 68 µm)
1 - white ground layer (max. thickness 12 µm)

Figure D74. Cross section of the sample **L3** - green from the wall of ***Fachada de porta soterrada - Roma***, viewed under reflected light.

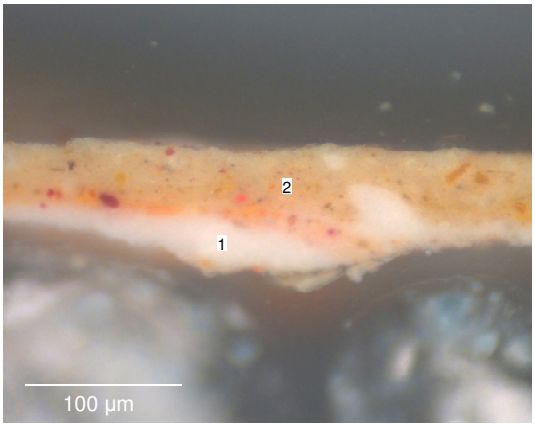

2 - orange paint layer (max. thickness 80 µm)
1 - white ground layer (max. thickness 46 µm)

Figure D75. Cross section of the sample **L4** - orange from the wall ***Fachada de porta soterrada - Roma***, viewed under reflected light.

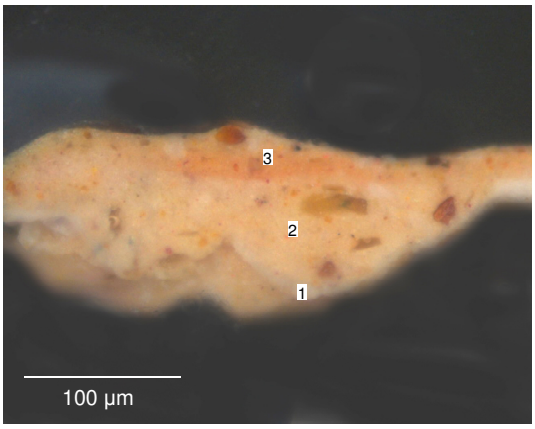

3 - orange paint layer (max. thickness 36 µm)
2 - orange paint layer (max. thickness 75 µm)
1 - white ground layer (max. thickness 13 µm)

Figure D76. Cross section of the sample **L5** - brown from the wall of ***Fachada de porta soterrada - Roma***, viewed under reflected light.

- Miragem de Nápoles

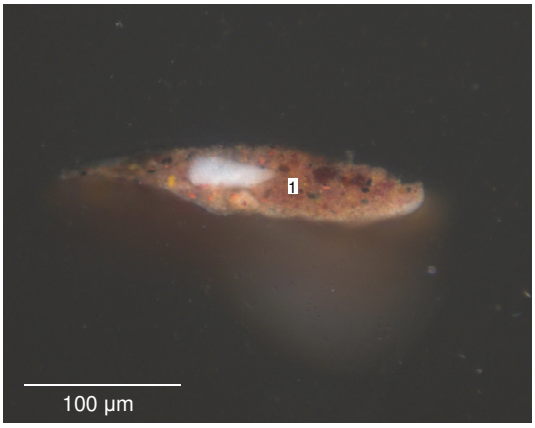

1 - brown paint layer (max. thickness 54 µm)

Figure D77. Cross section of the sample **M1** - brown from the ground of ***Miragem de Nápoles***, viewed under reflected light.

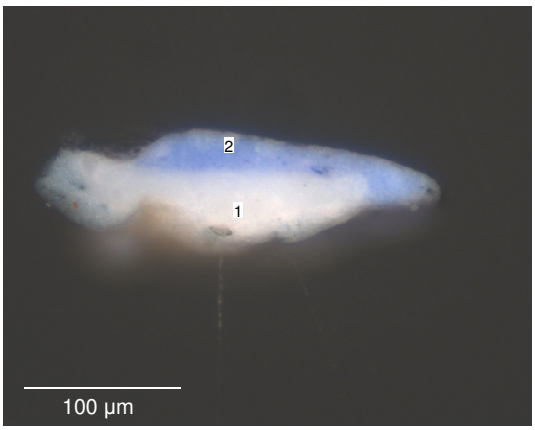

2 - blue paint layer (max. thickness 35 µm)
1 - white ground layer (max. thickness 56 µm)

Figure D78. Cross section of the sample **M2** - blue from the water of ***Miragem de Nápoles***, viewed under reflected light.

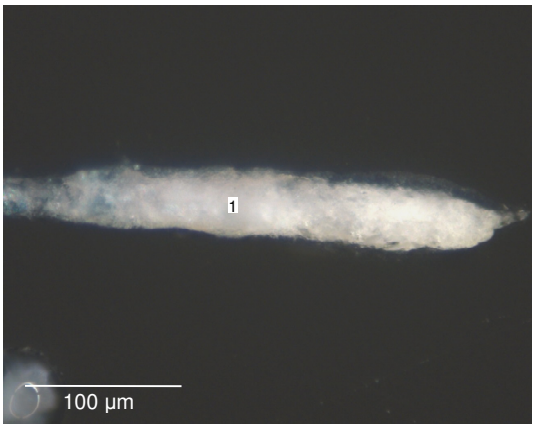

1 - white paint layer (max. thickness 50 µm)

Figure D79. Cross section of the sample **M3** - white of ***Miragem de Nápoles***, viewed under reflected light.

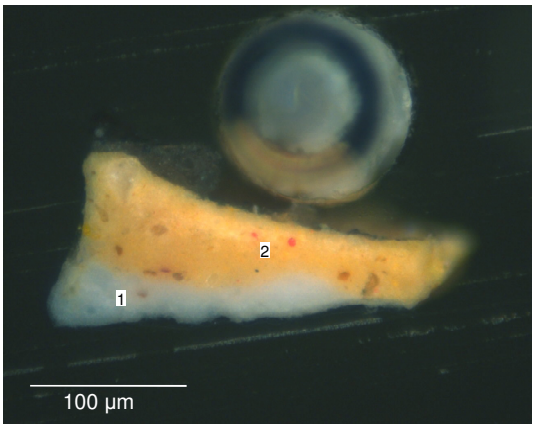

2 - orange paint layer (max. thickness 94 µm)
1 - white ground layer (max. thickness 40 µm)

Figure D80. Cross section of the sample **M4** - beige from the wall of ***Miragem de Nápoles***, viewed under reflected light.

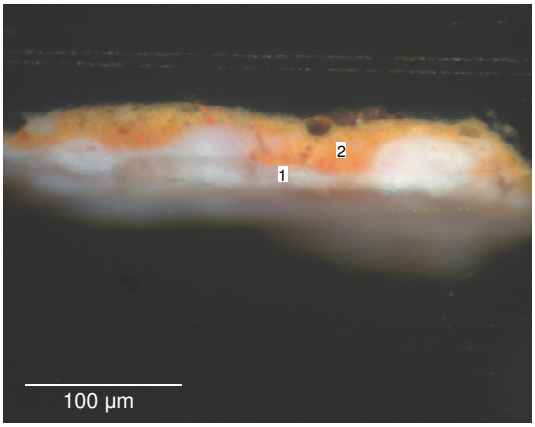

2 - orange paint layer (max. thickness 40 µm)
1 - white ground layer (max. thickness 15 µm)

Figure D81. Cross section of the sample **M5** - orange from the wall of ***Miragem de Nápoles***, viewed under reflected light.

- Portão

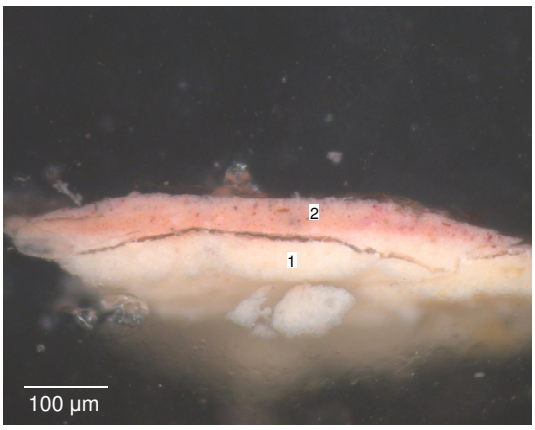

2 - pink paint layer (max. thickness 63 µm)
1 - white ground layer (max. thickness 58 µm)

Figure D82. Cross section of the sample **N1** - beige from the ground of ***Portão***, viewed under reflected light.

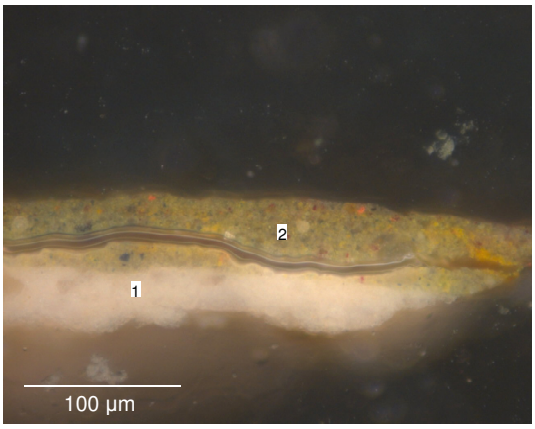

2 - green paint layer (max. thickness 49 µm)
1 - white ground layer (max. thickness 44 µm)

Figure D83. Cross section of the sample **N2** - green from the trees of ***Portão***, viewed under reflected light.

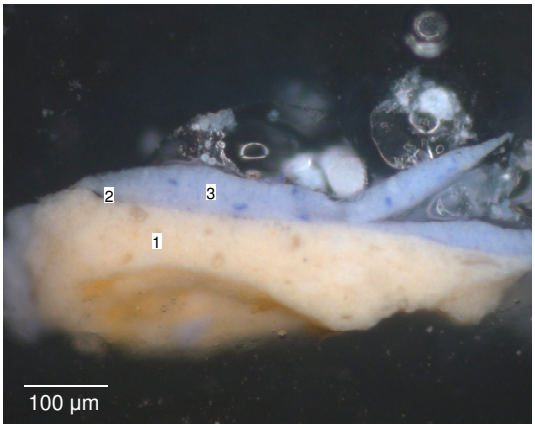

3 - blue paint layer (max. thickness 72 µm)
2 - black paint layer (max. thickness 4 µm)
1 - white ground layer (max. thickness 161 µm)

Figure D84. Cross section of the sample **N3** - blue from the sky of ***Portão***, viewed under reflected light.

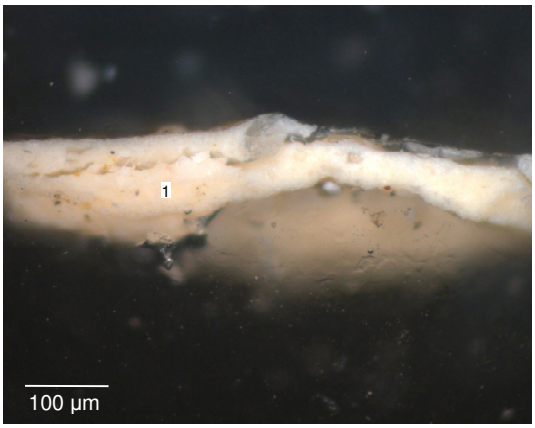

1 - white ground layer (max. thickness 108 µm)

Figure D85. Cross section of the sample **N4** - beige from the wall of ***Portão***, viewed under reflected light.

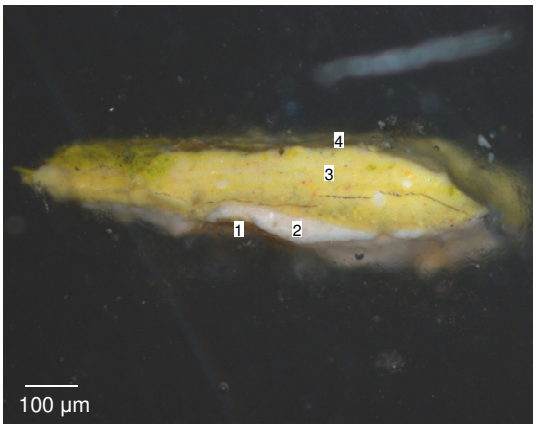

4 - varnish
3 - greenish paint layer (max. thickness 123 µm)
2 - white ground layer (max. thickness 38 µm)
1 - support

Figure D86. Cross section of the sample **N5** - green from the ground of ***Portão***, viewed under reflected light.

- Rapariga de Anacapri

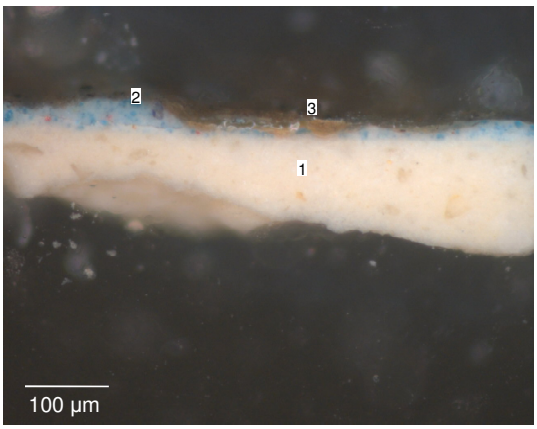

3 - varnish
2 - blue paint layer (max. thickness 49 µm)
1 - white ground layer (max. thickness 175 µm)

Figure D87. Cross section of the sample **O1** - blue from the background of ***Rapariga de Anacapri***, viewed under reflected light.

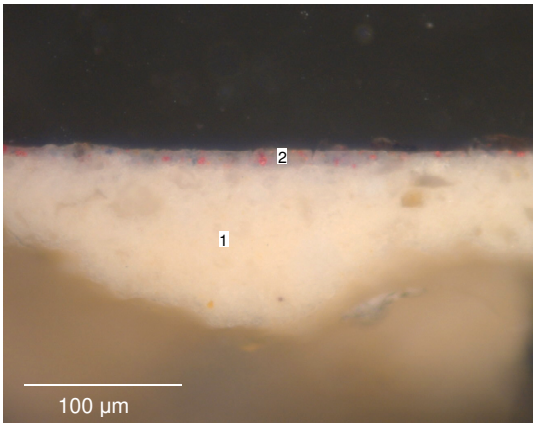

2 - pink paint layer (max. thickness 15 µm)
1 - white ground layer (max. thickness 124 µm)

Figure D88. Cross section of the sample **O2** - pink from the neckerchief of **Rapariga de Anacapri**, viewed under reflected light.

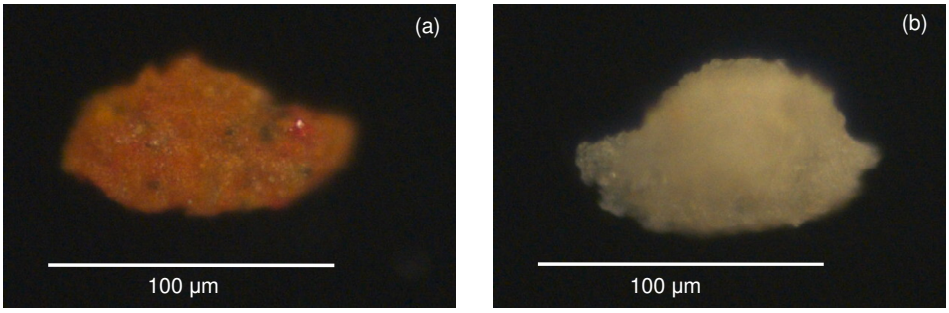

Figure D89. Unmounted sample **O3** - red from the neckerchief of ***Rapariga de Anacapri***, under reflected light. (a) top surface, (b) bottom surface.

- Rua de Roma

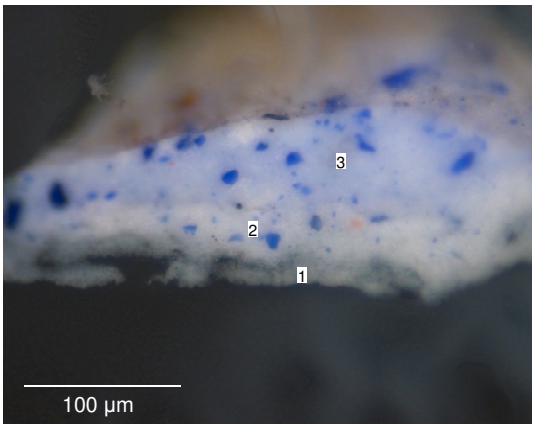

3 - blue paint layer (max. thickness 87 µm)
2 - blue paint layer (max. thickness 36 µm)
1 - white ground layer (max. thickness 28 µm)

Figure D90. Cross section of the sample **P1** - blue from the sky of ***Rua de Roma***, viewed under reflected light.

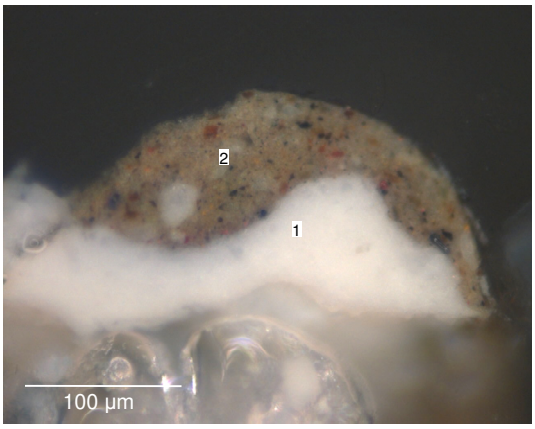

2 - brown paint layer (max. thickness 104 µm)
1 - white ground layer (max. thickness 102 µm)

Figure D91. Cross section of the sample **P2** - brown from the roof of ***Rua de Roma***, viewed under reflected light.

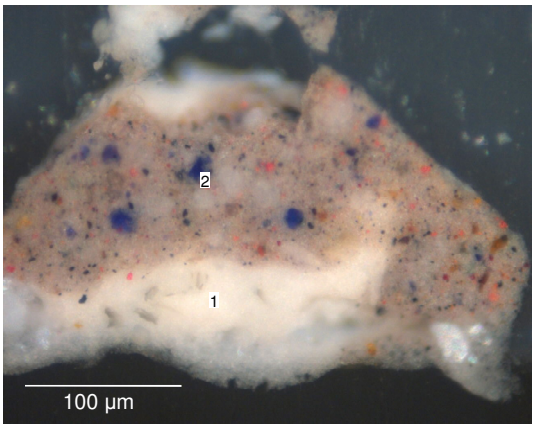

2 - brown paint layer (max. thickness 142 µm)
1 - white ground layer (max. thickness 98 µm)

Figure D92. Cross section of the sample **P3** - grey from the ground of ***Rua de Roma***, viewed under reflected light.

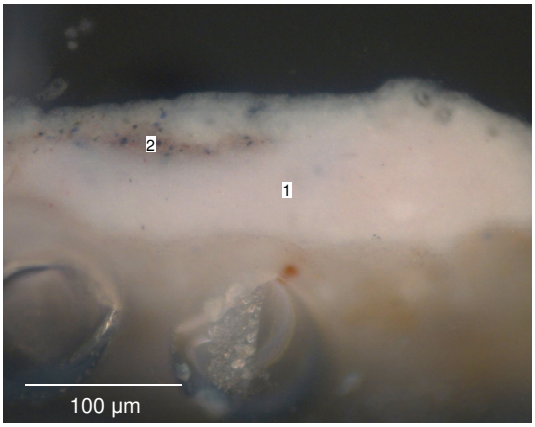

2 - brown paint layer (max. thickness 30 µm)
1 - white paint layer (max. thickness 84 µm)

Figure D93. Cross section of the sample **P4** - white from the ground of ***Rua de Roma***, viewed under reflected light.

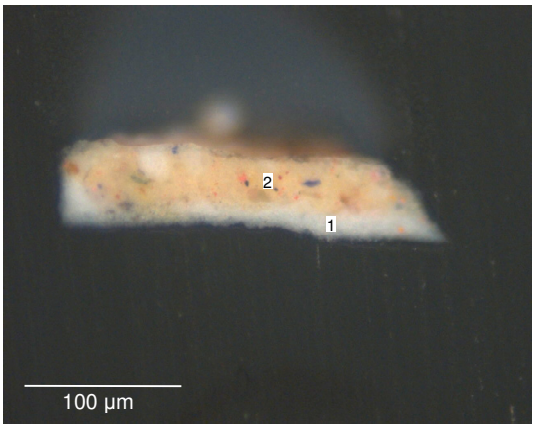

2 - orange paint layer (max. thickness 48 µm)
1 - white ground layer (max. thickness 21 µm)

Figure D94. Cross section of the sample **P5** - beige from the wall of ***Rua de Roma***, viewed under reflected light.

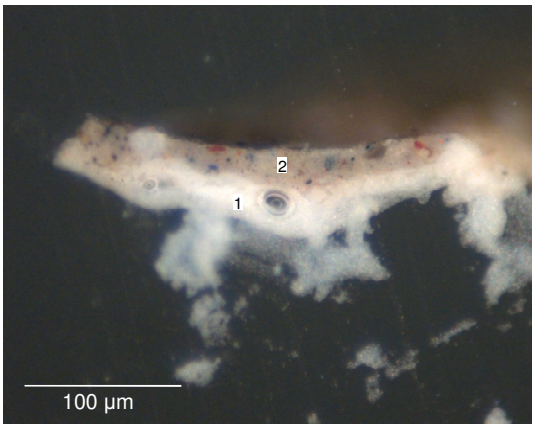

2 - grey paint layer (max. thickness 32 µm)
1 - white ground layer (max. thickness 48 µm)

Figure D95. Cross section of the sample **P6** - grey from the wall of ***Rua de Roma***, viewed under reflected light.

- Senhora vestida de preto

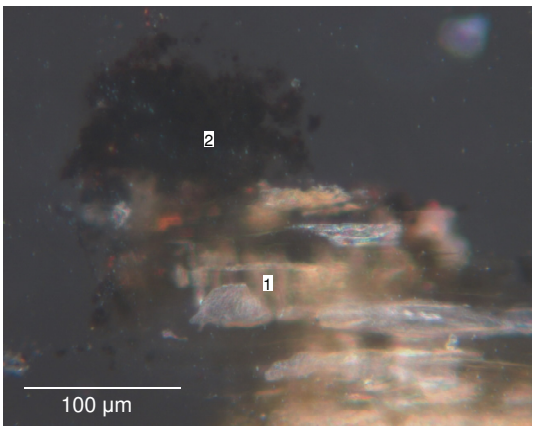

2 - black paint layer (max. thickness 57 µm)
1 – wood panel

Figure D96. Cross section of the sample **Q1** - black from the dress of ***Senhora vestida de preto***, viewed under reflected light.

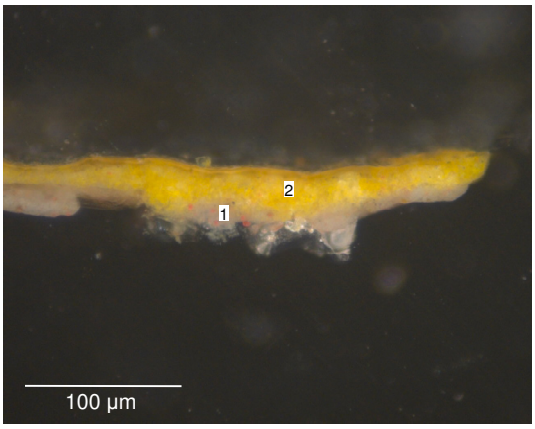

2 - amarelo paint layer (max. thickness 38 µm)
1 - grey paint layer (max. thickness 22 µm)

Figure D97. Cross section of the sample **Q2** - yellow from the chair of ***Senhora vestida de preto***, viewed under reflected light.

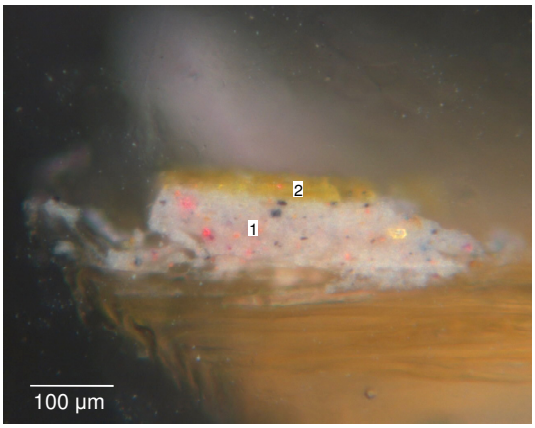

2 - yellow paint layer (max. thickness 15 µm)
1 - grey paint layer (max. thickness 65 µm)

Figure D98. Cross section of the sample **Q3** - yellow from the back of ***Senhora vestida de preto***, viewed under reflected light.

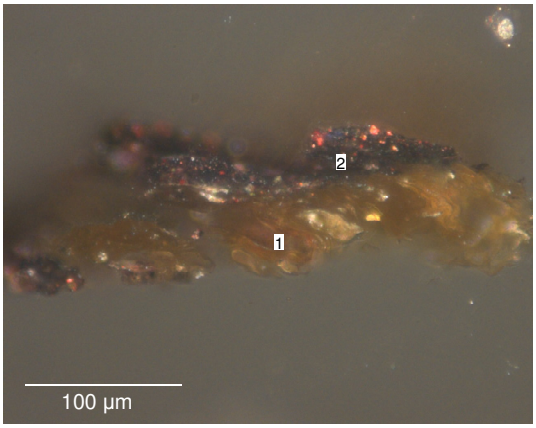

2 - black paint layer (max. thickness 41 µm)
1 – wood panel

Figure D99. Cross section of the sample **Q4** - black from the dress of ***Senhora vestida de preto***, viewed under reflected light.

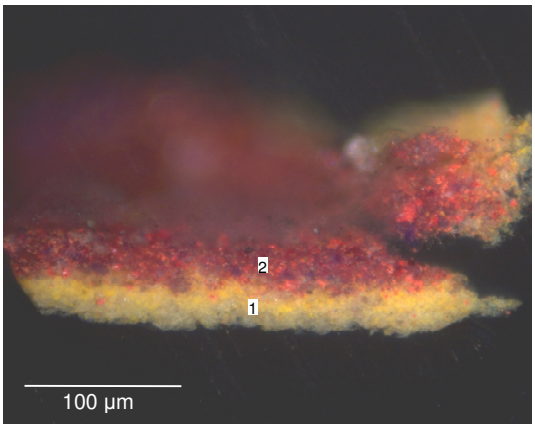

2 - red paint layer (max. thickness 40 µm)
1 - yellow paint layer (max. thickness 27 µm)

Figure D100. Cross section of the sample **Q5** - brown from the chair of ***Senhora vestida de preto***, viewed under reflected light.

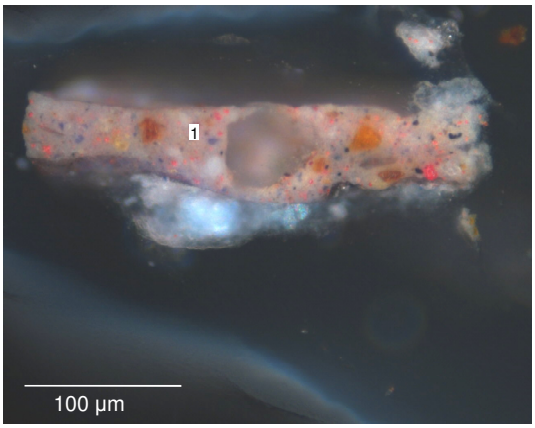

1 - grey paint layer (max. thickness 73 µm)

Figure D101. Cross section of the sample **Q6** - grey from the back of ***Senhora vestida de preto***, viewed under reflected light.

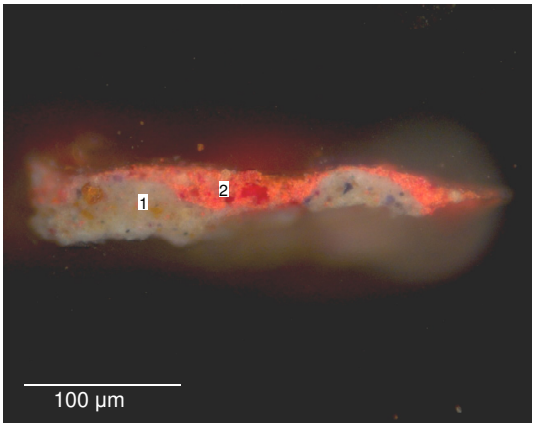

2 - red paint layer (max. thickness 32 µm)
1 - grey paint layer (max. thickness 45 µm)

Figure D102. Cross section of the sample **Q7** - red from the background of ***Senhora vestida de preto***, viewed under reflected light.

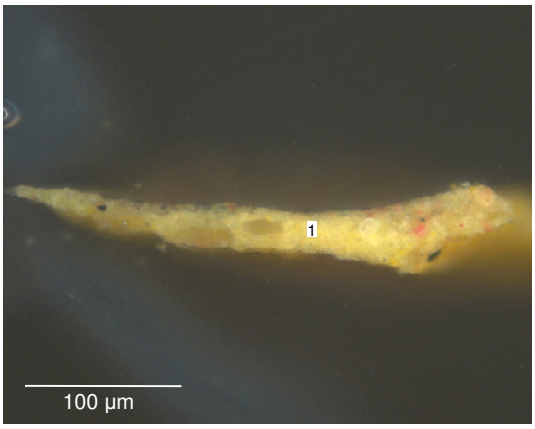

1 - yellow paint layer (max. thickness 54 µm)

Figure D103. Cross section of the sample **Q8** - yellow from the back of ***Senhora vestida de preto***, viewed under reflected light.

- Janela das persianas azuis

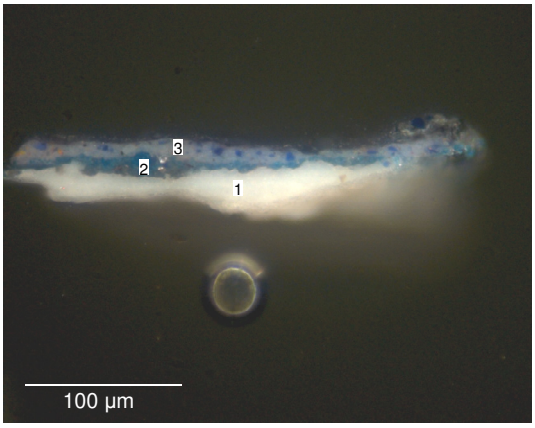

3 - blue paint layer (max. thickness 17 µm)
2 - blue paint layer (max. thickness 18 µm)
1 - white ground layer (max. thickness 31 µm)

Figure D104. Cross section of the sample **R1** - blue from the wall of ***Janela das persianas azuis***, viewed under reflected light.

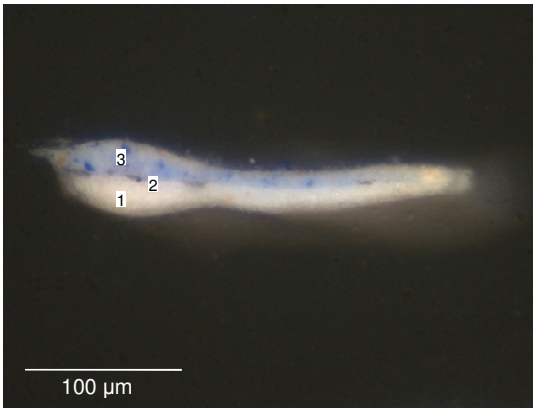

3 - white paint layer (max. thickness 26 µm)
2 - black paint layer (max. thickness 5 µm)
1 - white ground layer (max. thickness 31 µm)

Figure D105. Cross section of the sample **R2** - light blue from the wall of ***Janela das persianas azuis***, viewed under reflected light.

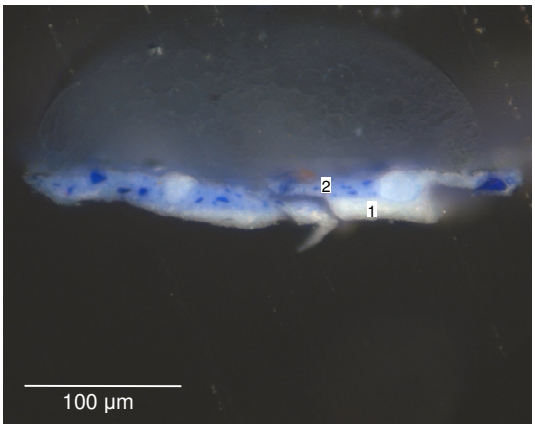

2 - blue paint layer (max. thickness 20 µm)
1 - white ground layer (max. thickness 18 µm)

Figure D106. Cross section of the sample **R3** - dark blue from the wall of ***Janela das persianas azuis***, viewed under reflected light.

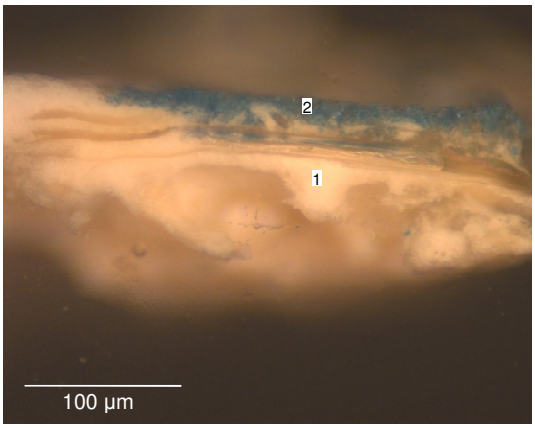

2 - blue paint layer (max. thickness 23 µm)
1 - white ground layer (max. thickness 87 µm)

Figure D107. Cross section of the sample **R4** - greenish from the wall of ***Janela das persianas azuis***, viewed under reflected light.

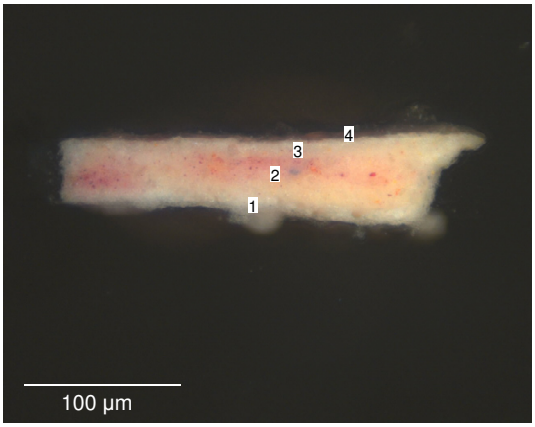

4 - varnish
3 - white paint layer (max. thickness 11 µm)
2 - beige paint layer (max. thickness 43 µm)
1 - white ground layer (max. thickness 12 µm)

Figure D108. Cross section of the sample **R5** - orange from the roof of ***Janela das persianas azuis***, viewed under reflected light.

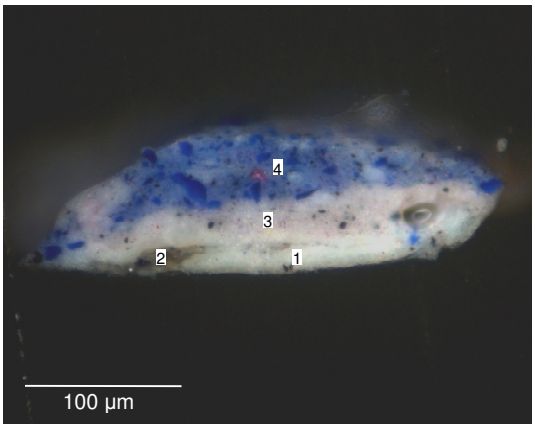

4 - blue paint layer (max. thickness 59 µm)
3 - pink paint layer (max. thickness 32 µm)
2 - organic layer (max. thickness 15 µm)
1 - white ground layer (max. thickness 19 µm)

Figure D109. Cross section of the sample **R6** - grey from the shadow of the clothes of ***Janela das persianas azuis***, viewed under reflected light.

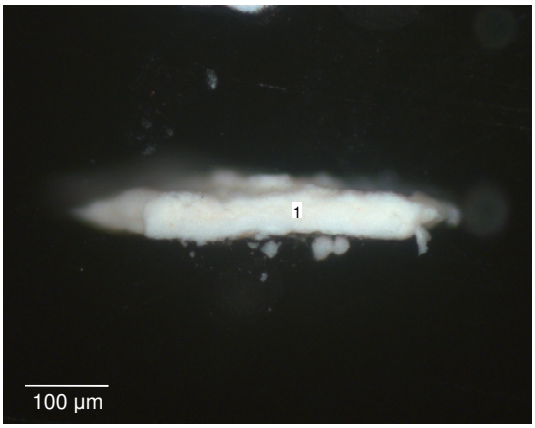

1 - white paint layer (max. thickness 64 µm)

Figure D110. Cross section of the sample **R7** - white from the clothes of ***Janela das persianas azuis***, viewed under reflected light.

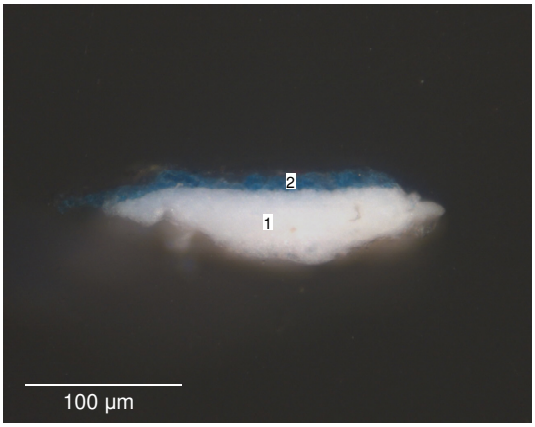

2 - blue paint layer (max. thickness 14 µm)
1 - white ground layer (max. thickness 56 µm)

Figure D111. Cross section of the sample **R8** - blue from the wall of ***Janela das persianas azuis***, viewed under reflected light.

- Mulher da água

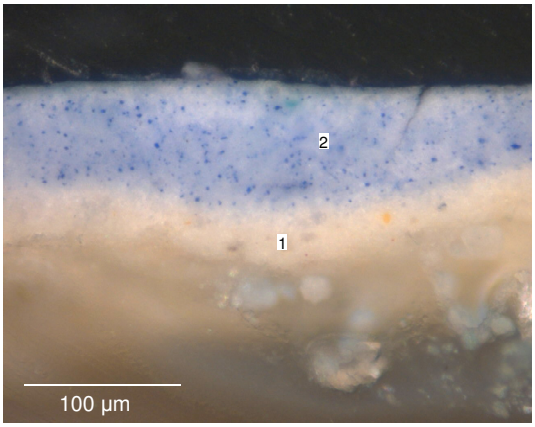

2 - blue paint layer (max. thickness 100 µm)
1 - white ground layer (max. thickness 39 µm)

Figure D112. Cross section of the sample **S1** - blue from the sky of ***Mulher da água***, viewed under reflected light.

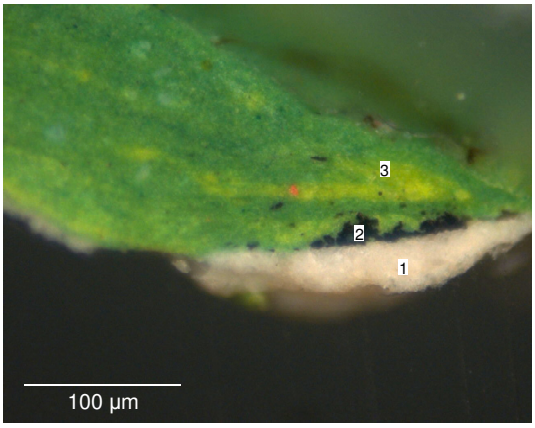

3 - green paint layer (max. thickness 182 µm)
2 - black paint layer (max. thickness 19 µm)
1 - white ground layer (max. thickness 35 µm)

Figure D113. Cross section of the sample **S2** - green from the bushes of ***Mulher da água***, viewed under reflected light.

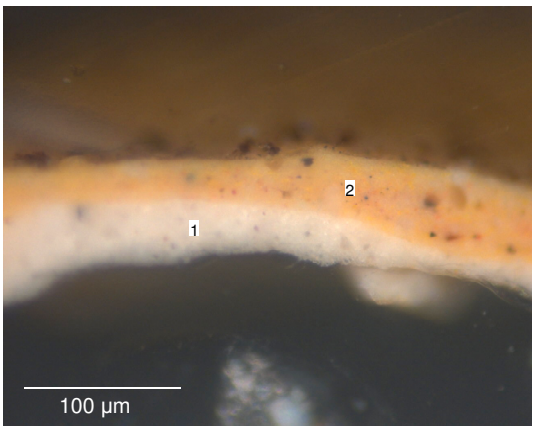

2 - beige paint layer (max. thickness 69 µm)
1 - white ground layer (max. thickness 48 µm)

Figure D114. Cross section of the sample **S3** - beige from the wall of ***Mulher da água***, viewed under reflected light.

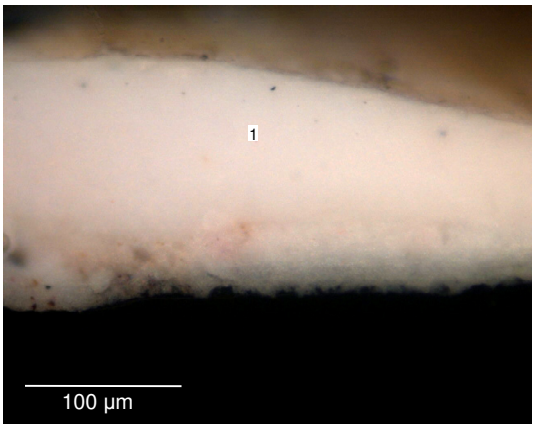

1 - white ground layer (max. thickness 190 µm)

Figure D115. Cross section of the sample **S4** - white from the kerchief of ***Mulher da água***, viewed under reflected light.

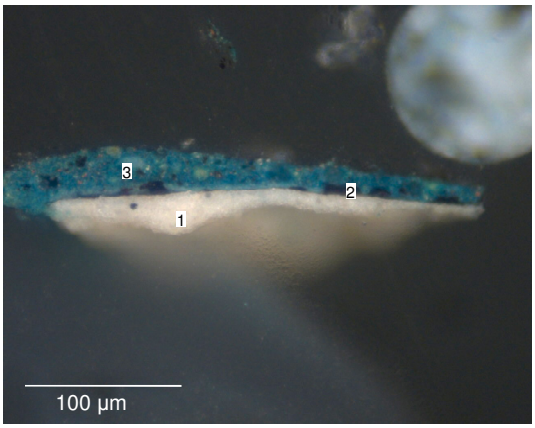

3 - blue paint layer (max. thickness 37 µm)
2 - black paint layer (max. thickness 6 µm)
1 - white ground layer (max. thickness 33 µm)

Figure D116. Cross section of the sample **S5** - blue from the blouse of ***Mulher da água***, viewed under reflected light.

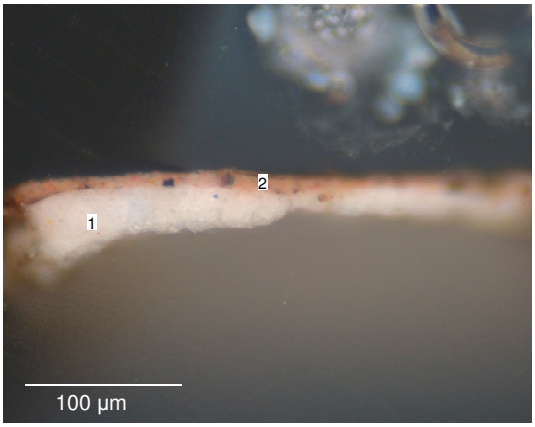

2 - orange paint layer (max. thickness 14 µm)
1 - white paint layer (max. thickness 45 µm)

Figure D117. Cross section of the sample **S6** - carnation from the hand of ***Mulher da água***, viewed under reflected light.

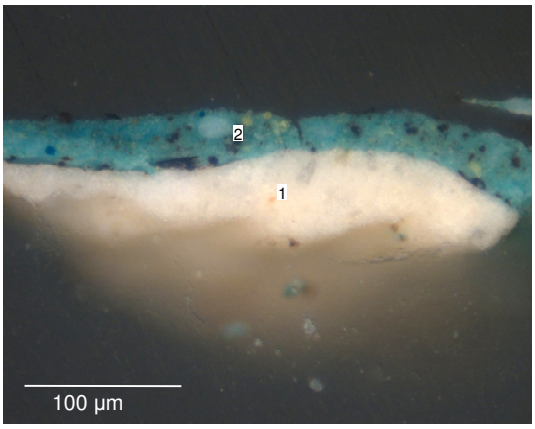

2 - blue paint layer (max. thickness 47 µm)
1 - white ground layer (max. thickness 74 µm)

Figure D118. Cross section of the sample **S7** - blue from the skirt of ***Mulher da água***, viewed under reflected light.

- Paisagem de Anacapri

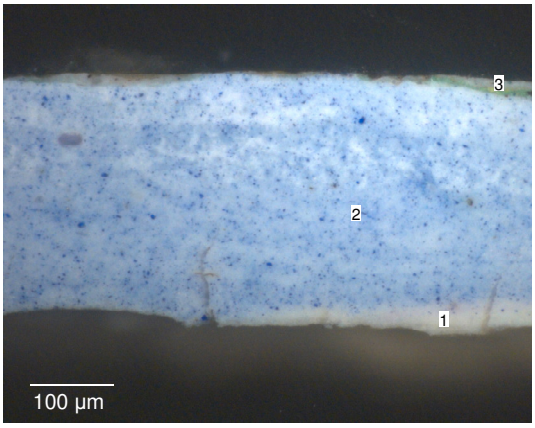

3 - green paint layer (max. thickness 8 µm)
2 - blue paint layer (max. thickness 358 µm)
1 - white paint layer (max. thickness 48 µm)

Figure D119. Cross section of the sample **T1** - blue from the sky of ***Paisagem de Anacapri***, viewed under reflected light.

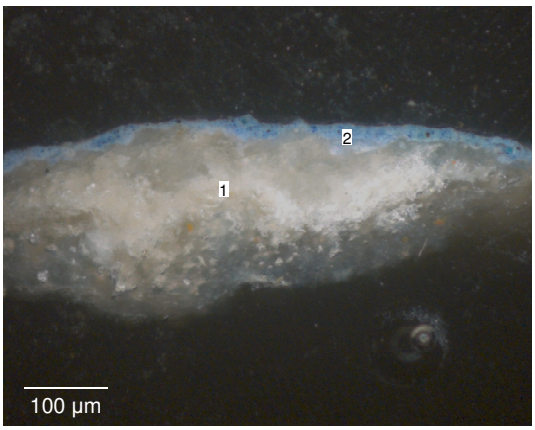

2 - blue paint layer (max. thickness 35 µm)
1 - white paint layer (max. thickness 280 µm)

Figure D120. Cross section of the sample **T2** - blue from the sea of ***Paisagem de Anacapri***, viewed under reflected light.

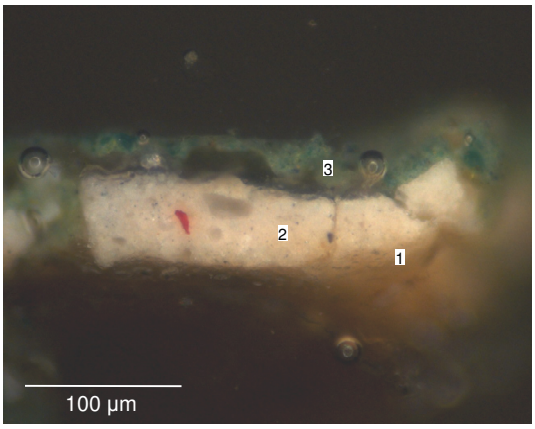

3 - green paint layer (max. thickness 27 µm)
2 - white ground layer (max. thickness 66 µm)
1 - size

Figure D121. Cross section of the sample **T3** - green from the trees of ***Paisagem de Anacapri***, viewed under reflected light.

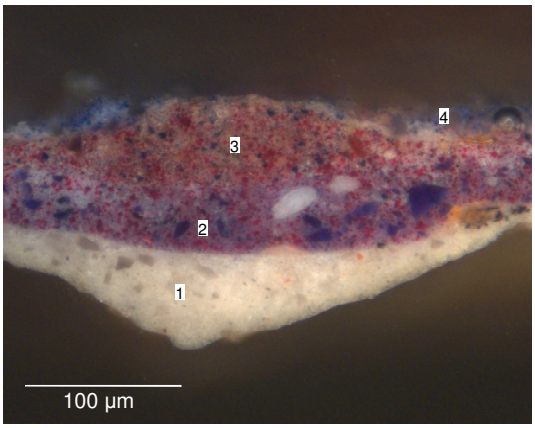

4 - blue paint layer (max. thickness 17 µm)
3 - brown paint layer (max. thickness 68 µm)
2 - purple paint layer (max. thickness 56 µm)
1 - white ground layer (max. thickness 76 µm)

Figure D122. Cross section of the sample **T4** - grey from the shadow on the ground of ***Paisagem de Anacapri***, viewed under reflected light.

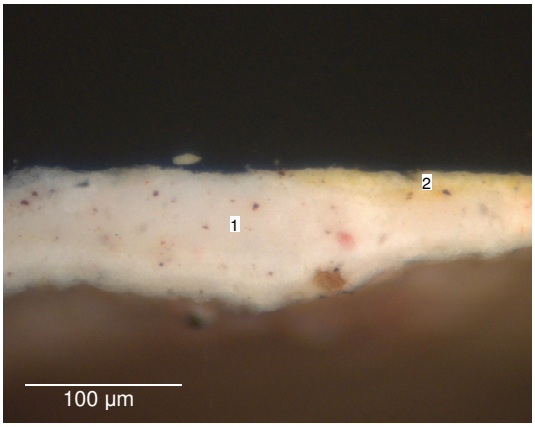

2 - yellow paint layer (max. thickness 23 µm)
1 - pink paint layer (max. thickness 96 µm)

Figure D123. Cross section of the sample **T5** - beige from the ground of ***Paisagem de Anacapri***, viewed under reflected light.

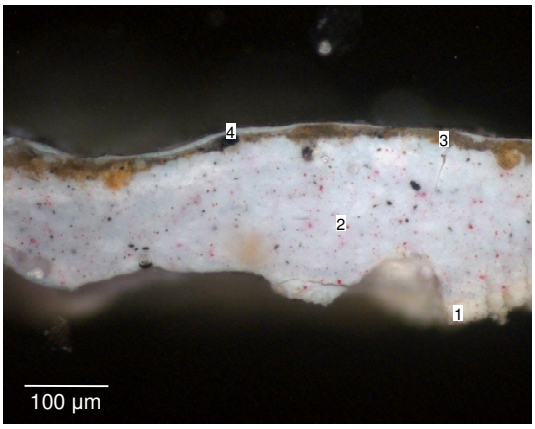

4 - grey paint layer (max. thickness 9 µm)
3 - brown layer (max. thickness 28 µm)
2 - grey paint layer (max. thickness 243 µm)
1 - white paint layer (max. thickness 31 µm)

Figure D124. Cross section of the sample **T6** - grey from the stone wall of ***Paisagem de Anacapri***, viewed under reflected light.

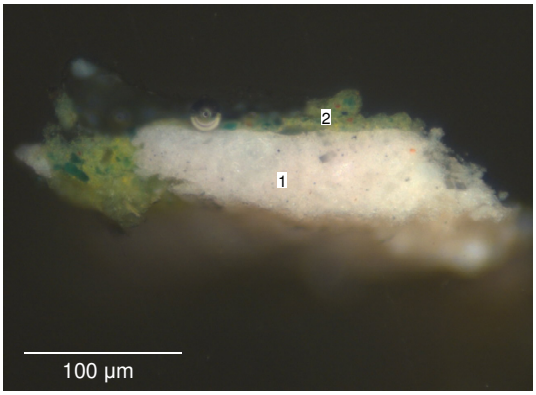

2 - green paint layer (max. thickness 32 µm)
1 - white ground layer (max. thickness 64 µm)

Figure D125. Cross section of the sample **T7** - green from the tree of ***Paisagem de Anacapri***, viewed under reflected light.

- Rapariga deitada no tronco de uma árvore

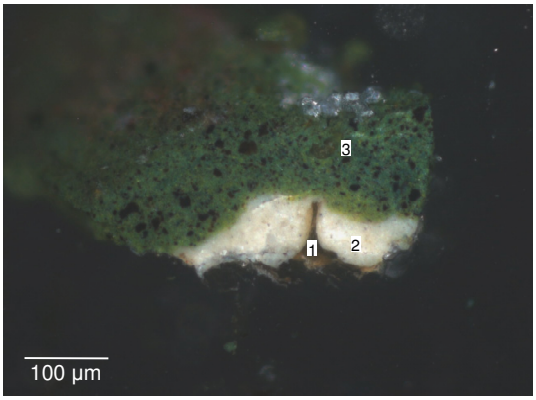

3 - green paint layer (max. thickness 167 µm)
2 - white paint layer (max. thickness 102 µm)
1 - size

Figure D126. Cross section of the sample **U1** - dark green from leafs of ***Rapariga deitada no tronco de uma árvore***, viewed under reflected light.

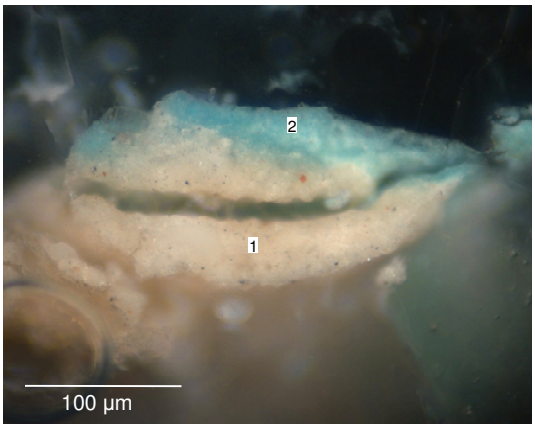

2 - blue paint layer (max. thickness 38 µm)
1 - white ground layer (max. thickness 47+42 µm)

Figure D127. Cross section of the sample **U2** - light blue of ***Rapariga deitada no tronco de uma árvore***, viewed under reflected light.

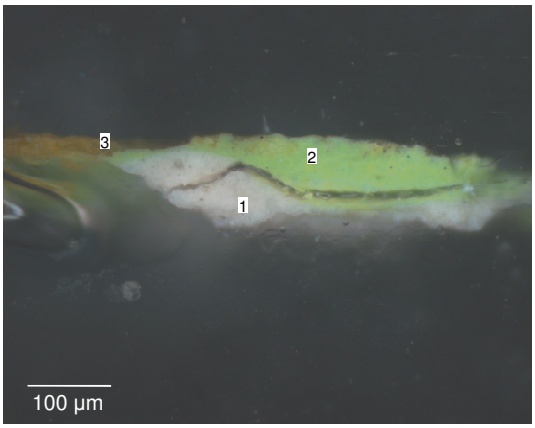

3 - varnish (max. thickness 23 µm)
2 - green paint layer (max. thickness 86+9 µm)
1 - white ground layer (max. thickness 86 µm)

Figure D128. Cross section of the sample **U3** - light green from leafs of ***Rapariga deitada no tronco de uma árvore***, viewed under reflected light.

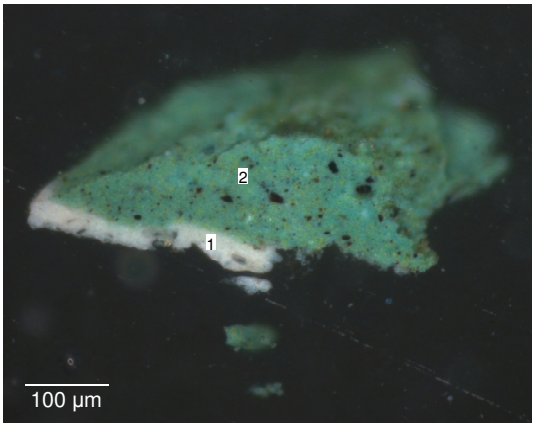

2 - green paint layer (max. thickness 169 µm)
1 - white ground layer (max. thickness 38 µm)

Figure D129. Cross section of the sample **U4** - green from leafs of ***Rapariga deitada no tronco de uma árvore***, viewed under reflected light.

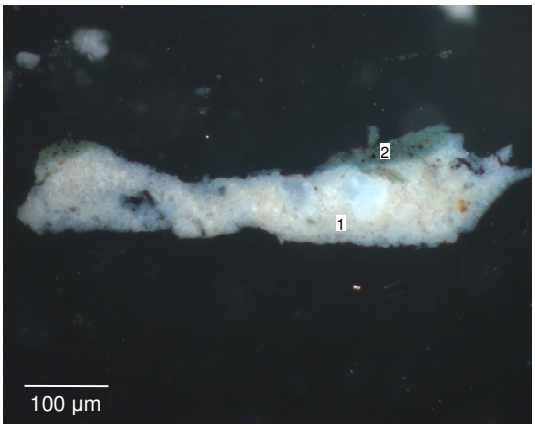

2 - grey paint layer (max. thickness 38 µm)
1 - white ground layer (max. thickness 115 µm)

Figure D130. Cross section of the sample **U5** - background grey of ***Rapariga deitada no tronco de uma árvore***, viewed under reflected light.

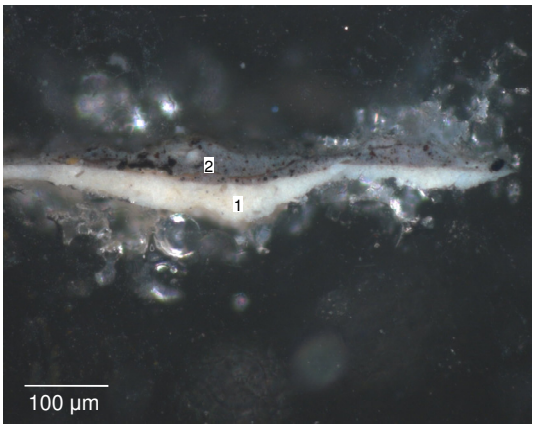

2 - grey paint layer (max. thickness 65 µm)
1 - white ground layer (max. thickness 56 µm)

Figure D131. Cross section of the sample **U6** - background grey of ***Rapariga deitada no tronco de uma árvore***, viewed under reflected light.

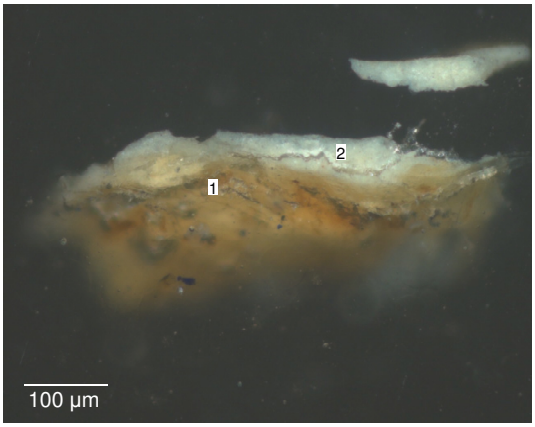

2 - white ground layer (max. thickness 62 µm)
1 - size/canvas

Figure D132. Cross section of the sample **U7** - ground from the back of ***Rapariga deitada no tronco de uma árvore***, viewed under reflected light.

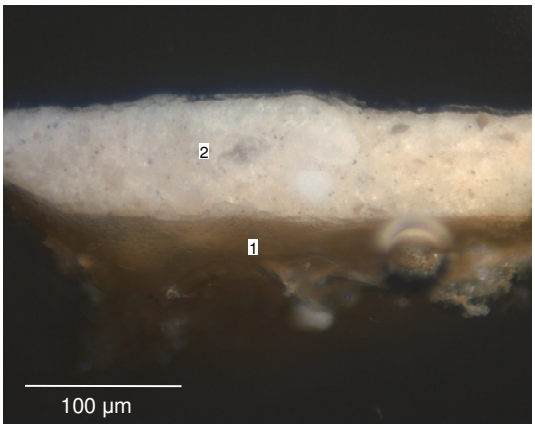

2 - white ground layer (max. thickness 98 µm)
1 - size

Figure D133. Cross section of the sample **U8** - ground layer from the back of ***Rapariga deitada no tronco de uma árvore***, viewed under reflected light.

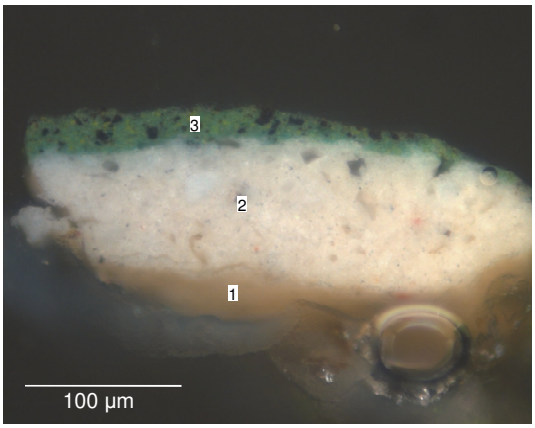

3 - green paint layer (max. thickness 24 µm)
2 - white ground layer (max. thickness 107 µm)
1 - size

Figure D134. Cross section of the sample **U9** - green from leafs of ***Rapariga deitada no tronco de uma árvore***, viewed under reflected light.

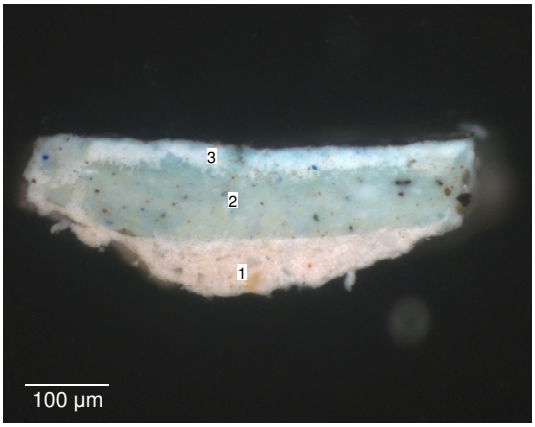

3 - white paint layer (max. thickness 35 µm)
2 - blue paint layer (max. thickness 123 µm)
1 - white ground layer (max. thickness 82 µm)

Figure D135. Cross section of the sample **U10** - bluish from the tree bench of ***Rapariga deitada no tronco de uma árvore***, viewed under reflected light.

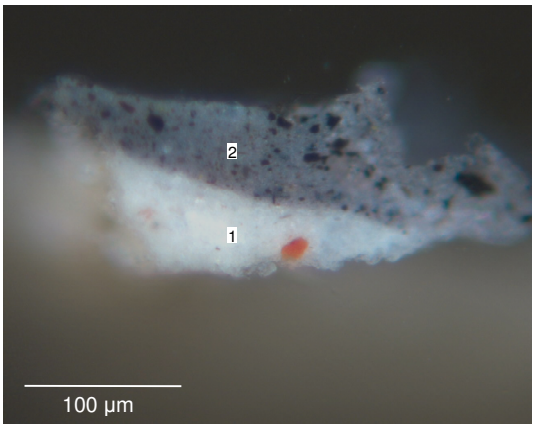

2 - grey paint layer (max. thickness 58 µm)
1 - white ground layer (max. thickness 52 µm)

Figure D136. Cross section of the sample **U11** - grey from the tree bench of ***Rapariga deitada no tronco de uma árvore***, viewed under reflected light.

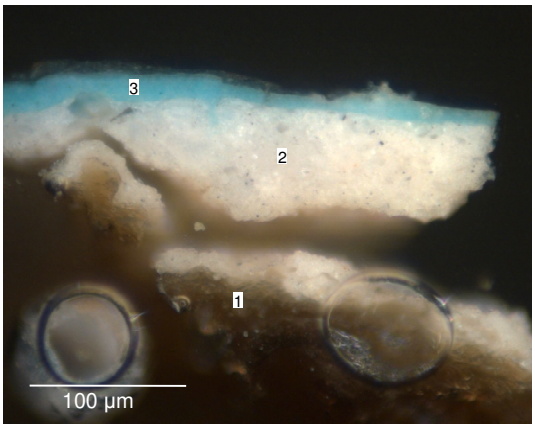

3 - blue paint layer (max. thickness 27 µm)
2 - white ground layer (max. thickness 88 µm)
1 - size

Figure D137. Cross section of the sample **U12** - light blue of ***Rapariga deitada no tronco de uma árvore***, viewed under reflected light.

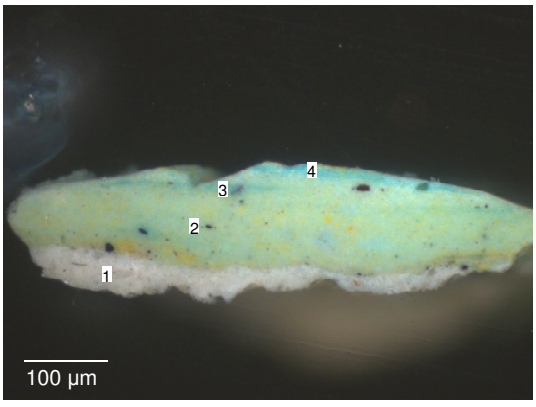

4 - blue paint layer (max. thickness 17 µm)
3 - green paint layer (max. thickness 10 µm)
2 - green paint layer (max. thickness 114 µm)
1 - white paint layer (max. thickness 64 µm)

Figure D138. Cross section of the sample **U13** - light green from leafs of ***Rapariga deitada no tronco de uma árvore***, viewed under reflected light.

- Cais de Barcelona

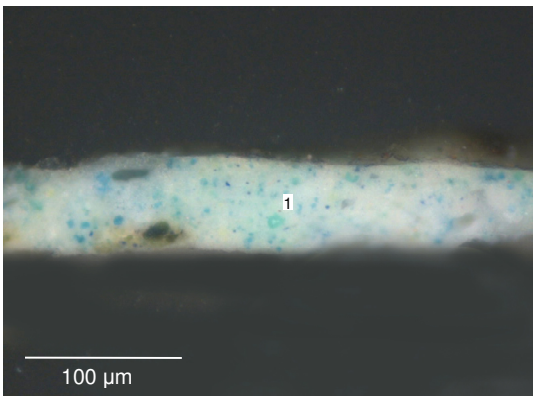

1 - blue paint layer (max. thickness 72 µm)

Figure D139. Cross section of the sample **V1** - blue from the sea of ***Cais de Barcelona***, viewed under reflected light.

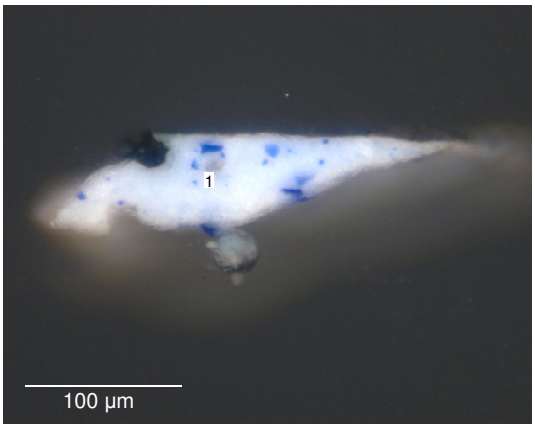

1 - blue paint layer (max. thickness 65 µm)

Figure D140. Cross section of the sample **V2** - blue from the sky of ***Cais de Barcelona***, viewed under reflected light.

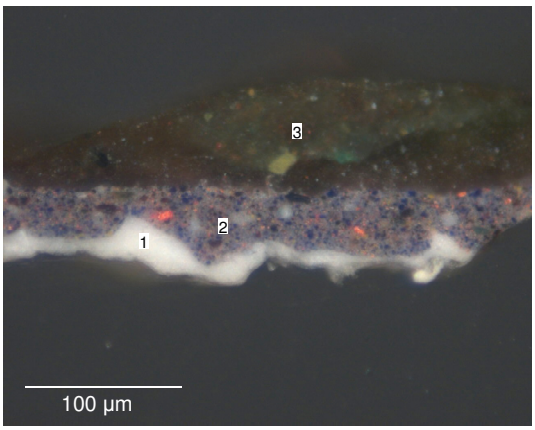

3 - green paint layer (max. thickness 89 µm)
2 - blue paint layer (max. thickness 52 µm)
1 - white ground layer (max. thickness 33 µm)

Figure D141. Cross section of the sample **V3** - black from the boat of ***Cais de Barcelona***, viewed under reflected light.

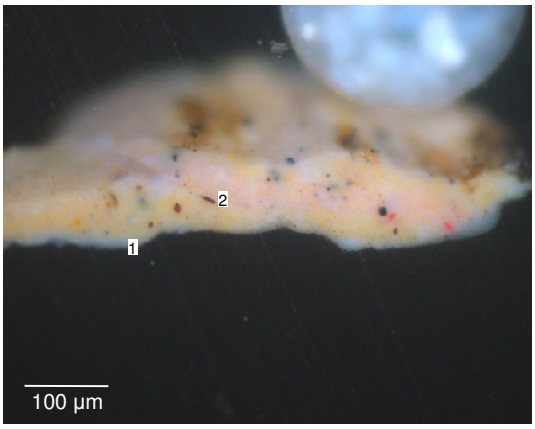

2 - beige paint layer (max. thickness 117 µm)
1 - white ground layer (max. thickness 19 µm)

Figure D142. Cross section of the sample **V4** - beige from the ground of ***Cais de Barcelona***, viewed under reflected light.

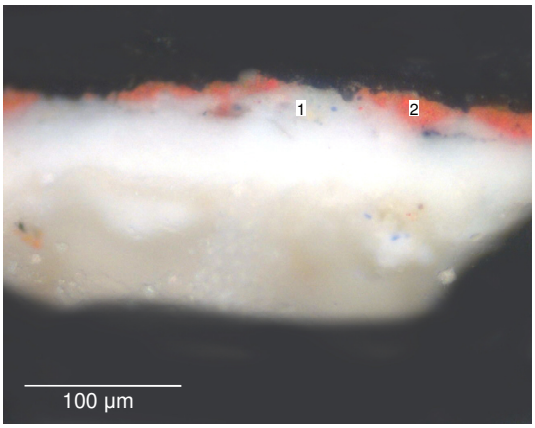

2 - red paint layer (max. thickness 22 µm)
1 - white paint layer (max. thickness 78 µm)

Figure D143. Cross section of the sample **V5** - brown from the crane of ***Cais de Barcelona***, viewed under reflected light.

- Flores Campestres

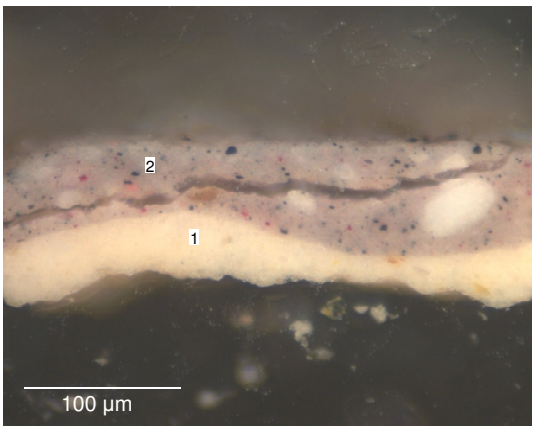

2 - grey paint layer (max. thickness 82 µm)
1 - white ground layer (max. thickness 52 µm)

Figure D144. Cross section of the sample **W1** - grey from the back of ***Flores Campestres***, viewed under reflected light.

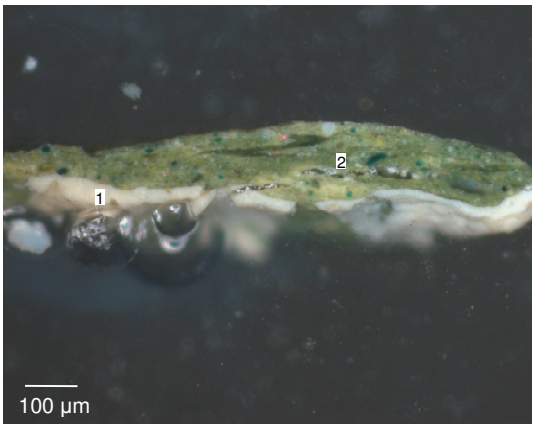

2 - green paint layer (max. thickness 192 µm)
1 - white ground layer (max. thickness 28 µm)

Figure D145. Cross section of the sample **W2** - green from the flowers of ***Flores Campestres***, viewed under reflected light.

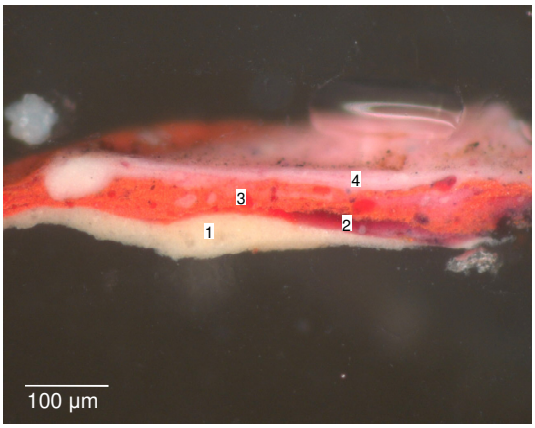

4 - pink paint layer (max. thickness 27 µm)
3 - red paint layer (max. thickness 60 µm)
2 - red paint layer (max. thickness 22 µm)
1 - white ground layer (max. thickness 63 µm)

Figure D146. Cross section of the sample **W3** - red from the flower of ***Flores Campestres***, viewed under reflected light.

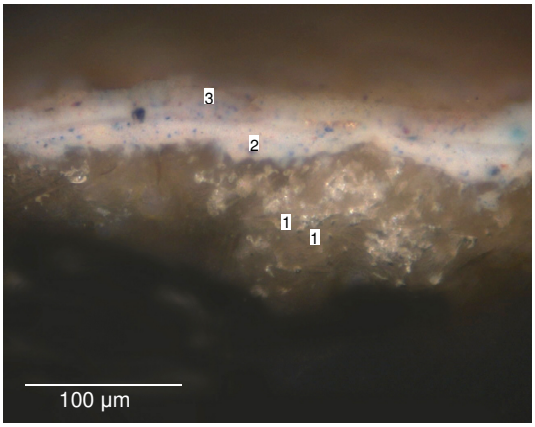

3 - grey paint layer (max. thickness 26 µm)
2 - grey paint layer (max. thickness 23 µm)
1 - brownish layer (max. thickness 103 µm)

Figure D147. Cross section of the sample **W4** - grey from the back of ***Flores Campestres***, viewed under reflected light.

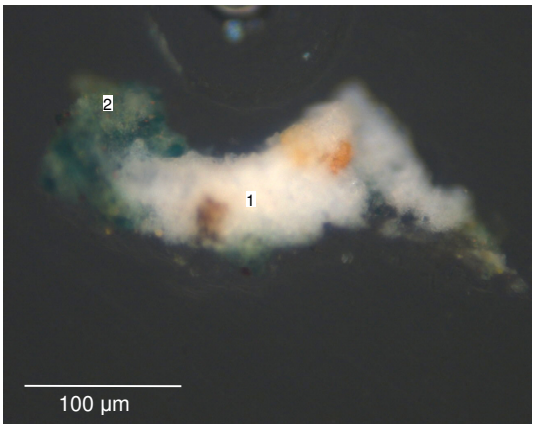

2 - green paint layer (max. thickness 46 µm)
1 - white ground layer (max. thickness 80 µm)

Figure D148. Cross section of the sample **W5** - green from the flowers of ***Flores Campestres***, viewed under reflected light.

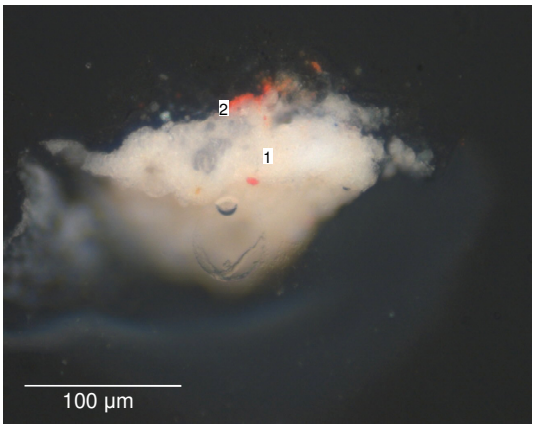

2 - red paint layer (max. thickness 4 µm)
1 - white ground layer (max. thickness 58 µm)

Figure D149. Cross section of the sample **W6** - red from the flower of ***Flores Campestres***, viewed under reflected light.

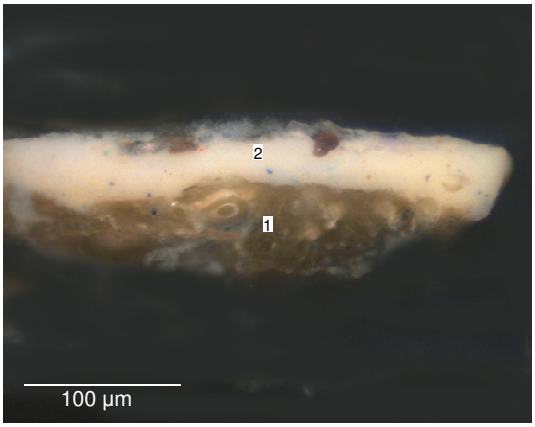

2 - white paint layer (max. thickness 50 µm)
1 - brownish layer (max. thickness 47 µm)

Figure B150. Cross section of the sample **W7** - light grey from the back of ***Flores Campestres***, viewed under reflected light.

Appendix E

Backscattered-electron image of the samples

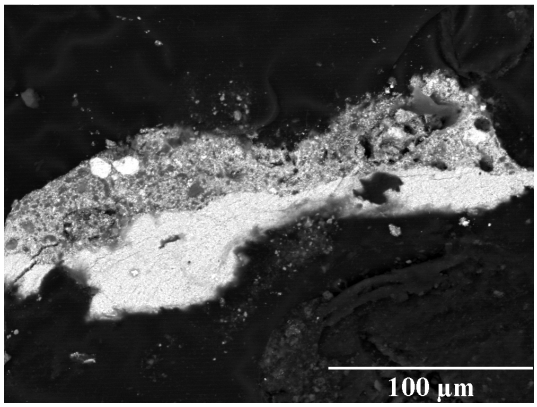

Figure E1. Backscattered-electron image of sample **A3** (***Casa rústica de Campanhã***).

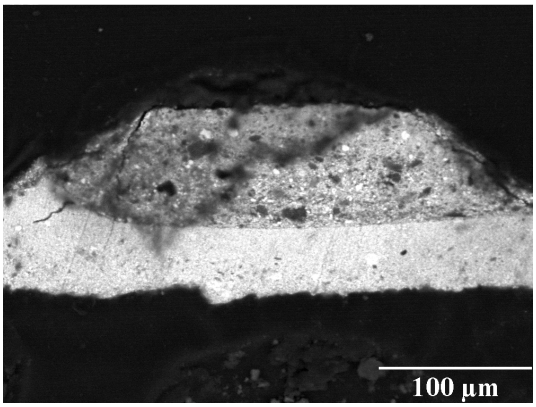

Figure E2. Backscattered-electron image of sample **B3** (***O mendigo Lapita***).

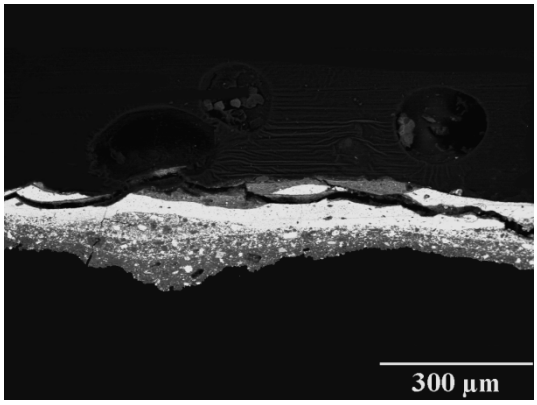

Figure E3. Backscattered-electron image of sample **C4** (***Paisagem - Abertura da Rua Alexandre Herculano***).

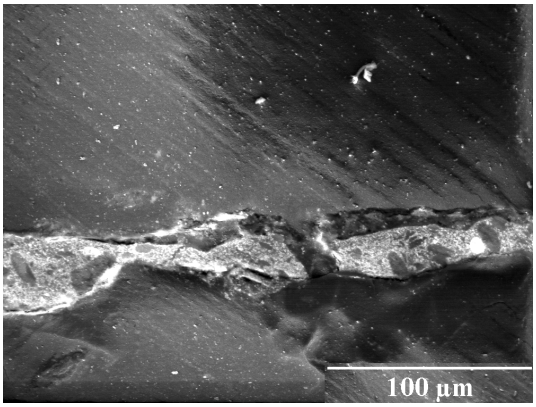

Figure E4. Backscattered-electron image of sample **D2** (***Jardim de Luxemburgo (estudo)***).

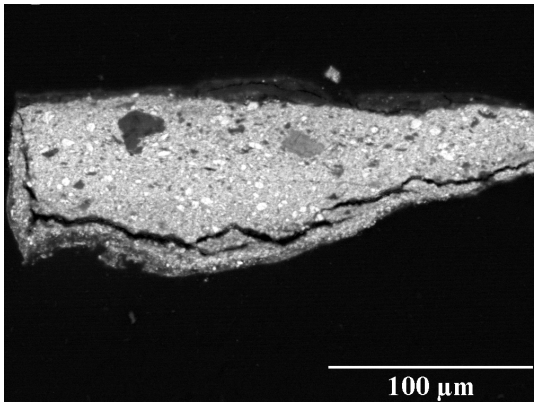

Figure E5. Backscattered-electron image of sample **E1** (***Aldeia St. Sauves***).

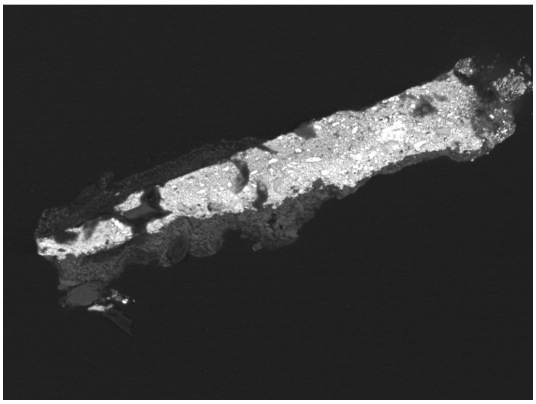

Figure E6. Backscattered-electron image of sample **F1** (***Paisagem St. Sauves***).

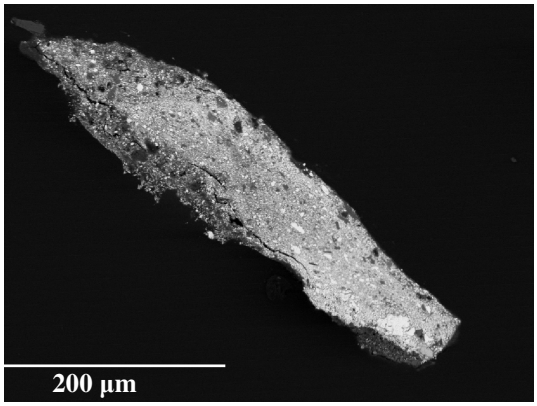

Figure E7. Backscattered-electron image of sample **F5** (***Paisagem St. Sauves***).

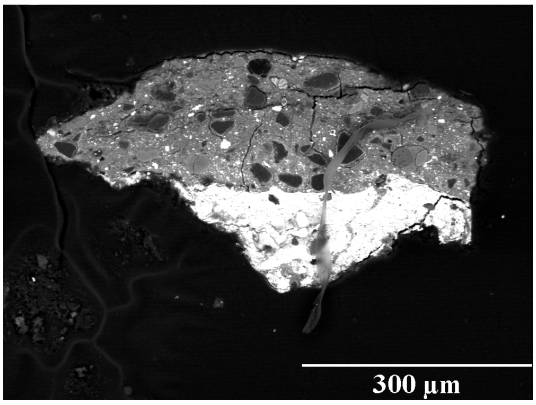

Figure E8. Backscattered-electron image of sample **F6** (***Paisagem St. Sauves***).

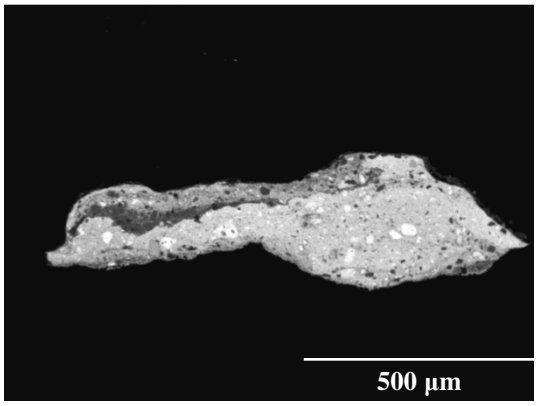

Figure E9. Backscattered-electron image of sample **H1** (***Casas brancas de Capri***).

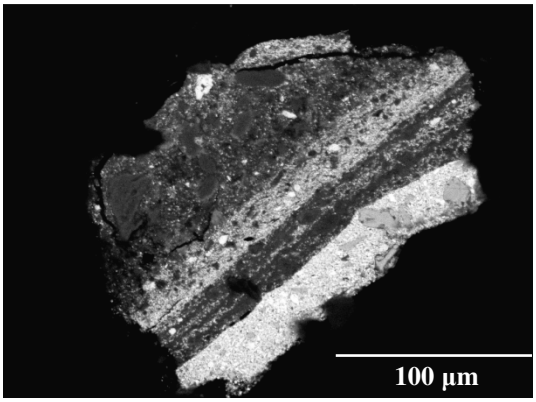

Figure E10. Backscattered-electron image of sample **H5** (***Casas brancas de Capri***).

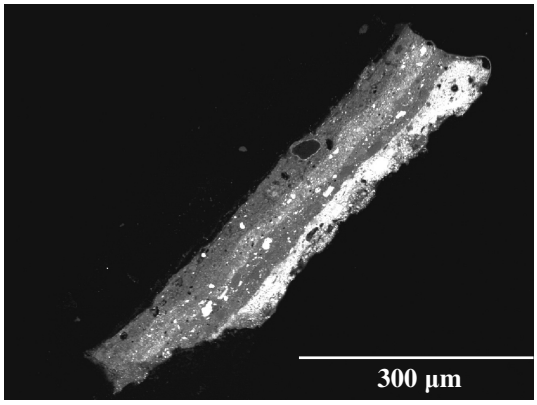

Figure E11. Backscattered-electron image of sample **I1** (***Cecília***)

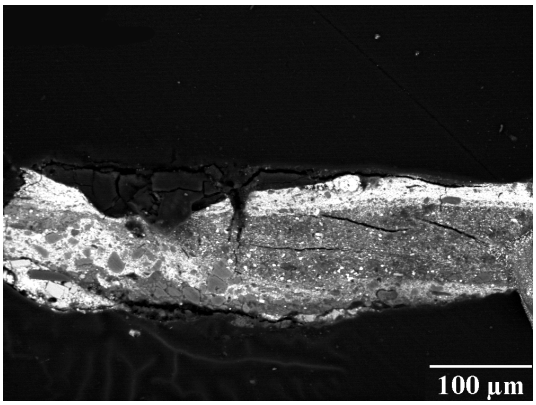

Figure E12. Backscattered-electron image of sample **I7** (***Cecília***)

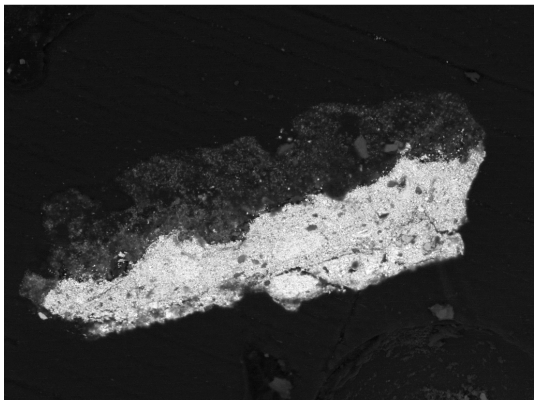

Figure E13. Backscattered-electron image of sample **J2** (***Escadas de um pardieiro - Roma***).

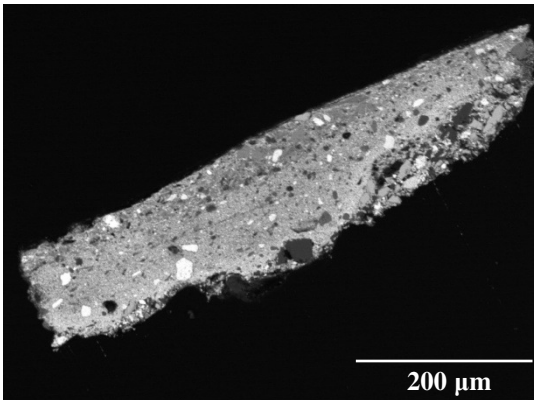

Figure E14. Backscattered-electron image of sample **K7** (***Esperando o Sucesso***).

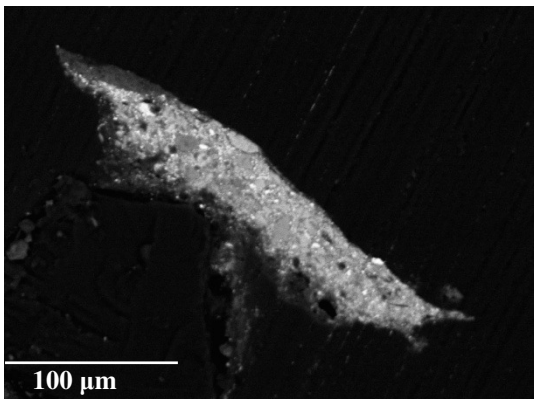

Figure E15. Backscattered-electron image of sample **L3** (***Fachada de casa soterrada - Roma***).

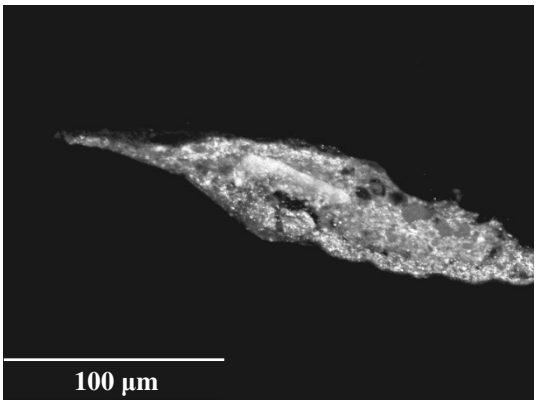

Figure E16. Backscattered-electron image of sample **M1** (***Miragem de Nápoles***)

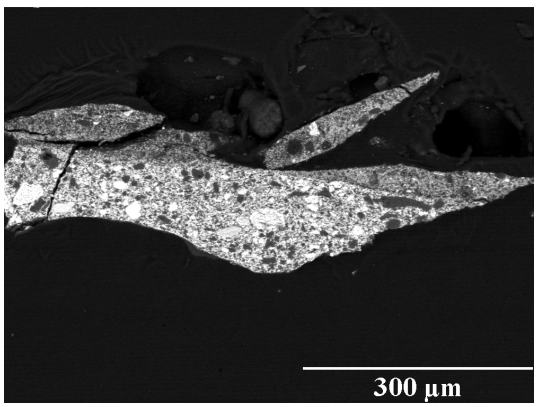

Figure E17. Backscattered-electron image of sample **N3** (***Portão***).

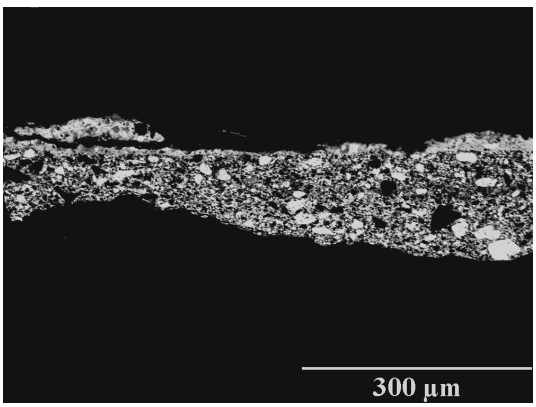

Figure E18. Backscattered-electron image of sample **O1** (***Rapariga de Anacapri***).

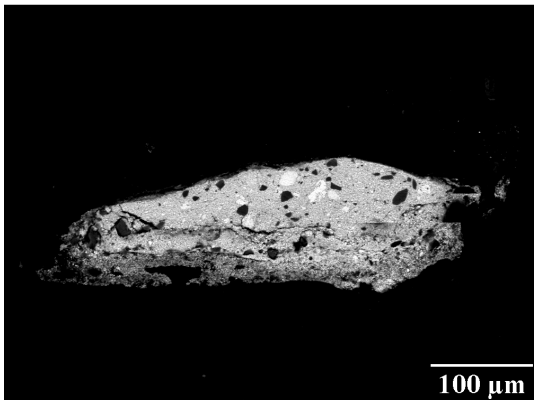

Figure E19. Backscattered-electron image of sample **P1** (***Rua de Roma***).

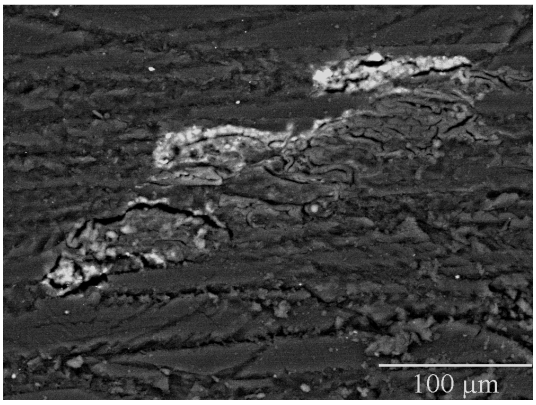

Figure E20. Backscattered-electron image of sample **Q4** (***Senhora vestida de preto***).

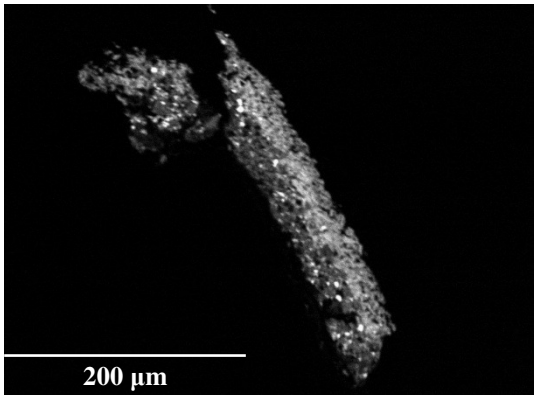

Figure E21. Backscattered-electron image of sample **Q5** (***Senhora vestida de preto***).

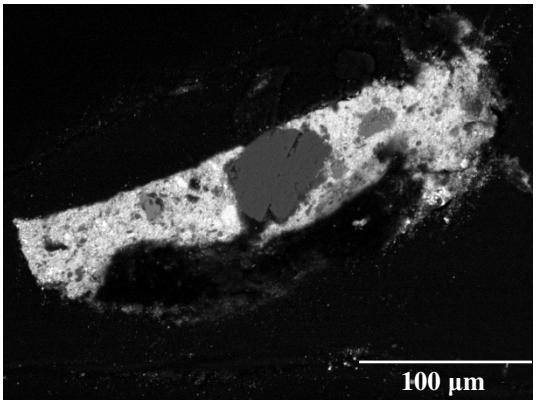

Figure E22. Backscattered-electron image of sample **Q6** (***Senhora vestida de preto***).

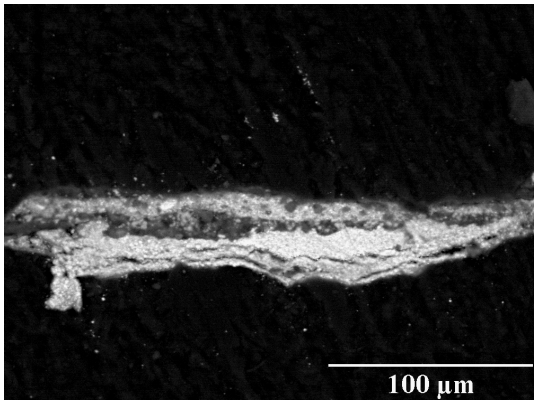

Figure E23. Backscattered-electron image of sample **R1** (***Janela das persianas azuis***).

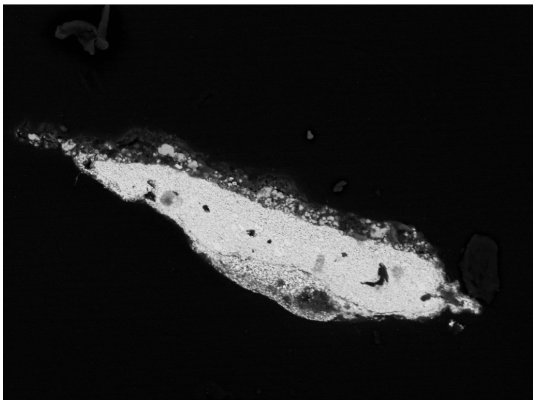

Figure E24. Backscattered-electron image of sample **R8** (***Janela das persianas azuis***).

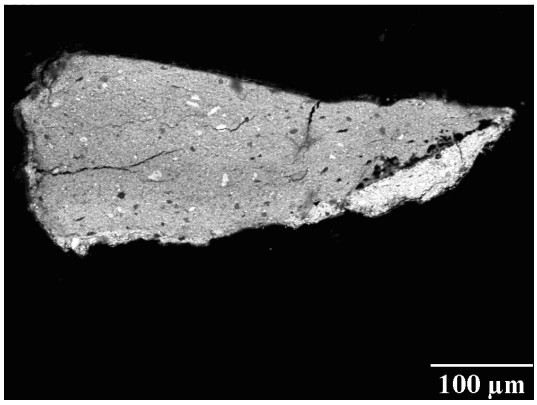

Figure E25. Backscattered-electron image of sample **S2** (***Mulher da água*)**.

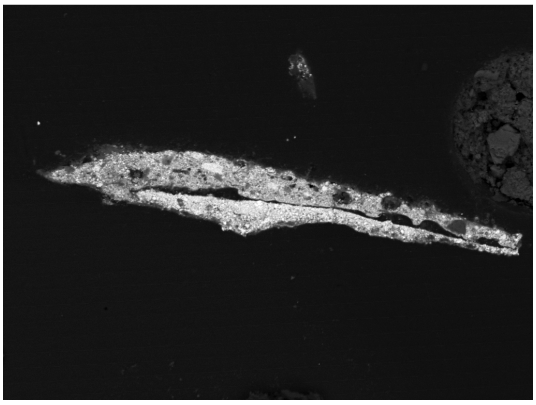

Figure E26. Backscattered-electron image of sample **S5** (**Mulher da água)**.

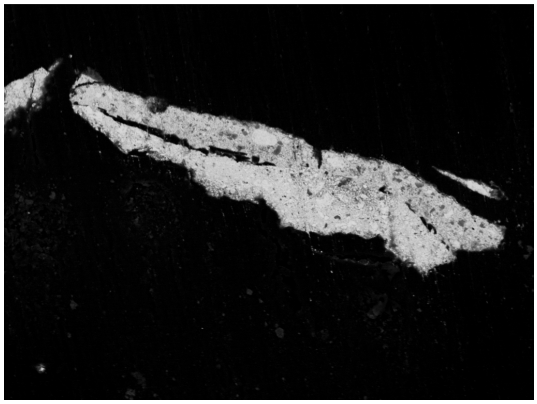

Figure E27. Backscattered-electron image of sample **S7** (***Mulher da água*)**.

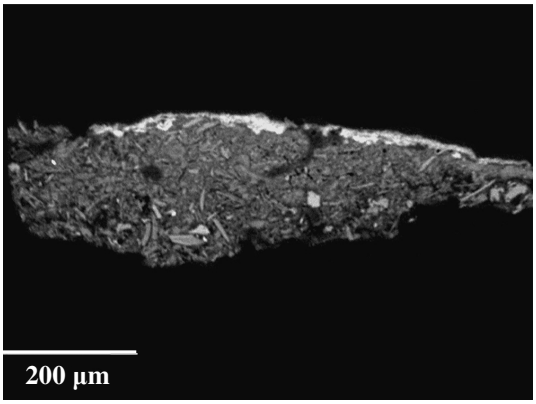

Figure E28. Backscattered-electron image of sample **T2** (***Paisagem de Anacapri*)**.

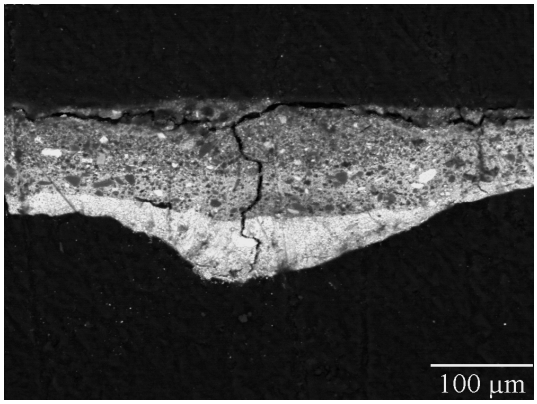

Figure E29. Backscattered-electron image of sample **T4** (***Paisagem de Anacapri*)**.

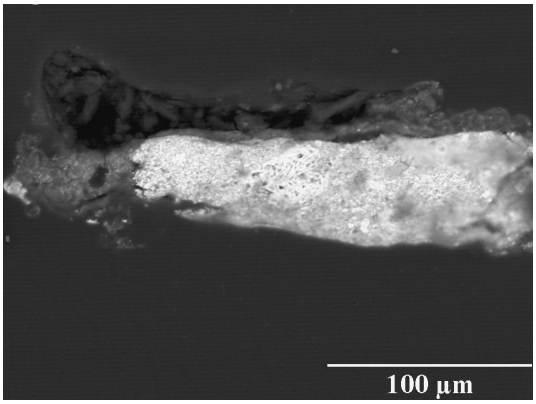

Figure E30. Backscattered-electron image of sample **T7** (***Paisagem de Anacapri*)**.

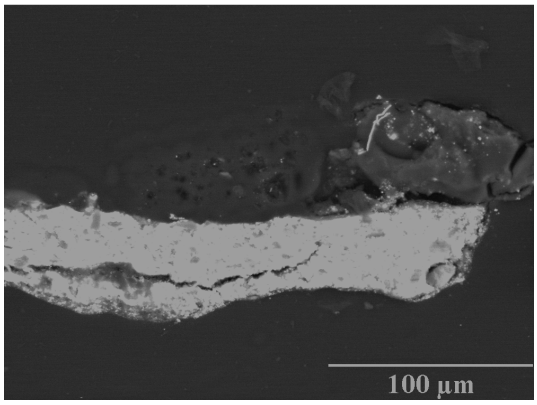

Figure E31. Backscattered-electron image of sample **V3** (***Cais de Barcelona***).

Appendix F

Samples viewed under ultraviolet light

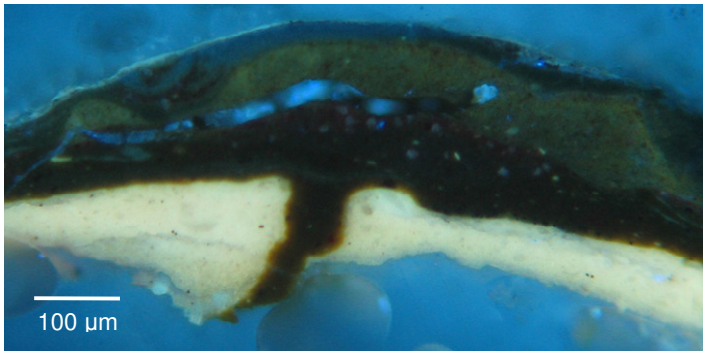

Figure F1. Cross section of the sample **C2** - green from the trees of ***Paisagem - Abertura da Rua Alexandre Herculano***, viewed under UV light (A cube).

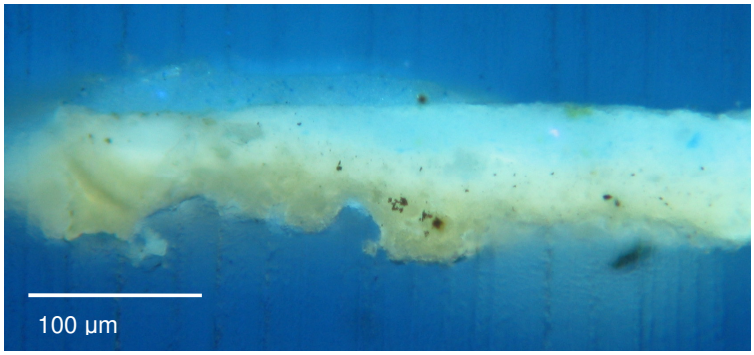

Figure F2. Cross section of the sample **F1** - blue from the sky of ***Paisagem St. Sauves***, viewed under UV light (A cube).

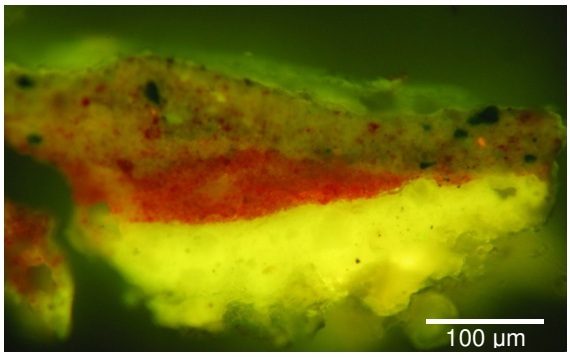

Figure F3. Cross section of the sample **F4** - green from the ground of ***Paisagem St. Sauves***, viewed under UV light (I 2/3 cube).

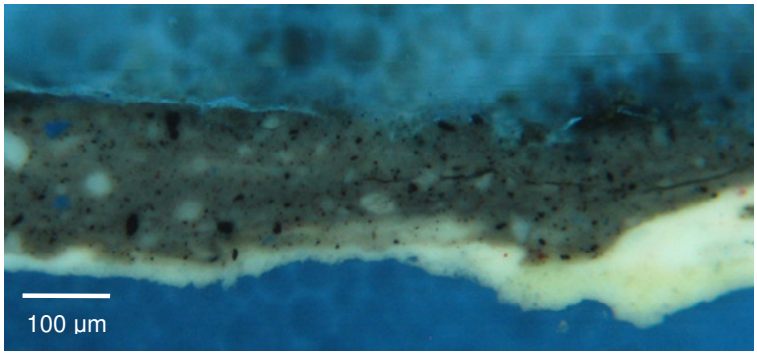

Figure F4. Cross section of the sample **G3** - grey from the leaf of ***Cansada (Cachopa de Capri)***, viewed under UV light (A cube).

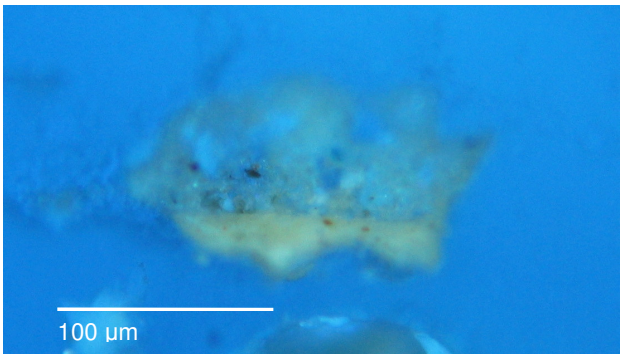

Figure F5. Cross section of the sample **J2** - beige from the ground of ***Escadas de um pardieiro - Roma***, viewed under UV light (A cube).

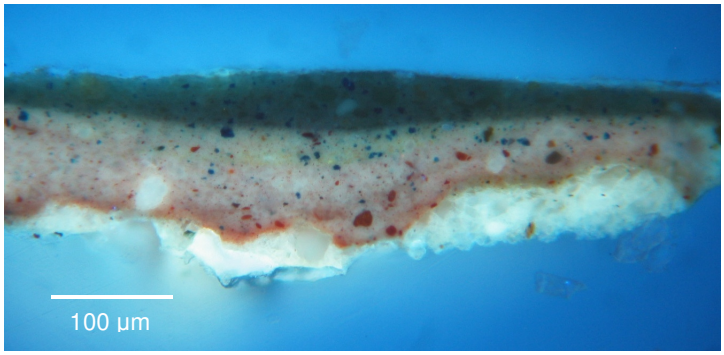

Figure F6. Cross section of the sample **K7** - green from the ground of ***Esperando o Sucesso***, viewed under UV light (A cube).

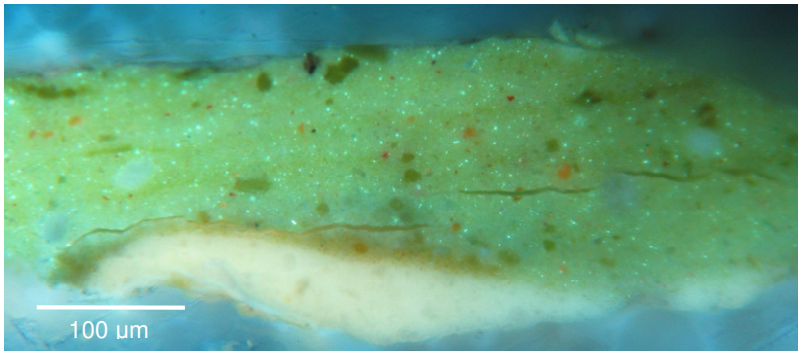

Figure F7. Cross section of the sample **N5** - green from the ground of ***Portão***, viewed under UV light (A cube).

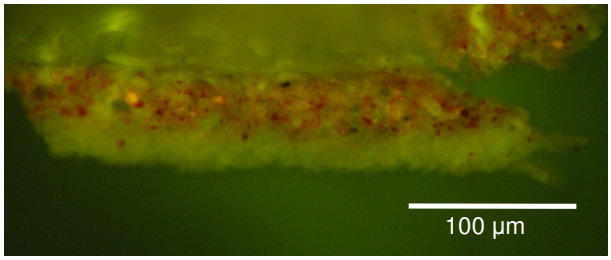

Figure F8. Cross section of the sample **Q5** - brown from the chair of ***Senhora vestida de preto***, viewed under UV light (I 2/3 cube).

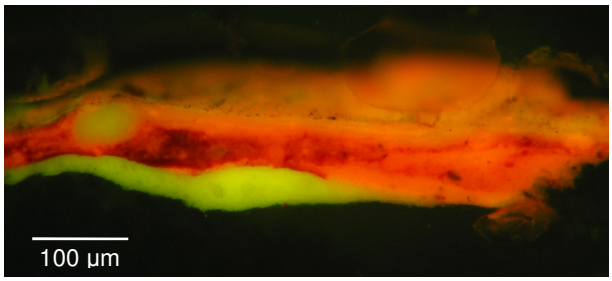

Figure F9. Cross section of the sample **W3** - red from the flower of ***Flores Campetres***, viewed under UV light (I 2/3 cube).